



Cimbri, Davide (2023) *Accurate quantum transport modelling and epitaxial structure design of high-speed and high-power In<sub>0.53</sub>Ga<sub>0.47</sub>As/AlAs double-barrier resonant tunnelling diodes for 300-GHz oscillator sources*. PhD thesis.

<https://theses.gla.ac.uk/83642/>

Copyright and moral rights for this work are retained by the author

A copy can be downloaded for personal non-commercial research or study, without prior permission or charge

This work cannot be reproduced or quoted extensively from without first obtaining permission in writing from the author

The content must not be changed in any way or sold commercially in any format or medium without the formal permission of the author

When referring to this work, full bibliographic details including the author, title, awarding institution and date of the thesis must be given

Enlighten: Theses

<https://theses.gla.ac.uk/>  
[research-enlighten@glasgow.ac.uk](mailto:research-enlighten@glasgow.ac.uk)

# Accurate Quantum Transport Modelling and Epitaxial Structure Design of High-Speed and High-Power $\text{In}_{0.53}\text{Ga}_{0.47}\text{As}/\text{AlAs}$ Double-Barrier Resonant Tunnelling Diodes for 300-GHz Oscillator Sources



Candidate: **Daide Cimbri** 

A dissertation submitted in fulfilment of the requirements  
for the degree of Doctor of Philosophy (PhD)  
in Electronics and Electrical Engineering

Division of Electronics and Nanoscale Engineering  
James Watt School of Engineering  
College of Science and Engineering  
University of Glasgow, United Kingdom

February 2023

© Davide Cimbri, 2023

# Declaration of originality and copyright

Unless otherwise and explicitly acknowledged and/or referenced (for instance, this includes some of the Figures reported in Chapters 1 and 2), the whole content of this dissertation, including its drafting, are the original and sole work of the author. All the results presented in this dissertation were achieved, peer-reviewed, and published during the PhD programme, i.e., prior to its submission. Moreover, no portion of this dissertation has been submitted by the author in support of any application for any degree or qualification at the University of Glasgow, or at any other university or institute of learning. Furthermore, the views expressed in this work are those of the author, and not necessarily those of the University of Glasgow.

Attention is drawn to the fact that copyright of this dissertation, apart from the aforementioned acknowledged/referenced third party content, rests with the author. This copy has been supplied on condition that anyone who consults it is understood to recognise that no content belonging to it, or information derived from it, may be used and/or published without prior written and explicit consent of the author. Acknowledgment is permitted via proper referencing.

The author declares that this dissertation has been produced in accordance with the University of Glasgow's Code of Good Practice in Research. This work was conducted as part of TeraApps, Doctoral Training Network in Terahertz Technologies for Imaging, Radar, and Communication Applications, and received funding from the European Union's Horizon 2020 research and innovation program under the Marie Skłodowska-Curie Innovative Training Network (ITN) grant agreement no. 765426.

# Acknowledgements

Pursuing a PhD is like embarking on a journey, and when this reaches its end, final thoughts go to travelling companions and the people met during the years, with whom the whole PhD adventure has been experienced and shared.

My profound gratitude goes, first of all, to Prof. Edward Wasige, who offered me the chance to join his group at the University of Glasgow and undertake research on the terahertz (THz) resonant tunnelling diode (RTD) (a device which keeps fascinating me after four and a half years of hard study and intense research activities), gave me the possibility to grow scientifically and professionally, supervised and guided me in my research and throughout the whole PhD programme, and patiently helped and supported me during the difficult and challenging time caused by the COVID-19 pandemic.

Second, I would like to thank all my colleagues at the University of Glasgow for the support received during these years of hard work. In particular, Dr. Jue Wang, Dr. Abdullah Al-Khalidi, Dr. Andrei Cornescu (now at fitbit, Google), Dr. Qusay Raghieb Ali Al-Taai, Dr. Maira Elksne, Dr. Eugenio Di Gaetano, and Dr. Francesco Mirando (Kelvin Nanotechnology) for the precious advices received during clean-room microfabrication; Dr. Afesomah Ofiare for helping me with S-parameters measurements and electromagnetic simulations in Ansys HFSS; and Dr. Razvan Morariu (now at Microchip Technology) for his help with RTD small-signal equivalent circuit modelling in ADS. Moreover, I would like to thank Mr. Aniket Dhongde and Mr. Kaivan Karami for the nice time spent together in the James Watt Nanofabrication Centre (JWNC) during the past years. Special thanks go to Prof. Richard Hogg for the interesting chats on RTD physics and for a collaboration on RTD wafer characterisation, which has led to a peer-reviewed co-authored journal paper.

Third, I would like to thank all the other early stage researchers (ESR), supervisors, partner organisations, and staff members of TeraApps for their contribute to the project and for the invaluable role they had in helping me becoming a researcher, inspiring me and conveying their knowledge and experience, as well as for the great time spent together during meetings, summer schools, and conferences. In particular, Michele and Thomas, with whom I shared part of my life

here in Glasgow, Simone (University of Duisburg-Essen), for all our discussions about science, engineering, and life, and Matteo, for the long conversations on quantum physics in RTDs, all of whom have become very dear friends before being colleagues; Zoltan (TU Wien) and Saif (University of Lisbon), for the advices with RTD modelling and simulations; and Robin (Keysight Technologies), Mahdi (Scuola Normale Superiore), and Sebastian (University of Montpellier) for the great time together during business trips.

Moreover, I would like to thank Prof. Nils Weimann (University of Duisburg-Essen) for his help with mask design; Dr. Werner Prost (University of Duisburg-Essen) for the enlightening discussions on RTD technology; Dr. Fabian Hartmann (University of Würzburg) for growing some of the RTD wafer structures reported in this work; Prof. José Figueiredo (University of Lisbon) for the frightful conversations on RTDs; and Prof. Michael Feiginov (TU Wien), whose talks helped me understanding better the RTD physical insight. Furthermore, I would like to express special thanks to Prof. Safumi Suzuki and Prof. Masahiro Asada (Tokyo Institute of Technology), and to Prof. Tadao Nagatsuma, Prof. Masayuki Fujita, and Prof. Julian Webber (Osaka University), for providing precious details about their work on RTDs.

In the end, I would like to express my profoundest gratitude to my family. My parents, Luisa and Maurizio, who supported and encouraged me throughout my entire academic career; and my sister Giorgia, for being the best sister a brother could desire. A special mention goes to Ada, my soulmate, without whom this work would not be possible. Further, I would like to thank all my new friends met in Glasgow for sharing such a nice time together within the past years.

Finally, I take this opportunity to thank the JWNC staff at the University of Glasgow for the training provided and the help offered during clean-room microfabrication, and to the European Commission for the financial support offered regarding my fellowship.

# Abstract

Terahertz (THz) wave technology is envisioned as an appealing and conceivable solution in the context of several potential high-impact applications, including sixth generation (6G) and beyond consumer-oriented ultra-broadband multi-gigabit wireless data-links, as well as high-resolution imaging, radar, and spectroscopy apparatuses employable in biomedicine, industrial processes, security/defence, and material science. Despite the technological challenges posed by the THz gap, recent scientific advancements suggest the practical viability of THz systems. However, the development of transmitters (Tx) and receivers (Rx) based on compact semiconductor devices operating at THz frequencies is urgently demanded to meet the performance requirements calling from emerging THz applications.

Although several are the promising candidates, including high-speed III-V transistors and photo-diodes, resonant tunnelling diode (RTD) technology offers a compact and high performance option in many practical scenarios. However, the main weakness of the technology is currently represented by the low output power capability of RTD THz Tx, which is mainly caused by the underdeveloped and non-optimal device, as well as circuit, design implementation approaches. Indeed, indium phosphide (InP) RTD devices can nowadays deliver only up to around 1 mW of radio-frequency (RF) power at around 300 GHz. In the context of THz wireless data-links, this severely impacts the Tx performance, limiting communication distance and data transfer capabilities which, at the current time, are of the order of few tens of gigabit per second below around 1 m.

However, recent research studies suggest that several milliwatt of output power are required to achieve bit-rate capabilities of several tens of gigabits per second and beyond, and to reach several metres of communication distance in common operating conditions. Currently, the short-term target is set to 5–10 mW of output power at around 300 GHz carrier waves, which would allow bit-rates in excess of 100 Gb/s, as well as wireless communications well above 5 m distance, in first-stage short-range scenarios. In order to reach it, maximisation of the RTD high-frequency RF power capability is of utmost importance. Despite that, reliable epitaxial structure design approaches, as well as accurate physical-based numerical simulation tools, aimed at RF power maximisation in the 300 GHz-band are lacking at the current time.

This work aims at proposing practical solutions to address the aforementioned issues. First, a physical-based simulation methodology was developed to accurately and reliably simulate the static current-voltage ( $IV$ ) characteristic of indium gallium arsenide/aluminium arsenide (In-GaAs/AlAs) double-barrier RTD devices. The approach relies on the non-equilibrium Green's function (NEGF) formalism implemented in Silvaco Atlas technology computer-aided design (TCAD) simulation package, requires low computational budget, and allows to correctly model  $\text{In}_{0.53}\text{Ga}_{0.47}\text{As}/\text{AlAs}$  RTD devices, which are pseudomorphically-grown on lattice-matched to InP substrates, and are commonly employed in oscillators working at around 300 GHz. By selecting the appropriate physical models, and by retrieving the correct materials parameters, together with a suitable discretisation of the associated heterostructure spatial domain through finite-elements, it is shown, by comparing simulation data with experimental results, that the developed numerical approach can reliably compute several quantities of interest that characterise the DC  $IV$  curve negative differential resistance (NDR) region, including peak current, peak voltage, and voltage swing, all of which are key parameters in RTD oscillator design.

The demonstrated simulation approach was then used to study the impact of epitaxial structure design parameters, including those characterising the double-barrier quantum well, as well as emitter and collector regions, on the electrical properties of the RTD device. In particular, a comprehensive simulation analysis was conducted, and the retrieved output trends discussed based on the heterostructure band diagram, transmission coefficient energy spectrum, charge distribution, and DC current-density voltage ( $JV$ ) curve. General design guidelines aimed at enhancing the RTD device maximum RF power gain capability are then deduced and discussed.

To validate the proposed epitaxial design approach, an  $\text{In}_{0.53}\text{Ga}_{0.47}\text{As}/\text{AlAs}$  double-barrier RTD epitaxial structure providing several milliwatt of RF power was designed by employing the developed simulation methodology, and experimentally-investigated through the microfabrication of RTD devices and subsequent high-frequency characterisation up to 110 GHz. The analysis, which included fabrication optimisation, reveals an expected RF power performance of up to around 5 mW and 10 mW at 300 GHz for  $25 \mu\text{m}^2$  and  $49 \mu\text{m}^2$ -large RTD devices, respectively, which is up to five times higher compared to the current state-of-the-art. Finally, in order to prove the practical employability of the proposed RTDs in oscillator circuits realised employing low-cost photo-lithography, both coplanar waveguide and microstrip inductive stubs are designed through a full three-dimensional electromagnetic simulation analysis.

In summary, this work makes an important contribution to the rapidly-evolving field of THz RTD technology, and demonstrates the practical feasibility of 300-GHz high-power RTD devices realisation, which will underpin the future development of Tx systems capable of the power levels required in the forthcoming THz applications.

# Publications and conference presentations

- **Peer-reviewed journal papers:**

1. **D. Cimbri**, B. Yavas-Aydin, F. Hartmann, F. Jabeen, L. Worschech, S. Höfling, and E. Wasige, "Accurate quantum transport modeling of high-speed In<sub>0.53</sub>Ga<sub>0.47</sub>As/AlAs double-barrier resonant tunneling diodes," *IEEE Transactions on Electron Devices*, vol. 69, no. 8, pp. 4638-4645, 2022, doi: 10.1109/TED.2022.3178360.
2. **D. Cimbri**, J. Wang, A. Al-Khalidi, and E. Wasige, "Resonant tunneling diode high-speed terahertz wireless communications - a review," *IEEE Transactions on Terahertz Science and Technology*, vol. 12, no. 3, pp. 226-244, 2022, doi: 10.1109/TTHZ.2022.3142965.
3. M. Cito, **D. Cimbri**, D. Childs, R. Baba, B. A. Harrison, A. Watt, T. Mukai, E. Wasige, and R. A. Hogg, "Micro-PL analysis of high current density resonant tunneling diodes for THz applications," *Applied Physics Letters*, vol. 119, no. 7, pp. 072102, 2021, doi: 10.1063/5.0059339.

- **Peer-reviewed conference proceedings:**

4. **D. Cimbri**, R. Morariu, A. Ofiare, and E. Wasige, "A high-power InP resonant tunnelling diode heterostructure for 300-GHz oscillator sources," *2022 17th European Microwave Integrated Circuits Conference (EuMIC)*, Milan, Italy, 26-27th September 2022, doi: 10.23919/EuMIC54520.2022.9923482.
5. **D. Cimbri**, R. Morariu, A. Ofiare, and E. Wasige, "In<sub>0.53</sub>Ga<sub>0.47</sub>As/AlAs double-barrier resonant tunnelling diodes with high-power performance in the low-terahertz band," *2022 Fifth International Workshop on Mobile Terahertz Systems (IWMTS)*, Duisburg, Germany, 4-6th July 2022, doi: 10.1109/IWMTS54901.2022.9832442.
6. **D. Cimbri**, J. Wang, and E. Wasige, "Epitaxial structure simulation study of In<sub>0.53</sub>Ga<sub>0.47</sub>As/AlAs double-barrier resonant tunnelling diodes," *2022 Fifth International Workshop on Mobile Terahertz Systems (IWMTS)*, Duisburg, Germany, 4-6th July 2022, doi: 10.1109/IWMTS54901.2022.9832441.
7. **D. Cimbri**, N. Weimann, Q. R. A. Al-Taai, A. Ofiare, and E. Wasige, "Ohmic contacts optimisation for high-power InGaAs/AlAs double-barrier resonant tunnelling

diodes based on a dual-exposure e-beam lithography approach," *3rd International Conference on Applied Photonics and Electronics (InCAPE)*, Perlis, Malaysia, 6th October 2021, published in *International Journal of Nanoelectronics and Materials (IJNeaM)*, vol. 14 (Special Issue), pp. 11-19, 2021.

- **Book chapters:**

8. **D. Cimbri** and E. Wasige, "Terahertz communications with resonant tunnelling diodes: status and perspectives," in *Next Generation Wireless Terahertz Communication Networks*, CRC Press, pp. 25-87, 2021, doi: 10.1201/9781003001140-3.

- **Conference presentations:**

9. **D. Cimbri** and E. Wasige, "An advanced TCAD quantum transport-based simulation approach for InP RTD device simulation," *International School on Terahertz Photonics and Electronics*, Pisa, Italy, 9-14th May 2022.
10. **D. Cimbri** and E. Wasige, "Modelling, design, microfabrication, and DC/RF characterisation of  $\text{In}_{0.53}\text{Ga}_{0.47}\text{As}/\text{AlAs}$  double-barrier resonant tunnelling diodes for low-terahertz sources," *2022 24th European Microwave Week (EuMW)*, London, United Kingdom, 2-7th April 2022.
11. **D. Cimbri**, B. Yavas-Aydin, F. Hartmann, F. Jabeen, and E. Wasige, "Modeling of high-power resonant tunneling diodes through the non-equilibrium Green's function method," *44th Workshop on Compound Semiconductor Devices and Integrated Circuits held in Europe (WOCSDICE)*, Bristol, United Kingdom, 14-17th June 2021.

# Contents

<b>List of Figures</b>	<b>xxii</b>
<b>List of Tables</b>	<b>xxiv</b>
<b>Lists of Acronyms, Units, Symbols, Abbreviations, Quantities, and Constants</b>	<b>xxv</b>
<b>Overview</b>	<b>xlviii</b>
<b>1 Terahertz radiation: technology and applications</b>	<b>1</b>
1.1 The terahertz spectrum . . . . .	1
1.2 Terahertz sources . . . . .	3
1.2.1 Photonic THz sources . . . . .	4
1.2.2 Electronic THz sources . . . . .	6
1.2.3 Consumer-oriented THz solid-state integrated sources: state-of-play . .	10
1.3 Terahertz applications . . . . .	11
1.3.1 High-resolution THz imaging and spectroscopy . . . . .	11
1.3.2 Ultra-broadband THz wireless communications . . . . .	15
1.3.2.1 The need for ultra-high-speed wireless connectivity . . . . .	15
1.3.2.2 Increasing the speed of wireless transmissions . . . . .	17
1.3.2.3 Link budget and THz antennas . . . . .	20
1.3.2.4 THz wireless data-links: state-of-play . . . . .	21
1.3.2.5 Hybrid photonic/electronic-based THz wireless data-links . .	22
1.3.2.6 Electronic-based THz wireless data-links . . . . .	25
1.3.2.7 Challenges in realising THz wireless communications . . . . .	29
<b>2 Terahertz resonant tunnelling diode</b>	<b>31</b>
2.1 Overview . . . . .	31
2.2 Historical notes . . . . .	33
2.3 Principle of operation . . . . .	35
2.4 Physical modelling . . . . .	37
2.4.1 Electronic states quantisation in quantum well structures . . . . .	37

2.4.1.1	Infinitely-deep rectangular potential well . . . . .	37
2.4.1.2	Finite-depth rectangular potential well . . . . .	41
2.4.2	Tunnelling and electron transport through potential barriers . . . . .	45
2.4.2.1	Tunnelling through a finite-height rectangular potential barrier . . . . .	45
2.4.2.2	Tunnelling through a double-barrier quantum well structure: the global coherent resonant tunnelling picture . . . . .	47
2.4.2.3	The sequential scattering-assisted resonant tunnelling picture: phase-decoherence and dissipative processes . . . . .	49
2.4.3	The Wentzel-Kramer-Brillouin (WKB) approximation . . . . .	51
2.4.4	Self-consistent solution of RTD devices: space charge build-up . . . . .	52
2.5	Equivalent circuit modelling . . . . .	60
2.6	Technology . . . . .	68
2.7	RTD THz oscillators . . . . .	73
2.7.1	Principle of operation . . . . .	73
2.7.2	Evolution . . . . .	75
2.7.3	Technology . . . . .	78
2.8	RTD THz detectors . . . . .	85
2.9	RTD THz applications . . . . .	89
2.9.1	Ultra-high-speed THz wireless communications . . . . .	89
2.9.1.1	RTD THz wireless TRx systems architecture . . . . .	90
2.9.1.2	RTD THz wireless data-links . . . . .	90
2.9.2	High-resolution THz imaging and radar systems . . . . .	96
<b>3</b>	<b>Resonant tunnelling diode microfabrication technology</b>	<b>102</b>
3.1	Mask design . . . . .	102
3.2	Lithography . . . . .	105
3.3	Metal evaporation and lift-off . . . . .	110
3.4	Wet etching . . . . .	113
3.5	Dry etching . . . . .	115
3.6	Metrology . . . . .	117
3.7	RTD devices fabrication process . . . . .	119
3.8	TLM structures design and fabrication process . . . . .	127
<b>4</b>	<b>Accurate quantum transport modelling of high-speed <math>\text{In}_{0.53}\text{Ga}_{0.47}\text{As}/\text{AlAs}</math> double-barrier resonant tunnelling diodes</b>	<b>135</b>
4.1	Introduction . . . . .	135
4.2	NEGF method . . . . .	137
4.3	Simulation of the RTD epitaxial structure DC $JV$ curve . . . . .	143
4.3.1	Epitaxial structures design . . . . .	143

4.3.2	NEGF simulation approach based on Silvaco Atlas TCAD . . . . .	145
4.3.3	RTD devices fabrication and DC characterisation . . . . .	149
4.3.4	Simulation versus experimental results: comparison and discussion . .	153
4.3.4.1	Peak, valley, and available current densities . . . . .	154
4.3.4.2	Peak, valley, and valley-to-peak voltages . . . . .	157
4.3.4.3	Maximum RF power . . . . .	160
4.4	Summary . . . . .	160
<b>5</b>	<b>Epitaxial structure simulation study of <math>\text{In}_{0.53}\text{Ga}_{0.47}\text{As}/\text{AlAs}</math> double-barrier resonant tunnelling diodes for low-terahertz sources</b>	<b>162</b>
5.1	Introduction . . . . .	162
5.2	RTD epitaxial structure simulation study . . . . .	164
5.2.1	Barriers . . . . .	165
5.2.2	Quantum well . . . . .	166
5.2.3	Lightly-doped spacers . . . . .	168
5.2.3.1	Emitter lightly-doped spacer . . . . .	168
5.2.3.2	Collector lightly-doped spacer . . . . .	171
5.2.4	High-band gap emitter . . . . .	172
5.3	RTD epitaxial structure design for high-power low-THz sources: general considerations . . . . .	173
5.4	Summary . . . . .	176
<b>6</b>	<b>A high-power <math>\text{In}_{0.53}\text{Ga}_{0.47}\text{As}/\text{AlAs}</math> double-barrier resonant tunnelling diode epitaxial structure for 300-GHz oscillators</b>	<b>177</b>
6.1	RTD heterostructure design . . . . .	177
6.2	RTD devices microfabrication . . . . .	178
6.3	RTD devices DC and RF characterisation . . . . .	179
6.4	High-frequency RF power analysis . . . . .	188
6.5	RF stubs for 300 GHz oscillator circuit design . . . . .	192
6.6	Summary . . . . .	196
<b>7</b>	<b>Conclusions and future perspectives</b>	<b>198</b>
7.1	Conclusions . . . . .	198
7.2	Challenges and future perspectives . . . . .	200
7.2.1	RTD modelling and simulation . . . . .	200
7.2.2	RTD epitaxial structure design and material systems . . . . .	202
7.2.3	RTD oscillator circuit design implementation and realisation . . . . .	203
<b>A</b>	<b>RTD devices fabrication recipe</b>	<b>207</b>

<b>B</b>	<b>TLM structures fabrication recipe</b>	<b>213</b>
<b>C</b>	<b>Extraction of the specific contact resistivity through the transfer length model</b>	<b>216</b>
<b>D</b>	<b>Silvaco Atlas TCAD RTD device simulation deck</b>	<b>218</b>
<b>E</b>	<b>RTD small-signal equivalent circuit ADS schematic</b>	<b>224</b>
	<b>Bibliography</b>	<b>225</b>

# List of Figures

1.1	Electromagnetic spectrum frequency bands ranging from the upper bound of radio-frequencies (RF) ( $f < 300$ MHz, $\lambda_0 > 1$ m) to the lower bound of visible light ( $f > 430$ THz, $\lambda_0 < 0.7$ $\mu$ m), including microwaves (MW), mm-waves, and FIR, mid-infrared (MIR), and near-infrared (NIR) light. . . . .	2
1.2	CMBR spectral radiance in the range 30–600 GHz (reproduced from [9]). The orange void dots represent the measured data captured by the FIRAS, while the solid blue line models the black-body radiation spectrum through Planck’s law at $T = 2.735 \pm 0.06$ K. . . . .	3
1.3	In a), schematic of the typical band diagram of an UTC-PD device under forward bias (adapted and reprinted from [72]); in b) to e), schematics of the layer structure and device layout, together with photo-micrographs of the fabricated device and complete module, respectively, of the InP antenna-integrated CW UTC-PD THz photo-mixer source reported in [70] (adapted and reprinted from [70]). . .	5
1.4	In a), schematic of a typical Gunn device mesa; in b), schematic of the waveguide-based oscillator cavity in InP Gunn technology reported in [106, 108] aimed at third-harmonic power extraction in the 400–500 GHz range (reprinted from [106]). . . . .	7
1.5	RF power versus operation frequency of THz solid-state integrated sources, including UTC-PD-based photo-mixers, transistor-based TMICs, and RTD-based oscillators in the 0.2–2 THz range, outlining some of the most relevant results reported in the literature. Reference number is provided for key results. . . . .	10
1.6	Visible (a and d), THz (b and e), and MRI (c and f) images of the healthy and tumor-affected fresh rat brains analysed in [199] (adapted and reprinted from [199]). . . . .	12
1.7	Imaging experiment employing the 100-GHz body scanner proposed in [202] (adapted and reprinted from [202]). A body-borne belt carrying explosives (in a)), as well as a firearm (in b)) hidden below a fabric-based jacket, could be identified at 3 m distance. . . . .	13

1.8	Stand-off real-life visualization of body-borne concealed explosives at 25 m distance carried out through the 675-GHz radar system reported in [203] (adapted and reprinted from [203]). The explosive charge (in d) and c)) hidden beneath a sweatshirt (in a)) could be clearly identified (in b)) at 25 m distance. . . . .	14
1.9	Illustrations of the real-time pulsed THz spectroscopic imaging system proposed in [228] (adapted and reprinted from [228]). In a), representation of the broadband multi-channel spectrometer, composed by THz lenses and a diffraction grating; in b), schematic of the THz imaging apparatus, including a ytterbium (Yb):potassium gadolinium tungstate (KGW) crystal-based laser source, uncooled camera, and optical components. . . . .	14
1.10	Imaging results of the experiment reported in [228] employing the proposed THz spectroscopic imaging apparatus (reprinted from [228]). In a) and b), test sample no. 1 and 2, respectively; on the left: optical images; in the middle: lactose distributions; on the right: D-fructose distributions. . . . .	15
1.11	Data-rate demand versus time trend for wireline, nomadic, and wireless communication technologies between 1970 and 2020, pointing out the faster exponential increase associated with wireless systems compared to wireline technologies (reprinted from [230]). . . . .	16
1.12	Wireless channel data-rate versus carrier frequency trend (reprinted from [3]). . . . .	18
1.13	Some potential applications of THz wireless communications. . . . .	19
1.14	Data-rate versus link distance of solid-state integrated THz wireless communication technologies, outlining some of the most relevant literature results. Reference number is provided for key results. . . . .	22
1.15	Block diagram of the 300 GHz-band wireless TRx system reported in [59] (adapted and reprinted from [59]). In a), Tx; in b), Rx; in c), optical signal generator. . . . .	24
1.16	Block diagram of the 400-GHz wireless TRx setup reported in [292] (adapted and reprinted from [292]). In a), optical signal generator; in b), modulation and mixing module; in c), THz wireless TRx. In the above, Pol.M stands for polarization maintaining. . . . .	24
1.17	Scenario representation of the long-range multi-channel THz wireless communication data link reported in [53] (reprinted from [53]). . . . .	25
1.18	InP HEMT TMIC TRx system reported in [155, 284] (adapted and reprinted from [155] [284]). In a), block diagram of the THz data-link used to carry out wireless communication experiments; in b), photograph of the employed InP HEMT mixer chip; in c), photograph of the employed InP HEMT PA chip. . . . .	27

1.19	InP HBT TMIC TRx system reported in [285] (adapted and reprinted from [285]). In a), block diagrams of the InP HBT Tx and Rx chips, together with schematic of the Tx/Rx modules packaging concept; in b), photograph of the Tx module. . . . .	28
1.20	Si-based CMOS TMIC TRx system reported in [299,302] (adapted and reprinted from [299,304]). In a), block diagram of the TRx; in b), micrograph of the Tx circuit board; in c), micrograph of the Tx die. . . . .	28
1.21	Atmospheric specific attenuation versus frequency up to 1 THz for dry (RH $\sim$ 0 %) and moist (RH $\sim$ 50 %) indoor conditions (reprinted from [247]). . . . .	29
2.1	In a), schematic illustration of the $IV$ curve of a generic $n$ -type intra-band RTD device; in b), associated simplified CB diagram, assuming a generic bias point and QW quasi-bound state energy level $E$ . In the above, $E_c$ is the CB edge, $z =  z $ the broken-symmetry (longitudinal) direction modulus, while $e^-$ represents the tunnelling electrons. . . . .	32
2.2	Measured conductance (left axis) and current (right axis)-voltage characteristics at $T = 77$ K of the GaAs/Al <sub>0.7</sub> Ga <sub>0.3</sub> As double-barrier heterostructure reported in [335], featuring 8 nm-thick barriers and an 5 nm-thick QW (reprinted from [335]). . . . .	34
2.3	Simplified illustration of the operation principle of an $n$ -type intra-band DBQW RTD device: a) thermal equilibrium; b) first PDR region; c) peak resonance; d) NDR region; e) valley point; and f) second PDR region. In this representation, the blue regions represent the emitter and collector Fermi sea. . . . .	36
2.4	Illustration of the electronic eigenstates and eigenenergies of a generic infinitely-deep rectangular potential well computed through Eq. (2.15) and (2.13), respectively, outlining the first four subbands (i.e., $q = 1, 2, 3, 4$ ). . . . .	40
2.5	Illustration of the electronic quasi-bound states of a generic finite-depth rectangular potential well computed numerically through Eq. (2.31) to (2.34), outlining the first four subbands (i.e., $q = 1, 2, 3, 4$ ). . . . .	44
2.6	In a), illustration of tunnelling through a finite-height rectangular potential barrier; in b), illustration of resonant tunnelling through a DBQW structure thanks to the first subband $E_1$ . . . . .	46
2.7	Schematic illustration of the transmission coefficient of a generic DBQW structure computed through Eq. (2.61), outlining the resonances associated with three quasi-bound state resonant levels $E_q$ ( $q = 1, 2, 3$ ). . . . .	48

2.8	Illustration of the band diagram of a DBQW RTD device: a), thermal equilibrium; and b), peak resonance (forward bias). In this representation, $E_F$ , $E_{Fn}^c$ and $E_{Fn}^e$ are the Fermi level and the emitter and collector quasi-Fermi level at the domain boundaries (contacts), respectively, $V$ is the applied bias voltage, while the blue regions represent the emitter and collector Fermi sea. . . . .	53
2.9	Block diagram illustrating the loop at the base of a self-consistent Schrödinger-Poisson solver within the Hartree approximation. . . . .	55
2.10	Illustration describing the openness nature of the RTD device. In this context, the emitter and collector boundary states $ \psi_{k_e}\rangle$ and $ \psi_{k_c}\rangle$ and their first derivative must be continuous at the interface with the RTD ensemble. . . . .	58
2.11	Unified RTD high-frequency small-signal equivalent circuit model. . . . .	61
2.12	RTD oscillator RF large-signal equivalent circuit. In this representation, $R_s(V)$ and $L_{qw}(V)$ are not included since the RTD maximum RF power is of interest. . . . .	66
2.13	In a), illustration of the typical layer structure of a generic InGaAs/AlAs double-barrier RTD device, outlining the DBQW region (layers nomenclature assumes the top contact to be forward biased with respect to the bottom one); in b), the corresponding simplified CB diagram at peak resonance. . . . .	69
2.14	In a), illustration of the RTD epitaxial structure employed in the realisation of the 260 GHz oscillator reported in [169]; in b), the measured static $IV$ characteristic of a fabricated $16 \mu\text{m}^2$ large device; in c), SEM image of a fabricated device (adapted and reprinted from [169]). . . . .	70
2.15	Illustration of the RTD epitaxial structure employed in the realisation of the 1.92 THz and 1.98 THz oscillators reported in [168, 470] (reprinted from [168, 470]). . . . .	71
2.16	In a), the RTD-based sinusoidal oscillator lumped-element equivalent circuit topology; in b), the approximate RF large-signal equivalent circuit; in c), the equivalent circuit at start-up. In b) and c), $R_s$ and $L_{qw}$ are neglected for the sake of simplicity. . . . .	74
2.17	Schematic representation of the rectangular waveguide-based resonator employed in the 200 GHz and 420 GHz oscillators reported in [364, 450] (reprinted from [364]). . . . .	76
2.18	In a), a schematic representation of the circuit topology of the single-element slot-antenna SRTD oscillator; in b), a photo-micrograph of a fabricated array element, including a SEM picture of the T-gate SRTD air-bridge-based device (adapted and reprinted from [528]). . . . .	77
2.19	Output power versus fundamental frequency of oscillation for some of the most relevant reported single-device RTD THz oscillators to date, including some results below 100 GHz. Reference number is provided for key results. . . . .	80

2.20	Photo-micrograph of the fabricated 0.26 THz microstrip RTD oscillator reported in [169] (reprinted from [169]). Here, $C_e$ and $R_e$ are the decoupling capacitor and stabilising resistors. . . . .	81
2.21	Measured output spectrum of the 0.26 THz microstrip RTD oscillator reported in [169] (reprinted from [169]). Down-conversion mixers were used to display the probed signal on the employed 50 GHz spectrum analyser. The resolution bandwidth was set to 3 MHz. . . . .	81
2.22	Layout illustration of an RTD THz oscillator integrated with a slot-antenna operating way above 300 GHz (reprinted from [437]). . . . .	82
2.23	Illustration of the circuit layout employed in the realisation of the 1.92 THz oscillator reported in [470] (reprinted from [470]). . . . .	83
2.24	In a), illustration of the 1.92 THz oscillator layout cross-section, showing the integration of the RTD device with the slot-antenna through the air-bridge structure (reprinted from [470]); in b), illustration showing the oscillator chip mounted onto the hemispherical Si lens for field collection and focusing (reprinted from [464]). . . . .	84
2.25	Oscillation frequency versus RTD mesa area for different antenna electrode thicknesses of the 1.98 THz oscillator reported in [168] (reprinted from [168]). The spectrum of oscillations, together with few details on the RTD epi-design and associated electrical quantities, are also provided. . . . .	85
2.26	Operation principle of a DBQW RTD THz detector based on the associated $IV$ curve. The device can be either biased close to the peak (marked as A and B depending on the polarisation region) in the case of a direct detector, as well as within the NDR region (highlighted in orange) if coherent detection is employed (reprinted from [568]). . . . .	86
2.27	Comparison of the measured output voltage versus the incoming 300-GHz signal RF power at 1.5 Gb/s in the wireless experiment reported in [568] (reprinted from [568]). . . . .	87
2.28	Schematic illustration of the operation principle of an RTD THz coherent detector (reprinted from [565]). . . . .	88
2.29	Comparison of the measured bit error rate versus Tx incoming RF power at 10 Gb/s in the wireless experiment reported in [287], where the RTD bias point was changed to switch from direct to coherent detection (reprinted from [287]). . .	89
2.30	Illustration of ASK/OOK modulation in RTD THz Tx (reprinted from [390]). . .	89
2.31	Block diagram of a THz wireless TRx system architecture employing an RTD-based Tx and/or Rx. . . . .	90

2.32	Block diagram of the THz wireless data transmission experimental setup employed in [585] (reprinted from [585]). . . . .	92
2.33	Results of the THz wireless communication experiment reported in [585] (adapted and reprinted from [585]). In a), the measured BER as a function of the data-rate, showing EF data transmission up to 22 Gb/s, and data-rates of up to 34 Gb/s with $BER \sim 1.9 \times 10^{-3}$ ; in b), the corresponding measured eye diagrams.	92
2.34	Illustration of the RTD THz oscillator circuit layout employed at the Tx side for wireless data transmission through FDM and PDM (reprinted from [587]). . . . .	93
2.35	Block diagram of the THz wireless communication experimental setup employed to perform data transmission through FDM and PDM (reprinted from [587]). . . . .	93
2.36	In a), the wireless experimental setup used for real-time high-resolution 4K video transmission; in b), a photograph of the direct THz RTD-based Rx front-end module reported in [573], with a zoom-in over the RTD integrated with a Si-based photonic crystal waveguide through a tapered-slot mode coupler (adapted and reprinted from [573]). . . . .	94
2.37	Results of the THz wireless communication experiment reported in [573] (adapted and reprinted from [573]). In a), the BER as a function of the data-rate; in b), the eye diagram at 32 Gb/s. . . . .	94
2.38	In a), photographs of the 300 GHz-band RTD coherent Rx front-end module, together with a photo-micrograph zoom-in over the RTD oscillator chip (reprinted from [565]); in b), measured BER versus data-rate of the wireless data transmission experiment reported in [565] (reprinted from [565]); in c), photograph of the 4K high-definition wireless transmission system reported in [287] (reprinted from [287]). . . . .	95
2.39	Illustration of the RTD THz reflection imaging system setup reported in [597] (reprinted from [597]). . . . .	97
2.40	Images of the characterised SUT (adapted and reprinted from [597]). In a), photograph of the SUT; in b), photograph of the closed box; in c), THz image of the closed box, revealing the hidden metallic content. . . . .	98
2.41	Block diagram of the AM CW THz radar experimental setup employing an RTD Tx and based on the lock-in phase measurement technique reported in [599] (reprinted from [599]). . . . .	99
2.42	Measurement error as a function of the target position employing the lock-in phase AM CW THz radar reported in [599] (reprinted from [599]). . . . .	100

2.43	Block diagram of the sub-carrier FM CW THz radar experimental setup employing an RTD Tx reported in [604] (reprinted from [604]). . . . .	100
2.44	Measurement error as a function of the target position employing the sub-carrier FM CW THz radar reported in [604] (reprinted from [604]). . . . .	101
3.1	Designed RTD lithographic mask. In a), mask layout; in b) and c), zooms-in over a $5 \times 5 \mu\text{m}^2$ -large device and associated RTD region, outlining the different lithographic windows, including top/bottom contact/mesa, passivation, and bond-pads; in d), designed optical alignment marks; in e), zoom-in over the two markers-set associated to the second lithographic step (top mesa); in f), check structure for via opening; in g), zoom-in over the via structures for the $3 \times 3 \mu\text{m}^2$ devices; in h), mask layout for conductive substrate processing; in i) and j), zooms-in over a $5 \times 5 \mu\text{m}^2$ -large device and associated RTD region. . . . .	103
3.2	In a), designed photo-mask layout; in b), zoom-in over the first two photo-windows (top mesa and bottom contact); in c), $5'' \times 5''$ engraved physical photo-mask. . . . .	104
3.3	Lithographic process flow: a) resist spin-coating; b) sample exposure through photo-lithography; c) sample exposure through EBL; d) development and plasma ashing. . . . .	106
3.4	In a), LAF cabinet for photo-resist spin-coating (E-beam resist ones are analogous); in b), hot-plate for sample soft-baking. . . . .	107
3.5	MA6 manual photo-mask aligner. . . . .	108
3.6	EBPG 5200 E-beam lithographic tool. . . . .	109
3.7	LAF cabinet for S1800 series photo-resists development (those for LOR-10A and PMMA are similar). . . . .	110
3.8	PlasmaFab 505 barrel asher. . . . .	111
3.9	MEB550S E-beam evaporator no. IV. . . . .	112
3.10	Dual lift-off process flow associated to metal EBPVD: a) sample spin-coating; b) exposure and development; c) metal evaporation; d) lift-off. . . . .	113
3.11	LAF cabinet for wet chemical etching, which can also be employed for development processes involving tetramethylammonium hydroxide. . . . .	114
3.12	Etching processes. In a) and b), anisotropic chemical wet etching; in c) and d), RIE of polyimide PI-2545 employing S1805 photo-resist as soft mask. . . . .	115
3.13	Plasmalab 80 Plus RIE tool. . . . .	116
3.14	Detected laser signal level during RIE of the polyimide PI-2545 passivation layer featuring two different thicknesses: in a), $1.2 \mu\text{m}$ , while in b), $1.8 \mu\text{m}$ , for a total of six and nine trace peaks, respectively. . . . .	117
3.15	UHR FE-SEM SU8240 scanning electron microscope. . . . .	118
3.16	DektakXT mechanical profiler. . . . .	119

3.17	Probe station for DC measurements. . . . .	120
3.18	Example of processed InGaAs/AlAs RTD epitaxial structure. The device mesa is shown, together with Ti/Pd/Au metal contacts, whose fabrication is described in the following. Layers nomenclature assumes forward bias operation. . . . .	121
3.19	RTD device fabrication flow: a), top contact; b), top mesa; c), bottom contact; d), bottom mesa; e), passivation and via opening; f), bond-pads. In e), the passivation layer extension for bond-pads insulation is also displayed with a lighter colour. In f), the bond-pads sit on the extended passivation layer as a comprehensive example. . . . .	122
3.20	T10XT10/OES/E UV/O <sub>3</sub> cleaning system. . . . .	123
3.21	Fabricated $5 \times 5 \mu\text{m}^2$ -large RTD device. In a), photograph of the processed sample and photo-micrograph of the fabricated device, together with a zoom-in over the RTD region; in b), SEM image of the RTD region. . . . .	126
3.22	Measured DC <i>IV</i> curve of the fabricated RTD device shown in Figure 3.21. . . . .	127
3.23	Top TLM structures E-beam lithographic mask. In a), mask layout, including a pair set of optical alignment markers at the four mask sides, as well as other markers for sample orientation and wet etching; in b), TLM structure layout; in c), zoom-in over the associated $1 \mu\text{m}$ -wide gap region. . . . .	129
3.24	Top TLM structure fabrication process: a), E-beam resist spin-coating; b), exposure, development, and surface cleaning; c), metallisation; d), lift-off; e), photoresist spin-coating; f), exposure, development, and plasma ashing; g), wet etching; h), resist stripping. . . . .	131
3.25	Photo-micrographs of a TLM structure after development. In a), the structure backbone; in b), a zoom-in over the $1 \mu\text{m}$ -wide gap region. . . . .	132
3.26	Photo-micrographs and SEM images of a TLM structure after lift-off. In a), the structure backbone; in b), a zoom-in over the $1 \mu\text{m}$ -wide gap area; in c), the $1 \mu\text{m}$ -wide gap seen through SEM; in d), a further zoom-in over the gap. . . . .	132
3.27	In a), b), and c), photo-micrographs of the $3 \mu\text{m}$ wide gap region of one of the fabricated structures, including two zooms-in over the gap; in d) and e), SEM images of the $5 \mu\text{m}$ -wide gap region of an analogous TLM, including a zoom-in over a mesa later side-wall. . . . .	133
4.1	Schematic representation of a 1D nanodevice, including contacts, leads, and active region. A generic longitudinal pure coherent state $ \psi_{k_z}\rangle$ is illustrated. . . . .	138
4.2	Coherent NEGF algorithm for the steady-state numerical solution of a 1D nanodevice (such as a 1D RTD), accounting for space charge effects. . . . .	142
4.3	Epitaxial structures under test, indicating layers name, thickness, and doping level. The DBQW region is highlighted. Layers nomenclature assumes the top contact to be forward biased with respect to the bottom one. . . . .	143

4.4	Computed CB edge energy profile and electron density distribution of the ESUT #1 at RT and thermal equilibrium close to the DBQW region, together with associated first and second quasi-bound resonant states (energies and envelope wave-functions), as well as a zoom-out over the entire device structure. In the above, $ \phi_i(z) ^2$ is given in arbitrary units and $E_F$ is the Fermi level (energy reference). . . . .	149
4.5	Computed transmission coefficient energy spectrum (linear (top) and log (bottom) scales) at RT at both thermal equilibrium and peak resonance ( $V = V_p$ ) of the ESUT #1. Peak and energy broadening $\Gamma_1$ values of the resonance associated with the first resonant metastable state are also shown in both conditions. The drop of the peak value and the increase of $\Gamma_1$ with bias, i.e., energy broadening, is attributed to the reduction of symmetry associated with the DBQW potential profile. . . . .	150
4.6	Computed CB edge energy profile and LDOS (log scale with arbitrary units) of the ESUT #1 at RT and peak resonance ( $V = V_p$ ) close to the DBQW region, revealing the first and second quasi-bound resonant states, as well as a third state (unbound). In the above, $E_F$ is the Fermi level. . . . .	151
4.7	Computed CB edge energy profile and LDOS (log scale with arbitrary units) of the ESUT #1 at RT and peak resonance ( $V = V_p$ ) close to the DBQW region, revealing the first and second quasi-bound resonant states, as well as a third state (unbound). In the above, $E_{Fn}$ is the electron quasi-Fermi level at the emitter/collector boundaries (contacts), as well as at the QW middle point. . . .	152
4.8	In a), a photo-micrograph of a fabricated $4 \times 4 \mu\text{m}^2$ -large RTD device, as well as a zoom-in over the RTD region; in b), an SEM image zoom-in over the opened via. . . . .	152
4.9	Extraction of the contact resistance $R_c$ , semiconductor sheet resistance $R_{sh} \propto \tan \theta$ , and transfer length $l_t =  l_r $ through linear fitting over the measured data. . . . .	153
4.10	Comparison between simulated and measured static $IV$ characteristics at RT and under forward bias of the RTD devices featuring the ESUT #1. . . . .	154
4.11	Comparison between simulated and measured static $IV$ characteristics at RT and under forward bias of the RTD devices featuring the ESUT #2. . . . .	155
4.12	Experimentally-extracted ESUT #1 and #2 RTD devices peak and valley currents as a function of the designed mesa area. . . . .	157
4.13	Experimentally-extracted ESUT #1 and #2 RTD devices peak voltage and voltage swing versus designed mesa area trends due to load line effects. . . . .	158

5.1	RTD reference epitaxial structure and associated design parameters (in red), as well as the overall set of simulation parameters (in black). . . . .	164
5.2	Computed resonant peak (linear scale) associated with the QW first quasi-bound state energy subband of the heterostructure transmission coefficient energy spectrum at RT for different barriers thicknesses. Thermal equilibrium is assumed as a general bias point. . . . .	166
5.3	Computed static $JV$ characteristic at RT for different QW thicknesses. . . . .	166
5.4	Computed transmission coefficient energy spectrum at RT for different QW thicknesses. Thermal equilibrium is assumed as a general bias point. . . . .	167
5.5	Computed static $JV$ characteristic at RT for different lightly-doped emitter spacer thicknesses and doping levels. The lightly-doped collector spacer thickness and doping level are set to 100 nm and $2 \times 10^{17} \text{ cm}^{-3}$ , respectively. * Computed assuming $t_{ls}^c = 100 \text{ nm}$ and $N_{D,ls}^c = 2 \times 10^{16} \text{ cm}^{-3}$ . . . . .	168
5.6	Computed CB edge energy profile and electron density at RT in the emitter region for different lightly-doped emitter spacer thicknesses and doping levels. The lightly-doped collector spacer thickness and doping level are set to 100 nm and $2 \times 10^{17} \text{ cm}^{-3}$ , respectively. Thermal equilibrium is assumed as arbitrary example. * Computed assuming $t_{ls}^c = 100 \text{ nm}$ and $N_{D,ls}^c = 2 \times 10^{16} \text{ cm}^{-3}$ . The black solid line represents the Fermi level (energy reference). . . . .	170
5.7	Computed static $JV$ characteristic at RT for different lightly-doped collector spacer thicknesses and doping levels. The lightly-doped emitter spacer thickness and doping level are set to 100 nm and $2 \times 10^{17} \text{ cm}^{-3}$ , respectively. . . . .	171
5.8	Computed CB edge energy profile at RT in proximity to the first barrier for different $\text{In}_{1-x-y}\text{Al}_y\text{Ga}_x\text{As}$ compositions. The black solid line represents the Fermi level (energy reference). Thermal equilibrium is assumed as reference example. . . . .	173
6.1	Proposed $n$ -type intra-band $\text{In}_{0.53}\text{Ga}_{0.47}\text{As}/\text{AlAs}$ RTD epitaxial structure. . . . .	178
6.2	In a), photo-micrograph of a fabricated RTD device; in b), SEM image zoom-in over the RTD region; in c), zoom-in over the opened via. . . . .	179
6.3	Measured and simulated static $IV$ characteristic of the designed RTD devices. . . . .	180
6.4	Experimental setup for RTD devices S-parameters measurement. . . . .	181
6.5	RTD device and bond-pads small-signal equivalent circuit. . . . .	182
6.6	In a), measured and modelled real and imaginary parts of $Z_{11}$ at $V = 0.3 \text{ V}$ ; in b), measured and modelled $S_{11}$ on Smith chart at $V = 0.3 \text{ V}$ . . . . .	183
6.7	In a), measured and modelled real and imaginary parts of $Z_{11}$ at $V = 2.7 \text{ V}$ ; in b), measured and modelled $S_{11}$ at $V = 2.7 \text{ V}$ . . . . .	184

6.8	Simulated transmission coefficient (linear scale) first subband resonance peak at RT ( $T = 300$ K), outlining the related energy broadening. Thermal equilibrium was assumed based on the bias-independency assumption of $\tau_{in}$ . . . . .	186
6.9	Measured static $IV$ characteristic and modelled NDR region. . . . .	187
6.10	In a), measured static $IV$ characteristic and modelled NDC; in b), modelled capacitance and QW inductance with the NDR region. . . . .	187
6.11	Extraction of the contact resistance $R_c$ , semiconductor sheet resistance $R_{sh} \propto \tan \theta$ , and transfer length $l_t =  l_t $ through linear fitting over the measured data. .	189
6.12	RF power density versus operation frequency performance of the analysed RTD heterostructure. . . . .	191
6.13	Cross section of the employed CPW (a)) and MLIN (b)). . . . .	193
6.14	Cross section of simulated $5 \mu\text{m}$ -long $26 \Omega$ CPW and $20 \mu\text{m}$ -long $10 \Omega$ MLIN stubs, showing the associated quasi-transverse electromagnetic mode standing wave two-dimensional electric field magnitude at $300$ GHz in proximity to a reference node. . . . .	194
6.15	Simulated $S_{11}$ parameter of $5 \mu\text{m}$ -long $26 \Omega$ CPW and $20 \mu\text{m}$ -long $10 \Omega$ MLIN stubs in the frequency range $250\text{--}350$ GHz. . . . .	195
6.16	Simulated inductance versus length of the analysed $26 \Omega$ CPW and $10 \Omega$ MLIN stubs at $300$ GHz. . . . .	195
7.1	Second proposed $n$ -type intra-band $\text{In}_{0.53}\text{Ga}_{0.47}\text{As}/\text{AlAs}$ RTD heterostructure. .	202
7.2	Third proposed $n$ -type intra-band $\text{In}_{0.53}\text{Ga}_{0.47}\text{As}/\text{AlAs}$ RTD heterostructure. . .	203
C.1	Cross-section view illustration of the TLM structure employed in the extraction of $\rho_c$ through four-point probe DC sensing, showing two generic contacts pairs. The dashed arrows indicate that $R_c$ is associated to the metal-semiconductor discontinuity region of the metal pads, while $R_{sh}$ to the region between the pads where current flow occurs. . . . .	216
E.1	ADS schematic for the extraction of the RTD high-frequency small-signal equivalent circuit parameters. Fitted values at $V = 0.3$ V are displayed as example. Here, $R_{rtd} = G_{rtd}^{-1}$ . . . . .	224

# List of Tables

1.1	Link budget examples for wireless transmission at 300 GHz [247]. . . . .	20
1.2	Hybrid photonic/electronic THz wireless communication data-links specifics. . .	23
1.3	Electronic-based THz wireless communication data-links specifics. . . . .	26
2.1	RTD III-V electronic physical parameters at RT ( $T = 300$ K). . . . .	68
2.2	RTD devices electrical quantities. . . . .	79
2.3	RTD THz oscillators specifics. . . . .	79
2.4	THz RTD wireless communication data-links specifics. . . . .	91
4.1	RTD epitaxial structures simulation material parameters*. . . . .	145
4.2	Measured/extracted parameters obtained from TLM structures characterisation*. .	153
4.3	Electrical quantities of the ESUT #1 and #2, and related RTD devices*. . . . .	155
4.4	Extracted RTD devices load-line parameters*. . . . .	159
5.1	Epi-structure simulation results for different barriers thicknesses. . . . .	165
5.2	Epitaxial structure simulation results for different QW thicknesses. . . . .	167
5.3	Epitaxial structure simulation results for different emitter lightly-doped spacer thicknesses and doping levels. . . . .	169
5.4	Epitaxial structure simulation results for different collector lightly-doped spacer thicknesses and doping levels*. . . . .	171
5.5	Epitaxial structure simulation results for different InAlGaAs compositions. . . .	172
6.1	RTD epitaxial structure extracted static $JV$ curve electrical quantities. . . . .	180
6.2	Extracted RTD device and bond-pads small-signal parameters at $V = 0.3$ V. . . .	185
6.3	Extracted RTD device and bond-pad small-signal parameters at $V = 2.7$ V. . . .	185
6.4	Employed polynomial expansion coefficients of the $IV$ curve within the NDR region. . . . .	186
6.5	RTD epitaxial structure extracted high-frequency electrical parameters. . . . .	188
6.6	Measured/extracted parameters obtained from TLM structures characterisation*. .	190
6.7	RTD epitaxial structure RF power performance and intrinsic frequency limit*. . .	191
6.8	RTD epitaxial structure high-frequency performance. . . . .	192

6.9	Oscillator design parameters for 300-GHz (fundamental) oscillations. . . . .	196
-----	--	-----

# Lists of Acronyms, Units, Symbols, Abbreviations, Quantities, and Constants

## Acronyms

1D	one-dimensional
1G	first generation
2D	two-dimensional
3D	three-dimensional
4G	fourth generation
5G	fifth generation
6G	sixth generation
AC	alternating current
ADC	analog-to-digital converter
ADS	Advance Design System
AI	artificial intelligence
AM	amplitude modulation
AR	augmented reality
ASK	amplitude-shift keying
AWG	arbitrary waveform generator
BER	bit error-rate
BERT	bit error-rate tester
BiCMOS	bipolar CMOS
BPF	band-pass filter
BPP	black polypropylene

BS	beam splitter
BSE	back-scattered electrons
BTE	Boltzmann transport equation
BWO	backward-wave oscillator
CB	conduction band
CCD	charged-coupled device
CD	cathodoluminescence
CDMA	code division multiple access
CMBR	cosmic microwave background radiation
CMOS	complementary metal-oxide-semiconductor
COBE	cosmic background explorer
COVID	coronavirus disease
CPS	coplanar stripline
CPU	central processing unit
CPW	coplanar waveguide
CW	continuous-wave
DBQW	double-barrier quantum well
DC	direct current
DDR4	double data rate 4
DFB	distributed feedback
DFG	difference frequency generation
DFT	density functional theory
DHBT	double HBT
DNA	deoxyribonucleic acid
DOS	density of states
DSO	digital storage oscilloscope
DSP	digital signal processing
EBL	electron-beam lithography
EBPVD	electron-beam physical vapour deposition
ECL	external cavity laser

EDFA	erbium-doped fibre amplifier
EDX	energy-dispersive X-ray spectroscopy
EF	error-free
EOAM	electro-optic amplitude modulator
EOPM	electro-optic phase modulator
EPM	empirical pseudo-potential method
ESUT	epitaxial structure under test
FD	finite difference
FDM	polarisation division multiplexing
FE	field-emission
FEC	forward error correction
FEL	free-electron laser
FEM	finite element method
FET	field-effect transistor
FIB	focused-ion beam
FIR	far-infrared
FIRAS	far-infrared absolute spectrophotometer
FL	femtosecond laser
FM	frequency modulated
FMBD	Fermi-level managed diode
FPU	field pick-up unit
FTIR	Fourier-transform infrared
FWA	fixed wireless access
GPRS	general packet radio service
GSG	ground-signal-ground
GSM	global system for mobile communications
HBT	heterojunction bipolar transistor
HBV	heterostructure barrier varactor
HEMT	high-electron-mobility transistor
HPF	high-pass filter

HSCSD	high-speed circuit-switched data
HSDPA	high-speed downlink packet access
HWP	half-wave plate
IC	integrated circuit
ICP-CVD	inductively-coupled chemical vapour deposition
IEEE	Institute of Electrical and Electronics Engineers
IF	intermediate frequency
IMPATT	impact ionization avalanche transit-time
IoT	internet of things
IPA	isopropyl alcohol
IQ	in-phase and quadrature
IQM	in-phase and quadrature imbalance
ISO	International Organization for Standardization
JWNC	James Watt Nanofabrication Centre
KGW	potassium gadolinium tungstate
LAF	laminar flow
LAN	local area network
LDOS	local density of states
LN	low-noise
LNA	low-noise amplifier
LO	local oscillator
LOP	longitudinal optical phonon
LOR	lift-off resist
LOS	line-of-sight
LPF	low-pass filter
LTE	long-term evolution
M2M	machine-to-machine
MBE	molecular beam epitaxy
MBPT	many-body perturbation theory
MDC	MICROPOSIT Developer Concentrate

MEMS	micro electro-mechanical system
MFTx	multi-format transmitter
MHEMT	metamorphic HEMT
MIBK	methyl isobutyl ketone
MID	mid-infrared
MIM	metal-insulator-metal
MIMO	multiple-input multiple-output
ML	monolayer
MLL	mode-locked laser
MMIC	monolithic microwave integrated circuit
MOVPE	metal-organic vapour phase epitaxy
MRI	magnetic resonance imaging
MW	microwave
NASA	national aeronautics and space administration
NDC	negative differential conductance
NDR	negative differential resistance
NEGF	non-equilibrium Green's function
NEMS	nano electro-mechanical system
NEP	noise equivalent power
NIR	near-infrared
NLO	non-linear optical
NLOS	non-line-of-sight
NRZ	non-return to zero
OBPF	optical band-pass filter
OFCG	optical frequency comb generation
OFDM	orthogonal frequency-division multiplexing
OOK	ON-OFF keying
OPO	optical parametric oscillator
OR	optical rectification
PA	power amplifier

PC	photo-conductor, polarisation controller, personal computer
PCA	photo-conductive antenna
PCB	printed circuit board
PD	photo-diode
PDM	polarisation division multiplexing
PDR	positive differential resistance
PER	packet error rate
PHEMT	pseudomorphic HEMT
PLL	phase-locked loop
PM	phase modulator
PMMA	polymethyl methacrylate
P-MP	point-to-multipoint
PNA	programmable network analyser
P-P	point-to-point
PPG	pulse pattern generator
PSK	phase-shift keying
PVC	polyvinyl chloride
PVCR	peak-to-valley current ratio
PVD	physical vapour deposition
QAM	quadrature amplitude modulation
QCL	quantum cascade laser
QPSK	quadrature phase-shift keying
QPSKM	quadrature phase-shift keying modulator
QTBM	quantum transmitting boundary method
QW	quantum well
QWP	quarter wave plate
R&D	research and development
RAM	random-access memory
RBT	resonant tunnelling bipolar transistor
RBW	resolution bandwidth

RES	reference epitaxial structure
RF	radio-frequency
RH	relative humidity
RHET	resonant tunnelling hot-electron transistor
RIE	reactive ion etching
RLSA	radial-line slot antenna
RO	reverse osmosis
RT	room temperature
RTD	resonant tunnelling diode
RWH	Ridley-Watkins-Hilsum
SBA	self-consistent Born approximation
SBD	Schottky barrier diode
SDRAM	synchronous dynamic random-access memory
SE	secondary electrons
SEM	scanning electron microscopy
SG	signal generator
SHM	sub-harmonic mixer
SI	semi-insulating
SLED	superlattice electronic device
SNR	signal-to-noise ratio
SOM	self-oscillating mixer
SPA	semiconductor parameter analyser
SPICE	simulation program with integrated circuit emphasis
SRTD	Schottky-collector RTD
SSB	single-sideband
SUT	sample under test
TB	triple-barrier
TbE	telecommunications, broadcasting and electronic
TCAD	technology computer-aided design
TD	tunnel diode

TDS	time-domain spectroscopy
TED	transferred-electron device
TLM	transmission line measurement
TMAH	tetramethylammonium hydroxide
TMIC	terahertz monolithic integrated circuit
TOF	time-of-flight
TUNNETT	tunnel-injection transit-time
UMTS	universal mobile telecommunications system
US	United States
UTC-PD	uni-traveling-carrier photo-diode
UV	ultra-violet
VB	valence band
VCA	virtual crystal approximation
VCO	voltage-controlled oscillator
VCSEL	vertical-cavity surface-emitting lasers
VNA	vector network analysers
VOA	variable optical attenuator
VR	virtual reality
WG	waveguide
WiMAX	worldwide interoperability for microwave access
WKB	Wentzel-Kramers-Brillouin
WLAN	wireless local area network
WPAN	wireless personal area network
WR	rectangular waveguide
WS	wave-shaper

## Measurement units

Å	angstrom
nm	nanometre
μm	micrometre
mm	millimetre
cm	centimetre
m	metre
km	kilometre
K	kelvin
meV	millielectronvolt
eV	electronvolt
Hz	hertz
kHz	kilohertz
MHz	megahertz
GHz	gigahertz
THz	terahertz
pW	picowatt
nW	nanowatt
μW	microwatt
mW	milliwatt
W	watt
fs	femtosecond
ps	picosecond
ms	millisecond
s	second
min	minute
h	hour
kg	kilogram
sr	steradian

rpm	rounds per minute
nA	nanoampere
mA	milliampere
A	ampere
kA	kiloampere
MA	megaampere
mV	millivolt
V	volt
kV	kilovolt
$\Omega$	Ohm
M $\Omega$	megaohm
mho	siemens
mS	millisiemens
fF	femtofarad
pF	picofarad
F	farad
dB	decibel
dB <sub>i</sub>	decibel (isotropic)
dB <sub>m</sub>	decibel milliwatt
pJ	picojoule
nJ	nanojoule
mJ	millijoule
GB	gigabyte
ZB	zettabyte
C	coulomb
°C	degree Celsius
pH	picohenry
nH	nanohenry
□	square
Bit/s	bit per second

Kbit/s	kilobit per second
Mbit/s	megabit per second
Gbit/s	gigabit per second
Gb/s	gigabit per second
Tbit/s	terabit per second
GS/s	gigasample per second

## Chemical symbols

$(\text{CH}_3)_2\text{CO}$	acetone
Al	aluminium
AlSb	aluminium antimonide
AlAs	aluminium arsenide
AlGaAs	aluminium gallium arsenide
AlN	aluminium nitride
Ar	argon
$\text{Ar}^+$	argon cation
As	arsenic
$\text{AsH}_3$	arsine
Cr	chromium
Ga	gallium
GaSb	gallium antimonide
GaAs	gallium arsenide
GaN	gallium nitride
Ge	germanium
Au	gold
HCl	hydrochloric acid
$\text{H}_2\text{O}_2$	hydrogen peroxide
In	indium
InAlAs	indium aluminium arsenide
InAlGaAs	indium aluminium gallium arsenide
InAs	indium arsenide
InGaAs	indium gallium arsenide
InP	indium phosphide
$\text{C}_3\text{H}_8\text{O}$	isopropyl alcohol
Hg	mercury
$\text{CH}_3\text{OH}$	methanol

Mo	molybdenum
NiCr	nichrome
N <sub>2</sub>	nitrogen
H <sub>3</sub> PO <sub>4</sub>	orthophosphoric acid
O <sub>2</sub>	oxygen
O <sub>3</sub>	ozone
Pd	palladium
Si	silicon
SiO <sub>2</sub>	silicon dioxide
SiGe	silicon germanium
SiN <sub>x</sub>	silicon nitride
Si <sub>3</sub> N <sub>4</sub>	silicon nitride
S	sulfur
CF <sub>4</sub>	tetrafluoromethane
Ti	titanium
W	tungsten
H <sub>2</sub> O	water
Xe	xenon
Yb	ytterbium

### Mathematical/physical symbols

$\hat{\mathcal{H}}$	Hamiltonian operator
$\hat{a}$	creation operator
$\hat{a}^\dagger$	annihilation operator
$\nabla$	del operator
$\xi$	complex function
$N$	test/basis function
$\{a\}$	expansion eigenvector
$\{b\}$	boundary vector
$[F]$	global stiffness matrix

$[H]$	Hamiltonian matrix
$[M]$	stiffness matrix
$[T]$	finite-elements formulation matrix
$[S]$	finite-elements formulation matrix
$p$	expansion coefficient
$\eta$	$IV$ curve degree of non-linearity
$\hat{x}$	transverse direction component versor
$\hat{y}$	transverse direction component versor
$\hat{z}$	longitudinal direction versor
$\Gamma$	first Brillouin zone high-symmetry mid-point
$X$	first Brillouin zone high-symmetry point

## Abbreviations

Tx	transmitter
Rx	receiver
TRx	transceiver
G	ground
ATT	signal attenuator

## Physical quantities

$I$	current
$i$	source current
$J$	current density
$I_c$	collector current
$I_F$	forcing current
$I_p$	peak current
$I_v$	valley current
$\Delta I$	peak-to-valley current difference
$J_p$	peak current density
$J_v$	valley current density
$\Delta J$	peak-to-valley current density difference
$I_{p,m}$	measured peak current
$J_{p,m}$	measured peak current density
$I_{v,m}$	measured valley current
$J_{v,m}$	measured valley current density
$I_{p,s}$	simulated peak current
$J_{p,s}$	simulated peak current density
$I_{v,s}$	simulated valley current
$J_{v,s}$	simulated valley current density
$\Delta J_m$	measured available current density
$\Delta J_s$	simulated available current density
$V$	voltage
$V_{ac}$	voltage amplitude
$V_b$	bias voltage
$V_{bias}$	bias voltage
$V_G$	gate voltage
$V_S$	sensing voltage
$v$	output voltage, group velocity

$V_p$	peak voltage
$V_v$	valley voltage
$\Delta V$	valley-to-peak voltage difference
$V_{p,m}$	measured peak voltage
$V_{v,m}$	measured valley voltage
$V_{p,s}$	simulated peak voltage
$V_{v,s}$	simulated valley voltage
$\Delta V_m$	measured voltage swing
$\Delta V_s$	simulated voltage swing
PVCR	peak-to-valley current ratio
$PVCR_m$	measured peak-to-valley current ratio
$PVCR_s$	simulated peak-to-valley current ratio
$R$	resistance
$R_c$	contact resistance
$\rho_c$	specific contact resistivity
$R_s$	series resistance
$R_p$	parasitic resistance
$R_{rtd}$	RTD differential resistance
$R_{c,t}$	top contact resistance
$R_{c,b}$	bottom contact resistance
$R_b$	bias line resistance
$R_{bias}$	bias line resistance
$R_{st}$	stabilising resistance
$R_e$	stabilising resistance
$R_L$	load resistance
$R_t$	total resistance
$R_{sh}$	sheet resistance
$G_{rtd}$	RTD differential conductance
$\mathcal{G}_{rtd}$	RTD differential conductance density
$\bar{G}_{rtd}$	RTD average differential conductance

$G_L$	load conductance
$Z_L$	load impedance
$Z_{in}$	input impedance
$Z_0$	characteristic impedance
$Z_{11}$	one-port impedance parameter
$Y_{rtd}$	RTD input admittance
$Y_L$	load admittance
$Y_{in}$	input admittance
$S_{11}$	input reflection coefficient
$S_{21}$	forward transmission coefficient
$C$	capacitance
$C_p$	parasitic capacitance
$C_{rtd}$	RTD capacitance
$\mathcal{C}_{rtd}$	RTD capacitance density
$\bar{C}_{rtd}$	RTD average capacitance
$C_d$	RTD self-capacitance (depletion capacitance)
$C_{dc}$	decoupling capacitance
$C_{stab}$	decoupling capacitance
$C_e$	decoupling capacitance
$Q_c$	collector charge
$L$	inductance, length
$L_s$	series inductance
$L_{min}$	minimum inductance
$L_p$	parasitic inductance
$L_{qw}$	QW inductance
$\mathcal{L}_{qw}$	QW inductance density
$IL$	insertion loss
$\delta$	skin depth
$\sigma$	wet etching later undercut
$\theta$	extraction angle

$B$	brightness
$T$	temperature
$W$	width
$S$	width
$d$	link distance, metal patch length
$l$	length, transmission line length
$l_{max}$	maximum transmission line length
$w$	signal line width, metal patch width
$g$	gap width
$s$	ground line width
$l_t$	transfer length
$A_{eff}$	contact effective area
$A_b$	bottom contact area
$A$	RTD (top) mesa area
$A_{max}$	maximum RTD area
$U$	electrostatic potential energy
$V_H$	Hartree potential
$E$	energy
$E_1$	first quasi-bound state energy level
$E_2$	second quasi-bound state energy level
$E_F$	Fermi level
$E_{Fn}$	quasi-Fermi level
$E_c$	CB edge
$\Delta E_c$	CB offset
$E_g$	energy band gap
$\Delta E$	energy difference
$N$	states number, number of elements
$Q$	quality factor
$\Gamma$	full-width at half maximum
$N_D$	doping concentration (donors)

$N_{D,ls}$	lightly-doped spacer doping concentration (donors)
$\tau$	time constant
$\beta$	relaxation time constant, phase constant
$\tau_{dbqw}$	DBQW quasi-bound state lifetime
$\tau_e$	QW-to-emitter escape time constant
$\tau_c$	QW-to-collector escape time constant
$v_c$	QW-to-collector escape rate
$\tau_{in}$	intrinsic delay time
$\tau_t$	intrinsic transit time
$\tau_{rd}$	total delay time
$\tau_{ex}$	extrinsic delay time
$\tau_r$	relaxation time
$f$	frequency, focal length
$f_c$	carrier frequency, cut-off frequency
$f_{THz}$	carrier frequency
$f_{max}$	maximum oscillation frequency
$f_{in}$	intrinsic cut-off frequency
$f_{op}$	operation frequency
$f_{osc}$	oscillation frequency
$\omega$	angular frequency
$\omega_0$	fundamental mode
$\omega_{op}$	operation angular frequency
$\lambda$	wavelength
$\lambda_0$	free-space wavelength
$\lambda_{osc}$	radiation wavelength
$\lambda_{op}$	operation wavelength
$t$	time, thickness
$t_b$	barrier thickness
$t_{qw}$	quantum well thickness
$t_{ls}$	lightly-doped spacer thickness

$t_d$	equivalent depletion regions thickness
$\epsilon_{r,0}$	relative static dielectric constant
$\epsilon_{r,\infty}$	relative dielectric constant infinite limit
$\epsilon_{r,eff}$	relative effective permittivity
$\epsilon_{d,0}$	equivalent static dielectric constant
$v_{e,s}$	electron saturation velocity
$\mu_{e,l}$	low-field electron mobility
$n_r$	refractive index
$P_T$	transmitting power
$G_T$	transmitting antenna gain
$G_R$	receiving antenna gain
$P_{RF}$	RF power
$P_{RF,max}$	maximum RF power
$P_{RF,max,tot}$	total maximum RF power
$P_{RF,max,m}$	maximum RF power estimated from measured quantities
$P_{RF,max,s}$	maximum RF power estimated from simulated quantities
$P_{RF,out}$	output power
$P_t$	transmitted power
$\mathcal{P}_{RF}$	RF power density
$\mathcal{P}_{RF,max}$	maximum RF power density
$\mathcal{P}_{RF,in}$	intrinsic RF power density
$\mathbf{z}$	longitudinal direction vector
$\mathbf{r}_T$	transverse direction vector
$\mathbf{r}$	overall spatial direction vector
$x$	transverse direction component modulus, molar fraction
$y$	transverse direction component modulus, molar fraction
$z$	longitudinal direction modulus
$r$	overall spatial direction modulus
$\mathbf{k}$	wave-vector
$k$	wave-vector modulus

$p$	wave-vector modulus
$\rho$	wave-vector modulus
$\mathbf{p}$	momentum
$\psi$	wave-function
$ \psi\rangle$	quantum state
$\phi$	envelope function
$\varphi$	wave-function transverse component
$m_e^*$	electron effective mass
$m_v^*$	VB DOS effective mass
$n_{2D}$	QW sheet electron density
$n$	electron density
$n_i$	intrinsic carrier concentration
$g_{2D}$	QW DOS
$f_n$	Fermi-Dirac distribution function
$\mu$	electrochemical potential
$N_c$	CB effective DOS
$N_v$	VB effective DOS
$\chi_e$	electron affinity
$M$	number of equivalent energy minima
$\mathcal{T}$	transmission coefficient
$\mathcal{T}_b$	single-barrier transmission coefficient
$\mathcal{T}_{DBQW}$	DBQW transmission coefficient
$G$	correlation/Green's function
$G^R$	retarded Green's function
$G^A$	advanced Green's function
$G_n$	(electron) correlation/Green's function
$G^<$	correlation/lesser Green's function
$G^>$	correlation/greater Green's function
$G^p$	(hole) correlation/Green's function
$\Sigma$	self-energy

$\Sigma^R$	retarded self-energy
$\Sigma^A$	advanced self-energy
$\Sigma^{R,B}$	retarded boundary self-energy
$\Sigma^{R,A}$	retarded advanced self-energy
$\Sigma^{R,S}$	retarded scattering self-energy
$\Sigma^<$	correlation/lesser self-energy
$\Sigma^{<,B}$	correlation/lesser boundary self-energy
$\Sigma^{<,S}$	correlation/lesser scattering self-energy
$\Sigma^>$	correlation/greater self-energy
$\Sigma^{>,B}$	correlation/greater boundary self-energy
$\Sigma^{>,S}$	correlation/greater scattering self-energy
$\Sigma^{in}$	in-scattering function
$\Sigma^{out}$	out-scattering function
$\Gamma^B$	boundary broadening function
$\mathcal{A}$	spectral function

## Physical constants

$k_B$	Boltzmann constant	$\sim 8.617 \times 10^{-5} \text{ eV/K}$
$h$	Planck constant	$\sim 4.136 \times 10^{-15} \text{ eV/Hz}$
$\hbar$	normalised Planck constant	$\sim 6.582 \times 10^{-16} \text{ eV/Hz}$
$c$	vacuum speed of light	$\sim 2.998 \times 10^8 \text{ m/s}$
$e$	elementary charge	$\sim 1.602 \times 10^{-19} \text{ C}$
$\epsilon_0$	vacuum dielectric constant	$\sim 8.854 \times 10^{-12} \text{ F/m}$
$m_0$	electron rest mass	$\sim 9.109 \times 10^{-31} \text{ kg}$

# Overview

## Aims and objectives

Because of its intrinsic potential, the resonant tunnelling diode (RTD) has lately been sparking great interest among the scientific community and industry as possible leader technology aimed at emitting and detecting terahertz (THz) radiation in the near future, and this could provide with the required technological breakthrough in numerous application contexts. The aim of this work is to contribute to the swiftly advancing field of THz RTD technology by proposing device simulation and design methodologies aimed at maximising the output power capabilities of RTD THz oscillator sources working in the 300-GHz band, which are unavailable to date.

## Achievements and contributions to the field

The main achievements of this work are listed in the following:

- a) a low computational load numerical simulation method based on the non-equilibrium Green's function (NEGF) formalism provided in Silvaco Atlas technology computer-aided design (TCAD) simulation package is proposed to accurately simulate the static current-voltage ( $IV$ ) characteristic of indium gallium arsenide/aluminium arsenide ( $\text{In}_{0.53}\text{Ga}_{0.47}\text{As}/\text{AlAs}$ ) double-barrier RTDs lattice-matched to indium phosphide (InP) substrates. Through the accurate selection of physical models and materials parameters, as well as by suitably discretising the RTD heterostructure employing the finite element method (FEM), it is demonstrated, through a comprehensive analysis involving simulation data and experimental results, that the developed simulation approach can accurately retrieve the peak current density, peak voltage, and the negative differential resistance (NDR) region valley-to-peak voltage difference of the device DC  $IV$  curve, which are key quantities in the design of high-power RTD oscillators working at 300 GHz.
- b) a comprehensive device design analysis is then conducted employing the developed simulation methodology, investigating how epitaxial layers design, including double-barrier quantum well (DBQW), and emitter and collector extended leads spacer lay-

ers, influence the electrical characteristic of the RTD device. The results are analysed and discussed in terms of the retrieved outputs, including the heterostructure band diagram, transmission coefficient energy spectrum, charge density, and static current density-voltage ( $JV$ ) characteristic. General design guidelines aimed at maximising the maximum radio-frequency (RF) power of the RTD device are then derived and discussed.

- c) to practically-demonstrate the proposed design methodology, a pseudomorphically-grown lattice-matched to InP  $\text{In}_{0.53}\text{Ga}_{0.47}\text{As}/\text{AlAs}$  double-barrier RTD epitaxial structure delivering high RF power was carefully designed through the proposed simulation method, and experimentally investigated by fabricating and subsequently characterising RTD devices by means of both DC and RF measurements to 110 GHz. The results, which include microfabrication optimisation, show an expected RF power of up to around 5 mW and 10 mW for  $25 \mu\text{m}^2$  and  $49 \mu\text{m}^2$ -large devices, respectively, at 300 GHz oscillation frequency, which is up to five times higher compared to current-state-of-the-art results. In the end, both coplanar waveguide and microstrip distributed inductors are accurately designed through three-dimensional electromagnetic simulations to prove the practical employability of the proposed RTD devices in oscillator circuits fabricated using standard photo-lithography.

Overall, the results achieved in this work suggest the practical viability of high-power InP RTD devices delivering 5–10 mW of RF power at around 300 GHz operation frequencies. Therefore, RTD THz sources capable of several milliwatt of output power at around 300 GHz carrier waves can be achieved if proper oscillator circuit/antenna design methodologies are developed.

## Outline

The document is organised as following.

Chapter 1 introduces to the dissertation work by providing general knowledge on THz radiation, technology, and applications, while Chapter 2 gives an overview on the THz RTD device. These provide with the required insight needed to properly understand the context of the work and explain its motivations, and define the concepts needed to explain and justify it.

Chapter 3 describes the work conducted in clean-room, including the fabrication of the RTD devices and transmission line measurement test structures for the extraction of the associated contact resistance, while Chapter 4 presents the developed simulation approach and the experimental work carried out for its demonstration.

Chapter 5 includes the RTD epitaxial structure simulation study and discusses about device design guidances for high-power operation in the 300-GHz band, while Chapter 6 presents a high-power RTD epitaxial structure and its experimental investigation, as well as designed RF inductive stubs for 300-GHz oscillators.

In the end, Chapter 7 concludes with final considerations and discusses about future perspectives.

# Chapter 1

## Terahertz radiation: technology and applications

This Chapter aims at introducing the reader to the work by providing general concepts on terahertz radiation, technology, and related applications, with a specific focus on terahertz sources for ultra-high-speed wireless data-links. It begins with general considerations and brief historical notes on the terahertz spectrum, to then continue with an overview of both photonic- and electronic-based terahertz emitters. Applications are then briefly discussed, including terahertz imaging and spectroscopy apparatuses, together with a survey on next-generation multi-gigabit terahertz wireless communications.

### 1.1 The terahertz spectrum

Terahertz (THz) science is a relatively young research area whose applicability started to be investigated in astronomy and related sub-fields during the 1970s in the development of radio telescopes [1]. Indeed, it has been estimated that around 98 % of the total amount of photons emitted in the entire universe history since the Big Bang belongs to this frequency range [2].

By definition, THz radiation is referred as the part of the electromagnetic spectrum which covers the middle ground frequency window  $0.1 \text{ THz} \leq f \leq 10 \text{ THz}$  [3], corresponding to free-space wavelengths  $30 \mu\text{m} \leq \lambda_0 \leq 3 \text{ mm}$ , and overlapping millimetre-waves (mm-waves) ( $30 \text{ GHz} \leq f \leq 300 \text{ GHz}$ ,  $1 \text{ mm} \leq \lambda_0 \leq 1 \text{ cm}$ ) [4] and far-infrared (FIR) light ( $0.3 \text{ THz} \leq f \leq 20 \text{ THz}$ ,  $15 \mu\text{m} \leq \lambda_0 \leq 1 \text{ mm}$ ) [5] ranges, as schematically illustrated in Figure 1.1.

The main interest was detecting and analysing the oldest form of existing electromagnetic radiation, known as cosmic microwave background radiation (CMBR) [6], which consists of a background electromagnetic noise that isotropically permeates the whole space [7]. Discovered in 1965 [7], its origin dates back to the epoch of recombination, and it can be considered a land-

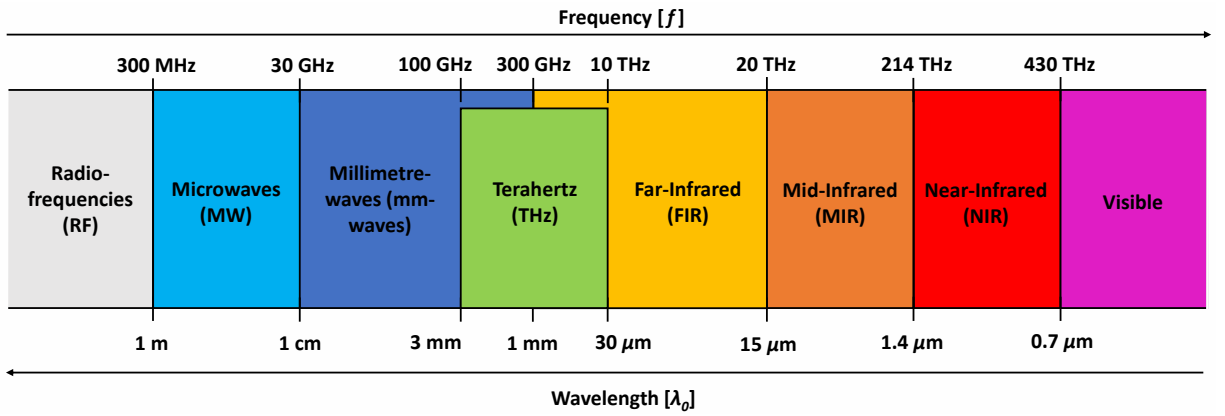


Figure 1.1: Electromagnetic spectrum frequency bands ranging from the upper bound of radio-frequencies (RF) ( $f < 300$  MHz,  $\lambda_0 > 1$  m) to the lower bound of visible light ( $f > 430$  THz,  $\lambda_0 < 0.7 \mu\text{m}$ ), including microwaves (MW), mm-waves, and FIR, mid-infrared (MIR), and near-infrared (NIR) light.

mark evidence of the Big Bang and, more generally, of the birth of the entire universe, and so a major source of data regarding the early stages of its formation [8].

A preliminary measurement of the CMBR was carried out in 1990 by the National Aeronautics and Space Administration (NASA) employing the FIR absolute spectrophotometer (FIRAS) aboard the cosmic background explorer (COBE) satellite [9]. In that occasion, it was discovered that the CMBR spectral radiance follows Planck's law of the black-body radiation [10]:

$$B \approx \frac{2hf^3}{c^2} \left[ \exp\left(\frac{hf}{k_B T}\right) - 1 \right]^{-1} \quad (1.1)$$

where  $B$  is the brightness,  $h$  the Planck constant,  $c$  the speed of light in vacuum,  $k_B$  the Boltzmann constant, while  $T$  the absolute temperature, featuring strong photon intensity in the lower THz limit (with peak around 160 GHz), as shown in Figure 1.2.

The successful detection of the CMBR led to a progressively growing interest in the THz range within the fields of cosmology and astrophysics, and it became, therefore, crucial to advance towards more sensitive antennas and radio receivers (Rx) capable to operate in this frequency window, which had been mentioned in the scientific literature already since the mid-1920s [11]. At the same time, due to its peculiar position within the electromagnetic spectrum, THz radiation started to gain great attention in the context of other research fields, with targeted applications including telecommunications, imaging, and spectroscopy [12].

However, due to the technological immaturity, this frequency band was originally nicknamed "THz gap", which was caused by the lack of systems able to reliably operate at frequencies which bridge between conventional electronics and photonics, including sources featuring suit-

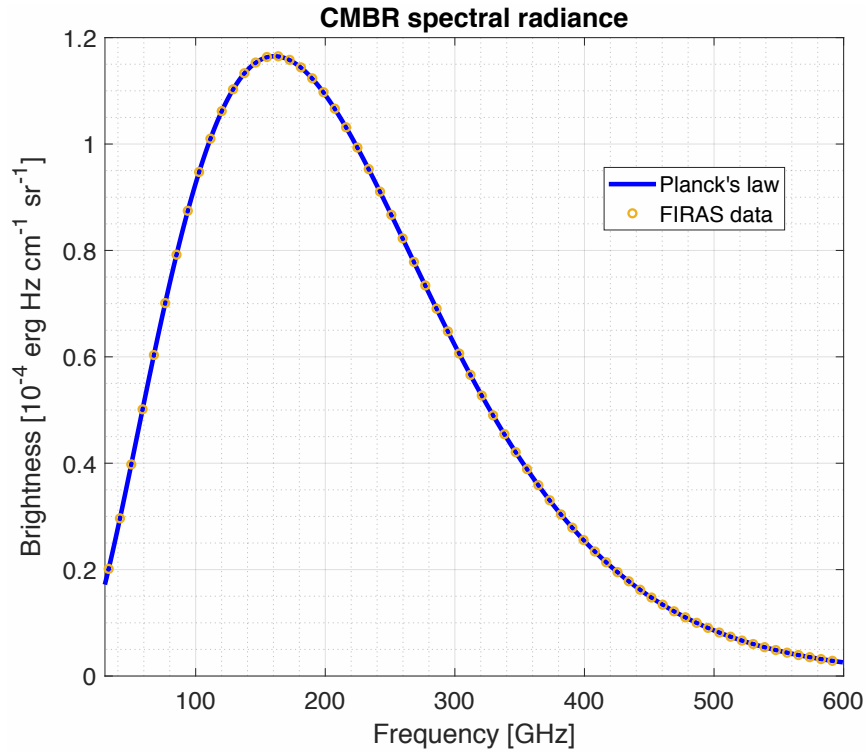


Figure 1.2: CMBR spectral radiance in the range 30–600 GHz (reproduced from [9]). The orange void dots represent the measured data captured by the FIRAS, while the solid blue line models the black-body radiation spectrum through Planck’s law at  $T = 2.735 \pm 0.06$  K.

able power levels and high-sensitivity detectors [13]. Indeed, although the THz spectral region had already been included in the internationally-recognised frequency bands at the end of the 1940s [14], its exploration had almost been entirely restricted to space-oriented applications due to the relatively strong signal losses experienced in the middle and lower portions of the atmosphere [15] caused by the high concentration of water ( $\text{H}_2\text{O}$ ) and oxygen ( $\text{O}_2$ ) molecules which are highly sensitive to THz waves. This will be discussed more in detail later on in this Chapter.

Nevertheless, starting with the development of mode-locked femtosecond lasers (FL) and photo-conductors (PC)/photo-conductive antennas (PCA) between the late 1980s and beginning of 1990s [16, 17], progressively increasing research efforts have been devoted to the technological advance, which have helped in the closure of the gap and allowed for the practical development of reliable THz emitters, detectors, antennas, and quasi-optical systems, paving the way for the future applicability of emerging THz technology [18, 19].

## 1.2 Terahertz sources

With the exception of very large-size systems, including gyrotrons [20] and synchrotrons [21], artificial THz sources can be divided in two main categories: 1) photonic; and 2) electronic [22].

### 1.2.1 Photonic THz sources

Photonic-based THz sources can naturally generate THz radiation or rely on optical-to-THz down-conversion approaches [23, 24]. In the first case, typical examples include optically-pumped molecular gas lasers [25, 26], solid-state impurity-doped  $p$ -type germanium (Ge) and  $n$ -type silicon (Si) lasers [27–29], and III-V/IV semiconductor-based quantum cascade lasers (QCL) [30–33].

While  $p$ -type Ge lasers typically work at extremely low temperatures  $T < 20$  K and generate high-output power ranging from the milliwatt to the watt level in the 1–4 THz frequency interval operating in pulsed mode [34], THz QCLs can usually operate up to around 250 K [35–37] and approximately in the range 1–5 THz [38, 39], but require strong external magnetic fields and vacuum conditions [40, 41], providing output powers of up to few hundreds of milliwatt in continuous-wave (CW) regime, and up to the watt range in pulsed mode [42, 43]. Although room temperature (RT,  $T = 300$  K) operation has been recently demonstrated [44], these systems are only at the first stages of their development.

In the second case, THz radiation is generated by employing optically-fed non-linear photonic devices, including non-linear optical (NLO) crystals [45] (as in optical rectification (OR) [46], difference frequency generation (DFG) [47], or optical parametric oscillators (OPO) [48]), photo-conductive emitters [49, 50], and high-speed photo-diodes (PD) [51, 52]. The photonic input signals are typically provided through pulsed FL-based sources [53] or, alternatively, through optical frequency comb generation (OFCG) by employing CW infrared laser diodes, such as distributed feedback (DFB) lasers [54–56], vertical-cavity surface-emitting lasers (VCSEL) [57], and QCLs [58], phase modulators (PM), and low-frequency local oscillators (LO) [59, 60]. More exotic solutions [61] include those based on spintronic multi-layers [62] and laser-filament-induced plasmas [63].

In this context, the uni-traveling-carrier photo-diode (UTC-PD) [64, 65] has attracted great interest for the generation of THz carrier signals in photonic-based THz transmitters (Tx) [66]. Proposed by Ishibashi *et al.* in 1997 [67, 68], the device working principle consists in optically mixing selected input infrared laser emission lines, known as to photo-mixing [69], where the output signal, known as THz "beat note", is the result of the difference of the input lines frequencies [70]. The optical-to-THz heterodyne down-conversion process based on DFG relies on second-order non-linear optical properties (susceptibility) which characterise the employed semiconductor materials at relatively high-input optical fields [71].

Figure 1.3a shows the band diagram of an UTC-PD device under forward bias [72, 73]. The semiconductor-based active region consists of a heavily-doped  $p$ -type narrow band gap absorp-

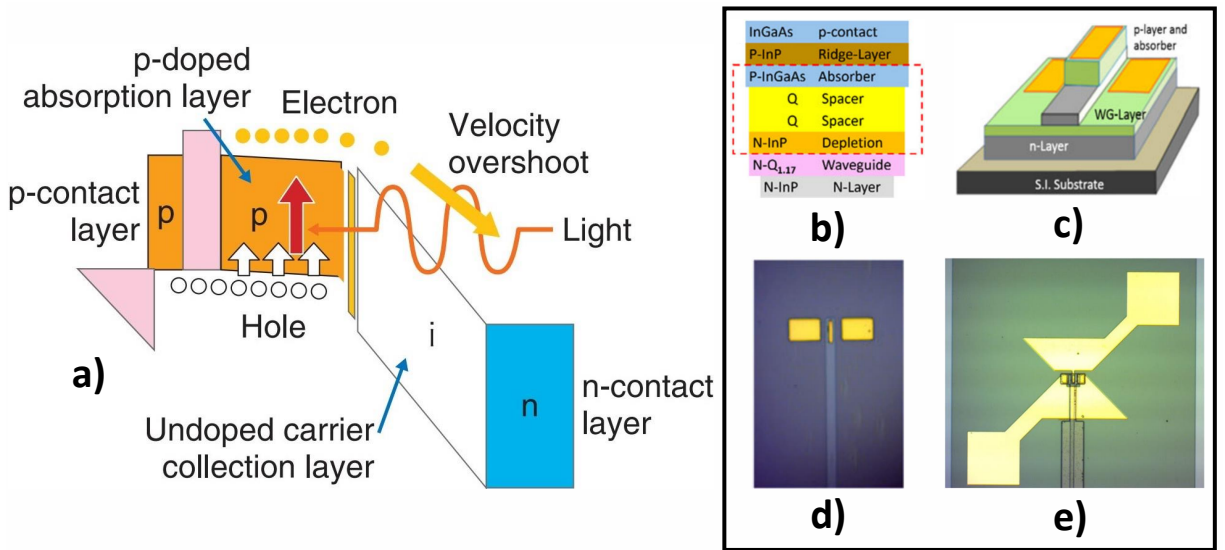


Figure 1.3: In a), schematic of the typical band diagram of an UTC-PD device under forward bias (adapted and reprinted from [72]); in b) to e), schematics of the layer structure and device layout, together with photo-micrographs of the fabricated device and complete module, respectively, of the InP antenna-integrated CW UTC-PD THz photo-mixer source reported in [70] (adapted and reprinted from [70]).

tion layer, typically made of indium gallium arsenide (InGaAs), and of an undoped, or  $n$ -type lightly-doped, wide band gap carrier collection layer, usually indium phosphide (InP)-based.

Upon light illumination and electron-hole pairs generation, the photo-generated majority holes in the quasi-neutral absorption layer quickly relax (being the dielectric relaxation time in  $p$ -type InGaAs as low as few tens of femtoseconds [74]) and diffuse towards the  $p$ -type contact (anode), while they are blocked by the carrier collection layer (a cliff layer might be added). On the other hand, the photo-generated minority electrons (mostly) diffuse into the depleted collection layer, while they are blocked by a wide band gap layer placed in between the absorption layer and the anode, and then drift towards the  $n$ -type contact (cathode) thanks to the built-in electric field and applied DC bias, taking advantage of velocity overshoot ("quasi-ballistic" transport [23]). The AC electrical signal arising across the device thanks to DFG is then fed to an on-chip/external antenna and THz radiation is emitted.

Several are the advantages of UTC-PDs versus conventional  $p$ - $i$ - $n$  devices. First, the response time of an UTC-PD is uniquely determined by high-velocity electron transport and mainly limited by the minority electrons diffusion time across the moderately-thick absorption layer (while both electrons and holes contribute to the operation of  $p$ - $i$ - $n$  PDs and low-velocity hole transport determines the associated frequency response), resulting in higher operational speed. Indeed, the InP electron saturation velocity is up to one order of magnitude higher than holes [75], so that electron transport through the carrier collection layer takes place at a superior speed, and

even beyond saturation thanks to velocity overshoot.

At the same time, although diffusion is generally considered slower than drift, the electron diffusion velocity in *p*-type InGaAs can be as high as around  $10^7$  cm/s in common operating conditions [76]. Furthermore, the associated diffusion time can be minimised by means of accurate design optimisation of the absorption layer (thickness, doping grading, etc.) [73]. Here, a thin absorption layer can be effectively adopted to attain ultra-fast operation by minimising the associated electron transit-time without sacrificing the device *RC* constant (i.e., switching speed) (where *R* and *C* are the associated resistance and capacitance, respectively) since, differently from standard *p-i-n* devices, depletion and absorption layers can be designed independently.

Another advantage resides in the higher output saturation current density (around one order of magnitude) at high-input optical fields due to the weaker space charge effects (i.e., reduced electric field degradation) within the absorption layer caused by electron-only operation and associated velocity overshoot, which widens the device range of linearity. Consequently, the high-speed/high-output power operation of the UTC-PD becomes possible at reduced or even zero (relying on the intrinsic built-in electric field only) bias voltage because velocity overshoot can take place at relatively lower electric fields, reducing power consumption and thermal dissipation, increasing efficiency, reducing cost, and improving reliability.

UTC-PDs can operate in CW regime at RT, and have proven to work well above 1 THz [64] (and up to around 4.5 THz [65]) with output powers up to the microwatt range, and beyond 1 mW at around 300 GHz, in InP technology [77]. Figures 1.3b to e show an example of InP UTC-PD photo-mixer module integrated with a planar bow-tie antenna for CW THz emission [70]. The device features a ridge-like absorption layer combined with a shallow optical waveguide structure to couple the optical input, and was able to generate output powers of 1 mW at 100 GHz and of few tens of nanowatt at 2.5 THz.

### 1.2.2 Electronic THz sources

On the electronic side [78], both vacuum [79] and solid-state [80] sources have been investigated. The former include backward-wave oscillators (BWO) [81, 82], which have proven to work above 1 THz and provide output powers in the watt range [83], and extended-interaction klystrons [84], traveling-wave tubes [85], and free-electron lasers (FEL) [86, 87], which can generate high-output power of up to tens of watt at several terahertz. However, these systems are bulky, costly, and necessitate of highly-strict operating conditions to correctly function, including cryogenic cooling and reduced pressure.

On the other hand, solid-state semiconductor-based electronic devices provide relatively

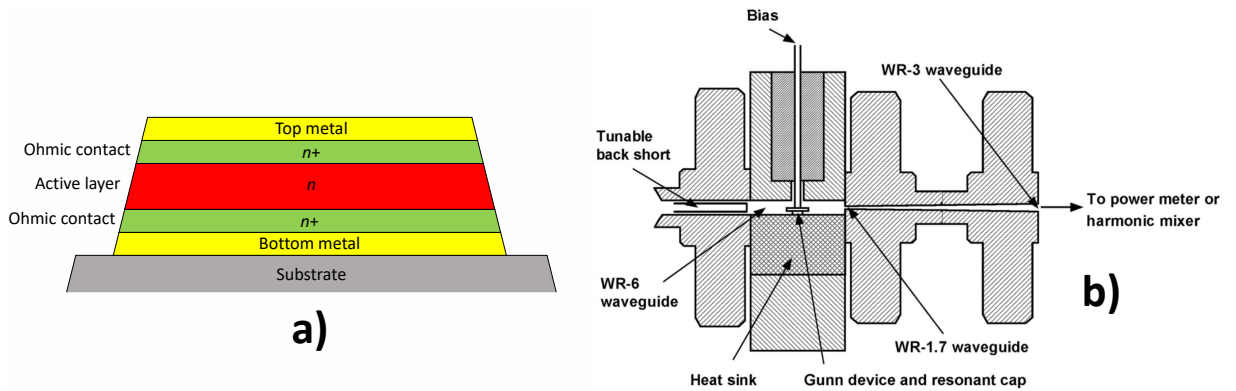


Figure 1.4: In a), schematic of a typical Gunn device mesa; in b), schematic of the waveguide-based oscillator cavity in InP Gunn technology reported in [106, 108] aimed at third-harmonic power extraction in the 400–500 GHz range (reprinted from [106]).

compact, cost-effective, and RT solutions capable of CW THz wave generation [18, 19]. Indeed, the progressive advancement of semiconductor technology over the last few decades has led to a tremendous boost in the frequency performance of solid-state sources. For example, two-terminal negative differential resistance (NDR) transit-time devices, such as tunnel-injection transit-time (TUNNETT) [88–90] and impact ionization avalanche transit-time (IMPATT) [91, 92] diodes, as well as superlattice electronic devices (SLED) [93, 94], have all shown to reliably operate at several hundreds of gigahertz [95–97].

The same applies to the transferred-electron device (TED) or Gunn diode [96], which takes the name from the homonymous physicist who discovered the effect associated to its operation in 1963 [98]. The physical mechanism is mainly described by the Ridley-Watkins-Hilsum (RWH) theory [99], which consists in the transfer of hot electrons from the active region conduction band (CB) valley with low effective mass and high mobility to one or more satellite upper valleys with higher effective mass and lower mobility, which is the case of many semiconductor materials with proper band structure, including gallium arsenide (GaAs) [100], InP [101], and gallium nitride (GaN) [102].

Figure 1.4a shows the typical structure of a Gunn device, mainly consisting of an  $n$ -type bulk active layer. At low electric fields, electrons stay in the lower valley and the device behaves ohmically (positive resistance). However, when the electric field overcomes a threshold value (material-dependent), electrons are promoted from the lower to the upper valley/s, giving rise to negative differential mobility and drift velocity drop, which makes the electron distribution across the device unstable and leads to a charge layer formation (domain). If the rate of transfer is high enough, current density decreases with increasing voltage, i.e., NDR [96].

The device frequency response mainly depends on the active region length and electron den-

sity. In this sense, due to the bulky nature of the diode, the dielectric relaxation time imposes fundamental physical limits to the maximum operating frequencies of Gunn devices with thin active layers. In GaN, the negative differential drift velocity instability can also be caused by negative effective mass mechanisms [103]. As a result of domain formation, a spatial electric field unbalance rises across the device and generates AC current pulses towards the anode. The material domain RF power release is then employed for noise energy amplification within the bandwidth characterising the employed resonator, resulting in sustained oscillations.

While IMPATT devices can provide relatively high RF power of several tens, and up to few hundreds, of milliwatt below around 200 GHz [91, 104] but suffer from the high phase noise due to the random nature of avalanche breakdown processes [105], Gunn diodes are characterised by better spectral purity and, similarly to TUNNETT devices (who have shown to work up to around 0.7 THz [88]), can work at higher frequency (up to around 0.5 THz [106]), providing several milliwatt of output power [102]. However, they suffer from thermal dissipation and related instability due to the high operating voltages [101, 107].

Figure 1.4b shows the schematic of a reported InP Gunn diode-based THz oscillator [106, 108]. The device features graded doping profile for enhanced performance, was mounted on a diamond-based heat sink to ensure thermal stability, and was embedded in a resonant-cap full-height waveguide-based cavity resonator, where a tunable back-short was adopted to tune the oscillation frequency and maximise the oscillator output power. The system was able to provide around 0.3 mW at 412 GHz, and around 0.1 mW at 479 GHz in the third-harmonic mode.

Although CW milliwatt-level output power operation in the 100 – 300 GHz frequency window has been already demonstrated employing either Si IMPATT [91], GaAs TUNNETT [109], InP Gunn [101, 110–112], and gallium arsenide/aluminium arsenide (GaAs/AlAs) SLED [93] technologies, these systems rely on inefficient waveguide cavity-based RF power extraction approaches, and are usually characterised by high DC power consumption (typically in the watt range), which unavoidably increase complexity, cost, and lowers the DC-to-RF conversion efficiency of the system typically well below 1 % above 300 GHz [101, 106]. At the same time, they suffer from thermal management issues and are generally incompatible with monolithic microwave integrated circuit (MMIC) technology, with the exception of planar Gunn diode-based oscillators [100, 113], which generally feature lower DC power consumption in the milliwatt range [114].

Furthermore, Schottky barrier diode (SBD) [115, 116] and heterostructure barrier varactor (HBV) diode [117, 118] frequency multipliers have proven to work as high as around 2.7 THz (27th harmonic) in GaAs technology [119], and generate up to around 2 mW of CW RF power at

1 THz [120]. Despite that, the inefficient circuitry dramatically lowers the DC-to-RF conversion efficiency, which is typically as low as  $10^{-3}$  % above 2.5 THz [121]. At the same time, being passive components, they require proper RF inputs, which limits these systems to be employed as terahertz up-conversion stages of lower frequency LO sources.

At the same time, three-terminal devices [122–124] are also making significant progresses in operation frequency thanks to the co-employment of high-mobility materials and scaling strategies [125]. While Si-based complementary metal-oxide-semiconductor (CMOS) field-effect transistor (FET) [126, 127], and silicon germanium (SiGe) heterojunction bipolar transistor (HBT) and bipolar CMOS (BiCMOS) [128, 129], technologies have attained maximum oscillation frequencies  $f_{max}$  of up to around 450 GHz [130] and 720 GHz [131], respectively, InP HBTs and double HBTs (DHBT) [132–134], and high-electron-mobility transistors (HEMT) [135], including pseudomorphic (PHEMT) [136] and metamorphic (MHEMT) designs [137], have shown values as high as 1.2 THz [138] and of up to 1.5 THz [139], respectively.

Therefore, it is clear that available transistor technologies can underpin terahertz monolithic integrated circuit (TMIC) sources realisations. Indeed, TMIC voltage-controlled oscillators (VCO) have shown to work at around 300 GHz in the fundamental mode [140], 430 GHz in the second harmonic [141], and 540 GHz in the third harmonic [142], with operation frequencies of up to around 850 GHz [143, 144] and milliwatt output power in the 0.3–0.9 THz range [145, 146] only enabled by extremely complex Tx designs, employing differential Colpitt [141, 147], cross-coupled [142, 148], buffer-feedback [149], or series-tuned [150] topologies, and including frequency multiplication chains, push-push/triple-push operation, sub-harmonic RF amplification stages, up-conversion mixers, and array configurations [139, 151–161], which inevitably lower the DC-to-RF conversion efficiency significantly below 1% above 300 GHz [143, 146] and make these systems complex and cumbersome. Moreover, they are usually characterized by higher phase noise compared to two-terminal NDR devices [162].

Resonant tunnelling diodes (RTD) have also been proposed and developed to build up THz emitters [163, 164]. Born as evolution of the Esaki tunnel diode (TD) [165], which typically works up to the X-band (8–12 GHz) due to the high associated capacitance [166, 167], the RTD is the fastest demonstrated solid-state semiconductor-based electronic device operating at RT, capable to drive oscillators whose fundamental oscillation frequency has already approached around 2 THz [168], and whose output power has reached the milliwatt level in the J-band (220–325 GHz) [169]. Since this device is the focus of this work, a comprehensive presentation of THz RTDs, including historical notes, operating principle, modelling, technology, as well as state-of-the-art RTD THz oscillators and detectors, Tx, Rx, and transceiver (TRx) systems, and associated short-range wireless data-links, is presented in Chapter 2.

More exotic sources include cryogenic Josephson's junctions-based devices [170–172], as well as those based on Bloch oscillations [173] and plasmonic resonances [174, 175].

### 1.2.3 Consumer-oriented THz solid-state integrated sources: state-of-play

Due to the progressive growing interest in next generation multi-gigabit wireless communication and high-resolution imaging/spectroscopy applications, the research community is nowadays focused towards the development of compact, low-cost, low-power, CW, and RT THz sources and detectors. On the emitters side, although several are the candidates, the most promising solid-state integrated technologies are semiconductor-based UTC-PDs, transistors, and RTDs.

Figure 1.5 shows the RF power versus operation frequency performance of some of the most relevant THz UTC-PD-based photo-mixers, transistor-based TMICs, and RTD-based oscillators working between 0.2–2 THz among those reported in the literature. As can be noticed, all three technologies can provide output powers up to the milliwatt threshold in the 300-GHz band ( $\sim 275$ – $325$  GHz [176]), while both UTC-PD- and RTD-based emitters have also demonstrated to operate above 1 THz, with associated output powers of up to few microwatt.

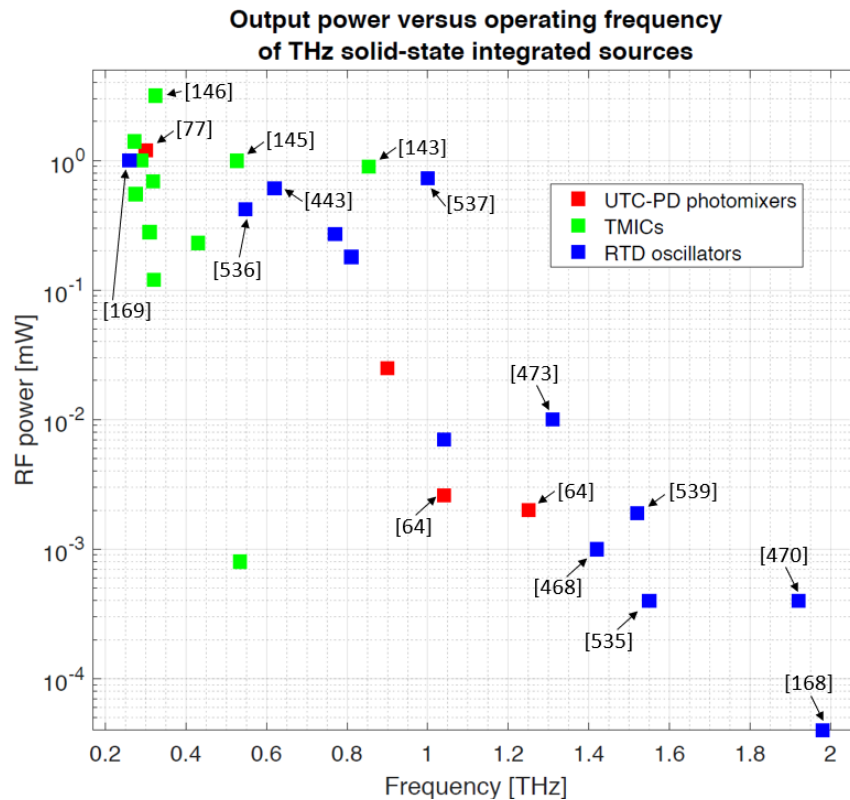


Figure 1.5: RF power versus operation frequency of THz solid-state integrated sources, including UTC-PD-based photo-mixers, transistor-based TMICs, and RTD-based oscillators in the 0.2–2 THz range, outlining some of the most relevant results reported in the literature. Reference number is provided for key results.

In this context, RTDs feature several advantages with respect to the other two technologies. Compared to UTC-PD photo-mixers, RTD THz oscillators do not require any external input laser diode source, LO, or optical component, such as modulators, filters, and combiners, since all the circuit elements are monolithically fabricated and integrated on the same chip, reducing production costs, and increasing compactness. At the same time, differently from transistor-based TMICs, they are characterised by relatively uncomplex circuit topologies and do not require any frequency multiplication or RF power amplification stage, but only a DC power supply, which drastically reduces fabrication complexity, cost, and increases integrability.

## 1.3 Terahertz applications

New and continuous advances in THz technology have made the previously unused frequency window exploitable in the context of different unexplored application scenarios, including high-resolution THz imaging and spectroscopy, and ultra-broadband THz wireless communications.

### 1.3.1 High-resolution THz imaging and spectroscopy

THz radiation features several properties that make it suitable for various novel high-resolution sensing applications [177, 178]. First, it is mostly transparent to common electrically-insulating mediums, including plastics [179], ceramics [180], paper [181], cardboard [182], woods [183, 184], and fabrics [185], meaning that THz signals can penetrate through and propagate with minimal attenuation, while it is reflected by conductive materials, such as metals and heavily-doped semiconductors [186].

At the same time, it is characterised by sub-millimetre (sub-mm) wavelength, which allows to acquire highly-defined two-dimensional (2D) images of samples/targets, and even sections or complete three-dimensional (3D) scans of objects (in which is known as THz tomography [187]) where higher-spatial resolution compared to current standard MW-based techniques is required [188]. Furthermore, it is non-ionizing, since THz photons energy is of the order of few millielectronvolt only [189], which makes it harmless towards biological material [190].

Since the development of THz time-domain spectroscopy (THz-TDS) and the demonstration of the first THz imaging apparatus in the middle of the 1990s [191], these properties have opened to new and innovative opportunities in the context of several scientific fields, including biology [14], medical diagnostic [192], and security screening [193]. For instance, non-invasive analysis of biological tissues [194], as well as in-vivo diagnosis of tumours and cancer cells [195, 196], become possible at relatively low-cost without the need of employing expensive magnetic resonance imaging (MRI) systems or resorting to standard in-vitro analysis, since

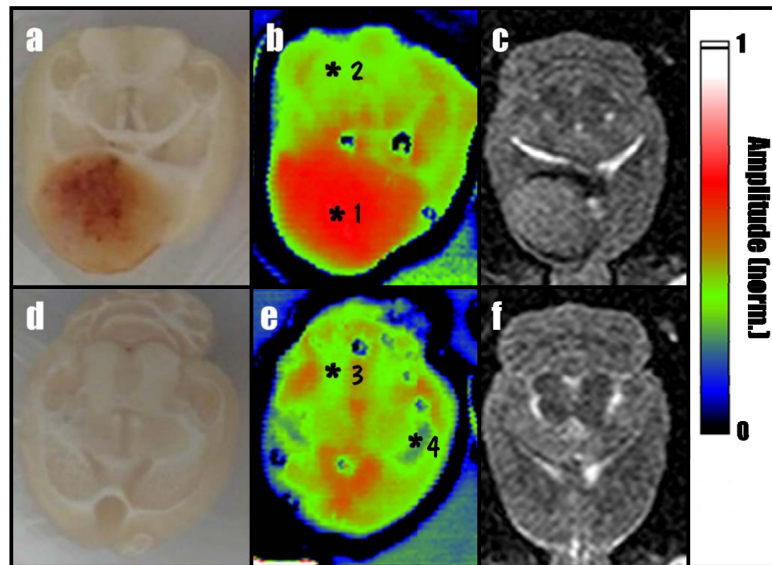


Figure 1.6: Visible (a and d), THz (b and e), and MRI (c and f) images of the healthy and tumor-affected fresh rat brains analysed in [199] (adapted and reprinted from [199]).

no health risks to the patient is posed, unlike with currently employed X-ray-based tomographic systems [197]. In this context, contrast imaging becomes possible thanks to the relatively-strong interaction between THz photons and polar water molecules, which abound in materials of biological origin [198].

Figure 1.6 shows visible, THz, and MRI images of a healthy and a diseased fresh rat brain after surgical explant, the latter affected by a glioma tumor, which it is considered liable for around 40 % of brain cancer clinical cases [199]. As it can be noticed, tumor regions could be clearly identified from the surrounding after THz scanning due to the larger water content compared to healthy brain tissue areas, providing similar diagnostic capabilities to MRI techniques.

For the same reason, people screening aimed at security purposes, including person-borne concealed objects identification (such as weapons, explosives, or contraband goods) at airports checkpoints, can be safely conducted due to the non-invasive character of THz radiation [200, 201]. Figure 1.7 shows an example of real-time short-range imaging experiment employing a low-THz ( $\sim 100\text{--}300$  GHz) security body scanner [202]. The system features six IMPATT diode-based CW sources delivering around 80 mW of output power each at 100 GHz, together with a plasmonic-based detector featuring a noise equivalent power (NEP) of around  $1 \text{ nW}/\sqrt{\text{Hz}}$ . The apparatus successfully demonstrated livestream sensing of body-borne concealed threats at 3 m distance with a moderate spatial resolution of around 3–6 cm, which was limited by the system operating frequency.

In a similar way, stand-off (i.e., radar) operation can be carried out. Figure 1.8 shows an

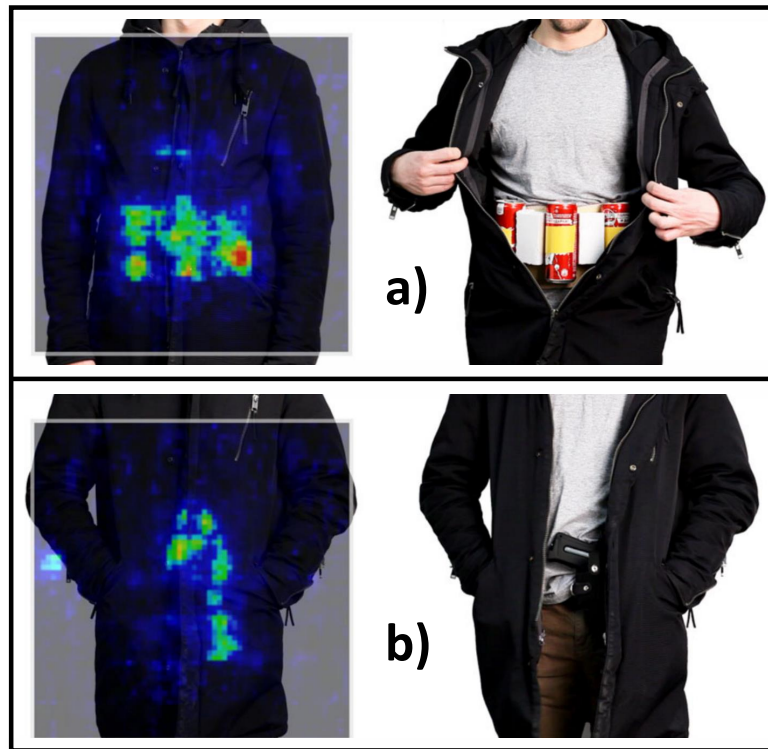


Figure 1.7: Imaging experiment employing the 100-GHz body scanner proposed in [202] (adapted and reprinted from [202]). A body-borne belt carrying explosives (in a)), as well as a firearm (in b)) hidden below a fabric-based jacket, could be identified at 3 m distance.

example of imaging experiment based on the THz radar system reported in [203]. In particular, successful real-time detection of concealed body-borne polyvinyl chloride (PVC) pipes was demonstrated employing a 675 GHz radar at 25 m distance. The employed THz imaging system comprised of a complex source based on a 110–115 GHz LO and a three-stage multiplier chain, together with power amplifiers (PA), while the Rx front-end consisted of a LO-driven 340 GHz tripler pumping a 675 GHz mixer, both designed and fabricated in GaAs SBD technology.

At the same time, THz imaging becomes a unique and powerful tool if combined with its capability of performing spectroscopy [204]. Indeed, THz radiation is sensitive to the rotational and vibrational modes of polar molecules [205], which allows to rely on absorption spectrum-based fingerprints characteristics to perform chemical composition analysis [206, 207], such as in THz-TDS [208, 209] or CW-based approaches [210, 211].

Non-destructive investigation, inspection, and testing applications of THz imaging and spectroscopy can be found in either medicine [14, 192] (e.g., non-invasive analysis of tissues [194]), biology [212] (e.g., study of THz radiation effects on biological material and molecules [213], as well as DNA investigation [214]), pharmaceutical industry [215] (including tablets inspections [216, 217]), industrial production processes [218] (e.g., characterisation of plastic materi-

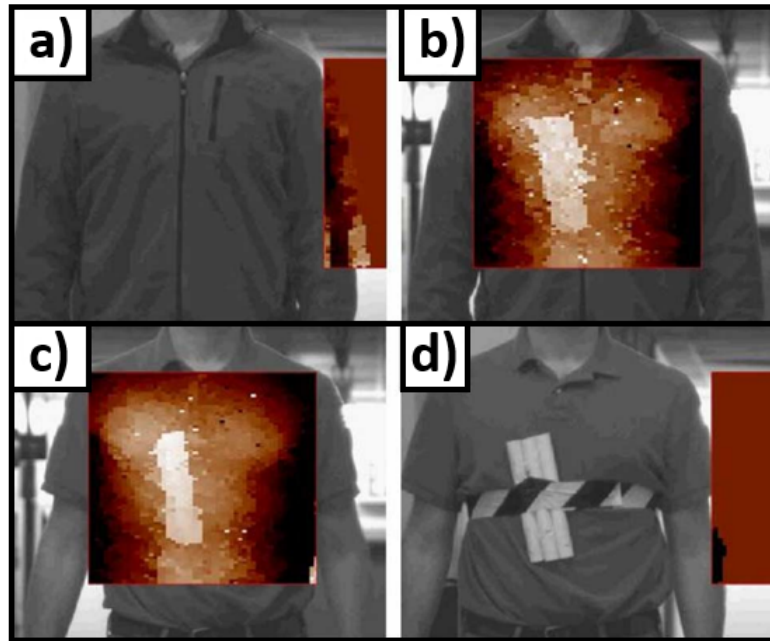


Figure 1.8: Stand-off real-life visualization of body-borne concealed explosives at 25 m distance carried out through the 675-GHz radar system reported in [203] (adapted and reprinted from [203]). The explosive charge (in d) and c)) hidden beneath a sweatshirt (in a)) could be clearly identified (in b)) at 25 m distance.

als [219] and food quality inspection [220, 221]), defence [193, 222] (e.g., detection of explosives [223] and chemical/biological warfare agents [224]), security/surveillance [225] (including people screening [200, 203]), and even restoration and archaeology (e.g., non-invasive analysis of artefacts [180], artworks [226], and ancient human remains [227]). For instance, Figure 1.9 shows a novel real-time pulsed THz spectroscopic imaging system which was reported in [228],

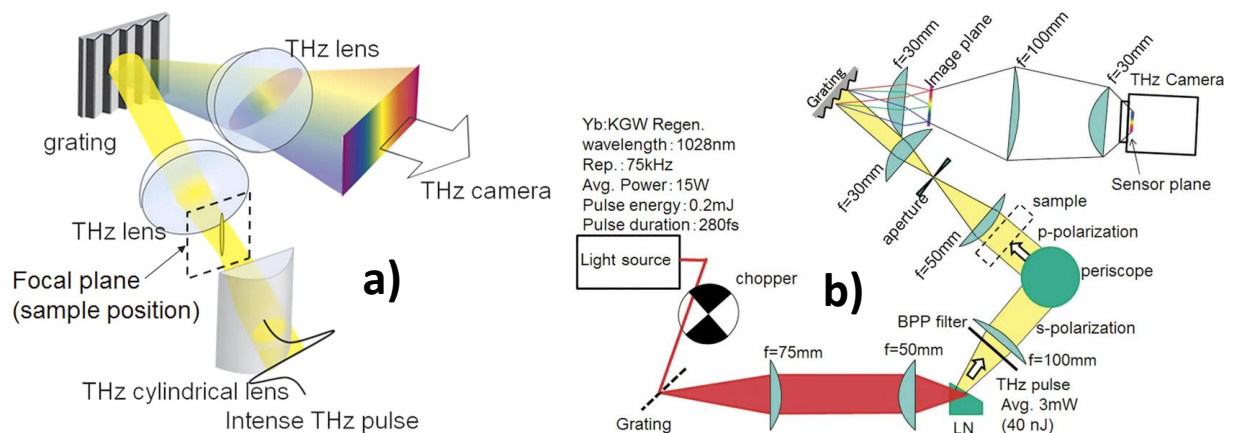


Figure 1.9: Illustrations of the real-time pulsed THz spectroscopic imaging system proposed in [228] (adapted and reprinted from [228]). In a), representation of the broadband multi-channel spectrometer, composed by THz lenses and a diffraction grating; in b), schematic of the THz imaging apparatus, including a ytterbium (Yb):potassium gadolinium tungstate (KGW) crystal-based laser source, uncooled camera, and optical components.

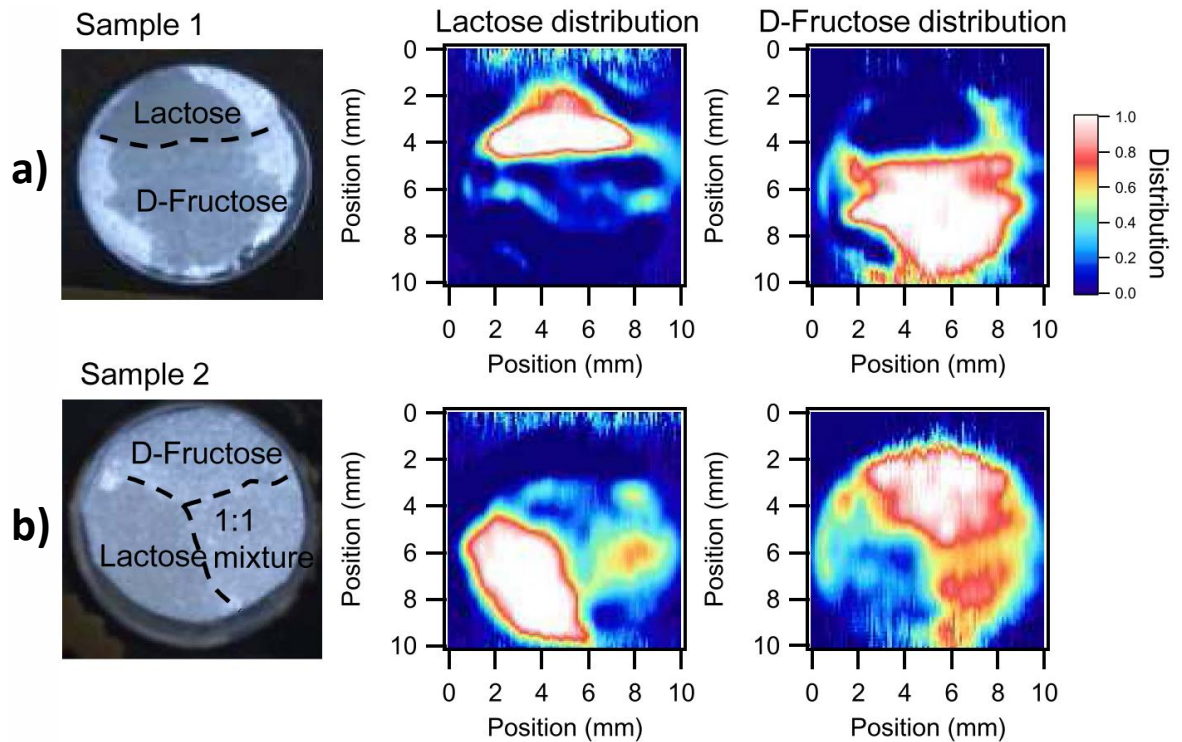


Figure 1.10: Imaging results of the experiment reported in [228] employing the proposed THz spectroscopic imaging apparatus (reprinted from [228]). In a) and b), test sample no. 1 and 2, respectively; on the left: optical images; in the middle: lactose distributions; on the right: D-fructose distributions.

consisting of a broadband multi-channel spectrometer working at 1 THz and a high-sensitivity THz camera. The system successfully demonstrated the capability of performing high-resolution identification of specific sugar molecules (in this case, lactose and D-fructose), together with the fast acquisition of the associated 2D images of their structure, as shown in Figures 1.10a and b.

### 1.3.2 Ultra-broadband THz wireless communications

For the last two decades, we have witnessed an extraordinarily fast evolution of mobile cellular networks, starting from first generation (1G) to fourth generation (4G), and with the fifth generation (5G) of wireless communication networks now being deployed [229]. Figure 1.11 shows the data-rate demand versus time trend for wireline, nomadic, and wireless communication technologies [230]. As it is possible to see, wireless networks data-transfer capability has been continuously increased at a speed much greater than wirelines over the last five decades.

#### 1.3.2.1 The need for ultra-high-speed wireless connectivity

The tremendous increase of mobile data traffic and widespread diffusion of wireless networks has generated an unceasing demand for ultra-broadband multi-gigabit wireless communication technologies capable of extremely large channel bandwidths and ultra-high data-rates required

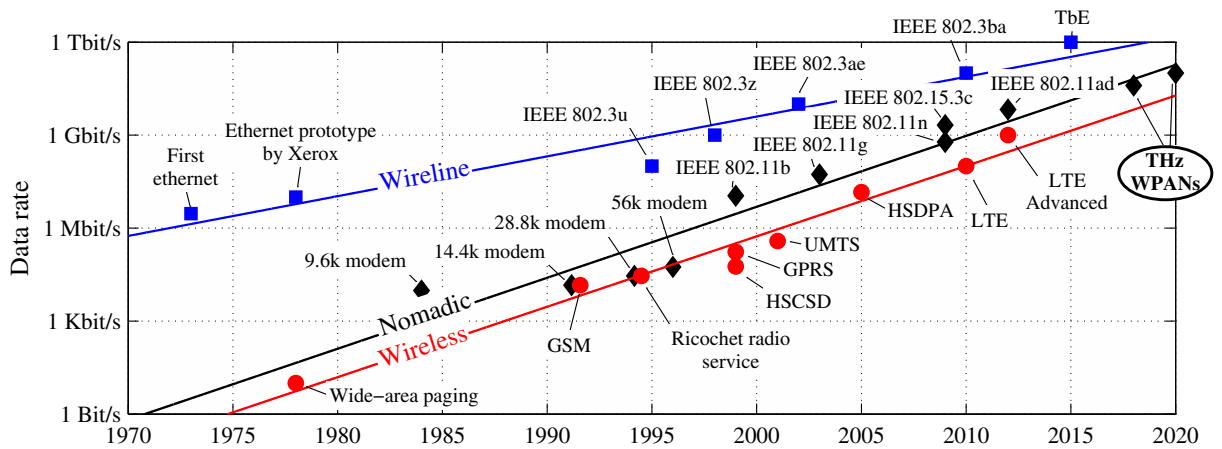


Figure 1.11: Data-rate demand versus time trend for wireline, nomadic, and wireless communication technologies between 1970 and 2020, pointing out the faster exponential increase associated with wireless systems compared to wireline technologies (reprinted from [230]).

by modern multimedia services [231], including the internet of things (IoT) [232]. It has been recently estimated that around two-third of the world population will have access to the internet network by 2023, with a total of more than 5 billion users, and more than 13 billion of interconnected mobile consumer devices [233], around 10 % of which capable of 5G high-speed connectivity, and with a forecasted global data traffic annual rate of around 5 ZB in 2030 enabled by what will be the sixth generation (6G) and beyond-6G networks [234, 235].

This is in line with Edholm’s law, which states that the demand for bandwidth performance in wireless communications has doubled every 18 months since 1980 [236], where data-rates of tens of gigabits per second had to be accommodated since around 2020 onwards [237], while hundreds of gigabit per second and even terabit per second wireless communication links [238] are expected within the next ten years thanks to next generation technologies [239, 240].

In this context, 5G technology will lead towards an era of ubiquitous high-capacity radio links with ever-lower levels of latency and extensive bandwidth capacity. For the path beyond 5G towards the upcoming 6G mobile communication systems, the mobile network is envisioned as becoming more advanced, since it can self-adapt to users’ experience thanks to intelligent learning mechanisms, allowing flexible and fast spectrum reallocation with resulting large bit-rates available to users with over 100 Gb/s single links speeds, ultra-low latency not exceeding 1 ms, and high-reliability featuring packet error-rate  $PER \leq 10^{-5}$  [241].

In addition, 3D and holographic-type communications will lead to an improvement of tele-interaction quality. By providing mobile edge computing and caching capability, including artificial intelligence (AI), to the proximity of end users, the beyond 5G networks will allow for powerful computational processing and massive data acquisition locally at edge networks

to support emerging applications, such as self-driving vehicles, intelligent transport systems, telesurgery, Industry 4.0, smart energy, augmented reality/virtual reality (AR/VR), e-health, and Machine-to-machine (M2M) services [242].

At the same time, new realities, such as the COVID-19 pandemic, has brought the need for more bandwidth and network flexibility into sharp focus, which will extend the use of online meetings to several kinds of human interactions, ranging from medical visits and client interactions, to real-time remote/tele-control applications, which will boost the need for more data capacity.

### 1.3.2.2 Increasing the speed of wireless transmissions

In order to accommodate this demand, there has been a significant amount of research and development (R&D) effort in digital signal processing (DSP), complex modulation schemes, and advanced transmission methods, including orthogonal frequency-division multiplexing (OFDM) [243] and very large-scale MIMO [244, 245], in the lower-MW frequency spectral region between 1–6 GHz and up to the 60 GHz-band. However, the narrow associated bandwidth limits the radio links data capacity from several hundreds of megabit per second to at most few gigabit per second in both long- and short-range scenarios [123].

Therefore, it has become increasingly difficult to accommodate, year after year, the performance requirements empirically predicted by Edholm's law, where spectral efficiencies of up to at least 14 bit/s/Hz would be required to attain bit-rates of the order of 100 Gb/s with currently-employed MW-based technology [230]. However, this is extremely challenging and practically unrealistic since it would inevitably involve extremely complex transmission approaches [246].

In this context, the largest globally-available frequency band currently allocated for mobile telecommunication services is set in V-band (40–75 GHz), at around 60 GHz (57–64 GHz) and with up to 7 GHz of continuous bandwidth [230, 247–250]. In order to meet the requirements imposed by 5G technology, the United States (US) has already started to extend the bandwidth up to 14 GHz by including the unlicensed portion 57–71 GHz [251, 252], and this trend is now approaching E-band (60–90 GHz). This adds to the total bandwidth belonging to the licensed standard low-frequency MW bands ( $< 6$  GHz), and high-frequency K-band (18–27 GHz) and Ka-band (27–40 GHz) portions (such as 24.25–27.5 GHz in Europe, and 27.5–28.35 GHz, 37–38.6 GHz, and 38.6–40 GHz in the US [248, 251, 253]).

However, in order to significantly increase data-rates and enable future proof scenarios and applications as foreseen in 6G and beyond, an increase in the bandwidth of several tens of gigahertz is required. Based on the current spectrum allocation, it is clear that future wire-

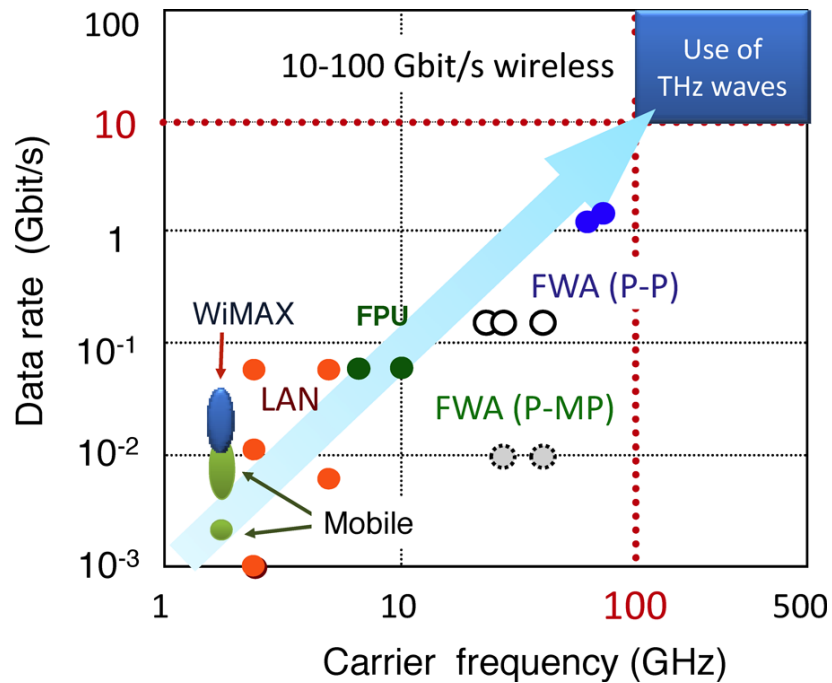


Figure 1.12: Wireless channel data-rate versus carrier frequency trend (reprinted from [3]).

less communications will have to operate in frequency bands where more spectral resources are available. Therefore, the exploitation of higher frequency regions in order to alleviate the spectrum scarcity and bandwidth limitations of current MW systems is inevitable, since higher carrier frequencies allow wider modulation bandwidths and higher data-rates [3] according to Shannon-Hartley theorem [254–256], as illustrated in Figure 1.12. Further, high-bandwidth systems have the tendency to decrease the end-to-end latency due to the high-rate data packet transfer, reason for which high frequencies are seen as opportunistic bands for haptic applications requiring seemingly "zero-perceptible" latency.

Although candidate bands are several, particularly interesting is the still unallocated yet unregulated "THz gap", which is attracting great interest due to the recent technological advances [257–259]. Figure 1.12, shows that THz carriers allow for data-rates beyond 10 Gb/s. Actually, different frequency sub-windows in this range have already been employed for several decades in radio astronomy, since they are in correspondence with specific vibrational and rotational resonant modes of molecules under study [260]. Therefore, a careful approach will have to be adopted to avoid any kind of possible conflict and interference between mobile telecommunication and radio astronomy systems [261]. Another advantage in choosing THz carrier waves is the sub-mm dimension of the antennas, which become cheaper and more integrable [262,263], even though integrated antenna solutions suffer from low gain ( $< 6$  dBi).

However, due to the lack of devices capable of generating and detecting THz waves reliably

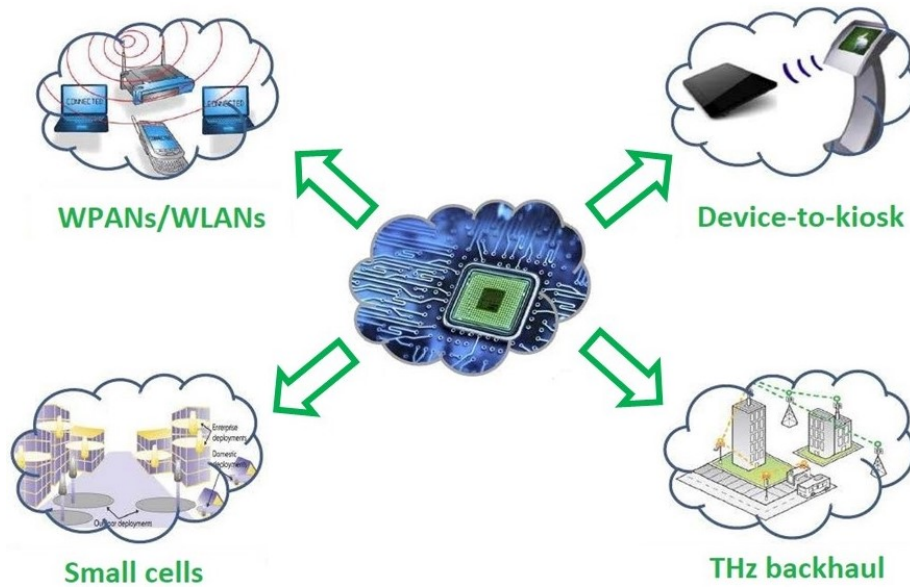


Figure 1.13: Some potential applications of THz wireless communications.

and efficiently in practical application circumstances, its usage in the scope of wireless communication links has been limited so far, but this is rapidly evolving [235]. Indeed, with the first demonstration of wireless communication in the THz band [66], first data-transmission systems working in the lowest part of the spectrum ( $< 150$  GHz) and able to provide several gigabit per second at a few kilometres distance have already started to be commercialised and successfully employed in Japan since 2014 [264], so it is hardly questionable if ultra-fast data-links capable of high data-rates beyond 100 Gb/s and operating at frequencies above 300 GHz will soon appear on the global market.

Typical THz wireless communication applications rely on both long- and short-range line-of-sight (LOS) and non-line-of-sight (NLOS) operation [230, 265]. Figure 1.13 shows some potential THz wireless communication applications, including wireless backhaul/fronthaul [266], wireless local area networks (WLAN) and wireless personal area networks (WPAN) [23], kiosk downloading [252, 267], and nano-networks [268]. In addition, THz technology results to be appealing in the contexts, including wireless data centres [269, 270], intra-chip connectivity [271, 272], and space communications [261].

Thus, it is possible to distinguish three categories of application scenarios: 1) short-range (few centimetres), like in the case of intra-device communication on electronic boards or kiosk downloading; 2) medium (few metres), like in data centres or computers in the same office space; and 3) long-range, like links (up to 100 m and beyond). It is worth noting that long-range links can reach kilometre distances or more in the case of wireless communication in space (no attenuation). Furthermore, it is evident that these communication scenarios impose very

different requirements on the sources, antennas, optics, and detectors from the point of view of power consumption, dimensions, weight, potential market volume, and price.

### 1.3.2.3 Link budget and THz antennas

To understand the basic TRx requirements, Table 1.1 reports some realistic 300-GHz link budget examples with 55 GHz transmission bandwidth assuming short-range LOS conditions [247], which can be considered of prime interest for first feasible applications. The analysis is based on Friss' model for transmission in free-space [273]. For the calculation, the signal-to-noise ratio (SNR) is assumed to be around 10 dB, as well as the implementation margin of signal degradation. Furthermore, estimates of the transmission loss and noise factor are also included, and perfect alignment between Tx and Rx is assumed, neglecting misalignment losses.

The results show that an antenna gain between 20–25 dBi is required, which can be provided either through the use of horn antennas, which need the integration of Tx/Rx chips within rectangular waveguides [155], or by mounting the chips on Si-based lenses [464]. Future systems might employ the traditional approach, which features the adoption of beam steering capability through the exploitation of phased-array antennas (hundreds of elements or more), but this remains to be seen. Indeed, the implementation of arrays at THz frequencies is non-trivial due to the small chips dimension and substrate effects. At the same time, it is also clear from Table 1.1 that Tx RF power levels of over several milliwatt are required to transmit over 1 m distance.

However, compact and cost-effective solid-state sources meeting these performance requirements are not readily available at the current time. Thus, the major hurdle which still prevents THz technology to be employed on an industrial basis is represented by the lack of compact, low-power, low-cost, and RT sources and detectors for CW THz emission and high-sensitivity detection, together with the lack of antenna arrays that can reliably operate in this frequency window [23]. Here, while the operation frequency of electronic devices is typically limited by carriers transit times [275], photonic devices face the tough requirements of band-to-band opti-

Table 1.1: Link budget examples for wireless transmission at 300 GHz [247].

Distance [m]	$P_T$ [mW]	$G_T$ [dBi]	$G_R$ [dBi]	Path loss [dB]	Noise factor [dB]
0.1	1.58	12	12	62	12
1	2.51	25	17	82	10
5	3.98	25	25	96	8

In the above,  $P_T$  is the RF power at the transmitting antenna,  $G_T$  and  $G_R$  the transmitting and receiving antenna gain, respectively,  $\lambda$  the transmission channel wavelength, while  $d$  the link distance.

cal transitions towards long emission wavelengths [276].

Although several are the solid-state competitor technologies which are being investigated and developed [277], none of them has made a real technological breakthrough yet. Moreover, in order to aid devices meeting links budget requirements, antennas gain could be enhanced, for instance, through innovative beam-steering solutions based on micro/nano electro-mechanical systems (MEMS/NEMS) or metamaterials [278–280].

#### 1.3.2.4 THz wireless data-links: state-of-play

Recent technological innovations regarding integrated THz mobile system components [281] indicate the practical viability of ultra-high-speed THz wireless communications [19, 235, 282]. Regarding Tx, two main approaches for THz signal generation are currently employed: 1) photonic; and 2) electronic. As already discussed, the first approach consists in photo-mixing two optical wavelengths employing a high-speed PD device, among which UTC-PDs, to generate the THz carrier wave signal, which requires the employment of telecom-based photonic components, including laser diodes, modulators, and low-loss optical fibre cables [66, 283].

Regarding approach 2), there are various candidates among semiconductor-based electronic THz emitters operating at RT, first of which transistor-based TMICs [284–286] and RTD oscillators [287]. At the Rx side, either sub-harmonic mixers (SHM) [155] or direct detectors [288, 289] are generally employed, so the approach is exclusively electronic.

Figure 1.14 shows the performance of solid-state integrated THz wireless communication technologies, including some of the most relevant literature results. As it is possible to notice, data-rates of several tens of gigabit per second, and of up to and over 100 Gb/s, have been achieved by different technologies, including group IV (such as Si and SiGe) and III-V (such as GaAs and InP) semiconductors, even though the link distance remains very limited to well below 10 m, and with the longer ranges largely enabled by the employment of extremely high-gain antennas (above 50 dBi), coherent Rx, and PA stages [286].

Therefore, in order to increase the link distance and realize practical THz wireless communications, a significant improvement in the performance of the associated compact semiconductor-based devices is required. Moreover, it is clear from Figure 1.14 that RTD technology demonstrates comparable performance with respect to the other competing technologies. However, while the latter typically employ complex transmission signalling procedures, such as quadrature amplitude modulation (QAM) and quadrature phase-shift keying (QPSK), RTD-based systems have relied on simple amplitude modulation (AM) schemes to achieve comparable speed performance, including ON-OFF keying (OOK) and amplitude-shift keying (ASK) [163].

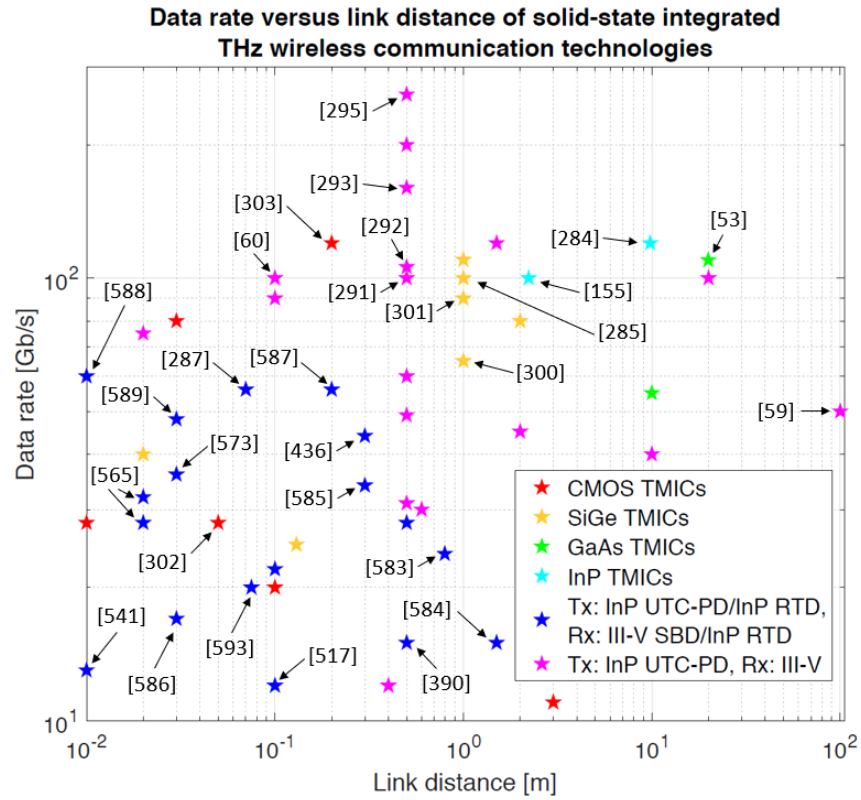


Figure 1.14: Data-rate versus link distance of solid-state integrated THz wireless communication technologies, outlining some of the most relevant literature results. Reference number is provided for key results.

Even though complex signalling, such as 16-QAM and higher constellations, feature high-spectral density, signal processing and synchronization become mandatory, which make the designed systems energy-hungry, especially at the Rx side. On the other hand, RTD TRx are characterized by simpler implementations, mainly square-law direct detectors, for which heavy signal processing is not required. These concepts will be discussed more in detail in Chapter 2.

### 1.3.2.5 Hybrid photonic/electronic-based THz wireless data-links

State-of-the-art hybrid photonic/electronic-based THz wireless data-links employ InP UTC-PD devices at the Tx side. Table 1.2 shows a summary of some of the reported links in the literature, and reveals that bit-rate capabilities beyond 100 Gb/s in the 200–500 GHz-band have been demonstrated. In particular, up to 160 Gb/s through QPSK [293,294] and up to 260 Gb/s through 16-QAM [295] over 50 cm-long links have been reported using multi-channel data transmission, both with bit error-rates (BER) below the forward error correction (FEC) limit and without employing any multiplexing [296] or MIMO [297] technique. In the following, few of these systems are discussed in detail.

Figure 1.15 shows the block diagram of the 300 GHz-band wireless communication system

Table 1.2: Hybrid photonic/electronic THz wireless communication data-links specifics.

Ref.	Rx	$f_c^*$ [GHz]	Modulation	Distance	Data-rate [Gb/s]	BER
[53]	GaAs HEMT	237.5	8/16-QAM	20 m	100	$< 4.5 \times 10^{-3}$
[59]	-	320	OOK	100 m	50	$9.5 \times 10^{-4}$
[60]	-	320	QPSK	5–10 cm	100	-
[290]	InP PC	287–325	QPSK	58 m	30	< FEC
[291]	-	280	16-QAM	50 cm	100	$< 4 \times 10^{-3}$
[292]	InP SBD	400	16-QAM	50 cm	106	$< 2 \times 10^{-2}$
[293]	InP SBD	300–500	QPSK	50 cm	160	$7 \times 10^{-3}$
[295]	InP SBD	300–500	QPSK	50 cm	260	< FEC

Some reported results from the literature employing InP UTC-PD-based Tx. \* Carrier frequency.

reported in [59], which features a CW InP UTC-PD-based Tx and an electronic SHM-based coherent Rx. The THz carrier signal is generated photonicly through OFCG by employing an infrared laser source, electro-optic phase modulators (EOPM), and a LO. After two of the comb lines are optically-selected, modulation takes place employing an electro-optic amplitude modulator (EOAM) or a quadrature phase-shift keying modulator (QPSKM), and the lines are then combined and sent to the UTC-PD through an optical fibre, where the modulated THz carrier signal is generated by photo-mixing and then irradiated through an antenna. The THz signal is then received and demodulated. The TRx system demonstrated single-channel wireless data transmission up to 50 Gb/s through OOK over a 100 m-long link [59], and up to 100 Gb/s through QPSK in the 5–10 cm range [60], both with BER below the FEC limit.

Another relevant single-channel wireless transmission experiment was reported in [292]. The employed 400-GHz wireless communication TRx setup was similar to the one employed in [59] and its block diagram is shown in Figure 1.16, comprising of a CW photonic-based Tx in InP UTC-PD technology and an electronic mixer-based coherent Rx. The input photonic signal is generated by OFCG, employing an infrared laser cavity, phase modulators, and a LO. A selected comb line is then modulated and photonicly-down-mixed with the LO signal through the antenna-integrated UTC-PD, generating and emitting the THz signal, which is afterwards demodulated at the Rx side. Data transmission up to 106 Gb/s through 16-QAM over 50 cm and with BER below the FEC limit was achieved, which is among the best single-channel wireless data transmission results ever reported.

Among the best multi-channel THz wireless communication results, data transmission up to

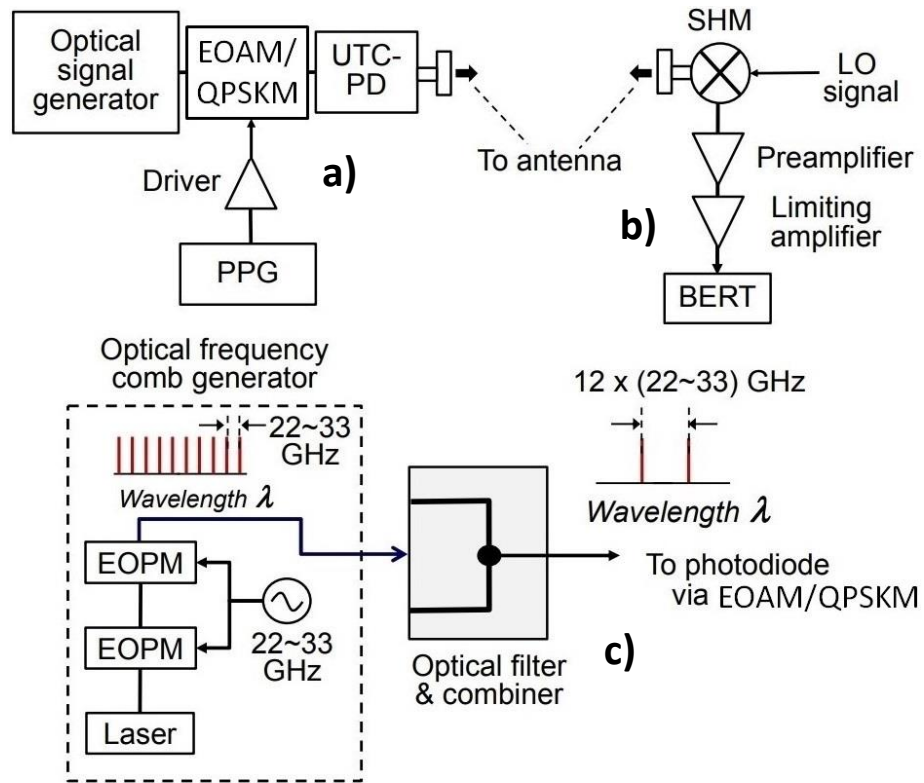


Figure 1.15: Block diagram of the 300 GHz-band wireless TRx system reported in [59] (adapted and reprinted from [59]). In a), Tx; in b), Rx; in c), optical signal generator.

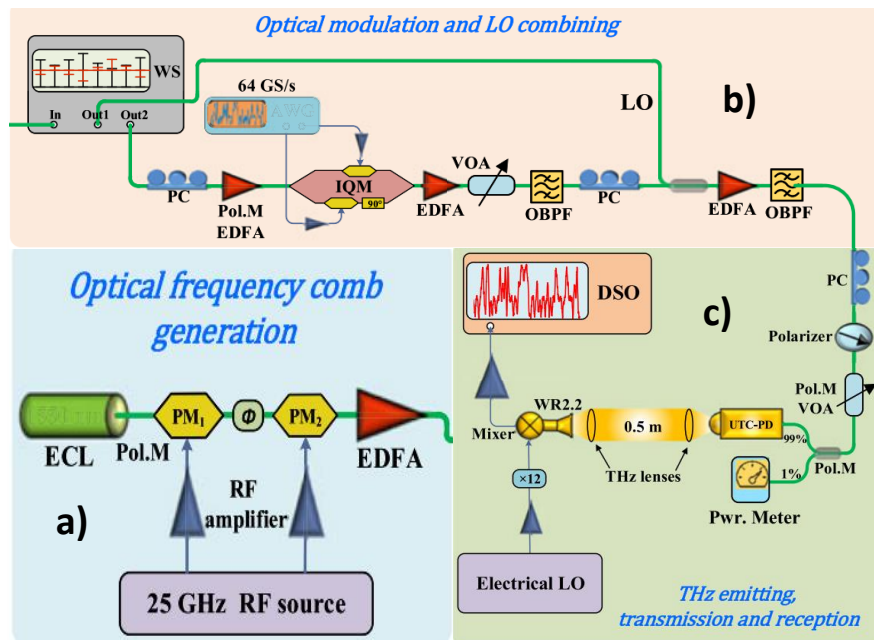


Figure 1.16: Block diagram of the 400-GHz wireless TRx setup reported in [292] (adapted and reprinted from [292]). In a), optical signal generator; in b), modulation and mixing module; in c), THz wireless TRx. In the above, Pol.M stands for polarization maintaining.

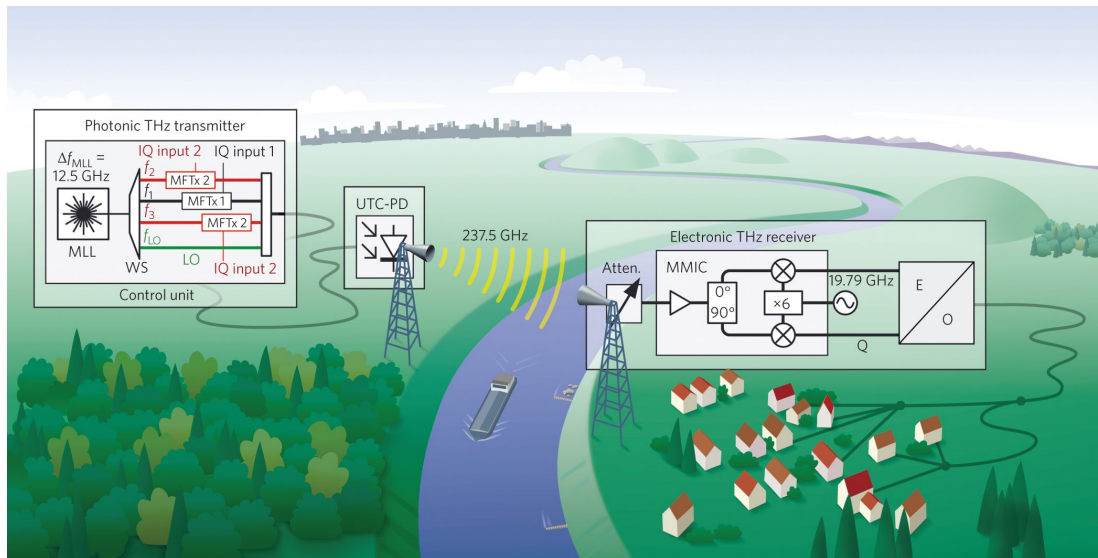


Figure 1.17: Scenario representation of the long-range multi-channel THz wireless communication data link reported in [53] (reprinted from [53]).

160 Gb/s (8-channel) [293] and up to 260 Gb/s (6-channel) [295] in the 300–500 GHz frequency band employing 16-QAM/QPSK over 50 cm-long links has been reported. Figure 1.17 shows a schematic of the 3-channel THz wireless data-link reported in [53]. The photonic input signals are generated by employing a single mode-locked laser and by heterodyning frequency-locked lines [298]. Four comb lines (three signals plus a LO reference) are selected by a wave-shaper (WS), and the three signals are then modulated through 8/16-QAM and sent to an InP UTC-PD by means of an optical fibre for THz signal generation, together with the un-modulated LO signal. The THz modulated carriers are then generated by photo-mixing the LO and the modulated signals through the UTC-PD, irradiated through an antenna, and then received and demodulated thanks to a SHM-based coherent Rx designed in GaAs mHEMT technology. The 237.5-GHz TRx system was able to demonstrate wireless data transmission up to 100 Gb/s through 8/16-QAM over 20 m, keeping the BER below the FEC limit.

Despite the impressive results, photonic-based THz Tx are still too complex and expensive to bring THz wireless communications technology to the consumer marketplace. They are bulky, including optical components, such as laser sources, modulators, filters, lenses, etc., they require cumbersome optical setups, and some need proper cryogenic cooling, which increase cost, complexity, reduce integrability, and increase reliability issues, posing practical limits in the context of consumer-oriented THz wireless communication applications.

### 1.3.2.6 Electronic-based THz wireless data-links

At the same time, transistor-based TMICs are also being developed for high-speed wireless communication applications. Table 1.3 shows a summary of various reported THz wireless

data-links of relevance employing TMIC-based TRx, revealing that bit-rates of over 100 Gb/s at several metres distance have been demonstrated in the 300 GHz-band [155, 284–286]. In the following, few of these systems are discussed in detail.

State-of-the-art results have been achieved employing HEMT technology. Figure 1.18a shows the block diagram of the InP HEMT THz wireless TRx used to carry out the high-speed wireless data transmission experiments reported in [284], while Figures 1.18b and c show photographs of the fabricated mixer and PA MMIC chips, respectively. At the CW Tx side, an intermediate frequency (IF) signal with central frequency of 20 GHz is generated by an arbitrary waveform generator (AWG) and modulated through 16-QAM. The signal is then mixed with a 15 GHz LO and up-converted by a  $18\times$  frequency extender and amplified, providing an output signal of frequency 270 GHz. The modulated up-converted THz signal is then sent to a high-pass filter (HPF) to suppress the LO leak and the image signal, amplified by a 300-GHz PA, sent to an antenna, radiated, and then received and demodulated. The PA and low-noise amplifier (LNA) at the Rx side, and both the LO PA and fundamental mixer stages at both the Tx and Rx sides, were designed in 80 nm InP HEMT technology. The system enabled single-channel wireless data transmission up to 120 Gb/s at 296 GHz using 16-QAM over a 9.8 m-long link, and with BER below the FEC limit, which is among the best results ever achieved by all-electronic single-channel THz wireless TRx.

SiGe HBT technology has also demonstrated great potential in this regard. Figure 1.19a shows the block diagram of the SiGe HBT-based THz TRx reported in [285], together with a schematic of its packaging concept, while Figures 1.19b and c show photographs of the associ-

Table 1.3: Electronic-based THz wireless communication data-links specifics.

Ref.	TRx	$f_c^*$ [GHz]	Modulation	Distance	Data-rate [Gb/s]	BER
[155]	InP HEMT	272–302	16-QAM	2.22 m	100	$10^{-3}$
[284]	InP HEMT	296	16-QAM	9.8 m	120	$10^{-3}$
[285]	SiGe HBT	220–255	16-QAM	1 m	100	$4 \times 10^{-3}$
[300]	SiGe HBT	225–255	QPSK	1 m	65	$\sim 10^{-3}$
[301]	SiGe HBT	230	16-QAM	1 m	90	$10^{-3}$
[302]	Si CMOS	300	16-QAM	5 cm	28	$< 10^{-3}$
[303]	Si CMOS	70–105	16-QAM	20 cm	120	$10^{-3}$
[286]	GaAs HEMT	240	8-PSK	850 m	64	$7.9 \times 10^{-5}$

Some of the reported results from the literature employing transistor-based TMIC TRx. \* Carrier frequency.

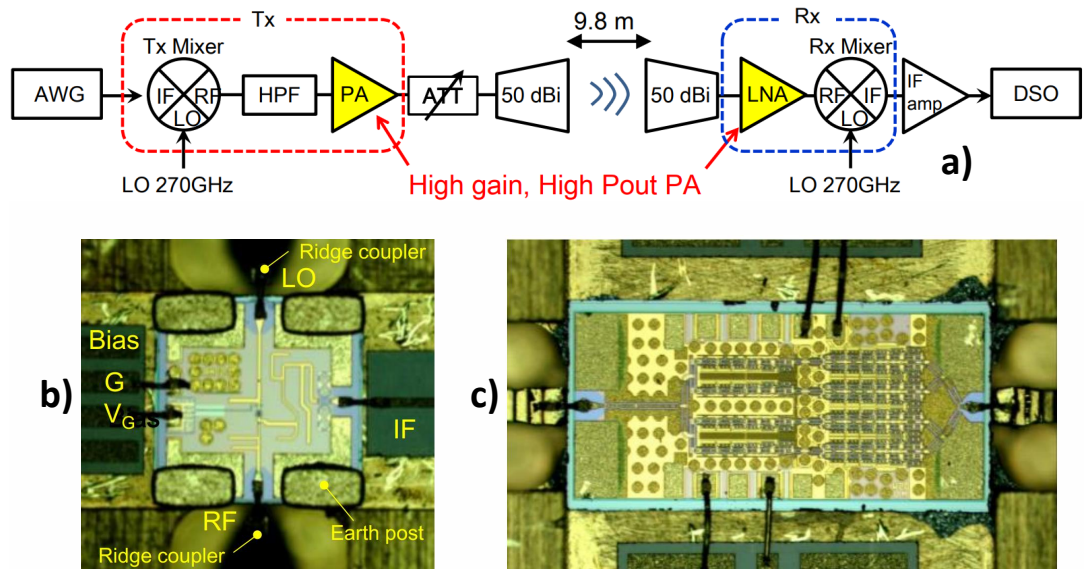


Figure 1.18: InP HEMT TMIC TRx system reported in [155, 284] (adapted and reprinted from [155] [284]). In a), block diagram of the THz data-link used to carry out wireless communication experiments; in b), photograph of the employed InP HEMT mixer chip; in c), photograph of the employed InP HEMT PA chip.

ated Tx and PA modules, respectively. The source features two 16-QAM modulated IF signals which are up-mixed with a LO within a double-balanced in-phase and quadrature (IQ) heterodyne up-conversion mixer-based architecture. The LO signal of frequency 230 GHz is generated through a Gilbert-cell-based  $16\times$  frequency multiplier followed by a differential three-stage PA. The modulated THz signal is amplified by a four-stage PA, sent to an antenna, and radiated, after which is demodulated after reception. Both the Tx and Rx front-end modules were designed in  $0.13\ \mu\text{m}$  SiGe HBT technology. Single-channel wireless data transfer was demonstrated up to 100 Gb/s in the 220–255 GHz frequency window over 1 m ( $\text{BER} < \text{FEC limit}$ ).

At the same time, Si-based CMOS THz Tx are already capable to provide single-channel data-rates of up to 28 Gb/s over 5 cm [302], and of up to 120 Gbps (2-channel) over 20 cm [303], both with BER below the FEC limit. Figure 1.20a shows the block diagram of the Si-based CMOS THz wireless TRx system reported in [299, 302], while Figures 1.20b and c show micrographs of the Tx circuit board [299] and associated die [304], respectively. A 16-QAM modulated IF signal is up-mixed with a LO followed by a frequency-tripler at the Tx side. After a driver stage, both the LO and the IF signals are mixed by a square mixer and the resulting 296 GHz signal sent to an antenna and radiated, followed by reception and demodulation. The system was able to demonstrate single-channel THz wireless data transmission up to 28 Gb/s over a 1 cm-long link, keeping the BER below FEC limit.

Moreover, wireless link distances of up to 850 m have been reported employing GaAs-based

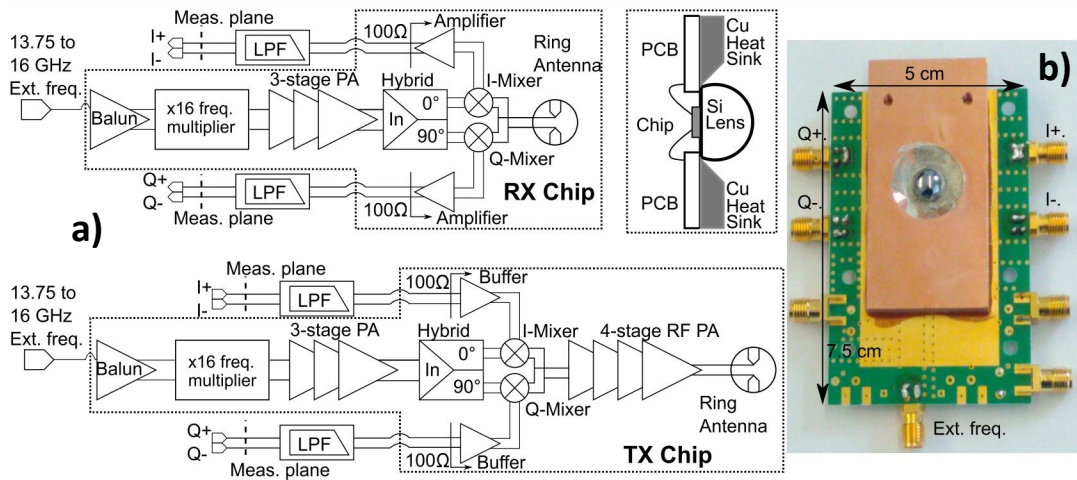


Figure 1.19: InP HBT TMIC TRx system reported in [285] (adapted and reprinted from [285]). In a), block diagrams of the InP HBT Tx and Rx chips, together with schematic of the Tx/Rx modules packaging concept; in b), photograph of the Tx module.

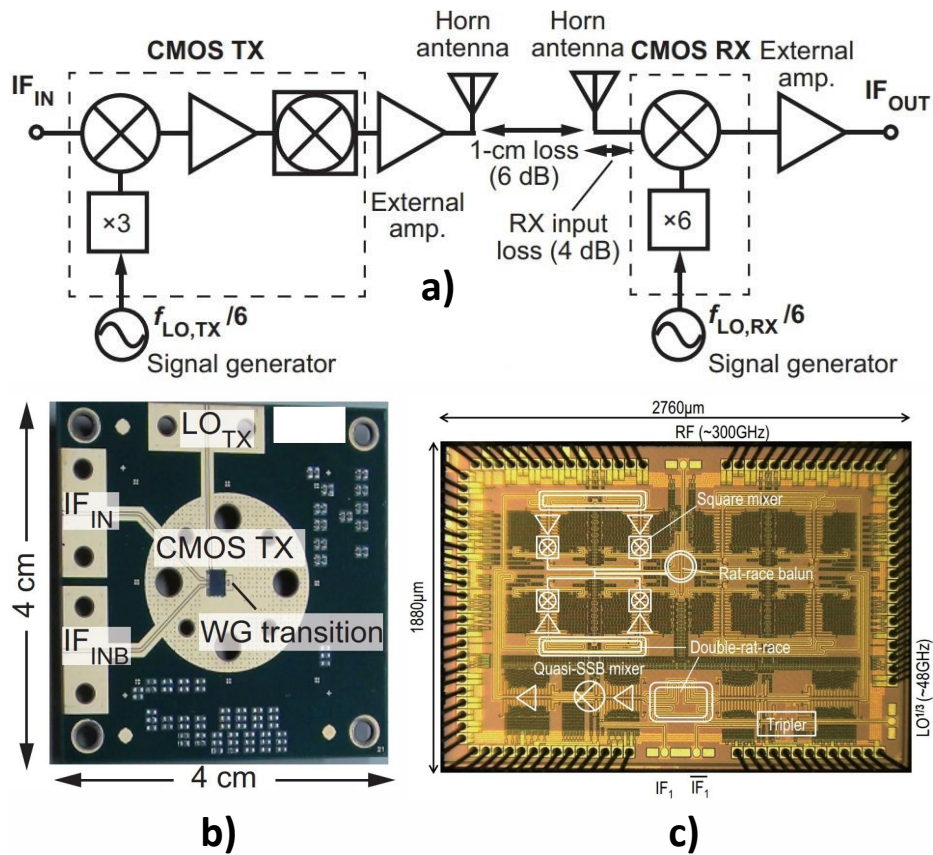


Figure 1.20: Si-based CMOS TMIC TRx system reported in [299, 302] (adapted and reprinted from [299, 304]). In a), block diagram of the TRx; in b), micrograph of the Tx circuit board; in c), micrograph of the Tx die.

TMIC Tx and Rx front-ends [286]. It is also worth underlining that, in addition to wireless communications, TMICs have proven to be great candidates for other potential THz applica-

tions, including high-resolution imaging [124] and radar systems [125]. However, as already discussed, these systems are extremely complex and inefficient.

In this context, NDR diodes have also been intensively investigated in the development of high-speed THz wireless TRx systems, in particular, RTDs [163]. Indeed, thanks to the recent technological advances, the RTD device is considered a promising compact and cost-effective solution to bring ultra-broadband multi-gigabit THz wireless communications technology to a widespread consumer marketplace. In this context, all-RTD 300-GHz wireless TRx have already reached single-channel bit-rates of up to 30 Gb/s error-free (EF), and of up to 56 Gb/s with BER below the FEC limit, through ASK over 7 cm [287]. An extensive review on RTD-based THz wireless communications is presented in Chapter 2.

### 1.3.2.7 Challenges in realising THz wireless communications

Despite the clear advantages, THz wireless communications are still quite challenging from a technological standpoint [257, 258]. As already mentioned, there are huge signal losses caused by strong absorption by  $O_2$ ,  $H_2O$ , and other gas molecules in the atmosphere, where the relative humidity (RH) can reach up to 100 % in outdoor rainy conditions [247]. Here, both the SNR and the link data capacity are strongly deteriorated by the ambient humidity.

The THz range is, therefore, mostly promising, in the short-term, for short-range indoor ap-

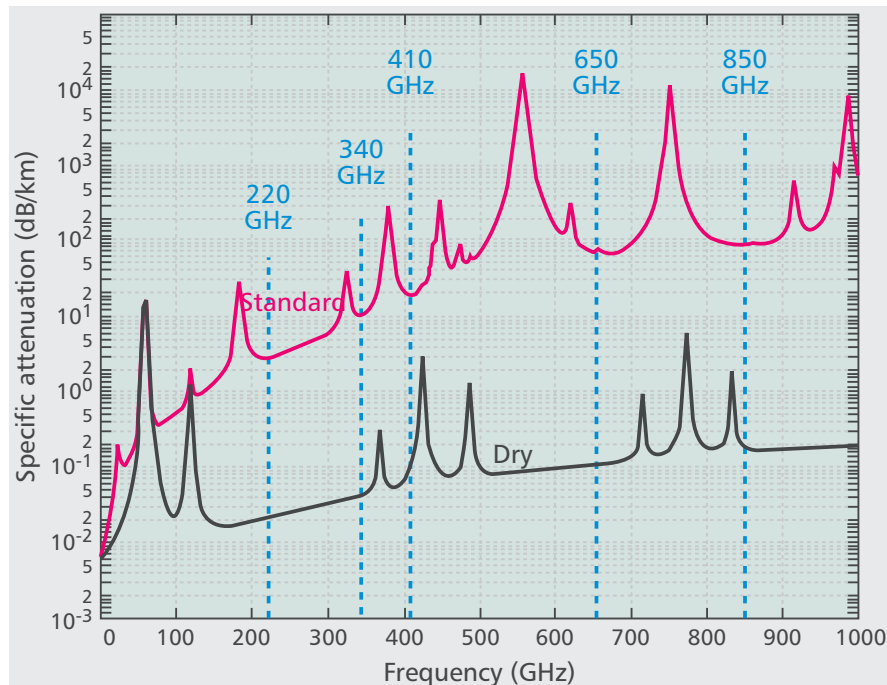


Figure 1.21: Atmospheric specific attenuation versus frequency up to 1 THz for dry (RH  $\sim$  0 %) and moist (RH  $\sim$  50 %) indoor conditions (reprinted from [247]).

plications, where the link distance is relatively short (metre range) and the environmental RH is a less stringent constrain (typically around 50 %) [247]. Figure 1.21 shows the atmospheric specific attenuation versus frequency up to 1 THz for dry (RH  $\sim$  0 %) and moist (RH  $\sim$  50 %) indoor conditions [247]. As it is possible to notice, of particular interest is the transmission window around the 300 GHz-band (275–325 GHz [176]), which features 55 GHz of continuous bandwidth with low attenuation (around 0.04 dB/m) [247, 305]. This is insignificant compared to free-space losses and, at the same time, there are no resonant absorption peaks, making short-range applications feasible.

Standardisation efforts for this band have been recently started through the IEEE standard 802.15.3d in the definition of physical layers for next generation ultra-high-speed WPANs [306]. For THz links, good alignment between the Tx and Rx antennas is required [307] and care has to be taken in the design and realisation of building structures in order to reduce signals attenuation through walls, ceilings, etc. [190, 308]. Long-distance outdoor applications (kilometre range) are feasible but will rely on future technological advances of both sources (output power) and detectors (sensitivity), together with antennas (gain, so both directivity and radiation efficiency) due to the higher attenuation at RHs of up to 100 %.

# Chapter 2

## Terahertz resonant tunnelling diode

The aim of this Chapter is to provide the reader with general knowledge on the resonant tunnelling diode, with specific focus on terahertz applications. It begins with an overview, including historical background and device operation principle, together with both physical and circuitual modelling. Thereafter, technology, as well as state-of-the-art sources and detectors, together with transceiver systems for ultra-high-speed terahertz wireless communications, are discussed in detail. Other applications, including high-resolution terahertz imaging and radar systems, are also briefly presented.

### 2.1 Overview

The resonant tunnelling diode (RTD) is a one-dimensional (1D) vertical transport unipolar two-terminal semiconductor-based active electronic device characterized by a highly non-linear current-voltage ( $IV$ ) characteristic, usually comprising of a negative differential resistance (NDR) region and of two positive differential resistance (PDR) regions [309].

Figure 2.1a depicts the (quasi)-static  $IV$  characteristic of a generic RTD device. The NDR region is characterised by  $I_p$  and  $I_v$ , which are the peak and valley current, respectively, and corresponding voltages  $V_p$  and  $V_v$ . Further, it can be described by the peak-to-valley and valley-to-peak current and voltage differences  $\Delta I = I_p - I_v$  and  $\Delta V = V_v - V_p$ , respectively, and peak-to-valley current ratio  $PVCR = I_p/I_v$  [310]. The  $IV$  curve can be considered a fingerprint of the RTD device, and its shape depends on different factors, among which device size, epitaxial design, operation frequency, and temperature [311, 312]. Indeed, although the ideal  $IV$  characteristic shows the typical triangular shape, temperature effects, including scattering processes caused by impurities and structural defects, make a realistic device featuring a smoother curve.

The non-linearities associated to the  $IV$  characteristic arise as a result of the quantum mechanical resonant tunnelling effect occurring within the core of the device, where current flow

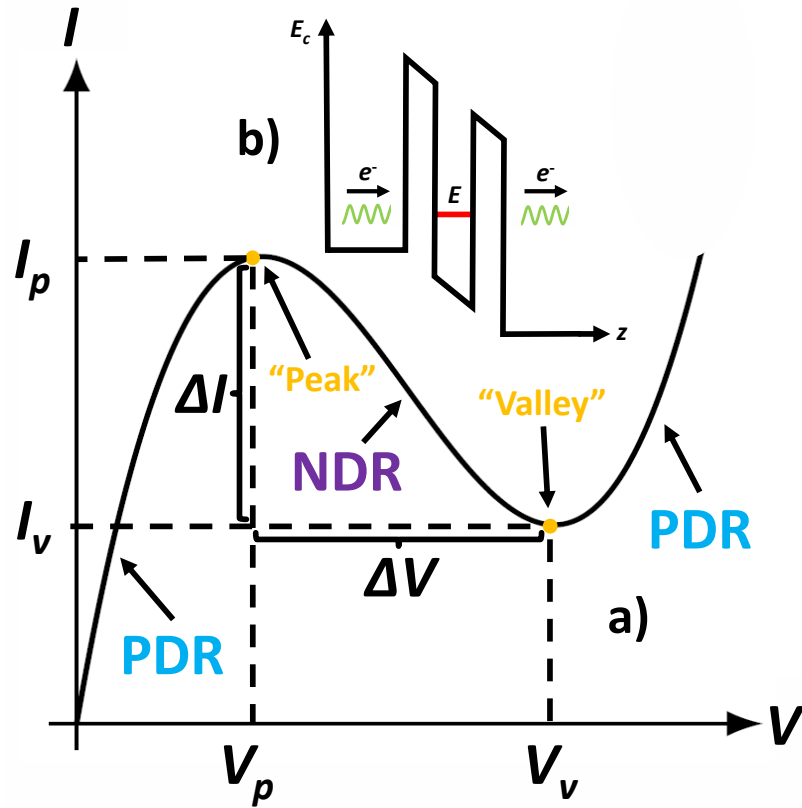


Figure 2.1: In a), schematic illustration of the  $IV$  curve of a generic  $n$ -type intra-band RTD device; in b), associated simplified CB diagram, assuming a generic bias point and QW quasi-bound state energy level  $E$ . In the above,  $E_c$  is the CB edge,  $z = |z|$  the broken-symmetry (longitudinal) direction modulus, while  $e^-$  represents the tunnelling electrons.

is either allowed or forbidden within resonant or non-resonant energy bands, respectively [313]. In this context, the heterostructure-based active region of the device typically consists of a semiconductor-based double-barrier quantum well (DBQW) structure, which is nanometric in thickness, so comparable to the electron de Broglie wavelength, and, therefore, thin enough to allow for electron resonant tunnelling [314].

In this context, the term "tunnelling" refers to the behaviour of electrons owning kinetic energy lower than the potential barriers but still able to travel across them with a certain degree of probability [315]. This is a consequence of the de-Broglie wave-particle duality, where the electron can be considered as a wave-packet [316]. In this context, inter-band electron tunnelling was experimentally observed for the first time by Esaki in 1957 working with heavily-doped germanium (Ge)-based  $p$ - $n$  junctions [317], and theoretically-modelled one year later [318]. On the other hand, "resonant" is associated with the possibility of undergoing tunnelling through the DBQW structure thanks to the presence of metastable, or quasi-bounded, resonant states [319].

The probability of resonant tunnelling through the DBQW is defined through the transmis-

sion coefficient  $\mathcal{T}_{DBQW}$ ; at the resonant condition,  $\mathcal{T}_{DBQW} \approx \mathcal{T}_{b,1} \mathcal{T}_{b,2} \sim 1$  (symmetric structure), whereas  $\mathcal{T}_{DBQW} \sim 0$  otherwise, where  $\mathcal{T}_{b,1} \sim 0$  and  $\mathcal{T}_{b,2} \sim 0$  are the tunnel transparencies associated with the first and second barrier, respectively [311]. In this sense, the resonant condition is met when electrons entering the DBQW region have energy close to one of the QW resonant states. Thus, as  $\mathcal{T}_{DBQW}$  changes with the applied bias voltage, the device  $IV$  curve exhibits NDR [320]. The details of how this happens are provided in Section 2.3.

This is possible thanks to the energy quantization inside the DBQW structure, that is, only certain electronic energy states are allowed inside the quantum well (QW), being the energy distribution spectrum discrete due to the associated stair-like density of states (DOS) [315]. Further details are provided in Section 2.4.1. Usually, the QW is designed to feature two quasi-bound states of energy  $E_1$  and  $E_2$ , respectively, which are mostly correlated to the first and second PDR region, respectively. The simplified conduction band (CB) diagram of a generic  $n$ -type intra-band RTD device at a generic bias point is depicted in Figure 2.1b. In the illustration, a generic resonant state  $E$  is assumed, and electrons tunnelling through the DBQW structure are schematically depicted as plane-waves travelling from the emitter to the collector side.

Since resonant tunnelling across the DBQW region can be an extremely-fast process (even though the concept of "tunnelling time" is still a controversial subject of debate [321, 322]), the bandwidth associated to the NDR can reach and overcome the THz range [323, 324]. For this reason, RTD devices can be successfully employed to develop ultra-fast THz sources and detectors. Although resonant tunnelling of holes has been also experimentally observed [325–327], electron operation is adopted due to the higher operational speed provided.

## 2.2 Historical notes

The concept of quantum-mechanical resonant tunnelling in crystals dates back to the early twentieth century with the idea of one-dimensional crystal proposed by Kronig and Penney in 1931 [328]. The problem of electron resonant tunnelling through a sequence of electrostatic potential barriers was originally studied theoretically and addressed similarly as for the resonant transmission of light through a Fabry-Pérot etalon [329]. In this regard, among the main contributions, it is worth mentioning the work of Iogansen (1964–1965) [330, 331] and Kane (1969) [332].

However, the major breakthrough took place only between 1970 and 1973, when Esaki, Tsu, and Chang (the former co-inventor of the (inter-band) tunnel diode (TD) in 1957 [317]) theoretically proved the attainability of ultra-fast electron resonant tunnelling and negative differential conductance (NDC) in semiconductor-based superlattices [333, 334], while the first experimen-

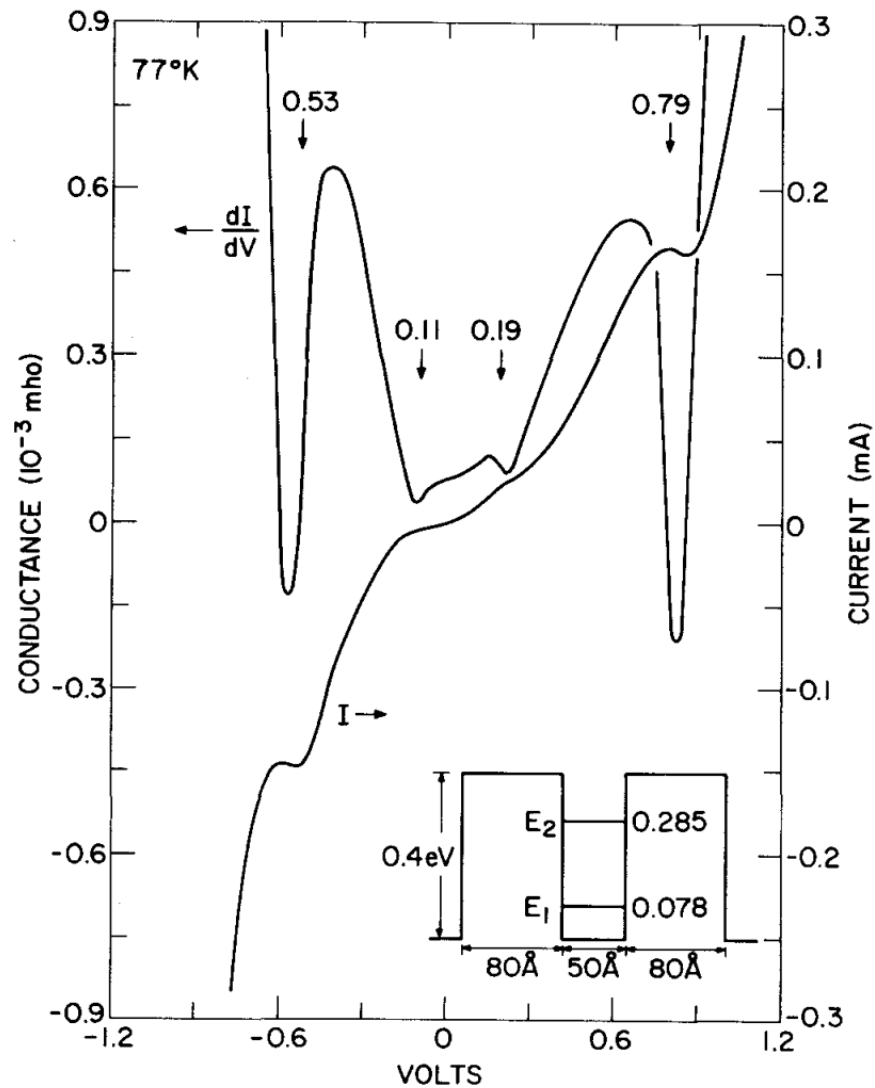


Figure 2.2: Measured conductance (left axis) and current (right axis)-voltage characteristics at  $T = 77$  K of the GaAs/ $\text{Al}_{0.7}\text{Ga}_{0.3}\text{As}$  double-barrier heterostructure reported in [335], featuring 8 nm-thick barriers and an 5 nm-thick QW (reprinted from [335]).

tal demonstration was reported by the same researchers in 1974 in gallium arsenide/aluminium gallium arsenide (GaAs/AlGaAs) heterostructures up to a temperature  $T = 125$  K [335–337]. Figure 2.2 shows the measured conductance and current as a function of the applied voltage of the double-barrier GaAs/ $\text{Al}_{0.7}\text{Ga}_{0.3}\text{As}$  heterostructure investigated in [335], where NDC with peak tunnelling current was experimentally observed at  $T = 77$  K.

The possibility of relying on extremely fast quantum-mechanical processes, together with the attainability of NDC in 1D vertical transport nanostructures, led to an intensive research work on resonant tunnelling in semiconductor-based double-barrier heterostructures [338–341] and superlattices [342–344]. However, this only began in the first half of the 1980s, thanks to the rapid progress of epitaxial crystal growth techniques achieved within the 1970s, including

molecular beam epitaxy (MBE) [345] and metal-organic vapour phase epitaxy (MOVPE) [346] technologies, which led to a significant improvement in high-quality heterostructures material growth [347]. Therefore, starting from the second half on the 1980s, extensive research was devoted to the development and realisation of high-speed resonant devices, including resonant tunnelling bipolar/hot-electron transistors (RBT/RHET) [348–350], and double-/triple-barrier RTDs [351–353].

The existence of NDC in epitaxially-grown RTD structures was experimentally-demonstrated for the first time by Sollner *et al.* in 1983 in GaAs/AlGaAs DBQW heterojunctions, reporting NDC at up to  $T = 200$  K and showing rectification at frequencies of up to around 2.5 THz at  $T = 25$  K [323]. However, room temperature (RT) responses of up to 3.9 THz were attained only in 1994 by Scott *et al.* employing the indium gallium arsenide/aluminium arsenide (In-GaAs/AlAs) material system [324]. The achievement of these two milestones indicated the practical viability of ultra-high-frequency THz sources and detectors based on the RTD device.

## 2.3 Principle of operation

The physical mechanism of the RTD is based on two key aspects: 1) the existence of quantised two-dimensional (2D) electronic states within the core of the device; and 2) the attainability of ultra-fast conduction based on quantum-mechanical resonant tunnelling through these metastable states [319]. The working principle of an  $n$ -type intra-band DBQW RTD device is illustrated in Figure 2.3. In the description,  $E_F$ ,  $E_{Fn}^e$ ,  $E_{Fn}^c$ ,  $E_c^e$ ,  $E_c^c$  are the Fermi level, and quasi-Fermi levels (electro-chemical potentials) and CB edges of the three-dimensional (3D) emitter and collector (supposed perfect conductors), respectively, while  $E_1$  and  $E_2$  are the QW quasi-bound state energy levels. Forward bias operation is assumed as example.

The device electrical behaviour can be sub-divided into six different operation regions [313]:

- a) *Thermal equilibrium*: the net current flow through the DBQW region is zero since no bias voltage is applied.
- b) *First PDR region*: when the right contact (collector) is biased with respect to the left one (emitter), a negligible non-resonant thermionic current component occurs for  $E_1 > E_{Fn}^e$ , while resonant current starts flowing as soon as  $E_1 \sim E_{Fn}^e$  and grows as  $E_1$  moves below  $E_{Fn}^e$ . In this regime, the current is roughly proportional to the number of tunnelling-available states belonging to the associated emitter Fermi sphere section, i.e. the current linearly increases with the applied bias and proportionally to  $E_{Fn}^e - E_1$  in the limit  $T \rightarrow 0$  K (neglecting scattering mechanisms), while a non-linear behaviour is observed at  $T > 0$  K due to thermally/scattering-activated components.

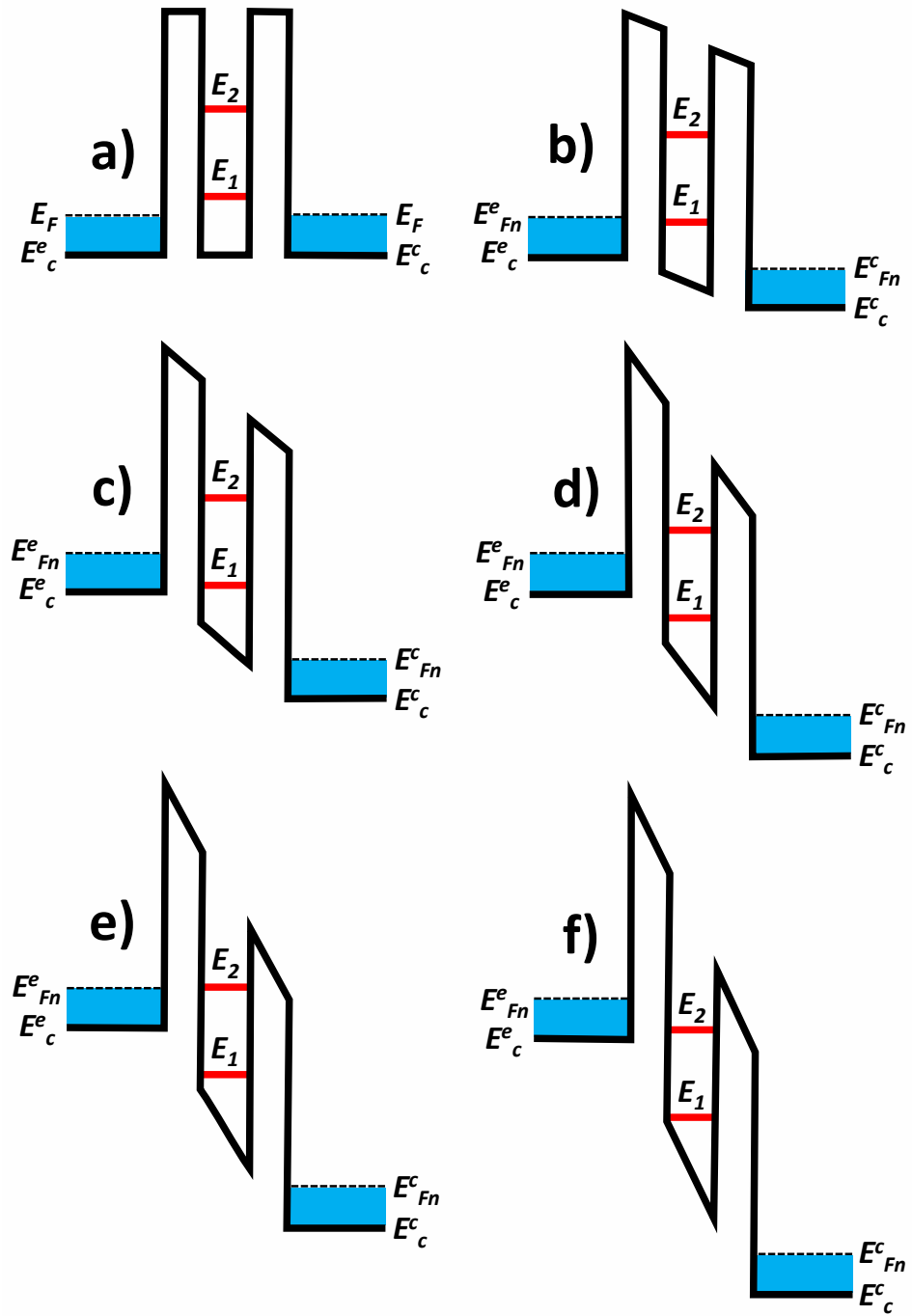


Figure 2.3: Simplified illustration of the operation principle of an  $n$ -type intra-band DBQW RTD device: a) thermal equilibrium; b) first PDR region; c) peak resonance; d) NDR region; e) valley point; and f) second PDR region. In this representation, the blue regions represent the emitter and collector Fermi sea.

- c) *Peak resonance*: the current keeps increasing with bias up to the peak resonance condition  $E_1 = E_c^e$ , i.e.,  $V = V_p$ , where  $\mathcal{T}_{DBQW}$  has a resonant peak.
- d) *NDR region*: if the bias voltage is increased further,  $E_1$  moves below  $E_c^e$  (emitter band gap) and no electronic states are available for resonant tunnelling assuming, so

the current drops, i.e., NDR.

- e) *Valley point*: if the bias voltage is increased even further, the current reaches a minimum when  $E_2 = E_{Fn}^e$ , i.e.,  $V = V_v$ .
- f) *Second PDR region*: at higher bias voltages, the current rises again thanks to the conduction channel given by  $E_2$ , similarly as for the first PDR region.

Further and more in-depth considerations on the RTD static  $IV$  characteristic will be discussed in Chapters 4 and 5.

## 2.4 Physical modelling

### 2.4.1 Electronic states quantisation in quantum well structures

The core of the RTD consists of a DBQW heterojunction, which is made of a narrow-band gap QW layer sandwiched between two wide-band gap thin barrier layers. In this system, electrons are confined along a longitudinal direction  $\hat{z}$  with translational broken symmetry, while quasi-free to move along the associated transverse plane defined by  $\mathbf{r}_T = x\hat{x} + y\hat{y}$ . Since the QW is nanometric in dimension, with thickness comparable or smaller than the electron wavelength, electronic states are quantised and distributed according to a set of energy subbands [354], generating a 2D electron gas [355]. In the following, approximate analytical expressions to model electronic states in rectangular QW structures are provided.

#### 2.4.1.1 Infinitely-deep rectangular potential well

The quantum nature of electrons in narrow potential wells can be analysed solving Schrödinger's equation for stationary states in the parabolic energy dispersion approximation [356]:

$$\hat{\mathcal{H}}\psi = \left[ -\frac{\hbar^2}{2m_e^*}\nabla^2 + U(r) \right] \psi = E\psi \quad (2.1)$$

where  $\hat{\mathcal{H}}$  is an hermitian operator representing the system Hamiltonian,  $E$  is the electron energy, while  $\psi$  the associated wave-function,  $U$  is the electrostatic potential energy,  $r = |\mathbf{r}| = (x, y, z)$ ,  $m_e^*$  is the electron effective mass (assumed subband-independent and isotropic in the Fourier space of the crystal),  $\nabla = \sum_j \hat{j} \partial / \partial j$  (where  $j = x, y, z$ ) is the del operator, and  $\hbar = h/2\pi$  the normalised Planck constant. For the sake of simplicity,  $\psi$  can be assumed factorisable as:

$$\psi(r) = \psi(x, y, z) = \phi_z(z) \prod_{s=x,y} \phi_s(s) \quad (2.2)$$

where  $\phi_z$  is an envelope wave-function describing electron confinement within the QW and providing a picture of the associated distribution of probability density as a function of  $z$ , while

$\varphi_s$  (where  $s = x, y$ ) are the components of  $\psi$  along the corresponding transverse (translational-invariant) directions. To simplify the treatment, the bottom of the well can be placed in correspondence to  $E = E_c = 0$ , where  $E_c$  is the CB edge. In this picture,  $E$  can be expressed as:

$$E = \sum_{s=x,y} E_s + E_z \quad (2.3)$$

where  $E_s$  ( $s = x, y$ ) and  $E_z$  are the transverse and longitudinal eigenenergies, respectively. For a specific component  $\psi_j$  (where  $j = x, y, z$ ), Eq. (2.1) can be re-written as [357]:

$$\frac{\partial^2 \psi_j(j)}{\partial j^2} + k_j^2 \psi_j(j) = 0 \quad (2.4)$$

whose general solution can be expressed in the following ansatz:

$$\psi_j(j) = \alpha \exp(ik_j j) + \beta \exp(-ik_j j) \quad (2.5)$$

where  $\alpha$  and  $\beta$  are arbitrary constants, while  $k_j = \sqrt{2m_e^*(E_j - U_j)}/\hbar$  is the electron wave-vector modulus component, (being  $U_j = U_s = 0$  if  $s = x, y$ ).

Assuming an infinitely-deep rectangular potential well of width  $W$  and with  $U$  of the following form:

$$U(r) = U_z(z) = \begin{cases} 0, & 0 < z < W \\ +\infty, & z < 0 \wedge z > W \end{cases} \quad (2.6)$$

solutions of Eq. (2.4) have the following general forms [357, 358] :

$$\varphi_x(x) = A_x \exp(ik_x x) + B_x \exp(-ik_x x) \quad (2.7)$$

$$\varphi_y(y) = A_y \exp(ik_y y) + B_y \exp(-ik_y y) \quad (2.8)$$

$$\phi_z(z) = C \sin(k_z z) + D \cos(k_z z) \quad (2.9)$$

where  $\varphi_s$  ( $s = x, y$ ) are quasi-free states,  $k_s = \sqrt{2m_e^* E_s}/\hbar$  are the wave-vector moduli along the corresponding transverse directions, while  $A_{x/y}$  and  $B_{x/y}$  arbitrarily constants. On the other hand,  $C$  and  $D$ , alongside with the longitudinal wave-vector modulus inside the QW  $k_z = \sqrt{2m_e^* E_z}/\hbar$ , can be retrieved imposing boundary conditions and enforcing normalisation to  $\phi_z$ . In this sense, the electron probability density outside the well is null, i.e., electronic states are fully enclosed within the QW region. Therefore, from the continuity of  $\phi_z$  at both  $z = 0$  and  $z = W$ :

$$\phi_z(0) = 0 \longrightarrow D = 0 \quad (2.10)$$

$$\phi_z(W) = 0 \longrightarrow \sin(k_z W) = 0 \longrightarrow k_z = \frac{\pi q}{W} \quad (2.11)$$

where  $q$  are integer numbers ( $q = 0, \pm 1, \pm 2, \dots$ ) that label the different energy subbands. In this sense, Eq. (2.11) states that  $k_z$  is quantized. It turns out that  $\phi_z$  and  $E_z$  can be written in the

following two forms [358]:

$$\phi_z(z) = \phi_q(z) = C \sin\left(\frac{\pi q}{W}z\right) \quad (2.12)$$

$$E_z = E_q = \frac{\hbar^2}{2m_e^*} \left(\frac{\pi q}{W}\right)^2 \quad (2.13)$$

where Eq. (2.13) reveals energy discretization along the confinement direction  $\hat{z}$ . Moreover, from the normalisation of  $\phi_z$ :

$$\int_0^W |\phi_z(z)|^2 dz = C^2 \int_0^W \sin^2\left(\frac{\pi q}{W}z\right) dz = 1 \longrightarrow C = \pm \sqrt{\frac{2}{W}} \quad (2.14)$$

Finally, assuming the potential well to be centred in  $z = 0$  ( $z \rightarrow z - W/2$ ), a general expression for the bound states  $\phi_q$  can be ultimately derived [315, 358]:

$$\phi_q(z) = \begin{cases} \sqrt{\frac{2}{W}} \sin\left(\frac{\pi q}{W}z\right), & q = 2, 4, 6, \dots \\ \sqrt{\frac{2}{W}} \cos\left(\frac{\pi q}{W}z\right), & q = 1, 3, 5, \dots \end{cases} \quad (2.15)$$

being  $\phi_{\pm q}$  states symmetric, which features anti-symmetric and symmetric shape according to even and odd subbands, respectively. A graphical representation of these states is shown in Figure 2.4. Therefore, the QW electronic states  $\psi$  and associated energies  $E$  expressions can be finally retrieved [359]:

$$\psi(r) = \begin{cases} \sqrt{\frac{2}{W}} \sin\left(\frac{\pi q}{W}z\right) \Pi_{s=x,y} [A_s \exp(ik_s r_s) + B_s \exp(-ik_s r_s)], & q = 2, 4, 6, \dots \\ \sqrt{\frac{2}{W}} \cos\left(\frac{\pi q}{W}z\right) \Pi_{s=x,y} [A_s \exp(ik_s r_s) + B_s \exp(-ik_s r_s)], & q = 1, 3, 5, \dots \end{cases} \quad (2.16)$$

$$E = \frac{\hbar^2}{2m_e^*} \left[ k_T^2 + \left(\frac{\pi q}{W}\right)^2 \right] \quad (2.17)$$

where  $k_T = \sqrt{\Sigma_{s=x,y} k_s^2} = \sqrt{2m_e^* E_T} / \hbar$  is the overall transverse wave-vector modulus, while  $E_T = \Sigma_{s=x,y} E_s$  the transverse energy.

The QW sheet electron density  $n_{2D}$ , i.e., the number of electrons per unit area and energy interval, at thermal equilibrium can be written on the basis of the system Fermi level  $E_F$  [359]:

$$n_{2D} = \sum_q n_q(E) = \int_0^{+\infty} g_{2D}(E) f_n(E) dE \quad (2.18)$$

where  $n_q$  is the electron density of the  $q$ -th subband,  $g_{2D}$  is the QW DOS, i.e., the number of allowed electronic states per unit area and energy interval, while  $f_n$  is the Fermi-Dirac distribution function:

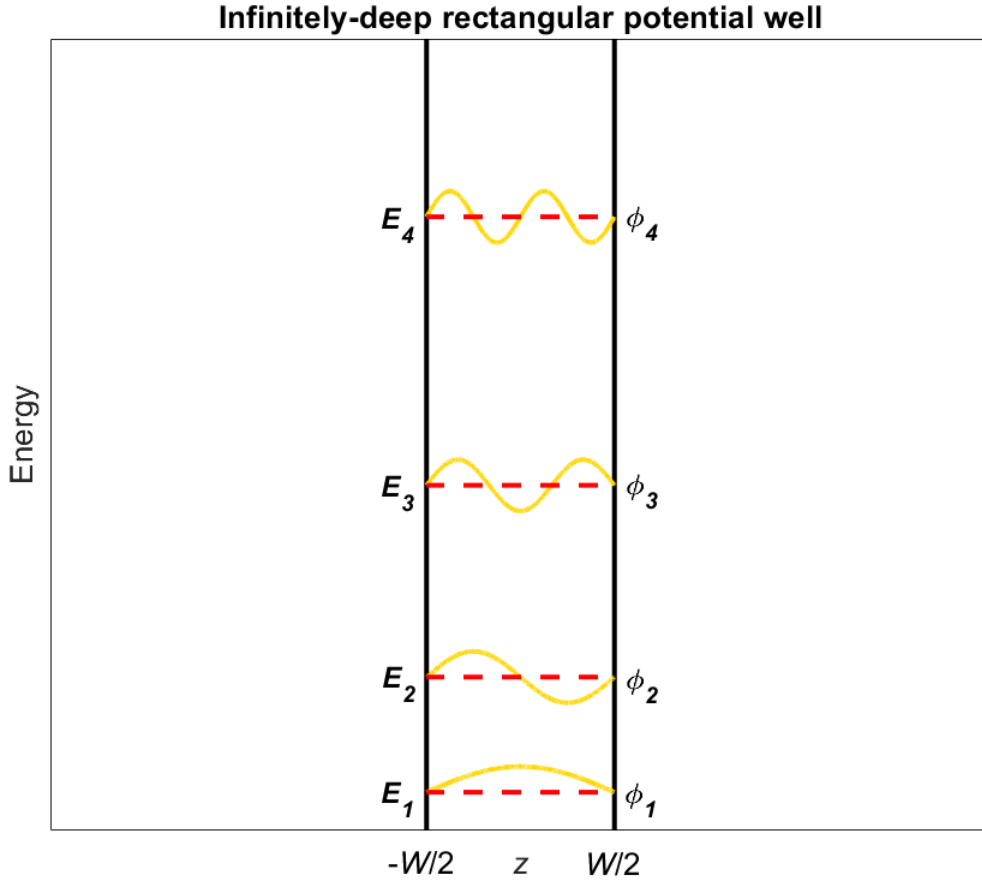


Figure 2.4: Illustration of the electronic eigenstates and eigenenergies of a generic infinitely-deep rectangular potential well computed through Eq. (2.15) and (2.13), respectively, outlining the first four subbands (i.e.,  $q = 1, 2, 3, 4$ ).

$$g_{2D}(E) = \sum_q g_q(E) \quad (2.19)$$

$$f_n(E) = \left[ \exp\left(\frac{E - E_F}{k_B T}\right) + 1 \right]^{-1} \quad (2.20)$$

being  $g_q$  the DOS of the  $q$ -th subband. To evaluate  $g_i$ , the quasi-free 2D electron gas is assumed enclosed in a transverse box region defined as  $(0 \leq x \leq L_x, 0 \leq y \leq L_y)$ , with  $L_x, L_y \gg W$ . Imposing Born-von Karman periodic boundary conditions to  $\varphi_x$  and  $\varphi_y$ , the normalisation constants  $A = 1/\sqrt{L_x}$   $B = 1/\sqrt{L_y}$  can be retrieved. Moreover, electronic states quantization in the transverse plane  $k_T = (k_x, k_y)$  occurs, giving  $k_x = 2\pi l/L_x$  and  $k_y = 2\pi m/L_y$ , being  $l$  and  $m$  integer numbers [360]. The allowed states belonging to the  $q$ -th subband of energy  $E_q$  and having energy  $E_T < E - E_q$  are the one belonging to the plane circle of radius  $k_T$  for which:

$$k_T < \frac{\sqrt{2m_e^*(E - E_q)}}{\hbar} \quad (2.21)$$

The number of these states  $N_q$  can be approximately derived by dividing the circle area by

the area associated with each state, which is  $k_x k_y = 4\pi^2/L_x L_y$ . Therefore, accounting for spin degeneracy,  $N_q$  can be written as [315, 358]:

$$N_q(E) = 2\pi \frac{2m_e^*(E - E_q) L_x L_y}{\hbar^2} \frac{L_x L_y}{4\pi^2} = \frac{m_e^* L_x L_y (E - E_q)}{\pi \hbar^2} \quad (2.22)$$

where  $N_q > 0$  if  $E > E_q$ , while  $N_q = 0$  if  $E \leq E_q$ . Therefore,  $g_q$  is given by [315, 358]:

$$g_q(E) = \frac{1}{L_x L_y} \frac{dN_q(E)}{dE} = \frac{1}{L_x L_y} \frac{m_e^* L_x L_y}{\pi \hbar^2} = \frac{m_e^*}{\pi \hbar^2} \quad (2.23)$$

where  $g_q > 0$  if  $E > E_q$ , while  $g_q = 0$  for  $E \leq E_q$ . In this sense, Eq. (2.23) states that the DOS in each subband is energy independent. The DOS can be then expressed by summing up over all the subbands, and the same for  $n_{2D}$ :

$$g_{2D}(E) = \sum_{q=1}^{+\infty} \frac{m_e^*}{\pi \hbar^2} u(E - E_q) \quad n_{2D} = \sum_{q=1}^{+\infty} n_q \quad (2.24)$$

where  $u$  is the Heviside step function. A stair-like energy behaviour is revealed.

Therefore,  $n_{2D}$  is finally given by [359]:

$$n_{2D} = \frac{m_e^*}{\pi \hbar^2} \sum_{q=1}^{+\infty} \int_{E_q}^{+\infty} \left[ \exp\left(\frac{E - E_F}{k_B T}\right) + 1 \right]^{-1} dE = \frac{m_e^*}{\pi \hbar^2} \sum_{q=1}^{+\infty} \log \left[ \exp\left(\frac{E_F - E_q}{k_B T}\right) + 1 \right] \quad (2.25)$$

where:

$$n_q = \frac{m_e^*}{\pi \hbar^2} \int_{E_q}^{+\infty} \left[ \exp\left(\frac{E - E_F}{k_B T}\right) + 1 \right]^{-1} dE = \frac{m_e^*}{\pi \hbar^2} \log \left[ \exp\left(\frac{E_F - E_q}{k_B T}\right) + 1 \right] \quad (2.26)$$

### 2.4.1.2 Finite-depth rectangular potential well

Despite that, realistic RTD heterostructures feature barriers with finite height, typically ranging between around 1–2 eV depending on the employed semiconductor materials [163], and this has an impact on the associated electronic structure. Assuming a rectangular potential well of depth  $U_b$ , width  $W$ , and centred in  $z = 0$  (similarly as sketched in Figure 2.3a):

$$U_z(z) = \begin{cases} 0, & |z| < W/2 \\ U_b, & |z| > W/2 \end{cases} \quad (2.27)$$

the longitudinal wave-vector modulus  $p_z(z)$  can be expressed as [315, 358]:

$$p_z(z) = \frac{\sqrt{2m_e^*[E_z - U_z(z)]}}{\hbar} = \begin{cases} \frac{\sqrt{2m_e^*E_z}}{\hbar} = k_z, & |z| < W/2 \\ \frac{i\sqrt{2m_e^*(U_b - E_z)}}{\hbar} = i\rho_z, & |z| > W/2 \end{cases} \quad (2.28)$$

where, for the sake of simplicity,  $m_e^*(z)$  is assumed constant along  $\hat{z}$ , i.e.,  $m_e^*(z) = m_e^*$ . The envelope functions  $\phi_z$  in Eq. (2.9) can be then re-written as [358]:

$$\phi_z(z) = \begin{cases} F \exp(-\rho_z z), & z < -W/2 \\ C \sin(k_z z) + D \cos(k_z z), & |z| < W/2 \\ G \exp(\rho_z z), & z > W/2 \end{cases} \quad (2.29)$$

where barriers regions are assumed infinitely-thick to simplify the treatment, while  $k_z$  and  $i\rho_z$  ( $0 < E_z < U_b$ ) are the longitudinal wave-vector moduli of the quasi-bound states in the QW and barriers regions, respectively. Scattering states ( $E_z > U_b$ ) are not considered. From Eq. (2.29), it is clear that the envelopes decay evanescently within the barriers. Imposing the continuity of  $\phi_z$  and  $\phi'_z = \partial\phi_z(z)/\partial z$  at  $z = \pm W/2$ , a linear system in the unknowns  $C$ ,  $D$ ,  $F$ , and  $G$  is obtained:

$$\begin{cases} F \exp(\rho_z \frac{W}{2}) + C \sin(k_z \frac{W}{2}) - D \cos(k_z \frac{W}{2}) = 0 \\ F \rho_z \exp(\rho_z \frac{W}{2}) + C k_z \cos(k_z \frac{W}{2}) + D k_z \sin(k_z \frac{W}{2}) = 0 \\ C \sin(k_z \frac{W}{2}) + D \cos(k_z \frac{W}{2}) - G \exp(\rho_z \frac{W}{2}) = 0 \\ C k_z \cos(k_z \frac{W}{2}) - D k_z \sin(k_z \frac{W}{2}) - G \rho_z \exp(\rho_z \frac{W}{2}) = 0 \end{cases} \quad (2.30)$$

whose associated matrix diagonalization leads, imposing the determinant  $\det = 0$ , to the following couple of non-linear equations in  $k_z$  and  $\rho_z$  [358]:

$$\tan\left(k_z \frac{W}{2}\right) = \frac{\rho_z}{k_z} \quad (2.31)$$

$$\cot\left(k_z \frac{W}{2}\right) = -\frac{\rho_z}{k_z} \quad (2.32)$$

In particular, Eq. (2.31) describes symmetric states:

$$\phi_{z,s}(z) = \phi_{q,s}(z) = \begin{cases} F \exp(-\rho_z z), & z < -W/2 \\ D \cos(k_z z), & |z| < W/2 \\ F \exp(\rho_z z), & z > W/2 \end{cases} \quad (2.33)$$

while Eq. (2.32) models anti-symmetric ones:

$$\phi_{z,a}(z) = \phi_{q,a}(z) = \begin{cases} -G \exp(-\rho_z z), & z < -W/2 \\ C \sin(k_z z), & |z| < W/2 \\ G \exp(\rho_z z), & z > W/2 \end{cases} \quad (2.34)$$

Assuming  $X = k_z W/2$  and  $Y = \rho_z W/2$ , Eq. (2.31) and (2.32) turn into:

$$X \tan(X) = Y \quad (2.35)$$

$$X \cot(X) = -Y \quad (2.36)$$

Moreover, if  $X$  and  $Y$  are squared and summed, a third equation is obtained:

$$X^2 + Y^2 = (k_z^2 + \rho_z^2) \left(\frac{W}{2}\right)^2 = \frac{m_e^* W^2 U_b}{2\hbar^2} = X_0^2 \quad (2.37)$$

Therefore, symmetric ( $q = 2, 4, 6, \dots$ ) and anti-symmetric ( $q = 1, 3, 5, \dots$ ) eigenvalues  $E_{q,s}$  and  $E_{q,a}$  are finally given by the following two-equation systems, respectively:

$$\begin{cases} X \tan(X) = Y \\ X^2 + Y^2 = X_0^2 \end{cases} \quad (2.38)$$

$$\begin{cases} X \cot(X) = -Y \\ X^2 + Y^2 = X_0^2 \end{cases} \quad (2.39)$$

which can be solved either graphically or numerically. To retrieve the associated eigenvectors,  $C$ ,  $D$ ,  $F$ , and  $G$  have to be determined, which can be done imposing the normalization of  $\phi_{q,s}$  and  $\phi_{q,a}$  states along  $\hat{z}$ . For the symmetric envelopes  $\phi_{q,s}$ :

$$\int_0^{+\infty} |\phi_{z,s}(z)|^2 dz = D^2 \int_0^{+W/2} \cos^2(k_z z) + F^2 \int_{W/2}^{+\infty} \exp(-2\rho_z z) = \frac{1}{2} \quad (2.40)$$

Coupling Eq. (2.40) and Eq. (2.31), general  $D$  and  $F$  expressions are obtained:

$$D = \left[ \frac{\cos^2(k_z \frac{W}{2})}{\rho_z} + \frac{\sin(k_z W)}{2k_z} + \frac{W}{2} \right]^{-1/2} \quad (2.41)$$

$$F = \exp(\rho_z W) \cos\left(k_z \frac{W}{2}\right) \left[ \frac{\cos^2(k_z \frac{W}{2})}{\rho_z} + \frac{\sin(k_z W)}{2k_z} + \frac{W}{2} \right]^{-1/2} \quad (2.42)$$

The coefficients  $C$  and  $G$  of the antisymmetric states  $\phi_{q,a}$  can be retrieved in a similar way:

$$C = \left[ \frac{\sin^2(k_z \frac{W}{2})}{\rho_z} + \frac{\sin(k_z W)}{2k_z} + \frac{W}{2} \right]^{-1/2} \quad (2.43)$$

$$G = \exp(\rho_z W) \sin\left(k_z \frac{W}{2}\right) \left[ \frac{\sin^2(k_z \frac{W}{2})}{\rho_z} - \frac{\sin(k_z W)}{2k_z} + \frac{W}{2} \right]^{-1/2} \quad (2.44)$$

obtaining the complete form of the eigenstates  $\phi_q$  [358], while  $\psi$  can be written similarly as in Eq. (2.16). A graphical representation of these states is shown in Figure 2.5. The complete form of the eigenenergies can be retrieved adding  $E_T$  to the solutions of Eq. (2.38) and Eq. (2.39),

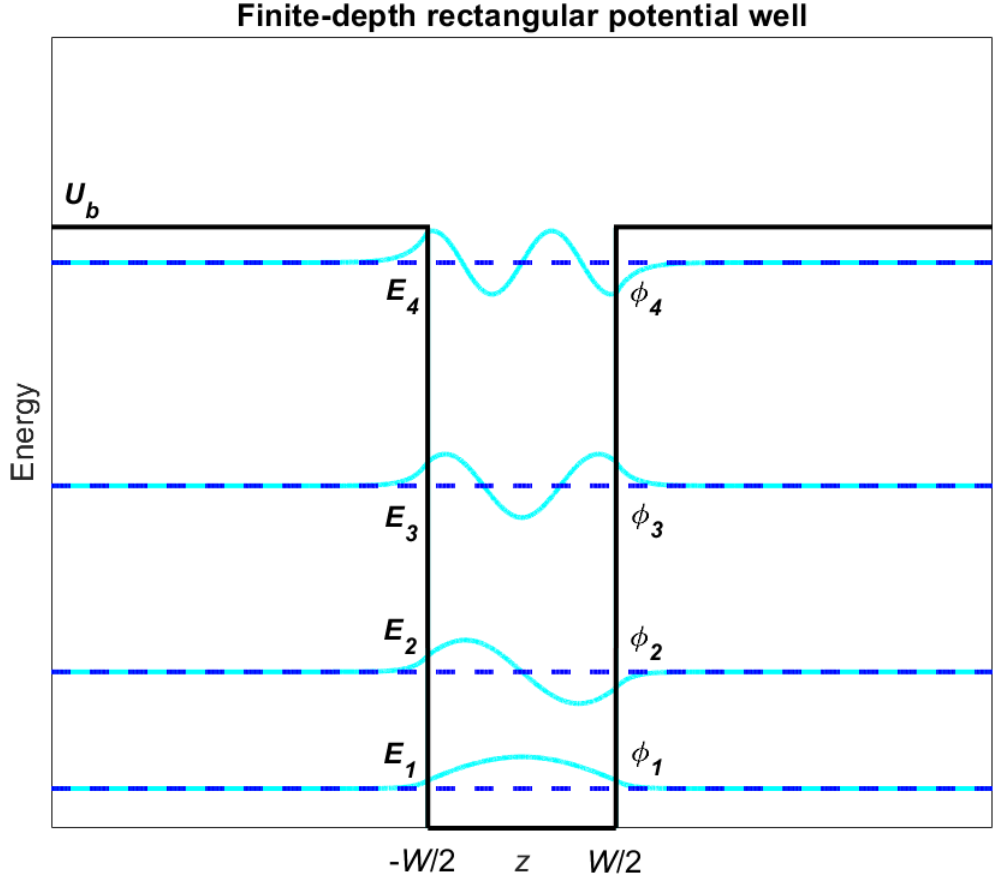


Figure 2.5: Illustration of the electronic quasi-bound states of a generic finite-depth rectangular potential well computed numerically through Eq. (2.31) to (2.34), outlining the first four subbands (i.e.,  $q = 1, 2, 3, 4$ ).

i.e.,  $E_z \rightarrow E_z + E_T$ , while the final expression can be obtained relaxing the  $E_c = 0$  assumption by accounting for the energy band gap.

The DOS  $g_{2D}$  and sheet electron density  $n_{2D}$  at thermal equilibrium can be, therefore, approximated similarly as in Eq. (2.24) and (2.25):

$$g_{2D}(E) = \sum_{q=1}^{+\infty} \frac{m_e^*}{\pi\hbar^2} u(E - E_q) \quad n_{2D} = \sum_{q=1}^{+\infty} n_q \quad (2.45)$$

$$\begin{aligned} n_{2D} &\approx \frac{m_e^*}{\pi\hbar^2} \sum_{q=1}^p \int_{-W/2}^{W/2} \phi_q^*(z) \phi_q(z) dz \int_{E_q}^{+\infty} \left[ \exp\left(\frac{E - E_F}{k_B T}\right) + 1 \right]^{-1} dE = \\ &= \frac{m_e^*}{\pi\hbar^2} \sum_{q=1}^p \int_{-W/2}^{W/2} |\phi_q(z)|^2 dz \log \left[ \exp\left(\frac{E_F - E_q}{k_B T}\right) + 1 \right] \end{aligned} \quad (2.46)$$

where  $\phi_q$  is the envelope eigenfunction belonging to the  $q$ -th subband, while  $p$  denotes the number of quasi-bound subbands. In this picture,  $n_{2D}(z)$  is obtained removing the integration along  $\hat{z}$ .

## 2.4.2 Tunnelling and electron transport through potential barriers

The transmission coefficient through a potential barrier can be defined as the ratio between the flux of particles (e.g., electrons) beyond the barrier and the one impinging it. Assuming the electrostatic potential energy profile  $U_z(z)$  to be a piecewise flat function, i.e.,  $k_z(z) = k_z$  constant within the left/right quasi-free regions and the barrier, general solutions of Eq. (2.4) along  $\hat{z}$  in each of these regions can be expressed, similarly to Eq. (2.5), as linear combinations of plane-waves [315, 357]:

$$\psi_z(z) = \psi_z^+ \exp(ik_z z) + \psi_z^- \exp(-ik_z z) \quad (2.47)$$

where the first and second term are the incident and reflected components of  $\psi_z$ , respectively, while  $\psi_z^+$  and  $\psi_z^-$  are the associated probability amplitudes.

Supposing an electron flux with energy  $E_z$  coming from  $-\infty$  and impinging on a potential barrier of height  $U_b$ , where  $E_z < U_b$ , the flux is partially transmitted to  $+\infty$  and partially reflected to  $-\infty$  thanks to quantum mechanical tunnelling. The barrier transmission coefficient, also called transmittance or transmission probability, is defined as [357]:

$$\mathcal{T}(E_z) = \frac{|\psi_z^+(+\infty)|^2 k_z(+\infty) m_e^*(+\infty)}{|\psi_z^+(-\infty)|^2 k_z(-\infty) m_e^*(-\infty)} \quad (2.48)$$

In this sense,  $\mathcal{T}$  represents the key element on which the operation principle of an RTD is based, and its form influences the associated electrical characteristics.

### 2.4.2.1 Tunnelling through a finite-height rectangular potential barrier

Assuming a finite-height rectangular potential barrier having height  $U_b$ , width  $W$ , and located between  $0 < z < W$ , as depicted in Figure 2.6a, the associated potential profile  $U_z$  can be written as:

$$U_z(z) = \begin{cases} 0, & z < 0 \wedge z > W \\ U_b, & 0 < z < W \end{cases} \quad (2.49)$$

Therefore, solutions in the form of Eq. (2.47) can be written as [358]:

$$\psi_z(z) = \begin{cases} \psi_1(z) = \psi_1^+ \exp(ik_1 z) + \psi_1^- \exp(-ik_1 z), & z < 0 \\ \psi_2(z) = \psi_2^+ \exp(-\rho_2 z) + \psi_2^- \exp(\rho_2 z), & 0 < z < W \\ \psi_3(z) = \psi_3^+ \exp(ik_3 z), & z > W \end{cases} \quad (2.50)$$

where  $\psi_{1,3}$  are scattering states and  $\psi_3^- = 0$  since there is no barrier which can reflect back for  $W < z < +\infty$ .

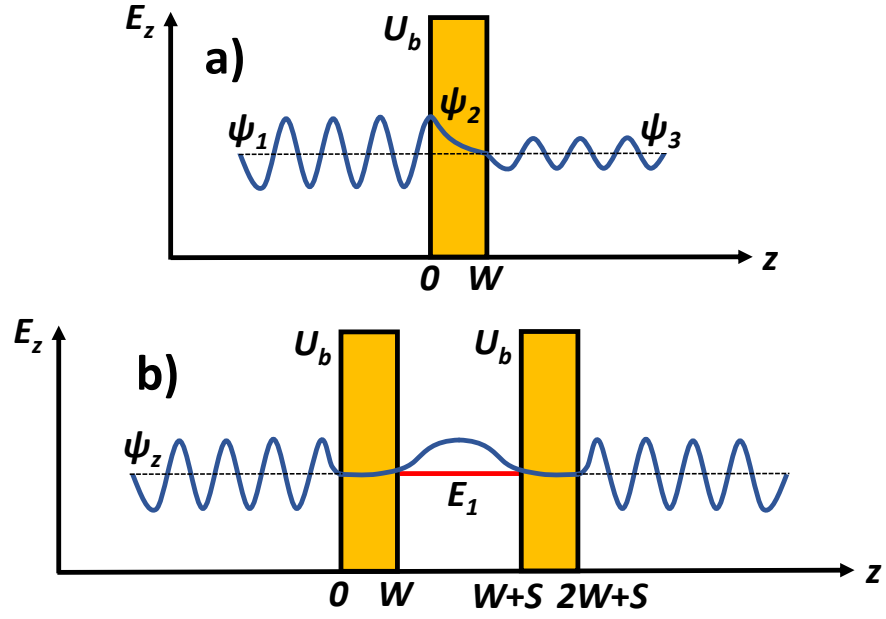


Figure 2.6: In a), illustration of tunnelling through a finite-height rectangular potential barrier; in b), illustration of resonant tunnelling through a DBQW structure thanks to the first subband  $E_1$ .

The associated wave-vector moduli are given similarly as in Eq. (2.28) [315, 358]:

$$p_z(z) = \frac{\sqrt{2m_e^*[E_z - U_z(z)]}}{\hbar} = \begin{cases} \frac{\sqrt{2m_e^*E_z}}{\hbar} = k_1, & z < 0 \\ i\sqrt{2m_e^*(U_b - E_z)} = k_2 = i\rho_2, & 0 < z < W \\ \frac{\sqrt{2m_e^*E_z}}{\hbar} = k_3 = k_1, & z > W \end{cases} \quad (2.51)$$

where  $0 < E_z < U_b$  and, for the sake of simplicity,  $m_e^*(z)$  is assumed constant along  $\hat{z}$ , i.e.,  $m_e^*(z) = m_e^*$ . By enforcing the continuity of  $\psi_z$  and  $\psi'_z = \partial\psi_z(z)/\partial z$  at  $z = W$ :

$$\psi_2(W) = \psi_3(W) \quad (2.52)$$

$$\psi'_2(W) = \psi'_3(W) \quad (2.53)$$

a linear system in the unknowns  $\psi_2^+$ ,  $\psi_2^-$ , and  $\psi_3^+$  is obtained:

$$\begin{cases} \psi_2^+ \exp(-\rho_2 W) + \psi_2^- \exp(\rho_2 W) = \psi_3^+ \exp(ik_1 W) \\ -\rho_2 \psi_2^+ \exp(-\rho_2 W) + \rho_2 \psi_2^- \exp(\rho_2 W) = ik_1 \psi_3^+ \exp(ik_1 W) \end{cases} \quad (2.54)$$

from which:

$$\frac{\psi_2^-}{\psi_3^+} = \frac{ik_1 + \rho_2}{2\rho_2} \exp[W(ik_1 - \rho_2)] \quad (2.55)$$

$$\frac{\psi_2^+}{\psi_3^+} = -\frac{ik_1 - \rho_2}{2\rho_2} \exp[W(ik_1 + \rho_2)] \quad (2.56)$$

Imposing the same conditions at  $z = 0$ , the following equation is obtained:

$$\psi_1^+ = \frac{k_1 + i\rho_2}{2k_1} \psi_2^+ + \frac{k_1 - i\rho_2}{2k_1} \psi_2^- \quad (2.57)$$

Substituting now Eq. (2.55) and (2.56) in Eq. (2.57) gives:

$$\begin{aligned} \frac{\psi_3^+}{\psi_1^+} &= \frac{(k_1 + i\rho_2)^2}{4ik_1\rho_2} \exp[W(ik_1 + \rho_2)] - \frac{(k_1 - i\rho_2)^2}{4ik_1\rho_2} \exp[W(ik_1 - \rho_2)] = \\ &= \left[ \cosh(\rho_2 W) - i \frac{k_1^2 - \rho_2^2}{2k_1\rho_2} \sinh(\rho_2 W) \right] \exp(ik_1 W) \end{aligned} \quad (2.58)$$

from which [315, 358]:

$$\frac{|\psi_3^+|^2}{|\psi_1^+|^2} = \left| \frac{\exp(-ik_1 W)}{\cosh(\rho_2 W) - i \frac{k_1^2 - \rho_2^2}{2k_1\rho_2} \sinh(\rho_2 W)} \right|^2 = \frac{4k_1^2 \rho_2^2}{4k_1^2 \rho_2^2 + (k_1^2 + \rho_2^2)^2 \sinh^2(\rho_2 W)} \quad (2.59)$$

The transmission coefficient  $\mathcal{T}_b$  is, therefore, given as [358]:

$$\begin{aligned} \mathcal{T}_b(E_z) &= \frac{|\psi_3^+|^2}{|\psi_1^+|^2} = \frac{4E_z(U_b - E_z)}{4E_z(U_b - E_z) + U_b^2 \sinh^2 \left[ \frac{W \sqrt{2m_e^*(U_b - E_z)}}{\hbar} \right]} = \\ &= \left\{ 1 + \frac{U_b^2}{4E_z(U_b - E_z)} \sinh^2 \left[ \frac{W \sqrt{2m_e^*(U_b - E_z)}}{\hbar} \right] \right\}^{-1} \sim \exp[-2\rho_2 W] \end{aligned} \quad (2.60)$$

#### 2.4.2.2 Tunnelling through a double-barrier quantum well structure: the global coherent resonant tunnelling picture

The transmission coefficient of a DBQW structure  $\mathcal{T}_{DBQW}$  [314] can be, as a first approximation, retrieved through the transfer matrix approach [315, 358]. Assuming two identical rectangular barriers of width  $W$ , height  $U_b$ , and separated by a QW region of width  $S$ , as depicted in Figure 2.6b,  $\mathcal{T}_{DBQW}$  can be expressed as [313]:

$$\begin{aligned} \mathcal{T}_{DBQW}(E_z) &\approx \left| \exp[-ik_z(2W + S)] \left\{ \left[ \cosh(\rho_z W) - i \frac{2E_z - U_b}{2\sqrt{E_z(U_b - E_z)}} \sinh(\rho_z W) \right]^2 \right. \right. \\ &\quad \left. \left. \exp(-ik_z S) + \frac{4U_b^2}{E_z(U_b - E_z)} \sinh^2(\rho_z W) \exp(ik_z S) \right\}^{-1} \right|^2 \end{aligned} \quad (2.61)$$

which features resonances in correspondence to the QW resonant subbands  $E_q$ . A graphical representation of  $\mathcal{T}_{DBQW}$  of a generic DBQW structure is shown in Figure 2.7. In particular, in proximity to the  $q$ -th resonance ( $E_z \sim E_q$ ), the following expression applies [313]:

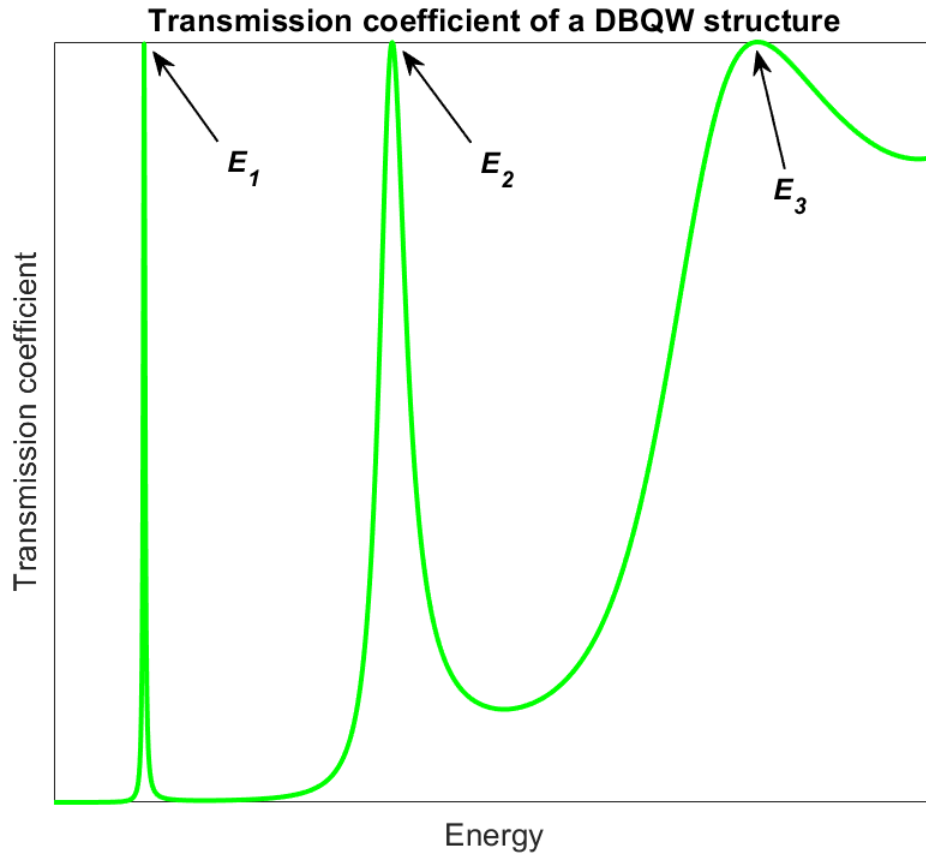


Figure 2.7: Schematic illustration of the transmission coefficient of a generic DBQW structure computed through Eq. (2.61), outlining the resonances associated with three quasi-bound state resonant levels  $E_q$  ( $q = 1, 2, 3$ ).

$$\mathcal{T}_{DBQW}(E_z) \approx \left| \frac{\Gamma_q}{(E_z - E_q) + i\Gamma_q} \exp[-ik_z(2W + S)] \right|^2 = \frac{\Gamma_q^2}{(E_z - E_q)^2 + \Gamma_q^2} \quad (2.62)$$

where  $\Gamma_q$  is the full-width at half maximum (FWHM) or intrinsic energy broadening parameter, of the  $q$ -th resonant subband, which can be modelled as [362]:

$$\Gamma_q = \frac{\hbar}{\tau_q} \quad (2.63)$$

being  $\tau_q$  the associated electron quasi-bound state lifetime [363], which can be within the picosecond and even femtosecond range depending on the specific DBQW structure [313] due to the thin employed barriers and QWs in THz RTD devices.

In this sense, Eq. (2.62), widely-known as Breit-Wigner's formula, shows that  $\mathcal{T}_{DBQW}$  has a Lorentzian shape with energy broadening  $\Gamma_q$ , which, generally-speaking, depends on different factors, including the relative energy position of the resonant subband  $E_q$  with respect to the barriers [366], i.e., on how much the electron is bounded in the QW (as can be seen in Figure 2.7), QW and barriers thickness, and the employed material system. This is the basic physical

principle on which the electrical operation of an RTD device is founded [309].

The treatment reported so far assumes thermal equilibrium, i.e., the net current through the DBQW is supposed null. If a constant external voltage  $V$  is applied, the steady-state current density  $J$  flowing through the  $q$ -th resonant subband channel can be approximated by the Landauer, or Tsu-Esaki, model for tunnelling through stationary states [313]:

$$J(V) \approx \frac{e}{2\pi^2} \left\{ \int_0^{+\infty} k_T dk_T \int_0^{+\infty} v_z(k_z) \mathcal{T}_{DBQW}(k_z, V) f_n^e(k_T, k_z) [1 - f_n^c(k_T, k_z)] dk_z + \int_0^{+\infty} k_T dk_T \int_{-\infty}^0 v_z(k_z) \mathcal{T}_{DBQW}(k_z, V) f_n^c(k_T, k_z) [1 - f_n^e(k_T, k_z)] dk_z \right\} \quad (2.64)$$

where  $f_n^{e/c}$  are the emitter/collector Fermi-Dirac distribution functions, while  $v_z = \hbar^{-1} dE_z/dk_z$  the wave-packet group velocity. Integrating over the transverse momentum  $k_T$  [334, 364]:

$$J(V) \approx \frac{em_e^* k_b T}{2\pi^2 \hbar^3} \int_0^{+\infty} \mathcal{T}_{DBQW}(E_z, V) \log \left[ \frac{1 + \exp\left(\frac{E_{Fn}^e - E_z}{k_B T}\right)}{1 + \exp\left(\frac{E_{Fn}^e - E_z - eV}{k_B T}\right)} \right] dE_z \quad (2.65)$$

where  $m_e^*$  is assumed isotropic along both transverse and longitudinal directions, and [361]:

$$\mathcal{T}_{DBQW}(E_z, V) \approx \frac{\left(\frac{\Gamma_q}{2}\right)^2}{[E_z - (E_q - \frac{eV}{2})]^2 + \left(\frac{\Gamma_q}{2}\right)^2} \quad (2.66)$$

where  $V = (E_{Fn}^e - E_{Fn}^c)/e$  (being  $e$  the elementary charge), which is supposed to split symmetrically with respect to the QW centre (but can be generalised). Since  $\Gamma_q \ll k_B T$ , which is usually the case even at RT, the integration along the longitudinal direction becomes analytical [361]:

$$J(V) \approx \frac{em_e^* k_b T \Gamma_q}{4\pi^2 \hbar^3} \log \left[ \frac{1 + \exp\left(\frac{E_{Fn}^e - E_q + \frac{eV}{2}}{k_B T}\right)}{1 + \exp\left(\frac{E_{Fn}^e - E_q - \frac{eV}{2}}{k_B T}\right)} \right] \left[ \cot\left(\frac{E_q - \frac{eV}{2}}{\frac{\Gamma_q}{2}}\right) + \frac{\pi}{2} \right] \quad (2.67)$$

In this sense, Eq. (2.67) is valid within the global coherent, or ballistic, limit, i.e., the electron wave-function is supposed not experiencing any phase coherence-breaking mechanism within the path between emitter and collector. In this work, the aforementioned quantum transport regime has been employed within a non-equilibrium Green's function (NEGF)-based framework. Further details will be provided in Chapter 4.

### 2.4.2.3 The sequential scattering-assisted resonant tunnelling picture: phase-decoherence and dissipative processes

The global coherent regime is, in principle, restricted to  $T = 0$  K operation and neglects any source of electron interaction. However, in realistic RTD devices working at RT, electrons un-

dergo scattering events [315] with the surrounding physical environment [365]. This can happen either during resonant tunnelling through the DBQW structure or transiting across the emitter and collector extended regions.

The former can be described by the sequential tunnelling picture [366, 367], where electron tunnelling is modelled as a two-stage process. First, the electron elastically-tunnels from the emitter into the QW. Here, scattering takes place and information on the electron wave-function phase is lost, i.e., phase-coherence is broken. At this stage, the electron can thermalise into locally-available quasi-equilibrium states if undergoes an inelastic scattering event. Second, the electron elastically-tunnels from the QW into the collector.

Mathematically speaking, the sequential tunnelling process can be modelled through a simple ad-hoc Hamiltonian [313]. In this picture, the phenomenological effect of phase-decoherence is reflected on  $\mathcal{T}_{DBQW}$  in terms of energy broadening of the specific resonant peak. If the electron wave-function phase is assumed to randomly change throughout the whole resonant tunnelling process, Eq. (2.66) can be re-written as [368]:

$$\mathcal{T}_{DBQW}(E_z, V) \approx \frac{\left(\frac{\Gamma_t}{2}\right)^2}{\left[E_z - \left(E_q - \frac{eV}{2}\right)\right]^2 + \left(\frac{\Gamma_t}{2}\right)^2} \frac{\Gamma_q}{\Gamma_t} \quad (2.68)$$

where  $\Gamma_t = \Gamma_q + \Gamma_{sq}$  is the total energy broadening associated to the  $q$ -th resonant level, while  $\Gamma_{sq}$  is the extrinsic scattering broadening parameter. Similarly as for the coherent case,  $J$  can be retrieved invoking Eq. (2.65). In this sense, the coherence breaking time can be defined as  $\tau_{qs} = \hbar/\Gamma_{sq}$ .

In this picture, whatever scattering mechanism that leads to phase-decoherence can be, in principle, phenomenologically-modelled through an ad-hoc  $\Gamma$  parameter. How scattering effects impact the static  $IV$  curve of RTDs will be discussed in Chapter 4. Mere, it is clear that, if  $\tau_{qs}/\tau_q \ll 1$ , the sequential resonant tunnelling regime dominates over the coherent one, which is the case of those thin DBQW heterostructures where the tunnelling time is much larger than the phase-breaking time [311]. Furthermore, it is also clear that, in the limit where no scattering takes place, the sequential tunnelling model reduces to an equivalent global coherent tunnelling Hamiltonian [369].

However, an RTD device is a much more complex system rather than the one which could be simply described by the sequential tunnelling model. Indeed, generally speaking, both elastic and inelastic scattering processes take place across the whole RTD structure, impacting the electrical behaviour of the device [370–372]. In this sense, electron transport can be regarded as a pure non-equilibrium, time-irreversible, and incoherent process, whose treatment should in-

clude, in principle, any scattering mechanism that leads to momentum and/or energy relaxation, including dissipative processes [373, 374]. Despite that, this physical insight is not accounted for in the present work. This will be extensively discussed in Chapter 4.

### 2.4.3 The Wentzel-Kramer-Brillouin (WKB) approximation

The treatment presented so far assumed the electrostatic potential energy  $U_z$  flat within the well, barriers, and quasi-free regions. However, in realistic DBQW structures, this assumption is not met due to several phenomena, including band bending caused by temperature-dependent space charge effects (accumulation/depletion), and the presence of an externally-applied electric field.

At the same time, the effective mass is a spatially-varying quantity along the whole domain, i.e.,  $m_e^* = m_e^*(z)$ , which has been neglected so far, and barriers are only few nanometres (nm)-thick. Therefore, these, as well as extended [314, 358, 375], simplified analytical models cannot be employed to accurately study the electronic properties of RTD devices, but just to give a rough idea on how electronic quantisation and tunnelling phenomena work in these heterostructure-based systems.

In this sense, if  $U_z$  is not uniform in a specific region ( $k_z$  not constant), solutions of Eq. (2.4) cannot be exactly given by Eq. (2.5). In such a case, approximate analytical solutions can be retrieved employing the Liouville-Green's method [376]. Suppose to express the solutions of Eq. (2.4) in the following ansatz [357]:

$$\psi_z(z) = A(z) \exp[\xi_z(z)] \quad (2.69)$$

where the amplitude  $A(z)$  is slowly-varying, while  $\xi_z$  is some complex function to be determined. By supposing to force Eq. (2.69) to be solution of Eq. (2.4) along  $\hat{z}$ , and assuming  $U_z = U_z(z)$  slowly-varying within a specific region, i.e.,  $|\partial^2 \xi_z(z)/\partial z^2| \ll \left| \left[ \partial \xi_z(z)/\partial z \right]^2 \right|$ , the associated zero-order solutions  $\xi_z = \xi_0$  can be written as:

$$\left[ \frac{\partial \xi_0(z)}{\partial z} \right]^2 \simeq -p_z^2(z) \longrightarrow \xi_0(z) \simeq \pm i \int p_z(z') dz' \quad (2.70)$$

Similarly, first-order solutions can be derived:

$$\left[ \frac{\partial \xi_1(z)}{\partial z} \right]^2 \simeq - \left[ p_z^2(z) \pm i \frac{\partial p_z(z)}{\partial z} \right] \longrightarrow \xi_1(z) \simeq \pm i \int \sqrt{p_z^2(z') \pm i \frac{\partial p_z(z')}{\partial z}} dz' \quad (2.71)$$

and so on. However, since  $U_z$  is a slowly-varying function, the following condition applies:

$$\left| \pm i \frac{\partial p_z(z)}{\partial z} \right| \ll |p_z^2(z)| \longrightarrow \left| \frac{1}{p_z(z)} \frac{\partial p_z(z)}{\partial z} \right| \ll |p_z(z)| \quad (2.72)$$

and the same for higher orders. Since the electron wavelength  $\lambda_z = 2\pi/|p_z|$ , Eq. (2.72) states that  $|p_z|$  variation along  $z$ , per unit of wavelength, is much smaller than  $|p_z|$  itself. This means that if  $U_z$  is slowly varying compared to  $\lambda_z$ ,  $\psi_z$  has a "quasi"-oscillatory behaviour with amplitude and wavelength which is slowly changing along  $z$ : this is the assumption behind the Wentzel-Kramer-Brillouin (WKB) approximation [316]. Therefore,  $\psi_z$  can be approximated as [357]:

$$\psi_z(z) \approx A(z) \exp \left[ \pm i \int p_z(z) dz \right] \quad (2.73)$$

which generalises Eq. (2.47), being  $p_z$  real or imaginary as following:

$$p_z(z) = \frac{\sqrt{2m_e^*[E_z - U_z(z)]}}{\hbar} = \begin{cases} \frac{\sqrt{2m_e^*[E_z - U_z(z)]}}{\hbar} = k_z(z), & E_z > U_z(z) \\ i\sqrt{2m_e^*[U_z(z) - E_z]} = i\rho_z(z), & 0 < E_z < U_z(z) \end{cases} \quad (2.74)$$

where  $A(z) \propto 1/\sqrt{p_z(z)}$ . Similarly, higher-order solutions can be derived. In this picture,  $E_z = U_z$  is called turning point, where the WKB approximation drops, and ad-hoc connection rules between classical and "non-classical" regions must be defined [316, 357].

Using this approach, the eigenstates of a bumpy-bottom infinite-depth QW of thickness  $W$  can be written as [357]:

$$E_q = \int_0^W k_z(z) dz = q\pi\hbar \quad (2.75)$$

generalising Eq. (2.13). Similarly, the transmission coefficient of a potential barrier with bumpy top and thickness  $W$  reads as [357]:

$$\mathcal{T}_b \sim \exp \left[ -2 \int_0^W \rho_z(z) dz \right] \quad (2.76)$$

generalising Eq. (2.60). From a general point of view, this approach allows to compute approximate solutions of Schrödinger's equation eigenstates  $\{\psi_z, E_z\}$  depending on the specific potential profile  $U_z(z, V)$ , including RTD structures [330, 331]. In this context,  $\mathcal{T}_{DBQW}$  and  $J$  can be computed similarly as already discussed.

#### 2.4.4 Self-consistent solution of RTD devices: space charge build-up

Although the WKB approach allows to study double-barrier and, more generally, multi-QW structures, the potential profile  $U_z(z, V)$  is, in principle, unknown. Indeed, temperature- and voltage-dependent carriers dynamics impact the electron density across the device, leading to the formation of space charge regions, and giving rise to a non-uniform potential distribution, which is strictly-dependent on the system doping profile. For this reason, although approximate analytical models can be employed for a preliminary study [377–379], an accurate analysis and design of RTD heterostructures must rely on self-consistent numerical solutions [380, 381].

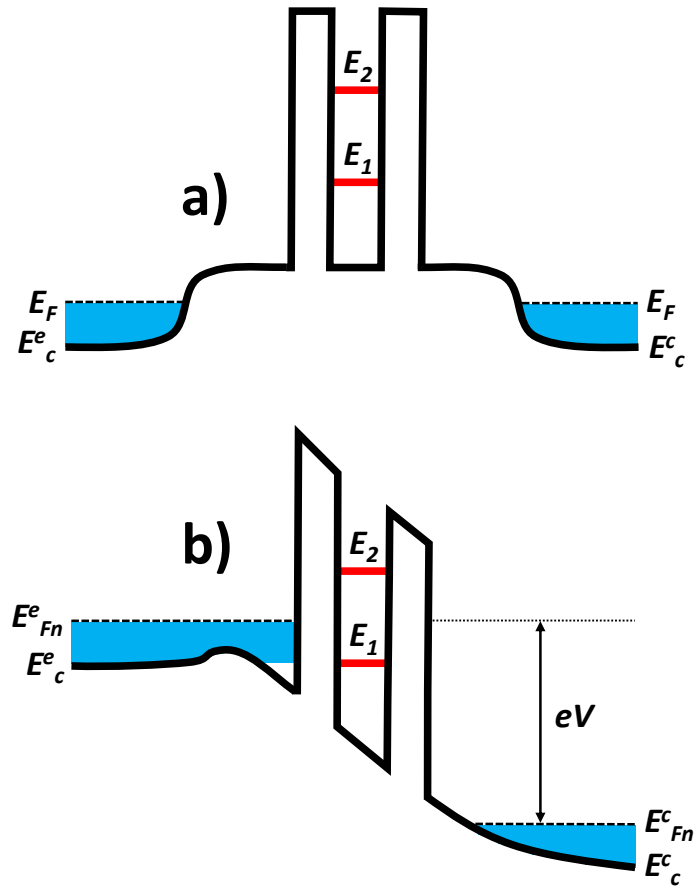


Figure 2.8: Illustration of the band diagram of a DBQW RTD device: a), thermal equilibrium; and b), peak resonance (forward bias). In this representation,  $E_F$ ,  $E_{Fn}^e$  and  $E_{Fn}^c$  are the Fermi level and the emitter and collector quasi-Fermi level at the domain boundaries (contacts), respectively,  $V$  is the applied bias voltage, while the blue regions represent the emitter and collector Fermi sea.

Figure 2.8 shows the realistic band diagram ( $T > 0$  K) of a generic DBQW RTD device at both thermal equilibrium and peak resonance (assuming forward bias conditions), outlining the non-linearity of the Hartree potential due to charge build-up. In Figure 2.8a, the bending of the potential within the emitter and collector region is due to the different charge concentration between the highly-doped contacts and the device core region. Moreover, as can be seen in Figure 2.8b, a "pseudo"-triangular potential well [358] arises at the emitter side in proximity to the first tunnelling barrier due to band bending at high bias voltages [382], which is the result of the potential drop across the emitter space charge region.

As a consequence, electrons transiting across the emitter and undergoing scattering processes can accumulate and thermalise into locally-available 2D quasi-bound states located in the triangular well and below the emitter CB edge before being injected into the DBQW. As a result, resonant tunnelling turns from being a purely 3D–2D process dominated by continuous scattering states, to an hybrid 3D/2D–2D phenomenon governed by a complex non-equilibrium

electron distribution function, and this can impact the static  $IV$  curve of the RTD device by providing additional features [382].

However, this is only the case of DBQW heterostructures featuring very-thick ( $\gtrsim 1 \mu\text{m}$ ) undoped/lightly-doped (with donor concentrations  $N_D \ll 10^{18} \text{ cm}^{-3}$ ) emitter regions [313], which are not employed in the design of THz RTDs due to frequency performance requirements. Therefore, the coherent (ballistic) regime can be assumed in this sense by employing a classic "quasi"-equilibrium Fermi-Dirac distribution to model the carriers statistic in the emitter region, where an energy-continuous spectrum is assumed. Further details in this regard will be provided in Chapter 4.

Since the charge distribution reflects the electron probability density, the non-equilibrium electron concentration  $n(z)$  along the RTD heterostructure is approximately given as [313]:

$$n(z) \approx \frac{k_B T}{2\pi^2 \hbar^2} \left\{ \int_0^{+\infty} m_e^*(z) |\psi_{k_z}(z)|^2 \log \left[ \exp \left( \frac{E_{Fn}^e - E_z}{k_B T} \right) + 1 \right] dk_z + \int_{-\infty}^0 m_e^*(z) |\psi_{k_z}(z)|^2 \log \left[ \exp \left( \frac{E_{Fn}^c - E_z}{k_B T} \right) + 1 \right] dk_z \right\} \quad (2.77)$$

and similar considerations apply to the non-equilibrium local density of states (LDOS) (as already discussed), where  $\psi_z[E_z(k_z), z] = \psi_{k_z}(E_{k_z}, z)$ . Eq. (2.77) is associated to Poisson's equation [383]:

$$\frac{\partial}{\partial z} \left[ \epsilon_{r,0}(z) \frac{\partial}{\partial z} \right] V_H(z, V) = -\frac{e}{\epsilon_0} [N_D(z) - n(z)] \quad (2.78)$$

where  $V_H$  is the Hartree potential and models charge build-up,  $\epsilon_{r,0}$  the relative static dielectric permittivity, and  $N_D$  is the doping (donor) concentration, all spatially-varying quantities along  $\hat{z}$ , while  $\epsilon_0$  the vacuum dielectric constant. In this picture, Schrödinger's equation can be written in the fashion of Eq. (2.1) by explicitly accounting for translational-broken symmetry, i.e.,  $k_z \rightarrow -i\partial_z$  [316, 383]:

$$\hat{\mathcal{H}}_z \psi_{k_z}(z) = -\frac{\hbar^2}{2} \frac{\partial}{\partial z} \left\{ \left[ \frac{1}{m_e^*(z)} \frac{\partial}{\partial z} \right] + U_z(z, V) \right\} \psi_{k_z}(z) = E_{k_z} \psi_{k_z}(z) \quad (2.79)$$

being  $\hat{\mathcal{H}}_z$  the longitudinal Hamiltonian operator, while the envelope functions  $\psi_z$  construct, as already seen, the heterostructure wave-functions ansatz  $\psi$ :

$$\psi(r) = \frac{1}{\sqrt{L_x L_y}} \psi_z(z) \Pi_{s=x,y} \exp(\pm i k_s s) \quad (2.80)$$

being  $s = x, y$  and  $L_x L_y$  the transverse cross-section of the normalization area, and where  $U_z$  is defined as:

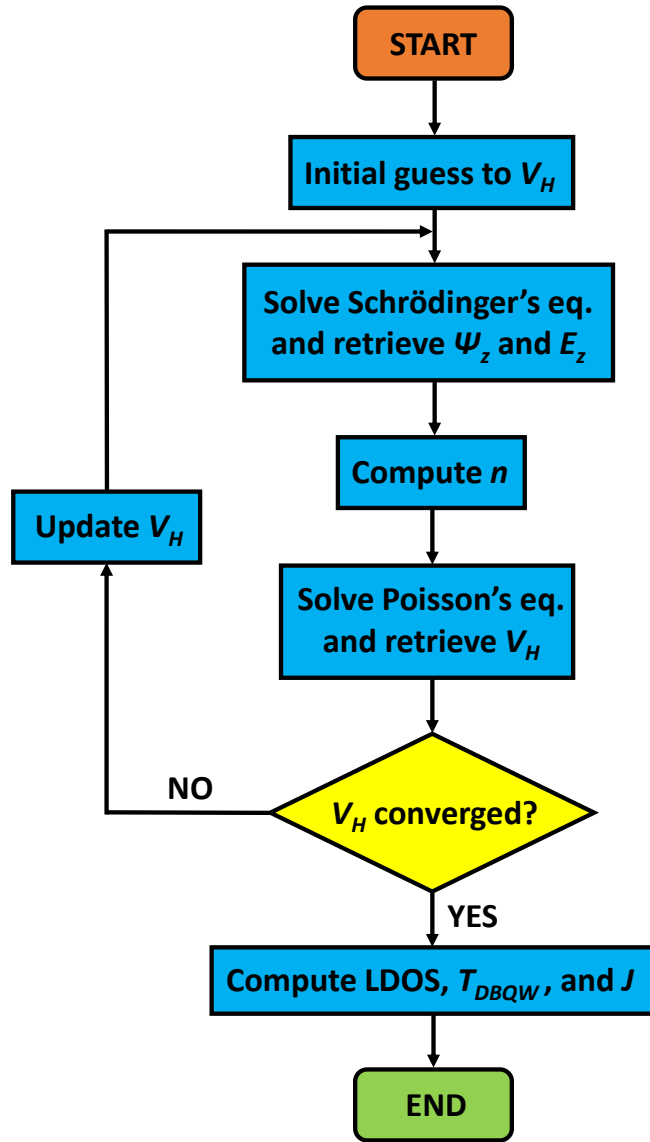


Figure 2.9: Block diagram illustrating the loop at the base of a self-consistent Schrödinger-Poisson solver within the Hartree approximation.

$$U_z(z, V) = -eV_H(z, V) + \Delta E_c(z) \quad (2.81)$$

being  $\Delta E_c$  the CB offset at the heterointerfaces, which is known and depends on the employed material system and RTD epi-design. In this simplified picture, exchange and correlation is not included since electron-electron interaction is neglected [356].

In order to compute the eigenstates  $\{\psi_z, E_z\}$  and the electron density  $n$ , Eq. (2.78) and (2.79) have to be iteratively solved numerically and self-consistently upon convergence. The flow-chart describing the working principle of a self-consistent Schrödinger-Poisson solver within the Hartree approximation is shown in Figure 2.9, and consists in the following iterative procedure [383]. First, Schrödinger's equation is solved, at a specific bias point, assuming an initial guess for the potential. In this sense, typically, the Hartree term  $V_H^0$  is either set equal to zero or

computed through approximate analytical expressions at thermal equilibrium. In principle, the better the chosen initial guess, the faster the convergence, and the more efficient the solver.

After computing the eigenstates, the electron density is retrieved and Poisson's equation is solved to extract the  $i$ -th iteration value  $V_H^i$ . Since the spatial dependency of the electron concentration along  $\hat{z}$  is modelled through the wave-function probability density and the emitter/collector contacts Fermi-Dirac distribution functions, the local quasi-Fermi level  $E_{Fn}(z)$  does not need to be formally-retrieved. The energy reference ( $E_z = 0$ ) is usually set equal to the Fermi level  $E_F$  at thermal equilibrium or to  $E_{Fn}^e$  under non-equilibrium conditions.

If the computed  $V_H^i$  does not meet the convergence criteria  $||V_H^i| - |V_H^{i-1}|| < \delta$ , where  $\delta > 0$  is numerically-assigned, Schrödinger's equation is solved with the updated term  $V_H^i$ , and the loop is repeated until convergence is reached. Finally, after  $\{\psi_z, E_z\}$  and  $n$  have been computed with the correct  $U_z$ , the LDOS,  $\mathcal{T}_{DBQW}$  and  $J$  are retrieved similarly as already discussed.

In this picture, the numerical solution of Schrödinger's and Poisson's equation is addressed either through finite differences (FD) [383, 384] or employing the finite element method (FEM) [385]. In the present work, the FEM has been employed.

Assuming to discretize the heterostructure domain along the symmetry-broken direction  $\hat{z}$  into a number of mesh elements  $g$ , the weak form [386] of Eq. (2.79) for the states  $\psi_z[E_z(k_z)] = \psi_{k_z}(E_{k_z})$  at a fixed bias point reads as:

$$-\frac{\hbar^2}{2} \int_z N_i(z) \frac{\partial}{\partial z} \frac{1}{m_e^*(z)} \frac{\partial \psi_{k_z}(z)}{\partial z} dz + \int_z N_i(z) U_z(z) \psi_{k_z}(z) dz = E_{k_z} \int_z N_i(z) \psi_{k_z}(z) dz \quad (2.82)$$

where  $N_i$  is a test function of a chosen basis set. Applying the Green's theorem:

$$\begin{aligned} \frac{\hbar^2}{2} \int_z \frac{\partial N_i(z)}{\partial z} \frac{1}{m_e^*(z)} \frac{\partial \psi_{k_z}(z)}{\partial z} dz + \int_z N_i(z) U_z(z) \psi_{k_z}(z) dz = \\ = E_{k_z} \int_z N_i(z) \psi_{k_z}(z) dz + \frac{\hbar^2}{2m_e^*(z)} \frac{\partial \psi_{k_z}(z)}{\partial z} \Big|_{z_1}^{z_N} \end{aligned} \quad (2.83)$$

where the last term sets the boundary conditions, where  $z_1$  and  $z_N$  are the boundary nodes. Expanding  $\psi_{k_z}$  in terms of a set of basis functions  $N_j = N_i$  according to Galerkin procedure [386]:

$$\psi_{k_z}(z) = \sum_{j=1}^N a_j N_j(z) \quad (2.84)$$

being  $N = g + 1$  the number of mesh nodes. By substituting Eq. (2.84) into Eq. (2.83), the

following expression is obtained:

$$\begin{aligned} \frac{\hbar^2}{2} \sum_{j=1}^N a_j \int_z \frac{\partial N_i(z)}{\partial z} \frac{1}{m_e^*(z)} \frac{\partial N_j(z)}{\partial z} dz + \sum_{j=1}^N a_j \int_z N_i(z) U_z(z) N_j(z) dz = \\ = E_{k_z} \sum_{j=1}^N a_j \int_z N_i(z) N_j(z) dz + \frac{\hbar^2}{2m_e^*(z)} \frac{\partial \psi_{k_z}(z)}{\partial z} \Big|_{z_1}^{z_N} \end{aligned} \quad (2.85)$$

Restricting Eq. (2.85) to a single mesh element  $s$  and assuming  $m_e^*$  and  $U_z$  constant within the element, i.e.,  $m_e^*(z) = m_s^*$  and  $U_z(z) = U_s$ :

$$\begin{aligned} \frac{\hbar^2}{2m_s^*} \sum_{j=1}^N a_j \int_s \frac{\partial N_i(z)}{\partial z} \frac{\partial N_j(z)}{\partial z} dz + U_s \sum_{j=1}^N a_j \int_s N_i(z) N_j(z) dz = \\ = E_{k_z} \sum_{j=1}^N a_j \int_s N_i(z) N_j(z) dz + \frac{\hbar^2}{2m_e^*(z)} \frac{\partial \psi_{k_z}(z)}{\partial z} \Big|_{z_1}^{z_N} \end{aligned} \quad (2.86)$$

which, in matrix form, reads as:

$$\left\{ \frac{\hbar^2}{2m_s^*} [T]_s + U_s [S]_s \right\} \{a\}_s = E_{k_z} [S]_s \{a\}_s + \frac{\hbar^2}{2m_e^*(z)} \frac{\partial \psi_{k_z}(z)}{\partial z} \Big|_{z_1}^{z_N} \quad (2.87)$$

where [386]:

$$[T]_s = \int_s \frac{\partial \{N\}^T}{\partial z} \frac{\partial \{N\}}{\partial z} dz \quad (2.88)$$

$$[S]_s = \int_s \{N\}^T \{N\} dz \quad (2.89)$$

Assembling over the mesh elements:

$$\sum_{s=1}^N \left\{ \frac{\hbar^2}{2m_s^*} [T]_s + U_s [S]_s \right\} \{a\}_s = E_{k_z} \sum_{s=1}^N [S]_s \{a\}_s + \frac{\hbar^2}{2m_e^*(z)} \frac{\partial \psi_{k_z}(z)}{\partial z} \Big|_{z_1}^{z_N} \quad (2.90)$$

a generalized eigenvalue problem is obtained:

$$[H] \{a\} = E_{k_z} [M] \{a\} + \frac{\hbar^2}{2m_e^*(z)} \frac{\partial \psi_{k_z}(z)}{\partial z} \Big|_{z_1}^{z_N} \quad (2.91)$$

where  $[H]$  and  $[M]$  are the Hamiltonian and mass (sparse) matrices, while  $E_{k_z}$  is a given quantity. The specific form of  $[T]_s$  and  $[S]_s$  depends on the choice of the test functions basis set. For instance, employing first-order Lagrange polynomials (line elements) [386]:

$$[T]_s = \frac{1}{l_s} \begin{bmatrix} 1 & -1 \\ -1 & 1 \end{bmatrix} \quad (2.92)$$

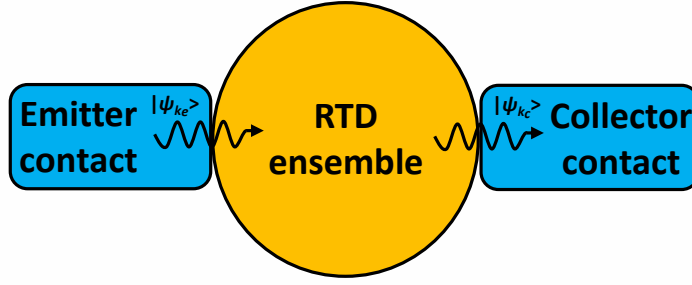


Figure 2.10: Illustration describing the openness nature of the RTD device. In this context, the emitter and collector boundary states  $|\psi_{k_e}\rangle$  and  $|\psi_{k_c}\rangle$  and their first derivative must be continuous at the interface with the RTD ensemble.

$$[S]_s = \frac{l_s}{6} \begin{bmatrix} 2 & 1 \\ 1 & 2 \end{bmatrix} \quad (2.93)$$

where  $l_s$  is the length of the  $s$ -th mesh element. In this picture, each mesh element is modelled through two linear basis functions. Similar considerations can be done for higher-order polynomials or other elements typologies [386]. Overall, Eq. (2.91) has to be solved for all the system  $\psi_{k_z}(E_{k_z})$  states. It has to be underlined that this treatment employs the effective mass approximation to model the RTD electronic structure, which is particular useful since the electron energy-momentum dispersion relation can be reversed analytically. Further considerations on RTD band structure modelling in the context of this work will be provided in Chapter 4.

To correctly pose the problem given by Eq. (2.91), the boundary term has to be determined. Indeed, neglecting it would impose Neumann ("natural") conditions at the domain boundaries, i.e.,  $\partial\psi_{k_z}(z)/\partial z|_{z_1, z_N} = 0$ , which is required for quasi-bound states computation (see Section 2.4.1.2). However, the RTD is an open quantum ensemble system, where current flow is made possible thanks to scattering states [387]. Therefore, open boundary conditions must be applied, which translates in enforcing the continuity of the wave-function and its first derivative across the device/contacts interface [388]. This concept is illustrated in Figure 2.10.

Assuming the contacts as fully-absorbing carrier reservoirs elements maintain thermal equilibrium and charge neutrality, and, at the same time, characterised by a flat potential energy distribution, the longitudinal emitter and collector states  $|\psi_{k_e}\rangle$  and  $|\psi_{k_c}\rangle$  at the domain boundaries  $z = z_1$  and  $z_N$  can be written as:

$$\psi_{k_e}(z_1) = \psi_{k_e}^+ \exp(ik_e z_1) + \psi_{k_e}^- \exp(-ik_e z_1) \quad (2.94)$$

$$\psi_{k_c}(z_N) = \psi_{k_c}^+ \exp(ik_c z_N) \quad (2.95)$$

being  $k_{e,c} = \sqrt{2m_{e,c}^*(E_z - U_{e,c})}/\hbar$ , and where subscripts  $e$  and  $c$  labels the emitter and collector

contacts, respectively. The associated first derivatives are, therefore, given by:

$$\left. \frac{\partial \psi_{k_e}(z)}{\partial z} \right|_{z_1} = ik_e \left[ \psi_{k_e}^+ \exp(ik_e z_1) - \psi_{k_e}^- \exp(-ik_e z_1) \right] = ik_e \left[ -\psi_{k_e}(z_1) + 2\psi_{k_e}^+ \exp(ik_e z_1) \right] \quad (2.96)$$

$$\left. \frac{\partial \psi_{k_c}(z)}{\partial z} \right|_{z_N} = ik_c \psi_{k_c}(z_N) \quad (2.97)$$

In this sense, Eq. (2.94) and (2.95) state the continuity of  $\psi_{k_z}$  at the domain boundaries, while Eq. (2.96) and (2.97) gives the overall transparent boundary conditions. Substituting Eq. (2.96) and (2.97) in Eq. (2.91), an inhomogeneous linear system is obtained:

$$[F]\{a\} = \{b\} \quad (2.98)$$

where  $[F] = E_{k_z}[M] - [H]$  is the global stiffness matrix of the FEM formulation incorporating the boundary conditions. The numerical computation of the eigenvector  $\{a\}$  (for each  $E_{k_z}$  of interest) can be carried in different ways, including a sparse direct approach based on the lower-upper (LU) decomposition of  $[F]$ .

Similarly as for Schrödinger's equation, Poisson's equation can be solved following the same approach. In this picture, the weak form of Eq. (2.78) at a specific bias point for the single mesh element, i.e.,  $\varepsilon_{r,0}(z) = \varepsilon_{s,0}$ ,  $N_D(z) = N_s$ , and  $n(z) = n_s$ , is given by:

$$\varepsilon_{s,0} \sum_{j=1}^N a_j \int_s \frac{\partial N_i(z)}{\partial z} \frac{\partial N_j(z)}{\partial z} dz = \frac{e}{\varepsilon_0} \left[ (N_s - n_s) \int_s N_i(z) dz \right] + \varepsilon_{r,0}(z) \frac{\partial V_H(z)}{\partial z} \Big|_{z_1}^{z_N} \quad (2.99)$$

However, differently from Schrödinger's equation, the boundary term can be dropped. Indeed, the potential is, by definition, flat in the emitter/collector contacts, i.e., Neumann conditions apply from the continuity of the Hartree term and its first derivative at the interface with the domain boundaries. Assembling over the mesh elements Eq. (2.99), the following matrix form is obtained:

$$\sum_{s=1}^N \varepsilon_{s,0} [T]_s \{a\}_s = \frac{e}{\varepsilon_0} \sum_{s=1}^N \left[ (N_s - n_s) \int_s N_i(z) dz \right] \quad (2.100)$$

which can be written similarly to Eq. (2.98).

In this work, the treatment described so far has been employed in the context of the NEGF formalism to numerically-simulate the static  $IV$  curve of designed  $\text{In}_{0.53}\text{Ga}_{0.47}\text{As}/\text{AlAs}$  double-barrier RTD devices. Further details on the NEGF method in the context of the present work will be provided in Chapter 4.

## 2.5 Equivalent circuit modelling

For the design and estimation of the high-frequency performance of RTDs, together with the practical realisation of associated THz circuits, the electrical characteristic and equivalent-circuit parameters of the device are required. In particular, oscillator and direct detector design relies on the non-linear DC  $IV$  curve, which is reliably measurable. In this context, semi-empirical approaches are widely adopted, which consist in fitting experimental data to either parameterised rigorous physical expressions derived from mesoscopic physics [361, 390] or arbitrary functions [391–394], which are then imported in technology computer-aided design (TCAD)-based tools for circuit design optimisation [395]. However, for a simplified analysis, a simple cubic function is typically employed [396]:

$$I(V) \approx -\alpha V + \beta V^3 \quad (2.101)$$

where  $\alpha$  and  $\beta$  can be written in terms of the NDR region electrical spans  $\Delta I$  and  $\Delta V$ :

$$\alpha = \frac{3\Delta I}{2\Delta V} \quad (2.102)$$

$$\beta = \frac{2\Delta I}{\Delta V^3} \quad (2.103)$$

and where the origin is shifted to the mid-point of the same region. In this sense, the maximum absolute value of the device NDC reads as [396]:

$$|G_{rd}(V)|_{max} = \left| \frac{dI(V)}{dV} \right|_{V=0} = \frac{3\Delta I}{2\Delta V} \quad (2.104)$$

where  $G_{rd} = dI/dV$  is the RTD "differential" conductance, which is negative in the NDR region. Similarly, higher-order polynomials can be adopted [396]. However, much of the device physics is lost within this picture which, among the things, assumes the  $IV$  curve symmetric with respect to the NDR region mid-point. On the other hand, as already mentioned, reliable and accurate approaches for RTD device analysis and design of THz sources and detectors rely on advanced self-consistent Schrödinger-Poisson numerical techniques [380], among which those based on the NEGF method [397]. Since this approach has been adopted in the present work, more details on the NEGF formalism will be provided in Chapter 4.

At the same time, the diode frequency response can be modelled through the associated small-signal equivalent circuit representation. The unified lumped small-signal  $RLC$  equivalent circuit model of the double-barrier RTD device was proposed in [398] as a result of the combination of previously-reported works [399, 401–407], and it is shown in Figure 2.11. In this representation, the device is modelled, at a specific bias point, by a capacitance  $C_{rd}$  in parallel with the series of  $G_{rd}$  and a QW inductance  $L_{qw}$ . According to the device operation region,  $G_{rd}$

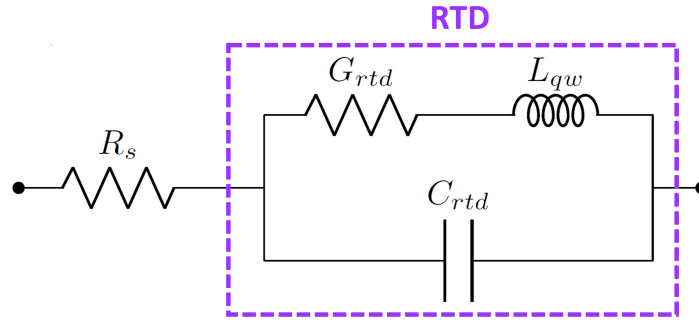


Figure 2.11: Unified RTD high-frequency small-signal equivalent circuit model.

models the resistive nature or radio-frequency (RF) gain capability of the diode, while  $L_{qw}$  and  $C_{rtd}$  account for the RTD self-capacitance and electron delay processes associated with resonant tunnelling through the DBQW structure.

In particular,  $L_{qw}$  models the lag associated with the diode current with respect to the voltage introduced by the charging, and consequent discharging, of the QW with bias due to electron resonant tunnelling [401]. Here, the delay arises from the time needed by the diode current to change in response to the QW charge build-up. Therefore, the time scale of this process is governed by the DBQW electron quasi-bound state lifetime  $\tau_{dbqw}$  [398]:

$$\tau_{dbqw} = \frac{\tau_e \tau_c}{\tau_e + \tau_c} = \frac{\hbar}{\Gamma_1} \quad (2.105)$$

or intrinsic "tunnelling" delay time, which depends on the adopted DBQW design, where  $\tau_e$  and  $\tau_c$  are the inverse of the electron QW-to-emitter and QW-to-collector escape rates  $\nu_e$  and  $\nu_c$ , respectively, while  $\Gamma_1$  is the FWHM associated with the first QW quasi-bound subband transmission coefficient resonant peak, similarly as in Eq. (2.63), and can be computed through quantum mechanical-based simulations [408]. In this picture,  $L_{qw}$  has a bias dependency which can be expressed as [401]:

$$L_{qw}(V) = \frac{\tau_{dbqw}}{G_{rtd}(V)} \quad (2.106)$$

where  $L_{qw} < 0$  holds in the NDR region. Here,  $\tau_{dbqw}$  is generally-assumed bias-independent, i.e.,  $\tau_{dbqw}(V) \sim \tau_{dbqw}$ , neglecting the weak dependence  $\Gamma_1(V)$  [398]. Moreover, space-charge effects in the DBQW are also not accounted as later discussed.

On the other hand,  $C_{rtd}$  can be written as [399]:

$$C_{rtd}(V) = C_d + C_{qw}(V) \quad (2.107)$$

In the above,  $C_d$  is the self-capacitance (which is only weakly bias-dependent, i.e.,  $C_d(V) \sim C_d$ ) and depends on the equivalent static dielectric constant and thickness  $\epsilon_{d,0}$  and  $t_d$  associated with the RTD depletion regions, respectively, and on device area  $A$ . On the other hand,  $C_{qw}$  is the

quantum capacitance [400], which arises due to the non-instantaneous QW discharge (screening) towards the collector, so it is proportional to the QW DOS. In particular, it models the variation of the charge seen by the collector  $\delta Q_c$  due to the change in the QW-to collector current  $\delta I_c$  with bias through the electron escape rate across the second barrier  $v_c$  [398]:

$$C_{qw}(V) = \frac{dQ_c}{dV} = -\frac{dQ_{qw}}{dV} = -\frac{1}{Av_c} \frac{dI_c}{dV} = -\frac{G_{rtd}(V)}{v_c} \quad (2.108)$$

where the QW-to-emitter capacitance is not accounted cause negligible, and where  $v_c$  is assumed bias-independent [398]. In this sense,  $C_{qw} < 0$  holds in the PDR regions.

The model is completed by a parasitic series resistance  $R_s$ , which models the emitter/collector access and contact resistance  $R_c = \rho_c A$ , where  $\rho_c$  is the specific contact resistivity extracted from transmission line measurements (TLM), the resistance of the device mesa, spreading resistance, and the resistance associated with emitter/collector contacts and bond-pads metallization [364]. A series inductance  $L_s$  might be, therefore, included, but this can be seen as part of the resonating inductance in oscillators [396], while it has to be accounted in direct detectors.

In this picture, the RTD input admittance  $Y_{rtd}$  reads as:

$$Y_{rtd} = \left\{ R_s + \left[ \frac{G_{rtd}}{1 + j\omega L_{qw} G_{rtd}} + j\omega C_{rtd} \right]^{-1} \right\}^{-1} \quad (2.109)$$

being  $\omega = 2\pi f$  the angular frequency and  $f$  the ordinary frequency, where the associated real and imaginary parts have the following form [395]:

$$\Re(Y_{rtd}) = \left\{ R_s + \frac{(1 - \omega^3 L_{qw} C_{rtd})^3 - \left(\frac{\omega C_{rtd}}{G_{rtd}}\right)^2}{G_{rtd}} \right\}^{-1} \quad (2.110)$$

$$\Im(Y_{rtd}) = \frac{(1 - \omega^3 L_{qw} C_{rtd})^3 - \left(\frac{\omega C_{rtd}}{G_{rtd}}\right)^2}{\omega \left( L_{qw} - \frac{C_{rtd}}{G_{rtd}^2} - \omega^2 L_{qw}^2 C_{rtd} \right)} \quad (2.111)$$

where  $R_s$ ,  $G_{rtd}$ ,  $C_{rtd}$ , and  $L_{qw}$  quantities depend upon the bias point and can be either estimated through physical-based models/simulations [409] in the case of device design, or extracted from high-frequency scattering (S)-parameters measurements [410] for device high-frequency performance analysis and circuit design purposes. The validity of this model has been demonstrated by characterising double-barrier InGaAs/AlAs RTDs in their entire bias range from DC up to 110 GHz [395, 411].

This modelling procedure is quite straightforward since Eq. (2.109) requires only the "low-frequency" estimates of the small-signal parameters which are, by definition, only weakly-

frequency dependent (since the diode frequency cut-off sits typically way above the measurement frequency range), and the high-frequency behaviour of the device is then modelled analytically. In this context, S-parameters are usually measured up to around 40 – 60 GHz, where available vector network analysers (VNA) do not require frequency extenders and where parasitics de-embedding (bond-pads) can be carried out reliably, even though on-wafer accurate parameters extraction has been successfully carried out up to several hundreds of GHz to date [412].

However, S-parameters measurement remains non-trivial due to the parasitic oscillations arising within the biasing circuit when the RTD operates in the NDR region [413, 414], especially employing high-current density or large area devices due to large associated NDC, which gives rise to unstable plateau-like/hysteretic behaviours [415]. The common practice adopted to suppress the oscillations triggered by the bias line inductance and stabilise the RTD device at low-frequency (typically in the megahertz range) consists in connecting a shunt resistor in parallel to the RTD, which is then de-embedded after measurement [395]. This approach is analogous to what done in oscillator design, so it will be discussed later on. However, this is tricky since very high-current density/large area devices would require, in principle, extremely small resistance values, which are unpractical from a technological realisation standpoint.

Both the static  $IV$  characteristic and its small-signal equivalent circuit parameters can be used to investigate the RF performance of the RTD device at high frequency [311]. Here, the unilateral power gain cut-off frequency, or maximum oscillation frequency,  $f_{max}$  of the RTD is defined as the frequency at which  $\Re(Y_{in})$  vanishes due to the NDC roll-off caused by the DBQW electron lifetime, i.e.,  $f_{max} \approx 1/2\pi\tau_{dbqw}$ , which, in the discussed equivalent circuit picture, reads as [401]:

$$f_{max} = \sqrt{\frac{1}{8\pi^2 L_{qw}^2 C_{rtd}}} \left\{ 2L_{qw} - \frac{C_{rtd}}{G_{rtd}^2} + \sqrt{\left(\frac{C_{rtd}}{G_{rtd}^2} - 2L_{qw}\right)^2 - \frac{4L_{qw}^2(1 + R_s G_{rtd})}{R_s G_{rtd}}} \right\}^{1/2} \quad (2.112)$$

Note that, for RTD direct detectors, Eq. (2.112) gives an imaginary quantity, so  $f_{max} = \Im(f_{max})$ . For practical device analysis, the following simplified expression is, however, adopted:

$$f_{max} \approx \frac{|G_{rtd}|}{2\pi C_{rtd}} \sqrt{\frac{1}{R_s |G_{rtd}|} - 1} \quad (2.113)$$

which assumes  $L_{qw} = 0$  (i.e.,  $\tau_{dbqw} = 0$ ). In this simple model, the frequency cut-off is associated to the  $RC$  charging/discharging time due to  $R_s$ . In this context,  $f_{max}$  corresponds to the frequency at which the device NDR is cancelled out by the equivalent circuit resistance. Although this is fundamentally-incorrect, Eq. (2.113) can be practically-employed in RTD characterisation and subsequent oscillator design since the frequency constrain posed by  $R_s$  in fabricated devices is

typically way more stringent than the one set by the DBQW lifetime.

The intrinsic cut-off frequency of the diode  $f_{in}$  can be estimated based on the electron total intrinsic delay time  $\tau_{in}$  [416]:

$$f_{in} = \frac{1}{2(2\tau_{dbqw} + \tau_t)} = \frac{1}{4\tau_{in}} \quad (2.114)$$

being [416]:

$$\tau_{in} = \tau_{dbqw} + \frac{\tau_t}{2} \quad (2.115)$$

where  $\tau_t$  is the intrinsic transit time across the depletion regions, which can be estimated through the electron saturation velocity  $v_{e,s}$  and depends upon emitter and collector regions design. Generally,  $f_{in} \gg f_{max}$ . In this context, the overall cut-off frequency of the RTD device  $f_c$  due to both intrinsic and extrinsic delay times can be written as:

$$f_c = \frac{1}{4\tau_{rtd}} \quad (2.116)$$

where  $\tau_{rtd} = \sqrt{\tau_{in}^2 + \tau_{ex}^2}$  is the total electron delay time, and  $\tau_{ex}$  the extrinsic delay time [417]:

$$\tau_{ex} = \frac{\pi C_{rtd}}{2} \sqrt{\frac{R_s}{|G_{rtd}|}} \quad (2.117)$$

Note that, in the limit  $\tau_{rtd} \rightarrow \tau_{ex}$  (i.e.,  $\tau_{in} \rightarrow 0$ ),  $f_c \rightarrow \approx f_{max}$  as it appears in Eq. (2.113). Moreover, if  $\tau_t$  is accounted in  $L_{qw}$ ,  $f_c$  and  $f_{max}$  (Eq. (2.112)) can be both used to quantify the overall cut-off frequency of the diode, even though their correlation has not yet been explicitly investigated in this context. However, Eq. (2.116) is employed in state-of-the-art RTD modelling methodologies to provide with an accurate estimate of the diode frequency response. Therefore, this high-frequency model has been used in this work to accurately analyse designed and subsequently investigated  $\text{In}_{0.53}\text{Ga}_{0.47}\text{As}/\text{AlAs}$  RTD devices.

Although it is widely accepted that  $\tau_{dbqw}$  ( $\tau_t \ll \tau_{dbqw}$  in typical THz RTDs, so  $\tau_{rtd} \sim \tau_{dbqw}$ ) poses the upper boundary to the frequency response of the device, it has been claimed that operation beyond around  $1/2\pi\tau_{dbqw}$  is possible in specific RTD structures thanks to Coulomb interaction-induced space-charge effects [418]. In the proposed picture, the Coulomb interaction affects the charge relaxation processes in the RTD [419], so the high-frequency dynamics of electron transport through the device is instead governed by a more general relaxation time  $\tau_r$  [311]:

$$\tau_r = \left(1 + \beta \frac{\tau_{dbqw}}{\tau_e}\right)^{-1} \tau_{dbqw} \quad (2.118)$$

where the parameter  $\beta$  models the variation of  $\tau_{dbqw}$  due to Coulomb interaction, and it is

proportional to the DOS associated with the first resonant subband  $E_1$  divided by the total DBQW quantum capacitance. In particular,  $\tau_r < \tau_{dbqw}$  ( $\beta > 0$ ) and  $\tau_r > \tau_{dbqw}$  ( $\beta < 0$ ) in the PDR and NDR regions [418], respectively, which has been experimentally verified through S-parameters measurements of low-current density InGaAs/AlAs RTDs up to 12 GHz [420]. A similar behaviour was observed in [395]. In this context, the charge relaxation processes with the DBQW limit the operation frequency of the RTD device when biased in the NDR region, i.e.,  $f_{max} \approx 1/2\pi\tau_r < 1/2\pi\tau_{dbqw}$ . Obviously, if space-charge effects are neglected,  $\tau_r = \tau_{dbqw}$ . As a result, the device high-frequency admittance  $Y_{in}$  changes profoundly compared to Eq. (2.109) [418, 419, 421].

At the same time, Coulomb interaction affects the current regime of RTDs by generating displacement current mechanisms, i.e., the device current can be considered as an hybrid combination of both real and displacement components [421]. From a small-signal equivalent circuit point of view, the *RLC* model in Figure 2.11 is extended to a more general *RLCR* description featuring an additional instantaneous current channel [418]. In this context, it has first been theorized and then experimentally-observed that, thanks to displacement current effects, peculiar RTD structures featuring thin and heavily-doped collector regions (where the first resonant subband is immersed in the collector Fermi sea) can show NDC beyond the lifetime and even relaxation time limit, i.e.,  $\Re(Y_{in})$  stays negative and oscillators can provide RF gain [420, 422–425].

Even though this advanced model, which can be considered as the most accurate and compact high-frequency linear representation of the RTD to date (alternative approached have also been proposed in the past [426–430]), opens to new ways of looking at the frequency limitations of RTDs [431], as well as to unique operation regimes, its validity and associated practical employability in the context of RTD-based THz oscillators design is still yet to be fully understood. For instance, it would be important to clarify more on how to reliably estimate/extract  $\beta$ , as well as elucidate more on the effects resulting from the co-presence of the displacement current in a generic RTD epi-structure. Therefore, this model has not been employed in the analysis conducted in this work.

Although linear modelling of the RTD based on the associated small-signal equivalent circuit parameters can be used to estimate the high-frequency performance of the device and associated NDC roll-off, a non-linear large-signal model is, in principle, needed to estimate the diode RF power capability and in the design of oscillator sources and coherent/direct detectors. This is crucial in the case of oscillators working well below the RTD cut-off frequency or direct detectors dealing with high-power input signals.

In this context, the RF power  $P_{RF}$  the RTD device can deliver to a load of conductance  $G_L$

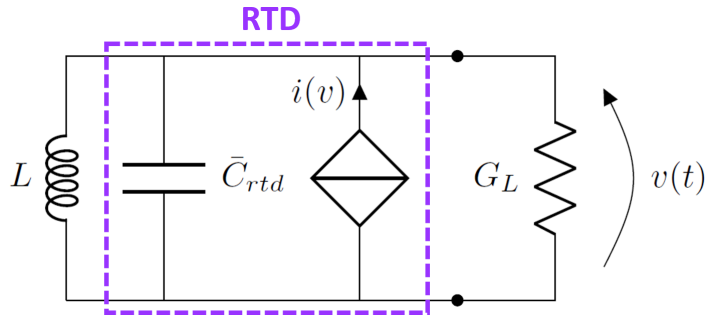


Figure 2.12: RTD oscillator RF large-signal equivalent circuit. In this representation,  $R_s(V)$  and  $L_{qw}(V)$  are not included since the RTD maximum RF power is of interest.

in steady-state conditions can be derived from non-linear forced oscillator theory by solving the Van der Pol equation associated to the oscillator large-signal equivalent circuit [432,433], which is depicted in Figure 2.12. In this simplified representation, the RTD device is modelled through an ideal voltage-dependent current source  $i(v)$  in parallel with a voltage-dependent or, for simplified analysis, "average" capacitance  $\bar{C}_{rtd}$  which, together with the resonating inductance  $L$ , forms the oscillator tank. The system is excited by an ideal signal generator and the steady-state output voltage  $v(t)$  across the load is assumed to carry only the fundamental mode  $\omega_0$ , i.e.,  $v(t) \sim V_{ac} \sin(\omega_0 t)$  (higher harmonics due to the NDC non-linearity are neglected), being the amplitude  $V_{ac}$  associated with the diode NDR voltage span.

By approximating the diode DC  $IV$  curve through Eq. (2.101),  $P_{RF}$  can be computed by equating the average power generated by the RTD device, with the average power dissipated in the load within one RF cycle, which corresponds to assuming the diode "average" NDC [434]  $\bar{G}_{rtd}(V_{ac}) = -G_L$ , replacing the non-linear signal generator with a linear load-dependent current source:

$$P_{RF} = -\frac{\Delta V^3}{3\Delta I} \bar{G}_{rtd}(\bar{G}_{rtd} + |G_{rtd}|_{max}) \quad (2.119)$$

If  $|G_{rtd}|_{max} = -2\bar{G}_{rtd} = 2G_L$  (matching condition), the diode maximum RF power  $P_{RF,max}$  can be derived [433]:

$$P_{RF,max} = \frac{3}{16} \Delta I \Delta V \quad (2.120)$$

From Eq. (2.120) it is clear that, in order to maximise  $P_{RF,max}$ , the NDR region electrical extension has to be enlarged. In this context,  $\Delta I = A\Delta J$ , where  $\Delta J$  is the available current density. Therefore,  $P_{RF,max}$  maximisation relies on the optimisation of both  $\Delta J$  and  $\Delta V$ , which are intimately related with the diode epitaxial design, together with the employment of large mesa areas. However, physical trade-offs limit the degrees of freedom associated with device design, leading to compromises in terms of output power and frequency performances. This will be discussed more in detail in Chapter 5.

However, the actual oscillator output power is lower than  $P_{RF,max}$  due to device NDC roll-off constrains [311], circuit parasitics [396], impedance mismatch at the output port [435], and the low radiation conductance of antennas at THz frequencies due to the reduced dimension [436]. For this reason, accurate design, including operation frequency and output power estimation, and full large-signal analysis of oscillator circuits, should be, in principle, carried out through either harmonic balance [391] or full-transient simulation approaches [396] employing high-frequency non-linear large-signal models of the RTD device in its NDR region.

Despite that, an unified and reliable large-signal model for oscillator/detector design at high-frequency based on full  $G_{rtd}(\omega, V_{ac})$ ,  $C_{rtd}(\omega, V_{ac})$ , and  $L_{qw}(\omega, V_{ac})$  expressions over the entire device bias range, generalising the model in Figure 2.12, is still yet to be developed, even though first-stage [401, 437] and fully-empirical [391, 438] approaches have already been proposed. Nevertheless, work in this direction is underway [311, 439]. Indeed, the frequency dependence of the  $IV$  curve should be considered in Figure 2.12 since the NDC roll-off flattens the NDR up to vanishing it [311].

However, the major hurdle is posed by the fact that the high-frequency  $IV$  characteristic is not directly measurable. Moreover, S-parameters measurement should be carried out up to the cut-off frequency of the diode, which is tough due to the lack of reliable equipment working at ultra-high frequencies  $\gg 1$  THz [440, 441] and the poor on-wafer measurement accuracy caused by probe mispositioning and misplanarity above 110 GHz [442]. To date, accurate impedance measurement of RTDs has been demonstrated up to around 0.5 THz [412]. Therefore, oscillator design is currently carried out with simple semi-empirical approaches based on the measured DC  $IV$  curve and associated extracted small-signal parameters of the RTD device, which are then imported in TCAD-based software's (e.g., SPICE, ADS, etc.) for circuitual analysis and subsequent optimisation.

Nonetheless, approximate but reliable semi-empirical analytical expressions can be currently used to estimate the RF power capability of THz RTDs at high-frequency. In this context, the diode RF power  $P_{RF}$  at the operation frequency  $f_{op}$  can be written as [443]:

$$P_{RF} \approx P_{RF,max} \cos(2\pi f_{op} \tau_{rtd}) \quad (2.121)$$

or, alternatively [444]:

$$P_{RF} \approx P_{RF,max} \left[ 1 - \left( \frac{f_{op}}{f_{max}} \right)^2 \right] \quad (2.122)$$

Note that, if  $f_{op} \rightarrow f_c$ ,  $P_{RF} \rightarrow 0$  in Eq. (2.121). Similarly, if  $f_{op} \rightarrow f_{max}$  (where  $f_{max}$  is given by Eq. (2.112)),  $P_{RF} \rightarrow 0$  in Eq. (2.122). Note also that both expressions take into account both the NDC roll-off due to intrinsic frequency limitations of the device, as well as the effect

of extrinsic parasitics. Indeed, a non-negligible  $R_s$  causes the diode RF power to drop since it poses a boundary to  $f_c$  and  $f_{max}$  [169]. However, Eq. (2.121) is the most acknowledged and used in state-of-the art RTD modelling. Therefore, this model has been employed in this thesis work.

## 2.6 Technology

RTD devices realized in III-V semiconductors show attractive characteristics for THz operation. The parameters of commonly-used III-V materials employed to design RTD-based THz sources and detectors are shown in Table 2.1, including the electron effective mass  $m_e^*$ , energy band gap  $E_g$ , conduction band offset  $\Delta E_c$ , and static relative dielectric constant  $\epsilon_{r,0}$  at RT. In general, small  $m_e^*$  leads to high drift mobility/current-density, with improved transport capabilities at THz frequencies, whereas high  $\Delta E_c$  increases the NDR region PVCR by suppressing the valley current due to thermionic emission across the DBQW structure.

Even though first attempts in RTD THz oscillators realization were based on high-quality

Table 2.1: RTD III-V electronic physical parameters at RT ( $T = 300$  K).

Material	$m_e^*$ [ $m_0$ ]	$E_g$ [eV]	$\epsilon_{r,0}$ [ $\epsilon_0$ ]	$\Delta E_c$ [eV]
GaAs	0.063	1.424	12.90	-0.28 <sup>[a]</sup>
AlAs	0.146	2.949 (2.153 <sup>**</sup> )	10.06	0 <sup>[a]</sup>
InAs	0.023	0.354	15.15	-1.35 <sup>[b]</sup>
AlSb	0.140	2.386	12.04	0 <sup>[b]</sup>
GaN	0.200	3.440	8.90	-2.00 <sup>[c]</sup>
AlN	0.400	6.130	9.14	0 <sup>[c]</sup>
$\text{Al}_x\text{Ga}_{1-x}\text{As}$	$0.063 + 0.083x$	$1.424 + 1.155x + 0.370x^2$	$12.90 - 2.84x$	$0.47 - 0.33x + 0.14x^2$ <sup>[d]</sup>
$\text{In}_{1-x}\text{Ga}_x\text{As}$	$0.023 + 0.035x + 0.009x^2$	$0.354 + 0.593x + 0.477x^2$	$15.15 - 2.87x + 0.67x^2$	$-4.88 + 0.81x$ <sup>[a]</sup>
$\text{In}_{0.53}\text{Ga}_{0.47}\text{As}$	0.042	0.738	13.90	-1.04 <sup>[a]</sup>

The parameters are taken/computed from the literature [75,445–448] at the  $\Gamma$  point. In the above, InAs stands for indium arsenide, AlSb for aluminium antimonide, GaN for gallium nitride, while AlN for aluminium nitride. In  $\text{Al}_x\text{Ga}_{1-x}\text{As}$ ,  $0.45 \leq x \leq 1$ , while, in  $\text{In}_{1-x}\text{Ga}_x\text{As}$ ,  $x \leq 0.47$ , being  $x$  the molar fraction associated with the ternary compound. Moreover,  $m_0 \sim 9.109 \times 10^{-31}$  kg is the electron rest mass, while  $\epsilon_0 \sim 8.854 \times 10^{-12}$  F/m the vacuum permittivity. Here,  $\Delta E_c$  is given with respect to a reference material (0 eV): [a], AlAs; [b], AlSb; [c], AlN; [d], GaAs. These parameters are general and strain-independent. <sup>\*\*</sup>X point value.

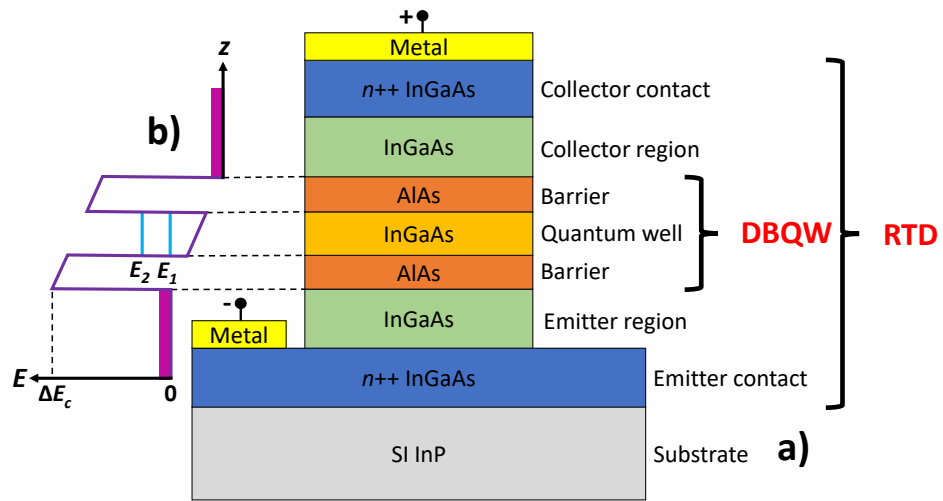


Figure 2.13: In a), illustration of the typical layer structure of a generic InGaAs/AlAs double-barrier RTD device, outlining the DBQW region (layers nomenclature assumes the top contact to be forward biased with respect to the bottom one); in b), the corresponding simplified CB diagram at peak resonance.

GaAs/AlGaAs [449] and GaAs/AlAs heterostructures [450] grown on semi-insulating (SI) GaAs substrates, the most dominant RTD technology for THz applications is nowadays based on the InGaAs/AlAs material system [451,452], in particular,  $\text{In}_{0.53}\text{Ga}_{0.47}\text{As}/\text{AlAs}$  [453,454], which is pseudomorphically-grown onto a lattice-matched SI indium phosphide (InP) substrate through either MBE [352] or MOVPE [455,456]. This is essentially due to the lower  $m_e^*$  of InGaAs, where the saturation drift velocity  $v_{e,s}$  is around  $3 \times 10^7$  cm/s [416] (at least three times higher than GaAs at RT [457]), larger  $\Delta E_c$ , which rises the PVCRR up to several tens [458,459] (while best reported values for AlGaAs/AlAs heterostructures are around 6 [460]), together with the lower  $\rho_c \sim 10^{-8} \Omega \text{ cm}^2$  [461] (around two orders of magnitude smaller than GaAs [462]), which enhances  $f_{max}$ . State-of-the-art InGaAs/AlAs RTDs have demonstrated to deliver current densities of up to around  $30 \text{ mA}/\mu\text{m}^2$ .

Figure 2.13 shows the typical layer structure of an  $n$ -type intra-band DBQW THz RTD device in the InGaAs/AlAs material system, together with a sketch of the associated CB diagram at peak resonance (forward bias). Generally-speaking, the core of the device comprises of a low-band gap InGaAs QW layer sandwiched between two high-band gap AlAs barrier layers. Often, either an indium (In)-rich InGaAs well [463–465], or an indium arsenide (InAs) sub-well [422], is employed in very-high current density designs.

Outside of the active region, InGaAs undoped/lightly-doped spacer layers are placed on both emitter and collector sides, together with  $n+$  emitter and collector regions, and heavily-doped  $n++$  contacts (silicon (Si) donor atoms are typically employed for doping), where titanium/palladium/gold (Ti/Pd/Au) metal stacks are usually employed since form good Ohmic

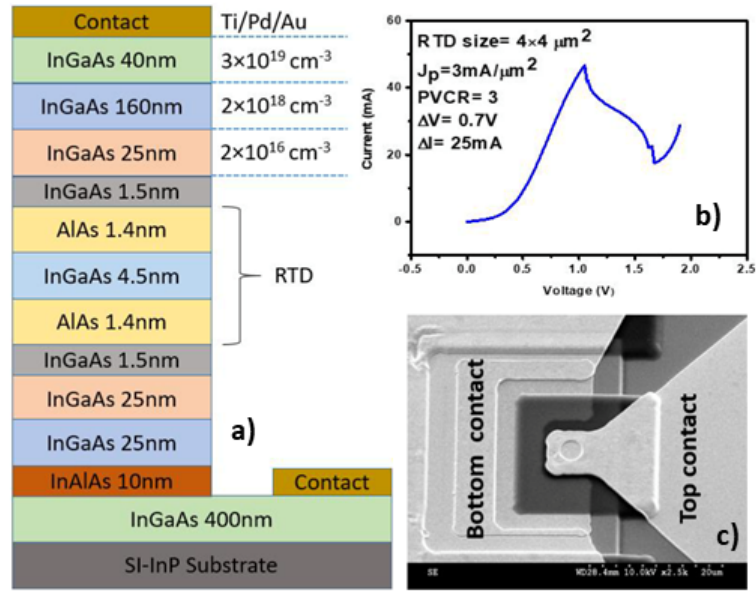


Figure 2.14: In a), illustration of the RTD epitaxial structure employed in the realisation of the 260 GHz oscillator reported in [169]; in b), the measured static  $IV$  characteristic of a fabricated  $16 \mu\text{m}^2$  large device; in c), SEM image of a fabricated device (adapted and reprinted from [169]).

contacts [169, 466]. Spacers are designed to avoid dopants diffusion into the DBQW active region, reduce the device self-capacitance, and enhance the RF power performance [467–469], while contacts doping level and In molar fraction are tuned to reduce  $\rho_c$  [464]. In this context, DBQW and emitter/collector regions design, including layers composition, thickness and/or doping level, reflect on the diode frequency and RF power performance [417].

An example of RTD epitaxial layer structure employed in THz sources up to around 300 GHz is depicted in Figure 2.14a [169]. It comprises of an  $\text{In}_{0.53}\text{Ga}_{0.47}\text{As}/\text{AlAs}$  DBQW with around 1.46 nm-thick barriers, 4.4 nm-thick  $\text{In}_{0.53}\text{Ga}_{0.47}\text{As}$  QW, and 25 nm-thick lightly-doped (Si,  $N_D = 2 \times 10^{16} \text{ cm}^{-3}$ ) spacers, and it was grown onto a SI InP substrate through MBE. The RTD electrical quantities of an around  $16 \mu\text{m}^2$ -large fabricated device are reported in Figure 2.14b, together with the measured static  $IV$  characteristic, featuring peak current density  $J_p = I_p/A \sim 3 \text{ mA}/\mu\text{m}^2$ ,  $\Delta I = 25 \text{ mA}$ ,  $\Delta V = 0.7 \text{ V}$ , and PVCR around 3. A scanning electron microscopy (SEM) image of the fabricated device is also shown in Figure 2.14c.

Figure 2.15 shows a high-speed InGaAs/AlAs DBQW heterostructure which has been used in RTD-based sources up to around 2 THz [168, 470]. It features an indium aluminium gallium arsenide (InAlGaAs)-based graded emitter, which allows to reduce the DC voltage needed to bias the RTD device in its NDR region by moving the emitter CB edge closer to  $E_1$ , thereby shifting  $V_p$  to lower bias [471]. This helps to prevent thermal breakdown due to ultra-high-current density operation. Moreover, it increases the DC-to-RF efficiency and prevents the generation of high-electric fields in the diode depletion regions, which could cause electrical breakdown.

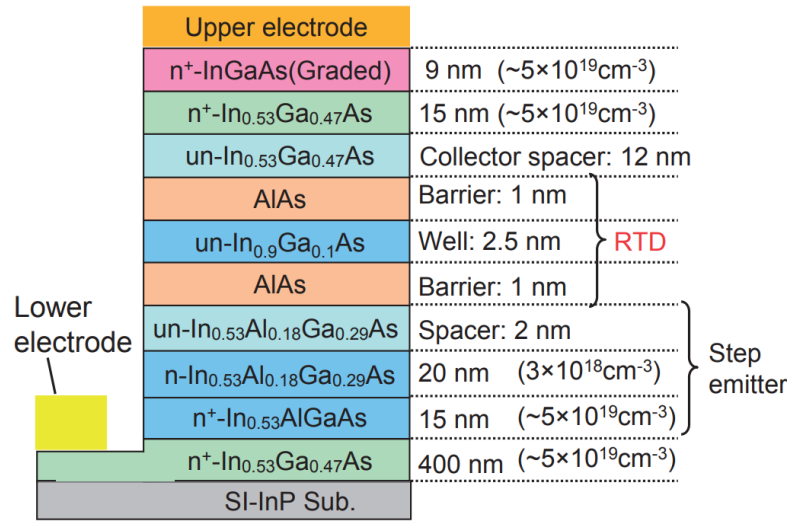


Figure 2.15: Illustration of the RTD epitaxial structure employed in the realisation of the 1.92 THz and 1.98 THz oscillators reported in [168, 470] (reprinted from [168, 470]).

An In-rich In<sub>0.9</sub>Ga<sub>0.1</sub>As QW is employed due to the thin QW and to further reduce the DC bias by depressing  $E_1$ , while the second quasi-bound subband stays almost in place, increasing the PVCR [464].

Furthermore, employing thin 1 nm-thick AlAs barriers and a thin 2.5 nm-thick QW increases current density and reduces the electron tunnelling time [473], increasing  $f_{in}$ , while a 12 nm-thick undoped collector spacer layer is used to trade off between depletion and carrier transit-related capacitances [468, 472]. The heavily-doped In-rich graded cap layer is designed to improve the Ohmic top contact by reducing the Schottky barrier height and the associated  $\rho_c$ . The static  $IV$  characteristic electrical quantities of an around  $0.2 \mu\text{m}^2$  large fabricated RTD device were reported in [168] and are  $J_p = 31 \text{ mA}/\mu\text{m}^2$ ,  $\Delta I = 2.8 \text{ mA}$ ,  $\Delta V = 0.5 \text{ V}$ , and PVCR= 1.8.

Recently, III-nitrides have also gained interest in the THz RTD community [474–478]. They feature large  $\Delta E_c$  (around 2.0 eV in the gallium nitride/aluminium nitride (GaN/AlN) material system), good  $v_{e,s}$  (around  $2 \times 10^7 \text{ cm/s}$  in GaN), and high-breakdown voltage. Despite that, they are characterized by large  $m_e^*$  (around 0.2 in GaN and 0.4 in AlN), and the Ohmic contacts are poor ( $\rho_c \sim 10^{-5} \Omega \text{ cm}^2$  [479]), resulting in reduced  $f_{max}$ . Moreover, the polar nature of the active region introduces broken symmetry effects, which deteriorates resonant current injection and tunneling dynamics [480, 481].

Furthermore, epitaxial growth is still immature, and the resulting PVCR too low at RT (usually below 1.5). Although demonstrated devices have exhibited  $J_p$  up to around  $10 \text{ mA}/\mu\text{m}^2$  to date, typical reported  $f_{max}$  values are under 200 GHz, so the jury is still out for this material systems to be employed in THz circuits.

Indium arsenide/aluminium antimonide (InAs/AlSb) heterostructures [482–485], as well as those based on gallium antimonide (GaSb) ternaries and quaternaries [486, 487], have also been investigated in the realisation of high-frequency RTDs thanks to their superior speed and RF power performance over InGaAs/AlAs devices. In this context, InAs has lower  $m_e^*$  over InGaAs, and the employment of AlSb offers a higher  $\Delta E_c$  [488]. In addition, the staggered type-II CB offset allows electrons to tunnel through the barriers with a reduced attenuation coefficient and increased tunnel transparency, resulting in enhanced current density and operating frequency compared to conventional type-I heterostructures, at the expense of a lower PVCR [489].

Further advantages include the absence of ternary/quaternary alloy-related scattering, the low associated electron-longitudinal optical phonon (LOP) scattering rate, and the small electron transit time across the depletion regions ( $v_{e,s} \sim 5 \times 10^7$  cm/s in InAs), enhancing  $f_{in}$  [489]. At the same time, a nearly ideal Ohmic contact can be formed at the metal-InAs junction since the Fermi level pins in the CB, lowering  $\rho_c$  down to around  $10^{-9} \Omega \text{ cm}^2$  [490, 491].

However, epitaxial growth quality is poor due to the lattice mismatch arising with commonly employed SI substrates, such as GaAs and GaSb [492, 493]. Moreover, InAs suffers from impact ionization due to the low threshold electric field caused by the reduced energy band gap, which can lead to subband population in the QW region, lowering the tunnelling injection efficiency [489, 494]. To date, InAs/AlSb RTD oscillators have been reported up to a fundamental operation frequency of 712 GHz and delivering around 0.3  $\mu\text{W}$  output power [482].

Furthermore, silicon/silicon-germanium (Si/SiGe) RTDs have been proposed due to monolithic integration possibilities with Si complementary metal-oxide-semiconductor (CMOS) technology [495–497]. However, due to the low electron mobility of Si and the limited  $\Delta E_c$  [498], performances are way below III-V heterojunctions. In this context,  $J_p$  of around 280 kA/cm<sup>2</sup> have been reported [496], which is one order of magnitude lower than state-of-the-art InP technology, and same applies to the PVCR. At the same time, the poor thermal conduction capabilities of Si makes large area devices to suffer from thermal management issues, resulting in severe performance degradation. For these reasons, this technology has been put aside and mostly investigated in the context of digital applications, including ultra-fast logic gates in the realisation of memory latches [499].

Moreover, Si/SiGe, as well as antimonides-based, RTD heterostructures relying on interband operation have been reported [486, 500–503]. The working mechanism is analogous to Esaki diodes and they typically show large PVCR [504, 505], however, they have not yet been employed in THz oscillator/detector circuits due to either poor frequency performance or technological limitations.

More exotic graphene-based RTDs have also been recently proposed as proof of concept [506, 507], however, their practical employability in THz circuits has not been investigated.

## 2.7 RTD THz oscillators

### 2.7.1 Principle of operation

RTD-based NDR oscillators can produce either sinusoidal or non-sinusoidal waveforms. The latter, called relaxation oscillators, have been demonstrated in both transmission line [508] or monolithic [509] forms, but they typically work at lower frequencies, and so they are not discussed here. On the other hand, state-of-the-art RTD THz transmitters (Tx) exclusively employ sinusoidal oscillators comprising of an inductor-capacitor ( $LC$ ) resonant tank, whose principle of operation conforms to classical NDR diode-based electronic oscillators.

When the RTD is biased within the NDR region, electronic noise in the circuit [162] is amplified by the NDC and the system filters out all frequency components, except those defined by the resonator passband. The shape of the spectrum defines its quality factor ( $Q$ ) and the corresponding bandwidth, which depend upon the resistor-inductor-capacitor ( $RLC$ ) lossy resonator damping nature [510]. If the large-signal NDC can compensate for circuit, device, and load (antenna) losses within the resonator bandwidth, a stable oscillating signal is obtained across the load [511].

Moreover, due to the non-linearity of the NDC, the oscillator spectrum is characterised by the fundamental mode of the resonator plus higher harmonics. An RTD oscillator can be, therefore, considered a DC-to-RF power converter, where the energy provided by the DC bias supply is transformed into an RF output signal with a certain efficiency, and then delivered to a load, usually, an antenna, to be radiated.

A representation of a generic RTD-based sinusoidal oscillator lumped-element equivalent circuit topology is shown in Figure 2.16a, together with its simplified RF equivalent circuits in large-signal (Figure 2.16b) and at start-up (Figure 2.16c). The DC part of the circuit is composed of the DC bias supply  $V_b$ , the bias line, which is modelled through its parasitic resistance  $R_b$  and inductance  $L_b$ , the decoupling capacitance  $C_{dc}$ , and the stabilising shunt resistance  $R_{st}$ , while the RF part of the circuit comprises the resonating inductance  $L$ , the RTD device, which provides RF gain and acts as resonating capacitance  $C_{rd}$ , and the load resistance  $R_L = 1/G_L$ .

The shunt resistor suppresses the low-frequency parasitic oscillations caused by the bias line inductance  $L_b$ , and it is designed so that  $R_{st} < 1/|G_{rd}|_{max}$  [512]. Therefore, the larger

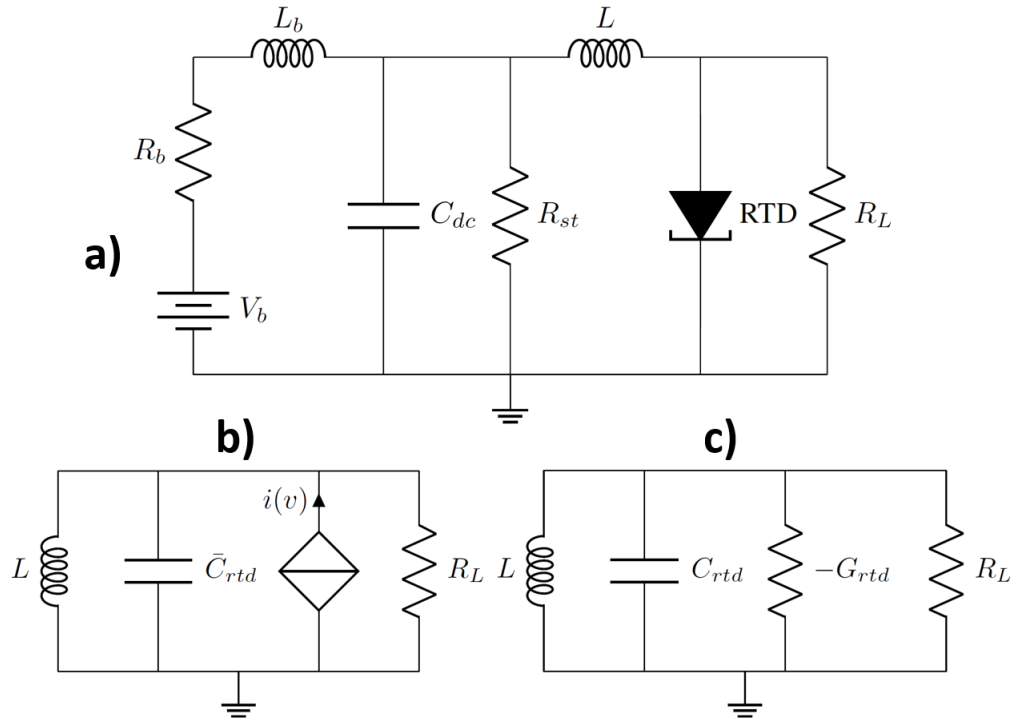


Figure 2.16: In a), the RTD-based sinusoidal oscillator lumped-element equivalent circuit topology; in b), the approximate RF large-signal equivalent circuit; in c), the equivalent circuit at start-up. In b) and c),  $R_s$  and  $L_{qw}$  are neglected for the sake of simplicity.

$|G_{rtd}|_{max}$ , the smaller has to be  $R_{st}$ . Note that  $R_{st} > L|G_{rtd}|_{max}/C_{rtd}$  has to be satisfied at the same time to avoid instability at very high-frequency [513]. However, this technique is quite unreliable since very small resistors with resistance way below  $10 \Omega$  needed at high  $|G_{rtd}|_{max}$  (either high-current density and/or large mesa areas) are technologically-unpractical since would feature too-high DC power dissipation at the oscillator bias point. Other approaches have been proposed to address on-wafer bias stabilisation [513, 514]. Generally-speaking,  $R_{st}$  limits the circuit efficiency and establishes the maximum device size  $A_{max} = 2\Delta V/3\Delta J R_{st}$  employable in oscillators [515], or stabilise the RTD device in its NDR region for high-frequency characterisation purposes [414].

Since the DC bias is fed via the resonating inductance, the decoupling capacitor is used to ground the inductor and to short-circuit  $R_{st}$  at the oscillation frequency  $f_{osc}$ , thereby decoupling the oscillator circuit from the DC bias supply. The decoupling capacitor is designed to be a short-circuit at  $f_{osc}$ , which is, by definition, the frequency at which the circuit susceptance is set to zero [396]:

$$f_{osc} = \frac{\sqrt{(L - C_{rtd}R_s^2)}}{2\pi L\sqrt{C_{rtd}(1 + R_sG_L)}} \quad (2.123)$$

(which simplifies to  $\approx 1/2\pi\sqrt{LC_{rtd}}$  if  $R_s \rightarrow 0$  [401]) i.e.,  $1/2\pi f_{osc}C_{dc} \rightarrow 0$ . The resonating in-

ductance  $L$  is usually realised from a short section of a transmission line (RF stub), such as a coplanar waveguide (CPW) [516], a coplanar stripline (CPS) [517], or a microstrip line [518], where  $2\pi f_{osc}L = Z_0 \tan(\beta l)$ , being  $\beta$  the imaginary part of the propagation constant,  $l$  the length of the stub, and  $Z_0$  its characteristic impedance, while the resonating capacitance is provided by the intrinsic parasitic capacitance of the RTD device. This is often the case of RTD oscillators operating below around 300 GHz, where an external load/antenna is employed [169]. At higher oscillation frequencies, an on-chip integrated antenna (mostly slot or patch) is usually employed, which works both as resonating inductance, as well as radiator, i.e., load resistance, resulting in highly-compact THz sources [466].

The oscillator output power is determined by the RF power capabilities of the RTD device, as already discussed in Section 2.5. Note that the load (antenna) is, in principle, "apparent", since it includes  $L$ , i.e.,  $G_L \rightarrow Y_L$ , with  $G_L(\omega, L)$  expression that does not present an ideal form for output power, i.e., the output power drops with increasing frequency due to impedance mismatch [396]. Therefore, at any given frequency, an optimum value of  $G_L$  may be found [515].

### 2.7.2 Evolution

The first experimental observation of high-frequency oscillations employing a QW-based resonant tunnelling device was reported by Sollner *et al.* in 1983, employing a GaAs/AlGaAs DBQW heterostructure and a coaxial cavity-based resonator [519]. The system was able to provide output powers of up to 5  $\mu\text{W}$  at a fundamental frequency of around 8 GHz, and oscillations up to 18 GHz, at  $T = 200$  K, while RT oscillations were first reported by Shewchuk *et al.* only one year after [449].

Considerable advances in operation frequency and output power were achieved in the following years working on GaAs technology. Fundamental frequencies of up to 56 GHz and second-harmonic operation up to 87 GHz, with output powers of 60  $\mu\text{W}$  and 18  $\mu\text{W}$ , respectively, were achieved at RT by Brown *et al.* in 1987 [520], while RT fundamental oscillations of up to 200 GHz and 420 GHz (both with output power of 0.2  $\mu\text{W}$ ) were reported by the same authors in 1988 [364] and 1989 [450], respectively. The system comprised an GaAs/AlAs DBQW RTD device and a waveguide-based resonator.

Figure 2.17 shows a sketch of the rectangular resonator reported in [364]. The RTD was placed below a whisker post and on top of the waveguide resonator floor. A tunable back-short, placed behind the device, allowed for a limited tuning of the oscillation power and frequency, while the RTD was DC-biased through a lossy coaxial line, which also provided low-frequency stabilization. This can be considered the first RTD-based THz oscillator.

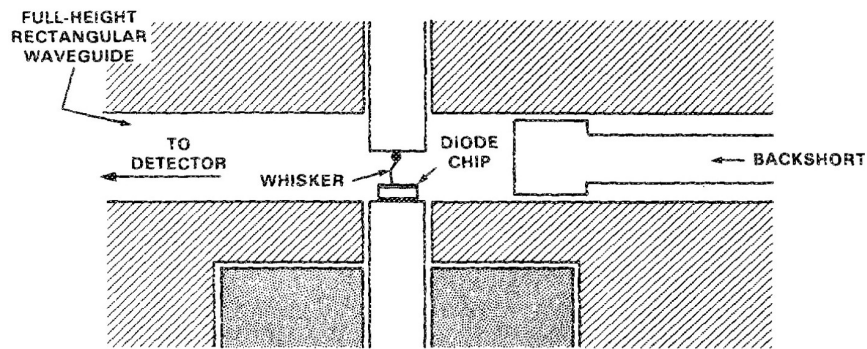


Figure 2.17: Schematic representation of the rectangular waveguide-based resonator employed in the 200 GHz and 420 GHz oscillators reported in [364, 450] (reprinted from [364]).

Two years later, record RT fundamental oscillations of up to 712 GHz were achieved by the same authors employing the InAs/AlSb material system, demonstrating output power of  $0.3 \mu\text{W}$  [482]. At that time, this was the highest experimentally-demonstrated oscillation frequency utilising an RTD device and, generally speaking, of a solid-state electronic oscillator at RT. However, waveguide-based oscillators were characterised by practical drawbacks, such as the non-monolithic bulky nature of the resonator, as well as the relatively inefficient oscillator circuitry used to suppress low-frequency parasitic oscillations caused by the large parasitic inductance introduced by the whisker used to connect the RTD device.

Despite the scientific relevance of these achievements, the immaturity of epitaxial growth techniques prevented further progresses. The scientific community gradually started losing faith in RTD technology, at the point where governmental and private funding ceased and the device was put aside and almost discarded as a research topic for the remaining part of the 1990s. Only few relevant works were reported, among which quasi-optical resonators for oscillator stabilisation [521–523] and coherent power combining [524], together with the first RTD terahertz monolithic integrated circuit (TMIC) oscillator [525]. Proposed by Reddy *et al.* in the second half of the 1990s, the oscillator concept consisted in the monolithic integration of the RTD with a slot-antenna on the same InP substrate thanks to T-gate air-bridge-based Schottky-collector RTD (SRTD) technology [514, 526, 527].

In this context, an approach based on oscillators arrays was proposed and developed to increase the system output power [528]. As shown in Figure 2.18a, each InGaAs/AlAs SRTD device was stabilised individually employing a non-linear biasing resistor [529] consisting in a low-impedance Schottky barrier diode (SBD) [530], and integrated with an on-chip planar slot-antenna element of length  $L$  which worked, at the same time, as a resonator and radiator. Silicon nitride ( $\text{SiN}_x$ ) metal-insulator-metal (MIM) capacitors ( $C_{stab}$ ) were used as reflectors for THz standing waves formation and the definition of the single array element, as well as for DC decoupling and SBD shunts. At the same time, the  $p$ -type collector Schottky contact in the SRTD

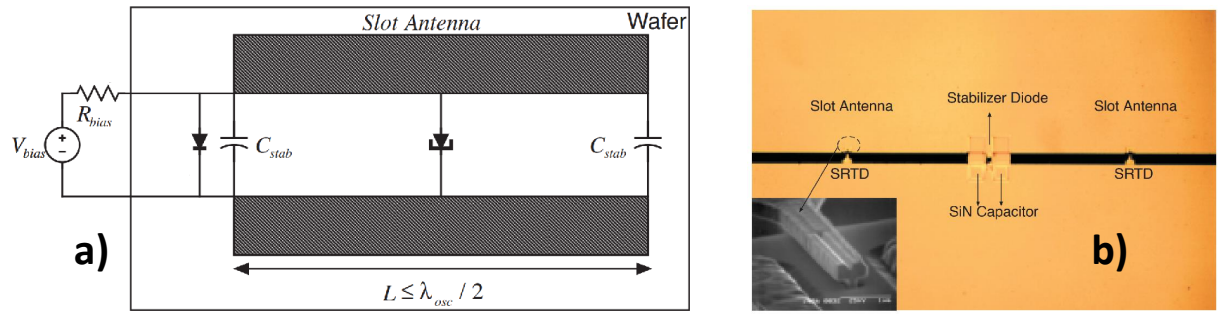


Figure 2.18: In a), a schematic representation of the circuit topology of the single-element slot-antenna SRTD oscillator; in b), a photo-micrograph of a fabricated array element, including a SEM picture of the T-gate SRTD air-bridge-based device (adapted and reprinted from [528]).

device reduced the associated  $\rho_c$ , being Ohmic for electrons, rising  $f_{max}$  [514]. In this sense, the RTD and passive components were fabricated on the same substrate, as shown in Figure 2.18b.

Each oscillator, consisting in a single radiator, was coupled with the other array elements but emitted independently at the radiation wavelength  $\lambda_{osc} \propto 1/n_r f_{osc}$  (being  $n_r$  the system refractive index), and power combining was achieved thanks to spatial interference of the corresponding radiation patterns. The array was mounted onto a Si-based lens to retrieve and collimate the THz field emitted mainly in the high-permittivity InP substrate. This because Si has similar refractive index compared to InP at THz frequencies, minimising reflection losses. Adopting this approach, 16-element and 64-element RTD-arrays could demonstrate output powers of up to 28  $\mu\text{W}$  at RT fundamental oscillations frequencies of 290 GHz and 650 GHz, respectively.

However, this concept suffered from different practical disadvantages. Indeed, phase-locking between the oscillators, which is needed to achieve coherent emission, increases circuit fabrication complexity, making coupling within large-scale arrays tough due to fabrication tolerances. Moreover, spatial power combining is critical to be achieved in a specific direction playing on the array geometry and without compromising mutual locking between the different elements. Despite that, the realization of the first fully-integrated RTD TMIC oscillator represented a crucial milestone due to the several advantages compared to waveguide-based counterparts, among which integrability and efficiency. As a result, RTDs started to progressively re-gain appeal within the scientific community.

A determining turning point occurred in 2005, when Orihashi *et al.* demonstrated RT third-harmonic oscillations up to around 1 THz with output power of 0.6 nW employing a single RTD device [531]. This was the first demonstration of an electronic oscillator working above 1 THz at RT. Details on the circuit layout are discussed in Section 2.7.3. RT fundamental oscillations of up to 831 GHz, 915 GHz, 1.04 THz, and 1.08 THz with output power of 1  $\mu\text{W}$ , few tens of nanowatt, 7  $\mu\text{W}$ , and 5.5  $\mu\text{W}$ , respectively, were then reported by the same research group in

2009 [472, 532], 2010 [471], and 2011 [533], respectively. To achieve that, the RTD epitaxial structure was improved by optimising the collector spacer layer, reducing barriers/QW thickness, and introducing a graded emitter.

Further improvements in oscillation frequency were then achieved by Feiginov *et al.* in 2011 employing an RTD membrane oscillator [422], reaching RT fundamental oscillations of up to 1.11 THz with output power of 0.1  $\mu\text{W}$ . Differently to what already implemented until then, the RTD device was integrated with a planar slot resonator and the THz signal was extracted and radiated in plane employing a broad-band Vivaldi antenna in order to improve the radiation efficiency. Both the resonator and the antenna were laid down onto a thin dielectric membrane and sustained by a Si-based holder.

In the following years, considerable advances in RT fundamental oscillation frequency were achieved. Kanaya *et al.* reported 1.31 THz with output power of 10  $\mu\text{W}$  in 2012 by further optimising the RTD active region [473], and then 1.42 THz with output power of 1  $\mu\text{W}$  in 2014 by further optimising the collector spacer layer thickness [468]. Then, around 1.4 THz with output powers of several nanowatt were achieved by Koyama *et al.* in 2013 employing a triple-barrier RTD device and a patch antenna (whose metal strip line acted as resonating inductance) for upwards emission, removing the bulky Si lens [534]. Feiginov *et al.* and Maekawa *et al.* reported 1.46 THz with output power of 0.36  $\mu\text{W}$  [425] and 1.55 THz with output power of 0.4  $\mu\text{W}$  [535] the same year by playing on the collector region doping and the slot-antenna length, respectively.

Record results were achieved by Maekawa *et al.* in 2016, reporting 1.92 THz with output power of 0.4  $\mu\text{W}$  [470], and by Izumi *et al.* in 2018, where around 2 THz RT fundamental oscillations were observed (with output power of around 40 nW) by optimising the air-bridge fabrication and antenna design [168]. This is the highest fundamental oscillation frequency reached by an RTD THz source and, generally-speaking, by an electronic oscillator at RT to date.

### 2.7.3 Technology

Different approaches have been adopted to develop InP-based RTD THz oscillators, featuring different device epitaxial structures and circuit implementations. The details of state-of-the-art oscillators are summarised in Tables 2.2 and 2.3, and Figure 2.19. The highest reported fundamental oscillation frequency at RT is 1.98 THz, with around 40 nW of output power  $P_{RF,out}$  (radiated) [168], while the highest reported  $P_{RF,out}$  (on-chip) is 1 mW at 0.26 THz [169].

Table 2.2 lists the electrical quantities of the employed RTD devices, while Table 2.3 reports the oscillator specifics, where provided. Note that, for frequencies far beyond 300 GHz, os-

Table 2.2: RTD devices electrical quantities.

Ref.	$J_p$ [mA/ $\mu\text{m}^2$ ]	$\Delta J$ [mA/ $\mu\text{m}^2$ ]	PVCR	$V_p$ [V]	$C_{rtd}$ [fF/ $\mu\text{m}^2$ ]	$\rho_c$ [ $\Omega \mu\text{m}^2$ ]	$f_{max}^*$
[536]	24	12	2	-	-	9.5 – 12	-
[470]	50	20.6	1.7	0.4	-	-	-
[168]	31	13.8	1.8	-	-	-	-
[443]	-	14	-	-	-	3	-
[537]	29	14.5	2	-	-	-	-
[169]	3	1.9	2.7	1	3.8	50	337 GHz
[390]	1.9	1.1	2.5	0.9	2.5	83	317 GHz
[538]	1.2	1.1	12	1.4	4.5	106	114 GHz
[539]	6.9	2	1.4	0.7	8.1	4.6	1.08 THz
[540]	6.7	1.9	1.4	0.6	-	-	-

\* Computed through Eq. (2.113). " - " stands for "not provided".

Table 2.3: RTD THz oscillators specifics.

Ref.	$A$ [ $\mu\text{m}^2$ ]	$\Delta I$ [mA]	$\Delta V$ [V]	$P_{RF,max}$ [mW]	Antenna	$f_{osc}$	$P_{RF,out}^*$
[536]	1.5–1.9	18–22.8	0.4	1.4–1.7	slot	548 GHz	0.4 mW
[470]	0.1	2.1	0.4	0.2	slot	1.92 THz	0.4 $\mu\text{W}$
[168]	0.2	2.8	0.5	0.3	slot	1.98 THz	40 nW
[443]	1.4	19.6	0.4	1.5	slot	620 GHz	0.6 mW <sup>[a]</sup>
[537]	0.5	7.2	0.3	0.4	dipole	1 THz	0.7 mW <sup>[b]</sup>
[169]	16	25	0.7	3.3	/	260 GHz	1 mW
[390]	16	18.2	0.8	2.7	/	84 GHz	2 mW <sup>[c]</sup>
[538]	26.4	29	1.3	7.1	/	62.5 GHz	3.1 mW
[539]	0.9	1.8	0.2	0.1	patch	1.52 THz	1.9 $\mu\text{W}$ <sup>[d]</sup>
[540]	1.6	3	0.2	0.1	dipole	675 GHz	47 $\mu\text{W}$ <sup>[e]</sup>

\* Reported values are "radiated" when the antenna type is specified, "on-chip" measured otherwise. [a], two-elements synchronised oscillators array; [b], 89-element unsynchronised oscillators array; [c], two-parallel RTDs oscillator; [d], triple-push configuration; [e], differential double-RTD oscillator. " - " and " / " stand for "not provided" and "not included", respectively.

cillator design employs integrated antennas and the devices are characterised by high  $J_p$  in the MA/cm<sup>2</sup> range and low  $\Delta V < 0.5$  V. Moreover, device sizes are small (around or well below 1  $\mu\text{m}^2$ ) and  $P_{RF,out}$  is low (microwatt range). On the other hand, in the low-THz band ( $\sim 100$ –300

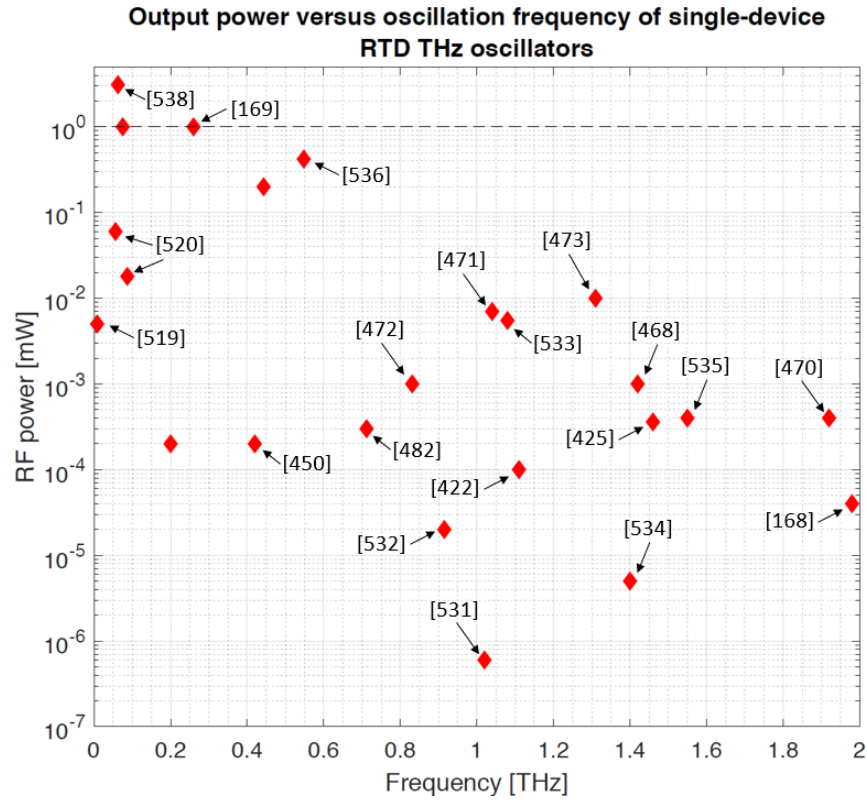


Figure 2.19: Output power versus fundamental frequency of oscillation for some of the most relevant reported single-device RTD THz oscillators to date, including some results below 100 GHz. Reference number is provided for key results.

GHz), moderate  $J_p \sim 300 \text{ kA/cm}^2$ , large  $\Delta V \gg 0.5 \text{ V}$ , and large mesa area ( $A \geq 16 \mu\text{m}^2$ ) devices are employed, as well as external antenna loads, with output powers in the milliwatt range. Indeed,  $\Delta I$ , as well as  $\Delta V$ , are high for devices operating below 600 GHz, while small for RTDs operating above 1 THz.

From Table 2.3, it can be seen that typical  $C_{rd}$  are in the range  $3\text{--}8 \text{ fF}/\mu\text{m}^2$ , while  $\rho_c$  are also very varied, ranging from  $3\text{--}106 \Omega \mu\text{m}^2$ , which mainly depends on the fabrication process of Ohmic contacts. The peak current density  $J_p$  also varies over a large range, between  $1\text{--}50 \text{ mA}/\mu\text{m}^2$ , which, in some ways, shows the relative immaturity of the epitaxial design approaches and associated oscillator circuit realisation.

Figure 2.19 shows the reported output power and corresponding operating frequency of these oscillators to date. Clearly, THz operation has been demonstrated, but the output power is still under 1 mW beyond 300 GHz, which is the main limitation of this technology. These results also show a wide variation in performance, which indicates the lack of established and optimal design practices.

A photo-micrograph of the fabricated 0.26 THz oscillator is shown in Figure 2.20, and its

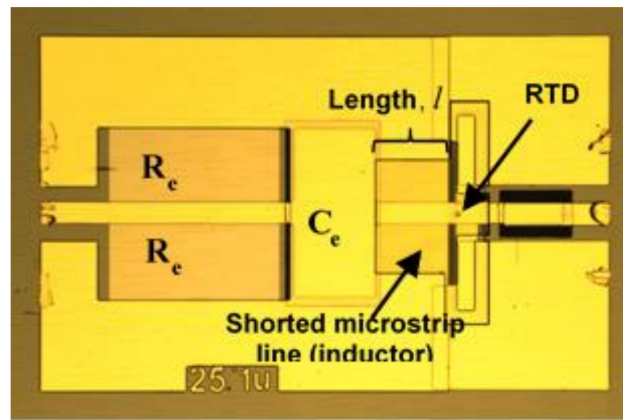


Figure 2.20: Photo-micrograph of the fabricated 0.26 THz microstrip RTD oscillator reported in [169] (reprinted from [169]). Here,  $C_e$  and  $R_e$  are the decoupling capacitor and stabilising resistors.

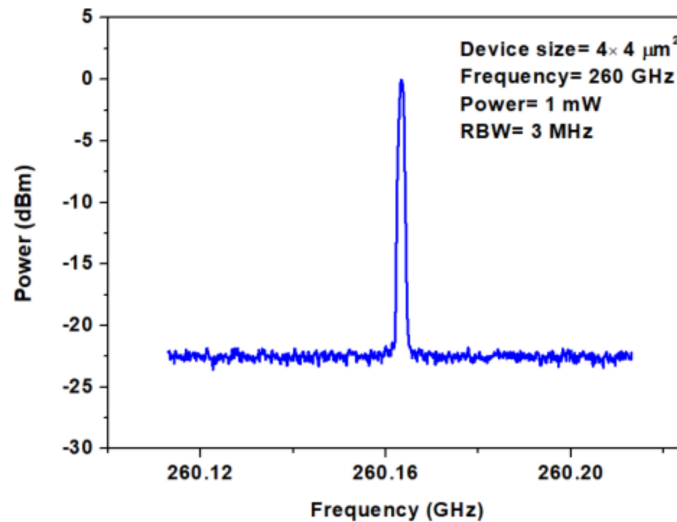


Figure 2.21: Measured output spectrum of the 0.26 THz microstrip RTD oscillator reported in [169] (reprinted from [169]). Down-conversion mixers were used to display the probed signal on the employed 50 GHz spectrum analyser. The resolution bandwidth was set to 3 MHz.

spectrum of oscillations is shown in Figure 2.21 [169]. The RTD source showed a high coherence level, where a coherence length of around 100 m was estimated from the measured spectrum. Also, from a broader analysis of the spectral profile, a line-width of 2 MHz at -10 dB below the 0.26 THz peak was measured, indicating the relatively-low phase noise of the oscillator. The corresponding measured output power was around 1 mW, which is the current record at low-THz frequencies, together with a corresponding DC-to-RF efficiency of around 0.7 %.

Circuit design was carried out employing a single RTD device and an 88  $\mu\text{m}$ -long microstrip-based resonating inductance with characteristic impedance  $Z_0 = 10.4 \Omega$ , where polyimide PI-2545 was used as dielectric. It features a 0.1 pF  $\text{SiN}_x$  MIM decoupling capacitor, a 1.3 pF

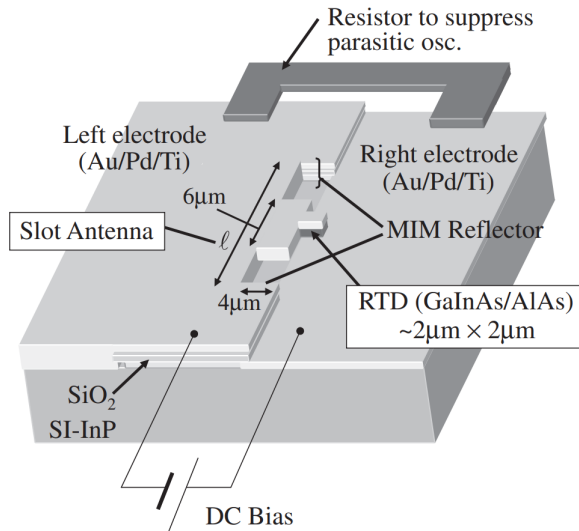


Figure 2.22: Layout illustration of an RTD THz oscillator integrated with a slot-antenna operating way above 300 GHz (reprinted from [437]).

$\text{SiN}_x$  MIM DC block capacitor, together with a nichrome (NiCr)-based stabilising resistor with  $R_{st} = 22 \Omega$ . The oscillator was designed for on-wafer probing and did not feature an on-chip antenna. In this context, the load consists in the input impedance of the spectrum analyser/power meter, which was  $50 \Omega$ . The modulation bandwidth of the system was estimated from 2-port S-parameters measurements of an unbiased oscillator and then deduced from the forward transmission coefficient  $S_{21}$ , and was around 110 GHz [541]. Moreover, microfabrication was carried out solely with optical lithography and wet etching, minimising production costs.

On the other hand, RTD THz oscillators operating far beyond 300 GHz employ integrated on-chip antenna loads featuring different designs, including slot [470,542], Vivaldi [422], radial-line slot [543], patch [539, 544–547], dipole [537, 540, 548], and bow-tie [549]. However, the most common on-chip antenna is the slot-antenna, which is used in conjunction with a hemispherical Si lens [525,531]. Because of the high dielectric permittivity of InP ( $\epsilon_{r,0} \sim 12.5$  [550],  $\epsilon_{r,\infty} \sim 9.6$  [551]), most of the output power is radiated into the substrate. Thus, the oscillator is mounted onto a Si lens to extract and collimate it, with the thickness of the chip and lens designed to maximise the power extraction efficiency [464].

Figure 2.22 shows the general layout of an RTD THz oscillator integrated with a slot-antenna [437]. In this configuration, the electrodes of the RTD device are connected to the left and right electrodes of the antenna, which have a silicon dioxide ( $\text{SiO}_2$ ) layer in between, forming a decoupling MIM capacitor, across which a stabilising resistor (usually InGaAs-based) is connected. The frequency of oscillation is mainly determined by the parallel resonance of  $L$  and  $C_{rtd}$ , where the resonating inductance is provided by the antenna. Indeed,  $L$  could also be viewed as the inductance of the metal connection between the decoupling capacitor and the RTD

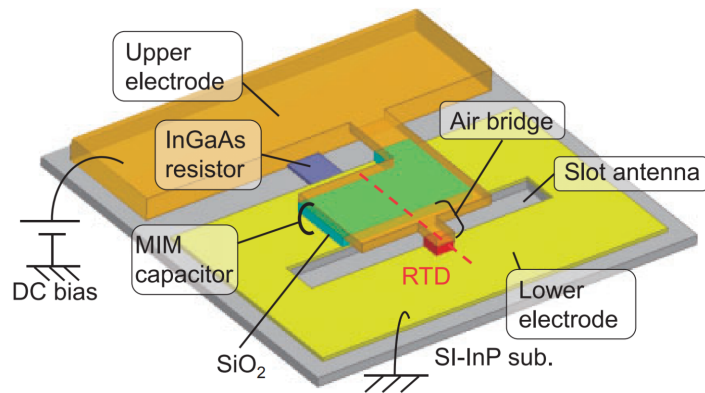


Figure 2.23: Illustration of the circuit layout employed in the realisation of the 1.92 THz oscillator reported in [470] (reprinted from [470]).

device. Therefore, the equivalent circuit of the antenna load can be seen as the parallel of its inductance  $L$  and resistance  $R_L$ , as shown in Figure 2.16b.

It is important to underline that, in Figure 2.22, the diode is located at the centre of the slot and THz standing waves form thanks to the MIM-based reflectors. However, since the input impedance of the antenna is infinity at the centre and zero at the edges of the slot, the RTD should be placed away from the centre for good impedance matching between the device and the antenna [552], where the exact location can be determined from 3D electromagnetic simulations. For this realisation, the dimension of the shorter part determines the antenna susceptance, which is mainly inductive and defines the oscillation frequency, while the dimensions of the longer part determine the radiation conductance, which determines the output power of the oscillator. Using this approach, output powers of up to 0.42 mW at 548 GHz have been demonstrated [536].

Furthermore, different oscillator cavity implementations have been proposed for frequency and output power enhancement in the THz range, including cylindrical [553–555], rectangular [556], and split-ring [557], as well as simplified layouts without MIM capacitors [558, 559]. In this context, circularly polarized emission of radiation has been demonstrated by employing cross-slot resonators and a radial-line slot antenna (RLSA) array for upward emission, which removes the polarization axis alignment constrain between transmitting and receiving antennas [543]. In addition, mutual injection locking between two synchronised RTD oscillators has been demonstrated, which provided around 0.61 mW of continuous-wave (CW) coherent radiation at a fundamental oscillation frequency of 620 GHz [443]. Large-scale arrays have also been proposed [537], featuring around 0.73 mW at 1 THz in pulsed-mode, but the oscillators were not phase-locked, destroying coherency in the emitter THz field.

Further, a varactor diode integrated with the RTD has been proposed to increase the frequency tunability range by overcoming the weak bias dependence of the device self-capacitance,

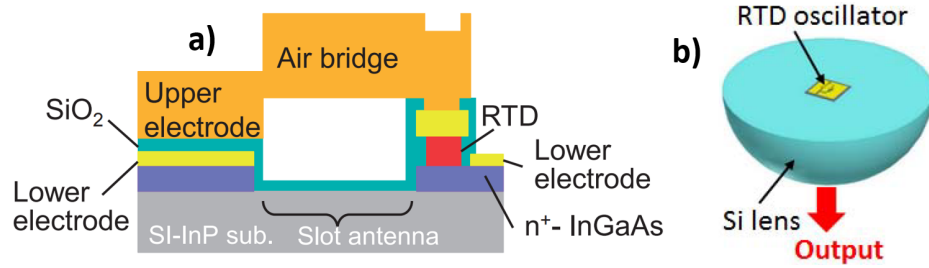


Figure 2.24: In a), illustration of the 1.92 THz oscillator layout cross-section, showing the integration of the RTD device with the slot-antenna through the air-bridge structure (reprinted from [470]); in b), illustration showing the oscillator chip mounted onto the hemispherical Si lens for field collection and focusing (reprinted from [464]).

e.g., up to 40 % [560], realising a voltage-controlled oscillator (VCO). Moreover, the use of phase-locked loops (PLL) with RTDs has also been proposed for spectral narrowing and  $Q$  enhancement [561].

The layout of the RTD THz slot-antenna oscillator operating at 1.92 THz is depicted in Figure 2.23. The upper RTD electrode is connected to the top antenna electrode along the back side of the slot through an air-bridge structure, as shown in Figure 2.24a, while the RTD bottom contact is connected to the bottom antenna electrode on the front side of the slot, integrating the RTD device with the antenna. The decoupling MIM capacitor is placed on the back side and was fabricated through a thin  $\text{SiO}_2$  layer sandwiched between the upper and lower Au-based antenna electrodes. The stabilising shunt resistor was realised from the heavily-doped InGaAs emitter contact under-sheet layer and connected between the upper and bottom electrodes of the MIM capacitor and RTD device. The oscillator chip was mounted onto a Si lens, as shown in Figure 2.24b.

The diode has a mesa area of around  $0.1 \mu\text{m}^2$  and the measured output power was  $0.4 \mu\text{W}$  at 1.92 THz [470]. By further optimising the slot-antenna electrode thickness (around  $3 \mu\text{m}$ ) to reduce the associated conduction losses, fundamental oscillations of up to 1.98 THz with output power of 40 nW were achieved employing an RTD device with a mesa size of around  $0.2 \mu\text{m}^2$  [168], as shown in Figure 2.25. In this context, the measurement of the oscillation frequency was carried out by employing a Fourier-transform infrared (FTIR) spectrometer with a liquid helium-cooled bolometer as a THz receiver (Rx), while, for the output power measurement, the radiated THz field was focused by a parabolic mirror and THz lenses, and then fed to a power meter via a horn-antenna.

RTD THz oscillator concepts other than the aforementioned ones have also been reported in the literature. Their output powers are low and so are not discussed here in detail. For instance, they include a 675 GHz differential double-RTD oscillator [540], and 165 GHz push-push [562]

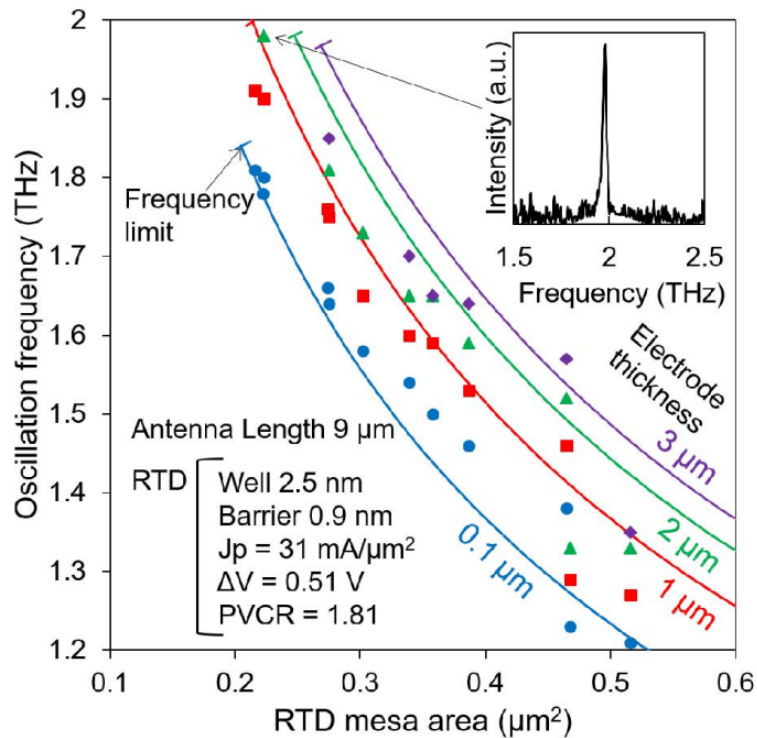


Figure 2.25: Oscillation frequency versus RTD mesa area for different antenna electrode thicknesses of the 1.98 THz oscillator reported in [168] (reprinted from [168]). The spectrum of oscillations, together with few details on the RTD epi-design and associated electrical quantities, are also provided.

and 1.52 THz triple-push [539] oscillators based on second- and third-harmonic modes, respectively. Moreover, travelling-wave microstrip RTD oscillators have also been suggested [563], as they have the potential to work at RT and THz frequencies by providing higher output power with respect to conventional lumped-element RTD oscillators due to the larger associated gain volume. Indeed, differently from standard mesa RTDs, the device can be seen as an "active" distributed element, where the gain medium is encapsulated within a metallic waveguide. Although an experimental proof of concept has not yet been provided, their development is ongoing [564].

## 2.8 RTD THz detectors

Due to their superior speed performance, RTDs can be also employed to realise high-sensitivity THz detectors, and can operate both as standard direct [517], as well as coherent [565], detectors according to the specific bias point [566], as illustrated in Figure 2.26. In the first case, the device is typically-biased in close proximity to  $V_p$  and can perform envelope detection of amplitude-modulated (AM) signals, as in on-off keying (OOK) or amplitude-shift keying (ASK), according to the square-law scheme by exploiting the large associated  $IV$  curve non-linearity [567, 568].

It is important to make it clear that, in contrast to SBDs, the non-linearity is not associated

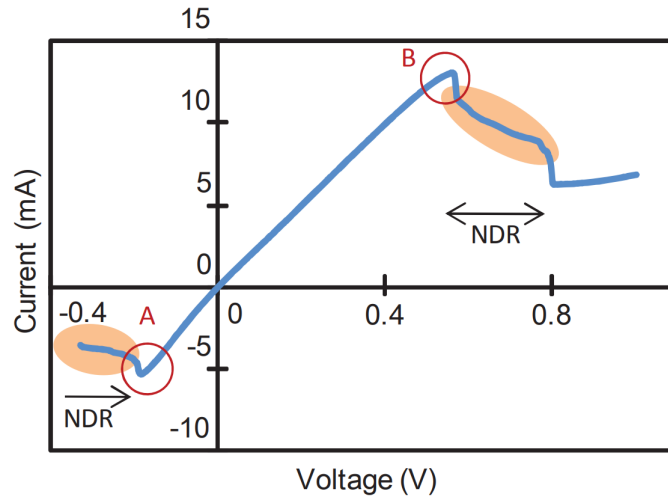


Figure 2.26: Operation principle of a DBQW RTD THz detector based on the associated  $IV$  curve. The device can be either biased close to the peak (marked as A and B depending on the polarisation region) in the case of a direct detector, as well as within the NDR region (highlighted in orange) if coherent detection is employed (reprinted from [568]).

with thermionic emission, but rather with the thermal broadening of the QW subbands, overcoming the thermal limit [311]. This makes the RT sensitivity of a THz RTD much higher than of a standard SBD, whose theoretical maximum DC current responsivity can go only up to around 19.7 A/W [569], while it is even lower for THz field-effect transistors (FET) [570, 571].

While III-V SBDs have shown voltage responsivities of up to 1 kV/W at 250 GHz [572], InP RTDs have demonstrated values of up to 4 kV/W [573] and 80 V/W [574] at 0.35 THz and 0.76 THz, respectively, together with current responsivities of up to 7.3 A/W at 0.78 THz [575]. Moreover, voltage responsivities of up to around 13 kV/W have been reported in the 26.5–50 GHz band [395]. Generally-speaking, the rectification response of the device is determined by the amplitude of the received signal across the RTD, and by the non-linearity of the  $IV$  curve  $\eta = [d^2I(V)/dV^2]/2[dI(V)/dV]$  [569], where the amplitude depends upon impedance matching between the RTD and waveguide/antenna, together with circuit parasitics.

Figure 2.27 shows the measured output voltage versus the incoming 300-GHz signal RF power of a wireless experiment where both InP-based RTD and SBD direct detectors were employed for performance comparison [568], revealing a factor of up to four times higher in sensitivity for the RTD detector. Here, the voltage responsivity of the RTD detector at around 300 GHz was up to 12 dB higher than for the SBD below the saturation voltage of the employed amplifier (which was around 5  $\mu$ W), and a maximum DC sensitivity of up to 30 dB higher was estimated from the  $IV$  curve degree of non-linearity. Note that, since the RTD is biased close to the NDR region, the amplitude of the detected signal must be reasonably small to avoid oscillation triggering due to the RTD NDC instability, which would distort the incoming waveform,

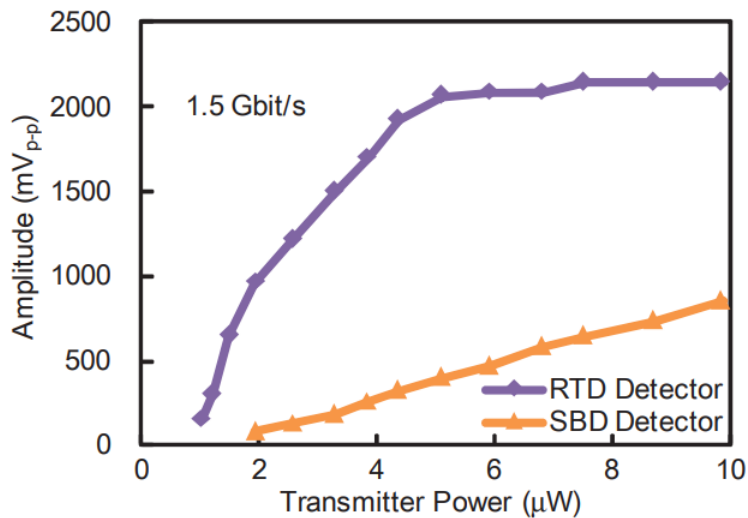


Figure 2.27: Comparison of the measured output voltage versus the incoming 300-GHz signal RF power at 1.5 Gb/s in the wireless experiment reported in [568] (reprinted from [568]).

resulting in a reduced dynamic range [311].

Triple-barrier (TB) RTDs have also been proposed as high-sensitivity THz direct detectors due to their superior performance compared to DBQW-based counterparts. The advantage lies in the strong current blocking thanks to the three-barrier configuration and in the misalignment of the first resonant subbands in the two adjacent asymmetric QWs, leading to a non-symmetric  $IV$  curve around 0 V. When bias is applied and the resonant condition is met, the pronounced current increase leads to a strong non-linearity, with associated responsivity that can exceed the thermal limit [311]. In this context, TB RTDs can be also used as high-sensitivity zero-bias detectors [576], with demonstrated voltage responsivities of up to 66 kV/W at 280 GHz [577]. However, this exceptional performance has not yet been exploited in system applications.

At the same time, TB RTDs have also been employed in THz sources [534, 578, 579] since they are, in principle, capable of higher PVCR (lower  $I_v$ ) compared to DBQW devices. Despite that, currently, their current density and RF power performance tend to be low compared to DBQW RTDs due to epitaxial growth limitations.

Although direct detection can provide a simple solution for THz Rx systems, it relies only on the incoming amplitude information of the signal, being its operation restricted to the Johnson-Nyquist noise limit [162], which reduces spectral efficiency and sensitivity, limiting transmission distance and/or the corresponding data-rate according to the specific signal-to-noise ratio (SNR) and link budget [567], which can nonetheless be partially offsetted by the large available bandwidth at THz frequencies. On the other hand, in the second type of RTD detector, the device is embedded in an oscillator circuit and operates as a coherent detector [566]. The

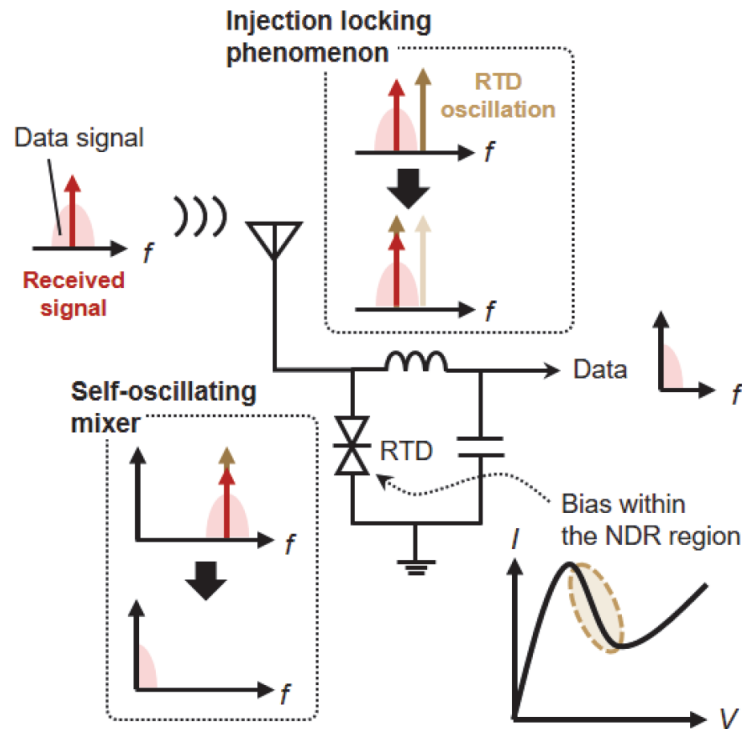


Figure 2.28: Schematic illustration of the operation principle of an RTD THz coherent detector (reprinted from [565]).

principle of operation of this detector is illustrated in Figure 2.28. In this case, the RTD is biased within its NDR region and the circuit acts as a local oscillator (LO) [580]. If the incoming carrier frequency is close enough to the LO one, injection locking [581] takes place and the two signals synchronise [582], performing coherent homodyne detection [565]. At the same time, the incoming signal is demodulated through the non-linear mixing properties of the NDR region [287], where the RTD acts as a self-oscillating mixer (SOM) [567].

Since the RTD works, at the same time, as a LO and mixer, this approach enables the realization of ultra-compact and high-sensitivity Rx chips. For instance, a sensitivity enhancement of up to 20 dB higher compared to direct detection was demonstrated in the wireless experiment reported in [287] employing a 300 GHz-band InP RTD transceiver (TRx), as shown in Figure 2.29. In another experiment, a minimum noise equivalent power (NEP) of  $7.7 \text{ pW}/\sqrt{\text{Hz}}$  was reported at 0.78 THz [566].

Together with the higher sensitivity due to the gain provided by the device NDC, better spectral efficiency is possible, where phase, frequency, and polarisation information of the received signal can be retrieved through injection locking, allowing for multi-channel division multiplexing approaches [567]. At the same time, duplex capability is, in principle, feasible since the same oscillator is employed at both the Tx and Rx front-ends. Despite all the positive attributes, however, the use of a coherent RTD Rx is still very new, and appropriate design methodologies

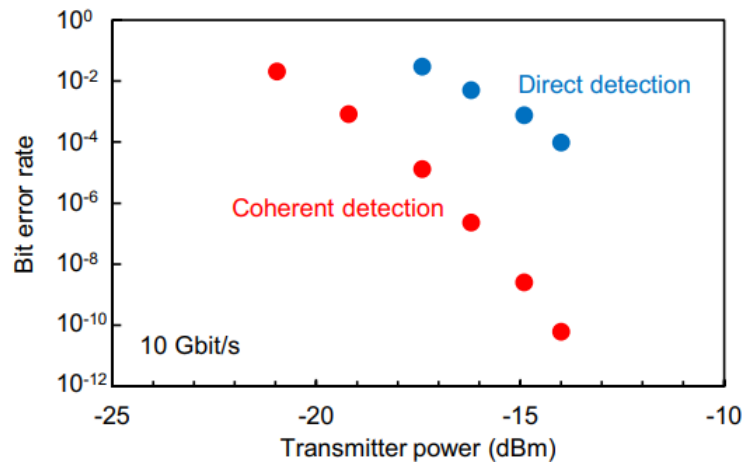


Figure 2.29: Comparison of the measured bit error rate versus Tx incoming RF power at 10 Gb/s in the wireless experiment reported in [287], where the RTD bias point was changed to switch from direct to coherent detection (reprinted from [287]).

to guarantee injection locking and maximise sensitivity need to be developed.

## 2.9 RTD THz applications

### 2.9.1 Ultra-high-speed THz wireless communications

In this Section, state-of-the-art THz wireless communications employing RTDs are discussed. In these experiments, an InP DBQW RTD THz oscillator is usually employed at the Tx side. Both ASK and OOK modulation are applicable to the Tx depending on the bias level and the amplitude of transmitting data, as illustrated in Figure 2.30. Here, ASK modulation has been widely used because of the advantages of being a simple, low cost, high-bandwidth, and high-

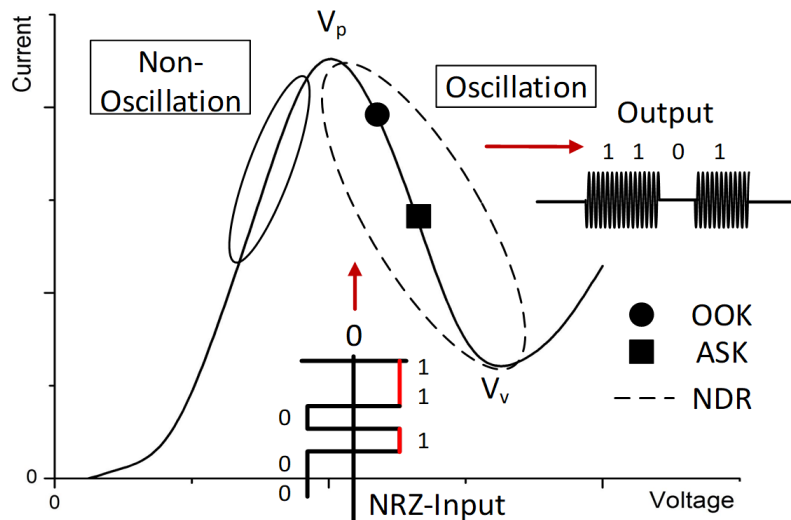


Figure 2.30: Illustration of ASK/OOK modulation in RTD THz Tx (reprinted from [390]).

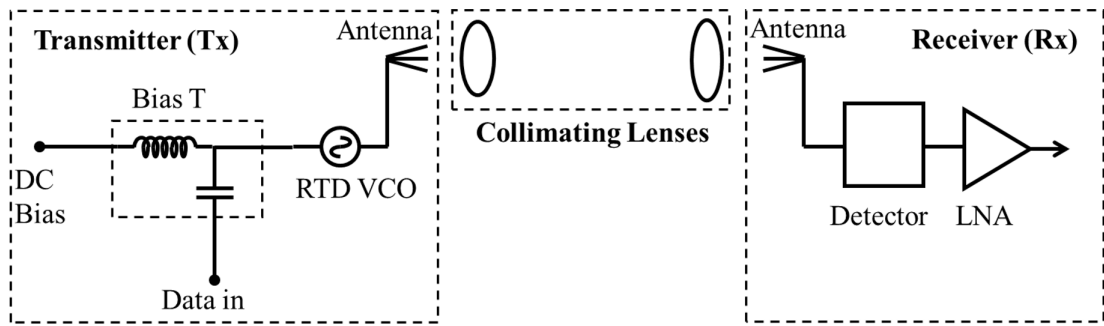


Figure 2.31: Block diagram of a THz wireless TRx system architecture employing an RTD-based Tx and/or Rx.

efficiency technique, while OOK, as a special case of ASK, implements data modulation by switching the carrier ON and OFF [567].

For ASK modulation, the RTD device is biased within its NDR region, while its bias point is set close to  $V_p$  for input non-return to zero (NRZ) data in the case of OOK, in order to switch ON and OFF the oscillator. Clearly, the input data amplitude for ASK is limited by the NDR voltage span, which is low. Since modulation of RTDs is via the bias line, the modulation bandwidth is mainly determined by the DC decoupling circuit comprising  $C_{dc}$  and  $R_{st}$ , as shown in Figure 2.16a, and has been measured to be around 110 GHz for 300 GHz oscillators [541].

### 2.9.1.1 RTD THz wireless TRx systems architecture

The block diagram of a THz wireless TRx employing an RTD-based Tx and/or Rx is illustrated in Figure 2.31. The Tx consists of an RTD ("voltage-controlled") oscillator and an external, or integrated on-chip, antenna mounted on a hemispherical Si lens. THz lenses are often employed between the Tx and Rx antennas to focus and collimate the beam. The data is superimposed over the DC bias through a bias-Tee.

Commercial power amplifiers are not yet available at THz frequencies, therefore, none is employed at the Tx. At the Rx side, an antenna, which may be external or integrated, is employed. The received signal is de-modulated using either square-law-based direct detection, by employing an SBD or an RTD direct detector, or employing a coherent RTD oscillator-based scheme. The low-frequency signal is then amplified by a low-noise amplifier (LNA).

### 2.9.1.2 RTD THz wireless data-links

Table 2.4 summarises some of the most recent wireless communication data-link results reported in the literature involving THz RTDs, either employed as a Tx, Rx, or both. In many cases, an SBD detector is used at the Rx while, in some other cases, an InP UTC-PD is employed at the Tx. In this context, the longest link distances of 50 cm [390], 80 cm [583], and 150 cm [584] feature

Table 2.4: THz RTD wireless communication data-links specifics.

Ref.	Tx	Rx	$f_c$ [GHz]	Modulation	Distance [cm]	Data-rate [Gb/s]	BER
[585]	RTD	SBD	490	ASK	20–30	22	EF
	RTD	SBD	490	ASK	20–30	34	$1.9 \times 10^{-3}$
[436]	RTD	SBD	650	ASK	20–30	25	EF
	RTD	SBD	650	ASK	20–30	44	$5 \times 10^{-4}$
[584]	RTD	SBD	62.5	OOK	30	10	EF
	RTD	SBD	62.5	OOK	150	15	$10^{-5}$
[586]	UTC-PD	RTD	297	OOK	3	17	EF
[565]	UTC-PD	RTD	322	OOK	2	27	EF
	UTC-PD	RTD	322	OOK	2	32	$2.7 \times 10^{-2}$
[573]	UTC-PD	RTD	350	OOK	3	32	EF
	UTC-PD	RTD	350	OOK	3	36	$9 \times 10^{-2}$
[517]	RTD	RTD	286	OOK	10	9	EF
	RTD	RTD	286	OOK	10	12	$4 \times 10^{-3}$
[593]	RTD	RTD	345	OOK	7.5	13	EF
	RTD	RTD	345	OOK	7.5	20	$2.1 \times 10^{-3}$
[287]	RTD	RTD	343	ASK	7	30	EF
	RTD	RTD	343	ASK	7	56	$1.39 \times 10^{-5}$
[587]	RTD	SBD	500–800	ASK	20	$56^{[a]}$	$10^{-4}–10^{-3}$
[588]	UTC-PD	RTD	324	16-QAM	1	60	$2 \times 10^{-3}$
[390]	RTD	SBD	84	ASK	50	15	$4.1 \times 10^{-3}$
[583]	RTD	SBD	278	ASK	80	12	EF
	RTD	SBD	278	ASK	80	22	$10^{-3}$
[541]	RTD	SBD	260	ASK	1	13	-
[589]	UTC-PD	RTD	324–335	OOK	2-3	$48^{[a]}$	EF
[590]	RTD	RTD	354	OOK	7	25	EF
	RTD	RTD	354	OOK	7	30	$2 \times 10^{-3}$

[a]: multi-channel link.

Tx operating below 0.3 THz. For higher carrier frequencies, link distances are way below 30 cm.

As can be noticed, there is a clear correlation between the link distance and the Tx output power, which is in the milliwatt range for the sub-100 GHz Tx, and in the microwatt range for the ones operating at higher frequencies. Data-rate results in the 9–60 Gb/s range have been demonstrated, including a 30 Gb/s error-free (EF) transmission over a 7 cm-long link through

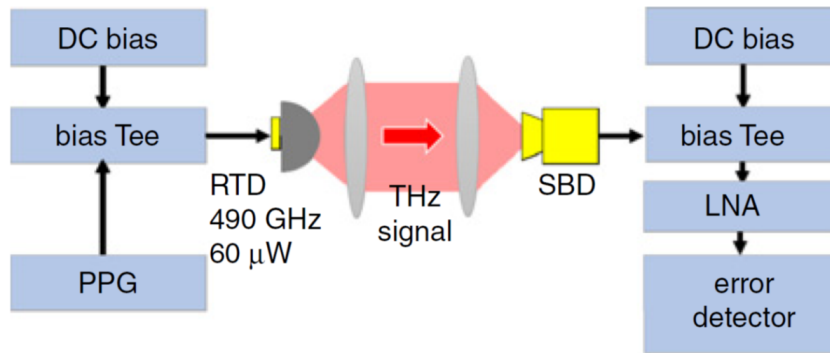


Figure 2.32: Block diagram of the THz wireless data transmission experimental setup employed in [585] (reprinted from [585]).

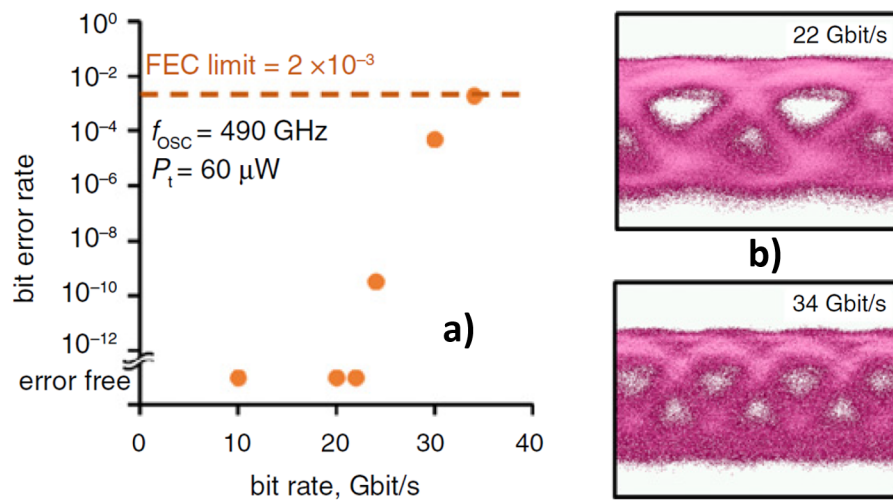


Figure 2.33: Results of the THz wireless communication experiment reported in [585] (adapted and reprinted from [585]). In a), the measured BER as a function of the data-rate, showing EF data transmission up to 22 Gb/s, and data-rates of up to 34 Gb/s with BER  $\sim 1.9 \times 10^{-3}$ ; in b), the corresponding measured eye diagrams.

an all-RTD TRx [287].

Here, some of the wireless transmission experiments are discussed in detail, the first in which a 490 GHz oscillator was used as a Tx [585]. Direct modulation was carried out by superimposing a modulation signal onto the bias voltage through ASK. The experimental setup is shown in Figure 2.32, where a pulse pattern generator (PPG) was used to impress digital data over the carrier. The modulated THz signal was then received through a horn-antenna, demodulated by an SBD direct detector, and amplified through a LNA. The link distance between the Tx and the Rx was set to 20–30 cm. The demodulated signal was then measured through an error detector (ED) and an oscilloscope. The results are shown in Figure 2.33. Clear eye opening and EF data transmission were obtained at a data-rate of 22 Gb/s, while data-rates of up to 34 Gb/s were achieved with bit error rate (BER) around  $1.9 \times 10^{-3}$ .

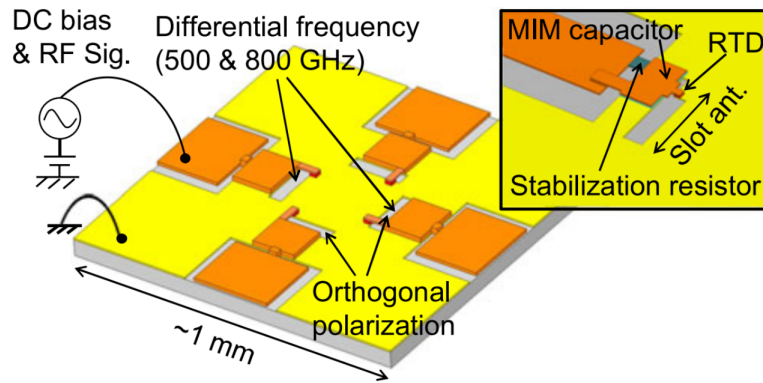


Figure 2.34: Illustration of the RTD THz oscillator circuit layout employed at the Tx side for wireless data transmission through FDM and PDM (reprinted from [587]).

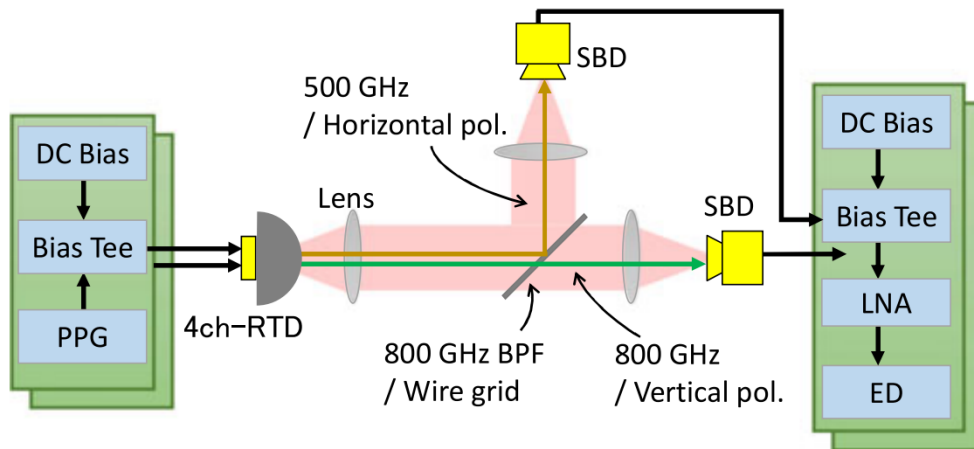


Figure 2.35: Block diagram of the THz wireless communication experimental setup employed to perform data transmission through FDM and PDM (reprinted from [587]).

Recently, multi-channel wireless data transmission employing polarisation and frequency division multiplexing (PDM/FDM) schemes have also been reported [587]. Figure 2.34 illustrates the Tx chip circuit layout. Four slot-antenna RTD oscillators are integrated together: two of them oscillate at 500 GHz, and the other two at 800 GHz for FDM, while the two oscillators, at each of these two frequencies, have polarizations that are orthogonal to each other, realised through the relative orientation of their antennas layouts (perpendicular to each other), for PDM.

The wireless communication setup is depicted in Figure 2.35, where SBD detectors were employed at the Rx front-ends, together with horn-antennas. Data-rates of up to 56 Gbps (28 Gbps per channel) were obtained using FDM in the 500 GHz and 800 GHz channels with BER around  $2.3 \times 10^{-4}$  and  $1.5 \times 10^{-3}$ , respectively, and through PDM at 500 GHz with BER around  $1.5 \times 10^{-3}$  and  $1.4 \times 10^{-4}$  for the vertical and horizontal polarization channels, respectively.

Figure 2.36a shows a THz wireless data transmission experimental setup involving an RTD

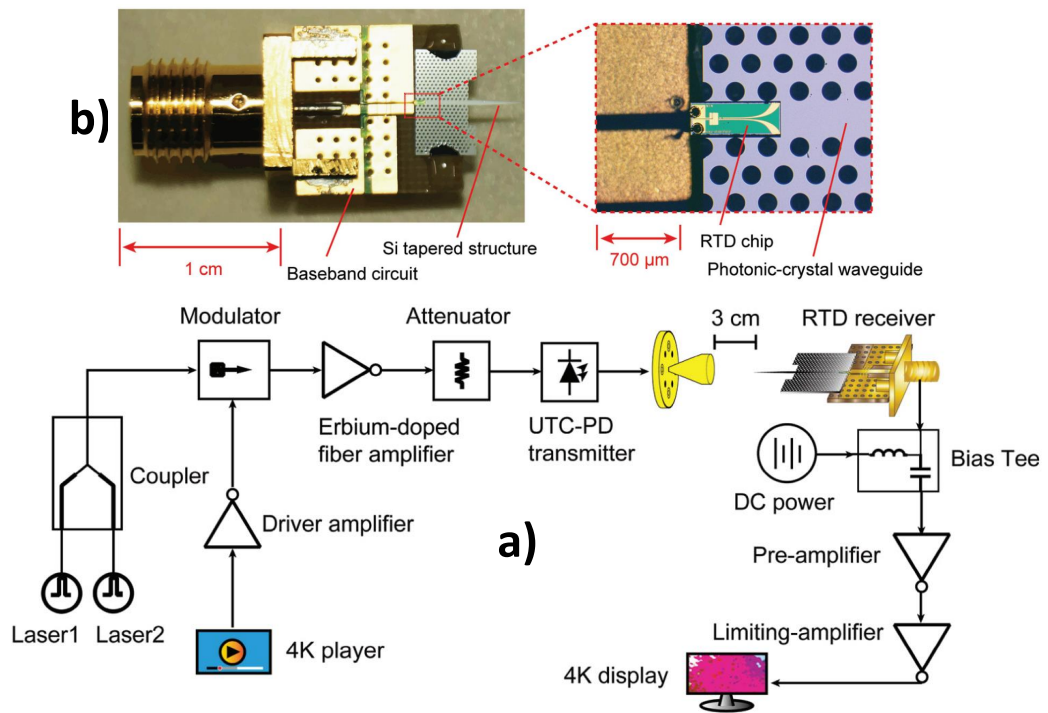


Figure 2.36: In a), the wireless experimental setup used for real-time high-resolution 4K video transmission; in b), a photograph of the direct THz RTD-based Rx front-end module reported in [573], with a zoom-in over the RTD integrated with a Si-based photonic crystal waveguide through a tapered-slot mode coupler (adapted and reprinted from [573]).

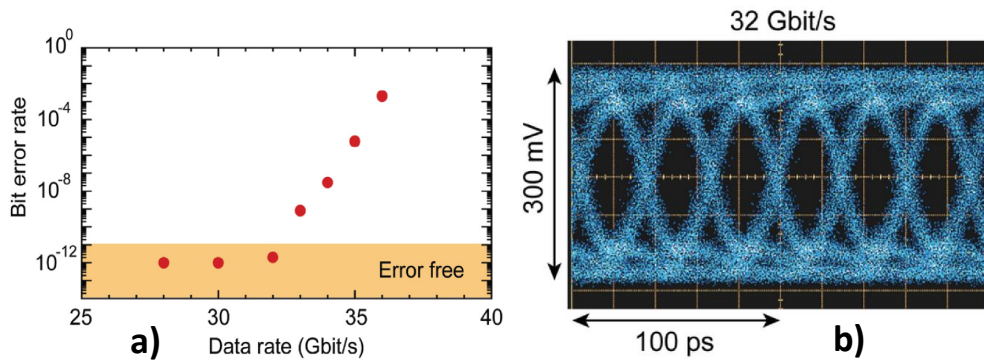


Figure 2.37: Results of the THz wireless communication experiment reported in [573] (adapted and reprinted from [573]). In a), the BER as a function of the data-rate; in b), the eye diagram at 32 Gb/s.

as a direct detector [573]. The Tx is based on an UTC-PD-based photo-mixer, providing  $f_c \sim 350$  GHz, which is modulated through OOK. The detector is integrated with a Si-based photonic crystal waveguide platform [591] and has a measured voltage responsivity of around 4 kV/W. Figure 2.36b shows a photograph of the Rx front-end module, outlining the metal-based tapered-slot mode converter and the photonic crystal waveguide.

Figure 2.37 shows the experimental results, where EF data transmission of up to 32 Gb/s,

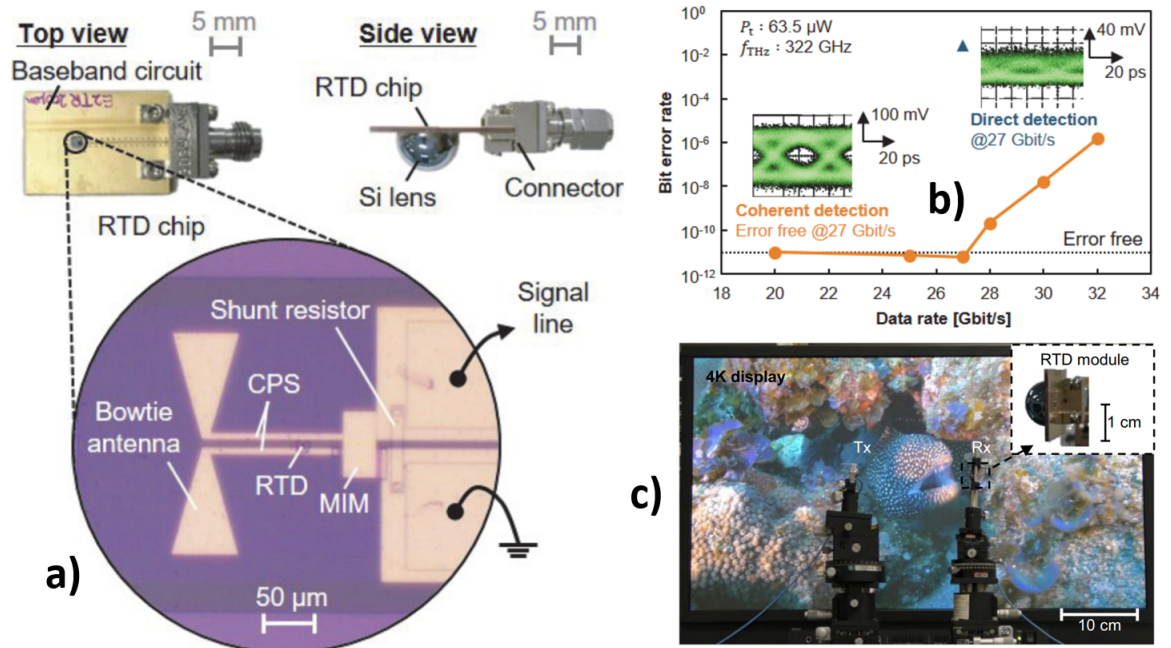


Figure 2.38: In a), photographs of the 300 GHz-band RTD coherent Rx front-end module, together with a photo-micrograph zoom-in over the RTD oscillator chip (reprinted from [565]); in b), measured BER versus data-rate of the wireless data transmission experiment reported in [565] (reprinted from [565]); in c), photograph of the 4K high-definition wireless transmission system reported in [287] (reprinted from [287]).

and data-rates of up to 36 Gb/s with  $\text{BER} \sim 9 \times 10^{-2}$ , were achieved over 3 cm distance. This allowed wireless transmission of a high-resolution 4K video in real-time. Using a similar setup and 16-QAM, record data-rates of up to 60 Gb/s with  $\text{BER} \sim 2 \times 10^{-3}$  over a 10 mm-long wireless link were demonstrated at 324 GHz [588]. In addition, multi-channel EF wireless data transmission through OOK of up to 48 Gb/s, together with real-time transmission of an 8K high-resolution video, was demonstrated in the 300 GHz-band over a distance of around 2–3 cm using a UTC-PD-based Tx and an RTD direct Rx [589].

When a coherent RTD detector is employed, a CPS is used to realise the resonator of the oscillator circuit and to connect the RTD device to a bow-tie antenna, while the Rx chip is mounted onto a Si lens to increase the antenna gain, as shown in Figure 2.38a. Here, the experimental wireless communication setup is similar to the one shown in Figure 2.36b. The link distance was set to 2 cm, while an oscilloscope was used to display the de-modulated signal. EF data transmission through OOK at around 322 GHz of up to 27 Gb/s, and data-rates of up to 32 Gb/s with  $\text{BER} \sim 2.7 \times 10^{-2}$ , were reported [565], with a sensitivity enhancement of around 10 dB with respect to the direct detection counterpart, as revealed in Figure 2.38b.

In the THz wireless data-links reported in [287,517,592,593], an RTD was employed at both the Tx and Rx sides by exploiting both the direct [517,592,593], as well as the coherent [287],

detection scheme. With an all-RTD wireless TRx setup and coherent detection, EF data transmission through ASK of up to 30 Gb/s, and data-rates of up to 56 Gb/s with  $\text{BER} \sim 1.39 \times 10^{-5}$ , were reported in the 300 GHz-band over a link distance of 7 cm [287]. In this context, a sensitivity enhancement of up to 40 dB with respect to the direct detection approach was observed. Moreover, the described data-link was employed to demonstrate real-time data transmission of a high-resolution 4K video, as shown in Figure 2.38c.

On the other hand, using a direct detection [517], EF wireless data transmission through OOK up to 9 Gb/s, and record data-rates of up to 12 Gb/s with  $\text{BER} \sim 4 \times 10^{-3}$ , have been reported in the 300 GHz-band over a distance of 10 cm. In the setup described in [592], data in the optical domain is converted into an electrical signal and used to modulate the RTD. OOK data is modulated using an intensity modulator and, after passing through a 1 km-long fibre, converted to an electrical signal using a photo-diode (PD). The output signal is added to the DC biasing voltage using a bias-Tee, and the resulting signal used to modulate the RTD at the Tx. Using multi-chip code division multiple access (CDMA), EF data rates of up to 13 Gb/s, and of up to 20 Gb/s with  $\text{BER} \sim 2.1 \times 10^{-3}$ , were demonstrated [593].

Although data-rates of several tens of gigabit per second have been achieved employing RTD devices at the Tx and/or Rx side, including single-channel EF data transmission at 30 Gb/s, and record data-rates of up to 56 Gb/s, employing an all-RTD TRx, the link distance is still limited to the centimetre range at carrier frequencies above around 300 GHz, while no wireless communication experiment has been reported above 0.8 THz, which is inherently caused by the low output power of the Tx.

Based on the aforementioned discussion, it would therefore seem that, in the 300 GHz-band and above, RTDs are more promising for practical THz wireless communication applications if compared to conventional transistor electronics for many reasons, including simplicity (a single RTD device can provide RF power in excess of 1 mW compared to transistor-based amplifiers with typically three to four stages), low-cost lithography requirements (micron-sized RTD devices vs. sub-100 nm-long transistor gates), and highly-sensitive RTD detectors (monolithic TRx can be realised). Moreover, the RTD can be epitaxially-integrated with transistors, where the latter can provide basic functionalities, which could lead to the desired versatile THz systems.

## 2.9.2 High-resolution THz imaging and radar systems

In addition to wireless communications, it is worth to mention that RTD technology is promising for other applications, including THz imaging/spectroscopy systems [164, 594] and radars [595, 596]. A compact THz imaging apparatus employing RTDs was proposed in [597]. In

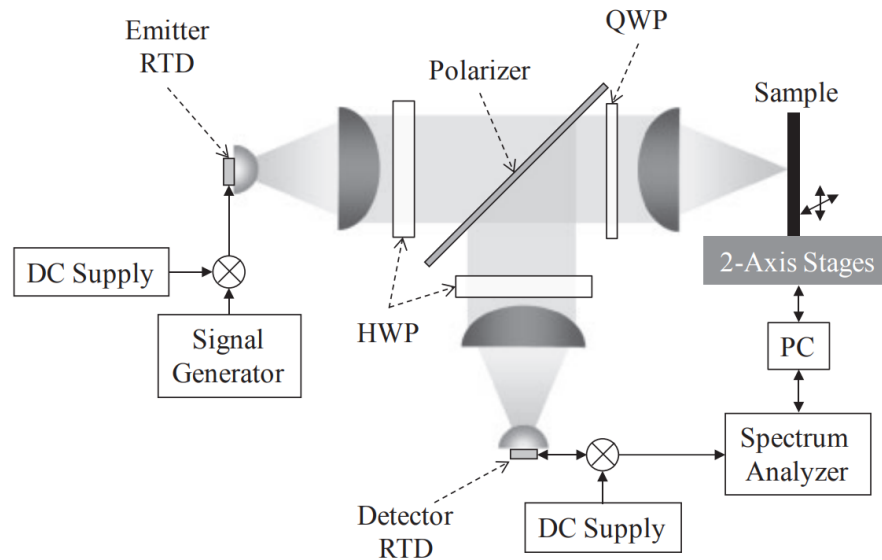


Figure 2.39: Illustration of the RTD THz reflection imaging system setup reported in [597] (reprinted from [597]).

this system, a CW 300 GHz-band RTD oscillator source and an RTD square-law direct detector are employed to acquire images of objects in reflection mode, where the RTDs consist in In-GaAs/AlAs DBQW heterostructures grown on SI InP substrates.

At the source, the RTD is integrated with a tapered slot-antenna and the chip is mounted onto a Si lens. The THz reflection imaging system setup is reported in Figure 2.39. The RTD oscillator radiates a linearly polarized THz field which is directed towards a polariser. In this context, THz collimating lenses and half-wave plates (HWP) are used to collimate the field and to keep the input/output polarisation, while the polariser allows to reduce the insertion loss of the system by acting as a beam splitter (BS). The beam passes through the polariser and it is converted into circularly polarised radiation by means of a quarter wave plate (QWP). Then, the beam impinges on the sample under test (SUT) and the reflected component passes through the QWP a second time, becoming orthogonal linearly polarised. The radiation is then reflected by the BS and focused onto the RTD detector, after which real-time THz imaging visualisation becomes possible on a screen after down-mixing, spectral analysis, and signal post-processing using a personal computer (PC).

An example of imaged SUT is shown in Figure 2.40, which consists in a plastic box containing metallic gadgets. As it is possible to see, THz imaging allowed to reveal the hidden metallic content inside of the closed plastic box. A spatial resolution of up to around 1 mm was achieved, which was limited by the diffraction limit since close to the emission wavelength of the RTD oscillator. However, significant improvements down to around  $3 \mu\text{m}$  were possible thanks to a Michelson-based interferometric imaging setup.

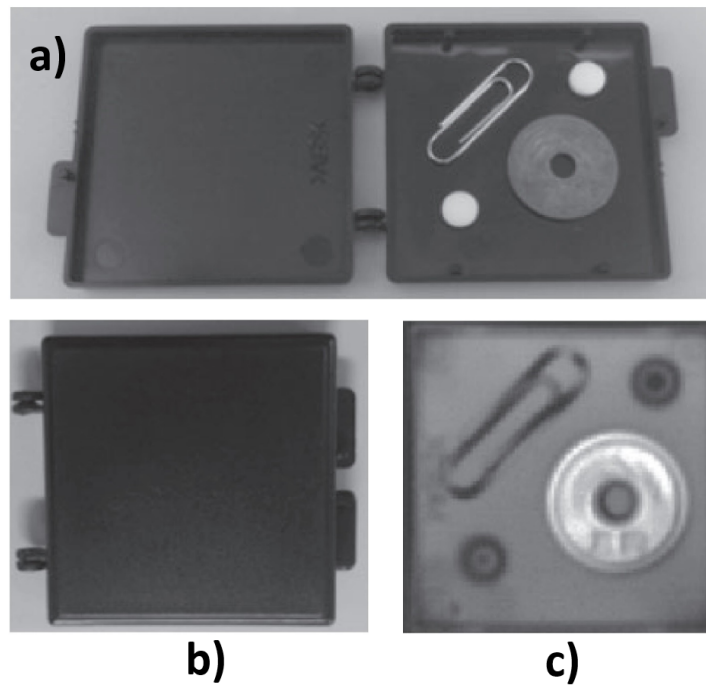


Figure 2.40: Images of the characterised SUT (adapted and reprinted from [597]). In a), photograph of the SUT; in b), photograph of the closed box; in c), THz image of the closed box, revealing the hidden metallic content.

An amplitude modulated CW THz radar [598] based on an InP RTD Tx was proposed in [599]. The working principle relies on the AM of a carrier signal by means of a sinusoidal wave and, after propagation, on the detection, demodulation, and comparison of the signal with the modulation one (taken as a reference). This approach fits well with RTDs since the oscillator output signal can be easily amplitude modulated by superimposing a modulation signal onto the DC bias.

In this system, an RTD oscillator is employed to generate the THz carrier wave, which is then sensed by an SBD direct detector after propagation. The radar functionality is realised by measuring the phase difference between the demodulated signal and the reference one in relationship with the time-of-flight (TOF) delay, and by correlating it with the propagation distance, retrieving the axial position of the target. The measurement is based on a two-step procedure, which allows to remove the " $2\pi$  ambiguity" arising from the periodic nature of the detected signal by repeating the phase measurement at a second modulation frequency.

In early development stages [600], the phase difference was determined by using a time-based measurement through the employment of an oscilloscope, which limited the distance resolution to around 0.29 mm. To reduce the estimation error, a THz lock-in phase experimental measurement setup was developed in [601], and it is shown in Figure 2.41. In this context, the 522 GHz radiation emitted by the RTD oscillator is modulated at frequencies of 5 GHz and 6

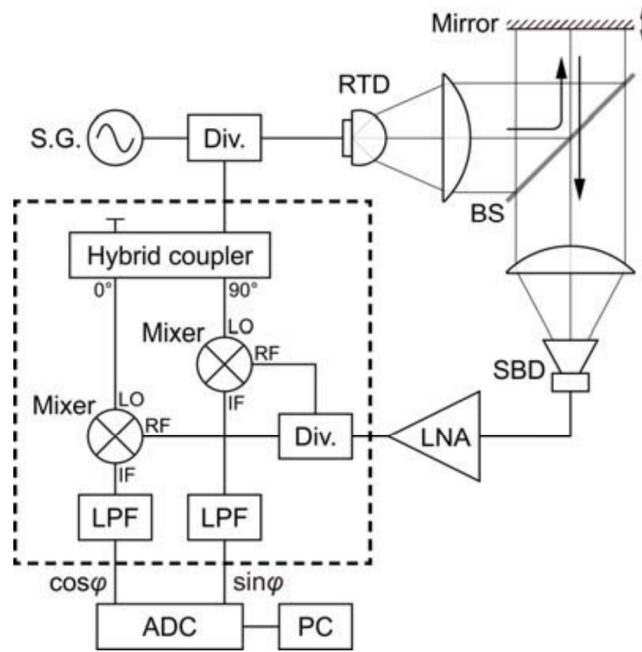


Figure 2.41: Block diagram of the AM CW THz radar experimental setup employing an RTD Tx and based on the lock-in phase measurement technique reported in [599] (reprinted from [599]).

GHz provided by a signal generator (SG), and it propagates towards the static target (consisting in a movable mirror) through a BS, where is partially reflected and directed towards an SBD direct detector. The signal is then demodulated and its phase measured and compared with the modulation one by means of the described two-step technique.

To carry out the lock-in phase measurement, a hybrid coupler produces two  $\pi/2$  shifted copies of the modulation signal, which are used as LO signals for two mixers that have the detected signal as input. The intermediate frequency (IF) outputs of the two mixers are then processed by a low-pass filter (LPF) and the resulting voltages, proportional to the cosine and the sine of the detected signal phase, are then calculated using a four-quadrant arctangent function after being processed by an analog-to-digital converter (ADC). Figure 2.42 shows the measurement error versus the target position, where a standard deviation of around  $63 \mu\text{m}$  was achieved. Recently, full-3D THz imaging has been successfully demonstrated by combining 2D scanning with the described AM CW radar technique [602].

A frequency modulated (FM) CW radar system [603] has also been proposed by the same research group [604]. In this technique, a source is amplitude-modulated with a signal whose frequency periodically ramps between two values. After propagation, the signal becomes delayed with respect to the source, resulting in frequency difference which carries information on the target distance. Differently from the AM technique, a FM CW radar has the advantage of being capable of measuring several distances simultaneously.

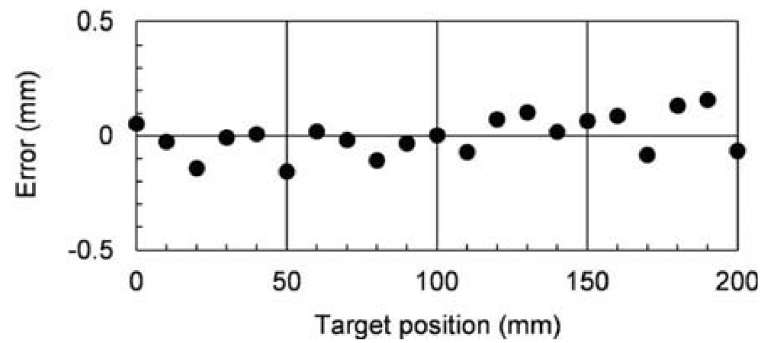


Figure 2.42: Measurement error as a function of the target position employing the lock-in phase AM CW THz radar reported in [599] (reprinted from [599]).

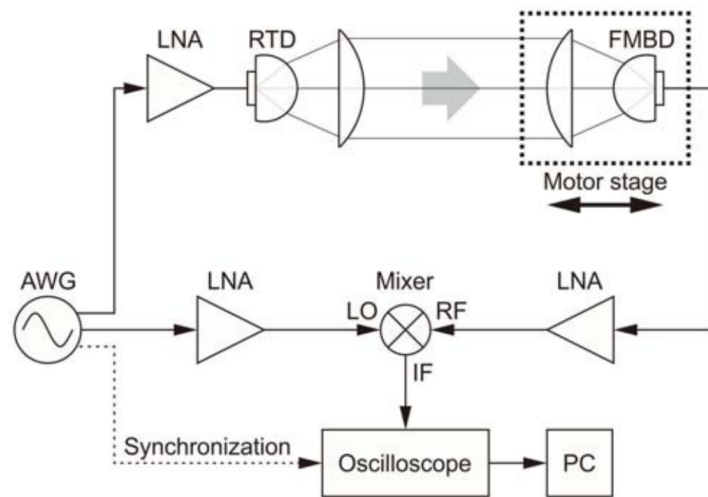


Figure 2.43: Block diagram of the sub-carrier FM CW THz radar experimental setup employing an RTD Tx reported in [604] (reprinted from [604]).

The experimental setup consisting in the proposed FM CW THz radar system is shown in Figure 2.43, where an RTD oscillator is employed as 511 GHz source, while a Fermi-level managed barrier diode (FMBD) [605] as a direct detector. An arbitrary waveform generator (AWG) is employed to provide a sinusoidal signal with frequency ranging between 3.4 GHz and 6.4 GHz, which is superimposed to a sub-carrier of the THz source [606]. The modulated THz beam is then focused, after propagation, onto the FMBD, which is movable thanks to a motor stage. Here, the detector position can be tuned by means of a motor stage.

To retrieve information on the frequency shift caused by the propagation delay, the detected output from the FMBD (used as RF input) is sent to a mixer for down-conversion, where the AWG modulation signal is used as LO, and the output analysed through a discrete Fourier transform approach to compute the frequency shift. Figure 2.44 shows the measurement error versus the target position, where a standard deviation of around 0.73 mm was achieved. Recently, this

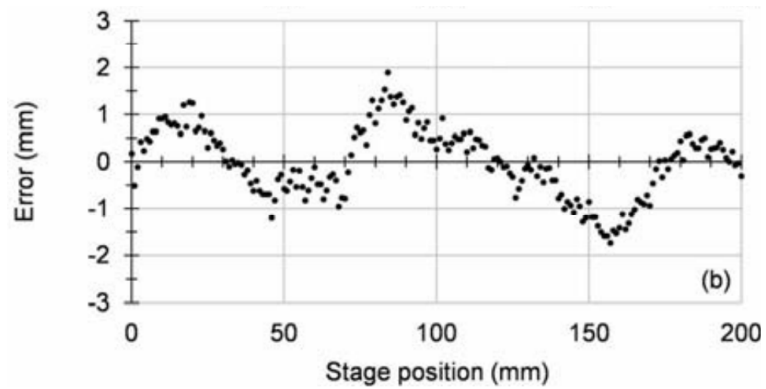


Figure 2.44: Measurement error as a function of the target position employing the sub-carrier FM CW THz radar reported in [604] (reprinted from [604]).

has been reduced down to around 0.42 mm, while a real-time measurement error of around 0.75 mm was reported for a moving ("dynamic") target [607].

# Chapter 3

## Resonant tunnelling diode microfabrication technology

This Chapter presents the microfabrication conducted in this work. In particular, it describes the fabrication process used to realise the designed micron-sized indium phosphide double-barrier resonant tunnelling diodes, which is based on hybrid electron-beam/optical lithography. After providing with the details on the employed mask layout, a brief explanation of the different adopted processes and associated fabrication tools is provided, including lithography, metal evaporation and lift-off, and wet/dry etching, as well as metrology, after which an in-depth description of the device full fabrication flow is presented. The fabrication of the test structures used to extract the devices Ohmic contacts resistance is also described. This work was carried out in the James Watt Nanofabrication Centre at the University of Glasgow, which consists in a 1400 m<sup>2</sup> class 1000 (ISO 6) clean-room facility.

### 3.1 Mask design

The lithographic mask employed in the fabrication of the resonant tunnelling diodes (RTD) was designed using Tanner L-Edit IC from Siemens EDA [608], and is shown in Figure 3.1a. It comprises of 32 devices per square top mesa area  $A$ , ranging between  $3 \times 3 \mu\text{m}^2$  and  $10 \times 10 \mu\text{m}^2$  with  $1 \mu\text{m}$  side increment, together with  $A = 15 \times 15 \mu\text{m}^2$ ,  $20 \times 20 \mu\text{m}^2$ , and  $30 \times 30 \mu\text{m}^2$ , and sub-divided in eight groups distributed across the whole mask area, for a total of 384 diodes. In each group, the devices are arranged according to vertical and horizontal  $30 \mu\text{m}$ -wide pitches.

An example of designed  $5 \times 5 \mu\text{m}^2$ -large device is shown in Figure 3.1b, together with a zoom-in over the associated RTD region in Figure 3.1c, outlining the different lithographic layers, whose fabrication will be described in Section 3.7. The bond-pads are designed in a coplanar waveguide (CPW) geometry with characteristic impedance  $Z_0 = 50 \Omega$  for scattering

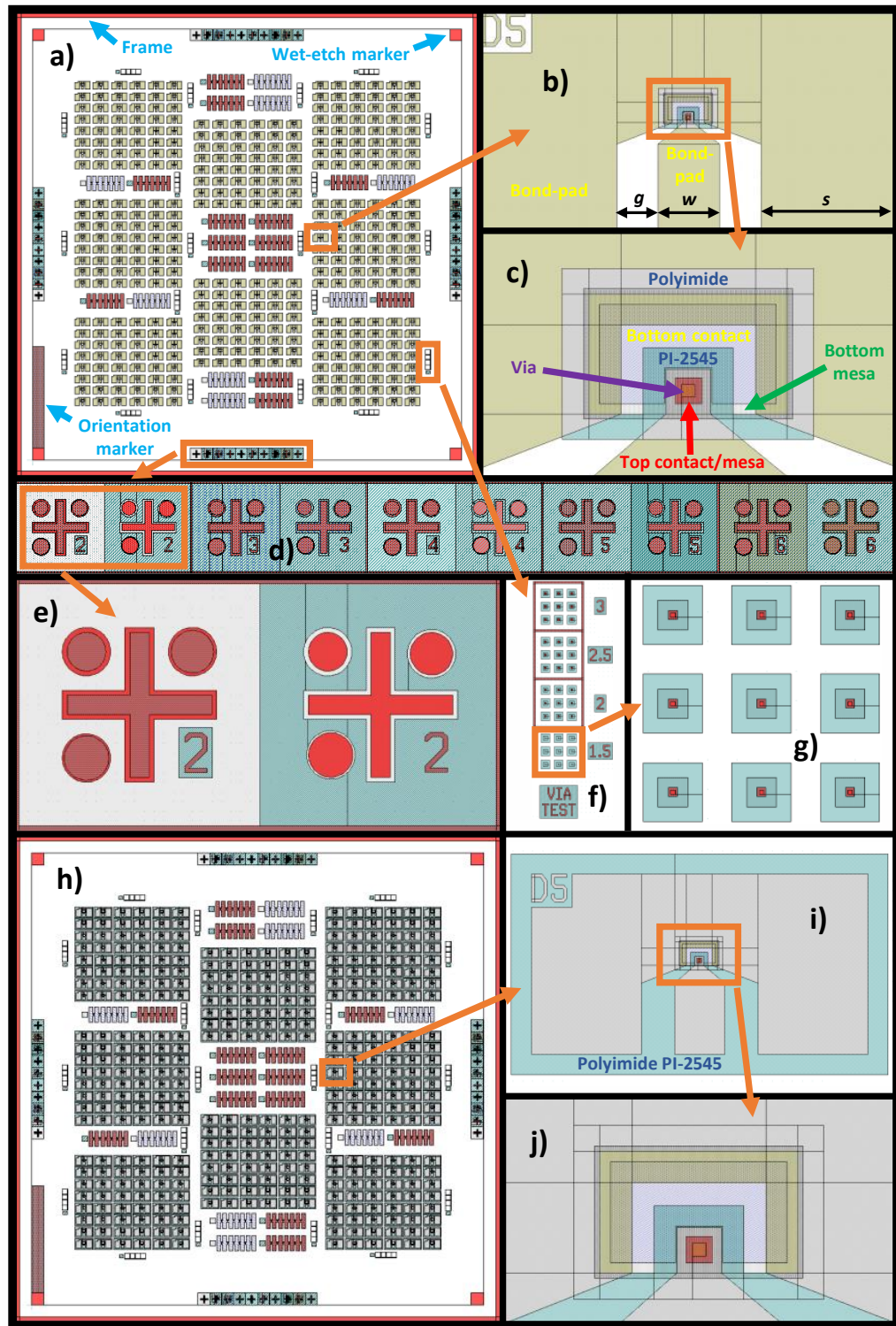


Figure 3.1: Designed RTD lithographic mask. In a), mask layout; in b) and c), zooms-in over a  $5 \times 5 \mu\text{m}^2$ -large device and associated RTD region, outlining the different lithographic windows, including top/bottom contact/mesa, passivation, and bond-pads; in d), designed optical alignment marks; in e), zoom-in over the two markers-set associated to the second lithographic step (top mesa); in f), check structure for via opening; in g), zoom-in over the via structures for the  $3 \times 3 \mu\text{m}^2$  devices; in h), mask layout for conductive substrate processing; in i) and j), zooms-in over a  $5 \times 5 \mu\text{m}^2$ -large device and associated RTD region.

(S)-parameters measurement, as will be discussed in Chapter 6. In particular, the signal pad width  $w$  is set to  $50 \mu\text{m}$ , and the gaps between signal and ground pads  $g$  to  $33.5 \mu\text{m}$ , while the ground pads width  $s$  to  $110 \mu\text{m}$ , with  $s > 5w/2$  to ensure minimal radiation losses and correct guiding of the coplanar mode upon excitation [609]. The pads are then tapered towards the RTD region by keeping the same  $Z_0$ .

At the same time, 22 transmission line measurement (TLM) test structures for the extraction of the devices contacts resistance are included, which will be discussed in detail in Section 3.8. The mask incorporates optical alignment markers at the four sides of each associated lithographic window (Figures 3.1d and e), for a total of six lithographic steps: the first, which consists in patterning the devices top contact, top TLMs, and the optical alignment markers (as well as further markers for chemical wet etching and sample orientation), is carried out through electron-beam (E-beam) lithography (EBL) for accurate shaping of the smaller devices ( $3 \times 3 - 5 \times 5 \mu\text{m}^2$ ) and of the top TLMs  $1 \mu\text{m}$ -wide gap, while the remaining five steps are processed through photo-lithography. Moreover, test structures for via opening of the small RTDs (Figure 3.1f and g) are also included, for a total framed mask area of around  $1 \text{ cm}^2$ .

Some of the epitaxial structures processed in this work were grown on conductive  $n$ -type indium phosphide (InP) substrates rather than standard semi-insulating (SI), which makes the mask in Figure 3.1a unsuitable. Indeed, the bond-pads lie on the substrate, which would short circuit the devices upon DC probing. To address this issue, a second mask layout was designed, which is shown in Figures 3.1h. This is a copy of the aforementioned one apart from the passivation layer, which is extended all over the device region, as shown in Figure 3.1i and j. In this case, the bond-pads sit on the insulating layer, allowing for a correct DC biasing of the RTDs. Note, however, that the processed TLMs cannot be measured in this case since there is no way to provide electrical isolation within the single structure and between the different structures.

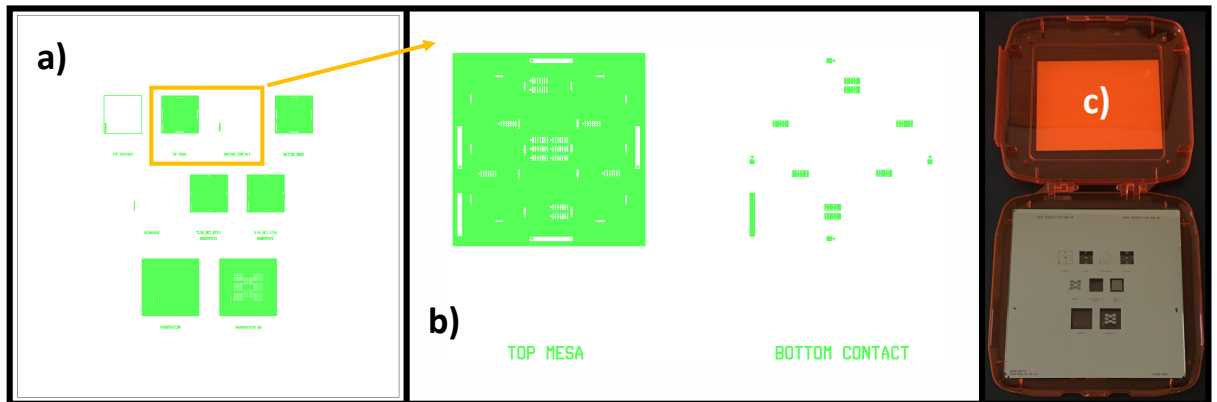


Figure 3.2: In a), designed photo-mask layout; in b), zoom-in over the first two photo-windows (top mesa and bottom contact); in c),  $5'' \times 5''$  engraved physical photo-mask.

All the lithographic windows (eleven in total: two E-beam and nine optical) were designed for positive resists, as discussed in Section 3.2. Figure 3.2a shows the designed photo-mask, comprising of the nine lithographic windows, while Figure 3.2b shows a zoom-in over the associated top mesa and bottom contact steps. Among the optical windows, an additional window (top contact) is included, which is identical to the one designed for EBL and was used in the early fabrication stages for comparison. Moreover, two other windows are also added for top TLMs processing (one of which for mere testing), as will be described in Section 3.8. The photo-windows have been engraved on a 5" × 5" physical mask by Compugraphics Photomasks, which consists in a quartz-based slab with a chromium (Cr)-based processed film on one side carrying the designed features, as shown in Figure 3.2c.

## 3.2 Lithography

The realisation of semiconductor-based electronic devices and associated monolithic integrated circuits (IC) relies on the progressive transfer of pre-designed features onto a sample/wafer via a coated thin layer named resist, in what is called lithographic patterning [105]. In this context, a resist is a substance which is sensitive to either photons (light) or electrons thanks to its chemical structure and composition, and it usually consists of a sensitiser (containing the photo/electron-active compound), a polymeric base resin (which gives mechanical/chemical strength), and an organic solvent (which allows spin-coating) [105]. Generally-speaking, each fabrication step, whether it consists in deposition or etching, requires a lithographic process.

Depending on their polarity, resists can be classified in two main categories: 1) positive; and 2) negative. Regarding optical resists, positive photo-resists reinforce their solubility towards developer agents if exposed to ultra-violet (UV) radiation thanks to photo-decomposition of the associated polymeric chains, while negative photo-resists tend to become less soluble according to photo-polymerisation/photo-cross-linking [105]. Similar considerations apply to E-beam resists. Due to the higher resolution and thermal stability that usually distinguish positive compared to negative resists, positive optical and E-beam resists were used in this work.

In particular, the MICROPOSIT S1800 G2 photo-resist series from Rohm & Haas Electronic Materials [610], including both S1805 and S1818, as well as LOR-10A lift-off resist (LOR) from MicroChem [611], were chosen. At the same time, polymethyl methacrylate (PMMA) no. 8 and 10 E-beam resists from Allresist [612] were adopted for the EBL steps. Further details on the employed E-beam resists are reported in Appendix A. All these resists are available in the James Watt Nanofabrication Centre (JWNC).

At each fabrication step, a thin layer or multiple layers of resist is(are) coated on the wafer

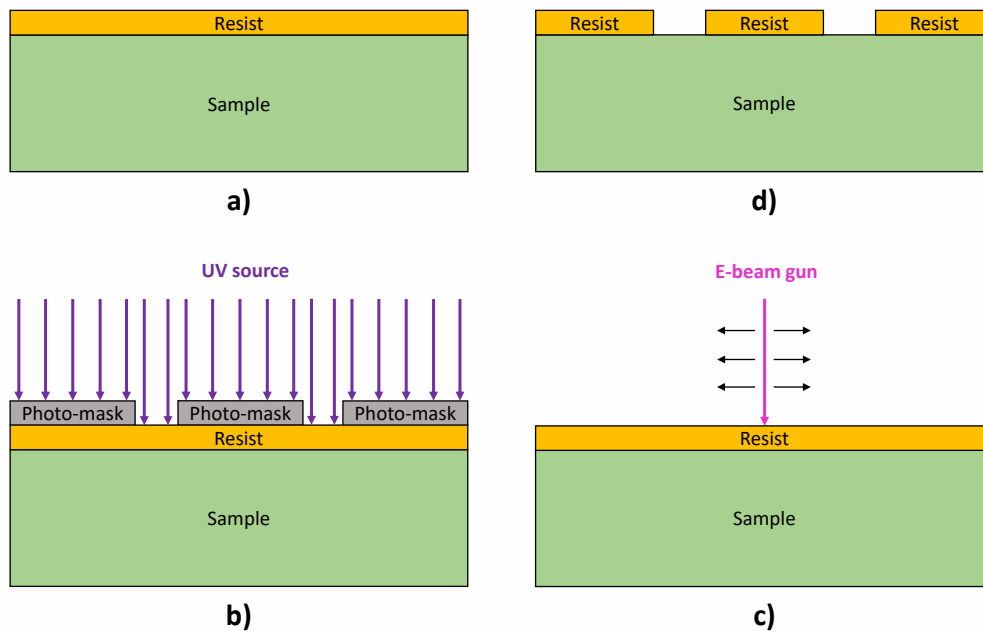


Figure 3.3: Lithographic process flow: a) resist spin-coating; b) sample exposure through photolithography; c) sample exposure through EBL; d) development and plasma ashing.

sample through a spin cycle, as depicted in Figure 3.3a, which can be either photo-resist(s) or E-beam resist(s) depending of the process requirements. Figure 3.4a shows an example of laminar flow (LAF) cabinet intended for resist spin-coating in the JWNC, which is equipped with a chemical fume hood and can process small samples up to full-size wafers. The sample is placed on top of a size-compatible chuck and mounted in the spinner, where a vacuum system firmly holds the sample to the chuck surface. Then, the resist is gently poured onto the sample surface by means of a filtered syringe and spun thanks to a controller, which allows to set the spin cycle recipe, including ramping, speed, and spinning time of the single or different spinning steps.

This determines the thickness of the coated film depending on its viscosity according to the associated spin curve, and it affects its lithographic resolution, so both the type of resist, as well as its spin recipe, have to be carefully selected according to the specific fabrication step. In this context, the amount of poured resist, its location on the sample surface, as well as the cleanness of the sample back side, play an important role for a successful lithographic patterning, and this is achieved based on the level of experience processing with the employed chucks, spinners, and resists.

Subsequently, the sample is soft-baked on a hot-plate, as shown in Figure 3.4b. This allows to improve the mechanical strength of the film by removing the solvent excess, which is required for a correct lithographic exposure. The temperature is set thanks to a controller, and it depends upon the spun resist. The entire process is repeated according to the number of required resist layers, which can be multiple for certain processes, such as in lift-off.

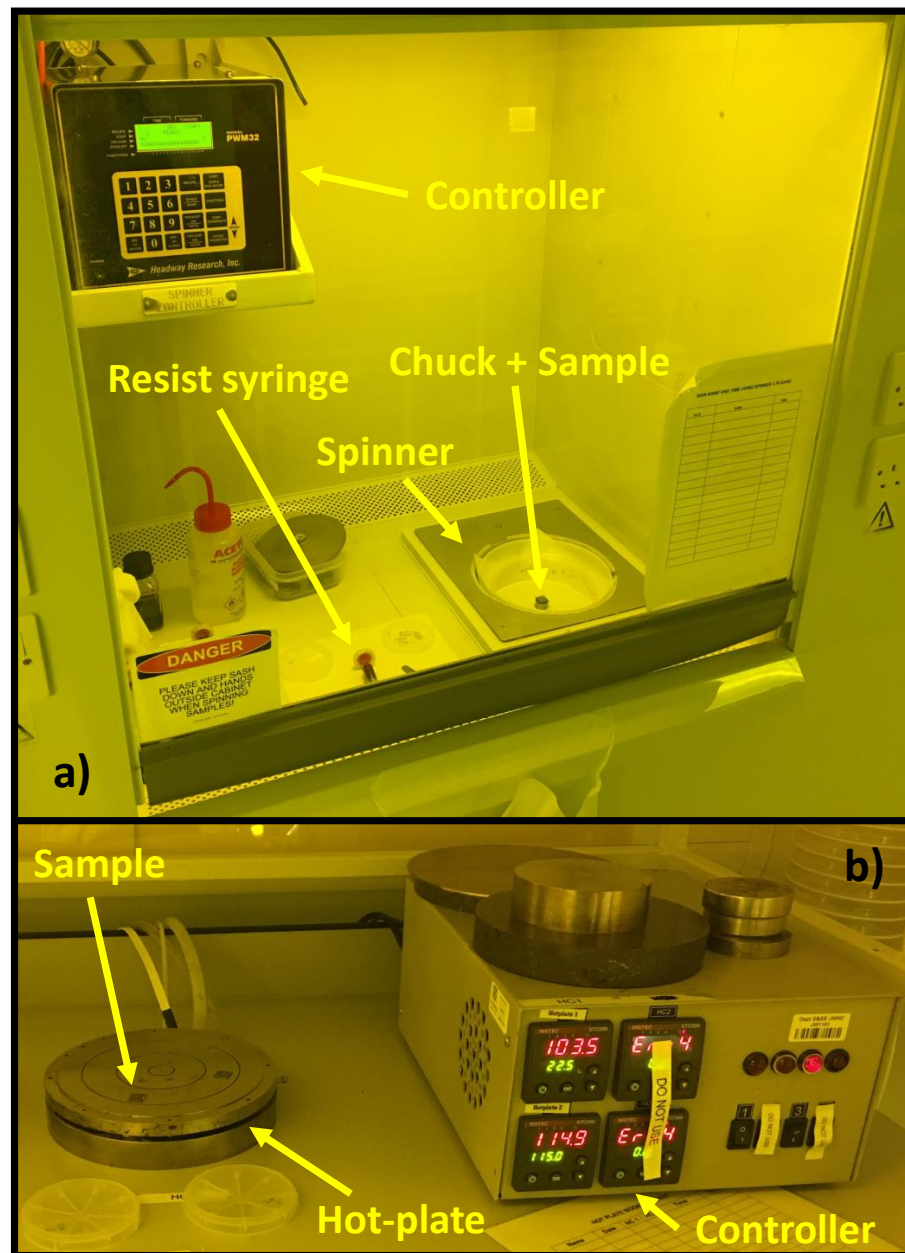


Figure 3.4: In a), LAF cabinet for photo-resist spin-coating (E-beam resist ones are analogous); in b), hot-plate for sample soft-baking.

According to the required resolution, standard optical lithography or highly-resolved EBL are typically employed depending on the dimension of the features intended to be patterned [105]. In the present work, both techniques were employed. In photo-lithography, the mask layout transfer is achieved by exposing the pre-spun sample by means of an UV light source via the photo-mask, as shown in Figure 3.3b. In this work, the MA6 manual photo-mask aligner from SÜSS MicroTec [613] in the JWNC was used in hard contact mode, which is shown in Figure 3.5. The tool can process small-size samples and up to 6" wafers in diameter. The incorporated mercury (Hg)-xenon (Xe)-based vapour lamp is capable of generating UV radiation

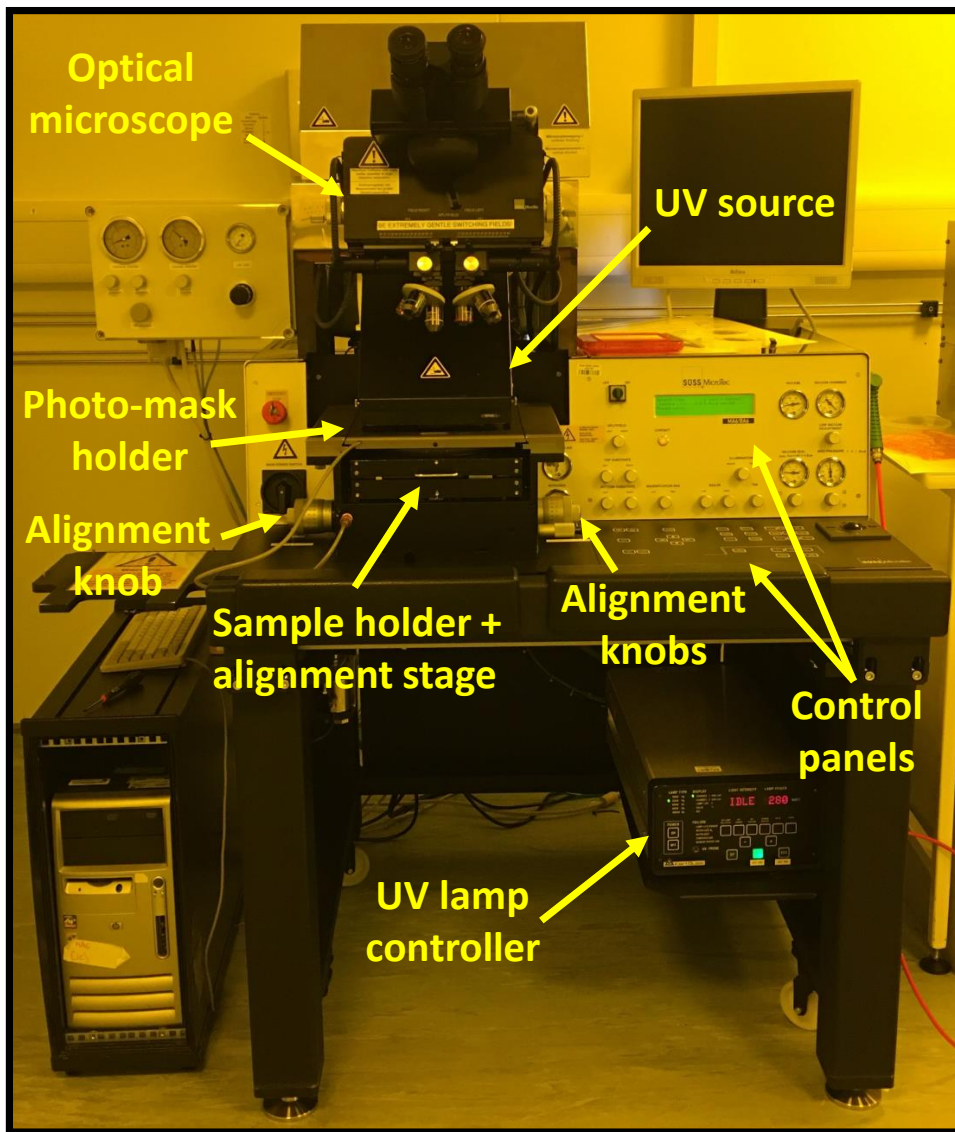


Figure 3.5: MA6 manual photo-mask aligner.

of around  $0.4 \mu\text{m}$  in wavelength, while the system allows alignment down to around  $0.5 \mu\text{m}$ , which meet most of the requirements dictated by the microfabrication of the RTD devices and TLM structures reported in this work. Generally-speaking, the resolution achieved during the lithographic process depends on the employed exposure tool and associated settings, as well as on the intrinsic properties of the coated resist film.

In the common operating procedure, the photo-mask is mounted on a suitable mask holder thanks to a vacuum system according to the specific optical window of interest. After defining the tool settings depending on the resist features, including exposure time (dose) and alignment distance, the sample is loaded under the photo-mask and put in contact with it, as well as firmly secured to the vacuum holder. The sample is then aligned to the optical window by means of an optical microscope and thanks to mechanical knobs, after which is eventually exposed. In this

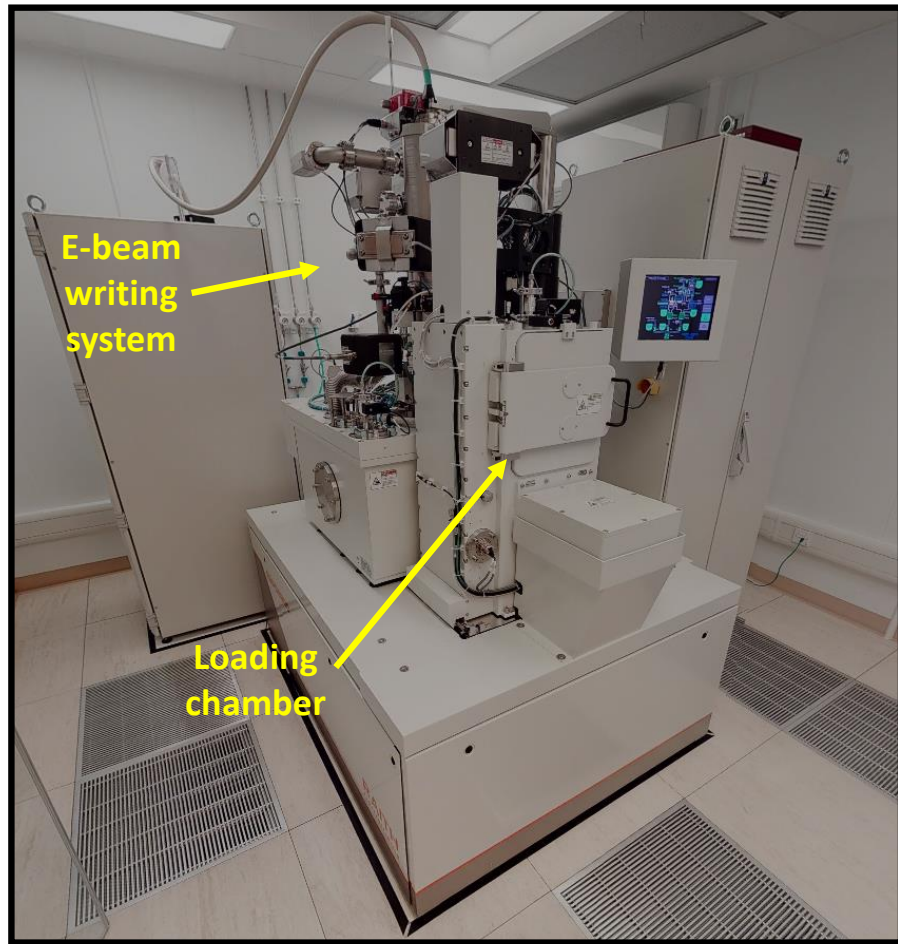


Figure 3.6: EBPG 5200 E-beam lithographic tool.

context, the features patterning is achieved thanks to the high-transmittance/reflectance of the quartz/Cr-based regions on the employed photo-mask.

If deep sub- $\mu\text{m}$  resolution is needed, EBL allows to pattern features below 20 nm in dimension [614,615]. The working principle of high-resolution EBL is based on the progressive scanning of the coated sample via a highly-accelerated nanometric E-beam under strict vacuum conditions, as shown in Figure 3.3c. In this context, an electron gun (E-gun) generates the electron flux typically by means of a high-current tungsten (W)-based filament thanks to either thermionic or field-effect emission. The superb achievable resolution compared to standard UV light exposer relies on the low electron wavelength at large acceleration voltages [616]. Although nanometric patterning was not required in this work, EBL was employed to carry out some critical fabrication steps, as discussed in later in this Chapter.

To do that, the EBPG 5200 E-beam lithographic tool from Raith [617] in the JWNC was used, which is shown in Figure 3.6. In this context, loading and exposure of the sample is not done by users themselves but, on the contrary, carried out by clean-room staff. The E-beam job

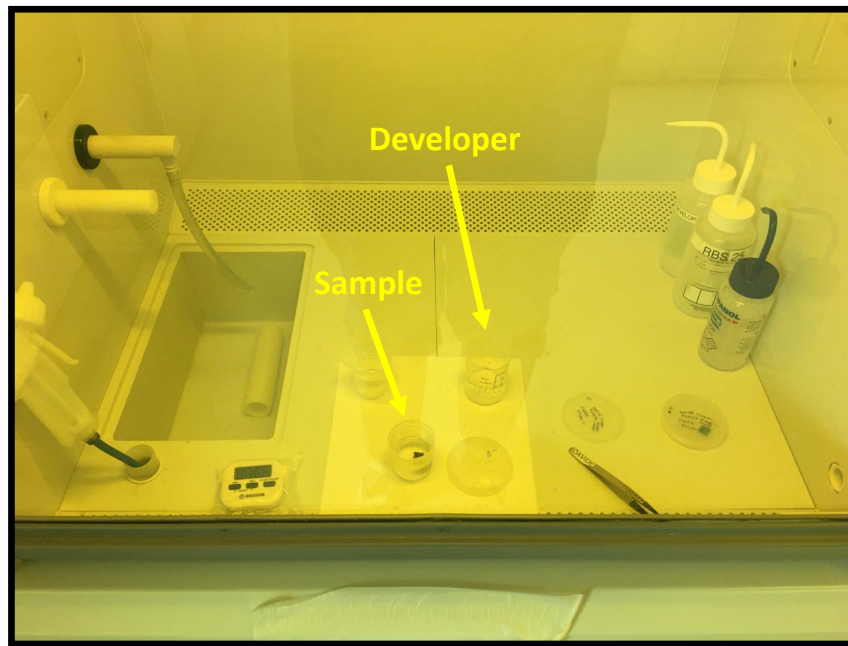


Figure 3.7: LAF cabinet for S1800 series photo-resists development (those for LOR-10A and PMMA are similar).

featuring the desired lithographic layout and exposure settings (e.g., dose, resolution, beam size, proximity correction, etc.) is created by the user through BEAMER from GenISys [618] and CJOB from Raith [619], and sent to the operator via server, who can then process the pre-coated sample. In this context, the minimum feature size ranges between 10 nm and 20 nm.

After lithography, the sample is developed [620] and the exposed resist regions removed, as shown in Figure 3.3d. An example of fume hood-equipped LAF cabinet devoted to samples development in the JWNC is shown in Figure 3.7. In this context, the developer solution, as well as the processing time, are chosen according to the exposed resist. Ultimately, low-temperature plasma ashing [620] is performed to remove any resist residuals which have not been dissolved during the development stage, making the sample ready for either metal deposition or wet etching. In particular, an oxygen ( $O_2$ ) plasma is used to turn the organic residues to ash in a reaction chamber, which are then pumped away. Figure 3.8 shows the used PlasmaFab 505 barrel asher in the JWNC. In this context, the generator power sets the etch-rate which, together with the processing time, must be suitable for the intended fabrication step.

### 3.3 Metal evaporation and lift-off

Metallisation is a key step in the fabrication of electronic devices and ICs, and it is typically carried out employing physical vapour deposition (PVD) [105], such as evaporation, sputtering, or electroplating. In this work, metal deposition was carried out through evaporation, in particular,

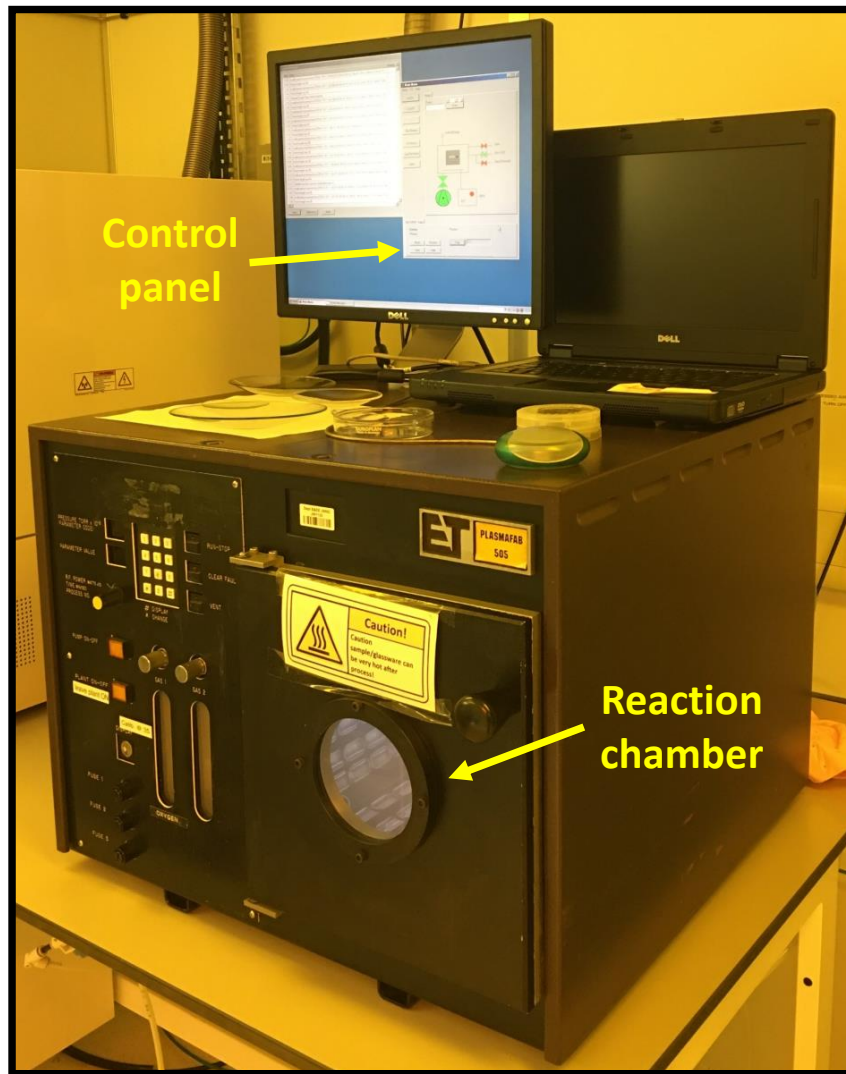


Figure 3.8: PlasmaFab 505 barrel asher.

electron-beam physical vapour deposition (EBPVD) [105], which was used in the realisation of the RTD devices Ohmic contacts and bond-pads, as well as for the TLMs metal structure. This process consists in bombarding a selected metal target thanks to a highly-accelerated E-beam under high-vacuum conditions.

Here, the beam is generated by means of an E-gun, similarly as in EBL. Electrons are then accelerated, directed, and focused towards a crucible target containing the metal intended to be evaporated. Upon striking, the kinetic energy of the beam electrons is high enough that the released thermal energy is sufficient to sublimate a localised volume of the target material. If the required evaporation/deposition chamber vacuum and temperature are sufficiently high to keep the vapour phase, the target desorbed atoms diffuse and then precipitate into solid form onto the sample surface. Since each metal has a different sublimation point, the E-beam current and acceleration voltage have to be set accordingly.

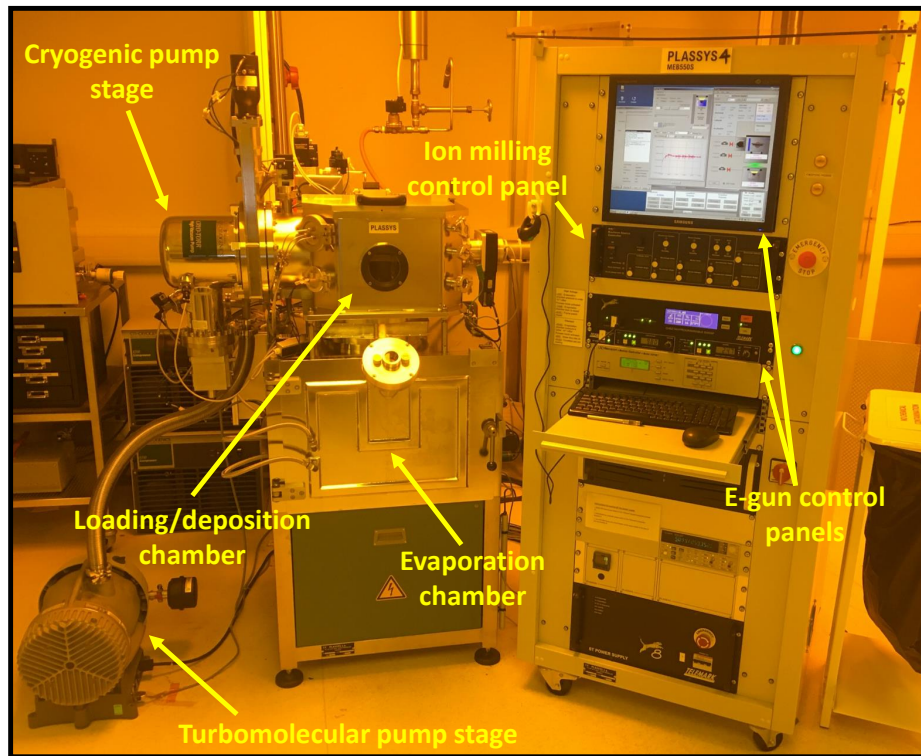


Figure 3.9: MEB550S E-beam evaporator no. IV.

Figure 3.9 shows the MEB550S E-beam evaporator no. IV from Plassys [621] in the JWNC, which was used for the metallisation steps. The system features two pumping stages: the first reaches around  $9 \times 10^{-2}$  mbar thanks to a turbomolecular pump, while the second allows to go down to  $1 \times 10^{-6}$  mbar by employing a cryogenic pump. Moreover, control panels allow to set the required E-gun acceleration voltage and beam current, and, more generally, to create/select the overall process recipe for the deposition of the intended metal film/stack. In this work, titanium (Ti), palladium (Pd), gold (Au), and molybdenum (Mo) were deposited using this tool.

At the same time, the system is equipped with an argon (Ar) ions-based gun for ion milling. In this context, a plasma-activated ion-beam made of heavy  $\text{Ar}^+$  ions is used to sputter-off the oxide thin layer at the sample surface by dislodging the associated atoms before metal deposition [622]. A control panel allows to set the acceleration voltage and etch time according to the process requirements. This technique is similar as to focused-ion beam (FIB) [623] and is analogous to a dry-etch process. This in-situ cleaning step is crucial in the fabrication of low-contact resistance Ohmic contacts in high-frequency electron devices, as will be explained in Sections 3.7 and 3.8, and further in the next Chapters. In this work, the aforementioned process was used to fabricate the RTDs contacts, as well as in the realisation of the TLM structures used to estimate their parasitic resistance.

The correct deposition of metal thin-layers through EBPVD requires a lift-off process [620].

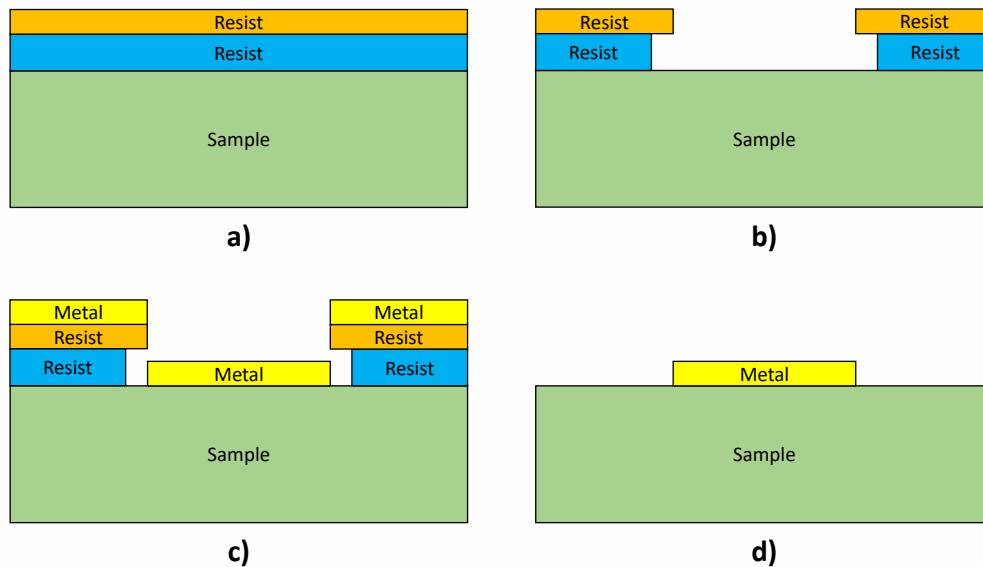


Figure 3.10: Dual lift-off process flow associated to metal EBPVD: a) sample spin-coating; b) exposure and development; c) metal evaporation; d) lift-off.

Figure 3.10 illustrates the dual lift-off process carried out in this work. First, a resist bi-layer is spun onto the sample surface and soft-baked (Figure 3.10a). Here, the first layer is used to create an under-cut profile, while the second one provides with the required lithographic resolution. The sample is then patterned through either photo-lithography or EBL, and subsequently developed. Figure 3.10b shows the sample after development. As may be seen, a pronounced under-cut profile is obtained, which is possible thanks to the different rate of solubility of the two resist layers towards the employed developer agents.

The sample is then subjected to metal deposition over its entire area, as shown in Figure 3.10c. In this context, metal coverage of the resist lateral side-walls is prevented thanks to the line-of-sight character of the evaporation process. As a final step, the sample is treated with a resist stripper solution and left in a hot water bath for the required time. This lets the protecting resist regions to dissolve, "lifting-off" the unwanted metal areas and leaving the intended metal pattern, as shown in Figure 3.10d. Clearly, the resist has to be thick enough to be correctly and easily dissolved by the stripper, so it is typically set to be at least three times thicker compared to the metal intended to be deposited. This, together with the created under-cut profile, guarantee a successful lift-off process.

### 3.4 Wet etching

The removal of semiconductor material from selected regions is carried out through etching [105], and this can be either wet or dry depending on the nature of the process. In this work, wet etching was employed for most of the required etching steps, including the RTDs and TLMs

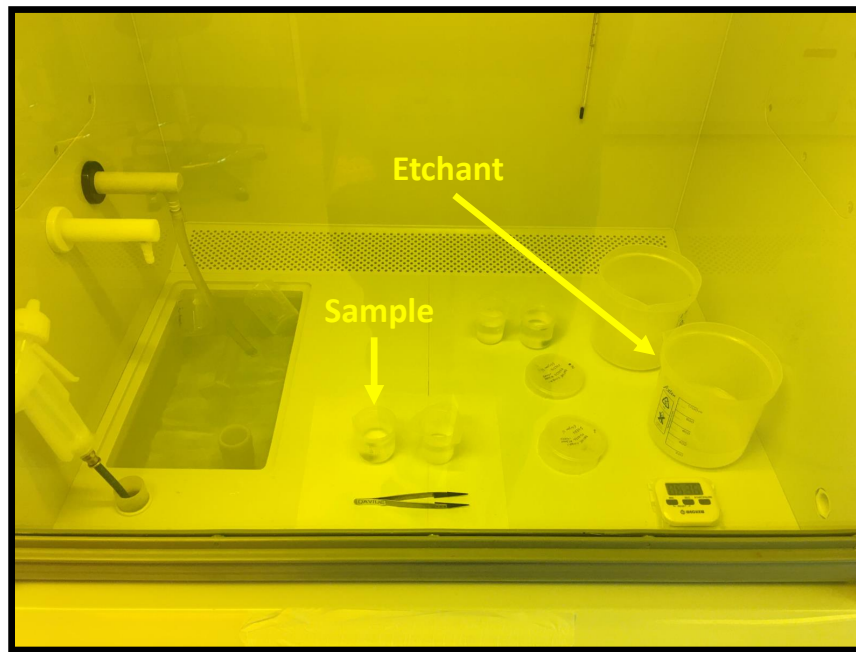


Figure 3.11: LAF cabinet for wet chemical etching, which can also be employed for development processes involving tetramethylammonium hydroxide.

mesas. This because of the low associated cost and processing time, as well as the compatibility with the designed large top mesa area RTD devices (above  $3 \times 3 \mu\text{m}^2$ ) and, partially, TLM structures. The process consists in dissolving the required epitaxial layers through acid-based solutions with high-degree of selectivity.

In the present work, indium gallium arsenide/aluminium arsenide (InGaAs/AlAs) RTD heterostructures epitaxially-grown on InP wafers were processed employing a highly-diluted dissolver composed of hydrogen peroxide ( $\text{H}_2\text{O}_2$ ) (which acts as oxidising agent, triggering and speeding-up the involved chemical reactions), orthophosphoric acid ( $\text{H}_3\text{PO}_4$ ), and water ( $\text{H}_2\text{O}$ ), with composition  $\text{H}_3\text{PO}_4:\text{H}_2\text{O}_2:\text{H}_2\text{O}=1:1:38$  [624], which has a rate of around 100 nm/min at room temperature (RT) in dissolving InGaAs, AlAs, and indium aluminium arsenide (InAlAs), while it is selective to InP. An example of fume-hood-equipped LAF cabinet devoted to wet chemical etching in the JWNC is shown in Figure 3.11.

Figure 3.12a and b illustrate a typical wet-etch process, where a hard mask is employed to protect the non-etching regions (Figure 3.12a). Wet chemical etching tends to be highly-anisotropic in III-V materials, i.e., the etch rate depends on the specific semiconductor crystal orientation, resulting in an overall vertical-to-lateral epi-stack-dependent etching rate. As a consequence, the processed layer(s) is(are) partially etched underneath the protecting etch mask, resulting in the undercut profile shown in Figure 3.12b. In the context of the present work, this limits the minimum dimension of processable RTD devices according to the associated layer-

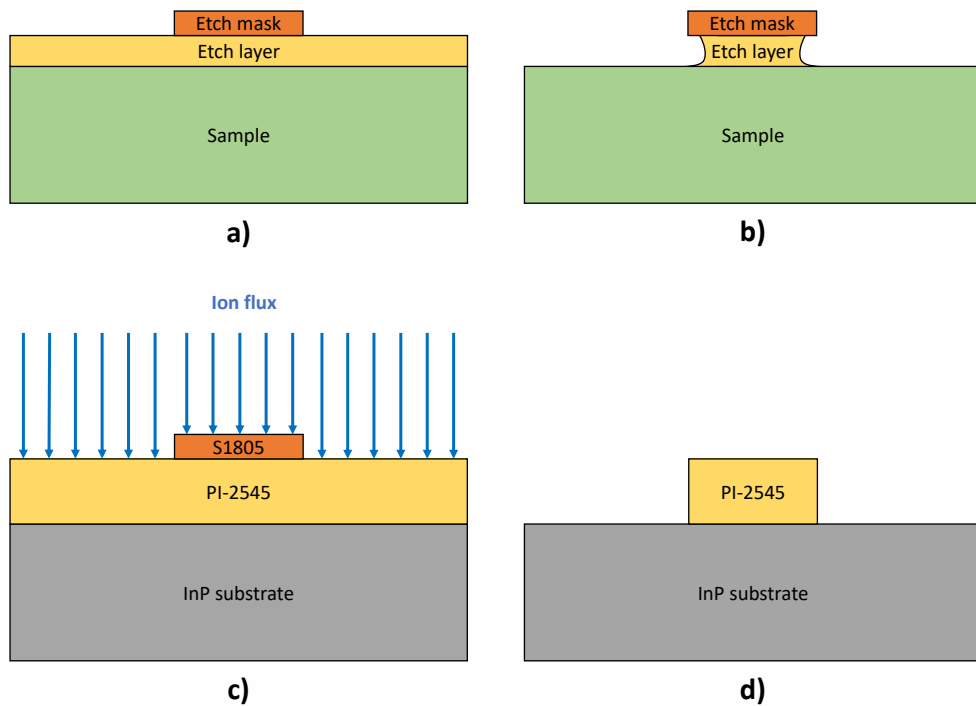


Figure 3.12: Etching processes. In a) and b), anisotropic chemical wet etching; in c) and d), RIE of polyimide PI-2545 employing S1805 photo-resist as soft mask.

stack and leads to a reduction of the effective RTD top mesa area compared to design.

### 3.5 Dry etching

Dry etching is a directional process and far more anisotropic than wet etching, and it usually consists in exposing the processing material to ion bombardment under reduced pressure [105]. A common technique is reactive ion etching (RIE), which consists in generating an ion flux through a chemically-reactive plasma [620]. The ions are then accelerated towards the sample surface and react with it, and the reactions by-products pumped away. At the same time, sputtering of the material can take place.

In the present work, this process was employed to open a via on top of the RTD device top contact after passivation, as will be discussed in Section 3.7. Figures 3.12c and d illustrate the associated RIE process. The passivation layer, which is spun across the whole sample, is realised with polyimide PI-2545 resin from HD Microsystems [625], while an S1805 photo-resist layer is used as protecting soft mask. here, a mixture of tetrafluoromethane ( $\text{CF}_4$ ) and  $\text{O}_2$  gases is used to generate the reactive plasma, which gives etch rates of around 215 nm/min and 150 nm/min for the employed resin and etch mask, respectively. To do that, the Plasmalab 80 Plus from Oxford Instruments [626] in the JWNC was used, which is shown in Figure 3.13. As for the EBPG 5200, this tool is operated by clean-room staff.

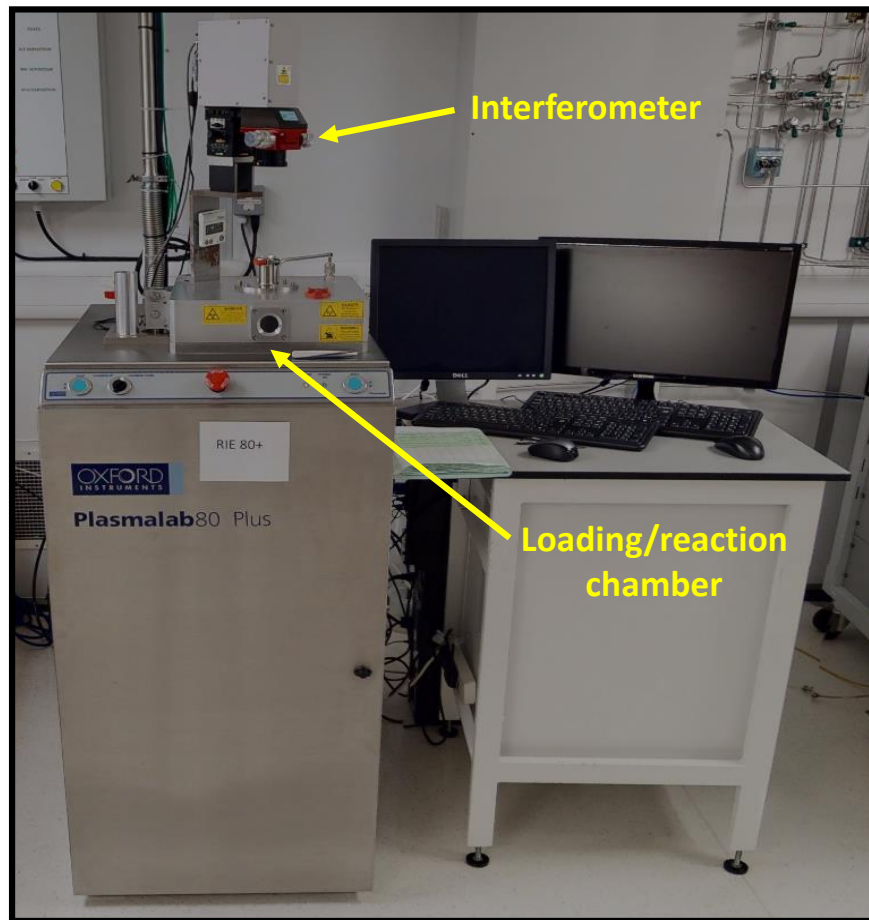


Figure 3.13: Plasmalab 80 Plus RIE tool.

To ensure a correct device passivation and via opening, the unwanted polyimide layer regions have to be etched away. To monitor the process, real-time laser interferometry was employed by means of a LEM end-point detector from Horiba Scientific [627]. In this technique, a narrow laser beam is impinged on the polyimide layer in a sample free region. Typically, the central part is chosen due to the smoother profile of the spun resin. As a result, part of the beam will be reflected at both the vacuum-polyimide and polyimide-InP substrate interfaces, with a total intensity that strictly depends on the passivation layer thickness, and which is detected through a charge-coupled device (CCD) camera.

As the polyimide layer is etched away, the intensity changes due to the phase difference of the two detected light beams, resulting in an oscillatory behaviour and allowing for real-time monitoring of the process. Obviously, when the passivation layer is entirely removed, the signal stays flat, indicating the completion of the etching process. Figure 3.14 shows two examples of detected signal intensity during RIE of fabricated RTD samples. In this context, the number of peaks and, more generally, the processing time, depend on the thickness of the polyimide layer, which depends upon processing requirements.

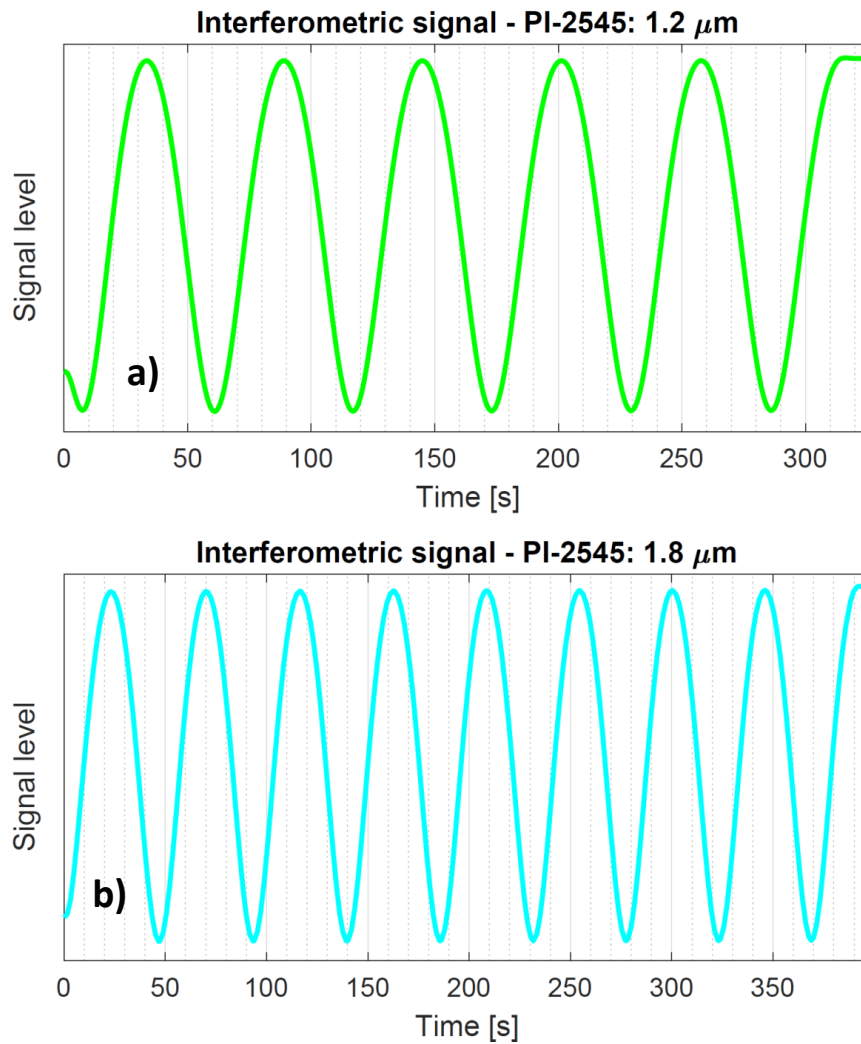


Figure 3.14: Detected laser signal level during RIE of the polyimide PI-2545 passivation layer featuring two different thicknesses: in a),  $1.2 \mu\text{m}$ , while in b),  $1.8 \mu\text{m}$ , for a total of six and nine trace peaks, respectively.

### 3.6 Metrology

Checking the sample at each fabrication step and associated sub-step is crucial to guarantee a smooth process flow. To do that, the JWNC offers various characterisation equipment. In this work, optical microscopes, as well as an electron microscope, a profilometer, and a probe station were intensively used.

Scanning electron microscopy (SEM) consists in probing the sample by means of a highly-accelerated nanometric E-beam [628]. This is produced by an E-gun in strict vacuum and cryogenic conditions, similarly as in EBL. As a result of the interaction between the beam and the specimen, several signals are produced, among which secondary electrons (SE), back-scattered electrons (BSE), characteristic X-rays, Auger electrons, photons (according to cathodoluminescence (CL)), and many more, which are detected by means of specific detectors. In this context,

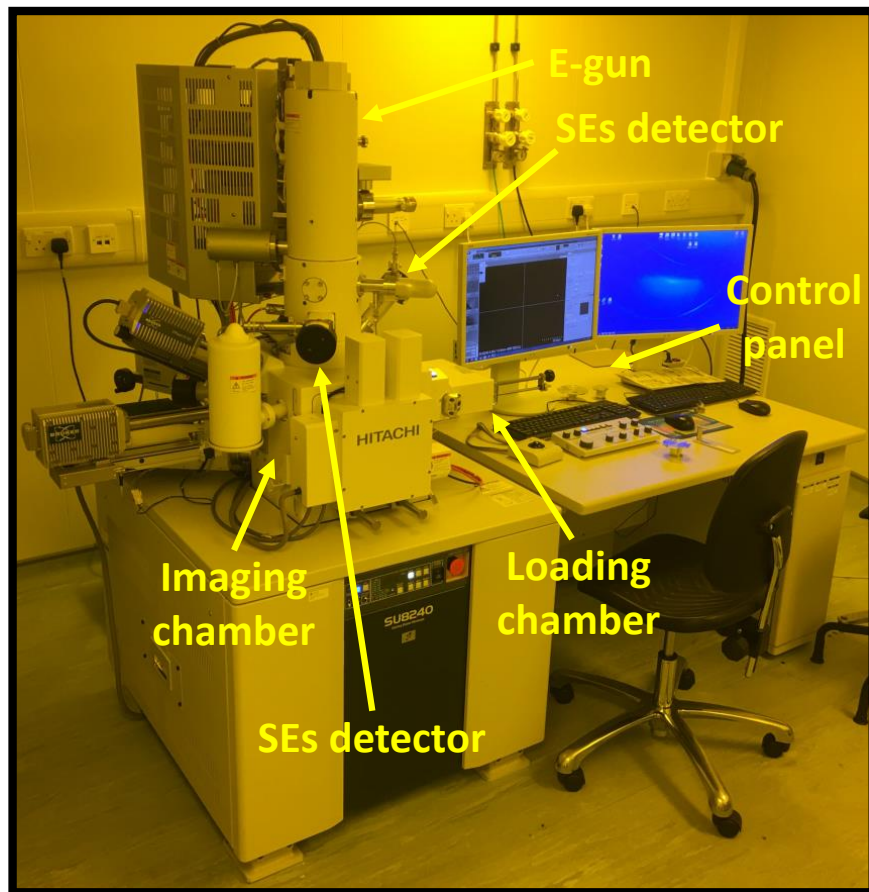


Figure 3.15: UHR FE-SEM SU8240 scanning electron microscope.

SEs provide with the topographical information of the sample surface, while BSEs allow for contrast imaging based on the specimen chemical composition or the analysis of its crystallographic structure. At the same time, elemental analysis or chemical characterisation can be carried out thanks to the detected characteristic X-rays, in what is called energy-dispersive X-ray spectroscopy (EDX).

Figure 3.15 shows the employed UHR FE-SEM SU8240 scanning electron microscope from Hitachi High-Technologies Corporation [629] in the JWNC. The system is equipped with a field-emission (FE) E-gun, SEs and BSEs detectors, and it allows for EDX. In this work, imaging of the RTD devices and TLM structures during fabrication and upon process completion was carried out employing the SEs Everhart-Thornley-like scintillator/photo-multiplier-based detectors. In this context, the resolution, which can be as high as around 1 nm, can be set according to the E-gun acceleration voltage (of the order of the kilovolt), while the two-stage magnification (up to around  $10^6$ ) is adjusted by means of a complex system of lenses.

Figure 3.16 shows the used DektakXT mechanical profiler from Bruker Corporation [630] in the JWNC. The tool is equipped with a diamond-based tip to contact the sample and allows

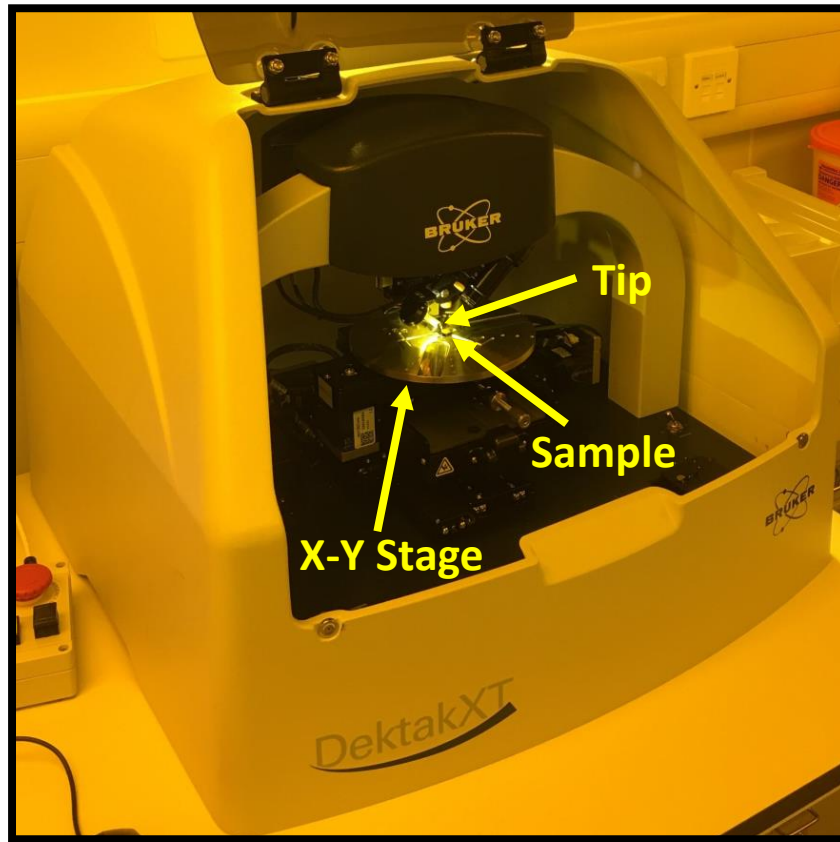


Figure 3.16: DektakXT mechanical profiler.

to measure its surface topography with a vertical resolution of up to 0.1 nm, where the stylus diameter can range between several micrometres down to few tens of nanometres. In this work, this tool was employed to accurately monitor the etch depth during the RTD devices fabrication.

Figure 3.17 shows the used probe station intended for DC measurements in the JWNC. The system features four DC probes and a 4155C semiconductor parameter analyser (SPA) from Keysight Technologies [631]. In the present work, this tool was intensively employed during microfabrication, as it will be discussed in Sections 3.7 and 3.8.

### 3.7 RTD devices fabrication process

The starting point of the fabrication flow is represented by the semiconductor wafer (typically ranging between 2" and 4" in diameter) constituting the designed  $n$ -type intra-band double-barrier RTD epitaxial structure based on the InGaAs/AlAs material system, which is epitaxially-grown on an InP substrate. To illustrate the fabrication flow, an example of processed epitaxial structure, which is depicted in Figure 3.18, is taken as a reference, which was investigated in the early stages of this work. A comprehensive discussion on RTD epitaxial design in the context of the present work is provided in the following Chapters.

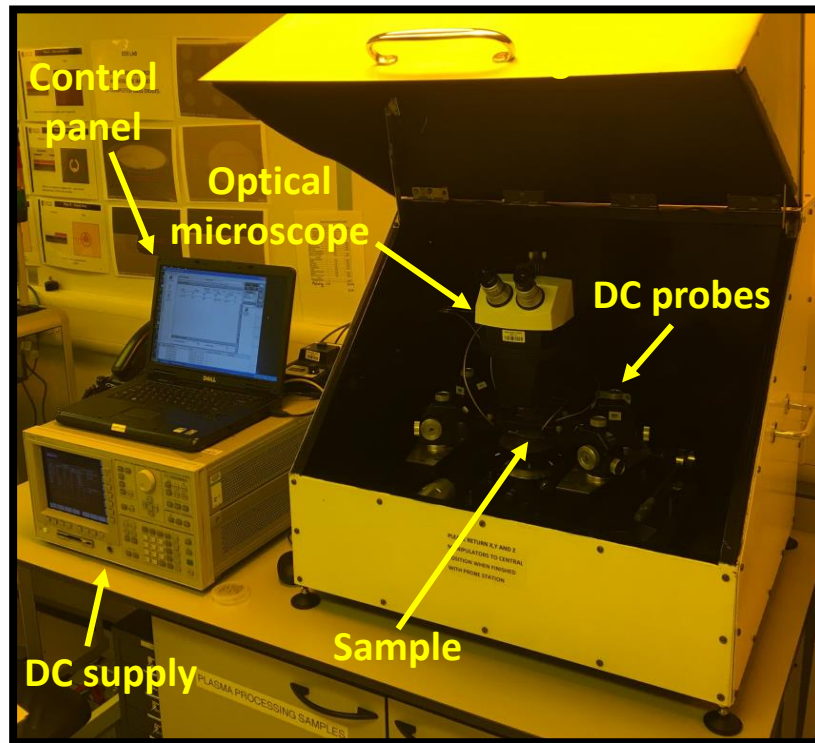


Figure 3.17: Probe station for DC measurements.

The heterostructure includes an  $\text{In}_{0.53}\text{Ga}_{0.47}\text{As}/\text{AlAs}$  double-barrier quantum well (DBQW) active region, consisting of an around 4.4 nm-thick (15 monolayers (ML), where  $1 \text{ ML} \simeq 0.293 \text{ nm}$ )  $\text{In}_{0.53}\text{Ga}_{0.47}\text{As}$  quantum well (QW) sandwiched by two AlAs barriers of around 1.5 nm (5 ML) in thickness. The DBQW region is surrounded by 5 ML-thick  $\text{In}_{0.53}\text{Ga}_{0.47}\text{As}$  undoped spacer layers, 25 nm-thick  $\text{In}_{0.53}\text{Ga}_{0.47}\text{As}$  lightly-doped spacers (with doping concentration  $N_D = 2 \times 10^{16} \text{ cm}^{-3}$ ), 160 nm-thick  $n+$   $\text{In}_{0.53}\text{Ga}_{0.47}\text{As}$  emitter and collector regions ( $N_D = 2 \times 10^{18} \text{ cm}^{-3}$ ), and 40 nm/400 nm-thick  $\text{In}_{0.53}\text{Ga}_{0.47}\text{As}$  heavily-doped collector cap/emitter contact layer ( $N_D = 3 \times 10^{19} \text{ cm}^{-3}$ ). The epi-stack was grown through molecular beam epitaxy (MBE) [632] by IQE on a lattice-matched  $650 \mu\text{m}$ -thick SI InP substrate employing a 200 nm-thick  $\text{In}_{0.52}\text{Al}_{0.48}\text{As}$  buffer layer and using silicon (Si) atoms as donors.

As initial step, a square sample with area of around  $1.2 \text{ cm}^2$  (11 mm-long sides) is cleaved from the wafer to accommodate the mask layout shown in Figure 3.1. In the present work, this was done through the high-precision ATV RV-129 diamond wafer scriber from ATV Technologie [633] in the JWNC. After that, the correct sample face has to be identified. Indeed, depending on the grower, wafers can be polished on both sides to enhance the lithographic degrees of freedom. In the present work, this was done through simple DC measurements employing the JWNC probe station shown in Figure 3.17. In this context, the highly-resistive InP substrate shows high impedance in the megaohm range, while the highly-doped top epi-layers can typically carry several tens of milliamperes at few volts. As already mentioned, some of the

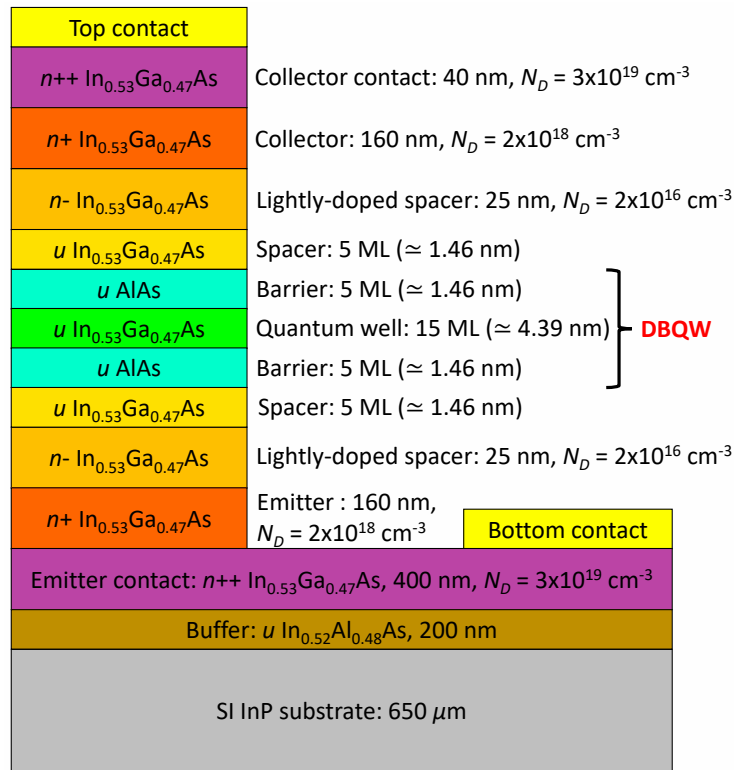


Figure 3.18: Example of processed InGaAs/AlAs RTD epitaxial structure. The device mesa is shown, together with Ti/Pd/Au metal contacts, whose fabrication is described in the following. Layers nomenclature assumes forward bias operation.

wafers processed in this work feature conductive substrates, so the aforementioned procedure could not be employed. However, these wafers were not polished on the substrate side, making electrical characterisation and sample back-side marking unnecessary.

Before processing, the sample requires a cleaning stage in an ultrasonic water bath, which consists in a three-step soaking procedure based on acetone ( $(\text{CH}_3)_2\text{CO}$ ), methanol ( $\text{CH}_3\text{OH}$ ), and isopropyl alcohol (IPA,  $\text{C}_3\text{H}_8\text{O}$ ). In this context, acetone and methanol, together with the physical action of the ultrasonic process, are used to chemically remove any organic and oily contaminants from the sample surface, respectively, while IPA cleans from potential residues caused by the high evaporation rate of acetone. Finally, a de-ionised water rinse based on reverse osmosis (RO) is used to wash the sample and finalise the process.

The RTD devices fabrication process comprises of one E-beam (top contact) and five optical lithographic steps, for a total of six steps. The complete fabrication recipe used in the present work is provided in Appendix A, which includes the realisation of top and bottom TLM structures during the same fabrication run (whose process will be described in detail in Section 3.8), as shown in Figure 3.1. This recipe was partially inherited as a result of past research work conducted within the High-Frequency Electronics group [396, 634], University of Glasgow, and

it was fully-revisited, improved, and extended for the purpose of this work.

The general fabrication flow is illustrated in Figure 3.19 and described in the below:

- a) *Top contact*: the first step consists in depositing the RTDs top metal Ohmic contacts (as well as the top TLMs metal structure), as shown in Figure 3.19a. Before that, the sample is subjected to an UV light/ozone (O<sub>3</sub>) treatment for 1 h. This is done to clean the sample from any residual organic (resist) contaminants [635] and, overall, to ox-

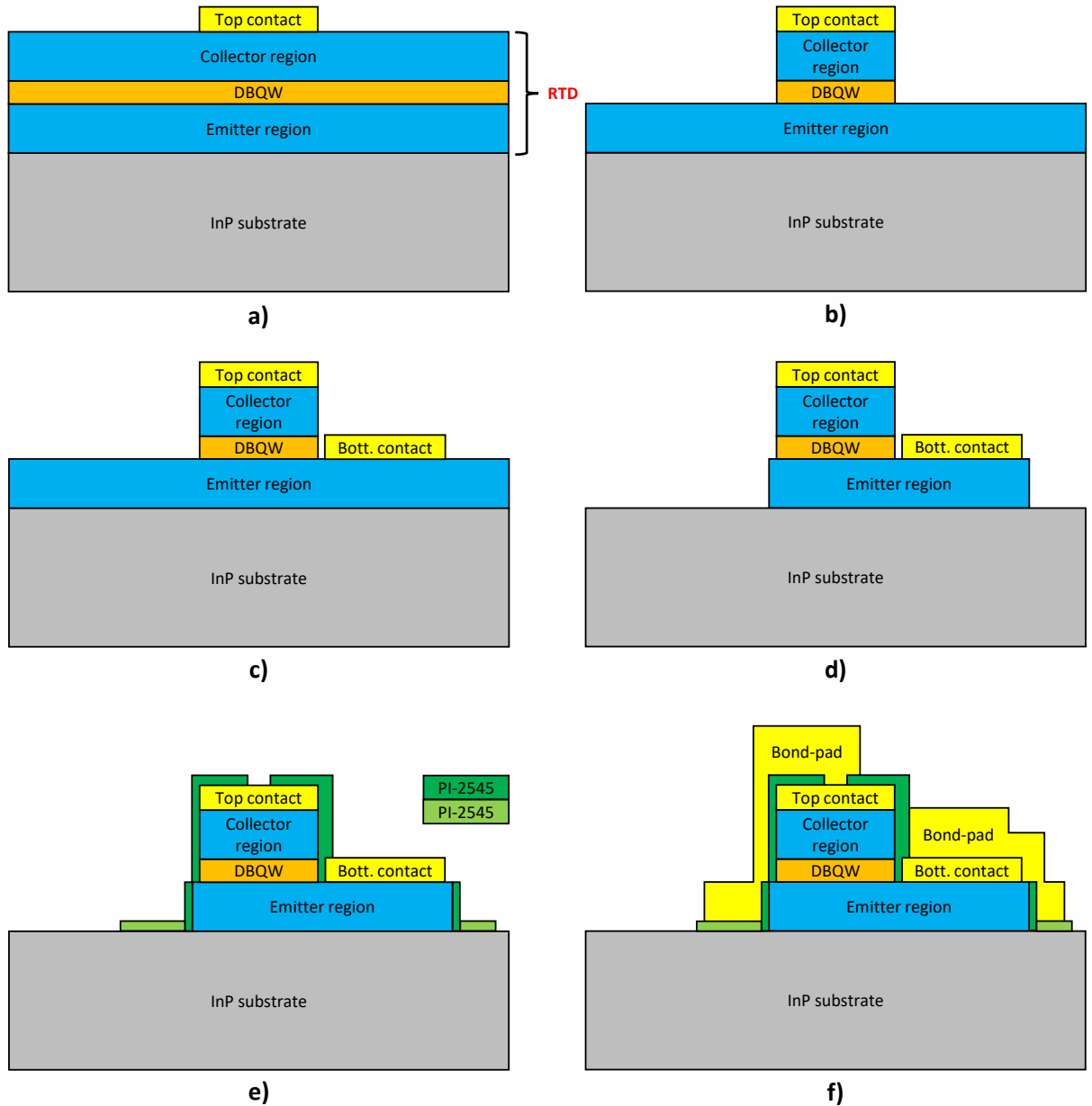


Figure 3.19: RTD device fabrication flow: a), top contact; b), top mesa; c), bottom contact; d), bottom mesa; e), passivation and via opening; f), bond-pads. In e), the passivation layer extension for bond-pads insulation is also displayed with a lighter colour. In f), the bond-pads sit on the extended passivation layer as a comprehensive example.

idise its surface. Indeed, the sample is exposed to air in normal conditions, making a thin native oxide layer forming at its surface. However, this is detrimental in the fabrication of Ohmic contacts, as it will be explained in Section 3.8.

To circumvent it, the sample surface is oxidised thanks to an UV/O<sub>3</sub> exposure, forming oxidizes species [636] that can be easily removed by a subsequent wet-etch chemical treatment [637]. In the context of the present work, this was carried out using the T10XT10/OES/E UV/O<sub>3</sub> cleaning system from UVOCS [638] in the JWNC, which is shown in Figure 3.20. The tool is equipped with a low-pressure Hg-based vapour lamp emitting UV rays mostly of 184.9 nm and 253.7 nm in wavelength. In this context, the first spectral line is used to decompose atmospheric oxygen molecules (O<sub>2</sub>) in atomic oxygen (O), i.e., O<sub>2</sub>→O+O, and to form O<sub>3</sub>, i.e., O+O<sub>2</sub>→O<sub>3</sub>, while the second one to make contaminant molecules reacting towards O, as well as to decompose O<sub>3</sub>, i.e., O<sub>3</sub>→O<sub>2</sub>+O. The continuous photo-sensitized formation and decomposition of O<sub>3</sub> generates an abundant population of reactive O, which acts as oxidising agent towards oxidizable species at the sample surface.

After that, a thin bi-layer made of around 780 nm-thick PMMA 8 and around 70 nm-thick PMMA 10 E-beam resists, for a total thickness of around 850 nm, is spin-coated on the sample surface and soft-baked. Both resists have resolution in the

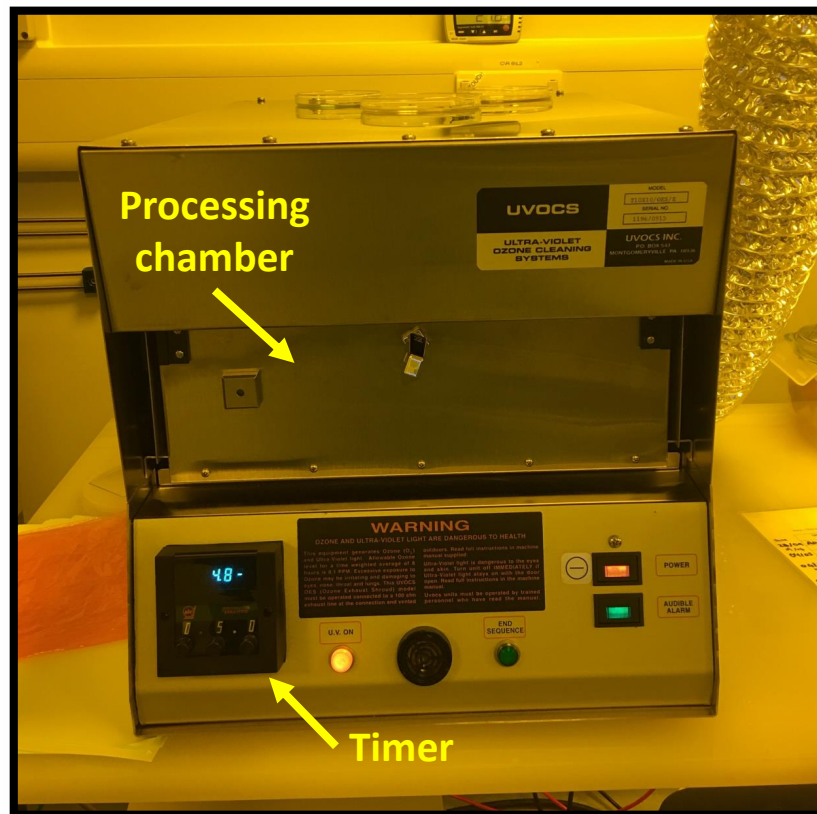


Figure 3.20: T10XT10/OES/E UV/O<sub>3</sub> cleaning system.

nanometre range. During spinning, the sample back side is protected with adhesive clean-room tape (the same applies to all the spin steps for both RTD devices and TLMs fabrication). The sample is then exposed with the EBPG 5200 through a dual E-beam exposure procedure (which will be described in Section 3.8) and developed in IPA:methyl isobutyl ketone (MIBK)=2.5:1.

Before metallisation, a further shorter treatment with UV/O<sub>3</sub> is performed to clean from resist residuals and to further oxidise the sample surface, followed by ex-situ wet chemical etching in an hydrochloric acid (HCl)-based diluted solution with concentration HCl:H<sub>2</sub>O=1:3 to clean the sample surface. The UV/O<sub>3</sub> processing time was optimised based on the tool etch rate and employed resist stack, allowing for a reliable lift-off. Afterwards, a Ti/Pd/Au=20/30/150 nm (or molybdenum/titanium/gold (Mo/Ti/Au)=20/20/150 nm) metal stack is deposited through EBPVD by using the MEB550S E-beam evaporator (Plassys IV) after a short in-situ Ar<sup>+</sup>-based dry-etch surface cleaning process, followed by lift-off in MICROPOSIT remover 1165 solution from Rohm & Haas Electronic Materials [639].

- b) *Top mesa*: the second step consists in creating the RTDs top mesa (and, partially, the top TLMs mesa), as shown in Figure 3.19b. After the photo-mask is properly cleaned (recipe provided in Appendix A), a thin S1805 photo-resist layer of around 500 nm in thickness is spun on the sample and soft-baked. After UV exposure with MA6, the sample is developed in a diluted solution based on MICROPOSIT Developer Concentrate (MDC) from Rohm & Haas Electronic Materials [640] with concentration MDC:H<sub>2</sub>O=1:1, and subsequently ashed.

Due to the large associated size, the RTDs and TLMs mesas are defined through chemical wet etching. In this context, the photo-resist is mainly used to protect the TLMs gaps and further mask features, including the optical alignment markers, while the RTDs top metal contact acts as etching hard mask for the devices top mesa. The process is carried out through the employment of a diluted acid-based solution of composition H<sub>3</sub>PO<sub>4</sub>:H<sub>2</sub>O<sub>2</sub>:H<sub>2</sub>O=1:1:38, where the sample is etched from the collector contact up to the emitter contact layer. By processing the structure in Figure 3.18, the measured etch depth with the DektakXT was around 520 nm, for a total processing time of 5 min and 20 s. Finally, the resist is stripped using 1165 solution.

- c) *Bottom contact*: the third step consists in depositing the RTDs bottom metal Ohmic contact (as well as the bottom TLMs metal structure), as shown in Figure 3.19c. This step is analogous to the top contact apart from the spin-coated resist, which consists in a thick bi-layer made of > 1 μm-thick LOR-10A and around 1.9 μm-thick S1818 photo-resists, for a total thickness of around 3 μm. This is done to cover and protect the RTDs and TLMs from metallisation, allowing for a correct lift-off.

In this context, the S1818 film has a resolution of around  $2\ \mu\text{m}$ , which is sufficient to pattern the intended large metal features. Moreover, differently from the top contact step, exposure is carried out through MA6, while development using the MICROP-OSIT MF-319 developer solution from Rohm & Haas Electronic Materials [641], which is based on tetramethylammonium hydroxide (TMAH). At the same time, UV/O<sub>3</sub> exposure is carried out entirely before EBPVD, which is possible thanks to the thick S1818 resist film, allowing for a correct lift-off. This is carried out through multiple subsequent short sub-steps to allow the sample cooling down, avoiding the resist to burn due to the high chamber temperature at prolonged processing times.

- d) *Bottom mesa*: the fourth step consists in creating the RTDs bottom mesa (and the (partially)top/bottom TLMs mesas), as shown in Figure 3.19d. This step is analogous to the top mesa apart from the spin-coated resist, which consists in a thick S1818 layer. This is done to additionally cover and protect the RTD devices from etching. As for the bottom contact, S1818 allows to process the intended large mesa features.

In this step, etching is carried out up to the InP substrate, which acts as etch stop, by entirely removing the emitter contact and potential buffer layers. This is checked either through mechanical profilometry and/or DC probing. In the case of the structure in Figure 3.18, the measured etch depth was around 500 nm with DektakXT, for a total processing time of 6 min.

- e) *Passivation and via opening*: the fifth step consists in passivating the RTDs, opening a via on top of the associated top contact to allow for bond-pad connection and, in the case of a conductive substrate, creating the bond-pads insulation support, as shown in Figure 3.19e. In this context, the square via area was designed to be half of the associated RTD top contact dimension. Moreover, the bottom mesa was framed to allow for a correct bottom pad deposition, as explained in the following.

To do that, a polyimide PI-2545 layer is spun onto the sample and cured at high temperature. Here, the thickness of the resin film is chosen according on the overall thickness of the RTD mesa structure. In this work, thicknesses of around  $1.2\ \mu\text{m}$  and  $1.8\ \mu\text{m}$  were adopted. After that, a thin layer of S1805 photo-resist is spin-coated and soft-baked. This layer acts as soft mask and it is designed to protect the device passivation region during RIE according to its corresponding etch-rate [634]. In the present work,  $0.9\ \mu\text{m}$  were found to be suitable for all the processed RTD hetero-structures.

After UV exposure through MA6 and development in MDC:H<sub>2</sub>O=1:1, the sample is ashed and post-baked on a hot plate for 10 min. This is done to smooth the resist edges and obtain a tapered polyimide layer profile after RIE, which ensures good step

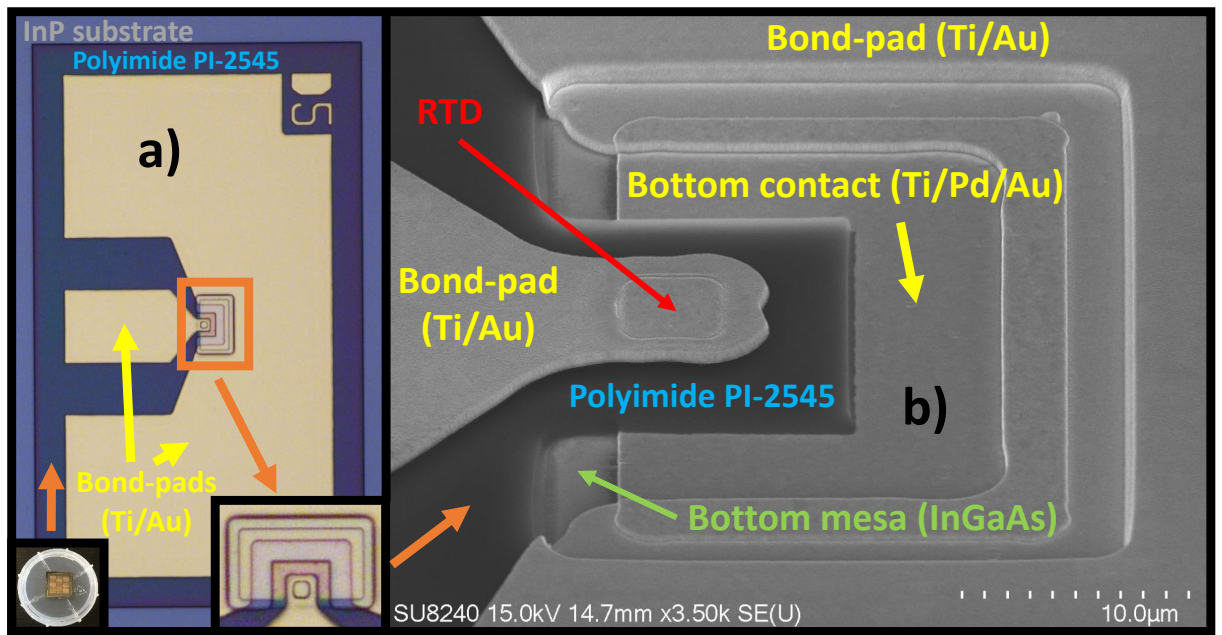


Figure 3.21: Fabricated  $5 \times 5 \mu\text{m}^2$ -large RTD device. In a), photograph of the processed sample and photo-micrograph of the fabricated device, together with a zoom-in over the RTD region; in b), SEM image of the RTD region.

coverage during the bond-pads EBPVD step, avoiding metal discontinuities. The sample is then processed with RIE80+ in a  $\text{CF}_4/\text{O}_2$ -based plasma and the process monitored using the installed interferometer.

- f) *Bond-pads*: the sixth and final step consists in depositing the RTDs bond-pads to allow for DC probing and S-parameter measurements, as shown in Figure 3.19f. This step is analogous to the bottom contact due to the similar lithographic requirements, apart from the evaporated film, which consists in a thick  $\text{Ti}/\text{Au}=20/400$  nm metal stack layer to ensure the associated integrity during device probing, and the missing pre-EBPVD  $\text{UV}/\text{O}_3$  and wet-etch cleaning treatments, which are replaced by a plasma ashing sub-step.

The processed sample featuring the epi-stack in Figure 3.18, together with one of the fabricated RTDs with designed top mesa area  $A = 5 \times 5 \mu\text{m}^2$ , are shown in Figures 3.21 and 3.22. Although the sample was characterised by a SI InP substrate, the RTDs bond-pads were deposited on the extended passivation layer, which was done at the beginning of the thesis work in testing the adhesion capabilities of Ti over polyimide PI-2545 in order to ensure a correct device probing.

The device features peak current  $I_p \simeq 40$  mA, peak-to-valley current ratio  $\text{PVCR} \simeq 4.4$ , peak voltage  $V_p \simeq 1.07$  V, and valley-to-peak voltage difference  $\Delta V \simeq 0.53$  V, while the associated maximum radio-frequency (RF) power  $P_{RF,max}$  was estimated to be around 1.3 mW.

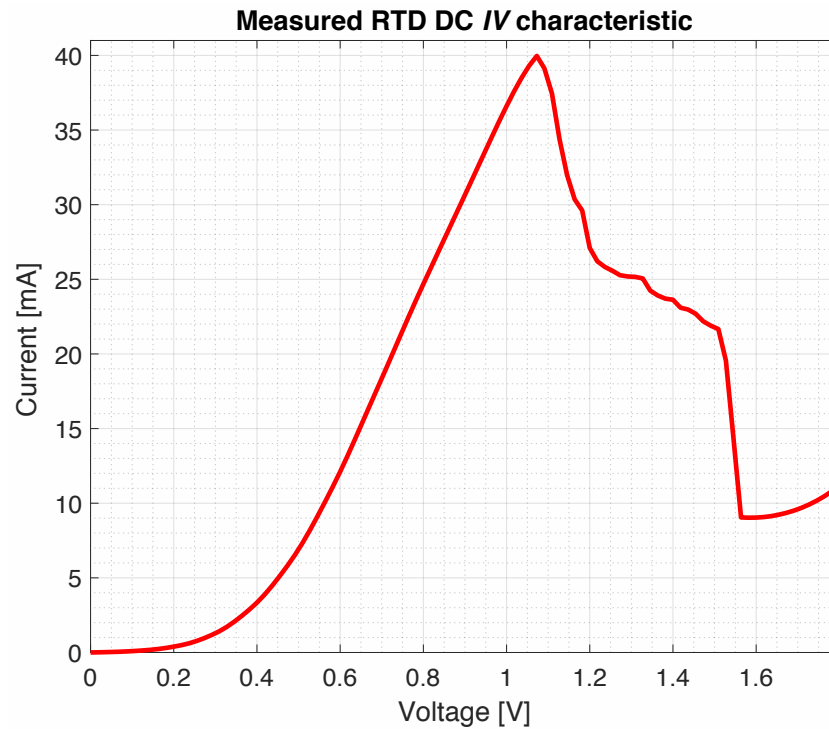


Figure 3.22: Measured DC  $IV$  curve of the fabricated RTD device shown in Figure 3.21.

### 3.8 TLM structures design and fabrication process

As broadly discussed in Chapter 2, the parasitic resistance associated with Ohmic contacts is one of the main factors that bottleneck the RF power capability of the RTD device at high-frequency. In particular, it limits the cut-off frequency at which the RTD can provide gain, as well as the maximum power the diode is able to deliver at a specific operation frequency. In the context of THz oscillators, this affects the resonator spectral line-width and quality factor ( $Q$ ), which determine the system phase-noise. As a consequence, together with affecting the transmitter (Tx) output power, this influences the wireless data-link signal-to-noise ratio (SNR) and associated data-rate.

Ohmic contacts of state-of-the-art THz RTD devices employed in both sources and detectors typically feature a specific contact resistivity  $\rho_c$  in the range  $2\text{--}10 \times 10^{-8} \Omega \text{ cm}^2$ , but it can reach over  $2 \times 10^{-6} \Omega \text{ cm}^2$  if care is not taken during fabrication. In the framework of high-power (above 1 mW) InGaAs/AlAs double-barrier RTDs aimed at oscillator realisation in the low-THz range ( $\sim 100\text{--}300$  GHz) [169, 390], the unoptimised metal-to-semiconductor junction fabrication process keeps  $\rho_c$  far from physical limiting values [642, 643], resulting in poor Ohmics.

The concept of parasitic resistance arising at metal-semiconductor contacts according to Schottky's theory is well established and explained in classic electron devices textbooks [165].

To maximise device performance, design and fabrication of the Ohmic contacts should be conducted to reduce the associated Schottky potential barrier, and  $\rho_c$  minimised towards the quantum limit dictated by the Landauer's conductance quantisation rule [643].

In this context, an accurate and reliable approach to experimentally-extract  $\rho_c$  is required to estimate the behaviour of the contacts and the extrinsic frequency response of the device. In the present work, this was done through transmission line measurements [644] by employing an ad-hoc test structure. The designed EBL mask and associated top contact TLM structure layouts are shown in Figure 3.23, featuring gap spacing ranging from  $6\ \mu\text{m}$  to  $1\ \mu\text{m}$  for accurate  $\rho_c$  extraction, for a total of 112 TLMs and an overall mask area of around  $1\ \text{cm}^2$ . The structure is analogous to the one included in the RTD mask in Figure 3.1, which is used to estimate the contact resistance associated to the top contact during the same fabrication run.

In principle, the same layout can be also employed for the bottom Ohmic contact. In this context, few bottom TLMs were included in the RTD photo-mask, as shown in Figure 3.1, featuring minimum gap spacing of  $3\ \mu\text{m}$  due to the associated photo-lithographic resolution constraints. However, although  $\rho_c$  associated with the bottom contact tends to be slightly higher compared to the top contact one due to the rough surface profile caused by chemical wet etching during the RTD top mesa fabrication step [395], the bottom contact resistance is negligible for the devices processed in this work due to the large associated contacts layout area, as will be explained in Chapter 4. Therefore, the accurate extraction procedure was adopted solely for the top contact, whose resistance represents the main contribute to the device parasitic series resistance.

The proposed test structure design, which is shown in Figure 3.23b, is similar to previously reported linear TLMs [645], where separate probes landing areas are provided far from the gaps to avoid common measurement artifacts arising due to manual probe mispositioning, which are well-known to give random measurement fluctuations, and unrepeatable and unreliable  $\rho_c$  extraction, in standard structures [646]. At the same time, metal interconnections are designed to reduce the associated parasitic resistance by employing a large patch width of  $80\ \mu\text{m}$ .

Although circular geometries [647] are widely employed since only require a single lithographic step and do not suffer from in-plane current crowding effects [648, 649], linear TLM structures can be reliably employed to accurately estimate  $\rho_c$  via four-point probe sensing [650]. Indeed, fringing currents can be easily eliminated through structure insulation by means of chemical wet etching and accurate mask alignment. Here, the small lateral undercut due to etching anisotropy does not pose a detrimental effect since current flow takes place horizontally and mostly at the sample surface, differently from an RTD device. This approach typically provides with an extraction error down to around  $\pm 0.1 \times 10^{-8}\ \Omega\ \text{cm}^2$  [461, 650], which is sufficient

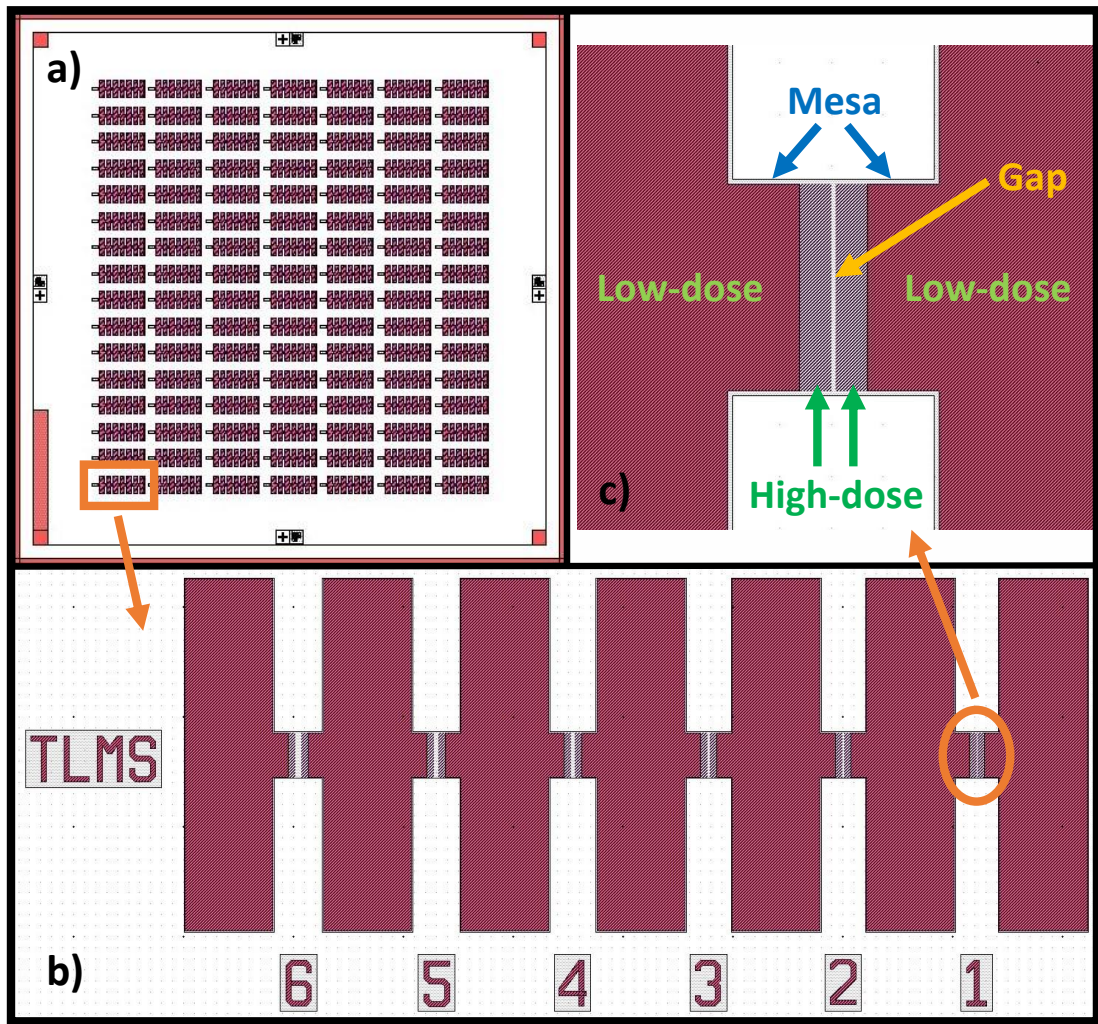


Figure 3.23: Top TLM structures E-beam lithographic mask. In a), mask layout, including a pair set of optical alignment markers at the four mask sides, as well as other markers for sample orientation and wet etching; in b), TLM structure layout; in c), zoom-in over the associated 1  $\mu\text{m}$ -wide gap region.

for RTD performance analysis, avoiding more complex design strategies [622].

EBL was adopted to pattern the TLMs due optical lithography unreliability in opening the 1  $\mu\text{m}$ -wide gap, which gives low reproducibility and needs careful SEM analysis after lift-off for each structure and at each fabrication run to remove any possible source of unwanted systematic error. Due to reflection phenomena occurring in proximity to the structure gaps during E-beam exposure, the resist profile takes a positive symmetric curved shape at both edges after development, resulting in a smaller equivalent gap width and, for short ones, complete gap closure after lift-off. Although this can be easily sorted by reducing the exposure dose, it results in the patterned regions to be left under-exposed. To address it, a dual-exposure process using two different doses is proposed based on experimental optimisation, as shown in Figure 3.23c.

A first high-dose (490) layer associated with the correct dose for reliable gaps shaping and opening was designed to cover the entire TLM structure, while a second low-dose one (310) is superimposed to the first one by keeping a distance of  $6\ \mu\text{m}$  from the gaps to compensate for under-exposure. The total dose (800) allows to correctly pattern the structure backbone and all the other mask features. Note that, as already pointed out in Sections 3.1 and 3.7, this process is compatible with the RTD top contact fabrication step, and this was experimentally-verified. At the same time, the mesa was shaped for fringing currents suppression by surrounding the whole metal structure with a tolerance of  $0.5\ \mu\text{m}$ , which corresponds to the resolution of the employed photo-resist.

The top TLM structure fabrication flow for a generic InGaAs/AlAs DBQW RTD hetero-structure grown onto an InP substrate is shown in Figure 3.24, and comprises of one E-beam and one optical lithographic step, which are analogous to the top contact and bottom mesa RTD fabrication ones. To illustrate the process, the epi-stack in Figure 3.18 is assumed. The complete fabrication recipe is provided in Appendix B, while the general process is described in the below:

- a) An E-beam resist bi-layer (PMMA 8/PMMA 10) is spin-coated and soft-baked on a cleaned sample of around  $1.2\ \text{cm}^2$  surface, and patterned through EBL (EBPG 5200) by means of the described dual-exposure process.
- b) The resist is developed and the  $\text{In}_{0.53}\text{Ga}_{0.47}\text{As}$  surface cleaned ( $\text{UV}/\text{O}_3 + \text{HCl}:\text{H}_2\text{O}$ ) ex-situ prior to metal evaporation. Figure 3.25 shows photo-micrographs of a TLM structure after development. As can be seen, the backbone was correctly exposed and developed. Moreover, all the gaps, including the  $1\ \mu\text{m}$ -wide, were correctly processed, revealing a straight profile.
- c) A  $\text{Ti}/\text{Pd}/\text{Au}=20/30/150\ \text{nm}$  (or  $\text{Mo}/\text{Ti}/\text{Au}=20/30/150\ \text{nm}$ ) metal stack is evaporated after an in-situ  $\text{Ar}^+$  ion milling treatment.
- d) Lift-off. Figure 3.26 shows photo-micrographs of a test structure after lift-off. As can be seen, the metal (in this case,  $\text{Ti}/\text{Pd}/\text{Au}$ ) was successfully-patterned and the gaps opened. To double-check, an SEM analysis was carried out on different structures, randomly selected across the sample, to obtain statistical significance. The analysis was focused on the  $1\ \mu\text{m}$ -wide gap (being the critical one) by measuring the associated width at different lateral positions. For instance, Figures 3.26c and d show SEM images of the  $1\ \mu\text{m}$ -wide gap belonging to one of the analysed structures. The investigation confirmed the correct opening of the gaps, with a tolerance of  $\pm 50\text{--}60\ \text{nm}$  between the different structures, which allows for a reliable  $\rho_c$  extraction. At the same time, metal corrugation was observed at the gaps edges perpendicularly with the sample surface, as can be seen in Figure 3.26d. This is explained by the

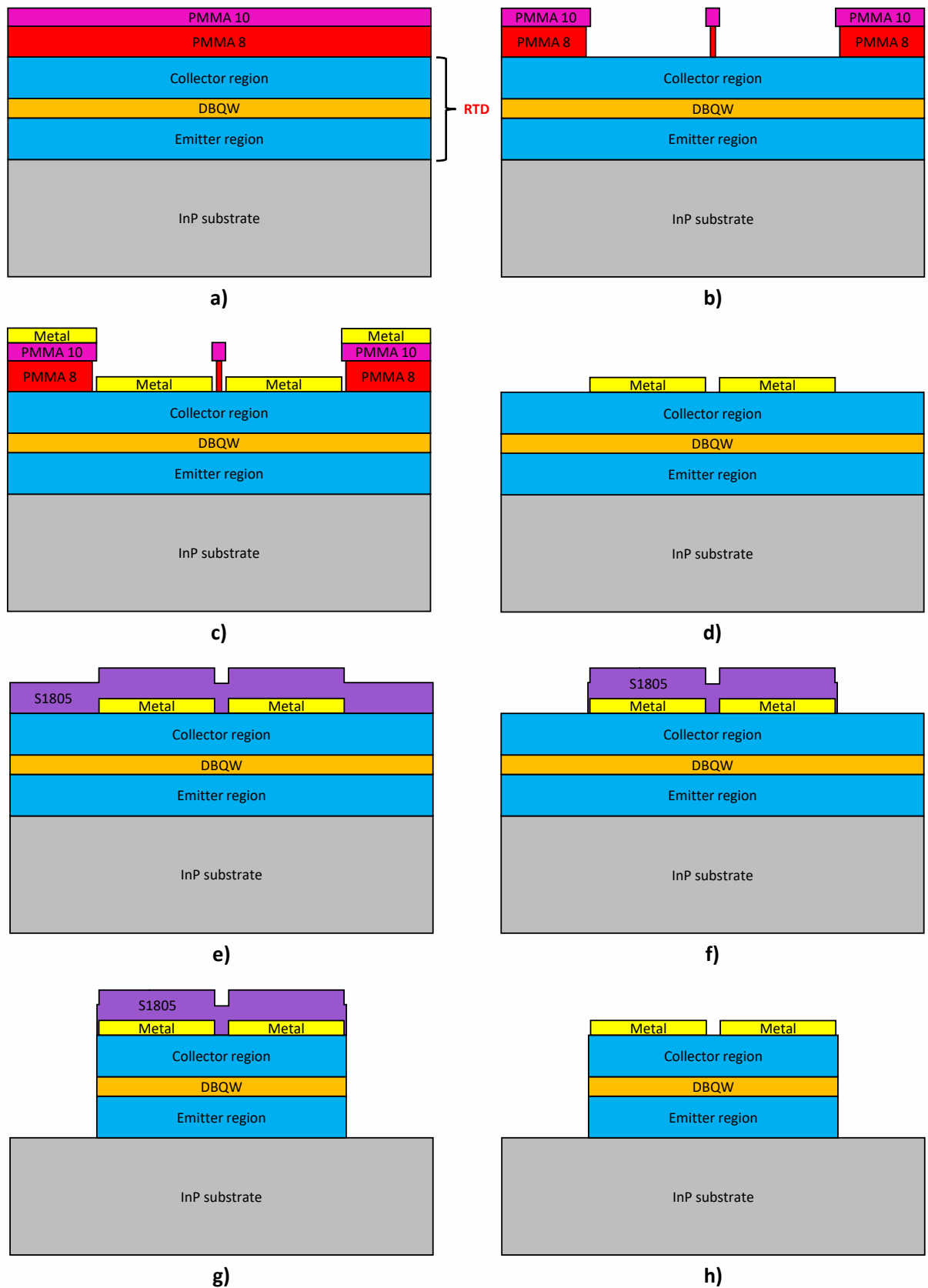


Figure 3.24: Top TLM structure fabrication process: a), E-beam resist spin-coating; b), exposure, development, and surface cleaning; c), metallisation; d), lift-off; e), photo-resist spin-coating; f), exposure, development, and plasma ashing; g), wet etching; h), resist stripping.

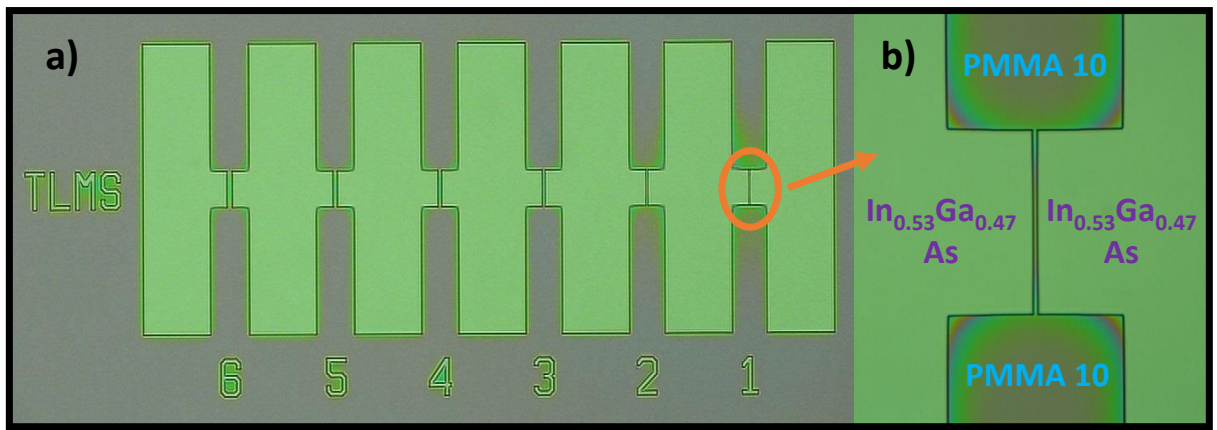


Figure 3.25: Photo-micrographs of a TLM structure after development. In a), the structure backbone; in b), a zoom-in over the 1 μm-wide gap region.

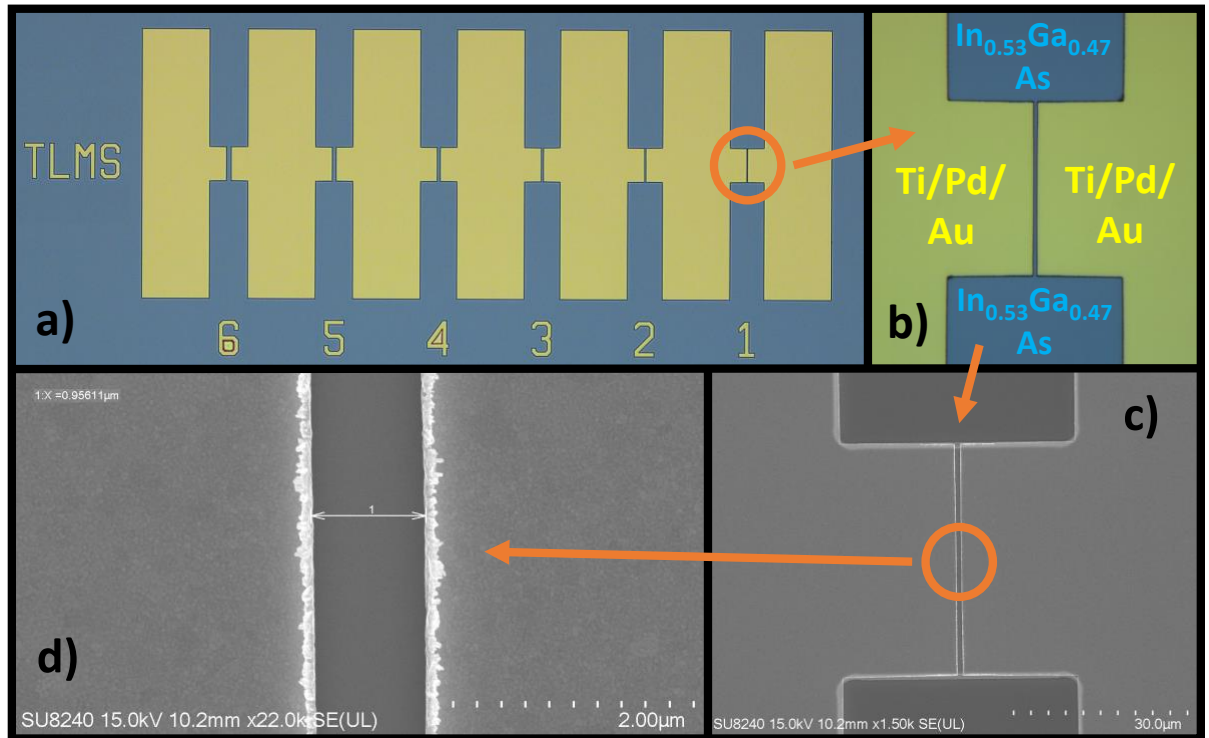


Figure 3.26: Photo-micrographs and SEM images of a TLM structure after lift-off. In a), the structure backbone; in b), a zoom-in over the 1 μm-wide gap area; in c), the 1 μm-wide gap seen through SEM; in d), a further zoom-in over the gap.

presence of a very thin deposited metal film on the resist later side-walls as a result of the evaporation process, resulting in metal flakes left along the surface edges in close proximity to the gaps after lift-off. However, this does not affect the reliability of the extraction procedure, since the actual gap width is measured at the In<sub>0.53</sub>Ga<sub>0.47</sub>As surface, where SEM imaging confirmed the gap edges to be smooth.

e) A photo-resist (S1805) layer is spin-coated, soft-baked, and patterned through optical

lithography (MA6).

- f) The resist is developed and the sample ashed.
- g) The TLMs mesa is defined and the structures electrically insulated from the surrounding through chemical wet etching up to the InP substrate ( $\text{H}_3\text{PO}_4:\text{H}_2\text{O}_2:\text{H}_2\text{O}=1:1:38$ ), for a total processing time of 10 min.
- h) The resist is stripped, finalising the fabrication process.

Figure 3.27 shows a photograph of a fabricated sample, and photo-micrographs and SEM images

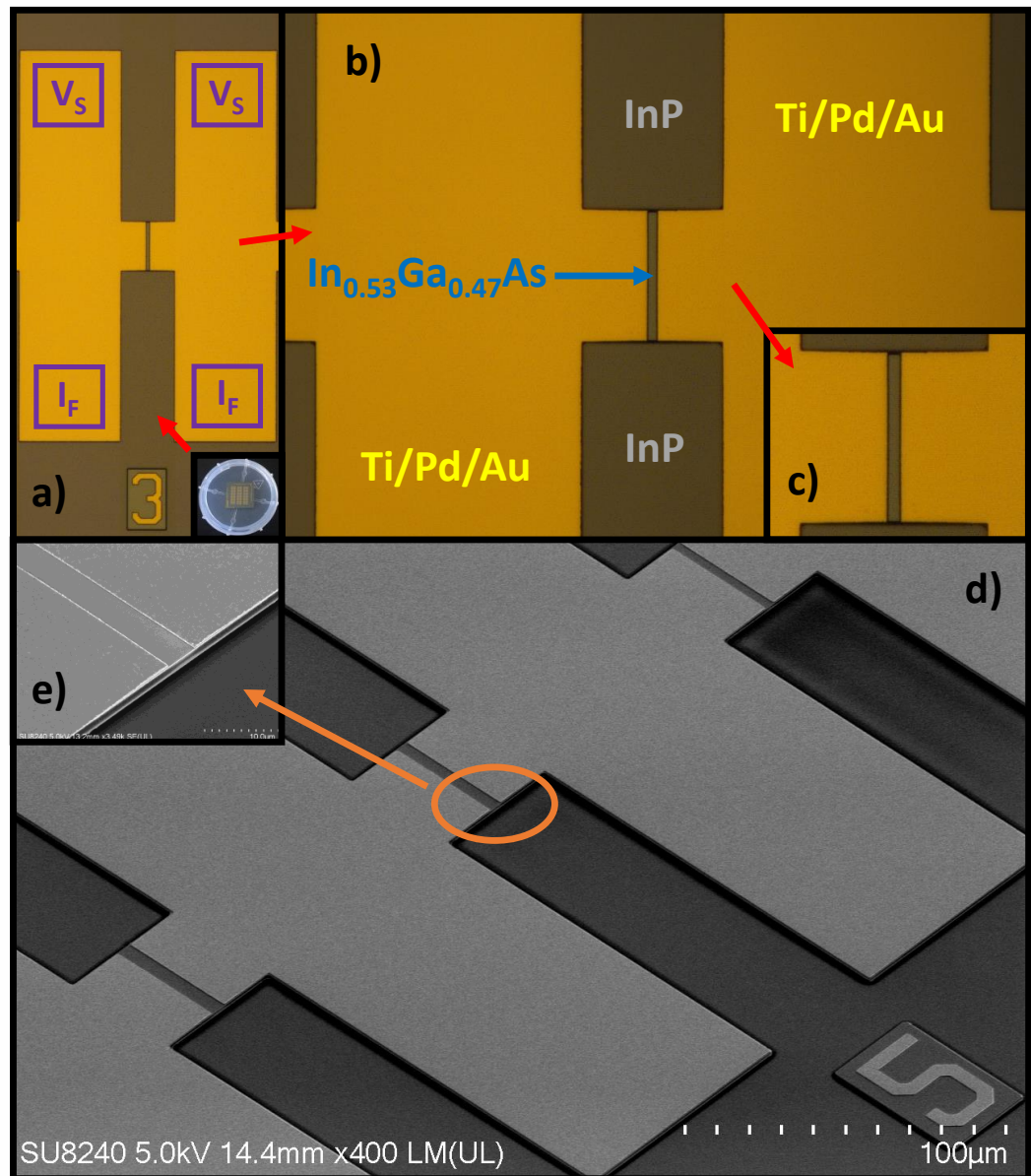


Figure 3.27: In a), b), and c), photo-micrographs of the 3  $\mu\text{m}$  wide gap region of one of the fabricated structures, including two zooms-in over the gap; in d) and e), SEM images of the 5  $\mu\text{m}$ -wide gap region of an analogous TLM, including a zoom-in over a mesa later side-wall.

of the 3  $\mu\text{m}$  and 5  $\mu\text{m}$ -wide gap measurement areas of fabricated structures for four-point probe sensing. As can be seen in Figures 3.27c and e, accurate photo-mask alignment for mesa definition was successfully achieved, which minimises in-plane current crowding effects. Within the adopted measurement technique, the bottom probes inject current ( $I_F$ ), while the top one sense voltage ( $V_S$ ). Based on the measurement data,  $\rho_c$  is extracted through the transfer length method [651]. Details on the extraction procedure are provided in Appendix C.

In the present work, the proposed TLM test structures were not used to optimise the RTD Ohmic contacts through an in-depth investigation study, but rather to extract  $\rho_c$  in the framework of RTD device modelling and characterisation, as it will be described in Chapters 4 and 6. Here, RTDs and TLMs fabrication was carried out employing Pd-based contacts, in particular, the Ti/Pd/Au metal stack, which is widely used in THz InP RTD technology [163, 466] and it has been proven to provide  $\rho_c$  down to around  $1 \Omega \mu\text{m}^2$  to heavily-doped InGaAs thanks to metal work-function compatibility and optimised pre-metallisation cleaning procedures [461, 490]. The role of Ti is to provide with mechanical adhesion to the InGaAs surface (as well as Au diffusion barrier), Pd works as semiconductor-metal interface layer, while Au allows for bond-pads connection. Same consideration apply to similar metal stacks, such as platinum (Pt)-based [646, 656].

Moreover, Mo-based contacts were also utilised, in particular, Mo/Ti/Au [622, 645, 650], due to the large associated melting point (around 2895 K [657]). Indeed, the employment of work-function-compatible refractory metals improves the thermal stability of Ohmic contacts, increasing device reliability [658]. Here, Mo directly contacts with InGaAs and acts as transition layer, while the Au layer adheres via a Ti thin film used to prevent diffusion of Au atoms across the metal-semiconductor interface. This metal stack has proven to provide similar  $\rho_c$  performance compared to Pd-based stacks [622, 658].

# Chapter 4

## Accurate quantum transport modelling of high-speed $\text{In}_{0.53}\text{Ga}_{0.47}\text{As}/\text{AlAs}$ double-barrier resonant tunnelling diodes

In this Chapter, a reliable physics-based simulation approach to accurately model high-speed indium gallium arsenide/aluminium arsenide double-barrier resonant tunnelling diodes (RTD) epitaxially-grown on lattice-matched indium phosphide substrates is demonstrated. It relies on the non-equilibrium Green's function formalism implemented in Silvaco Atlas technology computer-aided design quantum transport simulation package to closely mimic the actual device physics, together with the judicious choice of the material parameters, models, and suitable discretization of the associated epitaxial layer structure. The validity of the approach is proven by comparing simulated data with experimental measurements resulting from fabricated micrometer-sized RTD devices featuring two different epitaxially-grown layer stacks.

The results show that the simulation software can correctly compute the peak current density, peak voltage, and the valley-to-peak voltage difference associated with the negative differential resistance region of the RTD heterostructure static current density-voltage characteristic at room temperature, all of which are key parameters in the design of these devices for use in oscillator circuits working at low-terahertz frequencies.

### 4.1 Introduction

As broadly discussed in Chapter 2, resonant tunnelling diodes (RTD) represent a promising technology suitable to design high-speed and high-efficient emitters and detectors required by next-generation terahertz (THz) applications, among which multi-gigabit wireless communication data-links and high-resolution imaging apparatuses. However, the main limitation of the technology is represented by the sources output power, limiting practical applicability.

Currently, indium phosphide (InP) RTD-based transmitters (Tx) have achieved output powers of up to around 1 mW in the 300 GHz-band [169], which have demonstrated short-range wireless communication with data-rates of up to 22 Gb/s along an 80 cm-long data-link [289]. Nonetheless, link budget estimations show that several milliwatt of output power are required to both increase channel bandwidth by several tens of gigabits per second and further extend the link distance to several metres, meeting the requirements of practical application scenarios [247].

In this context, as explained in Chapter 2, the diode maximum radio-frequency (RF) power  $P_{RF,max}$  is intimately related with its static current-voltage ( $IV$ ) characteristic, in particular, with the span of the negative differential resistance (NDR) region. Therefore, an accurate estimation of both the device available current density  $\Delta J = \Delta I/A = J_p - J_v$  (being  $\Delta I = I_p - I_v$  the peak-to-valley current difference and  $A$  the RTD mesa area) and the valley-to-peak voltage difference  $\Delta V = V_p - V_v$ , is essential to maximise the associated RF power, where peak and valley current densities  $J_p$  and  $J_v$ , and voltages  $V_p$  and  $V_v$ , represent a fingerprint of the RTD epitaxial structure.

The establishment of a clear device design methodology aimed at maximising  $P_{RF,max}$  in the low-THz band ( $\sim 100\text{--}300$  GHz) is yet to be developed and requires a reliable physics-based simulation approach capable of accurately predicting the electrical behaviour of the RTD device. Although few but highly-complex and accurate numerical simulation tools have been developed in the past (see NEMO [659] and nextnano [660, 661]), as well as more basic ones (see Wingreen [408]), none of them has found practical applicability in this context since, due to the modelling complexity (and resulting computational load), only basic structures can be typically investigated. On the other hand, Silvaco TCAD offers a complete device simulation suit, including physical-based electrical (and thermal) device performance evaluation (DC, AC, transient, etc.), as well as semiconductor manufacturing processes virtualization.

However, RTD approaches based on Silvaco Atlas are unclear, with missing or incomplete information about the employed physical models and material parameters [379, 662, 663]. Further, no accurate comparison between simulated and fabricated devices aimed at establishing the reliability of the software has been conducted so far. Indeed, any device investigation analysis/design study and associated output data resulting from simulation tools/codes which have not been accurately tested and benchmarked with experimental data, i.e., fabricated and measured devices, lack of scientific validity.

To address this problem, a technology computer-aided design (TCAD)-based method to reliably simulate indium gallium arsenide/aluminium arsenide ( $\text{In}_{0.53}\text{Ga}_{0.47}\text{As}/\text{AlAs}$ ) double-barrier RTD devices epitaxially-grown on lattice-matched InP substrates was developed in this thesis. The approach relies on the non-equilibrium Green's function (NEGF) formalism im-

plemented in Silvaco Atlas TCAD suite to accurately account for the physics of the device, as well as on the careful selection of the epitaxial layers material parameters, physical models, and appropriate discretisation of the RTD wafer structure. The developed simulation approach was then used to carry out a comprehensive investigation study aimed at understanding general design rules for  $P_{RF,max}$  maximisation, which will be discussed in Chapter 5.

## 4.2 NEGF method

As discussed in the preceding Section, an accurate estimation of the static current density-voltage ( $JV$ ) characteristic of the epitaxial structure is of key importance to carry out RTD design for RF power performance maximisation. In this regards, approximate semi-empirical analytical methods and standard numerical approaches based on the self-consistent solution of the single-electron Schrödinger's and Poisson's equations are widely employed to model the electrical properties of RTDs within the Landauer-Büttiker limit [361, 380], as discussed in Section 2.4 of Chapter 2.

However, a complete quantum electron transport treatment based on kinetic models is preferred to treat carrier transport at a quantum level and formally-include many-body interactions that lead to a generalised mixed-state electron description [309, 664, 665], including electron-electron elastic scattering, and, more importantly, dissipative processes, such as electron-acoustic and (longitudinal) optical phonons, alloy, impurity, and interface roughness-related inelastic scattering [666]. Indeed, a realistic RTD device is far from being a closed quantum environment described by a conservative Hamiltonian, but it can be rather considered as an open particles ensemble governed by the laws of non-equilibrium quantum statistical mechanics.

In this regard, the NEGF approach is considered among the most accurate methods to describe the process of carrier transport in nanoscale devices beyond the semi-classical limit [667–669]. The electron wave-like nature is fully-preserved and accounted in the NEGF formalism, treating electron transport at a fully-quantum dynamic level [670], differently from classical drift-diffusion or semi-classical Boltzmann transport equation (BTE)-based kinetic approaches [671], such as those relying on the Wigner's function via Liouville's equation [672, 673]. Indeed, as the system characteristic length scales become smaller than the scattering mean free path, the electronic transport physics description changes from an incoherent semi-classical picture governed by the BTE, to a more coherent and purely quantum mechanical framework where currents are modelled in terms probability density fluxes injected from ideal carrier reservoirs.

The inclusion of contacts and electronic wave-function amplitude and phase-breaking mechanisms (i.e., a microscopic description of quantum transport including interactions beyond the

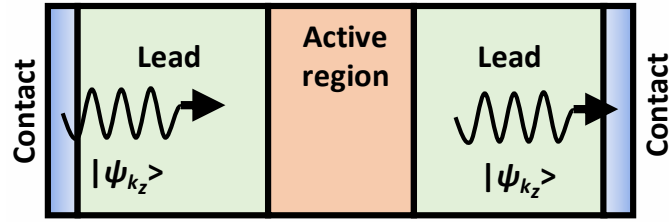


Figure 4.1: Schematic representation of a 1D nanodevice, including contacts, leads, and active region. A generic longitudinal pure coherent state  $|\psi_{k_z}\rangle$  is illustrated.

ballistic limit) is straightforward in the NEGF framework, and this can be accounted through the quantum field concept of scattering self-energy [674], contrarily to conventional BTE-based Monte Carlo numerical approaches [675], where scattering processes are included through computed scattering rates. Here, the electronic self-energy models the interaction between the electron and the surrounding environment. Indeed, electron transport in mesoscopic systems and nanostructures can be regarded as a co-existing regime governed by coherent, phase-breaking, and dissipative processes.

It would, therefore, seem that the NEGF method represents an appealing solution to accurately address the problem of quantum transport in nanoscale devices [676], including RTDs [397]. Due to the extensive mathematical treatment, only key concepts of the NEGF (or Keldysh) formalism are discussed in the below. Moreover, the treatment is restricted to the steady-state coherent picture, which is the limit considered in this work.

Conceptually-speaking, a one-dimensional (1D) nanodevice can be sub-divided into three regions: 1) contacts; 2) leads; and 3) active region. The contacts, modelled as semi-infinite regions, act as highly-doped carriers reservoirs described by the (equilibrium) Fermi-Dirac statistic according to a local electrochemical potential  $\mu_{e,c}$  (where  $e$  and  $c$  subscripts identify emitter and collector contacts) and the flat electrostatic potential  $U_z$  (being  $\hat{z}$  the longitudinal transport direction), from which a thermal equilibrium carrier flux is either injected into scattering states  $|\psi_{k_z}\rangle$  towards the device active region, or absorbed.

The leads connect the contacts to the device non-equilibrium core region and are modelled either through quasi-equilibrium or with ad-hoc non-equilibrium distributions obeying to the spatially-varying  $U_z$ . On the other hand, the active area is the main non-equilibrium regions. In this work, interaction mechanisms are not accounted and ballistic transport is assumed, as shown in Figure 4.1. In a double-barrier RTD device context, the extended emitter and collector regions are regarded as the leads, while the double-barrier quantum well (DBQW) represents the device active region.

In this context, a correct physical description of non-equilibrium quantum transport of carriers through the nanostructure requires the employment of many-body perturbation theory (MBPT) within a second quantisation scheme to account for correlation processes [677–679]. The quantum mixed-state description of the system is provided by a density matrix [680], generalising the classical Boltzmann distribution function model, where electron correlation is modelled through a correlation function  $G$ . Here,  $G$  can be interpreted as the reaction of the many-body interacting system to the "creation" of a particle at position  $\mathbf{r}$  (and state  $\mathbf{k}$ ) at time  $t$ , to its propagation to a position  $\mathbf{r}'$  (and state  $\mathbf{k}'$ ) and time  $t'$ , and to its final "annihilation". Generally speaking, the electronic correlation function  $G^n$  is modelled through the following expectation value [681]:

$$G^n(\mathbf{k}, \mathbf{k}', t, t') = \langle \hat{a}_{\mathbf{k}'}^\dagger(t') | \hat{a}_{\mathbf{k}}(t) \rangle \quad (4.1)$$

where  $\hat{a}$  and  $\hat{a}^\dagger$  (hermitian self-adjoint) are the creation and annihilation operators, respectively. In order to balance the outflow with the inflow of electrons inside the nanosystem for a correct kinetic description, a correlation function  $G^p$  can be introduced, which models the electrons inflow as an outflow of "missing electrons", i.e. conduction band (CB) holes.

Similarly, the semi-classical concept of scattering rate function  $S$ , which accounts for the rate at which electrons are scattered-in or out a state  $\mathbf{k}$ , is generalised to a scattering self-energy  $\Sigma$ . In this context, the Green's function, or correlation function,  $G$  has the role of propagator according to Feynman's diagram representation of quantum field theory [682, 683]. On the other hand, the self-energy acts as a non-local effective potential modelling the many-body interactions.

In the NEGF formalism,  $G^n$  and  $G^p$  are also identified as the lesser and greater Green's functions  $G^<$  and  $G^>$ , respectively, where  $G^n(\mathbf{k}, \mathbf{k}', E) \rightarrow -iG^<(\mathbf{k}, \mathbf{k}', E)$  and  $G^p(\mathbf{k}, \mathbf{k}', E) \rightarrow iG^>(\mathbf{k}, \mathbf{k}', E)$  [681]. On the other hand, the in-scattering and out-scattering functions  $\Sigma^{in}$  and  $\Sigma^{out}$  are associated with the corresponding lesser and greater self-energies  $\Sigma^<$  and  $\Sigma^>$ , respectively, where  $\Sigma^{in}(\mathbf{k}, \mathbf{k}', E) \rightarrow -i\Sigma^<(\mathbf{k}, \mathbf{k}', E)$  and  $\Sigma^{out}(\mathbf{k}, \mathbf{k}', E) \rightarrow i\Sigma^>(\mathbf{k}, \mathbf{k}', E)$  [681].

While the quantities  $G^n$ ,  $G^p$ ,  $\Sigma^{in}$ , and  $\Sigma^{out}$  (or  $G^{\lessgtr}$  and  $\Sigma^{\lessgtr}$ ) allow to describe correlation phenomena, i.e., keeping track of incoming/outcoming electrons in/out the system, the dynamics of electron transport inside the nanodevice is described through the retarded and advanced Green's functions  $G^R$  and  $G^A$ , and associated self-energies  $\Sigma^R$  and  $\Sigma^A$ , respectively, which are, as  $G^{\lessgtr}$  and  $\Sigma^{\lessgtr}$ , functions of the electron momentum and energy.

In particular,  $G^R$  describes the evolution of an electronic state from its injection into the system from the emitter contact, until its coherence is lost through either scattering into another state or absorption into the collector contact, while  $\Sigma^R$  models the many-body processes. On the other hand,  $G^A$  and  $\Sigma^A$  are the corresponding self-adjoints, i.e.,  $G^A = G^{R\dagger}$  and  $\Sigma^A = \Sigma^{R\dagger}$  [684].

Here, the self-energy is also used, through ad-hoc boundary terms, to model the coupling of the nanodevice inner region with the associated injection and "outjection" contacts.

The numerical solution of the NEGF problem of steady-state coherent electron transport in a nanodevice consists in computing the retarded and correlation Green's functions  $G^R$  and  $G^>$ , and associated self-energies  $\Sigma^R$  and  $\Sigma^<$ , from which all the physical observable of interest can be retrieved. To describe the numerical solution procedure in the case of a 1D nanostructure (uncoupled mode space approach), such as an  $n$ -type intra-band RTD, discretization of the problem in matrices form along  $\hat{z}$  is assumed by means of the finite element method (FEM), similarly as discussed in Section 2.4.4 of Chapter 2 in the case of a simple wave-function-based approach. Moreover, Datta's formalism is employed, which allows to deal with a single-electron Hamiltonian [684].

First, the retarded boundary self-energy of emitter and collector contacts  $\Sigma_{e,c}^{R,B}$  are computed imposing open boundary conditions to the system, analogously as described in Section 2.4.4 of Chapter 2. The total retarded boundary self-energy  $\Sigma^{R,B}$  is simply  $\Sigma_e^{R,B} + \Sigma_c^{R,B}$ . Then, Dyson's equation is solved for the retarded/advanced Green's function  $G^R$  [681]:

$$[G^R] = \{E_z[M] - [H_z] - [\Sigma^{R,B}]\}^{-1} \quad (4.2)$$

where  $E_z$  is the longitudinal energy, while  $[H_z]$  and  $[M]$  are the longitudinal Hamiltonian (modelling the electron dispersion relation and system electrostatic potential) and mass matrices of the FEM formulation.

Here, Dyson's equation can be regarded as the single-electron stationary Shrödinger's equation (see Chapter 2), in which  $\Sigma^{R,B}$  is added to model the openness of the system through the transparency of the contacts. However, differently from  $H_z$ ,  $\Sigma^{R,B}$  is non Hermitian ( $\Sigma^{R,B} \neq \Sigma^{R,A}$ ), i.e., it adds an imaginary part to the overall eigenvalues due to the form of the boundary terms.

This concept is represented by the contacts boundary broadening function  $\Gamma^B$  [681]:

$$[\Gamma^B] = i\{[\Sigma^{R,B}] - [\Sigma^{R,A}]\} = [\Gamma_e^B] + [\Gamma_c^B] = i \sum_{j=e,c} \{[\Sigma_j^{R,B}] - [\Sigma_j^{R,A}]\} \quad (4.3)$$

which has non-null boundary elements. From the above-mentioned considerations, it can be deduced that the NEGF method offers an elegant solution to deal with boundary effects.

Subsequently, the correlation (or lesser/greater) functions  $G^>$  are computed through Keldysh' equation [681]:

$$[G^>] = [G^R][\Sigma^<,B][G^A] \quad (4.4)$$

where the correlation (or lesser/greater) boundary self-energies  $\Sigma^{\gtrless,B}$  are retrieved invoking thermal equilibrium in the "fully-thermalised" contacts [681]:

$$\begin{aligned} [\Sigma^{<,B}] &= i f_n^e(E_z - \mu_e) [\Gamma^B] \\ [\Sigma^{>,B}] &= i \{ f_n^c(E_z - \mu_c) - 1 \} [\Gamma^B] \end{aligned} \quad (4.5)$$

where  $f_n^{e,c}$  are the equilibrium Fermi-Dirac distribution functions at the emitter and collector contacts defined in Chapter 2. In this context, the following equalities hold [681]:

$$\begin{aligned} [G^{<}] &= i f_n^e(E_z - \mu_e) [\mathcal{A}] \\ [G^{>}] &= i \{ f_n^c(E_z - \mu_c) - 1 \} [\mathcal{A}] \\ [\Gamma^B] &= i \{ [\Sigma^{>,B}] - [\Sigma^{<,B}] \} \end{aligned} \quad (4.6)$$

where  $\mathcal{A}$  is the spectral function [681]:

$$[\mathcal{A}] = i \{ [G^R] - [G^A] \} = i \{ [G^{>}] - [G^{<}] \} \quad (4.7)$$

which can be interpreted as the available local density of states (LDOS). In particular [681]:

$$[\mathcal{A}] = [G^R][\Gamma^B][G^A] = [\mathcal{A}_e] + [\mathcal{A}_c] = [G^R][\Gamma_e^B][G^A] + [G^R][\Gamma_c^B][G^A] \quad (4.8)$$

where  $\mathcal{A}_e$  and  $\mathcal{A}_c$  are the spectral functions of emitter and collector contacts, respectively.

Once  $G^R$  and  $G^{\gtrless}$  are computed, the system physical observables can be retrieved. Here,  $G^R$  contains information on  $\mathcal{T}_{DBQW}$ , wavefunctions (stationary eigenstates), and associated eigenenergies, while the electron density and LDOS can be retrieved through the diagonal elements of  $[G^{<}]$  and  $[\mathcal{A}]$  after accounting for multiplication constants derived from analytical integrations over the transverse wave-vector modulus  $k_T = (k_x, k_y)$ . For the electron density, an analytical integration in  $E_z$  is also required.

The flow-chart associated to a coherent NEGF solver is shown in Figure 4.2, which is similar to the one discussed in Section 2.4.4 of Chapter 2. Here, the electron density is used to solve Poisson's equation for the Hartree potential, from which the Hamiltonian is updated to retrieved  $G^R$  at the second iteration. Generally-speaking, at each bias point, Dyson's and Keldish' equations are iteratively and self-consistently solved with Poisson's equation (see Section 2.4.4 of Chapter 2) upon convergence starting from thermal equilibrium conditions in what, in NEGF terminology, is the "outer loop", analogously as seen in Section 2.4.4 of Chapter 2, where conservation laws for charge and current densities are met.

Assuming to deal with an  $n$ -type DBQW RTD device, the associated transmission coefficient  $\mathcal{T}_{DBQW}$  at a bias point  $V$  can be computed as [681]:

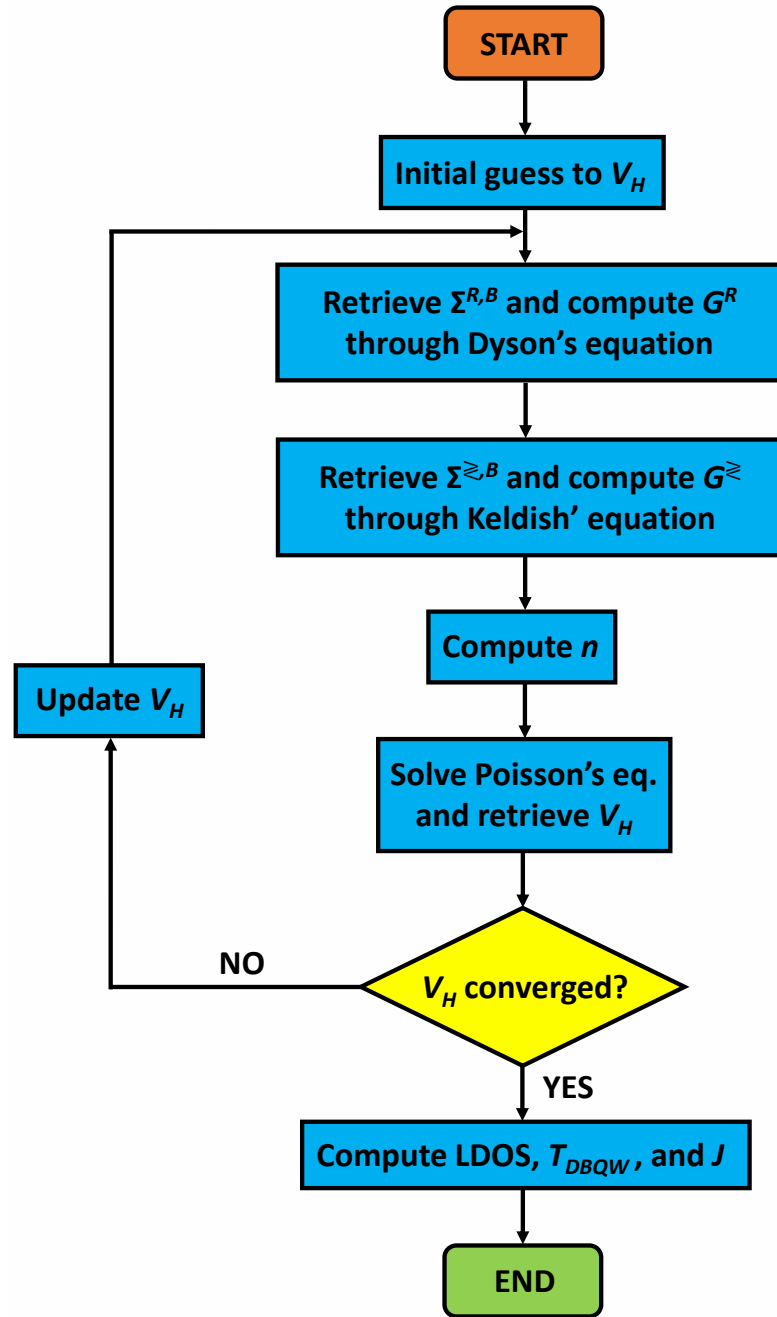


Figure 4.2: Coherent NEGF algorithm for the steady-state numerical solution of a 1D nanodevice (such as a 1D RTD), accounting for space charge effects.

$$\mathcal{T}_{DBQW}(E_z, V) = \hat{\text{Tr}}\{[\Gamma_e^B][G^R][\Gamma_c^B][G^A]\} \quad (4.9)$$

being  $\hat{\text{Tr}}$  the trace operator. The coherent component of the current density  $J$  in steady-state conditions is written as [684]:

$$J(V) \approx \frac{e}{2\pi\hbar} \int_0^{+\infty} \mathcal{T}_{DBQW}(E, V) [f_n^e(E - \mu_e) - f_n^c(E - \mu_c)] dE \quad (4.10)$$

Therefore [364, 681]:

$$\begin{aligned}
 J(V) &\approx \frac{em_e^*k_bT}{2\pi^2\hbar^3} \int_0^{+\infty} \mathcal{T}_{DBQW}(E_z, V) \log \left[ \frac{1 + \exp\left(\frac{\mu_e - E_z}{k_B T}\right)}{1 + \exp\left(\frac{\mu_e - E_z - eV}{k_B T}\right)} \right] dE_z = \\
 &= \frac{em_e^*k_bT}{2\pi^2\hbar^3} \int_0^{+\infty} \hat{\text{Tr}}\{[\Gamma_e^B][G^R][\Gamma_c^B][G^A]\} \log \left[ \frac{1 + \exp\left(\frac{\mu_e - E_z}{k_B T}\right)}{1 + \exp\left(\frac{\mu_e - E_z - eV}{k_B T}\right)} \right] dE_z
 \end{aligned} \tag{4.11}$$

where  $V = (\mu_e - \mu_c)/e$ . In this sense, Eq. (2.65) corresponds to the Landauer formula for ballistic transport (as discussed in Section 2.4.2.2 of Chapter 2) written within the NEGF framework.

In the present work, scattering processes are not included in the simulations, which are conducted within the ballistic limit. Indeed, it is shown in this Chapter that the coherent approach is more than sufficient to compute most of the features associated to the static  $JV$  characteristic of the RTD epitaxial structures considered in this work.

## 4.3 Simulation of the RTD epitaxial structure DC JV curve

### 4.3.1 Epitaxial structures design

To establish the RTD simulation approach, the static  $JV$  curve of two epitaxial structures under test (ESUT) was first simulated in Atlas through the NEGF method. The ESUT were then

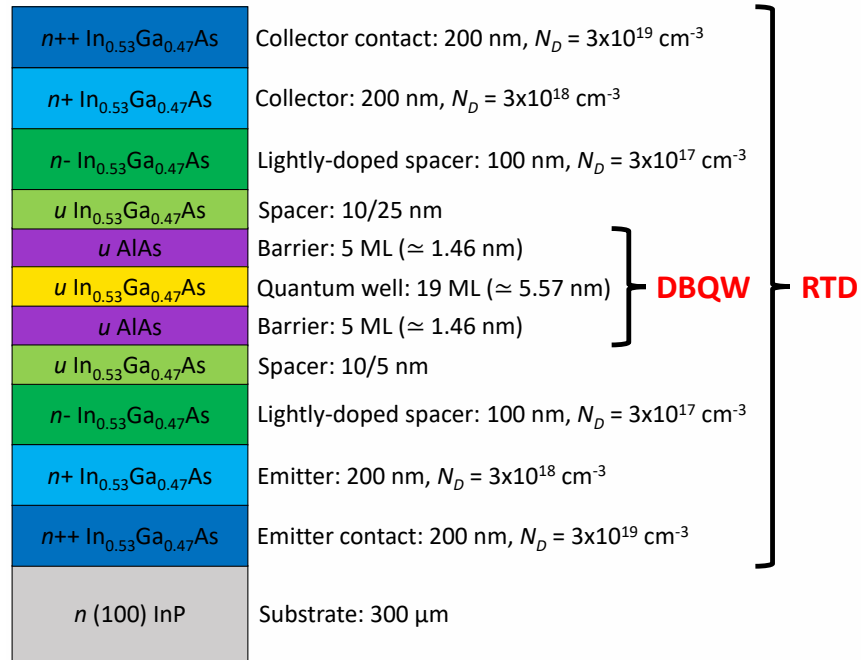


Figure 4.3: Epitaxial structures under test, indicating layers name, thickness, and doping level. The DBQW region is highlighted. Layers nomenclature assumes the top contact to be forward biased with respect to the bottom one.

epitaxially-grown through molecular beam epitaxy (MBE) on InP substrates, after which RTD devices were fabricated and measured. Experimental results were then compared with the simulations.

The  $n$ -type intra-band RTD ESUT are depicted in Figure 4.3. They consist of a lattice-matched to InP  $\text{In}_{0.53}\text{Ga}_{0.47}\text{As}/\text{AlAs}$  DBQW heterostructure, featuring moderate AlAs barrier thickness of around 1.46 nm (5 monolayers (ML)) and an around 5.57 nm-thick (19 ML)  $\text{In}_{0.53}\text{Ga}_{0.47}\text{As}$  quantum well (QW). Outside of the active region, undoped and 100 nm-thick lightly-doped ( $N_D = 3 \times 10^{17} \text{ cm}^{-3}$ ) spacer layers, 200 nm-thick emitter and collector regions ( $N_D = 3 \times 10^{18} \text{ cm}^{-3}$ ), and 200 nm-thick heavily-doped contact layers ( $N_D = 3 \times 10^{19} \text{ cm}^{-3}$ ) complete the heterostructures (where  $N_D$  is the associated doping concentration), which only differ in the undoped spacer layers thickness: the ESUT #2 emitter and collector spacers were set to 5 nm and 25 nm, respectively, while the ESUT #1 features 10 nm at both sides.

The wafer structures were grown by a partner in the TeraApps consortium at the University of Würzburg, in particular, using molecular beam epitaxy (MBE) on 300  $\mu\text{m}$ -thick lattice-matched 2" sulfur (S)-doped  $n$ -type (100)-oriented InP substrates. The growth temperature  $T$  was set to 475 °C, arsine ( $\text{AsH}_3$ ) was employed as gas precursor for arsenic (As), doping was carried out employing silicon (Si) donor atoms, while the conductive substrates were chosen to facilitate the growth schedule.

The idea behind the adopted design approach was to test the capability of the simulation software in capturing small variations in the DC  $JV$  characteristic due to a minor change at the epitaxial structure level. Barriers, QW, and emitter spacer layers were designed to achieve low peak voltage  $V_p < 2 \text{ V}$  and low current density operation ( $J_p < 150 \text{ kA/cm}^2$ ), which were intended to increase the accuracy of the comparison study by reducing thermal dissipation, while the collector spacer layers were designed to increase the NDR voltage span ( $\Delta V > 0.5 \text{ V}$ ), which is typically the case of epi-designs meant to operate in the low-THz range [169], as will be discussed in Chapter 5.

The estimated intrinsic cut-off frequency limit  $f_{in} = 1/4\tau_{in}$  of the ESUT #1 and #2 is around 362 GHz and 572 GHz, respectively, where the estimated electron intrinsic delay time  $\tau_{in} = \tau_{dbqw} + \tau_t/2$  (being  $\tau_{dbqw}$  and  $\tau_t$  the DBQW tunnelling time and transit time across the depletion regions, respectively) is around 0.69 ps and 0.44 ps, respectively, from the simulated transmission coefficient and assuming the  $\text{In}_{0.53}\text{Ga}_{0.47}\text{As}$  electron saturation velocity  $v_{e,s} \sim 3 \times 10^7 \text{ cm/s}$  [416]. However, the cut-off frequency could not be estimated from the measured scattering (S)-parameters due to the employed conductive substrates. Further details on the RTD heterostructure frequency-response estimation procedure are provided in Chapter 6.

Table 4.1: RTD epitaxial structures simulation material parameters\*.

Compound	$m_e^*$ [ $m_0$ ]	$m_v^*$ [ $m_0$ ]	$E_g$ [eV]	$N_c$ [ $\text{cm}^{-3}$ ]	$N_v$ [ $\text{cm}^{-3}$ ]
In <sub>0.53</sub> Ga <sub>0.47</sub> As	0.041	0.467	0.738	$2.12 \times 10^{17}$	$8.01 \times 10^{18}$
AlAs	0.146	0.79	2.153	$1.50 \times 10^{19}$	$1.76 \times 10^{19}$
Compound	$n_i$ [ $\text{cm}^{-3}$ ]	$\chi_e$ [eV]	$\epsilon_{r,0}$ [ $\epsilon_0$ ]	$\mu_{e,l}$ [ $\text{cm}^2\text{V}^{-1}\text{s}^{-1}$ ]	
In <sub>0.53</sub> Ga <sub>0.47</sub> As	$8.24 \times 10^{11}$	4.55	13.9	$2.52 \times 10^4$	
AlAs	13	3.50	10.1	$1.85 \times 10^2$	

\* In the above,  $m_e^*$  is the electron effective mass,  $m_v^*$  is the valence band density of states effective mass,  $m_0 \sim 9.109 \times 10^{-31}$  kg is the electron mass at rest,  $E_g$  is the energy band gap,  $N_c$  is the conduction band effective density of states,  $N_v$  is the valence band effective density of states,  $n_i$  is the intrinsic carriers concentration,  $\chi_e$  is the electron affinity,  $\epsilon_{r,0}$  is the static relative dielectric constant,  $\epsilon_0 \sim 8.854 \times 10^{-12}$  F/m is the vacuum permittivity, while  $\mu_{e,l}$  is the low-field electron mobility.

### 4.3.2 NEGF simulation approach based on Silvaco Atlas TCAD

In order to simulate the ESUT, a simulation deck was created and sub-divided into four main parts: 1) meshing and regions/electrodes definition; 2) material parameters; 3) models; and 4) computation. In order to achieve good balance between computational cost and simulation accuracy, the spatial mesh grid size was set to 0.01 nm within the non-equilibrium DBQW region, and progressively increased up to 0.05 nm in the quasi-equilibrium emitter and collector extended contacts. The full simulation deck is provided in Appendix D.

The material parameters associated to In<sub>0.53</sub>Ga<sub>0.47</sub>As or AlAs were both taken from the literature [75, 445–447] or derived, and are reported in Table 4.1. These include the electron  $m_e^*$  and valence band (VB) density of states (DOS)  $m_v^*$  effective mass, energy band gap  $E_g$ , electron affinity  $\chi_e$ , static relative dielectric constant  $\epsilon_{r,0}$ , and low-field electron mobility  $\mu_{e,l}$ . Here, the parameters of In<sub>0.53</sub>Ga<sub>0.47</sub>As are computed through Vegard’s law by linearly interpolating the associated binary compounds within the virtual crystal approximation (VCA) [375]:

$$P(\text{In}_{0.53}\text{Ga}_{0.47}\text{As}) = (1 - x)P(\text{InAs}) + xP(\text{GaAs}) \quad (4.12)$$

being  $x = 0.47$ , and quadratically-correcting through bowing parameters if available, where  $P$  is one of the aforementioned parameters. Conduction and valence band effective density of states  $N_c$  and  $N_v$ , respectively, as well as the intrinsic carriers concentration  $n_i$ , are then computed as [165]:

$$N_{c/v} = 2M_{c,v} \left[ \frac{2\pi m_{e/v}^* k_B T}{h^2} \right]^{\frac{3}{2}} \quad (4.13)$$

where  $M_{c,v}$  is the number of equivalent energy minima in the CB and VB, respectively, being  $M_c = 1$  and 3 for  $\text{In}_{0.53}\text{Ga}_{0.47}\text{As}$  and AlAs, respectively, and  $M_v = 1$ , while [165]:

$$n_i = (N_c N_v)^{1/2} \exp \left[ -\frac{E_g}{2k_B T} \right] \quad (4.14)$$

being  $k_B \sim 8.617 \times 10^{-5}$  eV/K the Boltzmann constant. Moreover, the employed CB offset  $|\Delta E_c|$  at the  $\text{In}_{0.53}\text{Ga}_{0.47}\text{As}/\text{AlAs}$  heterointerface discontinuity is set to 1.04 eV, which is compatible with experimentally-extracted values from photo-luminescence excitation spectroscopy measurements [685].

The formalism implemented in Silvaco Atlas TCAD deals with the NEGF heuristically by using elementary kinetic arguments based on a one-particle picture, as described in Section 4.2, which is intended to simplify the many-body, second quantisation, and diagrammatic theories for non-equilibrium processes based on quantum-field theory and non-equilibrium quantum statistical mechanics introduced by Kadanoff, Baym, and Keldysh thanks to the influence of Schwinger's school [686–688]. The 1D Schrödinger's and Poisson's equations are solved numerically and self-consistently upon convergence given the input mesh-grid at RT through finite-elements along the longitudinal transport direction  $\hat{z}$  to compute potential, bands profile, and DBQW resonant eigenstates and associated eigenenergies.

To do that, NEGF quantum transport equations in Dyson's and Keldish' forms (Eq. (4.2) and (4.4)) are iteratively and recursively solved at each bias point for both the retarded and correlation Green's functions  $G^R$  and  $G^<$ , respectively, starting from thermal equilibrium conditions (initial guess), similarly as illustrated in Figure 4.2. As already discussed,  $G^R$  carries information on the system eigenstates/eigenenergies and  $\mathcal{T}_{DBQW}$  (as well as on the LDOS through  $[\mathcal{A}]$ ), while  $G^<$  on electron and current densities. Since transport is 1D (being the electron wave-vector  $\mathbf{k} = k_z \hat{z}$ ), charge and current densities are obtained by analytically-integrating over  $k_T$ . Moreover, since current density is computed at a quantum level, continuity equation is not invoked and only Poisson's equation for the potential is solved.

At the moment, the software does not account for any scattering process and assumes ballistic transport [689], neglecting any incoherent conduction mechanism. In this limit, the electron is represented through a single-particle wave-function which keeps phase coherency over the entire nanodevice length, i.e., the eigenstate does not change its energy and momentum during its space/time evolution. Thus, resonant tunnelling is purely coherent rather than described by sequential tunnelling. However, it is worth to underline that, if scattering effects are neglected, the coherent and sequential tunnelling pictures give the same steady-state DC JV curve [311].

Therefore, the NEGF density matrix-like mixed-state description of the system is simplified to a "pure" single-electron Hamiltonian, without including any scattering self-energies. As a consequence, the only implemented self-energies are the retarded and correlation boundary self-energies  $\Sigma_{e,c}^{R,B}$  (and so  $\Gamma^B$  through Eq. (4.3)) and  $\Sigma_{e,c}^{<,B}$  (through Eq. (4.5)), respectively, which are folded into the system Hamiltonian to model the openness of the quantum ensemble through the semi-infinite emitter and collector contacts boundaries. In particular, while  $\Sigma_{e,c}^{R,B}$  carries information on the contacts LDOS,  $\Sigma_{e,c}^{<,B}$  accounts for their carriers statistics.

Neumann's boundary conditions are set for the potential to model Ohmic contacts, while open-boundary conditions are set for carriers which are, in the context of the FEM problem, numerically-implemented within the quantum transmitting boundary method (QTBM), which models Schrödinger's equation with open-boundary contacts [690, 691]. At the same time, the Fermi-Dirac distribution is adopted to model carrier statistics in the fully-thermalised anode and cathode, and quasi-equilibrium extended contacts regions. Further information about the NEGF solver implemented in Silvaco Atlas TCAD can be found in [692].

To simplify the electronic band structure treatment, the single-band effective mass approximation is adopted to model the electron dispersion relation in the CB. This prevents the employment of computationally-demanding multi-band approaches [693] needed to account for band warping and non-parabolicity around CB minima caused by conduction-to-valence band states coupling in very-narrow-gap semiconductor materials (whose  $E_g$  is typically way below 0.5 eV [694]), which would be required to study carrier transport under the effect of scattering processes, especially at high-(longitudinal) electric fields.

However, this can be neglected otherwise without excessively losing in physical accuracy and substantially reducing the amount of required computational resources, increasing simulation efficiency. In this context, typical RTD devices employed in oscillators operating below around 300 GHz make use of lattice-matched to InP  $\text{In}_{0.53}\text{Ga}_{0.47}\text{As}$  [169], whose room temperature (RT)  $E_g$  is around 0.74 eV [446], improving epitaxial growth quality and reproducibility levels. Further details with regard to this point will be provided in Chapter 5.

At the same time, the moderately-thick AlAs barriers are modelled at the  $X$  point of the associated first Brillouin zone through a normalised DOS effective mass  $m_e^* \sim 0.71$ , while  $\Gamma$ – $\Gamma$  transport ( $\text{In}_{0.53}\text{Ga}_{0.47}\text{As}$ –AlAs/AlAs– $\text{In}_{0.53}\text{Ga}_{0.47}\text{As}$ ) is assumed by means of a normalised tunnelling effective mass  $m_e^* \sim 0.146$ . Here,  $\Gamma$ – $X$  and  $X$ – $\Gamma$  transport is not accounted since negligible. Furthermore, strain effects in the DBQW region are also neglected, which results to be a good approximation since the lattice constant mismatch between the  $\text{In}_{0.53}\text{Ga}_{0.47}\text{As}$  QW and the AlAs barriers is only around 3 % [695], simplifying the assembling of the Hamiltonian

and FEM matrices. This modelling approach has successfully demonstrated to provide with physically-realistic current density levels for the RTD heterostructures analysed in this work.

Furthermore, the RTD parasitic series resistance  $R_s$  was neglected in the simulations. Indeed, although the effect of  $R_s$  on the device static  $IV$  characteristic is represented by the shift of the positive differential resistance (PDR) regions along the voltage axis [696], it is shown in this Chapter that this is negligible for small device sizes. However, load line effects can significantly affect the  $IV$  curve at large mesa areas, as discussed in Section 4.3.4.

The ESUT were simulated in steady-state-conditions and under forward bias, meaning that the device top contact (collector/cathode) was positively-biased with respect to the bottom one (emitter/anode). Indeed, RTD devices employed in THz oscillators are designed to work along one polarisation direction, typically, forward bias, therefore, emitter and collector regions are individually-designed for performance optimisation. The voltage range was set to 0–2 V with a step of 10 mV to trade-off between numerical convergence and computational time.

The simulations were carried out employing a Dell Precision 5820 workstation with the following computational capability; CPU: Intel Core i9-10900X; RAM: 32 GB DDR4 SDRAM. The simulation time was around 4 h and 50 min for the ESUT #1, and around 5 h and 35 min for the ESUT #2, which corresponds to around 1 min and 27 s, and 1 min and 40 s per bias point, respectively. The full simulation deck is provided in Appendix D. It would, therefore, seem that, in the context of the RTD heterostructures considered in this work, Silvaco Atlas offers an interesting TCAD simulation solution which can be run on commercial desktops/laptops by keeping low computational requirements.

From an  $n$ -type intra-band RTD epitaxial design perspective, RT ( $T = 300$  K) information on the CB edge energy profile, electron density distribution, DBQW quasi-bound resonant states, and transmission coefficient energy spectrum at thermal equilibrium and under non-equilibrium conditions are required, together with the static  $JV$  curve in steady-state conductions. Moreover, information about the LDOS energy spectrum in proximity to the DBQW region is also of interest.

For instance, Figures 4.4, 4.5, 4.6, and 4.7 show some of aforementioned quantities computed by simulating the ESUT #1. Figure 4.4 outlines the CB edge energy profile  $E_c(z)$  ( $\Gamma$  point) and electron density  $n(z)$  at RT and thermal equilibrium close to the DBQW region, as well as first ( $i = 1$ ) and second ( $i = 2$ ) quasi-bound states resonant energy levels  $E_i$  and corresponding envelope-function square modulus  $|\phi_i(z)|^2$ , where  $E_i = E_{i,z}$  and  $\phi_i(z)$  is the longitudinal component of the wave-function associated to the bottom of the corresponding subband.

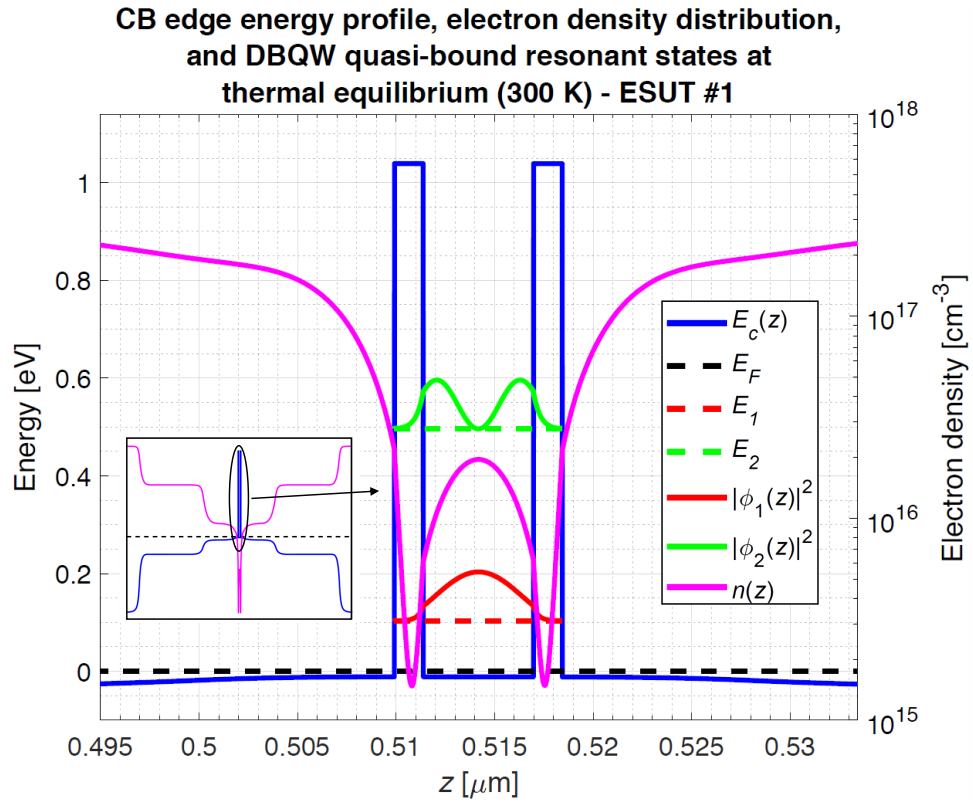


Figure 4.4: Computed CB edge energy profile and electron density distribution of the ESUT #1 at RT and thermal equilibrium close to the DBQW region, together with associated first and second quasi-bound resonant states (energies and envelope wave-functions), as well as a zoom-out over the entire device structure. In the above,  $|\phi_i(z)|^2$  is given in arbitrary units and  $E_F$  is the Fermi level (energy reference).

Figure 4.5 shows the transmission coefficient energy spectrum  $\mathcal{T}_{DBQW}(E_z, V)$  of the heterostructure at RT and thermal equilibrium, while Figure 4.6 the LDOS in proximity to the DBQW under the same operating conditions. Furthermore,  $\mathcal{T}_{DBQW}$  and the LDOS are also shown at peak resonance ( $V = V_p$ ) in Figures 4.5 and 4.7. This information provides insight to RTD operation and a basis for device design that gives a desired  $JV$  characteristic.

### 4.3.3 RTD devices fabrication and DC characterisation

RTD devices with square top mesa area  $A = 3 \times 3 \mu\text{m}^2$ ,  $4 \times 4 \mu\text{m}^2$ ,  $5 \times 5 \mu\text{m}^2$ ,  $6 \times 6 \mu\text{m}^2$ , and  $7 \times 7 \mu\text{m}^2$  were then fabricated through low-cost optical lithography on the grown wafers using the designed mask layout compatible with conductive substrates, as described in Chapter 3. The contacts were realised employing a titanium/palladium/gold metal stack (Ti/Pd/Au=20/30/150 nm), while the lateral undercut  $\sigma$  due to anisotropic wet etching in the mesas formation was estimated to be around 460 nm and 490 nm per side for the ESUT #1 and #2, respectively, through accurate scanning electron microscopy (SEM) inspection. To passivate the devices and provide bond-pads insulation, a 1.8  $\mu\text{m}$ -thick polyimide PI-2545 layer was employed.

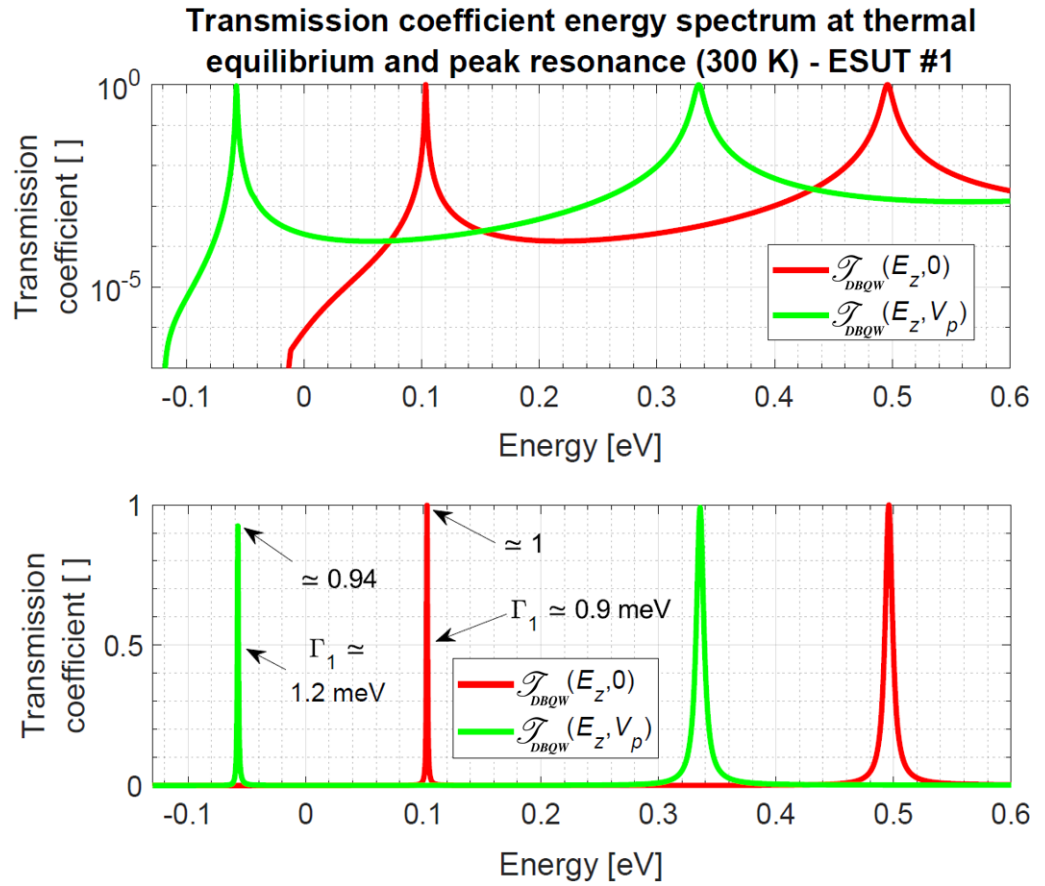


Figure 4.5: Computed transmission coefficient energy spectrum (linear (top) and log (bottom) scales) at RT at both thermal equilibrium and peak resonance ( $V = V_p$ ) of the ESUT #1. Peak and energy broadening  $\Gamma_1$  values of the resonance associated with the first resonant metastable state are also shown in both conditions. The drop of the peak value and the increase of  $\Gamma_1$  with bias, i.e., energy broadening, is attributed to the reduction of symmetry associated with the DBQW potential profile.

Moreover, the heavily-doped collector and emitter contacts surfaces were treated prior to metal evaporation through a basic ex-situ de-oxidation cleaning procedure based on ozone ( $O_3$ ) atmosphere exposure under ultra-violet (UV) light (UV/ $O_3$ ) for 4 min and 30 s, followed by a dip in a hydrochloric acid-based dilute solution ( $HCl:H_2O=1:3$ ) for 5 min. The loading time in the metal evaporator chamber was kept under 50 s. Furthermore, no extended pre-processing UV/ $O_3$  and in-situ argon (Ar) gun-based treatments were carried out during the two fabrication runs. A photo-micrograph and an SEM image of one of the fabricated  $4 \times 4 \mu m^2$ -large RTD device are shown in Figure 4.8 as visual example.

Since the processed wafers featured conductive substrates, the on-mask transmission line measurement (TLM) structures could not be probed. Therefore, a separate fabrication run employing another RTD wafer, featuring an analogous cap layer (composition and doping level) and a semi-insulating (SI) InP substrate, was carried out employing the TLM structures mask

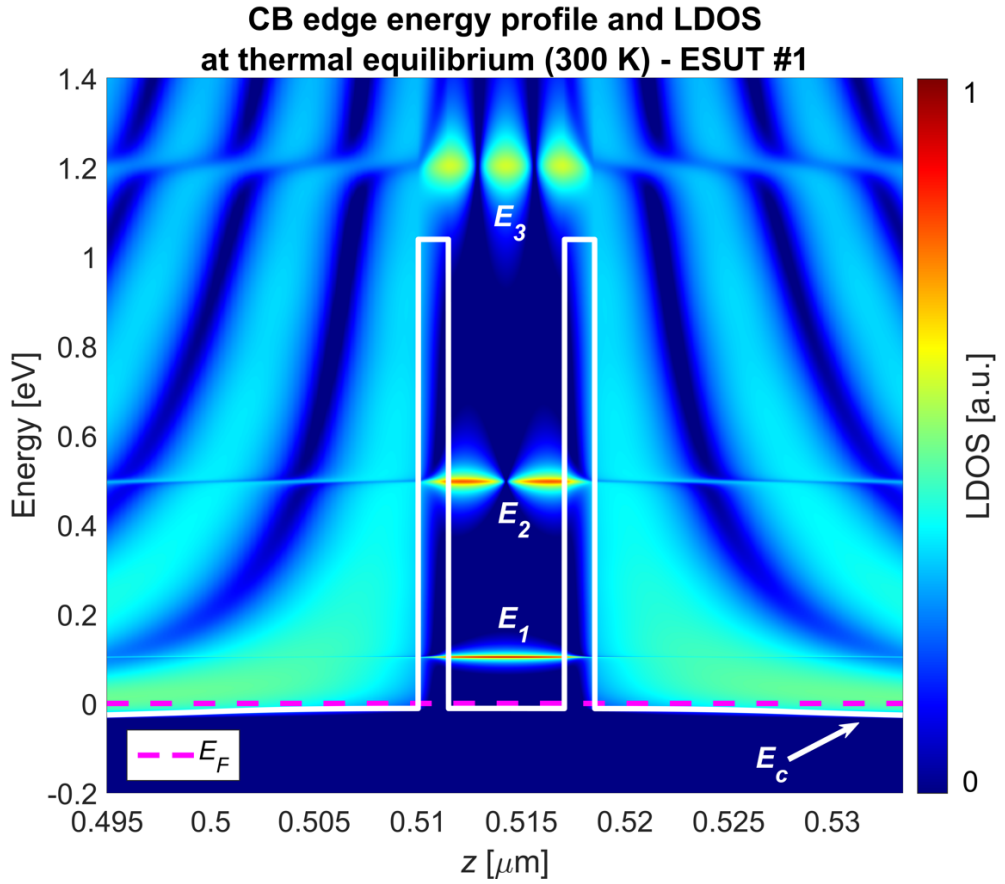


Figure 4.6: Computed CB edge energy profile and LDOS (log scale with arbitrary units) of the ESUT #1 at RT and peak resonance ( $V = V_p$ ) close to the DBQW region, revealing the first and second quasi-bound resonant states, as well as a third state (unbound). In the above,  $E_F$  is the Fermi level.

layout described in Chapter 3 and adopting the same Ohmic contacts fabrication procedure used for the RTD devices. The extraction procedure based on TLM structures measurements (as discussed in Appendix C) is illustrated in Figure 4.9, while an example of the associated extracted parameters for a measured structure are reported in Table 4.2. The estimated specific contact resistivity  $\rho_c$  was around  $13 \times 10^{-8} \Omega \text{ cm}^2 = 13 \Omega \mu\text{m}^2$ , with a discrepancy of around  $\pm 1 \Omega \mu\text{m}^2$  between different measured TLMs on both samples. This is around one order of magnitude higher compared to state-of-the-art Ohmic contacts to InGaAs [461], which is attributed to the unoptimised cleaning procedure adopted during fabrication. Despite that, the fabricated contacts can be regarded as good Ohmics in the context of RTD devices operating around 300 GHz.

The fabricated RTD devices were measured at RT and under forward bias (collector positively polarised with respect to the emitter one) through a DC sweep analysis within the voltage range 0–2 V with step 10 mV by using a 4155C semiconductor parameter analyser (SPA) from Keysight Technologies, as described in Chapter 3, in order to retrieve the experimental static  $IV$  characteristics.

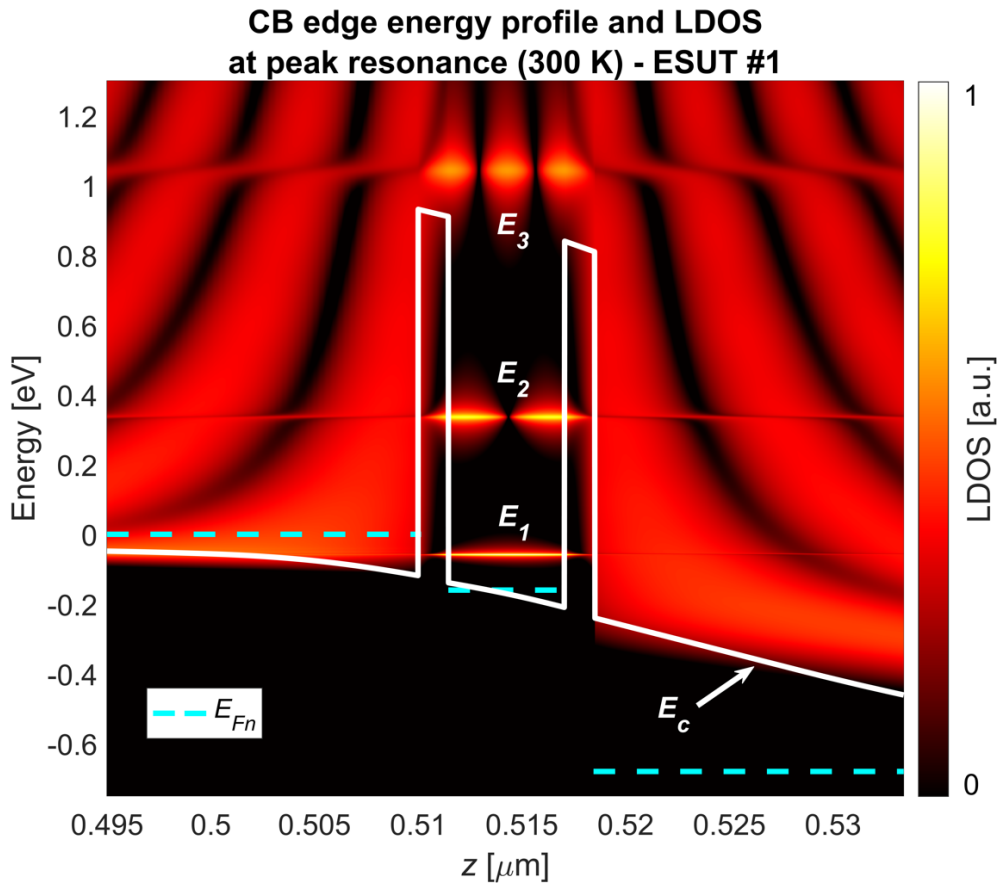


Figure 4.7: Computed CB edge energy profile and LDOS (log scale with arbitrary units) of the ESUT #1 at RT and peak resonance ( $V = V_p$ ) close to the DBQW region, revealing the first and second quasi-bound resonant states, as well as a third state (unbound). In the above,  $E_{Fn}$  is the electron quasi-Fermi level at the emitter/collector boundaries (contacts), as well as at the QW middle point.

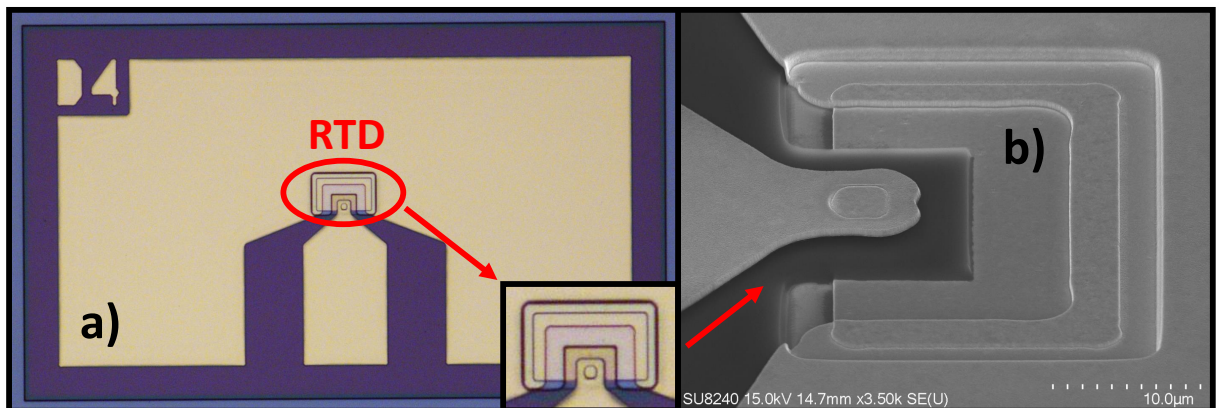


Figure 4.8: In a), a photo-micrograph of a fabricated  $4 \times 4 \mu\text{m}^2$ -large RTD device, as well as a zoom-in over the RTD region; in b), an SEM image zoom-in over the opened via.

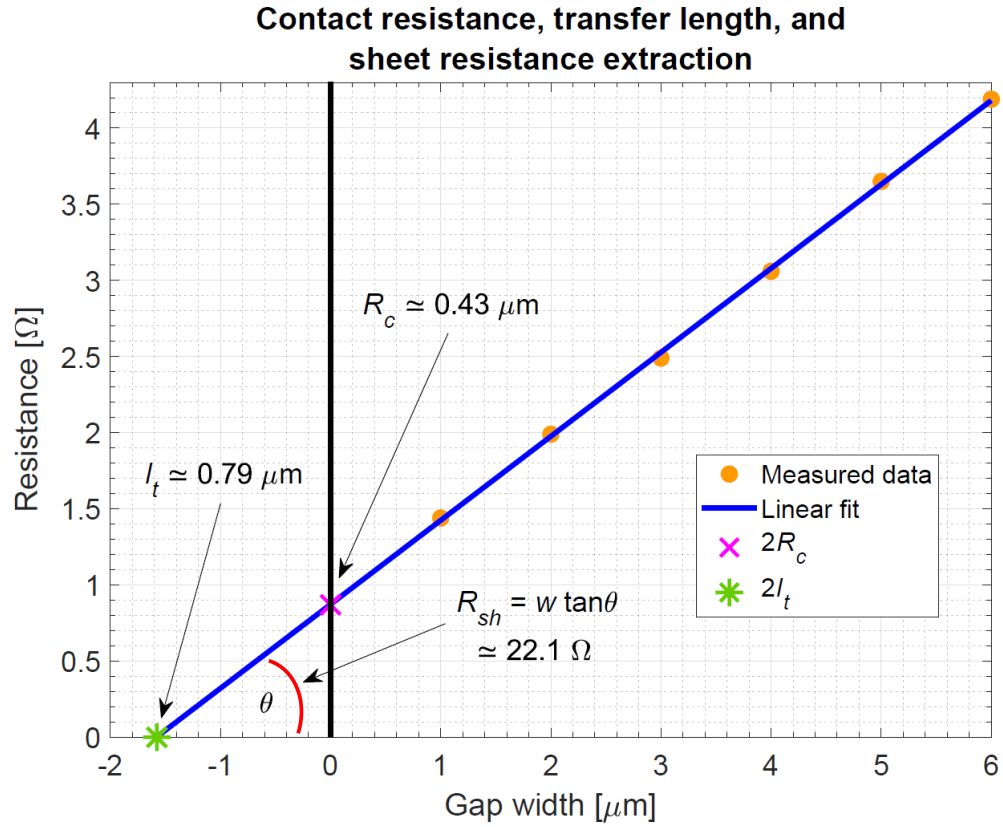


Figure 4.9: Extraction of the contact resistance  $R_c$ , semiconductor sheet resistance  $R_{sh} \propto \tan \theta$ , and transfer length  $l_t = |l_t|$  through linear fitting over the measured data.

Table 4.2: Measured/extracted parameters obtained from TLM structures characterisation\*.

$R_1$ [ $\Omega$ ]	$R_2$ [ $\Omega$ ]	$R_3$ [ $\Omega$ ]	$R_4$ [ $\Omega$ ]	$R_5$ [ $\Omega$ ]	$R_6$ [ $\Omega$ ]	$R_{sh}$ [ $\Omega$ ]	$R_c$ [ $\Omega$ ]	$l_t$ [ $\mu\text{m}$ ]	$\rho_c$ [ $\Omega \mu\text{m}^2$ ]
1.44	1.99	2.49	3.06	3.65	4.19	22.1	0.43	0.79	13

\* In the above,  $R_{t,i}$  (where  $i = 1, \dots, 6$ ) is the measured total resistance,  $R_{sh}$  is the extracted semiconductor sheet resistance,  $R_c$  is the extracted contact resistance, while  $l_t$  is the extracted transfer length.

#### 4.3.4 Simulation versus experimental results: comparison and discussion

Figures 4.10 and 4.11 compare the simulated with the measured static  $IV$  characteristics of the fabricated ESUT #1 and #2 RTD devices at RT and under forward bias, respectively. Several devices per mesa area, randomly distributed across the whole samples (around  $1.2 \text{ cm}^2$ -large), were measured to achieve statistical significance, and no differences in their electrical properties were revealed (i.e., smaller than the SPA set resolutions, which were 0.1 mA and 10 mV for currents and voltages, respectively), confirming the high wafer structural uniformity achieved during the growth process. Indeed, low-strain budget InP RTD heterostructures, such as the ones reported in this work, are characterised by high wafer structural uniformity and do not typ-

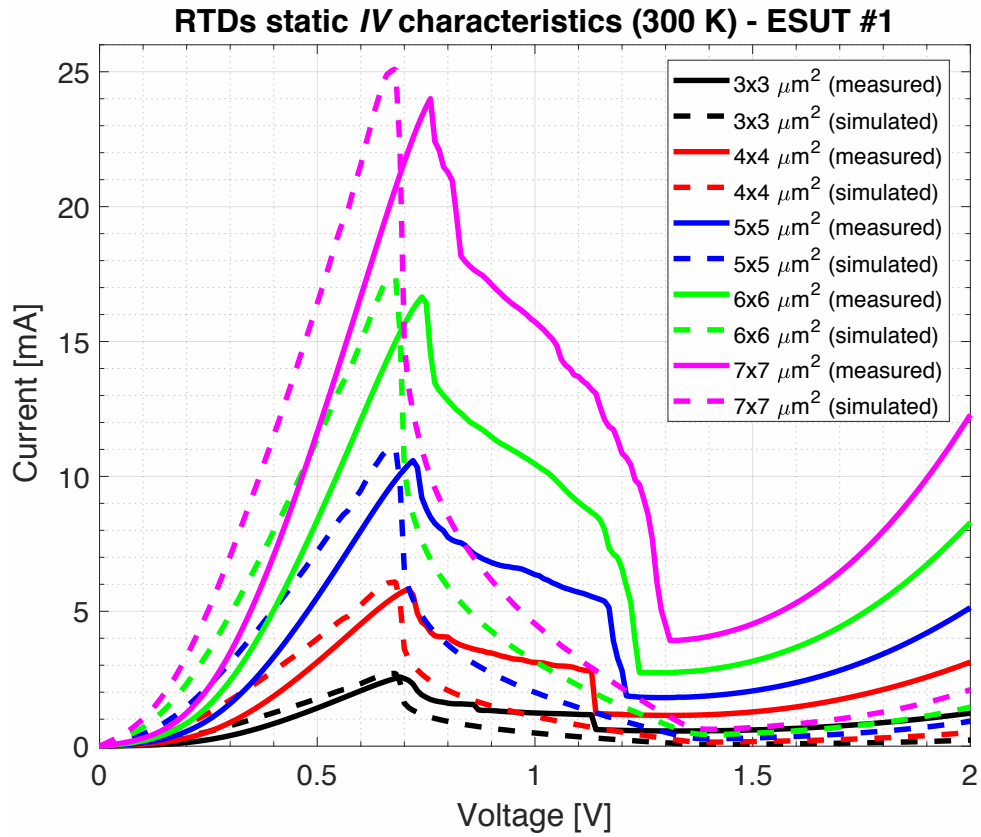


Figure 4.10: Comparison between simulated and measured static  $IV$  characteristics at RT and under forward bias of the RTD devices featuring the ESUT #1.

ically suffer from monolayer fluctuation and island formation [697].

The simulated and experimentally-extracted electrical quantities of both the ESUT #1 and #2, and related RTD devices, including  $J_p$ ,  $J_v$ ,  $V_p$ ,  $V_v$ , and  $\Delta V$ , are reported in Table 4.3. The simulated curves are smooth in the NDR region, while the measured ones show the typical plateau-like behaviour due to low-frequency parasitic bias oscillations [414]. An hysteretic fingerprint in the NDR region among polarisation switching was noticed for the measured devices, which is well-known to be caused by charge accumulation in the QW under non-equilibrium conditions, subsequently shifting the RTD internal electrostatic potential, i.e., intrinsic bistability [311, 698]. However, this effect was not taken into account in the analysis since it was observed that it doesn't play a significant role in influencing the electrical span of the NDR region, nor the electrical quantities associated with the DC  $IV$  curve (including  $V_p$ ).

#### 4.3.4.1 Peak, valley, and available current densities

The computed  $J_{p,s}$  and  $J_{v,s}$  of the ESUT #1 are around  $63 \text{ kA/cm}^2$  and  $2 \text{ kA/cm}^2$ , respectively, while the experimentally-extracted  $J_{p,m}$  and  $J_{v,m}$  are around  $60 \text{ kA/cm}^2$  and  $11 \text{ kA/cm}^2$ , respectively, after correcting the devices top mesa area due to anisotropic wet etching. On the other

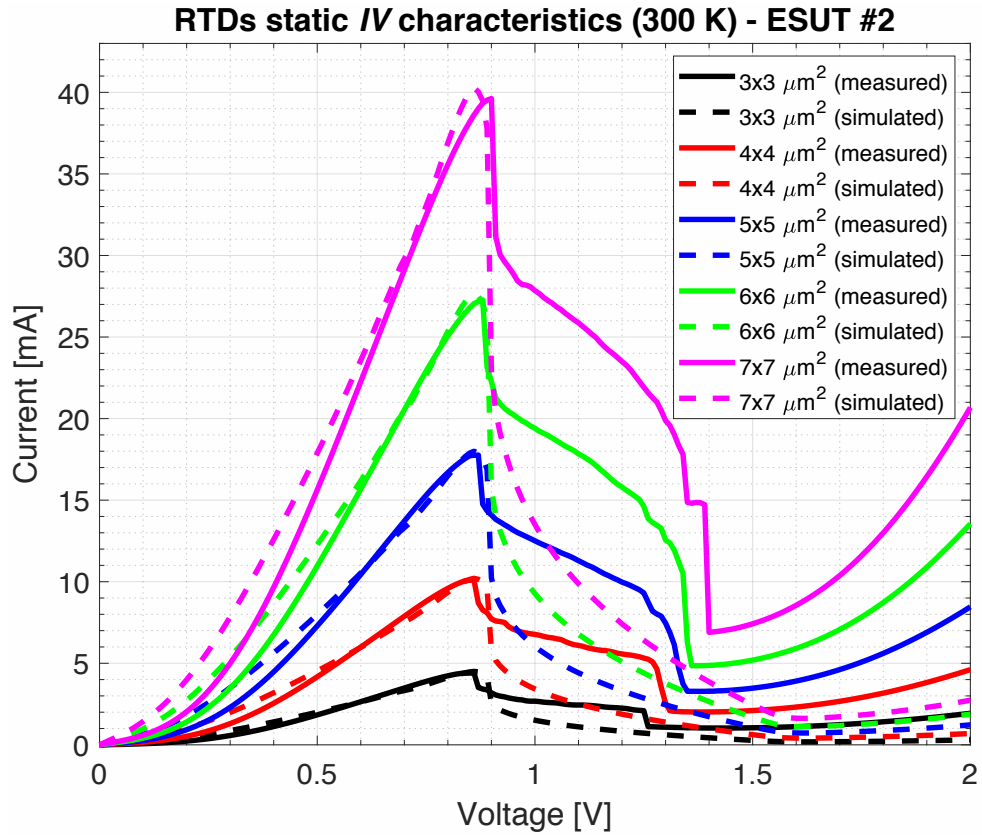


Figure 4.11: Comparison between simulated and measured static IV characteristics at RT and under forward bias of the RTD devices featuring the ESUT #2.

Table 4.3: Electrical quantities of the ESUT #1 and #2, and related RTD devices\*.

ESUT	$J_{p,s}$ [kA/cm <sup>2</sup> ]	$J_{v,s}$ [kA/cm <sup>2</sup> ]	$V_{p,s}$ [V]	$V_{v,s}$ [V]	$\Delta V_s$ [V]	$J_{p,m}$ [kA/cm <sup>2</sup> ]
#1	63	2	0.68	1.38	0.70	60
#2	110	5	0.86	1.57	0.71	108
ESUT	$J_{v,m}$ [kA/cm <sup>2</sup> ]	$V_{v,m}$ [V]	$A$ [ $\mu\text{m}^2$ ]	$V_{p,m}$ [V]	$\Delta V_m$ [V]	
#1	11	1.32	3 × 3	0.69	0.63	
			4 × 4	0.71	0.61	
			5 × 5	0.72	0.60	
			6 × 6	0.74	0.58	
			7 × 7	0.76	0.56	
#2	22	1.50	3 × 3	0.86	0.64	
			4 × 4	0.86	0.64	
			5 × 5	0.87	0.63	
			6 × 6	0.88	0.62	
			7 × 7	0.90	0.60	

\* In the above,  $s$  and  $m$  subscripts indicate simulated and measured quantities, respectively.

hand, the ESUT #2 values are  $J_{p,s} \simeq 110 \text{ kA/cm}^2$ ,  $J_{p,m} \simeq 108 \text{ kA/cm}^2$ ,  $J_{v,s} \simeq 5 \text{ kA/cm}^2$ , and  $J_{v,m} \simeq 22 \text{ kA/cm}^2$ .

This results in an estimated available current density  $\Delta J_s = J_{p,s} - J_{v,s}$  and peak-to-valley current ratio  $\text{PVCR}_s = J_{p,s}/J_{v,s}$  of around  $61 \text{ kA/cm}^2$  and  $31.5$ , respectively, for the ESUT #1, and of around  $105 \text{ kA/cm}^2$  and  $22$ , respectively, for the ESUT #2, while the extracted experimental values are  $\Delta J_m = J_{p,m} - J_{v,m} \simeq 49 \text{ kA/cm}^2$  and  $\text{PVCR}_m = J_{p,m}/J_{v,m} \simeq 5.5$ , respectively, for the ESUT #1, and around  $86 \text{ kA/cm}^2$  and  $4.9$ , respectively, for the ESUT #2.

To accurately extract  $J_{p,m}$  and  $J_{v,m}$ , the behaviour of the experimentally-measured peak and valley currents  $I_{p,m}$  and  $I_{v,m}$  as a function of the RTD mesa area was analysed for both heterostructures, which is shown in Figure 4.12. The analysis revealed a highly-linear trend, with associated maximum deviation from linearity of around  $4.5 \%$  for both the ESUT #1 and #2, confirming the linear dependencies  $I_{p,v}(A)$  and proving that the mesa lateral sidewall leakage current contribution was negligible in the measured RTD devices.

The small overestimation of  $J_{p,s}$  ( $\lesssim 5 \%$ ) and large underestimation of  $J_{v,s}$  ( $J_{v,m}/J_{v,s} \sim 5$ ), with resulting overestimations of both  $\Delta J_s$  ( $\sim 23 \%$ ) and  $\text{PVCR}_s$  ( $\text{PVCR}_s/\text{PVCR}_m \sim 5$ ), can be explained by the ballistic nature of the simulations, which neglects phase-breaking/dissipative scattering mechanisms mainly occurring in the DBQW region (including sequential tunnelling), as well as in the emitter and collector extended leads, at RT, such as electron-longitudinal optical (LO) phonon interactions [699], residual impurity and disorder scattering, etc., which can cause momentum and/or energy relaxation breaking electron coherency [397, 468, 700].

As a consequence, the peak of the transmission probability associated to the first resonant level  $E_1$  drops and broadens. This has two main effects on the DC JV curve. First,  $J_p$  is reduced due to the lower  $\mathcal{T}_{DBQW}$  at  $V = V_p$  (and scattering in the extended leads). However, at the same time,  $J_v$  rises because of the larger  $E_1$  energy broadening  $\Gamma_1$ . As a result, the heterostructure PVCR dramatically degrades compared to the coherent limit, i.e., the overall transparency associated with the NDR region increases, as well-reported in the literature [313].

Though, it has been shown that most of the valley current is not thermally-activated [701] (i.e., due to thermionic emission across the DBQW), and it is rather associated with scattering phenomena [380] caused by structural imperfections introduced during the epitaxial growth process of the RTD heterostructure [702], which increases the full-width at half maximum (FWHM) associated with the transmission probability peaks [397]. As a result, the current that can flow at  $V = V_v$  rises, enhancing  $J_v$  [703]. At the same time,  $E_2$  broadens too, i.e.,  $\Gamma_2$  increases, which makes  $J_v$  to rise even more. Indeed, the presence of the valley current is due to the co-presence

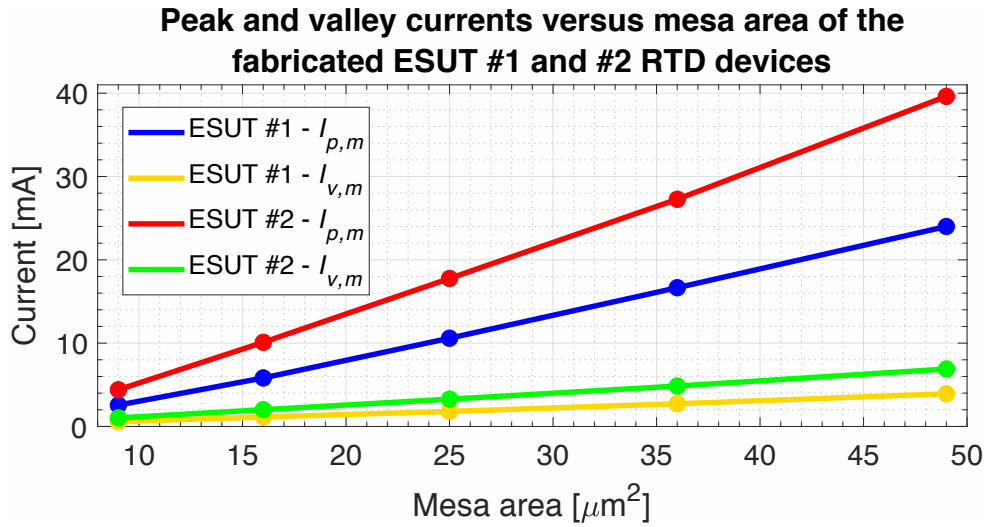


Figure 4.12: Experimentally-extracted ESUT #1 and #2 RTD devices peak and valley currents as a function of the designed mesa area.

of both  $E_1$  and  $E_2$  in terms of their overlapping broadening energy spectra. Another explanation for the underestimated valley current is represented by the simplified parabolic electronic energy dispersion relation at the emitter side [693].

In summary, the analysis shows that, while simulated and measured  $J_p$  values are in very good agreement, at the moment,  $J_v$ , and therefore  $\Delta J$  and the PVCR, cannot be accurately computed with the current version of the simulation software. However, attempts in including phase-breaking/dissipative processes on a computationally-efficient level in a new release of Atlas (called "Victory Atomistic Device and Nanostructure Simulator" [704]) are under development.

The inclusion of scattering processes will be, as already discussed in Section 4.2, straightforward in the context of the NEGF formalism and it will allow to accurately model the valley current, removing the currently in-place ballistic assumption and estimating the full  $JV$  curve. Moreover, simulation of RTD devices with realistically-thick emitter/collector extended regions of hundreds of nanometres in thickness by employing consumer desktops/laptops will be feasible thanks to the employed low-computational load techniques. In this context, standard and rigorous self-consistent Born approximation (SBA) approaches remain incompatible. However, the computational capability of modern hardware is increasing at an impressive rate, so this issue could be solved at some point in the near future.

#### 4.3.4.2 Peak, valley, and valley-to-peak voltages

The computed ( $s$ -labelled) and experimentally-extracted ( $m$ -labelled)  $V_p$ ,  $V_v$ , and  $\Delta V$  values of both the ESUT #1 and #2 RTD devices are reported in Table 4.3. Here,  $V_{p,s}$  is accurately com-

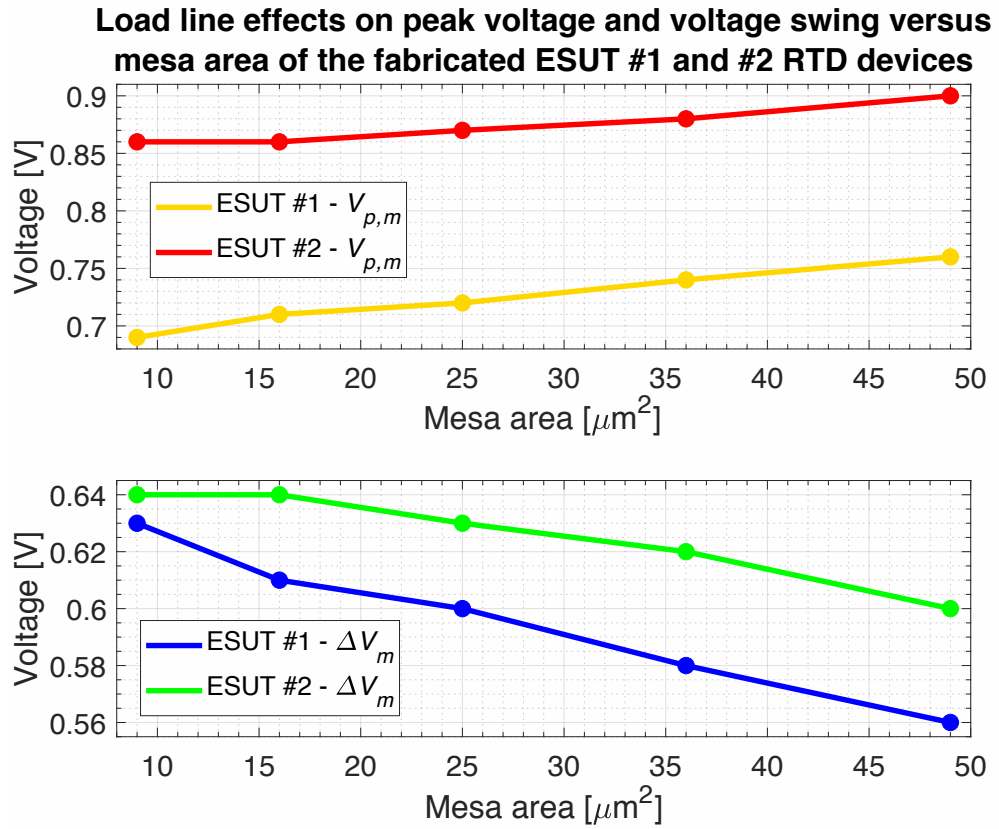


Figure 4.13: Experimentally-extracted ESUT #1 and #2 RTD devices peak voltage and voltage swing versus designed mesa area trends due to load line effects.

puted for the small  $3 \times 3 \mu\text{m}^2$  large devices, with 10 mV underestimation only (around 1.5 %) in the case of the ESUT #1, which can be attributed to a small (positive) fluctuation in  $\rho_c$  during fabrication or/and to the absence of scattering mechanisms in the simulation [660].

Simultaneously,  $\Delta V_s$  is also estimated quite accurately for the same mesa size, with around 11 % overestimation only (around 70 mV). This can be explained by the absence of dissipative processes in the simulation, which broaden  $E_1$  and  $E_2$  (increasing both  $\Gamma_1$  and  $\Gamma_2$ ), and makes the voltage associated with the onset of the valley current  $V_{v,m}$  to shift to lower values, shrinking the measured NDR region [705]. Indeed, the overestimation of  $\Delta V_s$  is mainly due to the overestimated  $V_{v,s}$  (around 4.5 %), which is correlated to the underestimation of  $J_{v,s}$ .

The mesa area trend of both  $V_{p,m}$  and  $\Delta V_m$  for larger device sizes is shown in Figure 4.13. It is clear that  $V_{p,m}$  shifts at higher voltage with increasing mesa area, resulting in  $V_{p,m}$  increasing and  $\Delta V_m$  shrinking. Indeed, when the RTD is biased within its first PDR region, the measured voltage lies across the series of  $R_s$  and the device resistance  $R_{rtd}(V) = dV/dI$ . If  $R_s \neq 0$ , the measured PDR region points shift at higher voltage values according to the ratio  $R_{rtd}/R_s$  due to the parasitic voltage drop across  $R_s$ , resulting in a higher and smaller measured  $V_{p,m}$  and  $\Delta V_m$ , respectively. From Table 4.4, it is clear that, while this effect is negligible for the  $3 \times 3 \mu\text{m}^2$ -large

Table 4.4: Extracted RTD devices load-line parameters\*.

ESUT	$A [\mu\text{m}^2]$	$R_c/R_p$	$R_{rtd}^*/R_s$	ESUT	$A [\mu\text{m}^2]$	$R_c/R_p$	$R_{rtd}^*/R_s$
	$3 \times 3$	15.0	84.0		$3 \times 3$	16.0	57.4
	$4 \times 4$	6.5	79.5		$4 \times 4$	7.0	53.8
#1	$5 \times 5$	3.5	73.0	#2	$5 \times 5$	4.0	48.8
	$6 \times 6$	2.5	59.6		$6 \times 6$	2.5	44.9
	$7 \times 7$	1.5	57.8		$7 \times 7$	1.5	43.6

\* Computed assuming  $R_{rtd}(V) = \bar{R}_{rtd}$  in the first PDR region.

devices (where the ratio  $R_{rtd}/R_s$  is around 84.0 and 57.4 for the ESUT #1 and #2, respectively), as the mesa area increases,  $R_{rtd}/R_s$  decreases.

Indeed, while  $R_{rtd}$  linearly scales with  $A$ ,  $R_s$  doesn't follow the same trend due to the parasitic resistance  $R_p$  mainly coming from the bond-pads metallisation, i.e.,  $R_s \approx R_p + R_c$ , where  $R_c$  is the RTD parasitic contact resistance. Here,  $R_p$  is estimated to be around  $0.2 \Omega$ , while the extracted value from the measured  $IV$  curves is  $1.9 \Omega$  for the fabricated RTD devices. However, the discrepancy is attributed to the DC probes used to bias the RTDs, so it was neglected during the analysis. Moreover,  $R_c = R_{c,t} + R_{c,b} = \rho_c/(A + A_b)$  (being  $R_{c,t}$  and  $R_{c,b}$  are the contact resistances associated with the RTD top and bottom Ohmic contacts, respectively, while  $A_b$  is the bottom contact area), where  $R_c \approx R_{c,t} = \rho_c/A$  since the ratio  $R_{c,t}/R_{c,b} = A_b/A$  was estimated to be around 22 for the fabricated devices.

While the influence of  $R_p$  on  $R_s$  is negligible for the  $3 \times 3 \mu\text{m}^2$  large devices, where  $R_c/R_p$  is around 15.0 and 16.0 for the ESUT #1 and #2, respectively, the ratio decreases for the bigger mesa areas. Therefore, the ratio  $R_{rtd}/R_s$ , in turn, drops. As a consequence, the NDR shrinks according to the load line slope [696]. If  $R_s = 1/|\bar{G}_{rtd}|$ , where  $\bar{G}_{rtd} < 0$  is the (average) RTD negative differential conductance (NDC), the device becomes extrinsically-bistable, i.e.,  $V_p = V_v$ , and the NDR vanishes, meaning that the RTD cannot be biased in this region [696].

In summary, the analysis shows that both  $V_p$  and  $\Delta V$  can be accurately computed for the  $3 \times 3 \mu\text{m}^2$  large RTD devices, being the simulation offset smaller than  $0.1 \text{ V}$ , which is the tolerance that is typically-adopted to quantify these parameters during wafer qualification. However, the estimation is not that accurate in the case of the larger area devices due to load-line effects. Therefore, small device sizes should be employed to correctly carry out accurate wafer qualification and estimate the associated  $V_p$  and  $\Delta V$  when the experimental RTD  $IV$  characteristics are measured.

Suitable mesa areas must be chosen according to the wafer electrical properties and the

Ohmic specific contact resistivity achieved during device fabrication. It is also clear that load-line effects alter the electrical behaviour of large device sizes. Indeed, even though both  $V_p$  and  $\Delta V$  are intimately-related with the RTD epitaxial-structure,  $R_s$  can mask the real wafer electrical performance if the measured devices are not sufficiently small, leading to poor qualification.

In conclusion, RTD design can currently rely on the quantities  $J_p$ ,  $V_p$  and  $\Delta V$ , which can be accurately estimated. During oscillator design, load line design and impedance matching between the RTD and the load can be carried out through the experimentally-extracted  $I_v$  and circuit design.

#### 4.3.4.3 Maximum RF power

The estimated  $P_{RF,max,m} \approx (3/16)\Delta J_m \Delta V_m$  evaluated from experimental data is around 0.06 mW/ $\mu\text{m}^2$  for the ESUT #1, and around 0.1 mW/ $\mu\text{m}^2$  for the ESUT #2, while the associated counterparts estimated from simulations  $P_{RF,max,s} \approx (3/16)\Delta J_s \Delta V_s$  are around 0.08 mW/ $\mu\text{m}^2$  and 0.14 mW/ $\mu\text{m}^2$ , respectively, with a discrepancy of around 30 % to 40 % due to the underestimated  $J_{v,s}$ , as already discussed. This means that a 16  $\mu\text{m}^2$ -large RTD device can deliver up to around 1 mW and 1.6 mW of RF power if featuring the ESUT #1 or #2, respectively.

Clearly, this value can be significantly increased through accurate device epitaxial structure design. In particular, barriers and QW thicknesses have to be optimised to achieve moderate current density operation, i.e.,  $150 < J_p < 300$  kA/cm<sup>2</sup>, and large PVCR  $> 3$ , resulting in  $\Delta J \gg 100$  kA/cm<sup>2</sup>. This allows the employment of large mesa areas above 9  $\mu\text{m}^2$  required for high-power operation without suffering from thermal breakdown issues.

At the same time, emitter and collector spacer layers thicknesses and doping levels have to be optimised to maximise the NDR voltage swing  $\Delta V$  and keep moderate  $V_p$  to minimise DC power consumption and increase efficiency. A discussion on RTD epitaxial structure design focused on the DC  $JV$  curve and aimed at low-THz oscillator sources is provided in the next Chapter.

## 4.4 Summary

This Chapter proposed a quantum transport numerical approach based on the non-equilibrium Green's function (NEGF) formalism to accurately and reliably model the electrical fingerprint of In<sub>0.53</sub>Ga<sub>0.47</sub>As/AlAs double-barrier RTDs, which are lattice-matched to InP substrates. It relies on Atlas TCAD simulation software, which numerically-solves the device physical equations through the FEM. The approach was demonstrated by means of a comprehensive experimental

analysis, which included microfabrication and measurement of epitaxially-grown RTD devices.

The results show that the simulation software correctly estimates the peak current density  $J_p$ , peak voltage  $V_p$ , and the valley-to-peak voltage difference  $\Delta V$  of the RTD heterostructure DC  $JV$  characteristic NDR region in RT conditions. On the other hand, the computed valley current density  $J_v$ , and so the available current density  $\Delta J$  and PVCR, do not match with the experimentally-extracted counterparts due to the ballistic nature of electron transport and simplified parabolic electronic dispersion relation, which will be solved through the implementation of scattering mechanisms and multi-band description. Nevertheless, successful epitaxial layer design for high-power low-THz (up to around 300 GHz) emitters can be conducted, and oscillator design carried out through the experimentally measured valley current.

## Chapter 5

# Epitaxial structure simulation study of $\text{In}_{0.53}\text{Ga}_{0.47}\text{As}/\text{AlAs}$ double-barrier resonant tunnelling diodes for low-terahertz sources

In this Chapter, an epitaxial structure simulation study of indium gallium arsenide/aluminium arsenide double-barrier resonant tunnelling diodes (RTD) epitaxially-grown on lattice-matched indium phosphide substrates is presented employing the approach described in Chapter 4, which is based on the non-equilibrium Green's function formalism implemented in Silvaco Atlas TCAD. In particular, the investigation focuses on how epitaxial layers design impacts the RTD heterostructure static current density-voltage characteristic, including barriers, quantum well, and spacer layers, as well as the employment of a high-band gap emitter region.

The analysis shows that, while barriers and QW thicknesses have a strong impact on the current operation of the RTD device, accurate asymmetric spacers design can provide a trade-off between the voltage span and relative position of its negative differential resistance region, while the employment of a high-band gap compound at the emitter side lowers the device bias point. This provides the required physical insight to accurately design and optimise high-power RTD devices employed in oscillator sources operating at low-terahertz frequencies.

### 5.1 Introduction

As discussed in Chapters 2 and 3, device epitaxial design optimisation is crucial to tailor oscillator performances according to the operational requirements. In this context, two approaches are commonly adopted to design indium gallium arsenide/aluminium arsenide ( $\text{InGaAs}/\text{AlAs}$ ) terahertz (THz) double-barrier resonant tunnelling diodes (RTD):

- a) the first approach relies on ultra-high peak current-density  $J_p$  in the megaampere per square centimetre (MA/cm<sup>2</sup>) range, and allows for a frequency response well-above 1 THz thanks to the very-thin employed double-barrier quantum well (DBQW) region [422, 465, 466], characterised by AlAs barriers thickness  $t_b$  around 0.88/1.17 nm (around 3/4 monolayers (ML)) and thin (typically below 3 nm in thickness [464]) high-indium (In) content (usually around or above 80 % [425, 470]) InGaAs (or indium arsenide (InAs) notch-based [422]) quantum wells (QW) [473] (to lower  $V_p$ ), which minimise the associated electron quasi-bound state tunneling lifetime. However, the associated radio-frequency (RF) power capability is remarkably limited. Indeed, the high available current density  $\Delta J = J_p - J_v$  (where  $J_v$  is the valley current density) is gained at the expense of a dramatic reduction in device area (around and below 1  $\mu\text{m}^2$ ) since large-size devices tend to be prone to thermal breakdown, and reduce the associated parasitic capacitance required to oscillate at THz frequencies which, together with the small valley-to-peak voltage difference  $\Delta V = V_p - V_v$  that characterises these epi-structures (typically below 0.5 V [466]), drastically lower the device RF gain. In addition,  $J_v$  is large at room temperature (RT), which reduces the peak-to-valley current ratio (PVCR) (which is, usually, below 2 [464]). This is due to the thin employed barriers and QW, and to the structural imperfections introduced during the growth of the highly-strained DBQW active region, which affects epitaxial growth uniformity and reproducibility, as well as device reliability [697]. Overall, the provided RF power is of the order of the microwatt above 1 THz oscillation frequencies.
- b) the second approach, which is the one considered in this work, is based on moderate  $J_p \sim 200\text{--}300$  kA/cm<sup>2</sup>, large device size (above 16  $\mu\text{m}^2$ ), and large  $\Delta V > 0.5$  V, and leads to high-power operation in the low-THz range ( $\sim 100\text{--}300$  GHz) [169, 516]. Due to the large employed mesa area, fabrication is fully-compatible with standard optical lithography, which diminishes the complexity and cost associated with electron-beam lithographic steps needed for micrometre square and sub-micrometre square sizes, while moderate current density operation reduces thermal stability issues. Furthermore, the active region is almost relaxed due to the employed lattice-matched to indium phosphide (InP) In<sub>0.53</sub>Ga<sub>0.47</sub>As QW, which increases epitaxial growth reproducibility and uniformity. However, in contrast with the previous approach, proper DBQW and spacer layers design aimed at performance maximisation has not yet been investigated in this context.

To address these device design challenges, a comprehensive discussion on epitaxial design of In<sub>0.53</sub>Ga<sub>0.47</sub>As/AlAs double-barrier RTDs is reported in the following. The analysis is focused on the DC current density-voltage ( $JV$ ) curve, which determines the device maximum

RF power per unit of area  $\mathcal{P}_{RF,max} \approx (3/16)\Delta J\Delta V$ . By tuning the parameters associated with epitaxial layers, including barriers, QW, and spacer layers, the impact on the heterostructure DC  $JV$  characteristic in terms of  $J_p$ ,  $V_p$ , and  $\Delta V$  (which are the quantities that can be accurately computed), is analysed employing the non-equilibrium Green's function (NEGF)-based simulation approach presented in Chapter 4, which relies on Silvaco Atlas TCAD.

At the same time, a qualitative analysis of  $J_v$ ,  $\Delta J$ , and  $PVCR = J_p/J_v$  in the context of barriers and QW design is carried out based on the simulated heterostructure transmission coefficient. Furthermore, the employment of a high-band gap material at the emitter side is also investigated. Device design considerations aimed at high-power low-THz sources are then briefly discussed.

## 5.2 RTD epitaxial structure simulation study

To study the impact of epitaxial structure design parameters on the heterostructure static  $JV$  characteristic, an  $n$ -type intra-band  $\text{In}_{0.53}\text{Ga}_{0.47}\text{As}/\text{AlAs}$  double-barrier RTD reference epitaxial structure (RES), which is depicted in Figure 5.1, was adopted, and features barriers thickness  $t_b = 1.46$  nm (around 5 ML), QW thickness  $t_{qw} = 4.39$  nm (around 15 ML), and emitter/collector lightly-doped spacer layers thickness  $t_{ls}^{e/c} = 100$  nm and doping level  $N_{D,ls}^{e/c} = 2 \times 10^{17} \text{ cm}^{-3}$ . The emitter and collector regions, as well as heavily-doped contacts, thicknesses and doping levels are set to 20 nm,  $2 \times 10^{18} \text{ cm}^{-3}$ , and 40/400 nm and  $2 \times 10^{19} \text{ cm}^{-3}$ , respectively. This choice was made based on reported epitaxial structures employed in oscillators operating at around 300 GHz [169].

$n++ \text{In}_{0.53}\text{Ga}_{0.47}\text{As}$	Collector contact: 40 nm, $N_D = 2 \times 10^{19} \text{ cm}^{-3}$
$n+ \text{In}_{0.53}\text{Ga}_{0.47}\text{As}$	Collector: 20 nm, $N_D = 2 \times 10^{18} \text{ cm}^{-3}$
$n- \text{In}_{0.53}\text{Ga}_{0.47}\text{As}$	Lightly-doped spacer: $t_{ls}^c = 50/100$ nm, $N_{D,ls}^c = 2 \times 10^{16/17} \text{ cm}^{-3}$
$u \text{In}_{0.53}\text{Ga}_{0.47}\text{As}$	Spacer: = 2 nm
$u \text{AlAs}$	Barrier: $t_b = 1.17/1.46/1.75$ nm (4/5/6 ML)
$u \text{In}_{0.53}\text{Ga}_{0.47}\text{As}$	Quantum well: $t_{qw} = 4.10/4.39/4.69$ nm (14/15/16 ML)
$u \text{AlAs}$	Barrier: $t_b = 1.17/1.46/1.75$ nm (4/5/6 ML)
$u \text{In}_{0.53}\text{Ga}_{0.47}\text{As}$	Spacer: = 2 nm
$n- \text{In}_{0.53}\text{Ga}_{0.47}\text{As}$	Lightly-doped spacer: $t_{ls}^e = 50/100$ nm, $N_{D,ls}^e = 2 \times 10^{16/17} \text{ cm}^{-3}$
$n+ \text{In}_{0.53}\text{Ga}_{0.47}\text{As}$	Emitter: 20 nm, $N_D = 2 \times 10^{18} \text{ cm}^{-3}$
$n++ \text{In}_{0.53}\text{Ga}_{0.47}\text{As}$	Emitter contact: 400 nm, $N_D = 2 \times 10^{19} \text{ cm}^{-3}$

Figure 5.1: RTD reference epitaxial structure and associated design parameters (in red), as well as the overall set of simulation parameters (in black).

Table 5.1: Epi-structure simulation results for different barriers thicknesses.

$t_b$ [nm]	$J_p$ [kA/cm <sup>2</sup> ]	$V_p$ [V]	$V_v$ [V]	$\Delta V$ [V]
1.17	656	1.2	2.7	1.5
1.46	263	1.2	2.7	1.5
1.75	101	1.2	2.7	1.5

Parameters associated with barriers, QW, and lightly-doped spacers were then tuned, as shown in Figure 5.1, and simulation results compared and discussed. Forward bias, i.e., collector contact (cathode) positively-biased with respect to the emitter contact (anode), and RT ( $T = 300$  K) operation, is assumed to model realistic RTD devices employed in THz sources, as discussed in Chapter 4.

### 5.2.1 Barriers

The RES was simulated setting  $t_b = 1.17$  nm, 1.46 nm, and 1.75 nm (around 4 ML, 5 ML, and 6 ML, respectively, where 1 ML  $\sim 0.293$  nm). Simulation results are shown in Table 5.1. The impact of  $t_b$  on the DC  $JV$  curve is revealed in terms of current density, while the effect on voltages is negligible ( $V_p \simeq 1.2$  V,  $V_v \simeq 2.7$  V, and  $\Delta V \simeq 1.5$  V).

In particular, as  $t_b$  increases,  $J_p$  decreases [409, 706] from around 656 kA/cm<sup>2</sup> assuming 4 ML, to around 263 kA/cm<sup>2</sup> and around 101 kA/cm<sup>2</sup> with 5 ML and 6 ML, respectively, revealing an exponential-like trend  $J_p \propto \exp(-\alpha t_b)$  ( $\alpha > 0$ ), which is explained by the drop of the full-width at half maximum (FWHM) energy broadening  $\Gamma_1$  of the resonance associated with the QW first quasi-bound state energy subband  $E_1$  of the heterostructure transmission coefficient energy spectrum  $\mathcal{T}_{DBQW}(E_z)$  (where  $E_z$  is the longitudinal energy component). This is shown in Figure 5.2, where thermal equilibrium is assumed as general example. Indeed, current density drops regardless of the specific bias point.

In particular,  $\Gamma_1$  decreases from around 7.5 meV assuming 4 ML, to around 2.9 meV and around 1.1 meV with 5 ML and 6 ML, respectively. This enhances carriers confinement and narrows the conduction channel due to the lower associated available local density of states (LDOS), reducing the double-barrier structure tunnelling transparency. However, although  $J_p$  increases by reducing  $t_b$ , the transmission coefficient FWHM energy broadening  $\Gamma_2$ , i.e.,  $\mathcal{T}_{DBQW}(E_z) \rightarrow E_2$  (where  $E_2$  is the QW second quasi-bound state resonant subband) increases more than  $\Gamma_1$  [451], from around 13.8 meV with 6 ML, to around 25.1 meV and around 47.6 meV with 5 ML and 4 ML, respectively, where  $\partial\Gamma_2/\partial t_b \gg \partial\Gamma_1/\partial t_b$  due to the weaker quantum confinement ( $E_2 > E_1$ ), making  $J_v \propto \exp(-\beta t_b)$  to rise more than  $J_p$  ( $\beta \ll \alpha$ ).

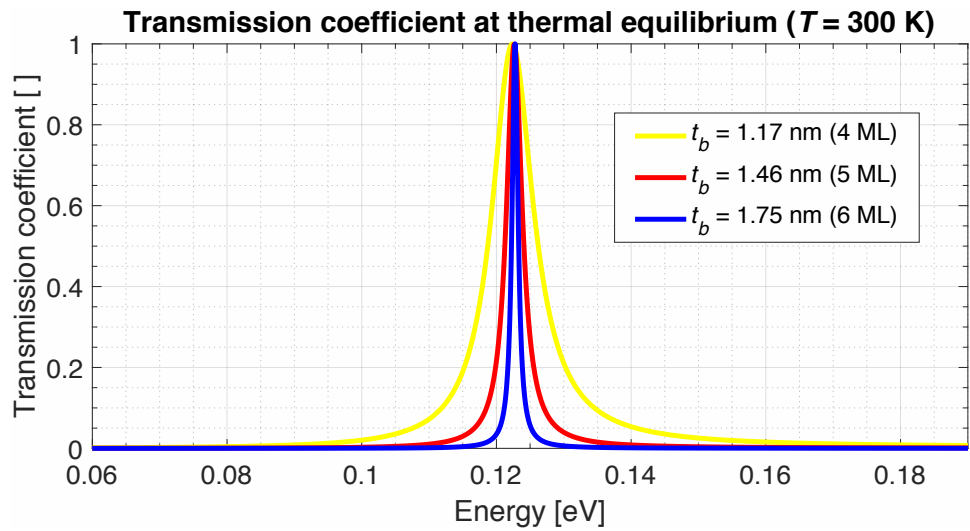


Figure 5.2: Computed resonant peak (linear scale) associated with the QW first quasi-bound state energy subband of the heterostructure transmission coefficient energy spectrum at RT for different barriers thicknesses. Thermal equilibrium is assumed as a general bias point.

In summary, the analysis shows that, while both  $J_p$  and  $\Delta J$  (because of the exponential increase of  $J_p$  and  $J_v$  [451]) increase reducing  $t_b$ , the PVCR drops, while  $V_p$  and  $\Delta V$  variations are negligible.

## 5.2.2 Quantum well

The RES was simulated setting  $t_{qw} = 4.10$  nm, 4.39 nm, and 4.69 nm (around 14 ML, 15 ML, and 16 ML). The computed static  $JV$  characteristics are shown in Figure 5.3, while the associ-

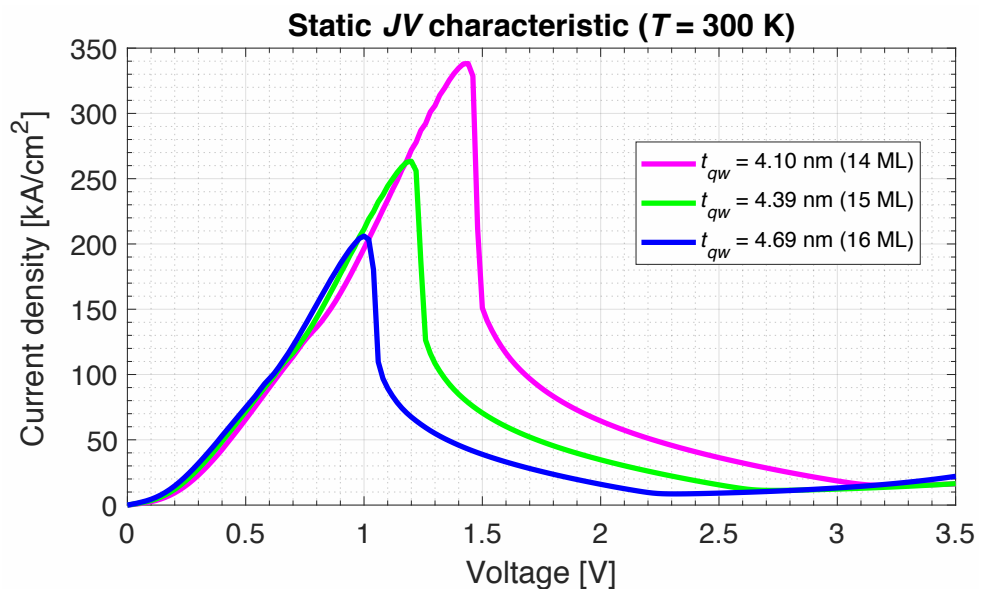


Figure 5.3: Computed static  $JV$  characteristic at RT for different QW thicknesses.

Table 5.2: Epitaxial structure simulation results for different QW thicknesses.

$t_{qw}$ [nm]	$J_p$ [kA/cm <sup>2</sup> ]	$V_p$ [V]	$V_v$ [V]	$\Delta V$ [V]
4.10	338	1.44	3.22	1.78
4.39	263	1.20	2.74	1.54
4.69	206	1.00	2.32	1.32

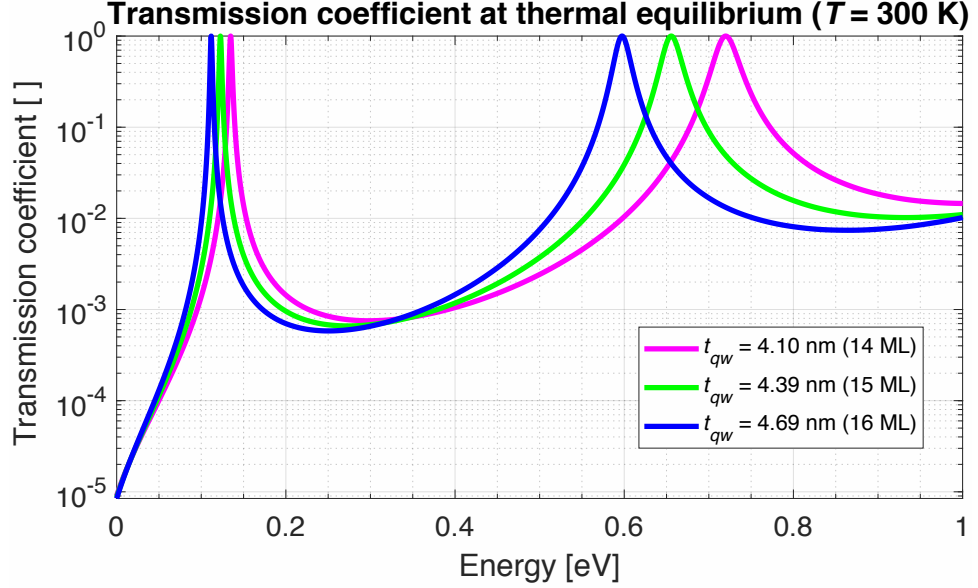


Figure 5.4: Computed transmission coefficient energy spectrum at RT for different QW thicknesses. Thermal equilibrium is assumed as a general bias point.

ated values are reported in Table 5.2, and are  $J_p \simeq 338$  kA/cm<sup>2</sup>,  $V_p \simeq 1.44$  V, and  $\Delta V \simeq 1.78$  V assuming 14 ML,  $J_p \simeq 263$  kA/cm<sup>2</sup>,  $V_p \simeq 1.20$  V, and  $\Delta V \simeq 1.54$  V with 15 ML, and  $J_p \simeq 206$  kA/cm<sup>2</sup>,  $V_p \simeq 1.00$  V, and  $\Delta V \simeq 1.32$  V assuming 16 ML.

To compare and explain the results,  $\mathcal{T}_{DBQW}$  of the different heterostructures at RT was computed and analysed, as shown in Figure 5.4. Thermal equilibrium conditions are assumed, analogously as done in Section 5.2.1. The increase in  $J_p$  and  $V_p$  with QW shrinking is explained by the rise of  $E_1$  [404,706], which increases from around 112 meV assuming 16 ML, to around 123 meV (with difference  $\Delta E_1 \simeq 11$  meV) and around 135 meV ( $\Delta E_1 \simeq 23$  meV) with 15 ML and 14 ML, respectively, and by the broadening of  $E_1$  caused by the weaker electronic wave-function confinement [706], where  $\Gamma_1$  increases from around 2.5 meV assuming 16 ML, to around 2.9 meV and around 3.3 meV with 15 ML and 14 ML, respectively.

Simultaneously,  $E_2$  rises more than  $E_1$  [706], and shifts from around 597 meV assuming 16 ML, to around 656 meV (with difference  $\Delta E_2 \simeq 59$  meV) and around 720 meV ( $\Delta E_2 \simeq 123$

meV) with 15 ML and 14 ML, respectively. This makes  $V_v$  to shift more than  $V_p$  ( $V_v \simeq 2.32$  V,  $\simeq 2.74$  V, and  $\simeq 3.22$  V with 16 ML, 15 ML, and 14 ML, respectively), making  $\Delta V$  to increase [417,473].

Moreover,  $\Gamma_2$  increases more than  $\Gamma_1$  [473], from around 20.6 meV with 16 ML, to around 25.1 meV and around 31.0 meV with 15 ML and 14 ML, respectively, because  $\partial\Gamma_2/\partial t_{qw} \gg \partial\Gamma_1/\partial t_{qw}$  due to the reduced quantum confinement. Therefore,  $J_v$  is expected to rise more than  $J_p$ , even though the resonant subbands energy separation rises. However, the impact of  $t_{qw}$  on both  $J_p$  and  $J_v$  is significantly weaker than of  $t_b$  [706].

In summary, the analysis shows that, while  $J_p$ ,  $\Delta J$  (similarly as discussed in Section 5.2.1 due to the increase of  $J_p$  and  $J_v$ ), and  $\Delta V$  increase reducing  $t_{qw}$ ,  $V_p$  rises and the PVCR drops.

## 5.2.3 Lightly-doped spacers

### 5.2.3.1 Emitter lightly-doped spacer

The RES was simulated setting  $t_{ls}^e = 50$  nm and 100 nm, and  $N_{D,ls}^e = 2 \times 10^{16}$  cm $^{-3}$  and  $2 \times 10^{17}$  cm $^{-3}$ , while the lightly-doped collector spacer thickness  $t_{ls}^c$  and doping level  $N_{D,ls}^c$  are set to 100 nm, and  $2 \times 10^{17}$  cm $^{-3}$  and  $2 \times 10^{16}$  cm $^{-3}$ , respectively. The computed static  $JV$  characteristics are shown in Figure 5.5, while the associated values are reported in Table 5.3.

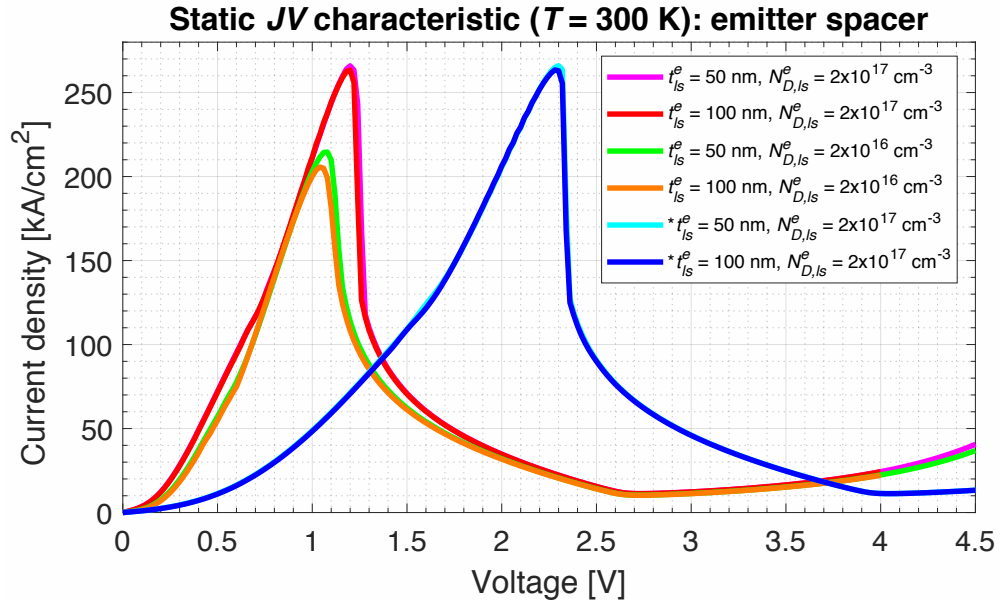


Figure 5.5: Computed static  $JV$  characteristic at RT for different lightly-doped emitter spacer thicknesses and doping levels. The lightly-doped collector spacer thickness and doping level are set to 100 nm and  $2 \times 10^{17}$  cm $^{-3}$ , respectively. \* Computed assuming  $t_{ls}^c = 100$  nm and  $N_{D,ls}^c = 2 \times 10^{16}$  cm $^{-3}$ .

Table 5.3: Epitaxial structure simulation results for different emitter lightly-doped spacer thicknesses and doping levels.

$t_{ls}^e$ [nm]	$N_{D,ls}^e$ [ $\text{cm}^{-3}$ ]	$J_p$ [ $\text{kA}/\text{cm}^2$ ]	$V_p$ [V]	$V_v$ [V]	$\Delta V$ [V]
*50	$2 \times 10^{17}$	265	1.20	2.74	1.54
*100	$2 \times 10^{17}$	265	1.20	2.74	1.54
*50	$2 \times 10^{16}$	215	1.08	2.74	1.66
*100	$2 \times 10^{16}$	206	1.04	2.74	1.70
**50	$2 \times 10^{17}$	265	2.28	4.04	1.76
**100	$2 \times 10^{17}$	265	2.28	4.04	1.76

\* Computed assuming  $t_{ls}^c = 100$  nm and  $N_{D,ls}^c = 2 \times 10^{17} \text{ cm}^{-3}$ . \*\* Computed assuming  $t_{ls}^c = 100$  nm and  $N_{D,ls}^c = 2 \times 10^{16} \text{ cm}^{-3}$ .

To compare and explain the results, the conduction band (CB) edge energy profile  $E_c(z)$  ( $\Gamma$  point) and electron density distribution  $n(z)$  in proximity to the first barrier at RT were computed, as shown in Figure 5.6, being  $\hat{z}$  the longitudinal broken symmetry (transport) direction. Thermal equilibrium is assumed as previously discussed (general visual example), even though specific considerations can be done at chosen bias points (forward bias).

In case of symmetric doping between emitter and collector lightly-doped spacers ( $N_{D,ls}^e = N_{D,ls}^c$ ), no significant variation in the DC  $JV$  curve is revealed when  $t_{ls}^e$  is tuned [707], which can be explained by the weak variation in the potential barrier arising in proximity to the first barrier at peak resonance ( $V = V_p$ ), which is confirmed by the smoothness of  $E_c$  at thermal equilibrium. Similar considerations apply to the asymmetric case  $N_{D,ls}^e > N_{D,ls}^c$ , which is confirmed by the positive curvature of the potential profile in proximity to the first barrier at thermal equilibrium.

On the other hand, if  $N_{D,ls}^e < N_{D,ls}^c$ ,  $J_p$  drops with increasing  $t_{ls}^e$ , which can be explained by the larger potential barrier seen by the tunnelling electrons when the equivalent voltage drop across the depletion region at the emitter side at peak resonance is not enough to compensate for the associated intrinsic built-in potential, which is the case if the emitter contact is heavily doped [707] (whose doping level  $N_{D,ls}^e$  is set to  $2 \times 10^{19} \text{ cm}^{-3}$  in the present analysis). This is confirmed by the negative profile of the potential at thermal equilibrium. Moreover,  $J_p$  decreases if  $N_{D,ls}^e$  is reduced due the lower available electron concentration [409], making  $E_c$  to shift towards and above the Fermi level  $E_F$  (or local quasi-Fermi level  $E_{Fn}$ ).

At the same time,  $V_p$  decreases in both cases since  $E_c$  and  $E_1$  get closer because of band warping caused by the larger potential drop at the emitter side, increasing  $\Delta V$  [706]. However,

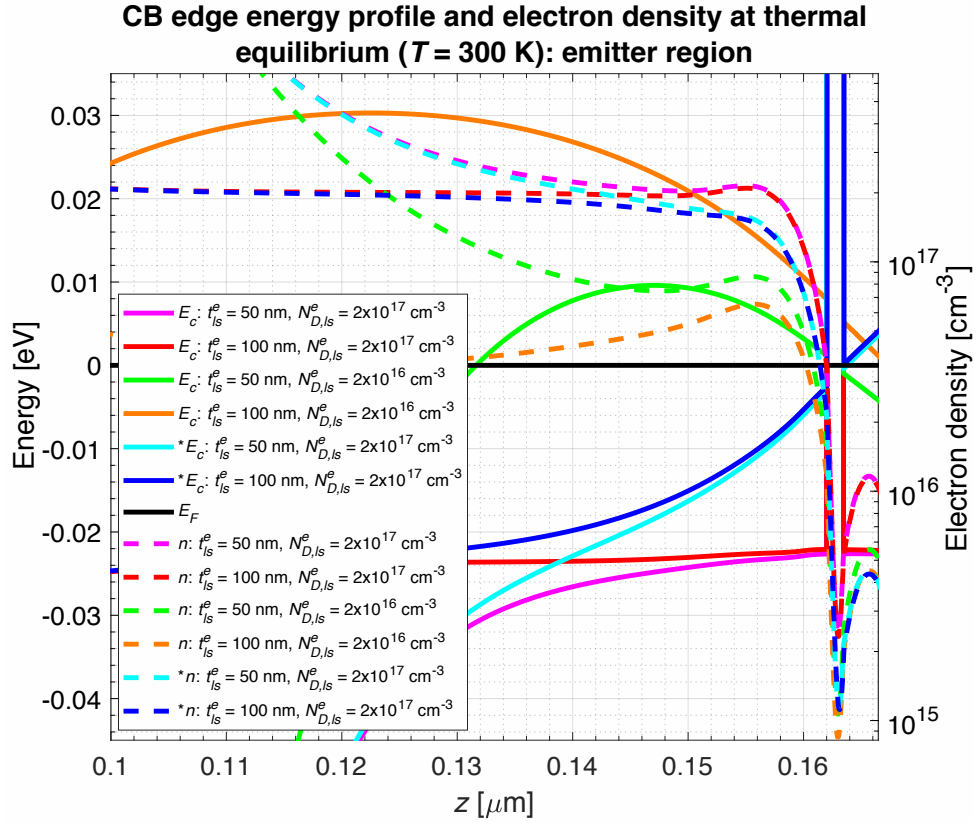


Figure 5.6: Computed CB edge energy profile and electron density at RT in the emitter region for different lightly-doped emitter spacer thicknesses and doping levels. The lightly-doped collector spacer thickness and doping level are set to 100 nm and  $2 \times 10^{17} \text{ cm}^{-3}$ , respectively. Thermal equilibrium is assumed as arbitrary example. \* Computed assuming  $t_{ls}^e = 100$  nm and  $N_{D,ls}^e = 2 \times 10^{16} \text{ cm}^{-3}$ . The black solid line represents the Fermi level (energy reference).

generally-speaking, the  $V_p(t_{ls}^e, N_{D,ls}^e)$  dependency is strictly dependent on Thomas-Fermi screening effects caused by charge accumulation/depletion due to band bending [708]. However, this is strictly correlated to the specific epitaxial structure under study, therefore, its accurate investigation has to be carried in the context of device design.

Furthermore,  $V_v$  results to be largely unaffected by both  $t_{ls}^e$  and  $N_{D,ls}^e$ , where the estimated  $V_v$  are around 2.74 V and around 4.04 V assuming  $N_{D,ls}^e = 2 \times 10^{17} \text{ cm}^{-3}$  and  $2 \times 10^{16} \text{ cm}^{-3}$ , respectively. However, it is expected that  $J_p$ ,  $V_p$ , and  $V_v$  vary as  $t_{ls}^e$  increases and/or  $N_{D,ls}^e$  decreases due to scattering processes in the emitter region [451], which were not included in the simulations, as already discussed in Chapter 4.

In summary, the analysis shows that, while  $J_p$ ,  $V_p$ , and  $\Delta V$  considerably change if  $N_{D,ls}^e$  is tuned, their dependency on  $t_{ls}^e$  turns to be notable only if  $N_{D,ls}^e/N_{D,ls}^c \ll 1$ . In particular, both  $J_p$  and  $V_p$  decreases, while  $\Delta V$  increases, if either  $N_{D,ls}^e$  is reduced or  $t_{ls}^e$  increased.

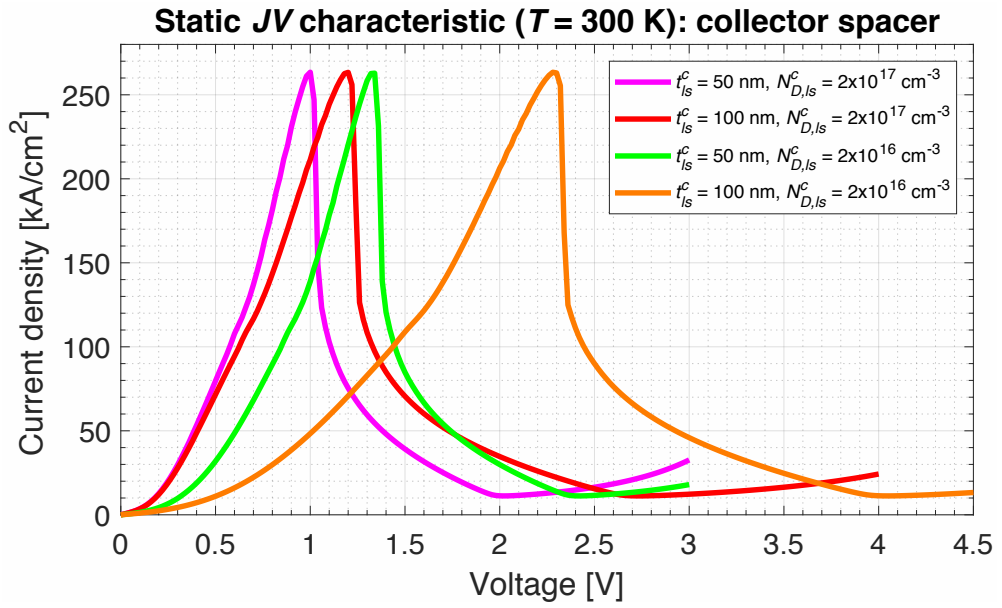


Figure 5.7: Computed static JV characteristic at RT for different lightly-doped collector spacer thicknesses and doping levels. The lightly-doped emitter spacer thickness and doping level are set to 100 nm and  $2 \times 10^{17} \text{ cm}^{-3}$ , respectively.

### 5.2.3.2 Collector lightly-doped spacer

The RES was simulated setting  $t_{ls}^c = 50$  nm and 100 nm, and  $N_{D,ls}^c = 2 \times 10^{16} \text{ cm}^{-3}$  and  $2 \times 10^{17} \text{ cm}^{-3}$ , while the lightly-doped emitter spacer thickness  $t_{ls}^e$  and doping level  $N_{D,ls}^e$  were set to 100 nm and  $2 \times 10^{17} \text{ cm}^{-3}$ , respectively. The computed static JV characteristics are shown in Figure 5.7, while the associated values are reported in Table 5.4.

The shift of  $V_p$  and  $V_v$  at higher voltage if  $t_{ls}^c$  is increased and/or  $N_{D,ls}^c$  decreased is explained by the larger voltage drop across the collector region, i.e., higher equivalent "series" resistance [709]. In particular,  $V_v$  shifts more than  $V_p$  since the inequality  $E_1 - E_c < E_2 - E_1$  is typically met in the QW, increasing  $\Delta V$ . In this context, the  $V_p(t_{ls}^c, N_{D,ls}^c)$  and  $V_v(t_{ls}^c, N_{D,ls}^c)$  depen-

Table 5.4: Epitaxial structure simulation results for different collector lightly-doped spacer thicknesses and doping levels\*.

$t_{ls}^c$ [nm]	$N_{D,ls}^c$ [ $\text{cm}^{-3}$ ]	$J_p$ [ $\text{kA}/\text{cm}^2$ ]	$V_p$ [V]	$V_v$ [V]	$\Delta V$ [V]
50	$2 \times 10^{17}$	265	1.00	2.02	1.02
100	$2 \times 10^{17}$	265	1.20	2.74	1.54
50	$2 \times 10^{16}$	265	1.34	2.42	1.08
100	$2 \times 10^{16}$	265	2.28	4.04	1.76

\* Computed assuming  $t_{ls}^e = 100$  nm and  $N_{D,ls}^e = 2 \times 10^{17} \text{ cm}^{-3}$ .

dencies are expected to depend on the resistive nature of the collector depletion region through the associated Debye length, which depends on the employed collector design. Therefore, this has to be accurately investigated in the context of the specific epitaxial structure under study.

At the same time,  $J_p$  does not change by tuning both  $t_{ls}^c$  and/or  $N_{D,ls}^c$ , where the computed  $J_p$  is around  $265 \text{ kA/cm}^2$ , unless a large potential barrier approaching  $E_1$  arises in proximity to the second barrier at peak resonance assuming  $N_{D,ls}^c \lll N_{D,ls}^e$ . Despite that, it is expected that  $J_p$ ,  $V_p$ , and  $V_v$  change as  $t_{ls}^c$  increases and/or  $N_{D,ls}^c$  decreases due to scattering mechanisms in the collector region [417, 468], which were not included in the simulations, as already discussed in Chapter 4.

In summary, the analysis showed that both  $V_p$  and  $\Delta V$  increase if  $t_{ls}^c$  is increased and/or  $N_{D,ls}^c$  is decreased, while  $J_p$  is unaffected.

### 5.2.4 High-band gap emitter

The impact of a high energy band gap  $E_g$  material employed at the emitter side was also investigated. In this context, an indium aluminium gallium arsenide (InAlGaAs) quaternary compound is assumed [464]. The RES was simulated setting  $t_{qw} = 4.10 \text{ nm}$  and assuming different  $\text{In}_{1-x-y}\text{Al}_y\text{Ga}_x\text{As}$  compositions  $\{x, y\} = \{0.43, 0.04\}$  ( $E_g \simeq 0.93 \text{ eV}$ ),  $\{0.4, 0.07\}$  ( $E_g \simeq 0.98 \text{ eV}$ ), and  $\{0.37, 0.1\}$  ( $E_g \simeq 1.04 \text{ eV}$ ) [375], where  $x$  and  $y$  are the gallium (Ga) and aluminium (Al) contents, respectively.

Simulations results are shown in Table 5.5, revealing a drop of  $V_p$  with increasing the Al concentration, where computed values are around  $0.84 \text{ V}$ ,  $0.66 \text{ V}$ , and  $0.52 \text{ V}$  with  $\{x, y\} = \{0.43, 0.04\}$ ,  $\{0.4, 0.07\}$ , and  $\{0.37, 0.1\}$ , respectively, reducing  $V_p$  up to around three times if compared to an equivalent heterostructure employing  $\text{In}_{0.53}\text{Ga}_{0.47}\text{As}$  ( $E_g \simeq 0.74 \text{ eV}$  [446]), whose  $V_p$  is estimated to be around  $1.44 \text{ V}$ . At the same time,  $J_p$  drops, where computed values decrease from around  $338 \text{ kA/cm}^2$  with  $y = 0$  to around  $220 \text{ kA/cm}^2$ ,  $180 \text{ kA/cm}^2$ , and  $145$

Table 5.5: Epitaxial structure simulation results for different InAlGaAs compositions.

Quaternary compound	$J_p$ [ $\text{kA/cm}^2$ ]	$V_p$ [V]
$\text{In}_{0.53}\text{Ga}_{0.47}\text{As}$	338	1.44
$\text{In}_{0.53}\text{Al}_{0.04}\text{Ga}_{0.43}\text{As}$	220	0.84
$\text{In}_{0.53}\text{Al}_{0.07}\text{Ga}_{0.4}\text{As}$	180	0.66
$\text{In}_{0.53}\text{Al}_{0.1}\text{Ga}_{0.37}\text{As}$	145	0.52

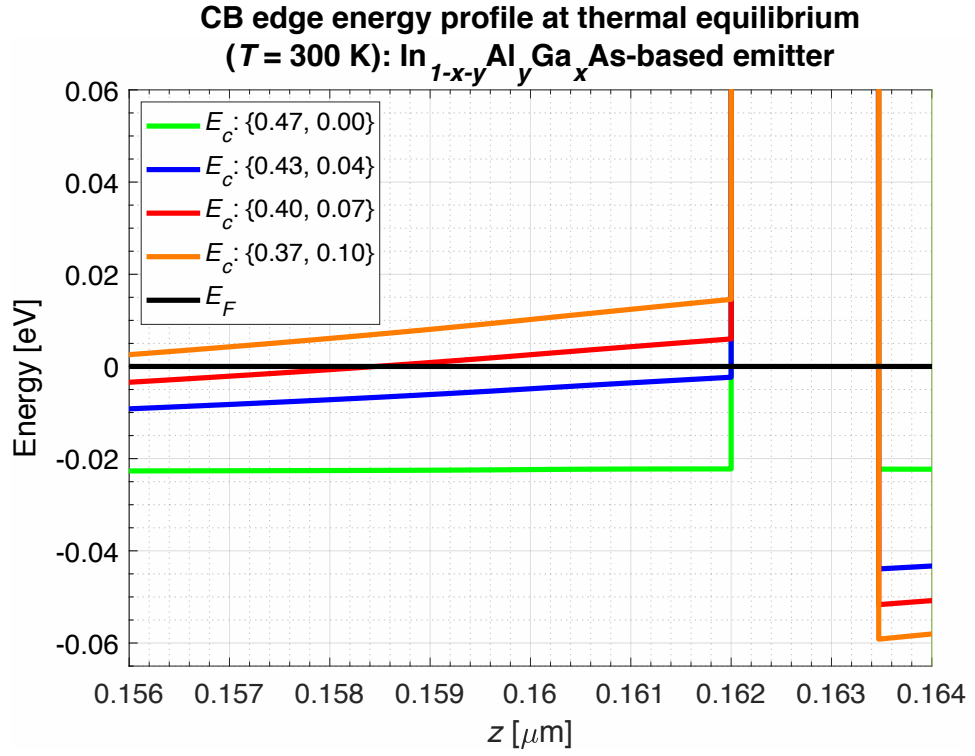


Figure 5.8: Computed CB edge energy profile at RT in proximity to the first barrier for different  $\text{In}_{1-x-y}\text{Al}_y\text{Ga}_x\text{As}$  compositions. The black solid line represents the Fermi level (energy reference). Thermal equilibrium is assumed as reference example.

$\text{kA/cm}^2$ , with  $\{x, y\} = \{0.43, 0.04\}$ ,  $\{0.4, 0.07\}$ , and  $\{0.37, 0.1\}$ , respectively.

To explain the results, the CB profile  $E_c(z)$  at RT close to the first barrier was simulated, which is shown in Figure 5.8. Thermal equilibrium was assumed as reference example. As can be seen, the drop of  $V_p$  can be explained by the shift of  $E_c$  in both emitter (upwards) and QW (downwards) regions, which makes  $E_c$  and  $E_1$  to approach, i.e.,  $E_1 - E_c$  to diminish. However,  $J_p$  drops at the same time, which is due to the higher electron effective mass  $m_e^*$  of  $\text{In}_{1-x-y}\text{Al}_y\text{Ga}_x\text{As}$  ( $0.047 \lesssim m_e^* \lesssim 0.053$ ) compared to  $\text{In}_{0.53}\text{Ga}_{0.47}\text{As}$  ( $m_e^* \sim 0.041$ ) [375].

In summary, the analysis showed that both  $V_p$  and  $J_p$  reduce employing an InAlGaAs-based emitter region.

### 5.3 RTD epitaxial structure design for high-power low-THz sources: general considerations

Based on the analysis in the preceding Section, a brief discussion on lattice-matched to InP  $n$ -type  $\text{In}_{0.53}\text{Ga}_{0.47}\text{As}/\text{AlAs}$  double-barrier RTD epitaxial structure design aimed at high-power low-THz oscillators working at around 300 GHz is hereby reported. The adopted design method-

### CHAPTER 5.3. RTD EPITAXIAL STRUCTURE DESIGN FOR HIGH-POWER LOW-THz SOURCES: GENERAL CONSIDERATIONS

ology focuses on  $\mathcal{P}_{RF,max}$  maximisation through the simulated static  $JV$  curve, i.e., maximisation of the associated negative differential resistance (NDR) region span.

In particular, the procedure consists in designing  $J_p$ ,  $V_p$ , and  $\Delta V$ , which can be accurately computed, according to the operational requirements, as well as analysing the heterostructure band diagram, electron density distribution, DBQW resonant states, LDOS, and transmission coefficient energy spectrum, which give qualitative information on  $J_v$  and  $\Delta J$ . The remaining parameters, including capacitance, QW inductance, as well as the valley current  $I_v = AJ_v$  (where  $A$  is the device mesa area), are then experimentally-retrieved through scattering (S)-parameters measurement and DC sweep of microfabricated RTD devices, through which load line and high-frequency circuit design (including impedance matching with the load/antenna) is accurately carried out.

Regarding the DBQW, moderately-thick AlAs barriers of thickness  $t_b = 1.17/1.46/1.75$  nm (4/5/6 ML) is recommended which, together with an  $\text{In}_{0.53}\text{Ga}_{0.47}\text{As}$  QW of thickness  $t_{qw} = 4.10/4.39/4.69$  nm (14/15/16 ML), can provide (depending on the overall epi-design) with  $J_p$  in the 200–300  $\text{kA/cm}^2$  range. The PVCr is typically above 3 in such structures [710]. This current density level is suggested for the design of large-size RTD devices aimed at oscillators operating at around 300 GHz [169], offering high-speed performance and thermal reliability. In this context,  $J_p$  up to around 400  $\text{kA/cm}^2$  can be employed.

Generally-speaking,  $t_b < 4$  ML is not advisable since makes  $J_p$  to increase well over 700  $\text{kA/cm}^2$ , and up to and above 1  $\text{MA/cm}^2$  [163], which is incompatible with large device sizes, and shrinks the PVCr well below 3 (rising  $J_v$ ), limiting the exploitable NDR extent available for RF gain. Moreover,  $t_b > 6$  ML dramatically lowers  $J_p$  (typically below 100  $\text{kA/cm}^2$ ) due to the pronounced associated exponential trend  $J_p(t_b)$ , as discussed in Section 5.2. At the same time, a moderate  $t_{qw} < 16$  ML helps in keeping  $J_p$  at the required level during emitter/collector spacers design, and enhances  $\Delta V$ . However, this shifts  $V_p$  and large bias, reducing the DC-to-RF efficiency, and lowers the PVCr, so care must be adopted during epi-design to balance/trade-off the different effects. On the other hand, the employment of  $t_{qw} \gg 16$  ML lowers  $V_p$  and significantly reduces  $J_p$ , so it is not recommended.

Shrinking the QW allows to reduce the electron quasi-bound-state resonant tunnelling lifetime, increasing the diode cut-off frequency (i.e., device bandwidth). Thus, moderately-thick DBQW regions featuring  $t_b = 5$  ML and  $t_{qw} = 15$  ML allow to realise high-speed RTD devices operating at 300 GHz, such as the one reported in [169], and similar performances are expected assuming  $t_b = 5 \pm 1$  ML and  $t_{qw} = 15 \pm 1$  ML. An example of designed and experimentally-demonstrated high-power RTD epitaxial structure is presented in Chapter 6.

Furthermore, the employment of  $\text{In}_{1-x}\text{Ga}_x\text{As}$  QWs with  $x = 0.47$ , i.e., low-strain budget  $\text{In}_{0.53}\text{Ga}_{0.47}\text{As}/\text{AlAs}$  DBQW heteroregions, improves the epitaxial growth uniformity, increasing microfabrication yield and device reliability. High-In content QWs, i.e.,  $x > 70\%$  [710], are not required in this context due to the moderate  $t_{qw}$  values (well above 3 nm), since it is not essential to counterbalance the rise of  $V_p$  by depressing the first quasi-bound resonant state  $E_1$ , which would dramatically reduce the structural quality of the grown wafers because of the highly-strained DBQW regions [697].

Regarding spacer layers, undoped spacers are used to avoid dopants diffusion from the emitter/collector extended regions into the DBQW. Thus, very-thin layers of around 1.5–2 nm (5–7 ML) in thickness are typically employed at both emitter/collector sides [163, 466]. At the same time, this prevents the formation of a large quasi-triangular potential (quantum) well at the emitter side close to the first barrier under forward bias (see Section 2.4.4 of Chapter 2), which would lead to significant charge accumulation, as well as the consequent formation of a parallel two-dimensional (2D)–2D electron tunnelling channel, impoverishing the designed  $JV$  curve.

On the other hand, lightly-doped spacers can be employed to tune  $J_p$  and  $V_p$ , and to enhance  $\Delta V$  [469]. Generally-speaking, a thick spacer layer at the collector side is recommended to greatly increase  $\Delta V$  above 1 V, and the associated shift of  $V_p$  at large bias (if significant) can be (partially) counteracted by playing on  $t_{qw}$ , by employing a high-band gap emitter alloy, such as  $\text{InGaAlAs}$  (as discussed in Section 5.2), or by tailoring the emitter lightly-doped spacer design. In this regard,  $V_p < 2$  V is recommended to keep the oscillator DC-to-RF efficiency to reasonable levels and to limit the dissipated power in the shunt resistor/s, which could lead to thermal breakdown.

The emitter lightly-doped spacer layer has to be designed to satisfy  $J_p$  and  $V_p$  requirements depending on the specific heterostructure, according to the considerations reported in Section 5.2. Here, an asymmetric thicknesses configuration is recommended to maximise  $\Delta V$ , i.e.,  $t_{ls}^e \ll t_{ls}^c$ , while the suggested doping levels  $N_{D,ls}^{e/c}$  are of the order of  $10^{16/17} \text{ cm}^{-3}$ . Generally-speaking, spacers thickness and doping level highly-influence the device self-capacitance (as well as the RTD overall frequency response), so this must be considered during device design.

Regarding emitter and collector regions, a high doping level  $N_D$  of the order of  $10^{18} \text{ cm}^{-3}$  is typically employed to guarantee highly-populated reservoirs for carriers injection [163], while heavily-doped contacts are designed to minimise the associated Ohmic contact resistance, i.e., lowering the metal-to-semiconductor Schottky barrier by maximising the doping level (where  $N_D$  is typically of the order of  $10^{19} \text{ cm}^{-3}$  [541]) and/or by increasing the associated In mo-

lar fraction (especially at the collector contact) [470]. In this regard,  $p$ -type Schottky contacts could be employed, as already discussed in Chapter 2 [444]. Further, the emitter contact layer thickness must be designed to allow practical wet-etching and according to the sheet resistance requirements of the employed shunt resistor/s.

To conclude, it is worth to underline that the aforementioned considerations have to be considered as general guidelines, while an ad-hoc investigation analysis, followed by subsequent design optimisation, must be achieved for any specific RTD heterostructure under study, according to the specific operation requirements. In the next Chapter, an example of designed and experimentally-investigated epitaxial structure is presented, demonstrating the validity of the proposed design approach for high-power 300-GHz RTD oscillator sources.

## 5.4 Summary

This Chapter presented an epitaxial structure investigation study of  $\text{In}_{0.53}\text{Ga}_{0.47}\text{As}/\text{AlAs}$  RTDs using the simulation approach demonstrated in Chapter 4, which is based on the non-equilibrium Green's function (NEGF) method implemented in Silvaco Atlas TCAD simulation package. The analysis focused on barriers, QW, and lightly-doped spacer layers design, as well as on the employment of a high energy band gap emitter alloy, and on the associated impact on several RTD heterostructure physical quantities, including the DC  $JV$  curve, transmission coefficient energy spectrum, electron density, and band profile at RT. The retrieved trends were analysed and general device design guidelines for high-power low-THz emitters deduced.

To summarise, RTD epitaxial design aimed at RF power maximisation focuses on the static  $JV$  curve, which is tailored to maximise the NDR region span defined by the available current  $\Delta I$  and voltage swing  $\Delta V$ . Within the developed simulation approach, the DBQW region and spacer layers of the RTD heterostructure must be designed and optimised to achieve moderate peak current density  $J_p$  and to maximise  $\Delta V$ , which allows the employment of large mesa areas. In the context of oscillator design, this requires a careful device analysis based on the specific requirements dictated by oscillator performance. Generally-speaking, device design optimization is always conducted based on RF power-cut-off frequency trade-offs.

## Chapter 6

# A high-power $\text{In}_{0.53}\text{Ga}_{0.47}\text{As}/\text{AlAs}$ double-barrier resonant tunnelling diode epitaxial structure for 300-GHz oscillators

In the present Chapter, an optimised high-power indium gallium arsenide/aluminium arsenide ( $\text{InGaAs}/\text{AlAs}$ ) double-barrier resonant tunnelling diode (RTD) epitaxial structure grown on indium phosphide (InP) is demonstrated. The heterostructure was designed using the non-equilibrium Green's function quantum transport simulation approach described in Chapter 4, and was experimentally investigated through the microfabrication and characterisation of RTD devices. The high-frequency radio-frequency (RF) power performance of the epitaxial structure is analysed based on the extracted small-signal equivalent circuit parameters.

The analysis shows that a  $16 \mu\text{m}^2$ -large RTD is capable of providing an RF power in excess of 3 mW at 300 GHz, while a  $49 \mu\text{m}^2$ -large device is expected to deliver up to around 10 mW, which is up to around five times higher compared to the current state-of-the-art. Distributed inductors in both coplanar and microstrip geometry are designed through full three-dimensional electromagnetic simulations, proving the feasibility of the proposed approach for the practical realisation of high-power 300-GHz oscillator sources employing low-cost optical lithography.

### 6.1 RTD heterostructure design

The proposed  $n$ -type intra-band RTD epitaxial structure is shown in Figure 6.1, which was designed to achieve moderate current density operation (with peak current density  $J_p \sim 200\text{--}300 \text{ kA}/\text{cm}^2$ ), which allows the employment of large mesa areas  $A \gg 1 \mu\text{m}^2$ , low peak voltage  $V_p < 2 \text{ V}$ , and large valley-to-peak voltage difference  $\Delta V = V_v - V_p \gg 0.5 \text{ V}$ . In particular, it consists of a lattice-matched to InP  $\text{In}_{0.53}\text{Ga}_{0.47}\text{As}/\text{AlAs}$  double-barrier quantum well (DBQW) structure, and it features moderately-thick AlAs barriers (around 1.46 nm-thick, which corresponds to five

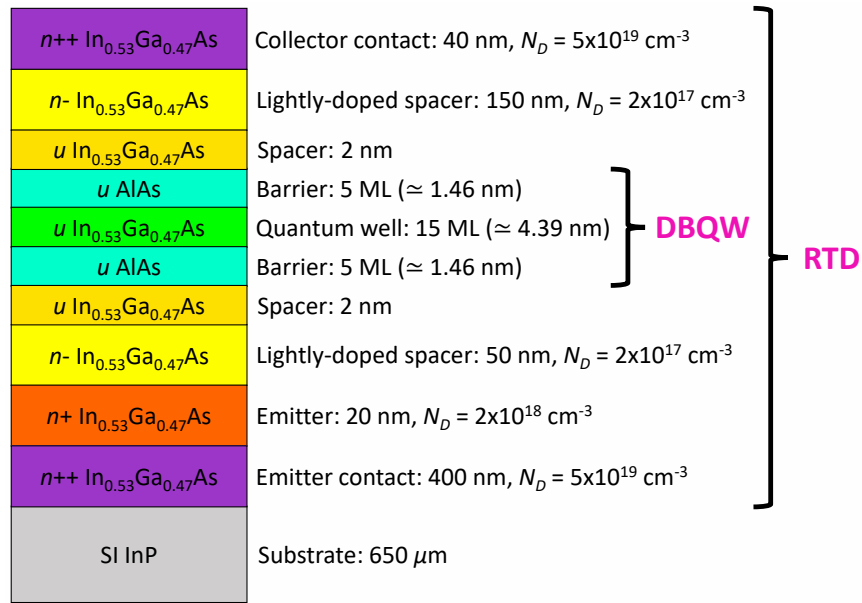


Figure 6.1: Proposed  $n$ -type intra-band  $\text{In}_{0.53}\text{Ga}_{0.47}\text{As}/\text{AlAs}$  RTD epitaxial structure.

atomic layers, where one monolayer (ML) is equal to around 0.293 nm) and an  $\text{In}_{0.53}\text{Ga}_{0.47}\text{As}$  QW of thickness of around 4.39 nm (15 ML). Two 2 nm-thick undoped spacers are placed close to the two barriers, while asymmetric lightly-doped spacers design is employed to achieve large  $\Delta V$ . In this context, the emitter lightly-doped spacer thickness and doping level  $N_D$  are set to 50 nm and  $2 \times 10^{17} \text{ cm}^{-3}$ , respectively, to satisfy  $J_p$  and  $V_p$  requirements, while the collector lightly-doped spacer to 150 nm and  $2 \times 10^{17} \text{ cm}^{-3}$  to guarantee large  $\Delta V$ .

At the same time, a 20 nm-thick emitter region (with doping level  $N_D = 2 \times 10^{18} \text{ cm}^{-3}$ ) is included, together with 40/400 nm-thick collector/emitter heavily-doped  $\text{In}_{0.53}\text{Ga}_{0.47}\text{As}$  contact layers ( $N_D = 5 \times 10^{19} \text{ cm}^{-3}$ ). The simulated current density-voltage ( $JV$ ) characteristic at room temperature (RT) was accurately tailored and features  $J_p \simeq 270 \text{ kA/cm}^2$ ,  $V_p \simeq 1.2 \text{ V}$  and  $\Delta V \simeq 1.7 \text{ V}$ . The wafer structure was grown through molecular beam epitaxy (MBE) by Intelligent Epitaxy Technology (IntelliEPI) on a 650  $\mu\text{m}$ -thick 3" (100) semi-insulating (SI) InP wafer substrate.

## 6.2 RTD devices microfabrication

RTD devices with square top mesa area  $A = 3 \times 3 \mu\text{m}^2$  were fabricated to accurately characterise the heterostructure. Microfabrication was carried out as described in Chapter 3. Ohmic contacts were processed using a titanium/palladium/gold (Ti/Pd/Au=20/30/150 nm) metal stack. Here, no surface cleaning procedure was adopted prior to metal evaporation. The mesas lateral undercut  $\sigma$  due to anisotropic chemical wet etching was estimated to be around  $3.5 \mu\text{m}^2$ , which was confirmed through scanning electron microscopy (SEM) analysis, resulting in an effective

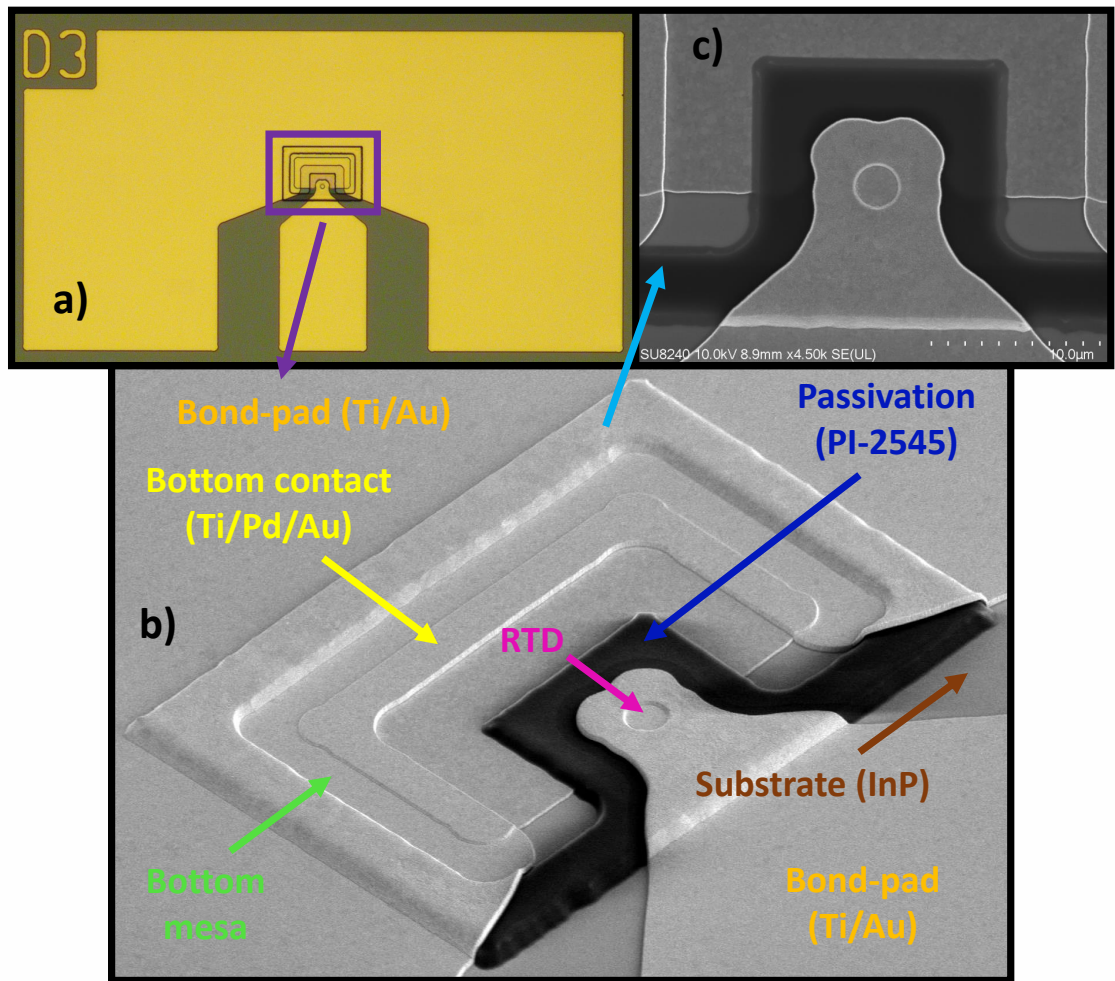


Figure 6.2: In a), photo-micrograph of a fabricated RTD device; in b), SEM image zoom-in over the RTD region; in c), zoom-in over the opened via.

$A \simeq 5.5 \mu\text{m}^2$ . Furthermore, passivation was carried out employing a  $1.2 \mu\text{m}$ -thick polyimide PI-2545 layer. A photo-micrograph and SEM images of a fabricated RTD device are shown in Figure 6.2.

### 6.3 RTD devices DC and RF characterisation

The devices were DC measured using a B1500A semiconductor parameter analyser (SPA) [711] from Keysight Technologies, and the associated static current-voltage ( $IV$ ) characteristic is shown in Figure 6.3 together with the simulated counterpart. Several RTDs on the processed sample were characterised, and no difference in their electrical characteristic was revealed. The heterostructure  $JV$  curve electrical quantities are reported in Table 6.1, where the measured  $J_p$  is around  $195 \text{ kA/cm}^2 = 1.95 \text{ mA}/\mu\text{m}^2$ ,  $J_v \simeq 0.57 \text{ mA}/\mu\text{m}^2$ ,  $\Delta J \simeq 1.38 \text{ mA}/\mu\text{m}^2$ ,  $\text{PVCR} \simeq 3.5$ ,  $V_p \simeq 1.36 \text{ V}$ ,  $V_v \simeq 2.55 \text{ V}$ , and  $\Delta V \simeq 1.2 \text{ V}$ , where  $J_v$  is the valley current density,  $\Delta J = J_p - J_v$  the available current density, while  $\text{PVCR} = J_p/J_v$  the peak-to-valley current ratio.

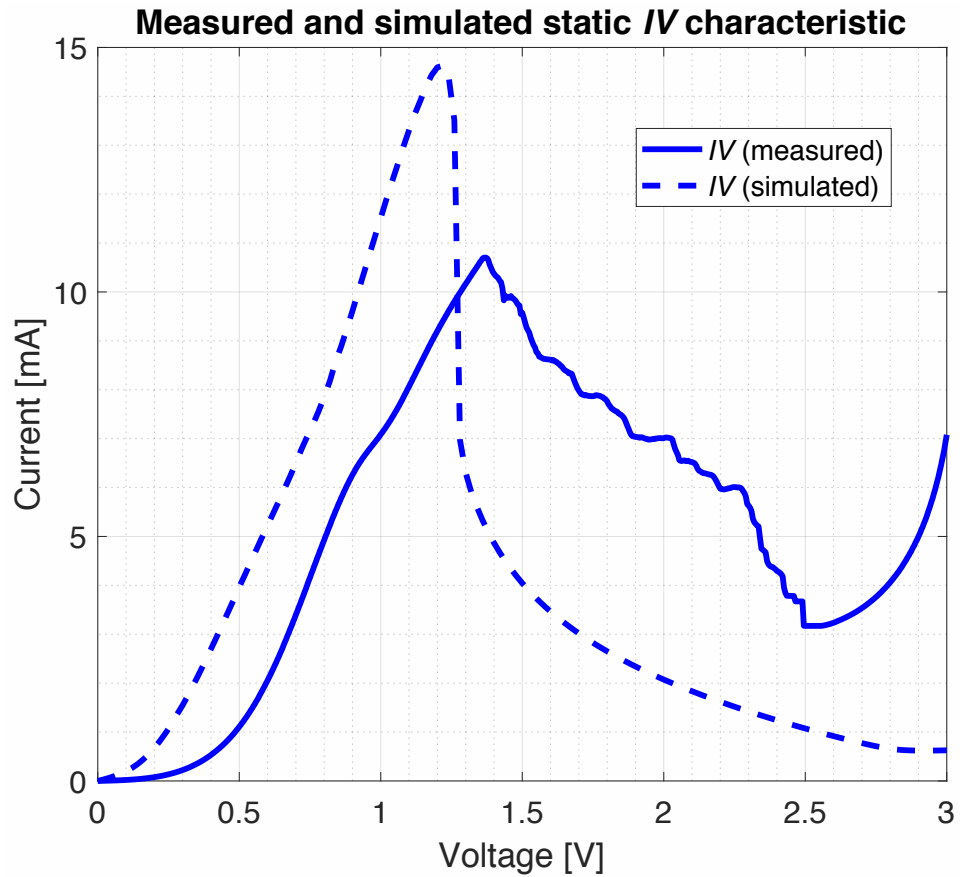


Figure 6.3: Measured and simulated static  $IV$  characteristic of the designed RTD devices.

Table 6.1: RTD epitaxial structure extracted static  $JV$  curve electrical quantities.

$J_p$ [mA/ $\mu\text{m}^2$ ]	$J_v$ [mA/ $\mu\text{m}^2$ ]	$\Delta J$ [mA/ $\mu\text{m}^2$ ]	PVCR	$V_p$ [V]	$V_v$ [V]	$\Delta V$ [V]
1.95	0.57	1.38	3.5	1.36	2.55	1.2

The poor electrical properties of the heterostructure compared to design is attributed to the lack of surface cleaning steps before Ohmics metallisation (which increases the associated contact resistance  $R_c$ , and leads to higher  $V_p$  and smaller  $\Delta V$ ) and, more importantly, to the poor quality achieved during epitaxial growth, where current density and the negative differential resistance (NDR) span (so  $J_p$ ,  $\Delta J$ ,  $V_v$ ,  $\Delta V$ , and the PVCR) are affected by structural defects and imperfections, shrinking the NDR region.

At the same time, this might also explain the kink shown at around 0.95 V. In particular, this can be attributed to random dopants fluctuations, as well as to crystalline defects and structural imperfections, at the emitter side. An accurate and precise description of this effect in the context of the fabricated wafer is unknown at present. However, this does not compromise the high-frequency operation of the RTD device when biased into the NDR region.

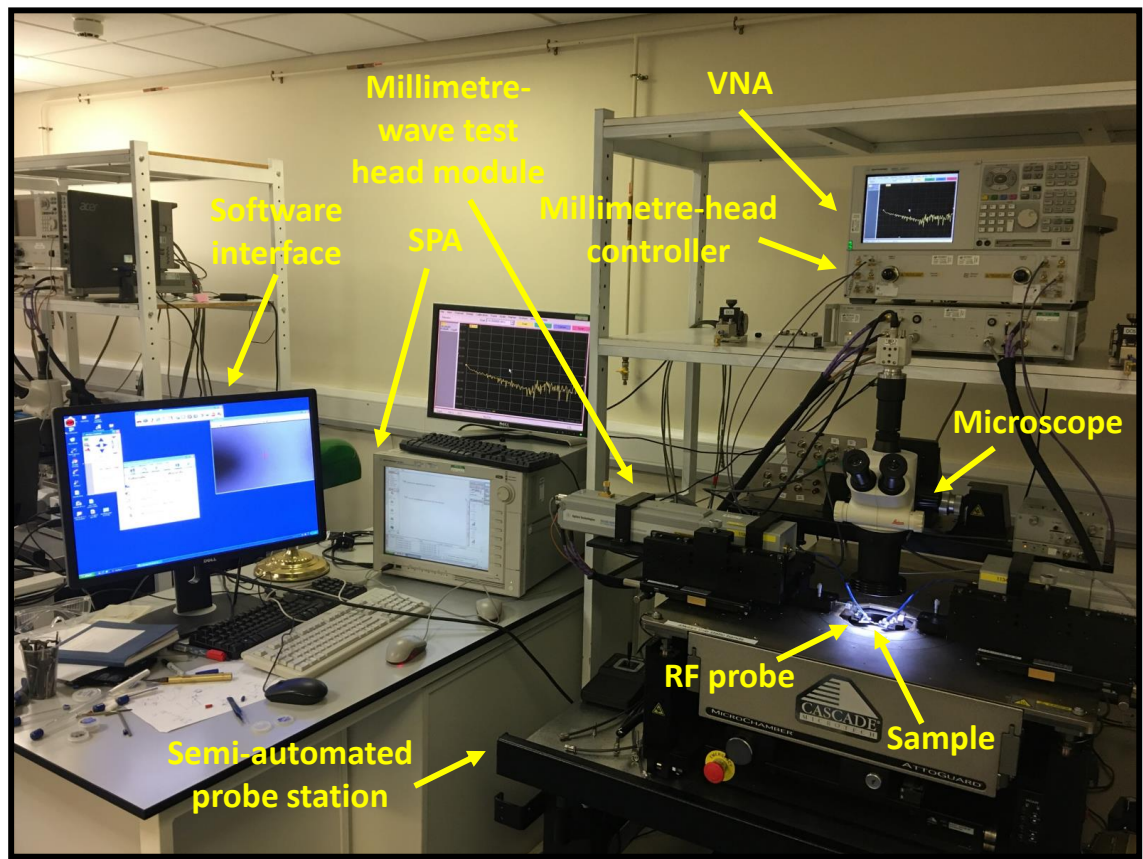


Figure 6.4: Experimental setup for RTD devices S-parameters measurement.

To determine the high-frequency performance of the proposed epitaxial structure, an estimate of the device small-signal equivalent circuit parameters within the NDR region is required, as discussed in Chapter 2. Since the moderate current RTDs (where the measured peak current  $I_p = AJ_p \simeq 11$  mA) exhibited instability within the NDR region due to low-frequency parasitic oscillations caused by the bias line inductance (as shown in Figure 6.3), direct scattering (S)-parameters measurement was not feasible. Therefore, the device high-frequency response was estimated according to the following approach.

First, S-parameters were measured in both the first and second positive differential resistance (PDR) regions, which are stable. To do that, after accurate calibration, on-wafer one-port measurements were carried out in the frequency range 10 MHz–110 GHz using an E8361A programmable network analyser (PNA) [712] system working in the frequency range 10 MHz–67 GHz, including an N5260A millimetre head controller [713] and an N5260-60013 67–110 GHz millimetre-wave test head module [714] (combiner assembly working as frequency extender including the bias-Tee), and a B1500A SPA [711] as power supply (also used for DC sweep, as already mentioned), all from Keysight Technologies, as well as a summit semi-automated probe station from CASCADE MICROTECH [715].

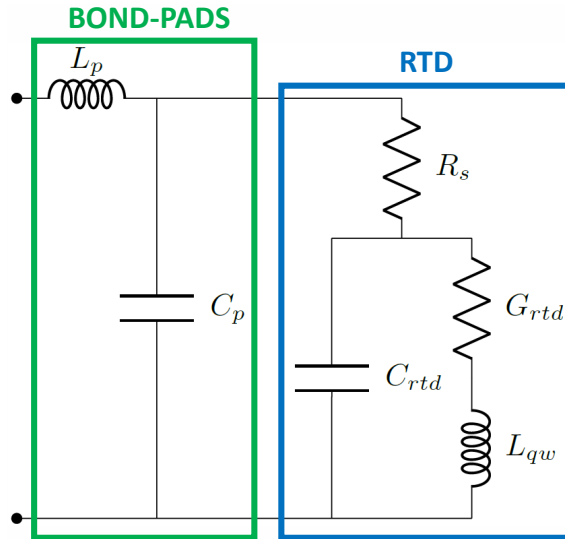


Figure 6.5: RTD device and bond-pads small-signal equivalent circuit.

The employed measurement experimental setup is shown in Figure 6.4. Here, the input signal power was set to -24 dBm. This allows to practically-retrieve the  $S_{11}$  parameter (i.e., input reflection coefficient/return loss of the RTD and bond-pads system) avoiding oscillations triggering if the device is biased close to the NDR region.

Based on the measured  $S_{11}$  parameter, the device small-signal equivalent circuit parameters were extracted through both  $S_{11}$  and the converted  $Z_{11}$  impedance parameter, where [609]:

$$Z_{11} = Z_0 \left[ \frac{1 + S_{11}}{1 - S_{11}} \right] \quad (6.1)$$

being  $Z_0 = 50 \Omega$  the characteristic impedance of the employed measurement setup. In this context, the designed and fabricated RTD devices bond-pads feature a coplanar waveguide (CPW) design with same  $Z_0$  (as discussed in Chapter 3) in order to match with the employed radio-frequency (RF) ground-signal-ground (GSG) probe from GGB INDUSTRIES (PICOPROBE MODEL 110H [716]), working from DC to 110 GHz and featuring  $100 \mu\text{m}$  pitch.

To do that, the small-signal equivalent circuit model of the RTD device and bond-pads, which is shown in Figure 6.5, was adopted (which was discussed in Chapter 2), comprising of the bond-pads inductance  $L_p$  and capacitance  $C_p$ , and of the RTD series resistance  $R_s \approx R_c$  (where  $R_c$  is the Ohmic contacts resistance), differential conductance  $G_{rtd}$ , capacitance  $C_{rtd}$ , and QW inductance  $L_{qw}$ . Here, the bond-pads resistance  $R_p$  was omitted since negligible, as discussed in Chapter 4. The model was imported in Advance Design System (ADS) and the measured  $S_{11}$  and converted  $Z_{11}$  parameters fitted at both first and second PDR regions bias points  $V = 0.3 \text{ V}$  and  $V = 2.7 \text{ V}$ , respectively. The adopted ADS schematic is reported in Appendix E.

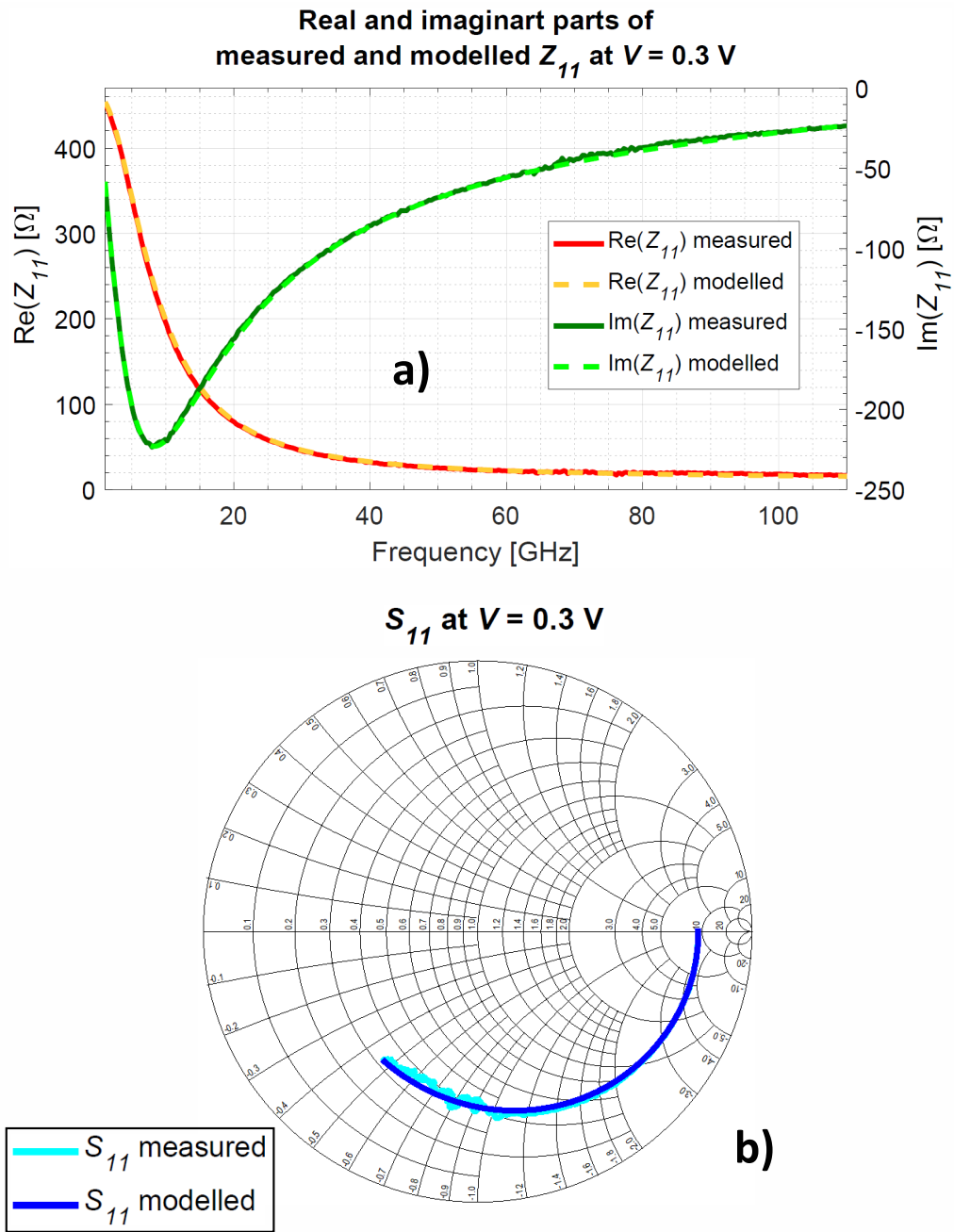


Figure 6.6: In a), measured and modelled real and imaginary parts of  $Z_{11}$  at  $V = 0.3$  V; in b), measured and modelled  $S_{11}$  on Smith chart at  $V = 0.3$  V.

Fitting results are shown in Figures 6.6 and 6.7, while the associated extracted small-signal parameters are reported in Tables 6.2 and 6.3, respectively. Good match between the extracted and modelled  $G_{rtd} = dI/dV$  values at the analysed bias points was met. The variation of  $R_s$  with bias is in agreement with recently-reported works [395]. This can be attributed to the change of the electrostatic Schottky potential barrier profile at the contacts (affecting  $R_c$ ), and to the electric field dependence of electron mobility, which affects the device access resistance [717].

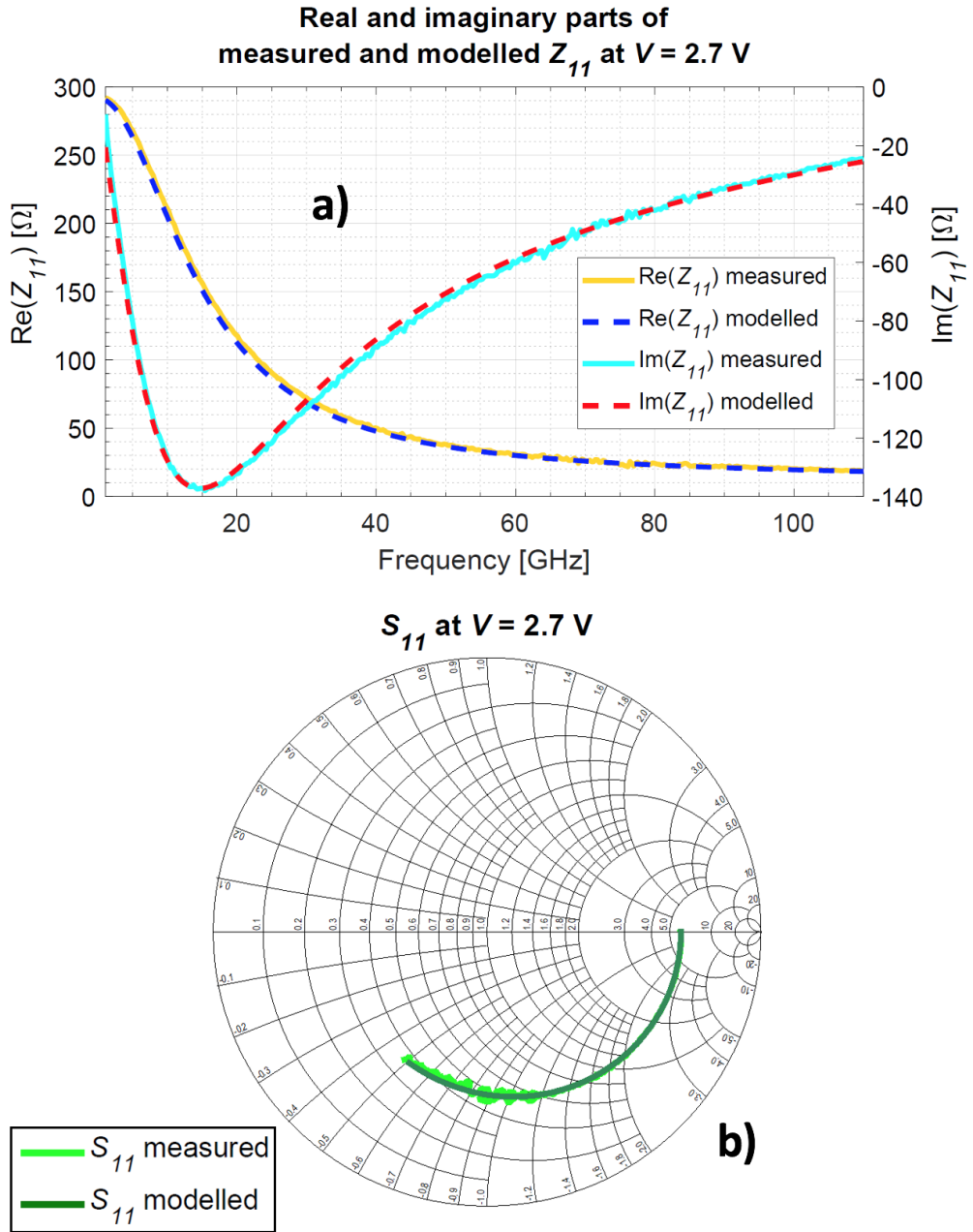


Figure 6.7: In a), measured and modelled real and imaginary parts of  $Z_{11}$  at  $V = 2.7$  V; in b), measured and modelled  $S_{11}$  at  $V = 2.7$  V.

Based on the extracted small-signal parameters, the electron QW-to-collector escape rate  $\nu_c$  and the total intrinsic delay time  $\tau_{in}$  at the analysed bias points, can be retrieved as:

$$\nu_c = -\frac{G_{rtd}(V)}{C_{qw}(V)} = -\frac{G_{rtd}(V)}{C_{rtd}(V) - C_d} \quad (6.2)$$

$$\tau_{in} = L_{qw}(V)G_{rtd}(V) \quad (6.3)$$

as discussed in Chapter 2, where  $C_{qw}$  is the quantum capacitance, while  $C_d$  the RTD self-capacitance, which was estimated to be around 26.7 fF for the fabricated devices from self-

Table 6.2: Extracted RTD device and bond-pads small-signal parameters at  $V = 0.3$  V.

$C_p$ [fF]	$L_p$ [pH]	$R_s$ [ $\Omega$ ]	$G_{rtd}$ [mS]	$C_{rtd}$ [fF]	$L_{qw}$ [pH]
17	21	42.1	2.4	27.3	130

 Table 6.3: Extracted RTD device and bond-pad small-signal parameters at  $V = 2.7$  V.

$C_p$ [fF]	$L_p$ [pH]	$R_s$ [ $\Omega$ ]	$G_{rtd}$ [mS]	$C_{rtd}$ [fF]	$L_{qw}$ [pH]
17	21	43.9	4.0	26.9	80

consistent Schrödinger-Poisson numerical simulations (using the approach described in Chapter 4) based on the heterostructure geometry, and around 27.9 fF if correcting with the parasitic capacitance of the passivation layer, which was estimated to be around 1.2 fF from the employed mask layout. This allows to accurately estimate  $v_c$ , which only depends on the epitaxial layer structure.

The extracted values are  $v_c \simeq 4.0$  THz ( $\tau_c = v_c^{-1} \simeq 0.25$  ps) and  $\tau_{in} \simeq 0.316$  ps, which are reasonable if compared to [411] due to the thinner employed barriers (5 ML instead of 9 ML) and QW (15 ML instead of 16 ML). In Eq. (6.3),  $L_{qw}$  is assumed to account for both  $\tau_{dbqw}$  and  $\tau_t$  ( $\tau_{in} = \tau_{dbqw} + \tau_t/2$ ), where  $\tau_{dbqw}$  is the electron DBQW quasi-bound state lifetime, while  $\tau_t$  the electron transit time across the emitter/collector depletion regions. Here, both  $v_c$  and  $\tau_{in}$  are treated as bias-independent, as discussed in Chapter 2, which was confirmed by the weak bias dependency of the extracted quantities.

In this context,  $\tau_{in}$  can be also easily-estimated from self-consistent Schrödinger-Poisson numerical simulations conducted in Atlas TCAD, which was described in Chapter 4. For the analysed heterostructure, the computed  $\tau_{dbqw}$  is around 0.26 ps from the simulated transmission coefficient first subband resonance peak energy broadening  $\Gamma_1$  (as discussed in Chapter 2), which was estimated to be around 2.6 meV, as shown in Figure 6.8.

Moreover,  $\tau_t$  was estimated to be around 13 fs assuming the  $\text{In}_{0.53}\text{Ga}_{0.47}\text{As}$  electron saturation velocity  $v_{e,s} \sim 3 \times 10^7$  cm/s [416]. This gives a total  $\tau_{in} \simeq 0.265$  ps, which is in good agreement with the extracted counterpart.

Then, the trend of  $G_{rtd}$ ,  $C_{rtd}$ , and  $L_{qw}$  with bias can be computed as:

$$G_{rtd}(V) = \frac{dI}{dV} \quad (6.4)$$

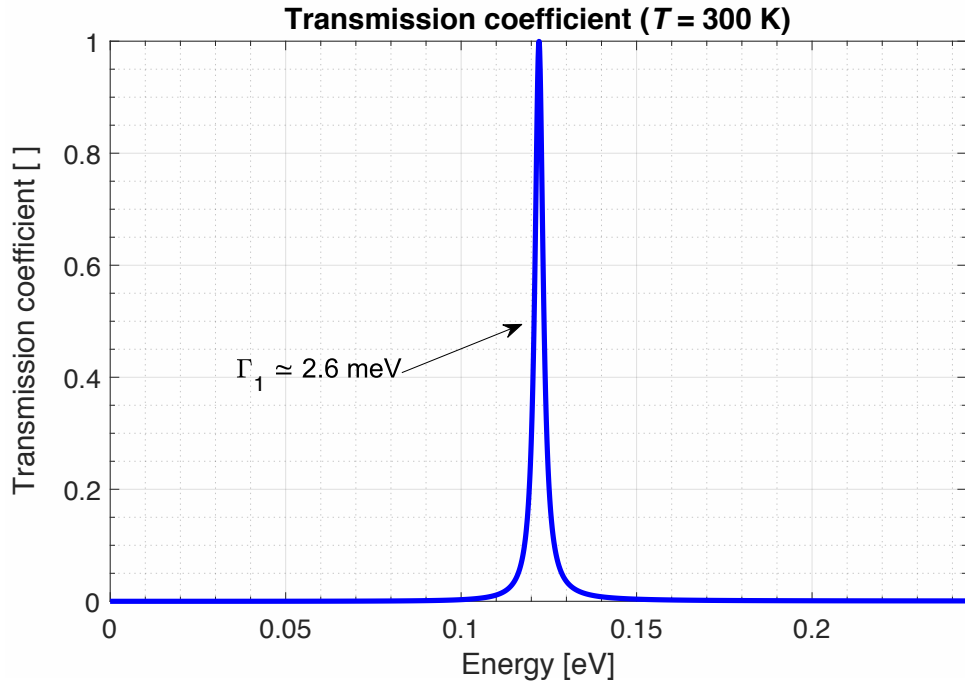


Figure 6.8: Simulated transmission coefficient (linear scale) first subband resonance peak at RT ( $T = 300$  K), outlining the related energy broadening. Thermal equilibrium was assumed based on the bias-independency assumption of  $\tau_{in}$ .

Table 6.4: Employed polynomial expansion coefficients of the  $IV$  curve within the NDR region.

$p_0$	$p_1$	$p_2$	$p_3$	$p_4$	$p_5$	$p_6$
-2092	6044	-7059	4300	-1446	255.2	-18.47

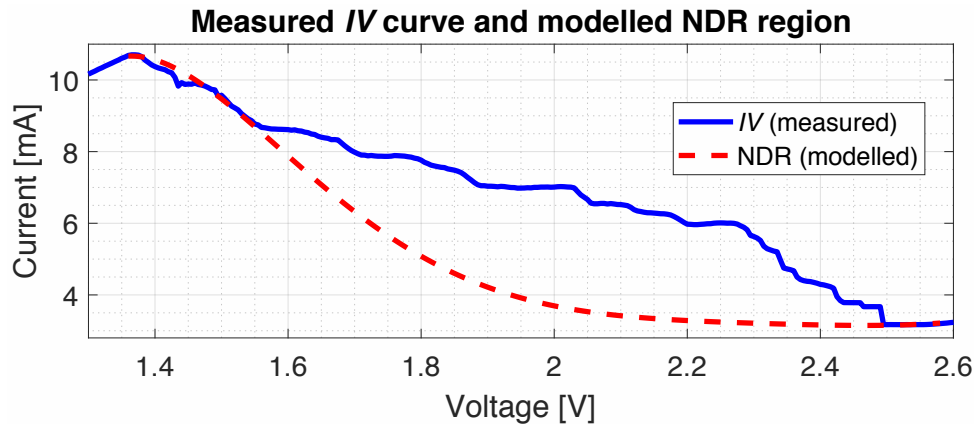
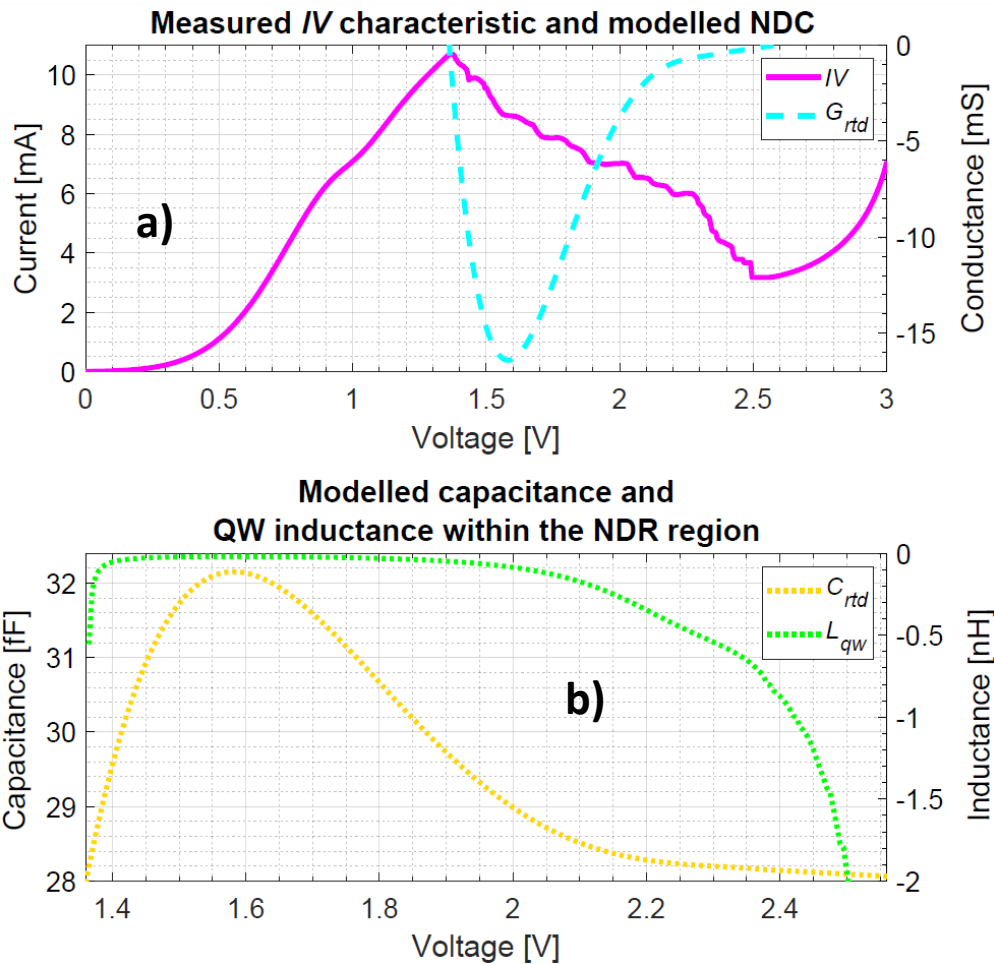
$$C_{rtd}(V) = C_d + C_{qw}(V) = C_d - \frac{G_{rtd}(V)}{v_c} \quad (6.5)$$

$$L_{qw}(V) = \frac{\tau_{in}}{G_{rtd}(V)} \quad (6.6)$$

Within the NDR region, the  $IV$  curve was accurately modelled in Matlab through a sixth-order polynomial function because of the associated instability:

$$I(V) = \sum_{i=0}^6 p_i V^i \quad (6.7)$$

where the employed coefficients  $p_i$  are reported in Table 6.4. To achieve that, the curve was fitted based on the behaviour in proximity of the peak and valley regions (i.e.,  $V \sim V_p$  and  $V \sim V_v$ ), as shown in Figure 6.9. Here, the sixth-order was found to be the highest and most suitable for accurate fitting of the analysed  $IV$  curve.


 Figure 6.9: Measured static  $IV$  characteristic and modelled NDR region.

 Figure 6.10: In a), measured static  $IV$  characteristic and modelled NDC; in b), modelled capacitance and QW inductance with the NDR region.

The RTD measured  $IV$  curve, as well as modelled negative differential conductance (NDC), and associated negative QW inductance and capacitance, are shown in Figure 6.10. Similar trends compared to previously-reported works are revealed [438]. Here, the estimated RTD NDC (corresponding to the maximum value  $|G_{rtd}|_{max}$  in the NDR region), and associated  $C_{rtd}$

Table 6.5: RTD epitaxial structure extracted high-frequency electrical parameters.

$\tau_{in}$ [ps]	$\nu_c$ [THz]	$\mathcal{G}_{rt}^*$ [mS/ $\mu\text{m}^2$ ]	$\mathcal{C}_{rt}^*$ [fF/ $\mu\text{m}^2$ ]	$\mathcal{L}_{qw}^*$ [pH/ $\mu\text{m}^2$ ]
0.316	4.0	-3.0	5.64	-3.47

\* Estimated in the NDR region.

and  $L_{qw}$ , are estimated to be around -16.5 mS, 32.2 fF, and -19.1 pH, respectively, at the bias point  $V = 1.58$  V.

These correspond to the RTD epitaxial structure density quantities  $\mathcal{G}_{rt} = G_{rt}/A \simeq -3.0$  mS/ $\mu\text{m}^2$ ,  $\mathcal{C}_{rt} = C_{rt}/A \simeq 5.64$  fF/ $\mu\text{m}^2$  (by correcting back with the parasitic contribute due to the passivation layer), and  $\mathcal{L}_{qw} = L_{qw}/A \simeq -3.47$  pH/ $\mu\text{m}^2$ . The relevant RTD heterostructure extracted high-frequency electrical parameters are summarised in Table 6.5.

## 6.4 High-frequency RF power analysis

As discussed in Chapter 2, the intrinsic response frequency limit  $f_{in}$  of the RTD heterostructure can be expressed as:

$$f_{in} = \frac{1}{4\tau_{in}} \quad (6.8)$$

which is estimated to be around 775 GHz for the analysed epitaxial structure, while the associated maximum RF power density  $\mathcal{P}_{RF,max}$  is given by:

$$\mathcal{P}_{RF,max} = \frac{P_{RF,max}}{A} = \frac{3}{16}\Delta J\Delta V \quad (6.9)$$

and is estimated to be around 0.31 mW/ $\mu\text{m}^2$  for the present heterostructure. On the other hand, the intrinsic RF power density at high-frequency  $\mathcal{P}_{RF,in}$  can be written as:

$$\mathcal{P}_{RF,in} = \mathcal{P}_{RF,max} \cos(2\pi f_{op}\tau_{in}) \quad (6.10)$$

and is estimated to be around 0.26 mW/ $\mu\text{m}^2$  at the operation frequency  $f_{op} = 300$  GHz.

The cut-off frequency limit of the RTD heterostructure due to external parasitics can be modelled through the extrinsic delay time  $\tau_{ex}$ :

$$\tau_{ex} \approx \frac{\pi\mathcal{C}_{rt}}{2} \sqrt{\frac{\rho_c}{|\mathcal{G}_{rt}|}} \quad (6.11)$$

where  $\rho_c = AR_c$  is the specific contact resistivity, and  $R_c = R_{c,t} + R_{c,b} = \rho_c/(A + A_b)$  (being  $R_{c,t}$

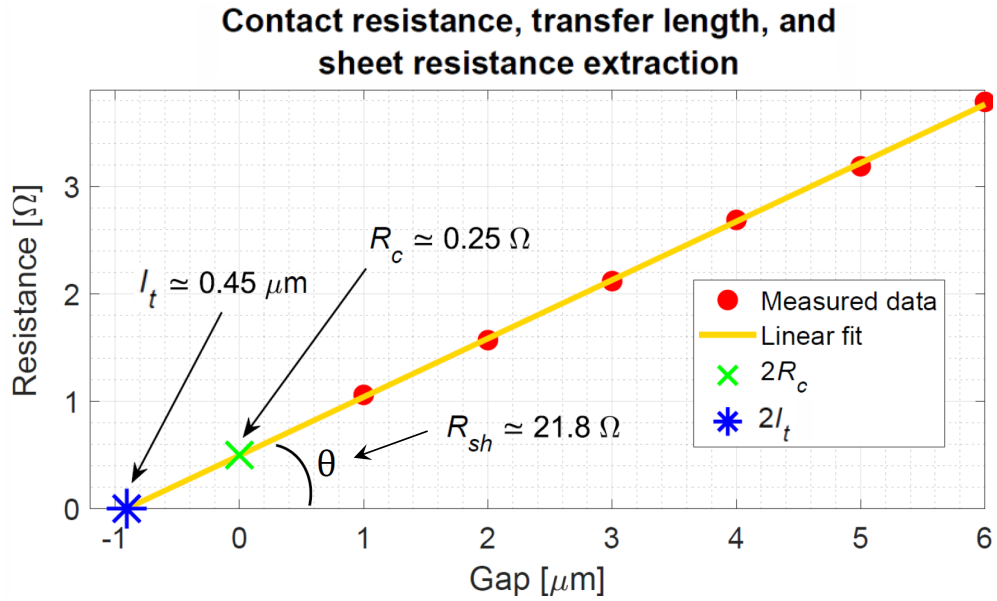


Figure 6.11: Extraction of the contact resistance  $R_c$ , semiconductor sheet resistance  $R_{sh} \propto \tan \theta$ , and transfer length  $l_t = |l_t|$  through linear fitting over the measured data.

and  $R_{c,b}$  the contact resistances associated with the RTD top and bottom Ohmic contacts, respectively, while  $A_b$  is the bottom contact area), where  $R_c \approx R_{c,t}$  since the ratio  $R_{c,t}/R_{c,b} = A_b/A$  was estimated to be around 22 for the fabricated devices. Since, no surface de-oxidation was carried out during Ohmics fabrication,  $\rho_c$  was estimated to be around  $231 \Omega \mu\text{m}^2$  from the measured S-parameters, which is comparable to previously-reported works [411], giving  $\tau_{ex} \simeq 2.46$  ps.

However,  $\tau_{ex}$  can be greatly reduced by appropriately fabricating the Ohmic contacts. For instance, assuming the procedure described in Chapter 4,  $\rho_c$  can be lowered to around  $13 \Omega \mu\text{m}^2$ , which gives  $\tau_{ex} \simeq 0.58$  ps. However, this can be reduced even further adopting the fabrication method described in Chapter 3 based on the molybdenum (Mo)/Ti/Au=20/20/150 nm metal stack. This includes a pre-evaporation cleaning step consisting of a 1 h + 4.5 min oxidation under ultra-violet (UV) light in a ozone ( $\text{O}_3$ )-based environment, followed by 2 min wet chemical etching (de-oxidation) in a hydrochloric acid (HCl)-based dilute solution (HCl:H<sub>2</sub>O=1:3), and a 40 s-long argon ions ( $\text{Ar}^+$ )-based ion milling. The deposition chamber loading time was kept around 30 s.

Figure 6.11 shows the extraction procedure of  $\rho_c$  based on the transfer length model of a processed transmission line measurement (TLM) structure, as discussed in Chapter 2. The extracted  $\rho_c$  was around  $4 \Omega \mu\text{m}^2$  (with  $\pm 1 \Omega \mu\text{m}^2$  variability among different TLMs) ( $R_c \simeq 0.7 \Omega$  for the fabricated RTDs), while the associated TLM parameters are reported in Table 6.6. This is close to state-of-the-art Ohmic contacts to InGaAs [461] and to previously-reported ex-situ values employing the same metal stack [622, 650], as well as to reported values for fabricated

Table 6.6: Measured/extracted parameters obtained from TLM structures characterisation\*.

$R_1$ [ $\Omega$ ]	$R_2$ [ $\Omega$ ]	$R_3$ [ $\Omega$ ]	$R_4$ [ $\Omega$ ]	$R_5$ [ $\Omega$ ]	$R_6$ [ $\Omega$ ]	$R_{sh}$ [ $\Omega$ ]	$R_c$ [ $\Omega$ ]	$l_t$ [ $\mu\text{m}$ ]	$\rho_c$ [ $\Omega \mu\text{m}^2$ ]
1.06	1.57	2.12	2.69	3.19	3.79	21.8	0.25	0.45	4

\* In the above,  $R_{t,i}$  (where  $i = 1, \dots, 6$ ) is the measured total resistance,  $R_{sh}$  is the extracted semiconductor sheet resistance,  $R_c$  is the extracted contact resistance, while  $l_t$  is the extracted transfer length.

RTD oscillators operating at terahertz (THz) frequencies [545, 546]. The discrepancy compared to in-situ results [658] can be attributed to the incomplete removal of the thin surface oxide layer, mainly due to atmosphere exposure between wet etching and loading into the evaporation chamber.

Hence,  $\tau_{ex}$  is estimated to be around 0.58 ps and 0.32 ps assuming  $\rho_c = 13 \Omega \mu\text{m}^2$  and  $4 \Omega \mu\text{m}^2$ , respectively. The RTD heterostructure maximum oscillation frequency  $f_{max}$  is, therefore, given by:

$$f_{max} \approx \frac{1}{4\tau_{ex}} \approx \frac{|\mathcal{G}_{rtd}|}{2\pi\mathcal{C}_{rtd}} \sqrt{\frac{1}{\rho_c|\mathcal{G}_{rtd}|} - 1} \quad (6.12)$$

which is estimated to be around 420 GHz and 768 GHz (approaching  $f_{in}$ ) assuming  $\rho_c = 13 \Omega \mu\text{m}^2$  and  $4 \Omega \mu\text{m}^2$ , respectively. The total delay time  $\tau_{rtd}$  due to both intrinsic and extrinsic contributes is then given by:

$$\tau_{rtd} = \sqrt{\tau_{in}^2 + \tau_{ex}^2} \quad (6.13)$$

and is estimated to be around 0.67 ps and 0.46 ps, which correspond to cut-off frequencies  $f_c$ :

$$f_c = \frac{1}{4\tau_{rtd}} \quad (6.14)$$

of around 375 GHz and 547 GHz assuming  $\rho_c = 13 \Omega \mu\text{m}^2$  and  $4 \Omega \mu\text{m}^2$ , respectively. If  $\rho_c = 231 \Omega \mu\text{m}^2$ ,  $f_c \simeq 101$  GHz, meaning that the heterostructure cannot operate at 300 GHz.

The RF power density of the proposed RTD heterostructure at high-frequency  $\mathcal{P}_{RF}$  is, therefore, given by:

$$\mathcal{P}_{RF} = \mathcal{P}_{RF,max} \cos(2\pi f_{op} \tau_{rtd}) \quad (6.15)$$

which is estimated to be around  $0.10 \text{ mW}/\mu\text{m}^2$  and  $0.20 \text{ mW}/\mu\text{m}^2$  assuming  $\rho_c = 13 \Omega \mu\text{m}^2$  and  $4 \Omega \mu\text{m}^2$ , respectively. The high-frequency RF power performance of the RTD heterostructure, including frequency limits and associated estimated parameters, are summarised in Figure 6.12 and Tables 6.7 and 6.8.

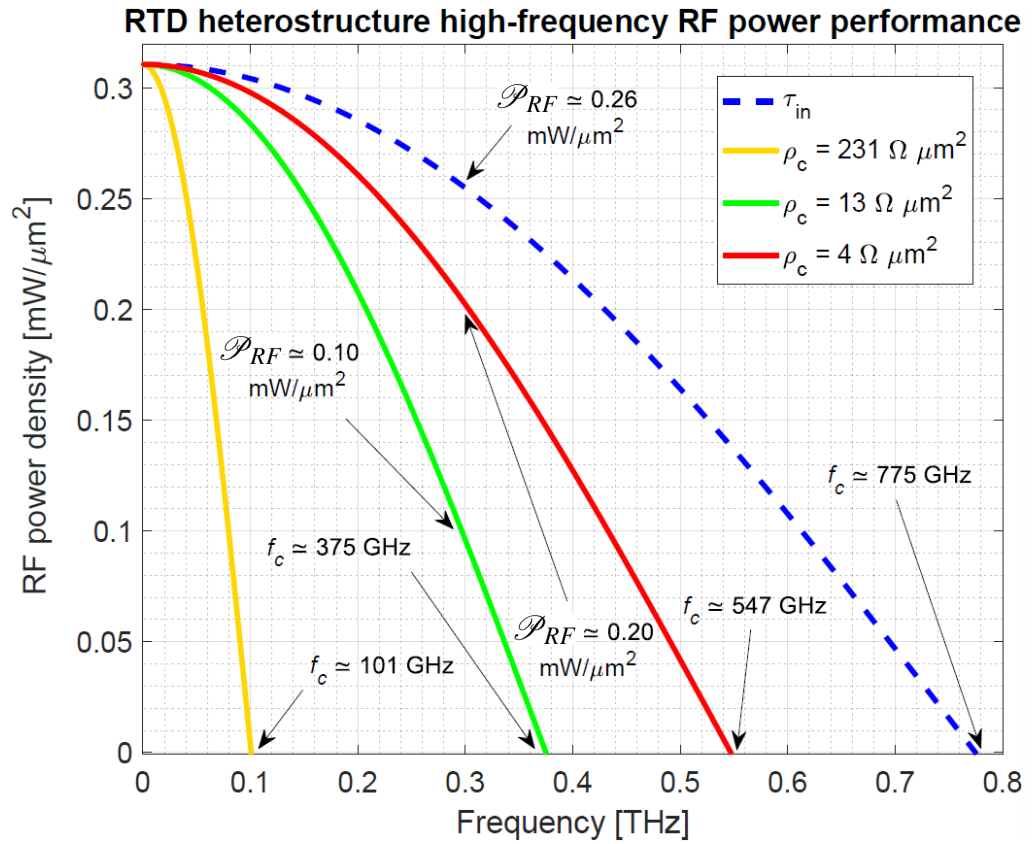


Figure 6.12: RF power density versus operation frequency performance of the analysed RTD heterostructure.

Table 6.7: RTD epitaxial structure RF power performance and intrinsic frequency limit\*.

$f_{in}$ [GHz]	$\mathcal{P}_{RF,max}$ [mW/ $\mu\text{m}^2$ ]	$\mathcal{P}_{RF,in}$ (300 GHz)* [mW/ $\mu\text{m}^2$ ]
775	0.31	0.26

\* Estimated assuming  $\tau_{ex} = 0$ .

Assuming to employ a shunt resistor with resistance  $R_{st} = 10 \Omega$  [513], the maximum device area  $A_{max}$  from low-frequency stabilisation criteria is given by:

$$A_{max} = \frac{2\Delta V}{3\Delta J R_{st}} \quad (6.16)$$

and is estimated to be around  $58 \mu\text{m}^2$ . Therefore,  $16 \mu\text{m}^2$ ,  $25 \mu\text{m}^2$ ,  $36 \mu\text{m}^2$ , and  $49 \mu\text{m}^2$ -large RTD devices are expected to deliver up to around 3.2 mW, 5.0 mW, 7.2 mW, and 9.8 mW of RF power at 300 GHz, respectively. For the estimation, the shift of  $V_p$  with increasing device area due to bond-pads parasitics (as discussed in Chapter 4) was neglected since not related to the epitaxial structure. This is up to around five times higher compared to state-of-the-art RTD epitaxial structures operating at around 300 GHz [169], where a  $16 \mu\text{m}^2$  RTD device feature  $P_{RF}$  (300 GHz)  $\sim 0.8$  mW only.

Table 6.8: RTD epitaxial structure high-frequency performance.

$\rho_c$ [ $\Omega \mu\text{m}^2$ ]	$f_{max}$ [GHz]	$\tau_{rtd}$ [ps]	$f_c$ [GHz]	$\mathcal{P}_{RF}$ (300 GHz) [ $\text{mW}/\mu\text{m}^2$ ]
13	420	0.67	375	0.10 $\text{mW}/\mu\text{m}^2$
4	768	0.46	547	0.20 $\text{mW}/\mu\text{m}^2$

Note that  $\tau_{in}$  was estimated in the PDR regions. However, as discussed in Chapter 2,  $\tau_{in}$  is expected to be slightly higher in the NDR region due to charge relaxation processes (Coulomb interaction) and displacement current effects, as experimentally-shown in recently reported works [395]. Therefore, the estimated  $f_{in}$ ,  $f_c$ ,  $\mathcal{P}_{RF,in}$ , and  $\mathcal{P}_{RF}$  values are, in this sense, slightly overestimated. Similar considerations would apply to  $\tau_c = v_c^{-1}$ , which influences  $f_{max}$ ,  $f_c$ , and  $\mathcal{P}_{RF}$ . However, the dependency is typically neglected in state-of-the-art modelling methodologies since weak [398].

## 6.5 RF stubs for 300 GHz oscillator circuit design

To demonstrate the practical employability of the proposed heterostructure in RTD-based THz emitters, shorted transmission line inductive stubs were designed to be employed as  $LC$  tank component in practical RTD oscillator circuits [163, 390] operating at around 300 GHz. Here, two different designs are proposed.

The first consists of a CPW line with low  $Z_0 = 26 \Omega$  and relative effective permittivity  $\epsilon_{r,eff} \simeq 6.4$ , featuring signal line width  $w = 46 \mu\text{m}$  and short gap width  $g = 3 \mu\text{m}$  to correctly support the associated coplanar mode at high-frequency. The second consists of a microstrip line (MLIN) with low  $Z_0 = 10 \Omega$  and  $\epsilon_{r,eff} \simeq 3.2$ , featuring  $w = 21 \mu\text{m}$  and a  $1.2 \mu\text{m}$ -thick polyimide PI-2545-based dielectric layer with static relative permittivity  $\epsilon_{r,0} = 3.5$  [625].

The RF stubs were designed employing the LineCalc tool included in ADS [718, 719] and then investigated in Ansys HFSS [720] through full finite elements-based three-dimensional (3D) high-frequency electromagnetic numerical simulations, accurately accounting for both conductors and dielectrics losses, as well as frequency dispersion.

Both structures were simulated on top of  $650 \mu\text{m}$ -thick InP substrates with  $\epsilon_{r,0} \simeq 12.5$  [550] assuming Au-based signal/ground lines of thickness  $t = 500 \text{ nm}$  (with  $t > 3\delta$  for low signal attenuation, being  $\delta \simeq 144 \text{ nm}$  the computed skin depth at 300 GHz) and ground lines width  $s > 5w/2$  to ensure minimal radiation losses. The cross section of the employed CPW and MLIN is illustrated in Figure 6.13.

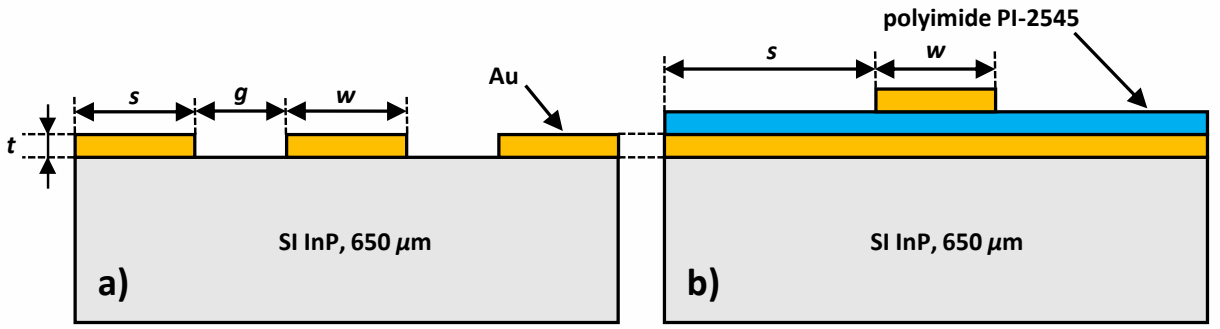


Figure 6.13: Cross section of the employed CPW (a) and MLIN (b).

From a circuit design perspective, the lines are shorted by 75 nm-thick silicon nitride ( $\text{Si}_3\text{N}_4$ ,  $\epsilon_{r,0} \simeq 6.8$  [395]) metal-insulator-metal (MIM) capacitors [169,390], which are designed to act as low impedance paths at the oscillation frequency, decoupling the RF part of the circuit from the DC bias supply. Figure 6.14 shows an example of simulated stubs in both the adopted CPW and MLIN topologies at 300 GHz. In the lossless limit, the stubs show inductive behaviour when their purely imaginary input impedance  $Z_{in}$  is positive [609]:

$$Z_{in} = j\mathfrak{I}Z_{in} = j\omega_{op}L = jZ_0 \tan(\beta l) > 0 \quad (6.17)$$

where  $L$  is the associated inductance,  $\beta l$  is the line phase length,  $l$  the length of the stub, and  $\beta \approx 2\pi f_{op} \sqrt{\epsilon_{r,eff}}/c$  [609] (assuming perfect transverse electromagnetic (TEM) operation) the imaginary part of the propagation constant, being  $f_{op} = \omega_{op}/2\pi$  the operation frequency (and  $\omega_{op}$  the angular frequency) and  $c$  the speed of light in vacuum. Eq. (6.17) is satisfied if:

$$\frac{p\pi}{2} < \beta l < \frac{q\pi}{2} \quad (6.18)$$

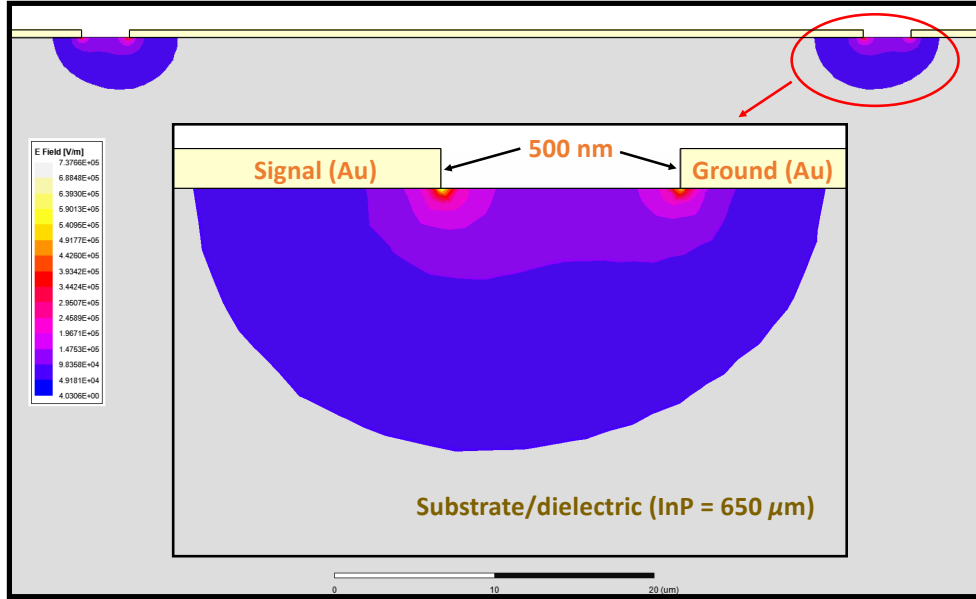
where  $p$  and  $q$  are positive whole even and positive odd integers, respectively. This approximately turns in  $0 < l < 98 \mu\text{m}$  and  $0 < l < 139 \mu\text{m}$  (where  $l \ll \lambda_{op}$  in both cases, i.e., lumped oscillator modelling can be adopted, as discussed in Chapter 2, being  $\lambda_{op}$  the operating wavelength) for short ( $\beta l < \pi/2$ , where  $l_{max} = \pi/2\beta$ ) adopted CPW and MLIN designs, respectively.

Figure 6.15 shows an example of simulated  $S_{11}$  parameter of designed CPW and MLIN stubs in the frequency range 250–350 GHz, confirming the inductive nature of the lines. The average insertion loss  $IL$  is around  $8.5 \times 10^{-3} \text{ dB}/\mu\text{m}$  and  $5.2 \times 10^{-3} \text{ dB}/\mu\text{m}$  at 300 GHz for the CPW and MLIN geometries, respectively, which was estimated from the simulated  $S_{21}$  parameters. Figure 6.16 shows the simulated inductance  $L = \mathfrak{I}(Z_{11})/2\pi f_{op}$  of both CPW and MLIN stubs at 300 GHz, resulting in linear densities of around  $0.33 \text{ pH}/\mu\text{m}$  and  $0.07 \text{ pH}/\mu\text{m}$ , respectively.

As discussed in Chapter 2, the oscillation frequency  $f_{osc}$  in the lumped limit is given as:

$$f_{osc} = \frac{\sqrt{L - C_{rtd}R_s^2}}{2\pi L \sqrt{C_{rtd}(1 + R_s G_L)}} \quad (6.19)$$

**Coplanar waveguide (CPW) stub**



**Microstrip line (MLIN) stub**

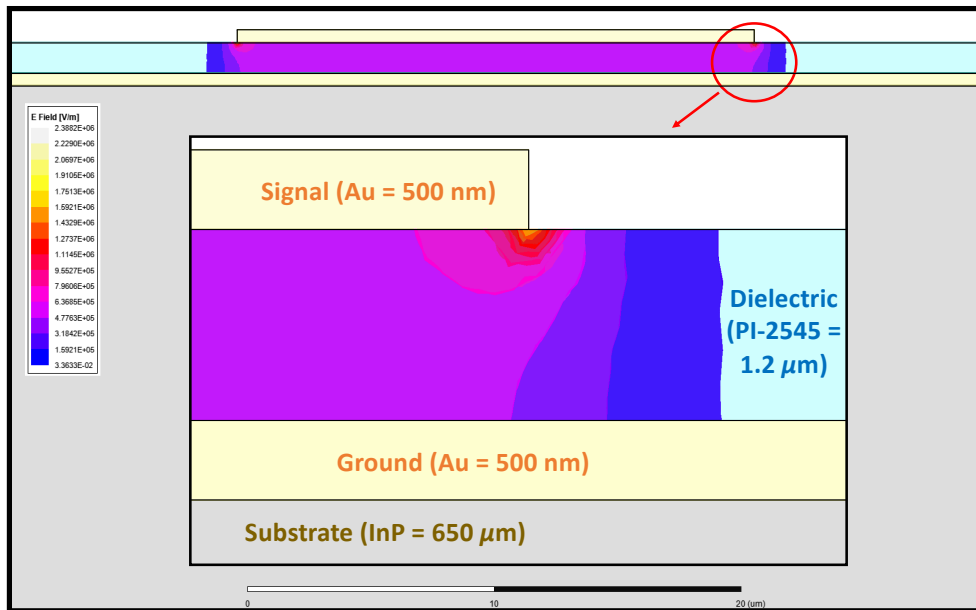


Figure 6.14: Cross section of simulated 5  $\mu\text{m}$ -long 26  $\Omega$  CPW and 20  $\mu\text{m}$ -long 10  $\Omega$  MLIN stubs, showing the associated quasi-transverse electromagnetic mode standing wave two-dimensional electric field magnitude at 300 GHz in proximity to a reference node.

where  $G_L$  is the load conductance and  $R_s \approx R_c$ . Therefore, the condition for the circuit to oscillate is given by:

$$L > L_{min} \approx C_{rt} R_c^2 \quad (6.20)$$

Table 6.9 lists the oscillator design parameters for 300-GHz oscillations assuming the fundamental mode, the proposed RTD heterostructure, and  $\rho_c = 4 \Omega \mu\text{m}^2$ . Clearly, the CPW geom-

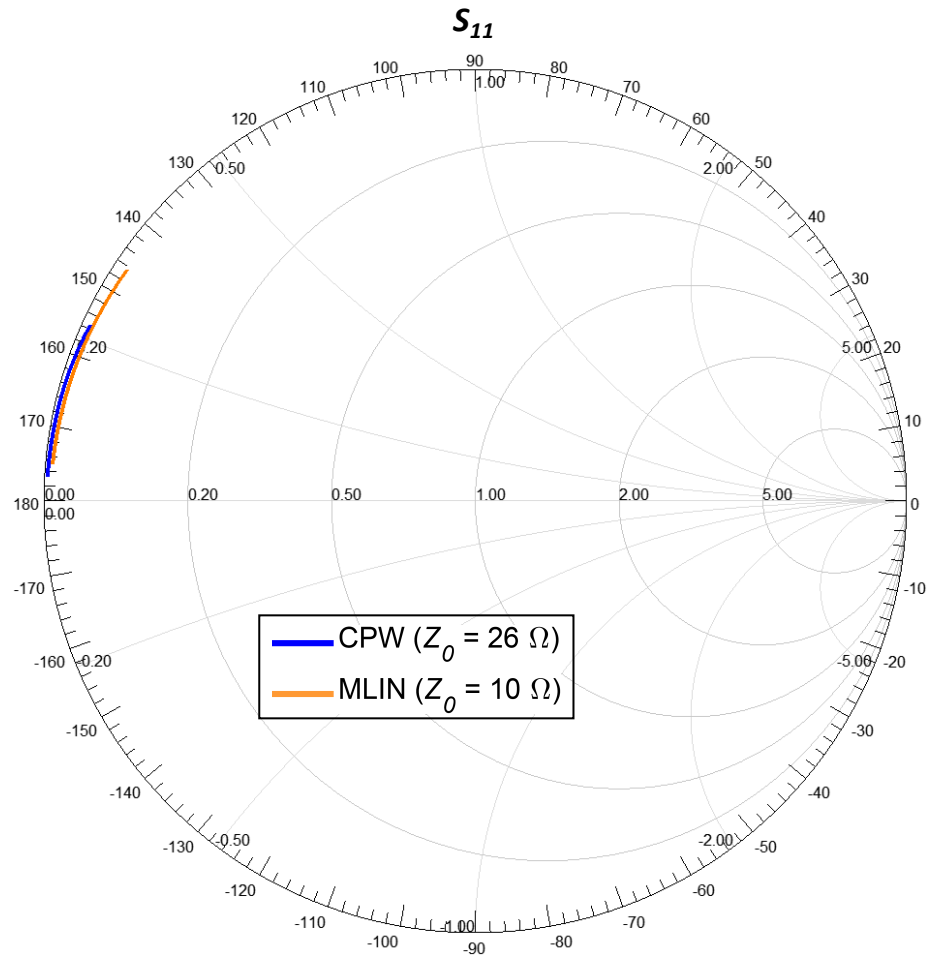


Figure 6.15: Simulated  $S_{11}$  parameter of 5  $\mu\text{m}$ -long 26  $\Omega$  CPW and 20  $\mu\text{m}$ -long 10  $\Omega$  MLIN stubs in the frequency range 250–350 GHz.

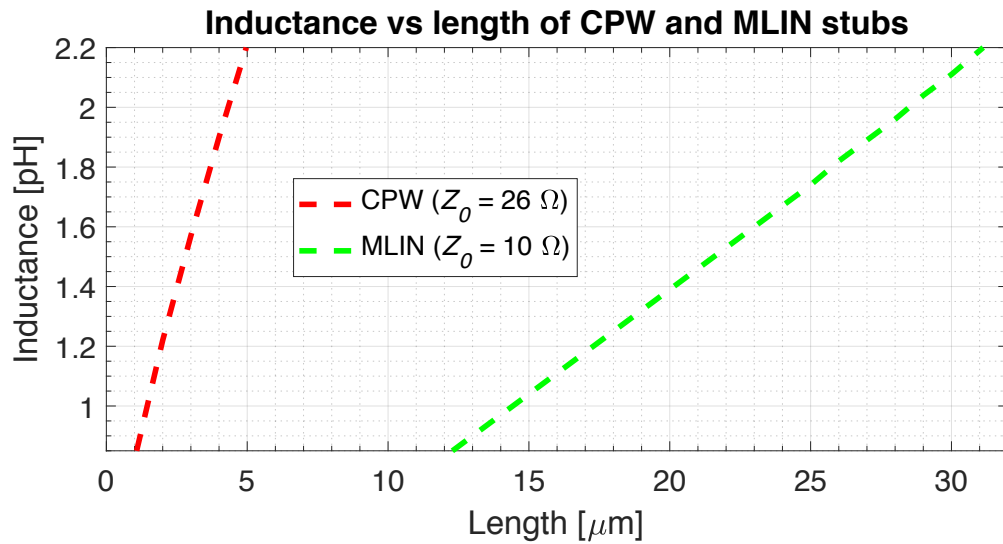


Figure 6.16: Simulated inductance versus length of the analysed 26  $\Omega$  CPW and 10  $\Omega$  MLIN stubs at 300 GHz.

Table 6.9: Oscillator design parameters for 300-GHz (fundamental) oscillations.

$A$	$16 \mu\text{m}^2$	$25 \mu\text{m}^2$	$36 \mu\text{m}^2$	$49 \mu\text{m}^2$
$R_c$	$0.25 \Omega$	$0.16 \Omega$	$0.11 \Omega$	$0.08 \Omega$
$C_{rtd}$	$90.2 \text{ fF}$	$141.0 \text{ fF}$	$203.0 \text{ fF}$	$276.4 \text{ fF}$
$L_{min}$	$5.64 \text{ fH}$	$3.61 \text{ fH}$	$2.51 \text{ fH}$	$1.84 \text{ fH}$
$L(300 \text{ GHz})^*$	$3.08 \text{ pH}$	$1.98 \text{ pH}$	$1.38 \text{ pH}$	$1.01 \text{ pH}$
$l(\text{CPW})$	$9 \mu\text{m}$	$6 \mu\text{m}$	$4 \mu\text{m}$	$3 \mu\text{m}$
$IL(\text{CPW})$	$0.076 \text{ dB}$	$0.051 \text{ dB}$	$0.034 \text{ dB}$	$0.025 \text{ dB}$
$l(\text{MLIN})$	$44 \mu\text{m}$	$28 \mu\text{m}$	$20 \mu\text{m}$	$14 \mu\text{m}$
$IL(\text{MLIN})$	$0.229 \text{ dB}$	$0.146 \text{ dB}$	$0.104 \text{ dB}$	$0.073 \text{ dB}$

\* Computed assuming a standard  $50 \Omega$  load ( $G_L = 20 \text{ mS}$ ).

etry, in addition to the short gap spacing of  $3 \mu\text{m}$ , requires ultra-short lines, which reach  $3 \mu\text{m} < l_{max} = 98 \mu\text{m}$  (with associated  $L = 1.01 \text{ pH} > L_{min} = 1.84 \text{ fH}$ ) in length if employing a  $49 \mu\text{m}^2$ -large RTD, approaching the optical lithographic resolution limit and resulting in fabrication issues in terms of both mask alignment and reliable lift-off.

On the other hand, the MLIN design allows for longer lines well above  $10 \mu\text{m}$  in length due to the lower inductance linear density, which is feasible and reliable with standard processing based on photolithography. In particular, a  $49 \mu\text{m}^2$ -large device requires a  $14 \mu\text{m}$ -long line (which is smaller than  $l_{max} = 139 \mu\text{m}$ ). At the same time, the smaller inductance density results in a lower oscillation frequency shift compared to design due to fabrication tolerances. Therefore, the MLIN design is preferred over the CPW one. However, this is gained at the expense of higher signal losses, where the insertion loss is estimated to be around nine times higher compared to the CPW design.

In the analysis, the parasitic series inductance of the RTD device and the parasitic inductance of the bond-pads were not accounted, which can lower the oscillation frequency. Therefore, accurate oscillator design must be carried out based on estimates of these quantities according to the specific adopted mask layout, which needs optimisation towards parasitics minimisation.

## 6.6 Summary

This Chapter presented an optimised  $\text{In}_{0.53}\text{Ga}_{0.47}\text{As}/\text{AlAs}$  double-barrier RTD epitaxial structure for high-power oscillators working at around 300 GHz. The heterostructure exhibits moderate available current density  $\Delta J \simeq 1.4 \text{ mA}/\mu\text{m}^2$  and large voltage swing  $\Delta V \simeq 1.2 \text{ V}$ , resulting in

## CHAPTER 6.6. SUMMARY

a maximum RF power  $P_{RF,max} \simeq 0.31 \text{ mW}/\mu\text{m}^2$  and over 540 GHz of bandwidth, being  $25 \mu\text{m}^2$ ,  $36 \mu\text{m}^2$ , and  $49 \mu\text{m}^2$  large RTD devices expected to deliver up to 5 mW, 7 mW, and 10 mW at 300 GHz, respectively, which is up to five times higher compared to the state-of-the art. The heterostructure features poorer electrical performance compared to design, which is attributed to structural defects introduced during epitaxial growth. This is also suggested by two other designed heterostructures grown by the same commercial supplier, which did not show NDR during wafer qualifications and so were not discussed here.

In order to demonstrate the practical feasibility of the presented RTD heterostructure in 300-GHz oscillator circuits fabricated through low-cost photo-lithography, distributed inductors featuring both coplanar and microstrip design were proposed performing full 3D electromagnetic simulations.

# Chapter 7

## Conclusions and future perspectives

### 7.1 Conclusions

Resonant tunnelling diode (RTD) technology seems to offer compact and high performance option for many practical and high-impact terahertz (THz) applications. However, the main weakness, which is nowadays the same for any other solid-state THz technology, is represented by the low output power of the sources, which is due to the underdeveloped and non-optimal device and circuit design implementation approaches, as well as to the poor epitaxial wafer crystal quality.

Currently, RTD-based THz emitters in indium phosphide (InP) technology can deliver up to around 1 mW of output power only, which is the highest value ever reported for a single RTD device operating in the 300-GHz band [169]. In the context of ultra-high-speed multi-gigabit wireless communications, the low output power capability of RTD-based sources severely impacts the practical applicability of THz transmitters (Tx), limiting communication distance and data transfer performances. For this reason, the employability of RTD THz Tx systems is currently restricted to short-range line-of-sight operation only, with maximum single-channel bit-rates of the order of few tens of gigabits per second and data transfer below 1 m.

However, recent research studies suggest that several milliwatt of output power are required in practical application scenarios to achieve bit-rate capabilities of several tens of gigabits per second and beyond, and to reach several metres of link distance in common operating conditions. Currently, the target is set to 5–10 mW at around 300 GHz carrier waves in the short-term, which would allow bit-rates in excess of 100 Gb/s and wireless communications well above 5 m distance. To achieve that, maximisation of the radio frequency (RF) power gain capability  $P_{RF}$  of the RTD device is of primal importance. However, reliable epitaxial design approaches, as well as accurate physical-based numerical simulation tools, aimed at  $P_{RF}$  maximisation in the 300 GHz-band are lacking at the current time. This work proposed and presented practical

solutions to address these issues. In particular, the main achievements can be summarised in the following:

- a) a simulation approach based on the non-equilibrium Green's function (NEGF) formalism implemented in Silvaco Atlas technology computer-aided design (TCAD) simulation package was proposed to accurately and efficiently simulate the static current-voltage ( $IV$ ) characteristic of  $\text{In}_{0.53}\text{Ga}_{0.47}\text{As}/\text{AlAs}$  double-barrier RTD heterostructures lattice-matched to InP. By choosing the appropriate physical models and materials parameters, as well as by means of a suitable discretisation of the heterostructure spatial domain through finite-elements, it was shown that the simulation package can reliably estimate the heterostructure peak current density  $J_p$ , peak voltage  $V_p$ , and the negative differential resistance (NDR) region voltage extent  $\Delta V$  of the DC current density-voltage ( $JV$ ) curve.

The demonstrated simulation approach will now assist in designing and optimizing  $\text{In}_{0.53}\text{Ga}_{0.47}\text{As}/\text{AlAs}$  double-barrier RTD devices through the associated static current-voltage ( $IV$ ) curve, and will assist in leveraging the Tx output power beyond the current 1 mW threshold at low-THz frequencies towards required levels, accelerating developments in the rapidly-evolving RTD technology for emerging THz applications, including next-generation ultra-broadband wireless communications, as well as high-resolution imaging/spectroscopy apparatuses and radar systems.

- b) the developed simulation approach was then employed to analyse how epitaxial structure design, including the double-barrier quantum well (DBQW), and emitter and collector regions, impact the electrical properties of the RTD heterostructure resulting from the tailored DC  $JV$  characteristic. To achieve that, a comprehensive simulation study was carried out, and the results analysed and discussed based on the retrieved output trends characterising the heterostructure band diagram, transmission coefficient energy spectrum, and static  $JV$  curve. As a result, general design guidelines aimed to maximise the RTD device maximum RF power gain capability  $P_{RF,max}$  were deduced, which mainly focus on maximising device area  $A$  and voltage swing  $\Delta V$ . The established design rules will now be adopted to design and optimise RTD devices by tailoring the device DC  $IV$  curve towards  $P_{RF,max}$  maximization.

- c) to prove the validity of the proposed epitaxial design approach, a lattice-matched to InP  $\text{In}_{0.53}\text{Ga}_{0.47}\text{As}/\text{AlAs}$  double-barrier RTD epitaxial structure capable of several milliwatt of RF power was accurately designed by means of the developed simulation approach, and experimentally-investigated through RTD devices microfabrication and subsequent high-frequency scattering (S)-parameters measurement up to 110 GHz, revealing an expected  $P_{RF}$  of up to around 5 mW and 10 mW at 300 GHz for  $25 \mu\text{m}^2$  and  $49 \mu\text{m}^2$ -large devices, respectively. To demonstrate the practical employ-

ability of the proposed RTDs for practical oscillator circuits realisation employing low-cost photolithography, both coplanar waveguide and microstrip inductive stubs were designed by means of a complete three-dimensional electromagnetic simulation analysis.

The results achieved in this work demonstrate that design and realisation of high-power InP RTD devices delivering 5–10 mW of RF power at 300 GHz oscillation frequencies is feasible, thus, RTD THz sources delivering several milliwatt of output power at 300 GHz can be achieved upon proper oscillator circuit/antenna design.

## 7.2 Challenges and future perspectives

### 7.2.1 RTD modelling and simulation

As discussed in Chapter 4, the valley current density  $J_v$ , and so the peak-to-valley current difference  $\Delta J$  and peak-to-valley current ratio  $PVCR = J_p/J_v$ , of the RTD heterostructure, cannot be correctly computed at the current time due to the lack of implemented scattering processes in Atlas TCAD. Here, if the coherent limit is dropped in favour of a more general many-body quantum transport description, phase-correlation and dissipative processes mechanisms can be simply and straightforwardly accounted through ad-hoc correlation (or lesser/greater) scattering self-energies  $\Sigma^{\lessgtr,S}$ , which add to the associated boundary self-energies  $\Sigma^{\lessgtr,B}$  as:

$$\Sigma^{\lessgtr} = \Sigma^{\lessgtr,B} + \Sigma^{\lessgtr,S} = \Sigma^{\lessgtr,B} + \sum_q \Sigma_q^{\lessgtr,S} \quad (7.1)$$

where  $q$  labels the different scattering processes. In this sense, Eq. (7.1) tells the real power of the NEGF method. However, while, in the coherent limit, the retarded boundary self-energy  $\Sigma^{R,B}$  is retrieved exactly and most of the computational burden consists in diagonalising the retarded Green's function  $G^R$  (which is a dense matrix),  $\Sigma^{\lessgtr,S}$  have to be computed perturbatively.

Within the rigorous self-consistent Born approximation (SBA) scheme [397], this has a profound impact on the NEGF algorithm, introducing an additional "inner loop", where self-consistency of the Green's functions  $G^R$  and  $G^{\lessgtr}$  (being  $G^{\lessgtr}$  the correlation Green's functions) and self energies  $\Sigma^R$  and  $\Sigma^{\lessgtr}$  (where an additional scattering retarded self-energy  $\Sigma^{R,S}$  is added) has to be met before entering the outer loop accounting for space-charge effects, obeying to charge and current conservation. Clearly, this massively increases the modelling complexity and the computational burden associated with the NEGF solver, where most of the simulation load would originate from the computation of the scattering self-energies, posing a limitation in the simulation of densely-meshed RTD devices with arbitrarily-thick epitaxial structures, including those employed in 300-GHz oscillators.

A practical solution to efficiently model these quantities, such as the electron-phonon Fock self-energy, could consist in adopting phenomenological models, such as Büttiker probes or Golizadeh self-energies [721], decoupling them from the Green's functions, or through local approximations in space.

Another possibility is the employment of empirical optical potential models, which have been extensively adopted in the context of RTDs simulation [408, 705, 722]. Here, scattering phenomena are accounted by adding a purely ad-hoc imaginary potential (also called "broadening parameter") to the nanosystem Hamiltonian. The same approach is sometimes employed to broaden the injected density of states (DOS) from the emitter, filling those states which are usually occupied by electrons scattered by inelastic phonons. This might help in improving convergence, where strong carriers localization resulting from the coherent description might lead to unphysically-sharp resonances in the computed spectral quantities.

However, most of the times, this parameter is treated empirically by fitting over experimental data resulting from fabricated and measured devices, which makes the approach unfeasible from an epitaxial structure design perspective. Furthermore, and more importantly, this approach violates current conservation, on which the NEGF method is based [674]. Therefore, its practical employment in the context of NEGF-based solvers is arguable. Currently, Silvaco is implementing computationally-efficient multi-scattering phenomenological approaches based on Büttiker probes [723, 724], which should allow to fully-model the  $JV$  curve towards the required level of accuracy needed for reliable epitaxial structure design optimization.

Moreover, more sophisticated modelling approaches should be considered and included in the future to increase the accuracy of the electronic band structure description, such as the empirical pseudo-potential method (EPM) [725, 726], or the  $\mathbf{k} \cdot \mathbf{p}$  [727, 728] and tight-binding [729] approaches, as well as ab initio techniques, such as the density functional theory (DFT) [730]. This would allow to accurately simulate RTDs featuring high indium (In) concentration QWs, such as  $\text{In}_{1-x}\text{Ga}_x\text{As}/\text{AlAs}$  DBQW-based devices with  $x \leq 0.2$ , indium arsenide/aluminium antimonide ( $\text{InAs}/\text{AlSb}$ ) RTDs, or inter-band epitaxial structures. At the same time, this would improve the emitter electronic structure picture (for instance, by employing a tight-binding approach [693]), which is desirable to ameliorate modelling of carriers injection into the device active region, leading to a more accurate electron transport description and giving better estimates of the valley current.

Currently, Atlas TCAD features an implemented 8-band  $\mathbf{k} \cdot \mathbf{p}$  solver [731, 732], but its applicability in the context of reliable RTD simulation has still to be fully investigated and demonstrated. Indeed, multi-band approaches tend to be computationally demanding, which poses a

major hurdle in designing realistic RTD epitaxial structures with a certain degree of complexity, including those employed in transceiver (TRx) systems operating at terahertz (THz) frequencies.

## 7.2.2 RTD epitaxial structure design and material systems

The analysis reported in Chapter 6 showed that the electrical performance of the proposed RTD heterostructure is poorer compared to design expectations. In particular, the experimentally-extracted  $J_p$  and  $\Delta V$  values are smaller than the simulated counterparts, which is attributed to the non-optimal epitaxial growth conditions and Ohmic contacts fabrication. This has a direct impact on the associated maximum RF power density performance  $\mathcal{P}_{RF,max}$ .

Indeed, setting both  $J_p$  and  $\Delta V$  to design values, and assuming the measured PVCR,  $\mathcal{P}_{RF,max}$  can be increased from around  $0.31 \text{ mW}/\mu\text{m}^2$  to around  $0.61 \text{ mW}/\mu\text{m}^2$ , which corresponds to  $P_{RF,max}$  of up to around 9.8 mW (instead of 5.0 mW), 15.4 mW (instead of 7.7 mW), 22.1 mW (instead of 11.2 mW) mW, and 30.1 mW (instead of 15.2 mW) for RTD devices with mesa area  $A$  ranging from  $16 \mu\text{m}^2$  to  $49 \mu\text{m}^2$  (neglecting the dependence  $\Delta V(A)$  due to bond-pads parasitics). Based on that, several milliwatt of additional RF power at 300 GHz are expected, with  $P_{RF} \gtrsim 7 \text{ mW}$  assuming  $A \geq 16 \mu\text{m}^2$ . This can be achieved through high-quality epitaxial growth procedures (such as by employing low growth rates), similarly as carried out in Chapter 4, and by appropriately fabricating Ohmic contacts, as described in Chapters 3 and 6.

Moreover,  $\mathcal{P}_{RF,max}$  can be further increased by tailoring the  $JV$  curve. Figures 7.1 and 7.2 show two examples of proposed epitaxial structures resulting from further optimisation of the

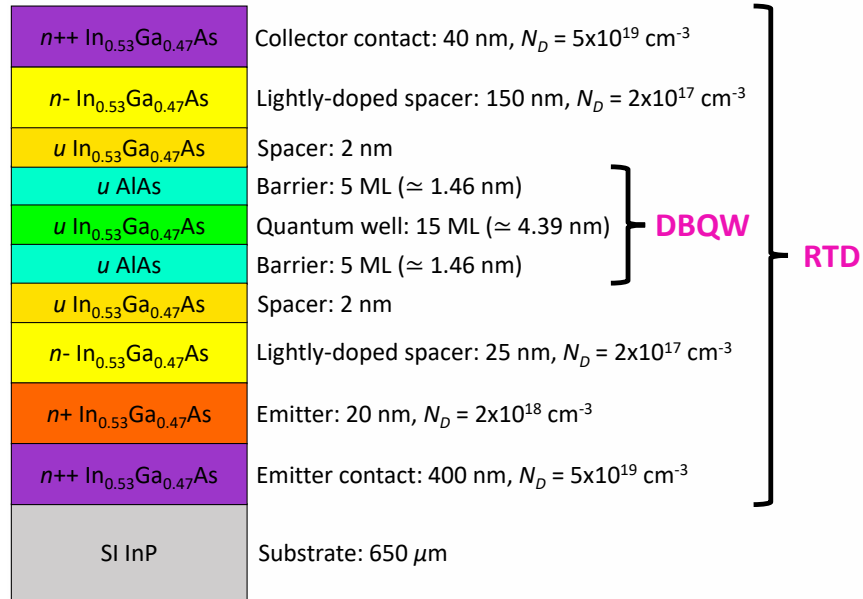


Figure 7.1: Second proposed  $n$ -type intra-band  $\text{In}_{0.53}\text{Ga}_{0.47}\text{As}/\text{AlAs}$  RTD heterostructure.

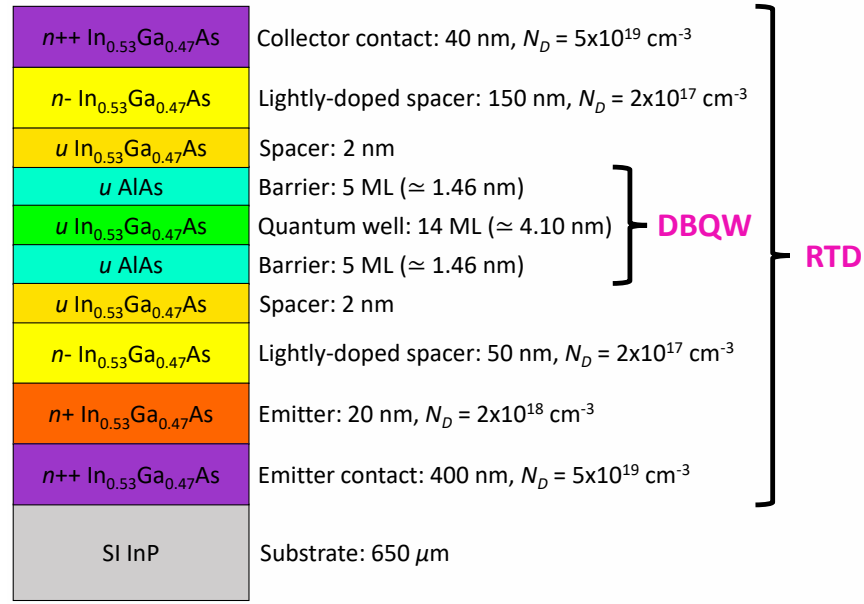


Figure 7.2: Third proposed  $n$ -type intra-band  $\text{In}_{0.53}\text{Ga}_{0.47}\text{As}/\text{AlAs}$  RTD heterostructure.

heterostructure reported in Chapter 6. The first features an emitter lightly-doped spacer layer of 25 nm in thickness rather than 50 nm, while the second is characterised by an around 4.10 nm-thick quantum well (QW) layer (14 monolayers (ML)) rather than 4.39 nm (15 ML).

Both the heterostructures feature  $J_p \simeq 300 \text{ kA/cm}^2 = 3 \text{ mA}/\mu\text{m}^2$ ,  $V_p \simeq 1.5 \text{ V}$ , and  $\Delta V \simeq 2.0 \text{ V}$ . Assuming the same PVCR (which is not expected to vary significantly), the expected  $\mathcal{P}_{RF,max}$  is around  $0.8 \text{ mW}/\mu\text{m}^2$ , meaning that  $P_{RF,max}$  expectation of  $16 \mu\text{m}^2$ ,  $25 \mu\text{m}^2$ ,  $36 \mu\text{m}^2$ , and  $49 \mu\text{m}^2$ -large RTDs can reach up to around 12.8 mW, 20.0 mW, 28.8 mW, and 39.2 mW, respectively. The expected  $P_{RF,max}$  at 300 GHz is significantly higher compared to the other heterostructure, with  $P_{RF}$  in excess of 9 mW with  $A \geq 16 \mu\text{m}^2$ .

Even though RTD THz technology is nowadays based on InP, the future may belong to antimonides or nitrides-based RTDs. Indeed, these material systems promise superior speed and power performances compared to InP technology, and so may underpin future THz Tx systems. However, this would require a considerable research effort towards extensive technological progress since, at present, both technologies still remain at early developmental stages.

### 7.2.3 RTD oscillator circuit design implementation and realisation

The proposed RTD heterostructures can be employed to realise oscillator sources working at low-THz frequencies ( $\sim 100\text{--}300 \text{ GHz}$ ). Here, no further process development is required since fabrication and circuit design methodologies have already been established [169,390]. The shunt resistors can be realised either by means of 33 nm-thick nichrome (NiCr) thin films with sheet

resistance of the order of  $50 \Omega/\square$ , which can be deposited through evaporation and dual lift-off using the same recipe developed for bond-pads (as described in Chapter 3), or through wet chemical etching of the heavily-doped InGaAs-based emitter (bottom) contact layer, resulting in around  $5 \Omega/\square$  sheet resistance. On the other hand, the metal-insulator-metal (MIM) capacitors can be realised employing 75 nm-thick silicon nitride ( $\text{Si}_3\text{N}_4$ ) thin layers, which are deposited through inductively-coupled plasma chemical vapour deposition (ICP-CVD) adopting the same lift-off procedure as for NiCr resistors.

However, effective design techniques aimed at matching the oscillator output with the waveguide transition and associated load, or emission THz antenna, have still to be fully-developed at the current time in order to maximise the RF power extraction from the RTD device. Indeed, accurate high-frequency measurement and modelling of the RTD in the key NDR region is still not possible due to device instability. It would be, therefore, advantageous to develop robust characterisation and modelling techniques to enable the development of a complete physics-based non-linear large-signal model of the RTD device at THz frequencies in both NDR and positive differential resistance (PDR) regions to be employed in circuit design. The availability of such a model would enable the full non-linear dynamic analysis of the device in its entire operation frequency range, and allow accurate oscillator design for output power maximisation [733]. Although some work has been recently conducted in this regard [734], reliable and universal design methodologies aimed at maximising impedance matching between the RTD and the load/antenna at THz frequencies still need to be properly developed.

Increasing the output power capability of single RTD device THz Tx must be considered of utmost importance. To do that, maximising device area is crucial, while the oscillation frequency can be tuned by appropriate design of the resonating inductance. Furthermore, individual THz sources with milliwatt-range output power would facilitate the employment of pulsed-amplitude modulation (AM) signalling. Such an approach would offer a way to dramatically reduce the receiver (Rx) complexity, as no carrier synchronization is required. In that case, the total energy-per-bit will be significantly improved and will make the system more energy efficient, with expected efficiencies well below  $10^{-1}$  pJ/bit/cm [583].

Arrays configurations can significantly assist in leveraging the output power capability of RTD THz Tx, especially at very-high carrier frequencies well in excess of 1 THz, where the RF power performance of the RTD device is intrinsically-limited due to physical constrains [163]. Here, overcoming the limitations associated with the high-permittivity InP substrate is an important challenge in RTD THz technology, since it has hindered the development of arrays of oscillators. Indeed, on-chip antennas have low gain, typically under around 6 dBi, and the radiation is directed into the substrate.

Therefore, the semiconductor dies are usually mounted on hemispherical silicon (Si) lenses to collimate and focus the radiation, but these are bulky and make the systems cumbersome. As such, efforts in designing sources with airside or upward radiation from the chips are underway. In this regard, on-chip radial-line slot antennas (RLSA) [543], together with dipole antenna arrays [537] and patch [534, 546, 547] antenna configurations, have been proposed, though further innovations to this challenge are needed.

At the same time, because of the high-permittivity substrate, surface waves cannot be avoided, which cause unintentional coupling of the oscillators and hinder proper synchronisation for spatial power combining. It thus remains a challenge to achieve mutual coupling with large-scale arrays. Even though arrays of RTD oscillators have been reported, they have fallen short of delivering the expected output power, where up to 0.61 mW at 620 GHz, 0.27 mW at 770 GHz, and 0.18 mW at 810 GHz have been reported by employing a two-element frequency-locked oscillator array for continuous-wave (CW) coherent emission [443].

Most realisations, however, remain unsynchronised. For instance, a 16-element and a 64-element arrays have provided output powers of up to around 28  $\mu$ W at fundamental frequencies of 290 GHz and 650 GHz, respectively [525]. Earlier efforts in this regard included quasi-optical resonators for oscillators stabilisation [523] and power combining [524]. In addition, pulsed-emission with RF powers of up to 0.73 mW at around 1 THz has been reported by employing an unsynchronised 89-element large-scale array [537], but the output power remained below the 1 mW level. Another approach based on patch antennas has been recently proposed, but the generated output power remains too low for practical applicability [545, 546]. Thus, new approaches for this challenge are required.

Recently, around 12 mW at 0.45 THz have been reported out of a 36-element array chip [735]. In this system, each element consists of an InP double-RTD oscillator integrated with a square patch antenna (similarly as in [545]), and mutual phase-locking was successfully achieved between the oscillators via a coupling microstrip line-based network, allowing for coherent emission without the need of a Si lens. This RTD chip was less than 10 mm<sup>2</sup> in dimension. However, since each element radiates independently, power combining is achieved in free space, which is more critical than emitting from a single antenna. Moreover, the effective RF power delivered by the single RTD at the emission frequency is low, around 0.16 mW. Despite that, this impressive result demonstrates the viability of arrays of RTD oscillators as CW compact high-power THz coherent sources, and opens to further research in this direction, for instance, towards beam-forming of RTD phased-arrays [736].

In addition to array configurations, the employment of several RTDs in the same oscilla-

tor circuit in order to maximise the associated output power could benefit from series devices connection [737]. In contrast to parallelisation [390, 738], where the overall NDR increases thanks to the available current density  $\Delta I$ , i.e.,  $P_{RF,max,tot} \propto N\Delta I$ , being  $P_{RF,max,tot}$  the total RF power and  $N$  the number of RTD devices, serially-connected RTDs feature a larger  $\Delta V$ , i.e.,  $P_{RF,max,tot} \propto N\Delta V$  [396].

However, although both approaches allow to increase the output power capability according to the number of employed devices ( $P_{RF,max,tot} = NP_{RF,max}$ ), while the overall capacitance of parallel configurations increases with increasing  $N$  [739], degrading oscillation frequency, it drops with  $1/N$  if the RTDs are arranged in series, increasing operation frequency. According to these considerations, an  $N \times N$  parallel-series configuration would provide  $P_{RF,max,tot} = N^2 P_{RF,max}$  without affecting the total capacitance.

It is, therefore, clear that parallel-series circuit design arrangements offer an appealing solution to maximise the output power capability of RTD THz sources at a specific oscillation frequency. Series devices can be monolithically-fabricated on the same wafer substrate, or epitaxially-grown one on top of each other [706, 740]. In the latter, the highly-doped transition layers avoid coupling between the devices thanks to wavefunction phase breaking, i.e., the RTDs behave as separate entities [740]. However, although experimental work has been done in the past [741, 742], proper oscillator design methodologies aimed at correctly stabilise series connected two-terminal NDR devices [743], such as RTDs, are still missing, so new and reliable solutions must be developed.

# Appendix A

## RTD devices fabrication recipe

### Sample preparation

- Cleave an  $11 \times 11 \text{ mm}^2$ -large sample with the ATV RV-129 wafer scriber
- Establish processing face through DC probing and mark back side (when necessary)

### Sample cleaning

- Ultrasonic bath in acetone for 5 min
- Ultrasonic bath in methanol for 5 min
- Ultrasonic bath in IPA for 5 min
- Wash in RO water for 2 min
- Blow dry with nitrogen ( $\text{N}_2$ )
- Check with optical microscope
- Repeat the process until sample surface is clean

### Step 1: top contact

- Expose to UV/ $\text{O}_3$  for 1 h
- Spin-coat anisole 12% 200k AR-P 642.12 (PMMA 8) at 4000 rpm for 1 min
- Soft-bake at  $180 \text{ }^\circ\text{C}$  for 2 min
- Spin-coat ethyl lactate 2% 950k AR-P 679.02 (PMMA 10) at 4000 rpm for 1 min

- Soft-bake at 180 °C for 2 min
- Expose with EBPG 5200: E-gun acceleration voltage=100 kV; main resolution=1 nm; E-beam current=32 nA; measured spot size=43 nm; E-beam aperture=300 μm; proximity correction: Gaussian approximation; high-dose=490; low-dose=310
- Develop in IPA:MIBK=2.5:1 for 1 min at 23 °C
- Dip in IPA for 1 min
- Blow dry with N<sub>2</sub>
- Check with optical microscope
- Expose with UV/O<sub>3</sub> for 4.5 min
- Wet-etch in HCl:H<sub>2</sub>O=1:3 for 5 min
- Wash in RO water for 3 s
- Blow dry with N<sub>2</sub> for 3 s
- Dry-etch with Ar<sup>+</sup> gun for 40 s and evaporate Ti/Pd/Au=20/30/150 nm (or Mo/Ti/Au=20/20/150 nm) with MEB550S (Plassys IV)
- Strip in 1165 solution at 50 °C for 30 min (or overnight)
- Wash in RO water for 2 min
- Blow dry with N<sub>2</sub>
- Check with optical microscope
- Check metal thickness with Dektak XT

## **Photo-mask cleaning**

- Ultrasonic bath in acetone for 10 min
- Ultrasonic bath in IPA for 10 min
- Wash in RO water for 3 min
- Blow dry with N<sub>2</sub>
- Check with optical microscope
- Repeat the process until photo-mask is clean

## Step 2: top mesa

- Spin-coat S1805 at 4000 rpm for 30 s (pour with 0.2  $\mu\text{m}$ -filtered syringe)
- Soft-bake at 115 °C for 1 min
- Expose with MA6: hard contact, 2.3 s, 40  $\mu\text{m}$  alignment gap
- Develop in MDC:H<sub>2</sub>O=1:1 solution for 1 min and 15 s
- Wash in RO water for 2 min
- Blow dry with N<sub>2</sub>
- Check with optical microscope
- Ash at 80 W for 2 min
- Wet-etch in H<sub>3</sub>PO<sub>4</sub>:H<sub>2</sub>O<sub>2</sub>:H<sub>2</sub>O=1:1:38 solution
- Wash in RO water for 2 min
- Blow dry with N<sub>2</sub>
- Check etch depth with Dektak XT
- Repeat the process until the required etch depth
- Strip in 1165 solution at 50 °C for 10 min
- Wash in RO water for 2 min
- Blow dry with N<sub>2</sub>
- Check with optical microscope

## Step 3: bottom contact

- Spin-coat LOR-10A at 6000 rpm for 30 s (pour with 0.45  $\mu\text{m}$ -filtered syringe)
- Soft-bake at 150 °C for 2 min
- Spin-coat S1818 at 4000 rpm for 30 s (pour with 0.45  $\mu\text{m}$ -filtered syringe)
- Soft-bake at 115 °C for 3 min
- Expose with MA6: hard contact, 6 s, 50  $\mu\text{m}$  alignment gap

- Develop in MF-319 solution for 2 min and 30 s
- Wash in RO water for 2 min
- Blow dry with N<sub>2</sub>
- Check with optical microscope
- Expose with UV/O<sub>3</sub> for 64.5 min (with 4/4.5 min process and 4 min cooling steps)
- Wet-etch in HCl:H<sub>2</sub>O=1:3 for 5 min
- Dry-etch with Ar<sup>+</sup> gun for 40 s and evaporate Ti/Pd/Au=20/30/150 nm (or Mo/Ti/Au=20/20/150 nm) with MEB550S (Plassys IV)
- Strip in 1165 solution at 50 °C for 2 h (or overnight)
- Wash in RO water for 2 min
- Blow dry with N<sub>2</sub>
- Check with optical microscope
- Check metal thickness with Dektak XT

#### **Step 4: bottom mesa**

- Spin-coat S1818 at 4000 rpm for 30 s (pour with 0.45 μm-filtered syringe)
- Soft-bake at 115 °C for 1 min
- Expose with MA6: hard contact, 6 s, 50 μm alignment gap
- Develop in MDC:H<sub>2</sub>O=1:1 solution for 1 min and 15 s
- Wash in RO water for 2 min
- Blow dry with N<sub>2</sub>
- Check with optical microscope
- Ash at 80 W for 2 min
- Wet-etch in H<sub>3</sub>PO<sub>4</sub>:H<sub>2</sub>O<sub>2</sub>:H<sub>2</sub>O=1:1:38 solution
- Wash in RO water for 2 min
- Blow dry with N<sub>2</sub>

- Check with probe station/Dektak XT
- Repeat the process until the InP substrate is reached
- Strip in 1165 solution at 50 °C for 30 min
- Wash in RO water for 2 min
- Blow dry with N<sub>2</sub>
- Check with optical microscope

## Step 5: passivation and via opening

- Allow polyimide PI-2545 to reach room temperature (wait for 3–4 h)
- Spin-coat polyimide PI-2545 with the following recipe:
  - Step 1: speed 500 rpm, ramp 100 rpm, 5 s
  - Step 2: speed 8000 (1.2 μm-thick)/4000 (1.8 μm-thick) rpm, ramp 1000 rpm, 30 s
  - Step 3: speed 0 rpm, ramp 1000 rpm, 1 s
- Hard-bake at 180 °C overnight inside Heraeus oven (or at least for 8 h)
- Spin-coat S1805 at 1500 rpm for 30 s (pour with 0.2 μm-filtered syringe)
- Clean sample corners with humid cotton sticks
- Soft-bake at 125 °C for 2 min
- Expose with MA6: hard contact, 2.6 s, 40 μm alignment gap
- Develop in MDC:H<sub>2</sub>O=1:1 solution for 1 min and 15 s
- Wash in RO water for 2 min
- Blow dry with N<sub>2</sub>
- Check with optical microscope
- Post-bake at 125 °C on hot-plate for 10 min
- Dry-etch with RIE 80+: CF<sub>4</sub>/O<sub>2</sub>=5/95 sccm, 200 W, 20 mTorr, 20 °C, use interferometer (6(1.2 μm-thick)/9(1.8 μm-thick) peaks)
- Strip in 1165 solution at 50 °C for 1 h

- Wash in RO water for 2 min
- Blow dry with N<sub>2</sub>
- Check with optical microscope

## **Step 6: bond-pads**

- Spin-coat LOR-10A at 6000 rpm for 30 s (pour with 0.45 μm-filtered syringe)
- Soft-bake at 150 °C for 2 min
- Spin-coat S1818 at 4000 rpm for 30 s (pour with 0.45 μm-filtered syringe)
- Soft-bake at 115 °C for 3 min
- Expose with MA6: hard contact, 6 s, 50 μm alignment gap
- Develop in MF-319 solution for 2 min and 30 s
- Wash in RO water for 2 min
- Blow dry with N<sub>2</sub>
- Check with optical microscope
- Ash at 150 W for 2 min
- Evaporate Ti/Au=20/400 nm with MEB550S (Plassys IV)
- Strip in 1165 solution at 50 °C for 2 h (or overnight)
- Wash in RO water for 2 min
- Blow dry with N<sub>2</sub>
- Check with optical microscope
- Check metal thickness with Dektak XT

# Appendix B

## TLM structures fabrication recipe

### Sample preparation

- Cleave an  $11 \times 11$  mm<sup>2</sup>-large sample with the ATV RV-129 wafer scriber
- Establish processing face through DC probing and mark back side (when necessary)

### Sample cleaning

- Ultrasonic bath in acetone for 5 min
- Ultrasonic bath in methanol for 5 min
- Ultrasonic bath in IPA for 5 min
- Wash in RO water for 2 min
- Blow dry with nitrogen (N<sub>2</sub>)
- Check with optical microscope
- Repeat the process until sample surface is clean

### Step 1: metallisation

- Expose to UV/O<sub>3</sub> for 60 min
- Spin-coat anisole 15% 200k AR-P 642 (PMMA 8) at 4000 rpm for 1 min
- Soft-bake at 180 °C for 2 min
- Spin-coat ethyl lactate 2% 950k AR-P 679 (PMMA 10) at 4000 rpm for 1 min

- Soft-bake at 180 °C for 2 min
- Expose with EBPG 5200: E-gun acceleration voltage=100 kV; main resolution=1 nm; E-beam current=32 nA; measured spot size=43 nm; E-beam aperture=300 μm; proximity correction: Gaussian approximation; high-dose=490; low-dose=310
- Develop in IPA:MIBK=2.5:1 for 1 min at 23 °C
- Dip in IPA for 1 min
- Blow dry with N<sub>2</sub>
- Check with optical microscope
- Expose with UV/O<sub>3</sub> for 4.5 min
- Dip in HCl:H<sub>2</sub>O=1:3 for 5 min
- Wash in RO water for 3 s
- Blow dry with N<sub>2</sub> for 3 s
- Treat with Ar<sup>+</sup> gun for 40 s and evaporate Ti/Pd/Au=20/30/150 nm or Mo/Ti/Au=20/20/150 nm with MEB550S (Plassys IV)
- Strip in 1165 solution at 50 °C for 30 min (or overnight)
- Wash in RO water for 2 min
- Blow dry with N<sub>2</sub>
- Check with optical microscope
- Check metal thickness with Dektak XT

## **Photo-mask cleaning**

- Ultrasonic bath in acetone for 10 min
- Ultrasonic bath in IPA for 10 min
- Wash in RO water for 3 min
- Blow dry with N<sub>2</sub>
- Check with optical microscope
- Repeat the process until photo-window is clean

## Step 2: wet etching

- Spin-coat S1805 at 4000 rpm for 30 s (pour with 0.2  $\mu\text{m}$ -filtered syringe)
- Soft-bake at 115 °C for 1 min
- Expose with MA6: hard contact, 2.3 s, 40  $\mu\text{m}$  alignment gap
- Develop in 1:1=MDC:H<sub>2</sub>O solution for 1 min and 15 s
- Wash in RO water for 2 min
- Blow dry with N<sub>2</sub>
- Check with optical microscope
- Ash at 80 W for 2 min
- Wet-etch in H<sub>3</sub>PO<sub>4</sub>:H<sub>2</sub>O<sub>2</sub>:H<sub>2</sub>O=1:1:38 solution
- Wash in RO water for 2 min
- Blow dry with N<sub>2</sub>
- Check with probe station
- Repeat the etching process up to the InP substrate
- Strip in 1165 solution at 50 °C for 30 min
- Wash in RO water for 2 min
- Blow dry with N<sub>2</sub>
- Check with optical microscope

# Appendix C

## Extraction of the specific contact resistivity through the transfer length model

In the context of electron devices Ohmic contacts characterisation [652], the most common employed method to experimentally extract the specific contact resistivity  $\rho_c$  is based on transmission line measurements (TLM) [653, 654], from which  $\rho_c$  is extracted through the transfer length model [651]. To do that, a TLM structure is employed, consisting of a number of pads (made of the intended metal stack) contacting the semiconductor surface of interest and with increasing separation gap distance, as shown in Figure C.1. The structure used in this work is described in Chapter 3.

Upon fabrication completion, the extraction procedure consists in DC probing the TLM structure through a four-point probe measurement setup [655]. In this work, needle-carrying

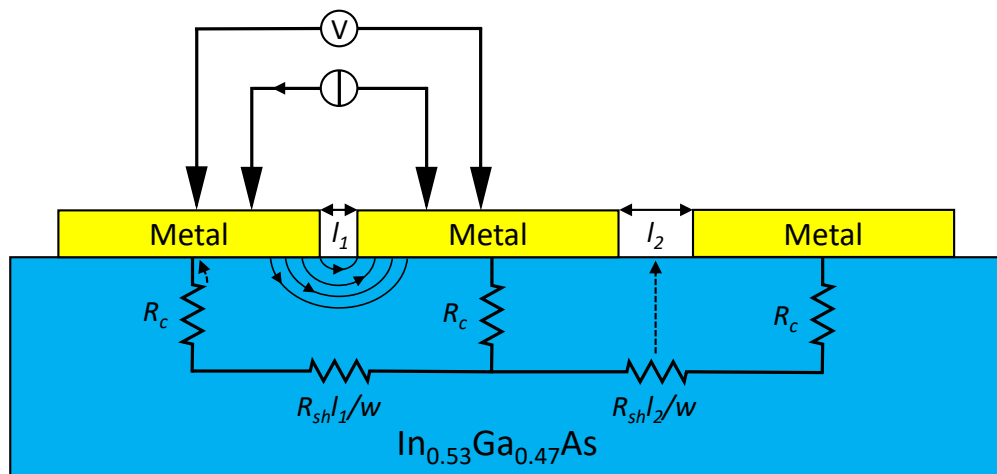


Figure C.1: Cross-section view illustration of the TLM structure employed in the extraction of  $\rho_c$  through four-point probe DC sensing, showing two generic contacts pairs. The dashed arrows indicate that  $R_c$  is associated to the metal-semiconductor discontinuity region of the metal pads, while  $R_{sh}$  to the region between the pads where current flow occurs.

DC probes, and a B1500A semiconductor device parameter analyser (SPA) bias supply from Keysight Technologies, were employed.

A constant current is injected between each pair of adjacent contact pads using two of the employed probes, while the remaining pair is used to measure the resulting voltage drop, as shown in Figure C.1. The total resistance  $R_{t,i}$ , for each contacts pair, can be expressed as:

$$R_{t,i} \approx 2R_c + R_{sh} \frac{l_i}{w} \quad (\text{C.1})$$

where  $R_c$  is the contact resistance,  $R_{sh}$  is the semiconductor sheet resistance,  $l_i$  is the gap width associated with the  $i$ -th pads pair ( $i = 1, \dots, 6$  for the designed TLM structure), while  $w$  is the pads width, which was set to  $40 \mu\text{m}$  for the employed TLMs. In this context, Eq. C.1 assumes  $R_c$  equal for all the probed contacts.

The acquired  $R_{t,i}(l_i)$  data can be then plotted, which should follow a linear behaviour since  $R_{sh}$  is supposed constant along the horizontal plane. From linear fitting, key parameters can be extracted, including  $R_c$ , which is obtained from half of the intersection value of the fitted line with the  $y$ -axis  $2R_c$  (i.e.,  $l = 0$ ),  $R_{sh}$ , which is retrieved from the line slope  $R_{sh}/w$ , and the transfer length  $l_t$ , which is obtained from half of the intersection value of the fitted line with the  $x$ -axis  $2l_t$  (i.e.,  $R_t = 0$ ). Practical examples are provided in Chapters 4 and 6.

Here,  $l_t$  represents a physical measure of the effective length of the contact or, alternatively, a characteristic decay length associated with the non-uniform (exponential) spatial distribution of the current flow in/out of the contact along the length of the contact itself, so that  $R_c = \rho_c/A_{eff} = \rho_c/wl_t$ , where  $A_{eff}$  is the contact effective area. In other words,  $l_t$  is the inverse of the average time electrons travel below the contact, or the average distance of the current flowing from the contact into the semiconductor [644]. This is the concept on which the transfer length model is based.

Finally,  $\rho_c$  can be estimated through the derived expressions below [644, 651]:

$$\rho_c \approx l_t^2 R_{sh} \approx wR_c l_t \tan\left(\frac{d}{l_t}\right) \quad (\text{C.2})$$

where  $d$  is the length associated with the gaps metal patches, which is  $20 \mu\text{m}$  for the designed structure reported in this thesis.

# Appendix D

## Silvaco Atlas TCAD RTD device simulation deck

In the following, the developed code for the ESUT #1 simulation is reported as an example.

```
#####  
#####  
# SILVACO Atlas TCAD simulation deck (ESUT #1) #  
#####  
#####  
  
go atlas simflags="-P 4"  
  
# Mesh-grid  
  
    mesh diag.flip (# mesh symmetrical with respect to the vertical center cross section)  
  
# Mesh-grid along x direction (assumed as transverse direction)  
  
    x.mesh loc=0.00 spac=0.001  
    x.mesh loc=0.001 spac=0.001  
  
# Mesh-grid along y direction (assumed as transport direction)  
  
# Emitter contact, In0.53Ga0.47As 40 nm (quasi-equilibrium)  
  
    y.mesh loc=-0.04 spac=0.0005
```

# Emitter,  $\text{In}_{0.53}\text{Ga}_{0.47}\text{As}$  200 nm (quasi-equilibrium)

y.mesh loc=0.0 spac =0.0005

# Lightly-doped spacer,  $\text{In}_{0.53}\text{Ga}_{0.47}\text{As}$  100 nm (quasi-equilibrium)

y.mesh loc=0.2 spac=0.0005

# Spacer,  $\text{In}_{0.53}\text{Ga}_{0.47}\text{As}$  10 nm (quasi-equilibrium)

y.mesh loc=0.3 spac=0.00001

# First barrier, AlAs 1.46 nm (non-equilibrium)

y.mesh loc=0.310 spac=0.00001

# Quantum well,  $\text{In}_{0.53}\text{Ga}_{0.47}\text{As}$  5.57 nm (non-equilibrium)

y.mesh loc=0.31146 spac=0.00001

# Second barrier, AlAs 1.46 nm (non-equilibrium)

y.mesh loc=0.31703 spac=0.00001

# Spacer,  $\text{In}_{0.53}\text{Ga}_{0.47}\text{As}$  10 nm (quasi-equilibrium)

y.mesh loc=0.31849 spac=0.00001

# Lightly-doped spacer,  $\text{In}_{0.53}\text{Ga}_{0.47}\text{As}$  100 nm (quasi-equilibrium)

y.mesh loc=0.32849 spac=0.0005

# Collector,  $\text{In}_{0.53}\text{Ga}_{0.47}\text{As}$  200 nm (quasi-equilibrium)

y.mesh loc=0.42849 spac=0.0005

# Collector contact,  $\text{In}_{0.53}\text{Ga}_{0.47}\text{As}$  40 nm (quasi-equilibrium)

y.mesh loc=0.62849 spac=0.0005

y.mesh loc=0.66849 spac=0.0005

### # Regions definition

# Emitter contact,  $\text{In}_{0.53}\text{Ga}_{0.47}\text{As}$  40 nm (quasi-equilibrium)

region num=1 material=InGaAs y.max=0.0 equil.negf

# Emitter,  $\text{In}_{0.53}\text{Ga}_{0.47}\text{As}$  200 nm (quasi-equilibrium)

region num=2 material=InGaAs y.min=0.0 y.max=0.2 equil.negf

# Lightly-doped spacer,  $\text{In}_{0.53}\text{Ga}_{0.47}\text{As}$  100 nm (quasi-equilibrium)

region num=3 material=InGaAs y.min=0.2 y.max=0.3 equil.negf

# Spacer,  $\text{In}_{0.53}\text{Ga}_{0.47}\text{As}$  10 nm (quasi-equilibrium)

region num=4 material=InGaAs y.min=0.3 y.max=0.310 equil.negf

# First barrier AlAs 1.46 nm (non-equilibrium)

region num=5 material=AlAs y.min=0.310 y.max=0.31146

# Quantum well,  $\text{In}_{0.53}\text{Ga}_{0.47}\text{As}$  5.6 nm (non-equilibrium)

region num=6 material=InGaAs y.min=0.31146 y.max=0.31703

# Second barrier, AlAs 1.46 nm (non-equilibrium)

region num=7 material=AlAs y.min=0.31703 y.max=0.31849

# Spacer,  $\text{In}_{0.53}\text{Ga}_{0.47}\text{As}$  10 nm (quasi-equilibrium)

region num=8 material=InGaAs y.min=0.31849 y.max=0.32849 equil.negf

# Lightly-doped spacer,  $\text{In}_{0.53}\text{Ga}_{0.47}\text{As}$  100 nm (quasi-equilibrium)

region num=9 material=InGaAs y.min=0.32849 y.max=0.42849 equil.negf

# Collector, In<sub>0.53</sub>Ga<sub>0.47</sub>As 200 nm (quasi-equilibrium)

region num=10 material=InGaAs y.min=0.42849 y.max=0.62849 equil.negf

# Collector contact, In<sub>0.53</sub>Ga<sub>0.47</sub>As 40 nm (quasi-equilibrium)

region num=11 material=InGaAs y.min=0.62849 y.max=0.66849 equil.negf

# Doping level

# Emitter contact, In<sub>0.53</sub>Ga<sub>0.47</sub>As 40 nm (quasi-equilibrium)

doping reg=1 y.max=0.0 uniform n.type conc=3e+19

# Emitter, In<sub>0.53</sub>Ga<sub>0.47</sub>As 200 nm (quasi-equilibrium)

doping num=2 y.min=0.0 y.max=0.2 uniform n.type conc=3e+18

# Lightly-doped spacer, In<sub>0.53</sub>Ga<sub>0.47</sub>As 100 nm (quasi-equilibrium)

doping num=3 y.min=0.2 y.max=0.3 uniform n.type conc=3e+17

# Lightly-doped spacer, In<sub>0.53</sub>Ga<sub>0.47</sub>As 100 nm (quasi-equilibrium)

doping num=9 y.min=0.32849 y.max=0.42849 uniform n.type conc=3e+17

# Collector, In<sub>0.53</sub>Ga<sub>0.47</sub>As 200 nm (quasi-equilibrium)

doping num=10 y.min=0.42849 y.max=0.62849 uniform n.type conc=3e+18

# Collector contact, In<sub>0.53</sub>Ga<sub>0.47</sub>As 40 nm (quasi-equilibrium)

doping reg=11 y.min=0.62849 y.max=0.66849 uniform n.type conc=3e+19

# Electrodes/contacts definition

```
elec num=1 name=emitter top
elec num=2 name=collector bottom
contact num=1 name=emitter reflect
contact num=2 name=collector reflect
```

```
# Material parameters
```

```
material material=InGaAs mc=0.041 mv=0.467 eg300=0.738 nc300=2.12e+17
nv300=8.01e+18 ni.min=8.24e+11 affinity=4.55 permittivity=13.9 mun=2.52e+4
```

```
material material=AlAs mc=0.146 mv=0.79 eg300=2.153 nc300=1.50e+19
nv300=1.76e+19 ni.min=13 affinity=3.50 permittivity=10.1 mun=1.85e+2
```

```
# Models
```

```
models n.negf_pl1d fermidirac esize.negf=10000 eig.ymin=0.0 eig.ymax=0.31849 print
```

```
# Computation
```

```
# Continuity equation is not solved for carriers
```

```
method carriers=0
```

```
# Bias-dependent quantities
```

```
# Transmission coefficient energy spectrum
```

```
probe transmission x=0 filename="ESUT1_T_"
```

```
# LDOS energy spectrum
```

```
set stepSize=0.000005
```

```
set startLoc=-0.04
```

```
set endLoc=0.66849
```

```
set loopCount=((endLoc-startLoc)/stepSize)+1
```

```
LOOP STEPS=loopCount
```

```
probe name="Local Density of States at startLoc" DOSVSE x=0.0005 y=startLoc
```

```
set startLoc=$startLoc+$stepSize
L.END

# Current density at each bias point

log outfile=ESUT1_JV.log

# Band diagram quantities

output eigen=100 band.param qfn

# Initial guess for potential/carrier density (thermal equilibrium)

solve init
save outfile=ESUT1_eq.str negf.log negf.eig

# Bias ramping

solve v2=0 name=collector vstep=0.01 vfinal=0.68 negf.eig
save outf=ESUT1_068.str negf.log negf.eig
solve name=collector vstep=0.01 vfinal=2 negf.eig

log off

quit
```

# Appendix E

## RTD small-signal equivalent circuit ADS schematic

To accurately extract the device small-signal equivalent circuit parameters, the measured  $S_{11}$  and converted  $Z_{11}$  parameters were fitted employing the small-signal equivalent circuit schematic shown in Figure E.1. To do that, the parameters tuning function included in ADS was employed.

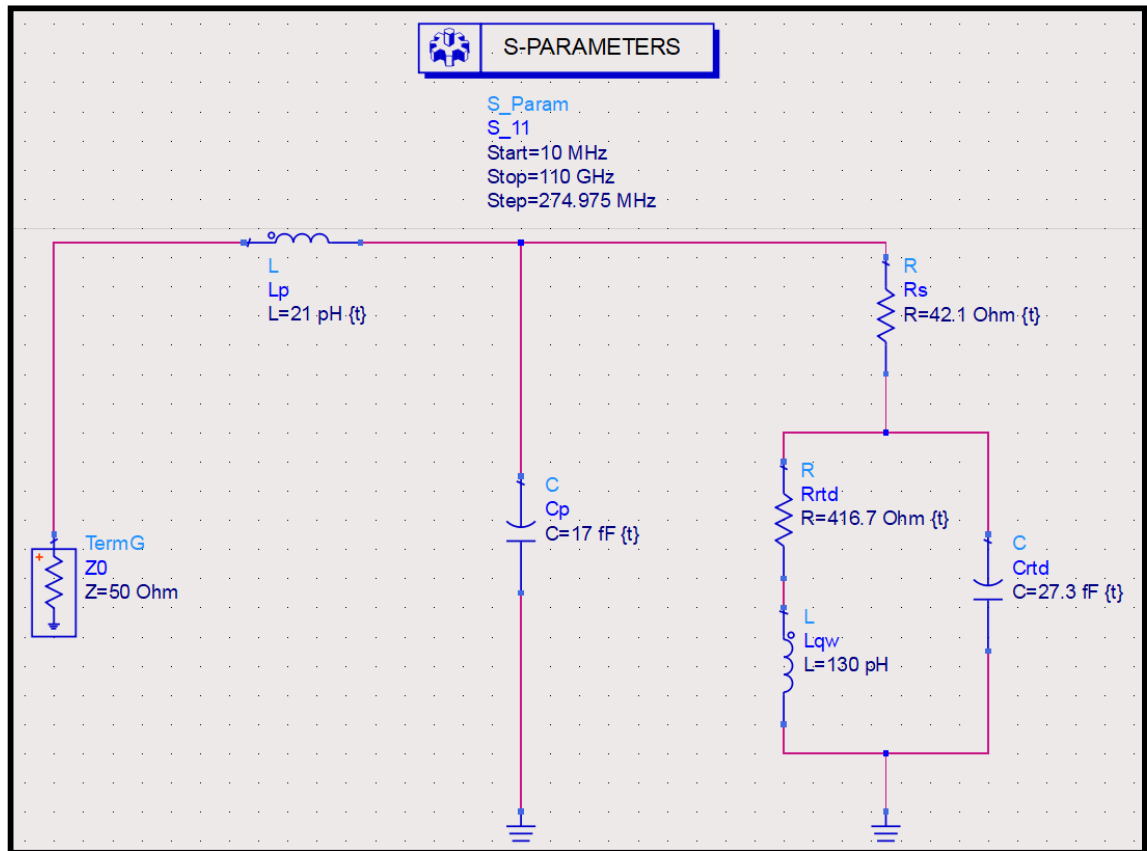


Figure E.1: ADS schematic for the extraction of the RTD high-frequency small-signal equivalent circuit parameters. Fitted values at  $V = 0.3 \text{ V}$  are displayed as example. Here,  $R_{rtd} = G_{rtd}^{-1}$ .

# Bibliography

- [1] E. Bründermann, H. -W. Hübers, and M. F. Kimmitt, "Terahertz techniques," *Springer*, 2012, doi: 10.1007/978-3-642-02592-1.
- [2] D. T. Leisawitz, W. C. Danchi, M. J. DiPirro, L. D. Feinberg, D. Y. Gezari, M. Hagopian, W. D. Langer, J. C. Mather, S. H. Moseley Jr., M. Shao, R. F. Silverberg, J. G. Staguhn, M. R. Swain, H. W. Yorke, and X. Zhang, "Scientific motivation and technology requirements for the SPIRIT and SPECS far-infrared/submillimeter space interferometers," *Proceedings of the SPIE, Astronomical Telescopes and Instrumentation*, vol. 4013, Munich, Germany, 2000, doi: 10.1117/12.393957.
- [3] T. Nagatsuma, "Terahertz technologies: present and future," *IEICE Electronics Express*, vol. 8, no. 14, pp. 1127-1142, 2011, doi: 10.1587/elex.8.1127.
- [4] P. H. Siegel, "Terahertz technology," *IEEE Transactions on Microwave Theory and Techniques*, vol. 50, no. 3, pp. 910-928, 2002, doi: 10.1109/22.989974.
- [5] J. Byrnes, "Unexploded ordnance detection and mitigation," *Springer*, 2009, doi: 10.1007/978-1-4020-9253-4.
- [6] R. W. Wilson, "History of the discovery of the cosmic microwave background radiation," *Physica Scripta*, vol. 21, no. 5, pp. 599-605, 1980, doi: 10.1088/0031-8949/21/5/001.
- [7] R. Durrer, "The cosmic microwave background: the history of its experimental investigation and its significance for cosmology," *Classical and Quantum Gravity*, vol. 32, no. 12, pp. 124007, 2015, doi: 10.1088/0264-9381/32/12/124007.
- [8] A. Wright, "Nobel prize 2006: mather and smoot," *Nature Physics*, vol. 2, no. 10, pp. 652, 2006, doi: 10.1038/nphys446.
- [9] J. C. Mather, E. S. Cheng, R. E. Jr. Eplee, R. B. Isaacman, S. S. Meyer, R. A. Shafer, R. Weiss, E. L. Wright, C. L. Bennett, N. W. Boggess, E. Dwek, S. Gulkis, M. G. Hauser, M. Janssen, T. Kelsall, P. M. Lubin, S. H. Jr. Moseley, T. L. Murdock, R. F. Silverberg, G. F. Smoot, and D. T. Wilkinson, "A preliminary measurement of the cosmic microwave background spectrum by the cosmic background explorer (COBE) satellite," *Astrophysical Journal Letters*, vol. 354, pp. L37, 1990, doi: 10.1086/185717.

- [10] G. F. Smoot, "Nobel lecture: cosmic microwave background radiation anisotropies: their discovery and utilization," *Reviews on Modern Physics*, vol. 79, no. 4, pp. 1349-1379, 2007, doi: 10.1103/revmodphys.79.1349.
- [11] F. F. Sizov, "Brief history of THz and IR technologies," *Semiconductor Physics, Quantum Electronics & Optoelectronics*, vol. 22, no. 1, pp. 67-79, 2019, doi: 10.15407/spqeo22.01.067.
- [12] M. Tonouchi, "Cutting-edge terahertz technology," *Nature Photonics*, vol. 1, no. 2, pp. 97-105, 2007, doi: 10.1038/nphoton.2007.3.
- [13] C. Sirtori, "Bridge for the terahertz gap," *Nature*, vol. 417, no. 6885, pp. 132-133, 2002, doi: 10.1038/417132b.
- [14] P. H. Siegel, "Terahertz technology in biology and medicine," *IEEE Transactions on Microwave Theory and Techniques*, vol. 52, no. 10, pp. 2438-2447, 2004, doi: 10.1109/TMTT.2004.835916.
- [15] M. Tamosiunaite, S. Tamosiunas, M. Zilinskas, and G. Valusis, "Atmospheric attenuation of the terahertz wireless networks," in *Broadband communications networks - recent advances and lessons from practice*, *IntechOpen*, 2017, doi: 10.5772/intechopen.72205.
- [16] D. Grischkowsky, S. Keiding, M. van Exter, and C. Fattinger, "Far-infrared time-domain spectroscopy with terahertz beams of dielectrics and semiconductors," *Journal of the Optical Society of America B*, vol. 7, no. 10, pp. 2006-2015, 1990, doi: 10.1364/JOSAB.7.002006.
- [17] M. B. Ketchen, D. Grischkowsky, T. C. Chen, C. -C. Chi, I. N. Duling III, N. J. Halas, J. -M. Halbout, J. A. Kash, and G. P. Li, "Generation of subpicosecond electrical pulses on coplanar transmission lines," *Applied Physics Letters*, vol. 48, no. 12, pp. 751-753, 1986, doi: 10.1063/1.96709.
- [18] G. Carpintero, L. E. G. Muñoz, H. L. Hartnagel, S. Preu, and A. V. Räisänen, "Semiconductor terahertz technology: devices and systems at room temperature operation," *Wiley*, 2015, doi: 10.1002/9781118920411.
- [19] D. Pavlidis, "Fundamentals of terahertz devices and applications," *Wiley*, 2021, doi: 10.1002/9781119460749.
- [20] N. Kumar, U. Singh, A. Bera, and A. K. Sinha, "A review on the sub-THz/THz gyrotrons," *Infrared Physics & Technology*, vol. 76, pp. 38-51, 2016, doi: 10.1016/j.infrared.2016.01.015.

- [21] R. A. Lewis, "A review of terahertz sources," *Journal of Physics D: Applied Physics*, vol. 47, no. 37, pp. 374001, 2014, doi: 10.1088/0022-3727/47/37/374001.
- [22] S. S. Dhillon, M. S. Vitiello, E. H. Linfield, A. G. Davies, M. C. Hoffmann, J. Booske, C. Paoloni, M. Gensch, P. Weightman, G. P. Williams, E. Castro-Camus, D. R. S. Cumming, F. Simoens, I. Escorcia-Carranza, J. Grant, S. Lucyszyn, M. Kuwata-Gonokami, K. Konishi, M. Koch, C. A. Schmuttenmaer, T. L. Cocker, R. Huber, A. G. Markelz, Z. D. Taylor, V. P. Wallace, J. A. Zeitler, J. Sibik, T. M. Korter, B. Ellison, S. Rea, P. Goldsmith, K. B. Cooper, R. Appleby, D. Pardo, P. G. Huggard, V. Krozer, H. Shams, M. Fice, C. Renaud, A. Seeds, A. Stöhr, M. Naftaly, N. Ridler, R. Clarke, J. E. Cunningham, and M. B. Johnston, "The 2017 terahertz science and technology roadmap," *Journal of Physics D: Applied Physics*, vol. 50, no. 4, pp. 043001, 2017, doi: 10.1088/1361-6463/50/4/043001.
- [23] H. -J. Song and T. Nagatsuma, "Handbook of terahertz technologies: devices and applications," *Jenny Stanford Publishing*, 2015, doi: 10.1201/b18381.
- [24] D. Saeedkia and S. Safavi-Naeini, "Terahertz photonics: optoelectronic techniques for generation and detection of terahertz waves," *Journal of Lightwave Technology*, vol. 26, no. 15, pp. 2409-2423, 2008, doi: 10.1109/JLT.2008.927614.
- [25] P. Chevalier, A. Amirzhan, F. Wang, M. Piccardo, S. G. Johnson, F. Capasso, and H. O. Everitt, "Widely tunable compact terahertz gas lasers," *Science*, vol. 366, no. 6467, pp. 856-860, 2019, doi: 10.1126/science.aay8683.
- [26] K. Zhong, W. Shi, D. G. Xu, P. X. Liu, Y. Y. Wang, J. L. Mei, C. Yan, S. J. Fu, and J. Q. Yao, "Optically pumped terahertz sources," *Science China Technological Sciences*, vol. 60, no. 12, pp. 1801-1818, 2017, doi: 10.1007/s11431-017-9057-3.
- [27] E. Bründermann, A. M. Linhart, L. Reichertz, H. P. Röser, O. D. Dubon, W. L. Hansen, G. Sirmain, and E. E. Haller, "Double acceptor doped Ge: a new medium for inter-valence-band lasers," *Applied Physics Letters*, vol. 68, no. 22, pp. 3075-3077, 1996, doi: 10.1063/1.116427.
- [28] A. Bergner, U. Heugen, E. Bründermann, G. Schwaab, M. Havenith, D. R. Chamberlin, and E. E. Haller, "New p-Ge THz laser spectrometer for the study of solutions: THz absorption spectroscopy of water," *Review of Scientific Instruments*, vol. 76, no. 6, pp. 063110, 2005, doi: 10.1063/1.1928427.
- [29] S. G. Pavlov, R. K. Zhukavin, V. N. Shastin, and H. -W. Hübers, "The physical principles of terahertz silicon lasers based on intracenter transitions," *physica status solidi B*, vol. 250, no. 1, pp. 9-36, 2013, doi: 10.1002/pssb.201248322.

- [30] R. Köhler, A. Tredicucci, F. Beltram, H. E. Beere, E. H. Linfield, A. G. Davies, D. A. Ritchie, R. C. Iotti, and F. Rossi, "Terahertz semiconductor-heterostructure laser," *Nature*, vol. 417, no. 6885, pp. 156-159, 2002, doi: 10.1038/417156a.
- [31] B. S. Williams, "Terahertz quantum-cascade laser," *Nature Photonics*, vol. 1, no. 9, pp. 517-525, 2007, doi: 10.1038/nphoton.2007.166.
- [32] S. Fatholouloumi, E. Dupont, C. W. I. Chan, Z. R. Wasilewski, S. R. Laframboise, D. Ban, A. Mátyás, C. Jirauschek, Q. Hu, and H. C. Liu, "Terahertz quantum cascade lasers operating up to  $\sim 200$  K with optimized oscillator strength and improved injection tunneling," *Optics express*, vol. 20, no. 4, pp. 3866-3876, 2012, doi: 10.1364/OE.20.003866.
- [33] D. J. Paul, "The progress towards terahertz quantum cascade lasers on silicon substrates," *Laser & Photonics Reviews*, vol. 4, no. 5, pp. 610-632, 2010, doi: 10.1002/lpor.200910038.
- [34] O. D. Dubon, D. R. Chamberlin, W. L. Hansen, E. E. Haller, L. A. Reichertz, G. Sinnain, E. Bründermann, A. M. Linhart, and H. P. Röser, "Terahertz emission from *p*-type germanium lasers doped from novel acceptors," *Eighth International Symposium on Space Terahertz Technology*, pp. 423-429, 1997.
- [35] S. Kumar, C. W. I. Chan, Q. Hu, and J. L. Reno, "A 1.8-THz quantum cascade laser operating significantly above the temperature of  $\hbar\omega/k_B$ ," *Nature Physics*, vol. 7, no. 2, pp. 166-171, 2011, doi: 10.1038/nphys1846.
- [36] L. Bosco, M. Franckić, G. Scalari, M. Beck, A. Wacker, and J. Faist, "Thermoelectrically cooled THz quantum cascade laser operating up to 210 K," *Applied Physics Letters*, vol. 115, no. 1, pp. 010601, 2019, doi: 10.1063/1.5110305.
- [37] B. Wen and D. Ban, "High-temperature terahertz quantum cascade lasers," *Progress in Quantum Electronics*, vol. 80, pp. 100363, 2021, doi: 10.1016/j.pquantelec.2021.100363.
- [38] G. Liang, T. Liu, and Q. J. Wang, "Recent developments of terahertz quantum cascade lasers," *IEEE Journal of Selected Topics in Quantum Electronics*, vol. 23, no. 4, pp. 1-18, 2017, doi: 10.1109/JSTQE.2016.2625982.
- [39] G. Scalari, C. Walther, M. Fischer, R. Terazzi, H. Beere, D. Ritchie, and J. Faist, "THz and sub-THz quantum cascade lasers," *Laser & Photonics Reviews*, vol. 3, no. 1-2, pp. 45-66, 2009, doi: 10.1002/lpor.200810030.
- [40] A. Wade, G. Fedorov, D. Smirnov, S. Kumar, B. S. Williams, Q. Hu, and J. L. Reno, "Magnetic-field-assisted terahertz quantum cascade laser operating up to 225 K," *Nature Photonics*, vol. 3, no. 1, pp. 41-45, 2009, doi: 10.1038/nphoton.2008.251.

- [41] G. Scalari, D. Turčinková, J. Lloyd-Hughes, M. I. Amanti, M. Fischer, M. Beck, and J. Faist, "Magnetically assisted quantum cascade laser emitting from 740 GHz to 1.4 THz," *Applied Physics Letters*, vol. 97, no. 8, pp. 081110, 2010, doi: 10.1063/1.3481698.
- [42] X. Wang, C. Shen, T. Jiang, Z. Zhan, Q. Deng, W. Li, W. Wu, N. Yang, W. Chu, and S. Duan, "High-power terahertz quantum cascade lasers with  $\sim 0.23$  W in continuous wave mode," *AIP Advances*, vol. 6, no. 7, pp. 075210, 2016, doi: 10.1063/1.4959195.
- [43] L. Li, L. Chen, J. Zhu, J. Freeman, P. Dean, A. Valavanis, A. G. Davies, and E. H. Linfield, "Terahertz quantum cascade lasers with  $> 1$  W output powers," *Electronics Letters*, vol. 50, no. 4, pp. 309-311, 2014, doi: 10.1049/el.2013.4035.
- [44] Q. Lu and M. Razeghi, "Recent advances in room temperature, high-power terahertz quantum cascade laser sources based on difference-frequency generation," *Photonics*, vol. 3, no. 3, pp. 42, 2016, doi: 10.3390/photonics3030042.
- [45] S. Hayashi, K. Nawata, T. Taira, J. Shikata, K. Kawase, and H. Minamide, "Ultrabright continuously tunable terahertz-wave generation at room temperature," *Scientific Reports*, vol. 4, no. 1, pp. 5045, 2014, doi: 10.1038/srep05045.
- [46] J. Hebling, K. -L. Yeh, M. C. Hoffmann, and K. A. Nelson, "High-power THz generation, THz nonlinear optics, and THz nonlinear spectroscopy," *IEEE Journal of Selected Topics in Quantum Electronics*, vol. 14, no. 2, pp. 345-353, 2008, doi: 10.1109/JSTQE.2007.914602.
- [47] Y. J. Ding, "Progress in terahertz sources based on difference-frequency generation," *Journal of the Optical Society of America B*, vol. 31, no. 11, pp. 2696-2711, 2014, doi: 10.1364/JOSAB.31.002696.
- [48] D. Molter, M. Theuer, and R. Beigang, "Nanosecond terahertz optical parametric oscillator with a novel quasi phase matching scheme in lithium niobate," *Optics Express*, vol. 17, no. 8, pp. 6623-6628, 2009, doi: 10.1364/OE.17.006623.
- [49] N. M. Burford and M. O. El-Shenawee, "Review of terahertz photoconductive antenna technology," *Optical Engineering*, vol. 56, no. 1, pp. 1-20, 2017, doi: 10.1117/1.OE.56.1.010901.
- [50] E. R. Brown, B. Globisch, G. Carpintero, A. Rivera, D. Segovia-Vargas, and A. Steiger, "Photoconductive THz sources driven at 1550 nm," in *Fundamentals of terahertz devices and applications*, Wiley, 2021, doi: 10.1002/9781119460749.ch3.
- [51] J. P. Seddon, M. Natrella, X. Lin, C. Graham, C. C. Renaud, and A. J. Seeds, "Photodiodes for terahertz applications," *IEEE Journal of Selected Topics in Quantum Electronics*, vol. 28, no. 2, pp. 1-12, 2022, doi: 10.1109/JSTQE.2021.3108954.

- [52] T. Nagatsuma, H. Ito, and T. Ishibashi, "High-power RF photodiodes and their applications," *Laser & Photonics Reviews*, vol. 3, no. 1-2, pp. 123-137, 2009, doi: 10.1002/lpor.200810024.
- [53] S. Koenig, D. Lopez-Diaz, J. Antes, F. Boes, R. Henneberger, A. Leuther, A. Tessmann, R. Schmogrow, D. Hillerkuss, R. Palmer, T. Zwick, C. Koos, W. Freude, O. Ambacher, J. Leuthold, and I. Kallfass, "Wireless sub-THz communication system with high data rate," *Nature Photonics*, vol. 7, no. 12, pp. 977-981, 2013, doi: 10.1038/nphoton.2013.275.
- [54] A. J. Deninger, A. Roggenbuck, S. Schindler, and S. Preu, "2.75 THz tuning with a triple-DFB laser system at 1550 nm and InGaAs photomixers," *Journal of Infrared, Millimeter, and Terahertz Waves*, vol. 36, no. 3, pp. 269-277, 2015, doi: 10.1007/s10762-014-0125-5.
- [55] S. -H. Yang, R. Watts, X. Li, N. Wang, V. Cojocaru, J. O'Gorman, L. P. Barry, and M. Jarrahi, "Tunable terahertz wave generation through a bimodal laser diode and plasmonic photomixer," *Optics Express*, vol. 23, no. 24, pp. 31206-31215, 2015, doi: 10.1364/OE.23.031206.
- [56] N. Kim, S. -P. Han, H. -C. Ryu, H. Ko, J. -W. Park, D. Lee, M. Y. Jeon, and K. H. Park, "Distributed feedback laser diode integrated with distributed Bragg reflector for continuous-wave terahertz generation," *Optics Express*, vol. 20, no. 16, pp. 17496-17502, 2012, doi: 10.1364/OE.20.017496.
- [57] M. T. Haidar, S. Preu, J. Cesar, S. Paul, A. S. Hajo, C. Neumeyr, H. Maune, and F. Küppers, "Systematic characterization of a 1550 nm microelectromechanical (MEMS)-tunable vertical-cavity surface emitting laser (VCSEL) with 7.92 THz tuning-range for terahertz photomixing systems," *Journal of Applied Physics*, vol. 123, no. 2, pp. 023106, 2018, doi: 10.1063/1.5003147.
- [58] L. Consolino, M. Nafa, M. De Regis, F. Cappelli, S. Bartalini, A. Ito, M. Hitaka, T. Dougakiuchi, T. Edamura, P. De Natale, and K. Fujita, "Direct observation of terahertz frequency comb generation in difference-frequency quantum cascade lasers," *Applied Sciences*, vol. 11, no. 4, pp. 1416, 2021, doi: 10.3390/app11041416.
- [59] T. Nagatsuma, K. Oogimoto, Y. Yasuda, Y. Fujita, Y. Inubushi, S. Hisatake, A. M. Agoues, and G. C. Lopez, "300-GHz-band wireless transmission at 50 Gbit/s over 100 meters," *41st International Conference on Infrared, Millimeter, and Terahertz waves (IRMMW-THz)*, pp. 1-2, 2016, doi: 10.1109/IRMMW-THz.2016.7758356.
- [60] T. Nagatsuma, Y. Fujita, Y. Yasuda, Y. Kanai, S. Hisatake, M. Fujiwara, and J. Kani, "Real-time 100-Gbit/s QPSK transmission using photonics-based 300-GHz-band wireless link," *IEEE International Topical Meeting on Microwave Photonics (MWP)*, pp. 27-30, 2016, doi: 10.1109/MWP.2016.7791277.

- [61] J. A. Fülöp, S. Tzortzakis, and T. Kampfrath, "Laser-driven strong-field terahertz sources," *Advanced Optical Materials*, vol. 8, no. 3, pp. 1900681, 2020, doi: 10.1002/adom.201900681.
- [62] G. Torosyan, S. Keller, L. Scheuer, R. Beigang, and E. T. Papaioannou, "Optimized spintronic terahertz emitters based on epitaxial grown Fe/Pt layer structures," *Scientific Reports*, vol. 8, no. 1, pp. 1311, 2018, doi: 10.1038/s41598-018-19432-9.
- [63] D. M. Lubenko, V. E. Prokopev, S. V. Alekseev, M. V. Ivanov, and V. F. Losev, "THz emission efficiency in femtosecond laser-induced filament under different pumping conditions," *Proceedings of the SPIE, XIV International Conference on Pulsed Lasers and Laser Applications*, vol. 11322, Tomsk, Russian Federation, 2019, doi: 10.1117/12.2550833.
- [64] T. Ishibashi, Y. Muramoto, T. Yoshimatsu, and H. Ito, "Unitraveling-carrier photodiodes for terahertz applications," *IEEE Journal of Selected Topics in Quantum Electronics*, vol. 20, no. 6, pp. 79-88, 2014, doi: 10.1109/JSTQE.2014.2336537.
- [65] T. Ishibashi and H. Ito, "Uni-Traveling Carrier Photodiodes: Development and Prospects," *IEEE Journal of Selected Topics in Quantum Electronics*, vol. 28, no. 2, pp. 1-6, 2022, doi: 10.1109/JSTQE.2021.3123383.
- [66] T. Nagatsuma, G. Ducournau, and C. Renaud, "Advances in terahertz communications accelerated by photonics," *Nature Photonics*, vol. 10, no. 6, pp. 371-379, 2016, doi: 10.1038/nphoton.2016.65.
- [67] T. Ishibashi, N. Shimizu, S. Kodama, H. Ito, T. Nagatsuma, and T. Furuta, "Uni-traveling-carrier photodiodes," *Ultrafast Electronics and Optoelectronics, OSA Trends in Optics and Photonics Series*, vol. 13, 1997, doi: 10.1364/UEO.1997.UC3.
- [68] T. Ishibashi and H. Ito, "Uni-traveling-carrier photodiodes," *Journal of Applied Physics*, vol. 127, no. 3, pp. 031101, 2020, doi: 10.1063/1.5128444.
- [69] S. Preu, G. H. Döhler, S. Malzer, L. J. Wang, and A. C. Gossard, "Tunable, continuous-wave terahertz photomixer sources and applications," *Journal of Applied Physics*, vol. 109, no. 6, pp. 061301, 2011, doi: 10.1063/1.3552291.
- [70] C. C. Renaud, M. Natrella, C. Graham, J. Seddon, F. Van Dijk, and A. J. Seeds, "Antenna Integrated THz Uni-Traveling Carrier Photodiodes," *IEEE Journal of Selected Topics in Quantum Electronics*, vol. 24, no. 2, pp. 1-11, 2018, doi: 10.1109/JSTQE.2017.2725444.
- [71] R. Boyd, "Nonlinear optics," *Academic Press*, 2003, doi: 10.1016/B978-0-12-121682-5.X5000-7.

- [72] A. Wakatsuki, Y. Muramoto, and T. Ishibashi, "Development of terahertz-wave photomixer module using a uni-traveling-carrier photodiode," *NTT Technical Review*, vol. 10, no. 2, 2012.
- [73] H. Ito, S. Kodama, Y. Muramoto, T. Furuta, T. Nagatsuma, and T. Ishibashi, "High-speed and high-output InP-InGaAs unitraveling-carrier photodiodes," *IEEE Journal of Selected Topics in Quantum Electronics*, vol. 10, no. 4, pp. 709-727, 2004, doi: 10.1109/JSTQE.2004.833883.
- [74] T. Ishibashi, S. Kodama, N. S. N. Shimizu, and T. Furuta, "High-speed response of uni-traveling-carrier photodiodes," *Japanese Journal of Applied Physics*, vol. 36, no. 10R, pp. 6263-6268, 1997, doi: 10.1143/jjap.36.6263.
- [75] O. Madelung, U. Rössler, and M. Schulz, "Semiconductors group IV elements, IV-IV and III-V compounds. Part b - electronic, transport, optical and other properties," *Springer Materials*, vol. 41A1 $\beta$ , 2002, doi: 10.1007/b80447.
- [76] E. S. Harmon, M. L. Lovejoy, M. R. Melloch, M. S. Lundstrom, D. Ritter, and R. A. Hamm, "Minority-carrier mobility enhancement in  $p^+$  InGaAs lattice matched to InP," *Applied Physics Letters*, vol. 63, no. 5, pp. 636-638, 1993, doi: 10.1063/1.109974.
- [77] H. -J. Song, K. Ajito, Y. Muramoto, A. Wakatsuki, T. Nagatsuma, and N. Kukutsu, "Uni-travelling-carrier photodiode module generating 300 GHz power greater than 1 mW," *IEEE Microwave and Wireless Components Letters*, vol. 22, no. 7, pp. 363-365, 2012, doi: 10.1109/LMWC.2012.2201460.
- [78] F. Aniel, G. Auton, D. Cumming, M. Feiginov, S. Gebert, T. González, C. Li, A. Lisauskas, H. Marinchio, J. Mateos, C. Palermo, A. Song, J. Treuttel, L. Varani, and N. Zerounian, "Terahertz electronic devices," in Springer handbook of semiconductor devices, *Springer*, 2021, doi: 10.1007/978-3-030-79827-7\_22.
- [79] J. H. Booske, R. J. Dobbs, C. D. Joye, C. L. Kory, G. R. Neil, G. -S. Park, J. Park, and R. J. Temkin, "Vacuum electronic high power terahertz sources," *IEEE Transactions on Terahertz Science and Technology*, vol. 1, no. 1, pp. 54-75, 2011, doi: 10.1109/TTHZ.2011.2151610.
- [80] J. Hesler, R. Prasankumar, and J. Tignon, "Advances in terahertz solid-state physics and devices," *Journal of Applied Physics*, vol. 126, no. 11, pp. 110401, 2019, doi: 10.1063/1.5122975.
- [81] C. Paoloni, D. Gamzina, L. Himes, B. Popovic, R. Barchfeld, L. Yue, Y. Zheng, X. Tang, Y. Tang, P. Pan, H. Li, R. Letizia, M. Mineo, J. Feng, and N. C. Luhmann, "THz backward-

- wave oscillators for plasma diagnostic in nuclear fusion," *IEEE Transactions on Plasma Science*, vol. 44, no. 4, pp. 369-376, 2016, doi: 10.1109/TPS.2016.2541119.
- [82] D. Gamzina, X. Li, C. Hurd, Y. Tang, X. Huang, Y. Zheng, L. Himes, M. Gonzalez, H. Li, P. Pan, R. Letizia, J. Feng, N. C. Luhmann Jr., and C. Paoloni, "Backward wave oscillator for high power generation at THz frequencies," *Proceedings of the SPIE, Terahertz Emitters, Receivers, and Applications VIII*, vol. 10383, San Diego, California, 2017, doi: 10.1117/12.2273256.
- [83] X. Xu, Y. Wei, F. Shen, H. Yin, J. Xu, Y. Gong, and W. Wang, "A watt-class 1-THz backward-wave oscillator based on sine waveguide," *Physics of Plasmas*, vol. 19, no. 1, pp. 013113, 2012, doi: 10.1063/1.3677889.
- [84] R. Li, C. Ruan, A. K. Fahad, C. Zhang, and S. Li, "Broadband and high-power terahertz radiation source based on extended interaction klystron," *Scientific Reports*, vol. 9, no. 1, pp. 4584, 2019, doi: 10.1038/s41598-019-41087-3.
- [85] R. Basu, L. R. Billa, R. Letizia, and C. Paoloni, "Design of sub-THz traveling wave tubes for high data rate long range wireless links," *Semiconductor Science and Technology*, vol. 33, no. 12, pp. 124009, 2018, doi: 10.1088/1361-6641/aae859.
- [86] P. Tan, J. Huang, K. F. Liu, Y. Q. Xiong, and M. W. Fan, "Terahertz radiation sources based on free electron lasers and their applications," *Science China Information Sciences*, vol. 55, no. 1, pp. 1-15, 2012, doi: 10.1007/s11432-011-4515-1.
- [87] N. Vinokurov, "Free electron lasers as a high-power terahertz sources," *Journal of Infrared, Millimeter, and Terahertz Waves*, vol. 32, no. 10, pp. 1123-1143, 2011, doi: 10.1007/s10762-011-9766-9.
- [88] J. Nishizawa, P. Plotka, T. Kurabayashi, and H. Makabe, "706-GHz GaAs CW fundamental-mode TUNNETT diodes fabricated with molecular layer epitaxy," *physica status solidi c*, vol. 5, no. 9, pp. 2802-2804, 2008, doi: 10.1002/pssc.200779256.
- [89] H. Eisele, "355 GHz oscillator with GaAs TUNNETT diode," *Electronics Letters*, vol. 41, no. 6, pp. 329-331, 2005, doi: 10.1049/el:20058165.
- [90] J. Nishizawa, P. Plotka, H. Makabe, and T. Kurabayashi, "GaAs TUNNETT diodes oscillating at 430 – 655 GHz in CW fundamental mode," *IEEE Microwave and Wireless Components Letters*, vol. 15, no. 9, pp. 597-599, 2005, doi: 10.1109/LMWC.2005.855381.
- [91] K. Chang, W. F. Thrower, and G. M. Hayashibara, "Millimeter-wave silicon IMPATT sources and combiners for the 110 – 260-GHz range," *IEEE Transactions on Microwave Theory and Techniques*, vol. 29, no. 12, pp. 1278-1284, 1981, doi: 10.1109/TMTT.1981.1130553.

- [92] A. Acharyya and J. P. Banerjee, "Prospects of IMPATT devices based on wide bandgap semiconductors as potential terahertz sources," *Applied Nanoscience*, vol. 4, no. 1, pp. 1-14, 2014, doi: 10.1007/s13204-012-0172-y.
- [93] H. Eisele, L. Li, and E. H. Linfield, "High-performance GaAs/AlAs superlattice electronic devices in oscillators at frequencies 100 – 320 GHz," *Applied Physics Letters*, vol. 112, no. 17, pp. 172103, 2018, doi: 10.1063/1.5020265.
- [94] H. Eisele, S. P. Khanna, and E. H. Linfield, "Superlattice electronic devices as high-performance oscillators between 60 – 220 GHz," *Applied Physics Letters*, vol. 96, no. 7, pp. 072101, 2010, doi: 10.1063/1.3324697.
- [95] H. Eisele, "Negative differential resistance devices for generation of terahertz radiation," *Proceedings of the SPIE, Terahertz Emitters, Receivers, and Applications VI*, vol. 9585, San Diego, California, 2015, doi: 10.1117/12.2187352.
- [96] H. Eisele and G. I. Haddad, "Two-terminal millimeter-wave sources," *IEEE Transactions on Microwave Theory and Techniques*, vol. 46, no. 6, pp. 739-746, 1998, doi: 10.1109/22.681195.
- [97] H. Eisele, A. Rydberg, and G. I. Haddad, "Recent advances in the performance of InP Gunn devices and GaAs TUNNETT diodes for the 100 – 300-GHz frequency range and above," *IEEE Transactions on Microwave Theory and Techniques* vol. 48, no. 4, pp. 626-631, 2000, doi: 10.1109/22.841952.
- [98] P. N. Butcher, "The Gunn effect," *Reports on Progress in Physics*, vol. 30, no. 1, pp. 97-148, 1967, doi: 10.1088/0034-4885/30/1/303.
- [99] B. K. Ridley and T. B. Watkins, "The possibility of negative resistance effects in semiconductors," *Proceedings of the Physical Society*, vol. 78, no. 2, pp. 293-304, 1961, doi: 10.1088/0370-1328/78/2/315.
- [100] A. Khalid, N. J. Pilgrim, G. M. Dunn, M. C. Holland, C. R. Stanley, I. G. Thayne, and D. R. S. Cumming, "A planar gunn diode operating above 100 GHz," *IEEE Electron Device Letters*, vol. 28, no. 10, pp. 849-851, 2007, doi: 10.1109/LED.2007.904218.
- [101] H. Eisele and R. Kamoua, "Submillimeter-wave InP Gunn devices," *IEEE Transactions on Microwave Theory and Techniques*, vol. 52, no. 10, pp. 2371-2378, 2004, doi: 10.1109/TMTT.2004.835974.
- [102] A. Khalid, N. J. Pilgrim, G. M. Dunn, M. C. Holland, C. R. Stanley, I. G. Thayne, and D. R. S. Cumming, "Reliable GaN-based THz Gunn diodes with side-contact and field-plate technologies," *IEEE Access*, vol. 8, pp. 84116-84122, 2020, doi: 10.1109/ACCESS.2020.2991309.

- [103] Z. S. Gribnikov, R. R. Bashirov, and V. V. Mitin, "Negative effective mass mechanism of negative differential drift velocity and terahertz generation," *IEEE Journal of Selected Topics in Quantum Electronics*, vol. 7, no. 4, pp. 630-640, 2001, doi: 10.1109/2944.974235.
- [104] M. Wollitzer, J. Buechler, F. Schäffler, and J. -F. Luy, "D-band Si-IMPATT diodes with 300 mW CW output power at 140 GHz," *Electronics Letters*, vol. 32, no. 2, pp. 122-123, 1996, doi: 10.1049/el:19960088.
- [105] S. M. Sze, "Semiconductor devices: physics and technology," *Wiley*, 1985.
- [106] H. Eisele, "480 GHz oscillator with an InP Gunn device," *Electronics Letters*, vol. 46, no. 6, pp. 422-426, 2010, doi: 10.1049/el.2010.3362.
- [107] J. -S. Rieh, "Introduction to terahertz electronics," *Springer*, 2021, doi: 10.1007/978-3-030-51842-4.
- [108] H. Eisele, "Third-harmonic power extraction from InP Gunn devices up to 455 GHz," *IEEE Microwave and Wireless Components Letters*, vol. 19, no. 6, pp. 416-418, 2009, doi: 10.1109/LMWC.2009.2020044.
- [109] H. Eisele and G. I. Haddad, "GaAs TUNNETT diodes on diamond heat sinks for 100 GHz and above," *IEEE Transactions on Microwave Theory and Techniques*, vol. 43, no. 1, pp. 210-213, 1995, doi: 10.1109/22.362989.
- [110] H. Eisele, "Dual Gunn device oscillator with 10mW at 280 GHz," *Electronics Letters*, vol. 43, no. 11, pp. 636-638, 2007, doi: 10.1049/el:20070936.
- [111] H. Eisele, "High performance InP Gunn devices with 34 mW at 193 GHz," *Electronics Letters*, vol. 38, no. 16, pp. 923-924, 2002, doi: 10.1049/el:20020612.
- [112] H. Eisele, "Second-harmonic power extraction from InP Gunn devices with more than 1 mW in 260 – 320 GHz frequency range," *Electronics Letters*, vol. 34, no. 25, pp. 2412-2413, 1998, doi: 10.1049/el:19981659.
- [113] A. Khalid, G. M. Dunn, R. F. Macpherson, S. Thoms, D. Macintyre, C. Li, M. J. Steer, V. Papageorgiou, I. G. Thayne, M. Kuball, C. H. Oxley, M. Montes Bajo, A. Stephen, J. Glover, and D. R. S. Cumming, "Terahertz oscillations in an  $\text{In}_{0.53}\text{Ga}_{0.47}\text{As}$  submicron planar Gunn diode," *Journal of Applied Physics*, vol. 115, no. 11, pp. 114502, 2014, doi: 10.1063/1.4868705.
- [114] C. Li, A. Khalid, S. H. Paluchowski Caldwell, N. J. Pilgrim, M. C. Holland, G. M. Dunn, and D. R. S. Cumming, "Enhancement of power and frequency in Planar Gunn diodes by introducing extra delta-doping layers," *Microwave and Optical Technology Letters*, vol. 53, no. 7, pp. 1624-1626, 2011, doi: 10.1002/mop.26071.

- [115] I. Mehdi, J. V. Siles, C. Lee, and E. Schlecht, "THz diode technology: status, prospects, and applications," *Proceedings of the IEEE*, vol. 105, no. 6, pp. 990-1007, 2017, doi: 10.1109/JPROC.2017.2650235.
- [116] A. Maestrini, I. Mehdi, J. V. Siles, R. Lin, C. Lee, G. Chattopadhyay, J. Pearson, and P. Siegel, "Frequency tunable electronic sources working at room temperature in the 1 to 3 THz band," *Proceedings of the SPIE, Terahertz Emitters, Receivers, and Applications III*, vol. 8496, San Diego, California, 2012, doi: 10.1117/12.929654.
- [117] J. Stake, A. Malko, T. Bryllert, and J. Vukusic, "Status and prospects of high-power heterostructure barrier varactor frequency multipliers," *Proceedings of the IEEE*, vol. 105, no. 6, pp. 1008-1019, 2017 doi: 10.1109/JPROC.2016.2646761.
- [118] J. Vukusic, T. Bryllert, T. Arezoo Emadi, M. Sadeghi, and J. Stake, "A 0.2-W heterostructure barrier varactor frequency tripler at 113 GHz," *IEEE Electron Device Letters*, vol. 28, no. 5, pp. 340-342, 2007 doi: 10.1109/LED.2007.895376.
- [119] J. C. Pearson, B. J. Drouin, A. Maestrini, I. Mehdi, J. Ward, R. H. Lin, S. Yu, J. J. Gill, B. Thomas, C. Lee, G. Chattopadhyay, E. Schlecht, F. W. Maiwald, P. F. Goldsmith, and P. Siegel, "Demonstration of a room temperature 2.48 – 2.75 THz coherent spectroscopy source," *Review of Scientific Instruments*, vol. 82, no. 9, pp. 093105, 2011, doi: 10.1063/1.3617420.
- [120] J. V. Siles, K. B. Cooper, C. Lee, R. H. Lin, G. Chattopadhyay, and I. Mehdi, "A New generation of room-temperature frequency-multiplier sources with up to 10× higher output power in the 160-GHz – 1.6-THz Range," *IEEE Transactions on Terahertz Science and Technology*, vol. 8, no. 6, pp. 596-604, 2018, doi: 10.1109/TTHZ.2018.2876620.
- [121] S. Martin, B. Nakamura, A. Fung, P. Smith, J. Bruston, A. Maestrini, F. Maiwald, P. Siegel, E. Schlecht, and I. Mehdi, "Fabrication of 200 to 2700 GHz multiplier devices using GaAs and metal membranes," *IEEE MTT-S International Microwave Symposium Digest*, vol. 3, pp. 1641-1644, 2001, doi: 10.1109/MWSYM.2001.967219.
- [122] U. R. Pfeiffer, R. Jain, J. Grzyb, S. Malz, P. Hillger, and P. Rodríguez-Vázquez, "Current status of terahertz integrated circuits - from components to systems," *IEEE BiCMOS and Compound Semiconductor Integrated Circuits and Technology Symposium (BCICTS)*, pp. 1-7, 2018, doi: 10.1109/BCICTS.2018.8551068.
- [123] U. Pfeiffer, "Integrated circuit design for terahertz applications," *6G Wireless Summit (6G SUMMIT)*, 2020.

- [124] P. Hillger, J. Grzyb, R. Jain, and U. R. Pfeiffer, "Terahertz imaging and sensing applications with silicon-based technologies," *IEEE Transactions on Terahertz Science and Technology*, vol. 9, no. 1, pp. 1-19, 2019, doi: 10.1109/TTHZ.2018.2884852.
- [125] M. Božanić and S. Sinha, "Emerging transistor technologies capable of terahertz amplification: a way to re-engineer terahertz radar sensors," *Sensors*, vol. 19, no. 11, pp. 2454, 2019, doi: 10.3390/s19112454.
- [126] T. H. Lee, "Terahertz CMOS integrated circuits," *IEEE International Symposium on Radio-Frequency Integration Technology*, pp. 1-2, 2014, doi: 10.1109/RFIT.2014.6933268.
- [127] S. Lee, B. Jagannathan, S. Narasimha, A. Chou, N. Zamdmer, J. Johnson, R. Williams, L. Wagner, J. Kim, J. Plouchart, J. Pekarik, S. Springer, and G. Freeman, "Record RF performance of 45-nm SOI CMOS technology," *IEEE International Electron Devices Meeting*, pp. 255-258, 2007, doi: 10.1109/IEDM.2007.4418916.
- [128] H. Rucker and B. Heinemann, "High-performance SiGe HBTs for next generation BiCMOS technology," *Semiconductor Science and Technology*, vol. 33, no. 11, pp. 114003, 2018, doi: 10.1088/1361-6641/aade64.
- [129] H. Rucker, B. Heinemann, and A. Fox, "Half-Terahertz SiGe BiCMOS technology," *IEEE 12th Topical Meeting on Silicon Monolithic Integrated Circuits in RF Systems*, pp. 133-136, 2012, doi: 10.1109/SiRF.2012.6160164.
- [130] H. -J. Lee, S. Rami, S. Ravikumar, V. Neeli, K. Phoa, B. Sell, and Y. Zhang, "Intel 22nm FinFET (22FFL) process technology for RF and mm wave applications and circuit design optimization for FinFET technology," *IEEE International Electron Devices Meeting (IEDM)*, pp. 14.1.1-14.1.4, 2018, doi: 10.1109/IEDM.2018.8614490.
- [131] B. Heinemann, H. Rucker, R. Barth, F. Bärwolf, J. Drews, G. G. Fischer, A. Fox, O. Fursenko, T. Grabolla, F. Herzel, J. Katzer, J. Korn, A. Krüger, P. Kulse, T. Lenke, M. Lisker, S. Marschmeyer, A. Scheit, D. Schmidt, J. Schmidt, M. A. Schubert, A. Trusch, C. Wipf, and D. Wolansky, "SiGe HBT with ft/fmax of 505 GHz/720 GHz," *IEEE International Electron Devices Meeting (IEDM)*, pp. 3.1.1-3.1.4, 2016, doi: 10.1109/IEDM.2016.7838335.
- [132] M. Urteaga, Z. Griffith, M. Seo, J. Hacker, and M. J. W. Rodwell, "InP HBT technologies for THz integrated circuits," *Proceedings of the IEEE*, vol. 105, no. 6, pp. 1051-1067, 2017, doi: 10.1109/JPROC.2017.2692178.
- [133] J. C. Rode, H. -W. Chiang, P. Choudhary, V. Jain, B. J. Thibeault, W. J. Mitchell, M. J. W. Rodwell, M. Urteaga, D. Loubychev, A. Snyder, Y. Wu, J. M. Fastenau, and A.

- W. K. Liu, "Indium phosphide heterobipolar transistor technology beyond 1-THz bandwidth," *IEEE Transactions on Electron Devices*, vol. 62, no. 9, pp. 2779-2785, 2015, doi: 10.1109/TED.2015.2455231.
- [134] M. Urteaga, R. Pierson, P. Rowell, V. Jain, E. Lobisser, and M. J. W. Rodwell, "130nm InP DHBTs with  $f_t > 0.52$  THz and  $f_{max} > 1.1$  THz," *69th Device Research Conference*, pp. 281-282, 2011, doi: 10.1109/DRC.2011.5994532.
- [135] W. R. Deal, "InP HEMT for sub-millimeter wave space applications: status and challenges," *39th International Conference on Infrared, Millimeter, and Terahertz waves (IRMMW-THz)*, pp. 1-3, 2014, doi: 10.1109/IRMMW-THz.2014.6956216.
- [136] D. -H. Kim, J. A. del Alamo, P. Chen, W. Ha, M. Urteaga, and B. Brar, "50-nm E-mode In<sub>0.7</sub>Ga<sub>0.3</sub>As PHEMTs on 100-nm InP substrate with  $f_{max} > 1$  THz," *International Electron Devices Meeting*, pp. 30.6.1-30.6.4, 2010, doi: 10.1109/IEDM.2010.5703453.
- [137] D. -H. Kim, B. Brar, and J. A. del Alamo, " $f_t = 688$  GHz and  $f_{max} = 800$  GHz in  $L_g = 40$  nm In<sub>0.7</sub>Ga<sub>0.3</sub>As MHEMTs with  $g_{m\_max} > 2.7$  mS/ $\mu$ m," *International Electron Devices Meeting*, pp. 13.6.1-13.6.4, 2011, doi: 10.1109/IEDM.2011.6131548.
- [138] A. M. Arabhavi, F. Ciabattini, S. Hamzeloui, R. Flückiger, T. Saranovac, D. Han, D. Marti, G. Bonomo, R. Chaudhary, O. Ostinelli, and C. R. Bolognesi, "InP/GaAsSb double heterojunction bipolar transistor emitter-fin technology with  $f_{MAX} = 1.2$  THz," *IEEE Transactions on Electron Devices*, vol. 69, no. 4, pp. 2122-2129, 2022, doi: 10.1109/TED.2021.3138379.
- [139] X. Mei, W. Yoshida, M. Lange, J. Lee, J. Zhou, P. Liu, K. Leong, A. Zamora, J. Padilla, S. Sarkozy, R. Lai, and W. R. Deal, "First demonstration of amplification at 1 THz using 25-nm InP high electron mobility transistor process," *IEEE Electron Device Letters*, vol. 36, no. 4, pp. 327-329, 2015, doi: 10.1109/LED.2015.2407193.
- [140] D. Kim and S. Jeon, "A 300-GHz high-power high-efficiency voltage-controlled oscillator with low power variation," *IEEE Microwave and Wireless Components Letters*, vol. 30, no. 5, pp. 496-499, 2020, doi: 10.1109/LMWC.2020.2986160.
- [141] P. Hillger, J. Grzyb, S. Malz, B. Heinemann, and U. Pfeiffer, "A lens-integrated 430 GHz SiGe HBT source with up to -6.3 dBm radiated power," *IEEE Radio Frequency Integrated Circuits Symposium (RFIC)*, pp. 160-163, 2017, doi: 10.1109/RFIC.2017.7969042.
- [142] W. Steyaert and P. Reynaert, "A 0.54 THz signal generator in 40 nm bulk CMOS with 22 GHz tuning Range and integrated planar antenna," *IEEE Journal of Solid-State Circuits*, vol. 49, no. 7, pp. 1617-1626, 2014, doi: 10.1109/JSSC.2014.2319251.

- [143] K. M. K. H. Leong, X. Mei, W. H. Yoshida, A. Zamora, J. G. Padilla, B. S. Gorospe, K. Nguyen, and W. R. Deal, "850 GHz receiver and transmitter front-ends using InP HEMT," *IEEE Transactions on Terahertz Science and Technology*, vol. 7, no. 4, pp. 466-475, 2017, doi: 10.1109/TTHZ.2017.2710632.
- [144] K. M. K. H. Leong, X. Mei, W. Yoshida, P. -H. Liu, Z. Zhou, M. Lange, L. -S. Lee, J. G. Padilla, A. Zamora, B. S. Gorospe, K. Nguyen, and W. R. Deal, "A 0.85 THz low noise amplifier using InP HEMT transistors," *IEEE Microwave and Wireless Components Letters*, vol. 25, no. 6, pp. 397-399, 2015, doi: 10.1109/LMWC.2015.2421336.
- [145] U. R. Pfeiffer, Y. Zhao, J. Grzyb, R. A. Hadi, N. Sarmah, W. Förster, H. Rucker, and B. Heinemann, "A 0.53THz reconfigurable source array with up to 1mW radiated power for terahertz imaging applications in 0.13 $\mu$ m SiGe BiCMOS," *IEEE International Solid-State Circuits Conference Digest of Technical Papers (ISSCC)*, pp. 256-257, 2014, doi: 10.1109/ISSCC.2014.6757424.
- [146] R. Han, C. Jiang, A. Mostajeran, M. Emadi, H. Aghasi, H. Sherry, A. Cathelin, and E. Afshari, "A SiGe terahertz heterodyne imaging transmitter with 3.3 mW radiated power and fully-integrated phase-locked loop," *IEEE Journal of Solid-State Circuits*, vol. 50, no. 12, pp. 2935-2947, 2015, doi: 10.1109/JSSC.2015.2471847.
- [147] S. P. Voinigescu, A. Tomkins, E. Dacquay, P. Chevalier, J. Hasch, A. Chantre, and B. Sautreuil, "A study of SiGe HBT signal sources in the 220 – 330-GHz Range," *IEEE Journal of Solid-State Circuits*, vol. 48, no. 9, pp. 2011-2021, 2013, doi: 10.1109/JSSC.2013.2265494.
- [148] J. Yun, D. Yoon, H. Kim, and J. -S. Rieh, "300-GHz InP HBT oscillators based on common-base cross-coupled topology," *IEEE Transactions on Microwave Theory and Techniques*, vol. 62, no. 12, pp. 3053-3064, 2014, doi: 10.1109/TMTT.2014.2364608.
- [149] B. Razavi, "A 300-GHz fundamental oscillator in 65-nm CMOS technology," *IEEE Journal of Solid-State Circuits*, vol. 46, no. 4, pp. 894-903, 2011, doi: 10.1109/JSSC.2011.2108122.
- [150] M. Seo, M. Urteaga, A. Young, V. Jain, Z. Griffith, J. Hacker, P. Rowell, R. Pierson, and M. Rodwell, ">300GHz fixed-frequency and voltage-controlled fundamental oscillators in an InP DHBT process," *IEEE MTT-S International Microwave Symposium*, pp. 272-275, 2010, doi: 10.1109/MWSYM.2010.5517660.
- [151] E. Öjefors, J. Grzyb, Y. Zhao, B. Heinemann, B. Tillack, and U. R. Pfeiffer, "A 820GHz SiGe chipset for terahertz active imaging applications," *IEEE International Solid-State Circuits Conference*, pp. 224-226, 2011, doi: 10.1109/ISSCC.2011.5746294.

- [152] Z. Hu, M. Kaynak, and R. Han, "High-power radiation at 1 THz in silicon: a fully scalable array using a multi-functional radiating mesh structure," *IEEE Journal of Solid-State Circuits*, vol. 53, no. 5, pp. 1313-1327, 2018, doi: 10.1109/JSSC.2017.2786682.
- [153] K. Sengupta and A. Hajimiri, "A 0.28 THz power-generation and beam-steering array in CMOS based on distributed active radiators," *IEEE Journal of Solid-State Circuits*, vol. 47, no. 12, pp. 3013-3031, 2012, doi: 10.1109/JSSC.2012.2217831.
- [154] A. Nikpaik, A. H. M. Shirazi, A. Nabavi, S. Mirabbasi, and S. Shekhar, "A 219-to-231 GHz frequency-multiplier-based VCO with  $\sim 3\%$  peak DC-to-RF efficiency in 65-nm CMOS," *IEEE Journal of Solid-State Circuits*, vol. 53, no. 2, pp. 389-403, 2018, doi: 10.1109/JSSC.2017.2759116.
- [155] H. Hamada, T. Fujimura, I. Abdo, K. Okada, H. -J. Song, H. Sugiyama, H. Matsuzaki, and H. Nosaka, "300-GHz. 100-Gb/s InP-HEMT wireless transceiver using a 300-GHz fundamental mixer," *IEEE/MTT-S International Microwave Symposium-IMS*, pp. 1480-1483, 2018, doi: 10.1109/MWSYM.2018.8439850.
- [156] F. Ahmed, M. Furqan, B. Heinemann, and A. Stelzer, "0.3-THz SiGe-based high-efficiency push-push VCOs with  $> 1$ -mW peak output power employing common-mode impedance enhancement," *IEEE Transactions on Microwave Theory and Techniques*, vol. 66, no. 3, pp. 1384-1398, 2018, doi: 10.1109/TMTT.2017.2767593.
- [157] A. H. M. Shirazi, A. Nikpaik, S. Mirabbasi, and S. Shekhar, "A quad-core-coupled triple-push 295-to-301 GHz source with 1.25 mW peak output power in 65nm CMOS using slow-wave effect," *IEEE Radio Frequency Integrated Circuits Symposium (RFIC)*, pp. 190-193, 2016, doi: 10.1109/RFIC.2016.7508283.
- [158] L. A. Samoska, "An overview of solid-state integrated circuit amplifiers in the submillimeter-wave and THz regime," *IEEE Transactions on Terahertz Science and Technology*, vol. 1, no. 1, pp. 9-24, 2011, doi: 10.1109/TTHZ.2011.2159558.
- [159] W. R. Deal, K. Leong, V. Radisic, S. Sarkozy, B. Gorospe, J. Lee, P. H. Liu, W. Yoshida, J. Zhou, M. Lange, R. Lai, and X. B. Mei, "Low noise amplification at 0.67 THz using 30 nm InP HEMTs," *IEEE Microwave and Wireless Components Letters*, vol. 21, no. 7, pp. 368-370, 2011, doi: 10.1109/LMWC.2011.2143701.
- [160] R. Han and E. Afshari, "A CMOS high-power broadband 260-GHz radiator array for spectroscopy," *IEEE Journal of Solid-State Circuits*, vol. 48, no. 12, pp. 3090-3104, 2013, doi: 10.1109/JSSC.2013.2272864.

- [161] K. Schmalz, R. Wang, J. Borngräber, W. Debski, W. Winkler, and C. Meliani, "245 GHz SiGe transmitter with integrated antenna and external PLL," *IEEE MTT-S International Microwave Symposium Digest*, pp. 1-3, 2013, doi: 10.1109/MWSYM.2013.6697430.
- [162] A. Van Der Ziel and E. R. Chenette, "Noise in solid state devices," *Advances in Electronics and Electron Physics*, vol. 46, pp. 313-383, 1978, doi: 10.1016/S0065-2539(08)60414-X.
- [163] D. Cimbri, J. Wang, A. Al-Khalidi, and E. Wasige, "Resonant tunnelling diode high-speed terahertz wireless communications - a review," *IEEE Transactions on Terahertz Science and Technology*, vol. 12, no. 3, pp. 226-244, 2022, doi: 10.1109/TTHZ.2022.3142965.
- [164] J. Wang, M. Naftaly, and E. Wasige, "An overview of terahertz imaging with resonant tunneling diodes," *Applied Sciences*, vol. 12, no. 8, pp. 3822, 2022, doi: 10.3390/app12083822.
- [165] S. M. Sze and K. K. Ng, "Physics of semiconductor devices," Wiley, 2006.
- [166] D. H. Hornbostel, "'5-10" Ghz YIG-tuned tunnel-diode oscillator," *Proceedings of the IEEE*, vol. 53, no. 11, pp. 1751-1751, 1965, doi: 10.1109/PROC.1965.4369.
- [167] D. Nelson and F. Sterzer, "Tunnel-diode microwave oscillators with milliwatt power outputs," *WESCON/60 Conference Record*, pp. 68-73, 1960, doi: 10.1109/WESCON.1960.1150474.
- [168] R. Izumi, S. Suzuki, and M. Asada, "1.98 THz resonant-tunneling-diode oscillator with reduced conduction loss by thick antenna electrode," *42nd International Conference on Infrared, Millimeter, and Terahertz Waves (IRMMW-THz)*, pp. 1-2, 2017, doi: 10.1109/IRMMW-THz.2017.8066877.
- [169] A. Al-Khalidi, K. H. Alharbi, J. Wang, R. Morariu, L. Wang, A. Khalid, J. M. L. Figueiredo, and E. Wasige, "Resonant tunneling diode terahertz sources with up to 1 mW output power in the J-Band," *IEEE Transactions on Terahertz Science and Technology*, vol. 10, no. 2, pp. 150-157, 2020, doi: 10.1109/TTHZ.2019.2959210.
- [170] L. Ozyuzer, A. E. Koshelev, C. Kurter, N. Gopalsami, Q. Li, M. Tachiki, K. Kadowaki, T. Yamamoto, H. Minami, H. Yamaguchi, T. Tachiki, K. E. Gray, W. -K. Kwok, and U. Welp, "Emission of coherent THz radiation from superconductors," *Science*, vol. 318, no. 5854, pp. 1291-1293, 2007, doi: 10.1126/science.1149802.
- [171] E. A. Borodianskyi and V. M. Krasnov, "Josephson emission with frequency span 1 – 11 THz from small Bi<sub>2</sub>Sr<sub>2</sub>CaCu<sub>2</sub>O<sub>8+δ</sub> mesa structures," *Nature Communications*, vol. 8, no. 1, pp. 1742, 2017, doi: 10.1038/s41467-017-01888-4.

- [172] U. Welp, K. Kadowaki, and R. Kleiner, "Superconducting emitters of THz radiation," *Nature Photonics*, vol. 7, no. 9, pp. 702-710, 2013, doi: 10.1038/nphoton.2013.216.
- [173] O. Schubert, M. Hohenleutner, F. Langer, B. Urbanek, C. Lange, U. Huttner, D. Golde, T. Meier, M. Kira, S. W. Koch, and R. Huber, "Sub-cycle control of terahertz high-harmonic generation by dynamical Bloch oscillations," *Nature Photonics*, vol. 8, no. 2, pp. 119-123, 2014, doi: 10.1038/nphoton.2013.349.
- [174] Y. M. Meziani, T. Otsuji, M. Hanabe, T. Ishibashi, T. Uno, and E. Sano, "Room temperature generation of terahertz radiation from a grating-bicoupled plasmon-resonant emitter: size effect," *Applied Physics Letters*, vol. 90, no. 6, pp. 061105, 2007, doi: 10.1063/1.2459879.
- [175] T. Otsuji, T. Komori, T. Watanabe, T. Suemitsu, D. Coquillat, and W. Knap, "Plasmon-resonant microchip emitters and detectors for terahertz sensing and spectroscopic applications," *Proceedings of the SPIE, Terahertz Physics, Devices, and Systems IV: Advanced Applications in Industry and Defense*, vol. 7671, Orlando, Florida, 2010, doi: 10.1117/12.850009.
- [176] T. Nagatsuma, S. Hisatake, M. Fujita, H. H. N. Pham, K. Tsuruda, S. Kuwano, and J. Terada, "Millimeter-wave and terahertz-wave applications enabled by photonics," *IEEE Journal of Quantum Electronics*, vol. 52, no. 1, pp. 1-12, 2016, doi: 10.1109/JQE.2015.2506992.
- [177] D. M. Mittleman, "Twenty years of terahertz imaging," *Optics Express*, vol. 26, no. 8, pp. 9417-9431, 2018, doi: 10.1364/OE.26.009417.
- [178] G. Valušis, A. Lisauskas, H. Yuan, W. Knap, and H. G. Roskos, "Roadmap of terahertz imaging 2021," *Sensors*, vol. 21, no. 12, pp. 4092, 2021, doi: 10.3390/s21124092.
- [179] R. Piesiewicz, C. Jansen, S. Wietzke, D. Mittleman, M. Koch, and T. Kürner, "Properties of building and plastic materials in the THz range," *International Journal of Infrared and Millimeter Waves*, vol. 28, no. 5, pp. 363-371, 2007, doi: 10.1007/s10762-007-9217-9.
- [180] M. Mikerov, R. Shrestha, P. van Dommelen, D. M. Mittleman, and M. Koch, "Analysis of ancient ceramics using terahertz imaging and photogrammetry," *Optics Express*, vol. 28, no. 15, pp. 22255-22263, 2020, doi: 10.1364/OE.399336.
- [181] T. Hattori, H. Kumon, and H. Tamazumi, "Terahertz spectroscopic characterization of paper," *35th International Conference on Infrared, Millimeter, and Terahertz Waves*, pp. 1-2, 2010, doi: 10.1109/ICIMW.2010.5612460.
- [182] Y. -S. Lee, "Principles of terahertz science and technology," *Springer*, 2009.

- [183] K. Krügener, S. Sommer, E. Stübling, R. Jachim, M. Koch, and W. Viöl, "THz properties of typical woods important for european forestry," *Journal of Infrared, Millimeter, and Terahertz Waves*, vol. 40, no. 7, pp. 770-774, 2019, doi: 10.1007/s10762-019-00601-4.
- [184] K. Krügener, E. -M. Stübling, R. Jachim, B. Kietz, M. Koch, and W. Viöl, "THz tomography for detecting damages on wood caused by insects," *Applied Optics*, vol. 58, no. 22, pp. 6063-6066, 2019, doi: 10.1364/AO.58.006063.
- [185] J. E. Bjarnason, T. L. J. Chan, A. W. M. Lee, M. A. Celis, and E. R. Brown, "Millimeter-wave, terahertz, and mid-infrared transmission through common clothing," *Applied Physics Letters*, vol. 85, no. 4, pp. 519-521, 2004, doi: 10.1063/1.1771814.
- [186] A. K. Azad, Y. Zhao, W. Zhang, and M. He, "Effect of dielectric properties of metals on terahertz transmission subwavelength hole arrays," *Optics Letters*, vol. 31, no. 17, pp. 2637-2639, 2006, doi: 10.1364/OL.31.002637.
- [187] T. Isogawa, T. Kumashiro, H. Song, K. Ajito, N. Kukutsu, K. Iwatsuki, and T. Nagatsuma, "Tomographic imaging using photonicly generated low-coherence terahertz noise sources," *IEEE Transactions on Terahertz Science and Technology*, vol. 2, no. 5, pp. 485-492, 2012, doi: 10.1109/TTHZ.2012.2208745.
- [188] W. L. Chan, J. Deibel, and D. M. Mittleman, "Imaging with terahertz radiation," *Reports on Progress in Physics*, vol. 70, no. 8, pp. 1325-1379, 2007, doi: 10.1088/0034-4885/70/8/r02.
- [189] M. Seo, J. -H. Kang, H. -S. Kim, J. H. Cho, J. Choi, Y. M. Jhon, S. Lee, J. H. Kim, T. Lee, Q-H. Park, and C. Kim , "Observation of terahertz-radiation-induced ionization in a single nano island," *Scientific Reports*, vol. 5, no. 1, pp. 10280, 2015, doi: 10.1038/srep10280.
- [190] C. M. Armstrong, "The truth about terahertz," *IEEE Spectrum*, vol. 49, no. 9, pp. 36-41, 2012, doi: 10.1109/MSPEC.2012.6281131.
- [191] B. B. Hu and M. C. Nuss, "Imaging with terahertz waves," *Optics Letters*, vol. 20, no. 16, pp. 1716-1718, 1995, doi: 10.1364/OL.20.001716.
- [192] J. -H. Son, S. J. Oh, and H. Cheon, "Potential clinical applications of terahertz radiation," *Journal of Applied Physics*, vol. 125, no. 19, pp. 190901, 2019, doi: 10.1063/1.5080205.
- [193] H. -B. Liu, H. Zhong, N. Karpowicz, Y. Chen, and X. -C. Zhang, "Terahertz spectroscopy and imaging for defense and security applications," *Proceedings of the IEEE*, vol. 95, no. 8, pp. 1514-1527, 2007, doi: 10.1109/JPROC.2007.898903.
- [194] L. Yu, L. Hao, T. Meiqiong, H. Jiaoqi, L. Wei, D. Jinying, C. Xueping, F. Weiling, and Z. Yang, "The medical application of terahertz technology in non-invasive detection of cells

and tissues: opportunities and challenges," *RSC Advances*, vol. 9, no. 17, pp. 9354-9363, 2019, doi: 10.1039/C8RA10605C.

- [195] Z. Vafapour, A. Keshavarz, and H. Ghahraloud, "The potential of terahertz sensing for cancer diagnosis," *Heliyon*, vol. 6, no. 12, pp. e05623, 2020, doi: 10.1016/j.heliyon.2020.e05623.
- [196] M. Danciu, T. Alexa-Stratulat, C. Stefanescu, G. Dodi, B. I. Tamba, C. T. Mihai, G. D. Stanciu, A. Luca, I. A. Spiridon, L. B. Ungureanu, V. Ianole, I. Ciortescu, C. Mihai, G. Stefanescu, I. Chirilă, R. Ciobanu, and V. L. Drug, "Terahertz spectroscopy and imaging: a cutting-edge method for diagnosing digestive cancers," *Materials*, vol. 12, no. 9, pp. 1519, 2019, doi: 10.3390/ma12091519.
- [197] J. P. Guillet, B. Recur, L. Frederique, B. Bousquet, L. Canioni, I. Manek-Hönniger, P. Desbarats, and P. Mounaix, "Review of Terahertz Tomography Techniques," *Journal of Infrared, Millimeter, and Terahertz Waves*, vol. 35, no. 4, pp. 382-411, 2014, doi: 10.1007/s10762-014-0057-0.
- [198] M. Borovkova, M. Khodzitsky, P. Demchenko, O. Cherkasova, A. Popov, and I. Meglinski, "Terahertz time-domain spectroscopy for non-invasive assessment of water content in biological samples," *Biomedical Optics Express*, vol. 9, no. 5, pp. 2266-2276, 2018, doi: 10.1364/BOE.9.002266.
- [199] S. J. Oh, Y. -M. Huh, S. -H. Kim, J. Yang, K. Jeong, Y. Park, C. Kang, J. -H. Son, and J. -S. Suh, "Terahertz pulse imaging of fresh brain tumor," *2011 International Conference on Infrared, Millimeter, and Terahertz Waves*, pp. 1-2, 2011, doi: 10.1109/irmmw-THz.2011.6105230.
- [200] R. Knipper, A. Brahm, E. Heinz, T. May, G. Notni, H. Meyer, A. Tünnermann, and J. Popp, "THz absorption in fabric and its impact on body scanning for security application," *IEEE Transactions on Terahertz Science and Technology*, vol. 5, no. 6, pp. 999-1004, 2015, doi: 10.1109/TTHZ.2015.2474115.
- [201] H. Quast and T. Löffler, "3D-terahertz-tomography for material inspection and security," *34th International Conference on Infrared, Millimeter, and Terahertz Waves*, pp. 1-2, 2009, doi: 10.1109/ICIMW.2009.5325639.
- [202] G. Tzydynzhapov, P. Gusikhin, V. Muravev, A. Dremin, Y. Nefyodov, and I. Kukushkin, "New real-time sub-terahertz security body scanner," *Journal of Infrared, Millimeter, and Terahertz Waves*, vol. 41, no. 6, pp. 632-641, 2020, doi: 10.1007/s10762-020-00683-5.

- [203] K. B. Cooper, R. J. Dengler, N. Llombart, B. Thomas, G. Chattopadhyay, and P. H. Siegel, "THz imaging radar for standoff personnel screening," *IEEE Transactions on Terahertz Science and Technology*, vol. 1, no. 1, pp. 169-182, 2011, doi: 10.1109/TTHZ.2011.2159556.
- [204] P. U. Jepsen, D. G. Cooke, and M. Koch, "Terahertz spectroscopy and imaging – modern techniques and applications," *Laser & Photonics Reviews*, vol. 5, no. 1, pp. 124-166, 2011, doi: 10.1002/lpor.201000011.
- [205] A. Oka and K. Tominaga, "Terahertz spectroscopy of polar solute molecules in non-polar solvents," *Journal of Non-Crystalline Solids*, vol. 352, no. 42-49, pp. 4606-4609, 2006, doi: 10.1016/j.jnoncrysol.2006.03.122.
- [206] H. Zhong, A. Redo-Sanchez, and X. -C. Zhang, "Identification and classification of chemicals using terahertz reflective spectroscopic focal-plane imaging system," *Optics Express*, vol. 14, no. 20, pp. 9130-9141, 2006, doi: 10.1364/OE.14.009130.
- [207] K. Ajito and Y. Ueno, "THz chemical imaging for biological applications," *IEEE Transactions on Terahertz Science and Technology*, vol. 1, no. 1, pp. 293-300, 2011, doi: 10.1109/TTHZ.2011.2159562.
- [208] M. Hangyo, M. Tani, and T. Nagashima, "Terahertz time-domain spectroscopy of solids: a review," *International Journal of Infrared and Millimeter Waves*, vol. 26, no. 12, pp. 1661-1690, 2005, doi: 10.1007/s10762-005-0288-1.
- [209] J. Neu and C. A. Schmuttenmaer, "Tutorial: an introduction to terahertz time domain spectroscopy (THz-TDS)," *Journal of Applied Physics*, vol. 124, no. 23, pp. 231101, 2018, doi: 10.1063/1.5047659.
- [210] J. -Y. Kim, H. -J. Song, M. Yaita, A. Hirata, and K. Ajito, "CW-THz vector spectroscopy and imaging system based on 1.55- $\mu$ m fiber-optics," *Optics Express*, vol. 22, no. 2, pp. 1735-1741, 2014, doi: 10.1364/OE.22.001735.
- [211] D. Stanze, A. Deninger, A. Roggenbuck, S. Schindler, M. Schlak, and B. Sartorius, "Compact cw terahertz spectrometer pumped at 1.5  $\mu$ m wavelength," *Journal of Infrared, Millimeter, and Terahertz Waves*, vol. 32, no. 2, pp. 225-232, 2011, doi: 10.1007/s10762-010-9751-8.
- [212] X. Yang, X. Zhao, K. Yang, Y. Liu, Y. Liu, W. Fu, and Y. Luo, "Biomedical applications of terahertz spectroscopy and imaging," *Trends in Biotechnology*, vol. 34, no. 10, pp. 810-824, 2016, doi: 10.1016/j.tibtech.2016.04.008.

- [213] A. R. Orlando and G. P. Gallerano, "Terahertz radiation effects and biological applications," *Journal of Infrared, Millimeter, and Terahertz Waves*, vol. 30, no. 12, pp. 1308-1318, 2009, doi: 10.1007/s10762-009-9561-z.
- [214] H. Cheon, H. -J. Yang, S. -H. Lee, Y. A. Kim, and J. -H. Son, "Terahertz molecular resonance of cancer DNA," *Scientific Reports*, vol. 6, no. 1, pp. 37103, 2016, doi: 10.1038/srep37103.
- [215] K. Ajito, "Terahertz spectroscopy for pharmaceutical and biomedical applications," *IEEE Transactions on Terahertz Science and Technology*, vol. 5, no. 6, pp. 1140-1145, 2015.
- [216] L. Ho, M. Pepper, and P. Taday, "Terahertz spectroscopy: signatures and fingerprints," *Nature Photonics*, vol. 2, no. 9, pp. 541-543, 2008, doi: 10.1038/nphoton.2008.174.
- [217] P. Bawuah, D. Markl, D. Farrell, M. Evans, A. Portieri, A. Anderson, D. Goodwin, R. Lucas, and J. A. Zeitler, "Terahertz-based porosity measurement of pharmaceutical tablets: a tutorial," *Journal of Infrared, Millimeter, and Terahertz Waves*, vol. 41, no. 4, pp. 450-469, 2020, doi: 10.1007/s10762-019-00659-0.
- [218] M. Naftaly, N. Vieweg, and A. Deninger, "Industrial applications of terahertz sensing: state of play," *Sensors*, vol. 19, no. 19, 2019, doi: 10.3390/s19194203.
- [219] S. Wietzke, C. Jansen, N. Krumbholz, O. Peters, N. Vieweg, C. Jördens, M. Scheller, D. Romeike, T. Jung, M. Reuter, S. Chatterjee, M. Koch, F. Physik, B. Baudrit, T. Zentgraf, T. Hochreinp, and M. Bastian, "Terahertz spectroscopy: a powerful tool for the characterization of plastic materials," *10th IEEE International Conference on Solid Dielectrics*, pp. 1-4, 2010, doi: 10.1109/ICSD.2010.5567915.
- [220] M. Karaliūnas, K. E. Nasser, A. Urbanowicz, I. Kašalynas, D. Bražinskienė, S. Asadauskas, and G. Valušis, "Non-destructive inspection of food and technical oils by terahertz spectroscopy," *Scientific Reports*, vol. 8, no. 1, pp. 18025, 2018, doi: 10.1038/s41598-018-36151-3.
- [221] L. Afsah-Hejri, P. Hajeb, P. Ara, and R. J. Ehsani, "A comprehensive review on food applications of terahertz spectroscopy and imaging," *Comprehensive Reviews in Food Science and Food Safety*, vol. 18, no. 5, pp. 1563-1621, 2019, doi: 10.1111/1541-4337.12490.
- [222] J. F. Federici, B. Schulkin, F. Huang, D. Gary, R. Barat, F. Oliveira, and D. Zimdars, "THz imaging and sensing for security applications-explosives, weapons and drugs," *Semiconductor Science and Technology*, vol. 20, no. 7, pp. S266-S280, 2005, doi: 10.1088/0268-1242/20/7/018.

- [223] C. Baker, T. Lo, W. R. Tribe, B. E. Cole, M. R. Hogbin, and M. C. Kemp, "Detection of concealed explosives at a distance using terahertz technology," *Proceedings of the IEEE*, vol. 95, no. 8, pp. 1559-1565, 2007, doi: 10.1109/JPROC.2007.900329.
- [224] D. L. Woolard, E. R. Brown, A. C. Samuels, J. O. Jensen, T. Globus, B. Gelmont, and M. Wolski, "Terahertz-frequency remote-sensing of biological warfare agents," *IEEE MTT-S International Microwave Symposium Digest*, vol. 2, pp. 763-766, 2003, doi: 10.1109/MWSYM.2003.1212483.
- [225] M. C. Kemp, P. F. Taday, B. E. Cole, J. A. Cluff, A. J. Fitzgerald, and W. R. Tribe, "Security applications of terahertz technology," *Proceedings of the SPIE, Terahertz for Military and Security Applications*, vol. 5070, Orlando, Florida, 2003, doi: 10.1117/12.500491.
- [226] C. Seco-Martorell, V. López-Domínguez, G. Arauz-Garofalo, A. Redo-Sanchez, J. Palacios, and J. Tejada, "Goya's artwork imaging with terahertz waves," *Optics Express*, vol. 21, no. 15, pp. 17800-17805, 2013, doi: 10.1364/OE.21.017800.
- [227] J. B. Jackson, J. Labaune, R. Bailleul-Lesuer, L. D'Alessandro, A. Whyte, J. W. Bowen, M. Menu, and G. Mourou, "Terahertz pulse imaging in archaeology," *Frontiers of Optoelectronics*, vol. 8, no. 1, pp. 81-92, 2015, doi: 10.1007/s12200-014-0446-y.
- [228] N. Kanda, K. Konishi, N. Nemoto, K. Midorikawa, and M. Kuwata-Gonokami, "Real-time broadband terahertz spectroscopic imaging by using a high-sensitivity terahertz camera," *Scientific Reports*, vol. 7, no. 1, pp. 42540, 2017, doi: 10.1038/srep42540.
- [229] M. Shafi, A. F. Molisch, P. J. Smith, T. Haustein, P. Zhu, P. De Silva, F. Tufvesson, A. Benjebbour, and G. Wunder, "5G: a tutorial overview of standards, trials, challenges, deployment, and practice," *IEEE Journal on Selected Areas in Communications*, vol. 35, no. 6, pp. 1201-1221, 2019, doi: 10.1109/JSAC.2017.2692307.
- [230] T. Kürner and S. Priebe, "Towards THz communications - status in research, standardization and regulation," *Journal of Infrared, Millimeter, and Terahertz Waves*, vol. 35, no. 1, pp. 53-62, 2014, doi: 10.1007/s10762-013-0014-3.
- [231] Z. Chen, X. Ma, B. Zhang, Y. Zhang, Z. Niu, N. Kuang, W. Chen, L. Li, and S. Li, "A survey on terahertz communications," *China Communications*, vol. 16, no. 2, pp. 1-35, 2019, doi: 10.12676/j.cc.2019.02.001.
- [232] A. Al-Fuqaha, M. Guizani, M. Mohammadi, M. Aledhari, and M. Ayyash, "Internet of things: a survey on enabling technologies, protocols, and applications," *IEEE Communications Surveys & Tutorials*, vol. 17, no. 4, pp. 2347-2376, 2015, doi: 10.1109/COMST.2015.2444095.

- [233] "Cisco annual internet report (2018-2023)," 2020.
- [234] F. Tariq, M. R. A. Khandaker, K.-K. Wong, M. A. Imran, M. Bennis, and M. Debbah, "A speculative study on 6G," *IEEE Wireless Communications*, vol. 27, no. 4, pp. 118-125, 2020, doi: 10.1109/MWC.001.1900488.
- [235] H. -J. Song and N. Lee, "Terahertz communications: challenges in the next decade," *IEEE Transactions on Terahertz Science and Technology*, vol. 12, no. 2, pp. 105-117, 2022, doi: 10.1109/TTHZ.2021.3128677.
- [236] S. Cherry, "Edholm's law of bandwidth," *IEEE Spectrum*, vol. 41, no. 7, pp. 58-60, 2004, doi: 10.1109/MSPEC.2004.1309810.
- [237] R. E. Miles, X. -C. Zhang, H. Eisele, and A. Krotkus, "Terahertz frequency detection and identification of materials and objects," *Springer*, 2007, doi: 10.1007/978-1-4020-6503-3.
- [238] T. Kürner, D. M. Mittleman, and T. Nagatsuma, "THz communications: paving the way towards wireless Tbps," *Springer*, 2022, doi: 10.1007/978-3-030-73738-2.
- [239] S. Dang, O. Amin, B. Shihada, and M. -S. Alouini, "What should 6G be?," *Nature Electronics*, vol. 3, no. 1, pp. 20-29, 2020, doi: 10.1038/s41928-019-0355-6.
- [240] P. Yang, Y. Xiao, M. Xiao, and S. Li, "6G wireless communications: vision and potential techniques," *IEEE Network*, vol. 33, no. 4, pp. 70-75, 2019, doi: 10.1109/MNET.2019.1800418.
- [241] M. Latva-aho and K. Leppänen, "Key drivers and research challenges for 6G ubiquitous wireless intelligence," *6G research visions*, 2019.
- [242] Y. Zhang, Z. Feng, H. Moustafa, F. Ye, U. Javaid, and C. Cui, "Guest editorial: edge intelligence for beyond 5G networks," *IEEE Wireless Communications*, vol. 28, no. 2, pp. 10-11, 2021, doi: 10.1109/MWC.2021.9430853.
- [243] Y. Li and G. L. Stüber, "Orthogonal frequency division multiplexing for wireless communications," *Springer*, 2006.
- [244] F. Rusek, D. Persson, B. K. Lau, E. G. Larsson, T. L. Marzetta, O. Edfors, and F. Tufvesson, "Scaling up MIMO: opportunities and challenges with very large arrays," *IEEE Signal Processing Magazine*, vol. 30, no. 1, pp. 40-60, 2013, doi: 10.1109/MSP.2011.2178495.
- [245] S. Yang and L. Hanzo, "Fifty years of MIMO detection: the road to large-scale MIMOs," *IEEE Communications Surveys & Tutorials*, vol. 17, no. 4, pp. 1941-1988, 2015, doi: 10.1109/COMST.2015.2475242.

- [246] T. Omiya, M. Yoshida, and M. Nakazawa, "400 Gbit/s 256 QAM-OFDM transmission over 720 km with a 14 bit/s/Hz spectral efficiency by using high-resolution FDE," *Optics Express*, vol. 21, no. 3, pp. 2632-2641, 2013, doi: 10.1364/OE.21.002632.
- [247] P. Smulders, "The road to 100 Gb/s wireless and beyond: basic issues and key directions," *IEEE Communications Magazine*, vol. 51, no. 12, pp. 86-91, 2013, doi: 10.1109/MCOM.2013.6685762.
- [248] "IEEE standard letter designations for radar-frequency bands," *IEEE Std 521-1984*, pp. 1-8, 1984, doi: 10.1109/IEEESTD.1984.81588.
- [249] T. Baykas, C. -S. Sum, Z. Lan, J. Wang, M. A. Rahman, H. Harada, and S. Kato, "IEEE 802.15.3c: the first IEEE wireless standard for data rates over 1 Gb/s," *IEEE Communications Magazine*, vol. 49, no. 7, pp. 114-121, 2011, doi: 10.1109/MCOM.2011.5936164.
- [250] T. S. Rappaport, J. N. Murdock, and F. Gutierrez, "State of the art in 60-GHz integrated circuits and systems for wireless communications," *Proceedings of the IEEE*, vol. 99, no. 8, pp. 1390-1436, 2011, doi: 10.1109/JPROC.2011.2143650.
- [251] "Fact sheet: spectrum frontiers rules identify, open up vast amounts of new high-band spectrum for next generation (5G) wireless broadband," *transition.fcc.gov*, 2019.
- [252] F. J. O'Hara, S. Ekin, W. Choi, and I. Song, "A perspective on terahertz next-generation wireless communications," *Technologies*, vol. 7, no. 2, 2019, doi: 10.3390/technologies7020043.
- [253] Y. Wang, J. Li, L. Huang, Y. Jing, A. Georgakopoulos, and P. Demestichas, "5G mobile: spectrum broadening to higher-frequency bands to support high data rates," *IEEE Vehicular Technology Magazine*, vol. 9, no. 3, pp. 39-46, 2014, doi: 10.1109/MVT.2014.2333694.
- [254] I. Hosako, N. Sekine, M. Patrashin, S. Saito, K. Fukunaga, Y. Kasai, P. Baron, T. Seta, J. Mendrok, S. Ochiai, and H. Yasuda, "At the dawn of a new era in terahertz technology," *Proceedings of the IEEE*, vol. 95, no. 8, pp. 1611-1623, 2007, doi: 10.1109/JPROC.2007.898844.
- [255] M. Hangyo, "Development and future prospects of terahertz technology," *Japanese Journal of Applied Physics*, vol. 54, no. 12, pp. 120101, 2015, doi: 10.7567/jjap.54.120101.
- [256] C. E. Shannon, "Communication in the presence of noise," *Proceedings of the IRE*, vol. 37, no. 1, pp. 10-21, 1949, doi: 10.1109/JRPROC.1949.232969.
- [257] J. Federici and L. Moeller, "Review of terahertz and subterahertz wireless communications," *Journal of Applied Physics*, vol. 107, no. 11, pp. 111101, 2010, doi: 10.1063/1.3386413.

- [258] T. Kleine-Ostmann and T. Nagatsuma, "A review on terahertz communications research," *Journal of Infrared, Millimeter, and Terahertz Waves*, vol. 32, no. 2, pp. 143-171, 2011, doi: 10.1007/s10762-010-9758-1.
- [259] G. Chattopadhyay, "Technology, capabilities, and performance of low power terahertz sources," *IEEE Transactions on Terahertz Science and Technology*, vol. 1, no. 1, pp. 33-53, 2011, doi: 10.1109/TTHZ.2011.2159561.
- [260] H. -J. Song and T. Nagatsuma, "Present and future of terahertz communications," *IEEE Transactions on Terahertz Science and Technology*, vol. 1, no. 1, pp. 256-263, 2011, doi: 10.1109/TTHZ.2011.2159552.
- [261] T. Nagatsuma and A. Kasamatsu, "Terahertz communications for space applications," *Asia-Pacific Microwave Conference (APMC)*, pp. 73-75, 2018, doi: 10.23919/APMC.2018.8617598.
- [262] T. Nagatsuma, "Antenna technologies for terahertz communications," *International Symposium on Antennas and Propagation (ISAP)*, pp. 1-2, 2018.
- [263] C. H. Chan, "THz antennas - design, fabrication and testing," *13th European Conference on Antennas and Propagation (EuCAP)*, pp. 1-4, 2019.
- [264] A. Hirata, T. Kosugi, H. Takahashi, J. Takeuchi, H. Togo, M. Yaita, N. Kukutsu, K. Aihara, K. Murata, Y. Sato, T. Nagatsuma, and Y. Kado, "120-GHz-band wireless link technologies for outdoor 10-Gbit/s data transmission," *IEEE Transactions on Microwave Theory and Techniques*, vol. 60, no. 3, pp. 881-895, doi: 10.1109/TMTT.2011.2178256.
- [265] I. F. Akyildiz, J. M. Jornet, and C. Han, "Terahertz band: next frontier for wireless communications," *Physical Communication*, vol. 12, pp. 16-32, 2014, doi: 10.1016/j.phycom.2014.01.006.
- [266] K. M. S. Huq, S. A. Busari, J. Rodriguez, V. Frascolla, W. Bazzi, and D. C. Sicker, "Terahertz-enabled wireless system for beyond-5G ultra-fast networks: a brief survey," *IEEE Network*, vol. 33, no. 4, pp. 89-95, 2019, doi: 10.1109/MNET.2019.1800430.
- [267] D. He, K. Guan, A. Fricke, B. Ai, R. He, Z. Zhong, A. Kasamatsu, I. Hosako, and T. Kürner, "Stochastic channel modeling for kiosk applications in the terahertz band," *IEEE Transactions on Terahertz Science and Technology*, vol. 7, no. 5, pp. 502-513, 2017, doi: 10.1109/TTHZ.2017.2720962.
- [268] A. Galal and X. Hesselbach, "Nano-networks communication architecture: modeling and functions," *Nano Communication Networks*, vol. 17, pp. 45-62, 2018, doi: 10.1016/j.nancom.2018.07.001.

- [269] A. Al-Khalidi, K. Alharbi, J. Wang, and E. Wasige, "THz electronics for data centre wireless links - the TERAPOD project," *9th International Congress on Ultra Modern Telecommunications and Control Systems and Workshops (ICUMT)*, pp. 445-448, 2017, doi: 10.1109/ICUMT.2017.8255202.
- [270] S. Mollahasani and E. Onur, "Evaluation of terahertz channel in data centers," *IEEE/IFIP Network Operations and Management Symposium (NOMS)*, pp. 727-730, 2016, doi: 10.1109/NOMS.2016.7502886.
- [271] S. Moghadami, F. Hajilou, P. Agrawal, and S. Ardalan, "A 210 GHz fully-integrated OOK transceiver for short-range wireless chip-to-chip communication in 40 nm CMOS technology," *IEEE Transactions on Terahertz Science and Technology*, vol. 5, no. 5, pp. 737-741, 2015, doi: 10.1109/TTHZ.2015.2459673.
- [272] V. Petrov, D. Moltchanov, M. Komar, A. Antonov, P. Kustarev, S. Rakheja, and Y. Koucheryavy, "Terahertz band intra-chip communications: can wireless links scale Modern x86 CPUs?," *IEEE Access*, vol. 5, pp. 6095-6109, 2017, doi: 10.1109/ACCESS.2017.2689077.
- [273] H. T. Friis, "A note on a simple transmission formula," *Proceedings of the IRE*, vol. 34, no. 5, pp. 254-256, 1946, doi: 10.1109/JRPROC.1946.234568.
- [274] S. Suzuki and M. Asada, "Room-temperature oscillation of resonant tunneling diodes close to 2 THz and their functions for various applications," *Journal of Infrared, Millimeter, and Terahertz Waves*, vol. 37, no. 12, pp. 1185-1198, 2016, doi: 10.1007/s10762-016-0321-6.
- [275] J. M. Chamberlain and R. E. Miles, "New directions in terahertz technology," *Springer*, 1997, doi: 10.1007/978-94-011-5760-5.
- [276] C. Corsi, and F. Sizov, "THz and security applications: detectors, sources and associated electronics for THz applications," *Springer*, 2014, doi: 10.1007/978-94-017-8828-1.
- [277] M. Shur, "Terahertz technology: devices and applications," *Proceedings of 35th European Solid-State Device Research Conference*, pp. 13-21, 2005, doi: 10.1109/ESSDER.2005.1546574.
- [278] K. -I. Maki, T. Shibuya, C. Otani, K. Suizu, and K. Kawase, "Terahertz beam steering via tilted-phase difference-frequency mixing," *Applied Physics Express*, vol. 2, no. 2, pp. 022301, 2009, doi: 10.1143/apex.2.022301.
- [279] Y. Monnai, V. Viereck, H. Hillmer, K. Altmann, C. Jansen, M. Koch, and H. Shinoda, "Terahertz beam steering using structured MEMS surfaces for networked wireless sensing," *Ninth International Conference on Networked Sensing (INSS)*, pp. 1-3, 2012, doi: 10.1109/INSS.2012.6240544.

- [280] X. Fu, F. Yang, C. Liu, X. Wu, and T. J. Cui, "Terahertz beam steering technologies: from phased arrays to field-programmable metasurfaces," *Advanced Optical Materials*, vol. 8, no. 3, pp. 1900628, 2020, doi: 10.1002/adom.201900628.
- [281] P. Hillger, M. van Delden, U. S. M. Thantrige, A. M. Ahmed, J. Wittemeier, K. Arzi, M. Andree, B. Sievert, W. Prost, A. Rennings, D. Erni, T. Musch, N. Weimann, A. Sezgin, N. Pohl, and U. R. Pfeiffer, "Toward Mobile Integrated Electronic Systems at THz Frequencies," *Journal of Infrared, Millimeter, and Terahertz Waves*, vol. 41, no. 7, pp. 846-869, 2020, doi: 10.1007/s10762-020-00699-x.
- [282] H. -J. Song, "Terahertz wireless communications: recent developments including a prototype system for short-range data downloading," *IEEE Microwave Magazine*, vol. 22, no. 5, pp. 88-99, 2021, doi: 10.1109/MMM.2021.3056935.
- [283] K. Sengupta, T. Nagatsuma, and D. M. Mittleman, "Terahertz integrated electronic and hybrid electronic-photonic systems," *Nature Electronics*, vol. 1, no. 12, pp. 622-635, 2018, doi: 10.1038/s41928-018-0173-2.
- [284] H. Hamada, T. Tsutsumi, G. Itami, H. Sugiyama, H. Matsuzaki, K. Okada, and H. Nosaka, "300-GHz 120-Gb/s wireless transceiver with high-output-power and high-gain power amplifier based on 80-nm InP-HEMT technology," *IEEE BiCMOS and Compound semiconductor Integrated Circuits and Technology Symposium (BCICTS)*, pp. 1-4, 2019, doi: 10.1109/BCICTS45179.2019.8972756.
- [285] P. Rodríguez-Vázquez, J. Grzyb, B. Heinemann, and U. R. Pfeiffer, "A 16-QAM 100-Gb/s 1-M wireless link with an EVM of 17% at 230 GHz in an SiGe technology," *IEEE Microwave and Wireless Components Letters*, vol. 29, no. 4, pp. 297-299, 2019, doi: 10.1109/LMWC.2019.2899487.
- [286] I. Kallfass, F. Boes, T. Messinger, J. Antes, A. Inam, U. Lewark, A. Tessmann, and R. Henneberger, "64 Gbit/s transmission over 850 m fixed wireless link at 240 GHz carrier frequency," *Journal of Infrared, Millimeter, and Terahertz Waves*, vol. 36, no. 2, pp. 221-233, 2015, doi: 10.1007/s10762-014-0140-6.
- [287] Y. Nishida, N. Nishigami, S. Diebold, J. Kim, M. Fujita, and T. Nagatsuma, "Terahertz coherent receiver using a single resonant tunnelling diode," *Scientific Reports*, vol. 9, no. 1, pp. 18125, 2019, doi: 10.1038/s41598-019-54627-8.
- [288] T. Nagatsuma, S. Horiguchi, Y. Minamikata, Y. Yoshimizu, S. Hisatake, S. Kuwano, N. Yoshimoto, J. Terada, and H. Takahashi, "Terahertz wireless communications based on photonics technologies," *Optics Express*, vol. 21, no. 20, pp. 23736-23747, 2013, doi: 10.1364/OE.21.023736.

- [289] J. Wang, A. Al-Khalidi, S. Ahearne, and E. Wasige, "22Gbps/80cm Low-Cost THz wireless system," *2021 51st European Microwave Conference (EuMC)*, pp. 209-212, 2022, doi: 10.23919/EuMC50147.2022.9784247.
- [290] T. Harter, S. Ummethala, M. Blaicher, S. Muehlbrandt, S. Wolf, M. Weber, M. M. H. Adib, J. N. Kemal, M. Merboldt, F. Boes, S. Nellen, A. Tessmann, M. Walther, B. Globisch, T. Zwick, W. Freude, S. Randel, and C. Koos, "Wireless THz link with optoelectronic transmitter and receiver," *Optica*, vol. 6, no. 8, pp. 1063-1070, 2019, doi: 10.1364/OP-TICA.6.001063.
- [291] V. K. Chinni, P. Latzel, M. Zègaoui, C. Coinon, X. Wallart, E. Peytavit, J. F. Lampin, K. Engenhardt, P. Szriftgiser, M. Zaknoune, and G. Ducournau, "Single-channel 100 Gbit/s transmission using III-V UTC-PDs for future IEEE 802.15.3d wireless links in the 300 GHz band," *Electronics Letters*, vol. 54, no. 10, pp. 638-640, 2018, doi: 10.1049/el.2018.0905.
- [292] S. Jia, X. Pang, O. Ozolins, X. Yu, H. Hu, J. Yu, P. Guan, F. Da Ros, S. Popov, G. Jacobsen, M. Galili, T. Morioka, D. Zibar, and L. K. Oxenløwe, "0.4 THz photonic-wireless link with 106 Gb/s single channel bitrate," *Journal of Lightwave Technology*, vol. 36, no. 2, pp. 610-615, 2018, doi: 10.1109/JLT.2017.2776320.
- [293] X. Yu, S. Jia, H. Hu, M. Galili, T. Morioka, P. U. Jepsen, and L. K. Oxenløwe, "160 Gbit/s photonics wireless transmission in the 300-500 GHz band," *APL Photonics*, vol. 1, no. 8, pp. 081301, 2016, doi: 10.1063/1.4960136.
- [294] O. Graydon, "Ultrafast wireless link," *Nature Photonics*, vol. 10, no. 11, pp. 691, 2016, doi: 10.1038/nphoton.2016.220.
- [295] X. Pang, S. Jia, O. Ozolins, X. Yu, H. Hu, L. Marcon, P. Guan, F. D. Ros, S. Popov, G. Jacobsen, M. Galili, T. Morioka, D. Zibar, and L. K. Oxenkwe, "260 Gbit/s photonic-wireless link in the THz band," *IEEE Photonics Conference (IPC)*, pp. 1-2, 2016, doi: 10.1109/IPCon.2016.7830951.
- [296] J. Yu, X. Li, J. Zhang, and J. Xiao, "432-Gb/s PDM-16QAM signal wireless delivery at W-band using optical and antenna polarization multiplexing," *The European Conference on Optical Communication (ECOC)*, pp. 1-3, 2014, doi: 10.1109/ECOC.2014.6963945.
- [297] R. Puerta, J. Yu, X. Li, Y. Xu, J. J. V. Olmos, and I. T. Monroy, "Demonstration of 352 Gbit/s photonic-enabled D-band wireless delivery in one 2x2 MIMO system," *Optical Fiber Communications Conference and Exhibition (OFC)*, pp. 1-3, 2017.

- [298] G. J. Schneider, J. A. Murakowski, C. A. Schuetz, S. Shi, and D. W. Prather, "Radiofrequency signal-generation system with over seven octaves of continuous tuning," *Nature Photonics*, vol. 7, no. 2, pp. 118-122, 2013, doi: 10.1038/nphoton.2012.339.
- [299] S. Lee, R. Dong, S. Hara, K. Takano, S. Amakawa, T. Yoshida, and M. Fujishima, "A 6-mW-DC-power 300-GHz CMOS receiver for near-field wireless communications," *IEEE MTT-S International Microwave Symposium (IMS)*, pp. 504-507, 2019, doi: 10.1109/MWSYM.2019.8700961.
- [300] P. Rodríguez-Vázquez, J. Grzyb, N. Sarmah, B. Heinemann, and U. R. Pfeiffer, "A 65 Gbps QPSK one meter wireless link operating at a 225-255 GHz tunable carrier in a SiGe HBT technology," *IEEE Radio and Wireless Symposium (RWS)*, pp. 146-149, 2018, doi: 10.1109/RWS.2018.8304970.
- [301] P. Rodríguez-Vázquez, J. Grzyb, N. Sarmah, B. Heinemann, and U. R. Pfeiffer, "Towards 100 Gbps: a fully electronic 90 Gbps one meter wireless link at 230 GHz," *48th European Microwave Conference (EuMC)*, pp. 1389-1392, 2018, doi: 10.23919/EuMC.2018.8541410.
- [302] K. Takano, K. Katayama, S. Amakawa, T. Yoshida, and M. Fujishima, "Wireless digital data transmission from a 300 GHz CMOS transmitter," *Electronics Letters*, vol. 52, no. 15, pp. 1353-1355, 2016, doi: 10.1049/el.2016.1148.
- [303] K. K. Tokgoz, S. Maki, J. Pang, N. Nagashima, I. Abdo, S. Kawai, T. Fujimura, Y. Kawano, T. Suzuki, T. Iwai, K. Okada, and A. Matsuzawa, "A 120Gb/s 16QAM CMOS millimeter-wave wireless transceiver," *IEEE International Solid-State Circuits Conference (ISSCC)*, pp. 168-170, 2018, doi: 10.1109/ISSCC.2018.8310237.
- [304] K. Takano, S. Amakawa, K. Katayama, S. Hara, R. Dong, A. Kasamatsu, I. Hosako, K. Mizuno, K. Takahashi, T. Yoshida, and M. Fujishima, "A 105Gb/s 300GHz CMOS transmitter," *IEEE International Solid-State Circuits Conference (ISSCC)*, pp. 308-309, 2017, doi: 10.1109/ISSCC.2017.7870384.
- [305] I. Kallfass, I. Dan, S. Rey, P. Harati, J. Antes, A. Tessmann, S. Wagner, M. Kuri, R. Weber, H. Massler, A. Leuther, T. Merkle, and T. Kürner, "Towards MMIC-based 300GHz indoor wireless communication systems," *IEICE Transactions on Electronics*, vol. E98.C, no. 12, pp. 1081-1090, 2015, doi: 10.1587/transele.E98.C.1081.
- [306] "802.15.3d-2017 - IEEE standard for high data rate wireless multi-media networks-amendment 2: 100 Gb/s wireless switched point-to-point physical layer," *IEEE Std 802.15.3d-2017 (Amendment to IEEE Std 802.15.3-2016 as amended by IEEE Std 802.15.3e-2017)*, pp. 1-55, 2017, doi: 10.1109/IEEESTD.2017.8066476.

- [307] T. Nagatsuma, K. Oogimoto, Y. Inubushi, and J. Hirokawa, "Practical considerations of terahertz communications for short distance applications," *Nano Communication Networks*, vol. 10, pp. 1-12, 2016, doi: 10.1016/j.nancom.2016.07.005.
- [308] J. Ma, R. Shrestha, L. Moeller, and D. M. Mittleman, "Channel performance for indoor and outdoor terahertz wireless links," *APL Photonics*, vol. 3, no. 5, pp. 051601, 2018, doi: 10.1063/1.5014037.
- [309] J. P. Sun, G. I. Haddad, P. Mazumder, and J. N. Schulman, "Resonant tunneling diodes: models and properties," *Proceedings of the IEEE*, vol. 86, no. 4, pp. 641-660, 1998, doi: 10.1109/5.663541.
- [310] D. J. Paul, "Nanoelectronics," in Encyclopedia of physical science and technology (Third Edition), pp. 285-301, *Academic Press*, 2003, doi: 10.1016/B0-12-227410-5/00469-5.
- [311] M. Feiginov, "Frequency limitations of resonant-tunnelling diodes in sub-THz and THz oscillators and detectors," *Journal of Infrared, Millimeter, and Terahertz Waves*, vol. 40, no. 4, pp. 365-394, 2019, doi: 10.1007/s10762-019-00573-5.
- [312] M. Asada, S. Suzuki, and T. Fukuma "Measurements of temperature characteristics and estimation of terahertz negative differential conductance in resonant-tunneling-diode oscillators," *AIP Advances*, vol. 7, no. 11, pp. 115226, 2017, doi: 10.1063/1.5007093.
- [313] H. Mizuta and T. Tanoue, "The Physics and applications of resonant tunnelling diodes," *Cambridge University Press*, 1995, doi: 10.1017/CBO9780511629013.
- [314] B. Ricco and M. Y. Azbel, "Physics of resonant tunneling. The one-dimensional double-barrier case," *Physical Review B*, vol. 29, no. 4, pp. 1970-1981, 1984, doi: 10.1103/PhysRevB.29.1970.
- [315] J. H. Davies, "The physics of low-dimensional semiconductors," *Cambridge University Press*, 1998, doi: 10.1017/CBO9780511819070.
- [316] D. Bohm, "Quantum theory," *Dover Publications Inc*, 1989.
- [317] L. Esaki, "Discovery of the tunnel diode," *IEEE Transactions on Electron Devices*, vol. 23, no. 7, pp. 644-647, 1976, doi: 10.1109/T-ED.1976.18466.
- [318] L. Esaki, "New phenomenon in narrow germanium  $p - n$  junctions," *Physical Review*, vol. 109, no. 2, pp. 603-604, 1958, doi: 10.1103/PhysRev.109.603.
- [319] E. R. Brown, "High-speed resonant-tunneling diodes," in Heterostructures and quantum devices, *VLSI Electronics Microstructure Science*, vol. 24, pp. 305-350, 1994, doi: 10.1016/B978-0-12-234124-3.50015-X.

- [320] L. L. Chang, E. E. Mendez, and C. Tejedor, "Resonant tunneling in semiconductors: physics and applications," *Springer*, 1991, doi: 10.1007/978-1-4615-3846-2.
- [321] M. Büttiker and R. Landauer, "Traversal time for tunneling," *Physical Review Letters*, vol. 49, no. 23, pp. 1739-1742, 1982, doi: 10.1103/PhysRevLett.49.1739.
- [322] R. Landauer and T. Martin, "Barrier interaction time in tunneling," *Reviews of Modern Physics*, vol. 66, no. 1, pp. 217-228, 1994, doi: 10.1103/RevModPhys.66.217.
- [323] T. C. L. G. Sollner, W. D. Goodhue, P. E. Tannenwald, C. D. Parker, and D. D. Peck, "Resonant tunneling through quantum wells at frequencies up to 2.5 THz," *Applied Physics Letters*, vol. 43, no. 6, pp. 588-590, 1983, doi: 10.1063/1.94434.
- [324] J. S. Scott, J. P. Kaminski, M. Wanke, S. J. Allen, D. H. Chow, M. Lui, and T. Y. Liu, "Terahertz frequency response of an  $\text{In}_{0.53}\text{Ga}_{0.47}\text{As}/\text{AlAs}$  resonant-tunneling diode," *Applied Physics Letters*, vol. 64, no. 15, pp. 1995-1997, 1994, doi: 10.1063/1.111717.
- [325] E. E. Mendez, W. I. Wang, B. Ricco, and L. Esaki, "Resonant tunneling of holes in  $\text{AlAs-GaAs-AlAs}$  heterostructures," *Applied Physics Letters*, vol. 47, no. 4, pp. 415-417, 1985, doi: 10.1063/1.96130.
- [326] T. Nakagawa, T. Fujita, Y. Matsumoto, T. Kojima, and K. Ohta, "Resonant tunneling of holes in  $\text{AlAs/GaAs}$  triple barrier diodes," *Applied Physics Letters*, vol. 50 no. 15, pp. 974-976, 1987, doi: 10.1063/1.98003.
- [327] H. C. Liu, D. Landheer, M. Buchanan, D. C. Houghton, M. D'Iorio, and S. Kechang, "Hole resonant tunneling in  $\text{Si/SiGe}$  heterostructures," *Superlattices and Microstructures*, vol. 5, no. 2, pp. 213-217, 1989, doi: 10.1016/0749-6036(89)90286-3.
- [328] R. D. L. Kronig, W. G. Penney, and R. H. Fowler, "Quantum mechanics of electrons in crystal lattices," *Proceedings of the Royal Society A: Mathematical, Physical and Engineering Sciences*, vol. 130, no. 814, pp. 499-513, 1931, doi: 10.1098/rspa.1931.0019.
- [329] S. Luryi, "Hot-electron injection and resonant-tunneling heterojunction devices," in Heterojunction band discontinuities: physics and device applications, *Elsevier Science*, pp. 489-564, 1987.
- [330] L. V. Iogansen, "The possibility of Resonance transmission of electrons in crystals through a system of barriers," *Journal of Experimental and Theoretical Physics*, vol. 18, no. 1, pp. 146-150, 1964.
- [331] L. V. Iogansen, "Resonance Tunneling of Electrons in Crystals," *Journal of Experimental and Theoretical Physics*, vol. 20, no. 1, pp. 180-185, 1965.

- [332] E. O. Kane, "Basic concepts of tunneling," in *Tunneling phenomena in solids*, Springer, pp. 1-11, 1969, doi: 10.1007/978-1-4684-1752-4\_1.
- [333] L. Esaki and R. Tsu, "Superlattice and negative differential conductivity in semiconductors," *IBM Journal of Research and Development*, vol. 14, no. 1, pp. 61-65, 1970, doi: 10.1147/rd.141.0061.
- [334] R. Tsu and L. Esaki, "Tunneling in a finite superlattice," *Applied Physics Letters*, vol. 22, no. 11, pp. 562-564, 1973, doi: 10.1063/1.1654509.
- [335] L. L. Chang, L. Esaki, and R. Tsu, "Resonant tunneling in semiconductor double barriers," *Applied Physics Letters*, vol. 24, no. 12, pp. 593-595, 1974, doi: 10.1063/1.1655067.
- [336] L. Esaki, "Long journey into tunneling," *Science*, vol. 183, no. 4130, pp. 1149-1155, 1974, doi: 10.1126/science.183.4130.1149.
- [337] L. Esaki and L. L. Chang, "New transport phenomenon in a semiconductor "superlattice"," *Physical Review Letters*, vol. 33, no. 8, pp. 495-498, 1974, doi: 10.1103/PhysRevLett.33.495.
- [338] T. H. H. Vuong, D. C. Tsui and W. T. Tsang, "Tunneling in  $\text{In}_{0.53}\text{Ga}_{0.47}\text{As}$ - $\text{InP}$  double-barrier structures," *Applied Physics Letters*, vol. 50, no. 4, pp. 212-214, 1987. doi: 10.1063/1.97664.
- [339] T. Inata, S. Muto, Y. Nakata, T. Fujii, H. Ohnishi, and S. Hiyamizu, "Excellent negative differential resistance of  $\text{InAlAs}/\text{InGaAs}$  resonant tunneling barrier structures grown by MBE," *Japan Journal of Applied Physics*, vol. 25, no. 12, part 2, pp. L983-L985, 1986, doi: 10.1143/jjap.25.1983.
- [340] H. C. Liu, D. Landheer, M. Buchanan, and D. C. Houghton, "Resonant tunneling in  $\text{Si}/\text{Si}_{1-x}\text{Ge}_x$  double-barrier structures," *Applied Physics Letters*, vol. 52, no. 21, pp. 1809-1811, 1988, doi: 10.1063/1.99632.
- [341] M. Tsuchiya, H. Sakaki, and J. Yoshino, "Room temperature observation of differential negative resistance in an  $\text{AlAs}/\text{GaAs}/\text{AlAs}$  resonant tunneling diode," *Japanese Journal of Applied Physics*, vol. 24, part 2, no. 6, pp. L466-L468, 1985, doi: 10.1143/jjap.24.1466.
- [342] F. Capasso, K. Mohammed, and A. Y. Cho, "Sequential resonant tunneling through a multiquantum well superlattice," *Applied Physics Letters*, vol. 48, no. 7, pp. 478-480, 1986, doi: 10.1063/1.97007.
- [343] K. K. Choi, B. F. Levine, R. J. Malik, J. Walker, and C. G. Bethea, "Periodic negative conductance by sequential resonant tunneling through an expanding high-field superlattice

- domain," *Physical Review B*, vol. 35, no. 8, pp. 4172-4175, 1987, doi: 10.1103/PhysRevB.35.4172.
- [344] A. Sibille, J. F. Palmier, H. Wang, and F. Mollot, "Observation of Esaki-Tsu negative differential velocity in GaAs/AlAs superlattices," *Physical Review Letters*, vol. 64, no. 1, pp. 52-55, 1990, doi: 10.1103/PhysRevLett.64.52.
- [345] M. Henini, "Molecular beam epitaxy: from research to mass production," *Elsevier Science*, 2013, doi: 10.1016/C2010-0-68986-3.
- [346] S. J. C. Irvine and P. Capper, "Metalorganic vapor phase epitaxy (MOVPE): growth, materials properties, and applications," *Wiley*, 2019, doi: 10.1002/9781119313021.
- [347] S. Kasap and P. Capper, "Springer handbook of electronic and photonic materials," *Springer*, 2007, doi: 10.1007/978-3-319-48933-9.
- [348] F. Capasso and R. A. Kiehl, "Resonant tunneling transistor with quantum well base and high-energy injection: a new negative differential resistance device," *Journal of Applied Physics*, vol. 58, no. 3, pp. 1366-1368, 1985, doi: 10.1063/1.336109.
- [349] F. Capasso, S. Sen, A. C. Gossard, A. L. Hutchinson, and J. H. English, "Quantum-well resonant tunneling bipolar transistor operating at room temperature," *IEEE Electron Device Letters*, vol. 7, no. 10, pp. 573-576, 1986, doi: 10.1109/EDL.1986.26478.
- [350] N. Yokoyama, K. Imamura, S. Muto, S. Hiyamizu, and H. Nishi, "A new functional, resonant-tunneling hot electron transistor (RHET)," *Japanese Journal of Applied Physics*, vol. 24, part 2, no. 11, pp. L853-L854, 1985, doi: 10.1143/jjap.24.l853.
- [351] C. I. Huang, M. J. Paulus, C. A. Bozada, S. C. Dudley, K. R. Evans, C. E. Stutz, R. L. Jones, and M. E. Cheney, "AlGaAs/GaAs double barrier diodes with high peak-to-valley current ratio," *Applied Physics Letters*, vol. 51, no. 2, pp. 121-123, 1987, doi: 10.1063/1.98588.
- [352] T. Inata, S. Muto, Y. Nakata, S. Sasa, T. Fujii, and S. Hiyamizu, "A pseudomorphic  $\text{In}_{0.53}\text{Ga}_{0.47}\text{As}/\text{AlAs}$  resonant tunneling barrier with a peak-to-valley current ratio of 14 at room temperature," *Japanese Journal of Applied Physics*, vol. 26, part 2, no. 8, pp. L1332-L1334, 1987, doi: 10.1143/jjap.26.l1332.
- [353] T. Nakagawa, H. Imamoto, T. Kojima, and K. Ohta, "Observation of resonant tunneling in AlGaAs/GaAs triple barrier diodes," *Applied Physics Letters*, vol. 49, no. 2, pp. 73-75, 1986, doi: 10.1063/1.97356.

- [354] G. Bastard and J. Brum, "Electronic states in semiconductor heterostructures," *IEEE Journal of Quantum Electronics*, vol. 22, no. 9, pp. 1625-1644, 1986, doi: 10.1109/JQE.1986.1073186.
- [355] C. Kittel, "Introduction to solid state physics," *Wiley*, 2004.
- [356] R. M. Martin, "Electronic structure: basic theory and practical methods," *Cambridge University Press*, 2008, doi: 10.1017/CBO9780511805769.
- [357] D. J. Griffiths, "Introduction to quantum mechanics," *Pearson Prentice Hall*, 2005.
- [358] O. Manasreh, "Semiconductor heterojunctions and nanostructures," *McGraw Hill*, 2005.
- [359] G. Ghione, "Semiconductor devices for high-speed optoelectronics," *Cambridge University Press*, 2009, doi: 10.1017/CBO9780511635595.
- [360] N. W. Ashcroft and N. D. Mermin, "Solid state physics," *Brooks/Cole*, 1976.
- [361] J. N. Schulman, H. J. De Los Santos, and D. H. Chow, "Physics-based RTD current-voltage equation," *IEEE Electron Device Letters*, vol. 17, no. 5, pp. 220-222, 1996, doi: 10.1109/55.491835.
- [362] P. J. Price, "Theory of resonant tunneling in heterostructures," *Physical Review B*, vol. 38, no. 3, pp. 1994-1998, 1988, doi: 10.1103/PhysRevB.38.1994.
- [363] S. Luryi, "Coherent versus incoherent resonant tunneling and implications for fast devices," *Superlattices and Microstructures*, vol. 5, no. 3, pp. 375-382, 1989, doi: 10.1016/0749-6036(89)90320-0.
- [364] E. R. Brown, W. D. Goodhue, and T. C. L. G. Sollner, "Fundamental oscillations up to 200 GHz in resonant tunneling diodes and new estimates of their maximum oscillation frequency from stationary-state tunneling theory," *Journal of Applied Physics*, vol. 64, no. 3, pp. 1519-1529, 1988, doi: 10.1063/1.341827.
- [365] K. Furuya, N. Machida, and Y. -C. Kang, "Analysis of phase breaking effect in resonant tunneling diodes using correlation function," *Japanese Journal of Applied Physics*, vol. 33, no. 5R, pp. 2511-2512, 1994, doi: 10.1143/JJAP.33.2511.
- [366] D. D. Coon and H. C. Liu, "Frequency limit of double barrier resonant tunneling oscillators," *Applied Physics Letters*, vol. 49, no. 2, pp. 94-96, 1986, doi: 10.1063/1.97362.
- [367] H. Morkoç, J. Chen, U. K. Reddy, T. Henderson, and S. Luryi, "Observation of a negative differential resistance due to tunneling through a single barrier into a quantum well," *Applied Physics Letters*, vol. 49, no. 2, pp. 70-72, 1986, doi: 10.1063/1.97355.

- [368] M. Jonson and A. Grincwajg, "Effect of inelastic scattering on resonant and sequential tunneling in double barrier heterostructures," *Applied Physics Letters*, vol. 51, no. 21, pp. 1729-1731, 1987, doi: 10.1063/1.98995.
- [369] T. Weil and B. Vinter, "Equivalence between resonant tunneling and sequential tunneling in double-barrier diodes," *Applied Physics Letters*, vol. 50, no. 18, pp. 1281-1283, 1987, doi: 10.1063/1.97884.
- [370] J. Bude, "Scattering mechanisms for semiconductor transport calculations," in Monte Carlo device simulation: full band and beyond, *Springer*, pp. 27-66, 1991, doi: 10.1007/978-1-4615-4026-7\_2.
- [371] W. R. Frensley, "Quantum transport modeling of resonant-tunneling devices," *Solid-State Electronics*, vol. 31, no. 3-4, pp. 739-742, 1988, doi: 10.1016/0038-1101(88)90378-4.
- [372] D. K. Ferry and H. L. Grubin, "Modeling of quantum transport in semiconductor devices," *Solid State Physics*, vol. 49, no. 3-4, pp. 283-448, 1996, doi: 10.1016/S0081-1947(08)60300-8.
- [373] E. Pop, "Energy dissipation and transport in nanoscale devices," *Nano Research*, vol. 3, no. 3, pp. 147-169, 2010, doi: 10.1007/s12274-010-1019-z.
- [374] T. Dittrich, P. Hänggi, G. -L. Ingold, B. Kramer, G. Schön, and W. Zwerger, "Quantum transport and dissipation," *Wiley-VCH*, 1998.
- [375] S. L. Chuang, "Physics of optoelectronic devices," *Wiley*, 1995.
- [376] D. W. Verzi, "Approximating with the Liouville-Green," *Journal of Interdisciplinary Mathematics*, vol. 8, no. 3, pp. 399-418, 2005, doi: 10.1080/09720502.2005.10700417.
- [377] D. R. Celino, A. M. de Souza, C. L. Machado Pereira Plazas, R. Ragi, and M. A. Romero, "A physics based RTD model accounting for space charge and phonon scattering effects," *Journal of Integrated Circuits and Systems*, vol. 17, no. 1, pp. 399-418, 2022, doi: 10.29292/jics.v17i1.545.
- [378] S. L. Yadav and H. Najeeb-ud-din, "A simple analytical model for the resonant tunneling diode based on the transmission peak and scattering effect," *Journal of Computational Electronics*, vol. 19, no. 3, pp. 1061-1067, 2020, doi: 10.1007/s10825-020-01531-4.
- [379] D. R. Celino, R. Ragi, and M. A. Romero, "Analytical physics-based compact current-voltage model for 2D-2D resonant tunneling diodes," *IEEE Transactions on Nanotechnology*, vol. 21, pp. 752-762, 2022, doi: 10.1109/TNANO.2022.3223019.

- [380] H. Ohnishi, T. Inata, S. Muto, N. Yokoyama, and A. Shibatomi, "Self-consistent analysis of resonant tunneling current," *Applied Physics Letters*, vol. 49, no. 19, pp. 1248-1250, 1986, doi: 10.1063/1.97428.
- [381] N. C. Klusdahl, A. M. Kriman, D. K. Ferry, and C. Ringhofer, "Self-consistent study of the resonant-tunneling diode," *Physical Review B*, vol. 39, no. 11, pp. 7720-7735, 1989, doi: 10.1103/PhysRevB.39.7720.
- [382] J. S. Wu, C. Y. Chang, C. P. Lee, K. H. Chang, D. G. Liu, and D. C. Liou, "Resonant tunneling of electrons from quantized levels in the accumulation layer of double-barrier heterostructures," *Applied Physics Letters*, vol. 57, no. 22, pp. 2311-2312, 1990, doi: 10.1063/1.103879.
- [383] I. -H. Tan, G. L. Snider, L. D. Chang, and E. L. Hu, "A self-consistent solution of Schrödinger–Poisson equations using a nonuniform mesh," *Journal of Applied Physics*, vol. 68, no. 8, pp. 4071-4076, 1990, doi: 10.1063/1.346245.
- [384] A. M. Cruz Serra and H. Abreu Santos, "A one-dimensional, self-consistent numerical solution of Schrödinger and Poisson equations," *Journal of Applied Physics*, vol. 70, no. 5, pp. 2734-2738, 1990, doi: 10.1063/1.349389.
- [385] L. R. Ram-Mohan, K. H. Yoo, and J. Moussa "The Schrödinger–Poisson self-consistency in layered quantum semiconductor structures," *Journal of Applied Physics*, vol. 95, no. 6, pp. 3081-3092, 2004, doi: 10.1063/1.1649458.
- [386] M. Koshiba, "Optical waveguide theory by the finite element method," *Springer*, 1992.
- [387] W. R. Frensley "Boundary conditions for open quantum systems driven far from equilibrium," *Reviews of Modern Physics*, vol. 62, no. 3, pp. 745-791, 1990, doi: 10.1103/RevModPhys.62.745.
- [388] A. Arnold "Mathematical concepts of open quantum boundary conditions," *Transport Theory and Statistical Physics*, vol. 30, no. 4-6, pp. 561-584, 2001, doi: 10.1081/TT-100105939.
- [389] M. Patriarca "Boundary conditions for the Schrödinger equation in the numerical simulation of quantum systems," *Physical Review E*, vol. 50, no. 2, pp. 1616-1622, 1994, doi: 10.1103/PhysRevE.50.1616.
- [390] J. Wang, A. Al-Khalidi, L. Wang, R. Morariu, A. Ofiare, and E. Wasige, "15-Gb/s 50-cm wireless link using a high-power compact III-V 84-GHz transmitter," *IEEE Transactions on Microwave Theory and Techniques*, vol. 66, no. 11, pp. 4698-4705, 2018, doi: 10.1109/TMTT.2018.2859983.

- [391] S. Diebold, S. Nakai, K. Nishio, J. Kim, K. Tsuruda, T. Mukai, M. Fujita, and T. Nagatsuma, "Modeling and simulation of terahertz resonant tunneling diode-based circuits," *IEEE Transactions on Terahertz Science and Technology*, vol. 6, no. 5, pp. 716-723, 2016, doi: 10.1109/TTHZ.2016.2592180.
- [392] C. E. Chang, P. M. Asbeck, K. -C. Wang, and E. R. Brown, "Analysis of heterojunction bipolar transistor/resonant tunneling diode logic for low-power and high-speed digital applications," *IEEE Transactions on Electron Devices*, vol. 40, no. 4, pp. 685-691, 1993, doi: 10.1109/16.202778.
- [393] E. R. Brown, O. B. McMahon, L. J. Mahoney, and K. M. Molvar, "SPICE model of the resonant-tunnelling diode," *Electronics Letters*, vol. 32, no. 10, pp. 938-940, 1996, doi: 10.1049/el:19960576.
- [394] G. Ternent and D. J. Paul, "SPICE modeling of the scaling of resonant tunneling diodes and the effects of sidewall leakage," *IEEE Transactions on Electron Devices*, vol. 59, no. 12, pp. 3555-3560, 2012, doi: 10.1109/TED.2012.2219867.
- [395] R. Morariu, "Accurate characterisation of Resonant Tunnelling Diodes for high-frequency applications," PhD thesis, University of Glasgow, 2021, doi: 10.5525/gla.thesis.81966.
- [396] L. Wang, "Reliable design of tunnel diode and resonant tunnelling diode based microwave sources," PhD thesis, University of Glasgow, 2012.
- [397] "R. Lake and S. Datta, "Nonequilibrium Green's-function method applied to double-barrier resonant-tunneling diodes," *Physical Review B*, vol. 45, no. 12, pp. 6670-6685, 1992, doi: 10.1103/PhysRevB.45.6670.
- [398] Q. Liu, A. Seabaugh, P. Chahal, and F. J. Morris, "Unified AC model for the resonant tunneling diode," *IEEE Transactions on Electron Devices*, vol. 51, no. 5, pp. 653-657, 2004, doi: 10.1109/TED.2004.825795.
- [399] R. Lake and J. Yang, "A physics based model for the RTD quantum capacitance," *IEEE Transactions on Electron Devices*, vol. 50, no. 3, pp. 785-789, 2003, doi: 10.1109/TED.2003.811390.
- [400] S. Luryi, "Quantum capacitance devices," *Applied Physics Letters*, vol. 52, no. 6, pp. 501-503, 1988, doi: 10.1063/1.99649.
- [401] E. R. Brown, C. D. Parker, and T. C. L. G. Sollner, "Effect of quasibound-state lifetime on the oscillation power of resonant tunneling diodes," *Applied Physics Letters*, vol. 54, no. 10, pp. 934-936, 1989, doi: 10.1063/1.100812.

- [402] J. M. Gering, D. A. Crim, D. G. Morgan, P. D. Coleman, W. Kopp, and H. Morkoç, "A small-signal equivalent-circuit model for GaAs-Al<sub>x</sub>Ga<sub>1-x</sub>As resonant tunneling heterostructures at microwave frequencies," *Journal of Applied Physics*, vol. 61, no. 1, pp. 271-276, 1987, doi: 10.1063/1.338872.
- [403] Y. Hu and S. P. Stapleton, "Capacitance of a resonant tunneling diode," *Japanese Journal of Applied Physics*, vol. 31, no. 1, part 1, pp. 23-25, 1992, doi: 10.1143/JJAP.31.23.
- [404] T. Wei, S. Stapleton, and E. Berolo, "Equivalent circuit and capacitance of double barrier resonant tunneling diode," *Journal of Applied Physics*, vol. 73, no. 2, pp. 829-834, 1993, doi: 10.1063/1.353345.
- [405] N. Shimizu, T. Waho, and T. Ishibashi, "Capacitance anomaly in the negative differential resistance region of resonant tunneling diodes," *Japanese Journal of Applied Physics*, vol. 36, no. 3B, part 2, pp. L330-L333, 1997, doi: 10.1143/JJAP.36.L330.
- [406] M. Long, H. Y. -Long, Z. Yang, W. Liang-Chen, Y. Fu-Hua, and Z. Yi-Ping, "A small signal equivalent circuit model for resonant tunnelling diode," *Chinese Physics Letters*, vol. 23, no. 8, pp. 2292-2295, 2006, doi: 10.1088/0256-307x/23/8/090.
- [407] T. P. E. Broekaert, B. Brar, J. P. A. van der Wagt, A. C. Seabaugh, F. J. Morris, T. S. Moise, E. A. Beam, and G. A. Frazier, "A monolithic 4-bit 2-Gsps resonant tunneling analog-to-digital converter," *IEEE Journal of Solid-State Circuits*, vol. 33, no. 9, pp. 1342-1349, 1998, doi: 10.1109/4.711333.
- [408] C. P. Allford and P. D. Buckle, "Strain compensated InGaAs/AlAs triple barrier resonant tunneling structures for THz applications," *IEEE Transactions on Terahertz Science and Technology*, vol. 7, no. 6, pp. 772-779, 2017, doi: 10.1109/TTHZ.2017.2758266.
- [409] P. Zhao, H. L. Cui, D. L. Woolard, K. L. Jensen, and F. A. Buot, "Equivalent circuit parameters of resonant tunneling diodes extracted from self-consistent Wigner-Poisson simulation," *IEEE Transactions on Electron Devices*, vol. 48, no. 4, pp. 614-627, 2001, doi: 10.1109/16.915658.
- [410] T. Wei, S. Stapleton, and O. Berolo, "Scattering parameter measurements of resonant tunneling diodes up to 40 GHz," *IEEE Transactions on Electron Devices*, vol. 42, no. 7, pp. 1378-1380, 1995, doi: 10.1109/16.391225.
- [411] R. Morariu, J. Wang, A. C. Cornescu, A. Al-Khalidi, A. Ofiare, J. M. L. Figueiredo, and E. Wasige, "Accurate small-signal equivalent circuit modeling of resonant tunneling diodes to 110 GHz," *IEEE Transactions on Microwave Theory and Techniques*, vol. 67, no. 11, pp. 4332-4340, 2019, doi: 10.1109/TMTT.2019.2939321.

- [412] S. Clochiatti, R. Schmidt, E. Mutlu, M. Dieudonne, W. Prost, D. Schreurs, and N. Weimann, "On-wafer characterization and modelling of InP resonant tunnelling diodes up to 500 GHz," *2022 52nd European Microwave Conference (EuMC)*, Milan, 27-29th September 2022, doi: 10.23919/EuMC54642.2022.9924370.
- [413] C. Kidner, I. Mehdi, J. R. East, and G. I. Haddad, "Bias circuit instabilities and their effect on the d.c. current-voltage characteristics of double-barrier resonant tunneling diodes," *Solid-State Electronics*, vol. 34, no. 2, pp. 149-156, 1991, doi: 10.1016/0038-1101(91)90081-9.
- [414] L. Wang, J. M. L. Figueiredo, C. N. Ironside, and E. Wasige, "DC characterization of tunnel diodes under stable non-oscillatory circuit conditions," *IEEE Transactions on Electron Devices*, vol. 58, no. 2, pp. 343-347, 2011, doi: 10.1109/TED.2010.2091507.
- [415] J. F. Young, B. M. Wood, H. C. Liu, M. Buchanan, D. Landheer, A. J. SpringThorpe, and P. Mandeville, "Effect of circuit oscillations on the dc current-voltage characteristics of double barrier resonant tunneling structures," *Applied Physics Letters*, vol. 52, no. 17, pp. 1398-1400, 1988, doi: 10.1063/1.99127.
- [416] M. Asada, S. Suzuki, and N. Kishimoto, "Resonant tunneling diodes for sub-terahertz and terahertz oscillators," *Japanese Journal of Applied Physics*, vol. 47, no. 6R, pp. 4375-4384, 2008, doi: 10.1143/jjap.47.4375.
- [417] H. Kanaya, T. Maekawa, S. Suzuki, and M. Asada, "Structure dependence of oscillation characteristics of resonant-tunneling-diode terahertz oscillators associated with intrinsic and extrinsic delay times," *Japanese Journal of Applied Physics*, vol. 54, no. 9, pp. 094103, 2015, doi: 10.7567/jjap.54.094103.
- [418] M. N. Feiginov, "Does the quasibound-state lifetime restrict the high-frequency operation of resonant-tunnelling diodes?," *Nanotechnology*, vol. 11, no. 4, pp. 359-364, 2000, doi: 10.1088/0957-4484/11/4/333.
- [419] M. N. Feiginov, "Effect of the Coulomb interaction on the response time and impedance of the resonant-tunneling diodes," *Applied Physics Letters*, vol. 76, no. 20, pp. 2904-2906, 2000, doi: 10.1063/1.126512.
- [420] M. N. Feiginov and D. R. Chowdhury, "Operation of resonant-tunneling diodes beyond resonant-state-lifetime limit," *Applied Physics Letters*, vol. 91, no. 20, pp. 203501, 2007, doi: 10.1063/1.2806922.
- [421] M. N. Feiginov, "Displacement currents and the real part of high-frequency conductance of the resonant-tunneling diode," *Applied Physics Letters*, vol. 78, no. 21, pp. 3301-3303, 2001, doi: 10.1063/1.1372357.

- [422] M. Feiginov, C. Sydlo, O. Cojocari, and P. Meissner, "Resonant-tunneling-diode oscillators operating at frequencies above 1.1 THz," *Applied Physics Letters*, vol. 99, no. 23, pp. 233506, 2011, doi: 10.1063/1.3667191.
- [423] M. Feiginov, C. Sydlo, O. Cojocari, and P. Meissner, "Operation of resonant-tunnelling oscillators beyond tunnel lifetime limit," *Europhysics Letters*, vol. 4, no. 94, pp. 48007, 2011, doi: 10.1209/0295-5075/94/48007.
- [424] M. Feiginov, C. Sydlo, O. Cojocari, and P. Meissner, "Operation of resonant-tunnelling diode oscillators beyond tunnel-lifetime limit at 564 GHz," *Europhysics Letters*, vol. 5, no. 97, pp. 58006, 2012, doi: 10.1209/0295-5075/97/58006.
- [425] M. Feiginov, H. Kanaya, S. Suzuki, and M. Asada, "Operation of resonant-tunneling diodes with strong back injection from the collector at frequencies up to 1.46 THz," *Applied Physics Letters*, vol. 104, no. 24, pp. 243509, 2014, doi: 10.1063/1.4884602.
- [426] J. P. Mattia, A. L. McWhorter, R. J. Aggarwal, F. Rana, E. R. Brown, and P. Maki, "Comparison of a rate-equation model with experiment for the resonant tunneling diode in the scattering-dominated regime," *Journal of Applied Physics*, vol. 84, no. 2, pp. 1140-1148, 1998, doi: 10.1063/1.368115.
- [427] H. P. Joosten, H. J. M. F. Noteborn, K. Kaski, and D. Lenstra, "The stability of the self-consistently determined current of a double-barrier resonant-tunneling diode," *Journal of Applied Physics*, vol. 70, no. 6, pp. 3141-3147, 1991, doi: 10.1063/1.349294.
- [428] W. -R. Liou and P. Roblin, "High frequency simulation of resonant tunneling diodes," *IEEE Transactions on Electron Devices*, vol. 41, no. 7, pp. 1098-1111, 1994, doi: 10.1109/16.293336.
- [429] J. Genoe, C. Van Hoof, W. Van Roy, J. H. Smet, K. Fobelets, R. P. Mertens, G. Borghs, "Capacitances in double-barrier tunneling structures," *IEEE Transactions on Electron Devices*, vol. 38, no. 9, pp. 2006-2012, 1991, doi: 10.1109/16.83722.
- [430] A. -P. Jauho, N. S. Wingreen, and Y. Meir, "Time-dependent transport in interacting and noninteracting resonant-tunneling systems," *Physical Review B*, vol. 50, no. 8, pp. 5528-5544, 1994, doi: 10.1103/PhysRevB.50.5528.
- [431] M. Villani, S. Clochiatti, W. Prost, N. Weimann, and X. Oriols, "There is plenty of room for THz tunneling electron devices beyond the transit time limit," *IEEE Electron Device Letters*, vol. 42, no. 2, pp. 224-227, 2021, doi: 10.1109/LED.2021.3049229.
- [432] B. van der Pol, "The nonlinear theory of electric oscillations", *Proceedings of the Institute of Radio Engineers*, vol. 22, no. 9, pp. 1051-1086, 1934, doi: 10.1109/JR-PROC.1934.226781.

- [433] C. Kim and A. Brandli, "High-frequency high-power operation of tunnel diodes," *IRE Transactions on Circuit Theory*, vol. 8, no. 4, pp. 416-425, 1961, doi: 10.1109/TCT.1961.1086849.
- [434] C. Brunetti, "The clarification of average negative resistance with extensions of its use," *Proceedings of the Institute of Radio Engineers*, vol. 25, no. 12, pp. 1595-1616, 1937, doi: 10.1109/JRPROC.1937.228824.
- [435] F. Han, H. Fujikata, K. Kobayashi, H. Tanaka, S. Suzuki, and M. Asada, "Impedance matching method in high-power RTD THz oscillator integrated with rectangular-cavity resonator," *2020 45th International Conference on Infrared, Millimeter, and Terahertz Waves (IRMMW-THz)*, pp. 1-2, 2020, doi: 10.1109/IRMMW-THz46771.2020.9370729.
- [436] M. Asada and S. Suzuki, "Terahertz oscillators using resonant tunneling diodes," *Asia-Pacific Microwave Conference (APMC)*, pp. 521-523, 2018, doi: 10.23919/APMC.2018.8617175.
- [437] N. Orihashi, S. Hattori, S. Suzuki, and M. Asada, "Experimental and theoretical characteristics of sub-terahertz and terahertz oscillations of resonant tunneling diodes integrated with slot antennas," *Japanese Journal of Applied Physics*, vol. 44, no. 11, pp. 7809-7815, 2005, doi: 10.1143/jjap.44.7809.
- [438] S. Clochiatti, K. Aikawa, K. Arzi, E. Mutlu, M. Suhara, N. Weimann, and W. Prost, "Large-signal modelling of sub-THz InP triple-barrier resonant tunneling diodes," *2020 Third International Workshop on Mobile Terahertz Systems (IWMTS)*, pp. 1-5, 2020, doi: 10.1109/IWMTS49292.2020.9166270.
- [439] M. Feiginov, C. Sydlo, O. Cojocari, and P. Meissner, "High-frequency nonlinear characteristics of resonant-tunnelling diodes," *Applied Physics Letters*, vol. 99, no. 13, pp. 133501, 2011, doi: 10.1063/1.3644491.
- [440] T. W. Crowe, J. L. Hesler, E. Bryerton, and S. A. Retzlöff, "Terahertz sources and receivers for science applications and test & measurement systems," *2016 IEEE Compound Semiconductor Integrated Circuit Symposium (CSICS)*, pp. 1-4, 2016, doi: 10.1109/CSICS.2016.7751069.
- [441] A. Rumiantsev and R. Doerner, "RF probe technology: history and selected topics," *IEEE Microwave Magazine*, vol. 14, no. 7, pp. 46-58, 2013, doi: 10.1109/MMM.2013.2280241.
- [442] R. Schmidt, S. Clochiatti, E. Mutlu, N. Weimann, A. Ferrero, M. Dieudonné, and D. M. M. -P. Schreurs, "Compensating probe misplacements in on-wafer S-parameters measurements," *IEEE Transactions on Microwave Theory and Techniques*, vol. 70, no. 11, pp. 5213-5223, 2022, doi: 10.1109/TMTT.2022.3205606.

- [443] S. Suzuki, M. Shiraishi, H. Shibayama, and M. Asada, "High-power operation of terahertz oscillators with resonant tunneling diodes using impedance-matched antennas and array configuration," *IEEE Journal of Selected Topics in Quantum Electronics*, vol. 19, no. 1, pp. 8500108-8500108, 2013, doi: 10.1109/JSTQE.2012.2215017.
- [444] M. Reddy, "Schottky-collector resonant tunnel diodes for sub-millimeter-wave applications," Ph.D. thesis, University of California Santa Barbara, 1997.
- [445] I. Vurgaftman, J. R. Meyer, and L. R. Ram-Mohan, "Band parameters for III-V compound semiconductors and their alloys," *Journal of Applied Physics*, vol. 89, no. 11, pp. 5815-5875, 2001, doi: 10.1063/1.1368156.
- [446] M. Levinshtein, S. Rumyantsev, and M. Shur, "Handbook series on semiconductor parameters," Volume 1 and 2, *World Scientific*, 1996, doi: 10.1142/2046.
- [447] O. Madelung, "Semiconductors: data handbook," *Springer*, 2004, doi: 10.1007/978-3-642-18865-7.
- [448] G. Martin, A. Botchkarev, A. Rockett, and H. Morkoç, "Valence-band discontinuities of wurtzite GaN, AlN, and InN heterojunctions measured by x-ray photoemission spectroscopy," *Applied Physics Letters*, vol. 68, no. 18, pp. 2541-2543, 1996, doi: 10.1063/1.116177.
- [449] T. J. Shewchuk, P. C. Chapin, P. D. Coleman, W. Kopp, R. Fischer, and H. Morkoç, "Resonant tunneling oscillations in a GaAs-Al<sub>x</sub>Ga<sub>1-x</sub>As heterostructure at room temperature," *Applied Physics Letters*, vol. 46, no. 5, pp. 508-510, 1985, doi: 10.1063/1.95574.
- [450] E. R. Brown, T. C. L. G. Sollner, C. D. Parker, W. D. Goodhue, and C. L. Chen, "Oscillations up to 420 GHz in GaAs/AlAs resonant tunneling diodes," *Applied Physics Letters*, vol. 55, no. 17, pp. 1777-1779, 1989, doi: 10.1063/1.102190.
- [451] H. Sugiyama, H. Yokoyama, A. Teranishi, S. Suzuki, and M. Asada, "Extremely high peak current densities of over  $1 \times 10^6$  A/cm<sup>2</sup> in InP-based InGaAs/AlAs resonant tunneling diodes grown by metal-organic vapor-phase epitaxy," *Japanese Journal of Applied Physics*, vol. 49, no. 5R, pp. 051201, 2010, doi: 10.1143/jjap.49.051201.
- [452] S. G. Muttalak, O. S. Abdulwahid, J. Sexton, M. J. Kelly, and M. Missous, "InGaAs/AlAs resonant tunneling diodes for THz applications: an experimental investigation," *IEEE Journal of the Electron Devices Society*, vol. 6, pp. 254-262, 2018, doi: 10.1109/JEDS.2018.2797951.
- [453] T. P. E. Broekaert and C. G. Fonstad, "In<sub>0.53</sub>Ga<sub>0.47</sub>As/AlAs resonant tunneling diodes with peak current densities in excess of 450 kA/cm<sup>2</sup>," *Journal of Applied Physics*, vol. 68, no. 8, pp. 4310-4312, 1990, doi: 10.1063/1.346226.

- [454] I. Mehdi and G. Haddad, "Lattice matched and pseudomorphic  $\text{In}_{0.53}\text{Ga}_{0.47}\text{As}/\text{In}_x\text{Al}_{1-x}\text{As}$  resonant tunneling diodes with high current peak-to-valley ratio for millimeter-wave power generation," *Journal of Applied Physics*, vol. 67, no. 5, pp. 2643-2646, 1990, doi: 10.1063/1.345472.
- [455] H. Sugiyama, H. Yokoyama, A. Teranishi, S. Suzuki, and M. Asada, "High-uniformity InP-based resonant tunneling diode wafers with peak current density of over  $6 \times 10^5$  A/cm<sup>2</sup> grown by metal-organic vapor-phase epitaxy," *Journal of Crystal Growth*, vol. 336, no. 1, pp. 24-28, 2011, doi: 10.1016/j.jcrysgro.2011.09.010.
- [456] H. Sugiyama, A. Teranishi, S. Suzuki, and M. Asada, "Structural and electrical transport properties of MOVPE-grown pseudomorphic AlAs/InGaAs/InAs resonant tunneling diodes on InP substrates," *Japanese Journal of Applied Physics*, vol. 53, no. 3, pp. 031202, 2014, doi: 10.7567/jjap.53.031202.
- [457] J. G. Ruch and G. S. Kino, "Transport properties of GaAs," *Physical Review*, vol. 174, no. 3, pp. 921-931, 1968, doi: 10.1103/PhysRev.174.921.
- [458] T. P. E. Broekaert, W. Lee, and C. G. Fonstad, "Pseudomorphic  $\text{In}_{0.53}\text{Ga}_{0.47}\text{As}/\text{AlAs}/\text{InAs}$  resonant tunneling diodes with peak-to-valley current ratios of 30 at room temperature," *Applied Physics Letters*, vol. 53, no. 16, pp. 1545-1547, 1988, doi: 10.1063/1.99951.
- [459] J. H. Smet, T. P. E. Broekaert, and C. G. Fonstad, "Peak-to-valley current ratios as high as 50:1 at room temperature in pseudomorphic  $\text{In}_{0.53}\text{Ga}_{0.47}\text{As}/\text{AlAs}/\text{InAs}$  resonant tunneling diodes," *Journal of Applied Physics*, vol. 71, no. 5, pp. 2475-2477, 1992, doi: 10.1063/1.351085.
- [460] V. K. Reddy, A. J. Tsao, and D. P. Neikirk, "High peak-to-valley current ratio Al-GaAs/AlAs/GaAs double barrier resonant tunnelling diodes," *Electronics Letters*, vol. 26, no. 21, pp. 1742-1744, 1990, doi: 10.1049/el:19901119.
- [461] A. M. Crook, E. Lind, Z. Griffith, M. J. W. Rodwell, J. D. Zimmerman, and A. C. Gossard, "Low resistance, nonalloyed Ohmic contacts to InGaAs," *Applied Physics Letters*, vol. 91, no. 19, pp. 192114, 2007, doi: 10.1063/1.2806235.
- [462] A. Piotrowska, A. Guivarc'h, and G. Pelous, "Ohmic contacts to III-V compound semiconductors: a review of fabrication techniques," *Solid-State Electronics*, vol. 26, no. 3, pp. 179-197, 1983, doi: 10.1016/0038-1101(83)90083-7.
- [463] H. Sugiyama, H. Matsuzaki, Y. Oda, H. Yokoyama, T. Enoki, and T. Kobayashi, "Metal-organic vapor-phase epitaxy growth of InP-based resonant tunneling diodes with a strained  $\text{In}_{0.8}\text{Ga}_{0.2}\text{As}$  well and AlAs barriers," *Japanese Journal of Applied Physics*, vol. 44, part 1, no. 10, pp. 7314-7318, 2005, doi: 10.1143/jjap.44.7314.

- [464] S. Suzuki and M. Asada, "Room-temperature oscillation of resonant tunneling diodes close to 2 THz and their functions for various applications," *Journal of Infrared, Millimeter, and Terahertz Waves*, vol. 37, no. 12, pp. 1185-1198, 2016, doi: 10.1007/s10762-016-0321-6.
- [465] K. J. P. Jacobs, B. J. Stevens, O. Wada, T. Mukai, D. Ohnishi, and R. A. Hogg, "A dual-pass high current density resonant tunneling diode for terahertz wave applications," *IEEE Electron Device Letters*, vol. 36, no. 12, pp. 1295-1298, 2015, doi: 10.1109/LED.2015.2491339.
- [466] M. Asada and S. Suzuki, "Terahertz emitter using resonant-tunneling diode and applications," *Sensors*, vol. 21, no. 4, pp. 1384, 2021, doi: 10.3390/s21041384.
- [467] N. Kishimoto, S. Suzuki, A. Teranishi, and M. Asada, "Frequency increase of resonant tunneling diode oscillators in Sub-THz and THz range using thick spacer layers," *Applied Physics Express*, vol. 1, no. 4, pp. 042003, 2008, doi: 10.1143/apex.1.042003.
- [468] H. Kanaya, R. Sogabe, T. Maekawa, S. Suzuki, and M. Asada, "Fundamental oscillation up to 1.42 THz in resonant tunneling diodes by optimized collector spacer thickness," *Journal of Infrared, Millimeter, and Terahertz Waves*, vol. 35, no. 5, pp. 425-431, 2014, doi: 10.1007/s10762-014-0058-z.
- [469] S. Javalagi, V. Reddy, K. Gullapalli, and D. Neikirk, "High efficiency microwave diode oscillators," *Electronics Letters*, vol. 28, no. 18, pp. 1699-1701, 1992, doi: 10.1049/el:19921080.
- [470] T. Maekawa, H. Kanaya, S. Suzuki, and M. Asada, "Oscillation up to 1.92 THz in resonant tunneling diode by reduced conduction loss," *Applied Physics Express*, vol. 9, no. 2, pp. 024101, 2016, doi: 10.7567/apex.9.024101.
- [471] S. Suzuki, M. Asada, A. Teranishi, H. Sugiyama, and H. Yokoyama, "Fundamental oscillation of resonant tunneling diodes above 1 THz at room temperature," *Applied Physics Letters*, vol. 97, no. 24, pp. 242102, 2010, doi: 10.1063/1.3525834.
- [472] S. Suzuki, A. Teranishi, K. Hinata, M. Asada, H. Sugiyama, and H. Yokoyama, "Fundamental oscillation of up to 831 GHz in GaInAs/AlAs resonant tunneling diode," *Applied Physics Express*, vol. 2, pp. 054501, 2009, doi: 10.1143/apex.2.054501.
- [473] H. Kanaya, H. Shibayama, R. Sogabe, S. Suzuki, and M. Asada, "Fundamental oscillation up to 1.31 THz in resonant tunneling diodes with thin well and barriers," *Applied Physics Express*, vol. 5, no. 12, pp. 124101, 2012, doi: 10.1143/apex.5.124101.

- [474] W. D. Zhang, T. A. Growden, E. R. Brown, P. R. Berger, D. F. Storm, and D. J. Meyer, "Fabrication and characterization of GaN/AlN resonant tunneling diodes," in High-frequency GaN electronic devices, pp. 249-281, *Springer*, 2020, doi: 10.1007/978-3-030-20208-8\_9.
- [475] T. A. Growden, D. F. Storm, W. Zhang, E. R. Brown, D. J. Meyer, P. Fakhimi, and P. R. Berger, "Highly repeatable room temperature negative differential resistance in AlN/GaN resonant tunneling diodes grown by molecular beam epitaxy," *Applied Physics Letters*, vol. 109, no. 8, pp. 083504, 2016, doi: 10.1063/1.4961442.
- [476] J. Encomendero, R. Yan, A. Verma, S. M. Islam, V. Protasenko, S. Rouvimov, P. Fay, D. Jena, and H. G. Xing, "Room temperature microwave oscillations in GaN/AlN resonant tunneling diodes with peak current densities up to 220 kA/cm<sup>2</sup>," *Applied Physics Letters*, vol. 112, no. 10, pp. 103101, 2018, doi: 10.1063/1.5016414.
- [477] T. A. Growden, W. Zhang, E. R. Brown, D. F. Storm, K. Hansen, P. Fakhimi, D. J. Meyer, and P. R. Berger, "431 kA/cm<sup>2</sup> peak tunneling current density in GaN/AlN resonant tunneling diodes," *Applied Physics Letters*, vol. 112, no. 3, pp. 033508, 2018, doi: 10.1063/1.5010794.
- [478] H. P. Zhang, J. S. Xue, Z. P. Sun, L. X. Li, J. J. Yao, F. Liu, X. Y. Yang, G. L. Wu, Z. M. Li, Y. R. Fu, Z. H. Liu, J. C. Zhang, and Y. Hao, "1039 kA/cm<sup>2</sup> peak tunneling current density in GaN-based resonant tunneling diode with a peak-to-valley current ratio of 1.23 at room temperature on sapphire substrate," *Applied Physics Letters*, vol. 119, no. 15, pp. 153506, 2021, doi: 10.1063/5.0064790.
- [479] H. Morkoç, "Metal contacts to GaN and processing," in Handbook of nitride semiconductors and devices: electronic and optical processes in nitrides, *Wiley*, vol. 2, pp. 1-119, 2008, doi: 10.1002/9783527628414.ch1.
- [480] J. Encomendero, V. Protasenko, B. Sensale-Rodriguez, P. Fay, F. Rana, D. Jena, and H. G. Xing, "Broken symmetry effects due to polarization on resonant tunneling transport in double-barrier nitride heterostructures," *Physical Review Applied*, vol. 11, no. 3, pp. 034032, 2019, doi: 10.1103/PhysRevApplied.11.034032.
- [481] J. Encomendero, V. Protasenko, B. Sensale-Rodriguez, P. Fay, F. Rana, D. Jena, and H. G. Xing, "Fighting broken symmetry with doping: toward polar resonant tunneling diodes with symmetric characteristics," *Physical Review Applied*, vol. 13, no. 3, pp. 034048, 2020, doi: 10.1103/PhysRevApplied.13.034048.
- [482] E. R. Brown, J. R. Soderstrom, C. D. Parker, L. J. Mahoney, K. M. Molvar, and T. C. McGill, "Oscillations up to 712 GHz in InAs/AlSb resonant tunnelling diodes," *Applied Physics Letters*, vol. 58, no. 20, pp. 2291-2293, 1991, doi: 10.1063/1.104902.

- [483] J. R. Söderström, D. H. Chow, and T. C. McGill, "InAs/AlSb double-barrier structure with large peak-to-valley current ratio: a candidate for high-frequency microwave devices," *IEEE Electron Device Letters*, vol. 11, no. 1, pp. 27-29, 1990, doi: 10.1109/55.46920.
- [484] L. F. Luo, R. Beresford, and W. I. Wang, "Resonant tunneling in AlSb/InAs/AlSb double-barrier heterostructures," *Applied Physics Letters*, vol. 53, no. 23, pp. 2320-2322, 1988, doi: 10.1063/1.100266.
- [485] E. Ozbay, D. M. Bloom, D. H. Chow, and J. N. Schulman, "1.7-ps, microwave, integrated-circuit-compatible InAs/AlSb resonant tunneling diodes," *IEEE Electron Device Letters*, vol. 14, no. 8, pp. 400-402, 1993, doi: 10.1109/55.225592.
- [486] J. N. Schulman, D. H. Chow, and T. C. Hasenberg, "InAs/antimonide-based resonant tunneling structures with ternary alloy layers," *Solid-State Electronics*, vol. 37, no. 4-6, pp. 981-985, 1994, doi: 10.1016/0038-1101(94)90341-7.
- [487] E. D. Guarín Castro, F. Rothmayr, S. Krüger, G. Knebl, A. Schade, J. Koeth, L. Worschech, V. Lopez-Richard, G. E. Marques, F. Hartmann, A. Pfenning, and S. Höfling, "Resonant tunneling of electrons in AlSb/GaInAsSb double barrier quantum wells," *AIP Advances*, vol. 10, no. 5, pp. 055024, 2020, doi: 10.1063/5.0008959.
- [488] H. Kroemer, "The 6.1 Å family (InAs, GaSb, AlSb) and its heterostructures: a selective review," *Physica E: Low-dimensional Systems and Nanostructures*, vol. 20, no. 3-4, pp. 196-203, 2004, doi: 10.1016/j.physe.2003.08.003.
- [489] E. R. Brown and C. D. Parker, "Resonant tunnel diodes as submillimetre-wave sources," *Philosophical Transactions of the Royal Society of London. Series A: Mathematical, Physical and Engineering Sciences*, vol. 354, no. 1717, pp. 2365-2381, 1996, doi: 10.1098/rsta.1996.0105.
- [490] T. Nittono, H. Ito, O. Nakajima, and T. Ishibashi, "Non-alloyed ohmic contacts to n-GaAs using compositionally graded  $\text{In}_x\text{Ga}_{1-x}\text{As}$  layers," *Japanese Journal of Applied Physics*, vol. 27, part 1, no. 9, pp. 1718-1722, 1988, doi: 10.1143/JJAP.27.1718.
- [491] C. A. Mead and W. G. Spitzer, "Fermi level position at metal-semiconductor interfaces," *Physical Review*, vol. 134, no. 3A, pp. A713-A716, 1964, doi: 10.1103/PhysRev.134.A713.
- [492] E. R. Brown, S. J. Eglash, G. W. Turner, C. D. Parker, J. V. Pantano, and D. R. Calawa, "Effect of lattice-mismatched growth on InAs/AlSb resonant-tunneling diodes," *IEEE Transactions on Electron Devices*, vol. 41, no. 6, pp. 879-882, 1994, doi: 10.1109/16.293296.

- [493] J. R. Söderström, E. R. Brown, C. D. Parker, L. J. Mahoney, J. Y. Yao, T. G. Andersson, and T. C. McGill, "Growth and characterization of high current density high-speed InAs/AlSb resonant tunneling diodes," *Applied Physics Letters*, vol. 58, no. 3, pp. 275-277, 1991, doi: 10.1063/1.104659.
- [494] K. F. Brennan and N. S. Mansour, "Monte Carlo calculation of electron impact ionization in bulk InAs and HgCdTe," *Journal of Applied Physics*, vol. 69, no. 11, pp. 7844-7847, 1991, doi: 10.1063/1.347516.
- [495] D. J. Paul, P. See, I. V. Zozoulenko, K. -F. Berggren, B. Kabius, B. Holländer, and S. Mantl, "Si/SiGe electron resonant tunneling diodes," *Applied Physics Letters*, vol. 77, no. 11, pp. 1653-1655, 2000, doi: 10.1063/1.1309020.
- [496] D. J. Paul, P. See, I. V. Zozoulenko, K. -F. Berggren, B. Holländer, S. Mantl, N. Griffin, B. P. Coonan, G. Redmond, and G. M. Creand, "n-type Si/SiGe resonant tunnelling diodes," *Materials Science and Engineering: B*, vol. 89, no. 1-3, pp. 26-29, 2002, doi: 10.1016/S0921-5107(01)00785-1.
- [497] D. J. Paul, P. See, R. Bates, N. Griffin, B. P. Coonan, G. Redmond, G. M. Crean, I. V. Zozoulenko, K. -F. Berggren, B. Holländer, and S. Mantl, "Si/SiGe electron resonant tunneling diodes with graded spacer wells," *Applied Physics Letters*, vol. 78, no. 26, pp. 4184-4186, 2001, doi: 10.1063/1.1381042.
- [498] L. Yang, J. R. Watling, R. C. W. Wilkins, M. Boriçi, J. R. Barker, A. Asenov, and S. Roy, "Si/SiGe heterostructure parameters for device simulations," *Semiconductor Science and Technology*, vol. 19, no. 10, pp. 1174, 2004, doi: 10.1088/0268-1242/19/10/002.
- [499] G. Ternent and D. J. Paul, "Si/SiGe tunneling static random access memories," *ECS Transactions*, vol. 50, no. 9, pp. 987-990, 2013, doi: 10.1149/05009.0987ecst.
- [500] P. Fay, J. Lu, Y. Xu, N. Dame, D. H. Chow and J. N. Schulman, "Microwave performance and modeling of InAs/AlSb/GaSb resonant interband tunneling diodes," *IEEE Transactions on Electron Devices*, vol. 49, no. 1, pp. 19-24, 2002, doi: 10.1109/16.974743.
- [501] S. -Y. Chung, R. Yu, N. Jin, S. -Y. Park, P. R. Berger, and P. E. Thompson, "Si/SiGe resonant interband tunnel diode with  $f_{r0}$  20.2 GHz and peak current density 218 kA/cm<sup>2</sup> for K-band mixed-signal applications," *IEEE Electron Device Letters*, vol. 27, no. 5, pp. 364-367, 2006, doi: 10.1109/LED.2006.873379.
- [502] N. Jin, S. -H. Chung, A. T. Rice, P. R. Berger, R. Yu, P. E. Thompson, and R. Lake, "151 kA/cm<sup>2</sup> peak current densities in Si/SiGe resonant interband tunneling diodes for high-power mixed-signal applications," *Applied Physics Letters*, vol. 83, no. 16, pp. 3308-3310, 2003, doi: 10.1063/1.1618927.

- [503] S. L. Rommel, T. E. Dillon, M. W. Dashiell, H. Feng, J. Kolodzey, P. R. Berger, P. E. Thompson, K. D. Hobart, R. Lake, A. C. Seabaugh, G. Klimeck, and D. K. Blanks, "Room temperature operation of epitaxially grown Si/Si<sub>0.5</sub>Ge<sub>0.5</sub>/Si resonant interband tunneling diodes," *Applied Physics Letters*, vol. 73, no. 15, pp. 2191-2193, 1998, doi: 10.1063/1.122419.
- [504] J. R. Söderström, D. H. Cho, and T. C. McGill, "New negative differential resistance device based on resonant interband tunneling," *Applied Physics Letters*, vol. 55, no. 11, pp. 1094-1096, 1989, doi: 10.1063/1.101715.
- [505] R. Beresford, L. F. Luo, K. F. Longenbach, and W. I. Wang, "Resonant interband tunneling through a 110 nm InAs quantum well," *Applied Physics Letters*, vol. 56, no. 6, pp. 551-553, 1990, doi: 10.1063/1.102742.
- [506] J. Gaskell, L. Eaves, K. S. Novoselov, A. Mishchenko, A. K. Geim, T. M. Fromhold, and M. T. Greenaway, "Graphene-hexagonal boron nitride resonant tunneling diodes as high-frequency oscillators," *Applied Physics Letters*, vol. 107, no. 10, pp. 103105, 2015, doi: 10.1063/1.4930230.
- [507] A. Y. Goharrizi, M. Zoghi, and M. Saremi, "Armchair graphene nanoribbon resonant tunneling diodes using antidote and BN doping," *IEEE Transactions on Electron Devices*, vol. 63, no. 9, pp. 3761-3768, 2016, doi: 10.1109/TED.2016.2586459.
- [508] E. R. Brown, C. D. Parker, S. Verghese, M. W. Geis, and J. F. Harvey, "Resonant-tunneling transmission-line relaxation oscillator," *Applied Physics Letters*, vol. 70, no. 21, pp. 2787-2789, 1997, doi: 10.1063/1.119059.
- [509] C. L. Chen, R. H. Mathews, L. J. Mahoney, S. D. Calawa, J. P. Sage, K. M. Molvar, C. D. Parker, P. A. Maki, and T. C. L. G. Sollner, "Resonant-tunneling-diode relaxation oscillator," *Solid-State Electronics*, vol. 44, no. 10, pp. 1853-1856, 2000, doi: 10.1016/S0038-1101(00)00105-2.
- [510] A. A. Andronov, A. A. Vitt, and S. E. Khaikin, "Theory of oscillators," *Pergamon Press*, 1966.
- [511] M. E. Hines, "High-frequency negative-resistance circuit principles for Esaki diode applications," *The Bell System Technical Journal*, vol. 39, no. 3, pp. 477-513, 1960, doi: 10.1002/j.1538-7305.1960.tb03933.x.
- [512] C. Kidner, I. Mehdi, J. R. East, and G. I. Haddad, "Power and stability limitations of resonant tunneling diodes," *IEEE Transactions on Microwave Theory and Techniques*, vol. 38, no. 7, pp. 864-872, 1990, doi: 10.1109/22.55778.

- [513] A. C. Cornescu, R. Morariu, A. Ofiare, A. Al-Khalidi, J. Wang, J. M. L. Figueiredo, and E. Wasige, "High-efficiency bias stabilization for resonant tunneling diode oscillators," *IEEE Transactions on Microwave Theory and Techniques*, vol. 67, no. 8, pp. 3449-3454, 2019, doi: 10.1109/TMTT.2019.2916602.
- [514] M. Reddy, M. J. Mondry, M. J. W. Rodwell, S. C. Martin, R. E. Muller, R. P. Smith, D. H. Chow, and J. N. Schulman, "Fabrication and dc, microwave characteristics of sub-micron Schottky-collector AlAs/In<sub>0.53</sub>Ga<sub>0.47</sub>As/InP resonant tunneling diodes," *Journal of Applied Physics*, vol. 77, no. 9, pp. 4819-4821, 1995, doi: 10.1063/1.359405.
- [515] L. Wang, "Output power analysis and simulations of resonant tunneling diode based oscillators," *International Computer Science Conference (ICSC): System Simulation and Scientific Computing*, pp. 47-55, 2012, doi: 10.1007/978-3-642-34381-0\_6.
- [516] J. Wang, A. Al-Khalidi, K. Alharbi, A. Ofiare, H. Zhou, E. Wasige, and J. Figueiredo, "High performance resonant tunneling diode oscillators as terahertz sources," *46th European Microwave Conference (EuMC)*, pp. 341-344, 2016, doi: 10.1109/EuMC.2016.7824348.
- [517] S. Diebold, K. Nishio, Y. Nishida, J. -Y. Kim, K. Tsuruda, T. Mukai, M. Fujita, and T. Nagatsuma, "High-speed error-free wireless data transmission using a terahertz resonant tunnelling diode transmitter and receiver," *Electronics Letters*, vol. 52, no. 24, pp. 1999-2001, 2016, doi: 10.1049/el.2016.2941.
- [518] E. Wasige, A. Al-Khalidi, K. Alharbi, and J. Wang, "High performance microstrip resonant tunneling diode oscillators as terahertz sources," *9th UK-Europe-China Workshop on Millimetre Waves and Terahertz Technologies (UCMMT)*, pp. 25-28, 2016, doi: 10.1109/UCMMT.2016.7873950.
- [519] T. C. L. G. Sollner, P. E. Tannenwald, D. D. Peck, and W. D. Goodhue, "Quantum well oscillators," *Applied Physics Letters*, vol. 45, no. 12, pp. 1319-1321, 1984, doi: 10.1063/1.95134.
- [520] E. R. Brown, T. C. L. G. Sollner, W. D. Goodhue, and C. D. Parker, "Millimeter-band oscillations based on resonant tunneling in a double-barrier diode at room temperature," *Applied Physics Letters*, vol. 50, no. 2, pp. 83-85, 1987, doi: 10.1063/1.97826.
- [521] K. D. Stephan, E. R. Brown, C. D. Parker, W. D. Goodhue, C. L. Chen, and T. C. L. G. Sollner, "Resonant-tunnelling diode oscillator using a slot-coupled quasioptical open resonator," *Electronics Letters*, vol. 27, no. 8, pp. 647-649, 1991, doi: 10.1049/el:19910406.
- [522] E. R. Brown, C. D. Parker, K. M. Molvar, and K. D. Stephan, "A quasioptically stabilized resonant-tunneling-diode oscillator for the millimeter- and submillimeter-wave regions,"

*IEEE Transactions on Microwave Theory and Techniques*, vol. 40, no. 5, pp. 846-850, 1992, doi: 10.1109/22.137389.

- [523] E. R. Brown, C. D. Parker, A. R. Calawa, M. J. Manfra, and K. M. Molvar, "A quasi-optical resonant-tunneling-diode oscillator operating above 200 GHz," *IEEE Transactions on Microwave Theory and Techniques*, vol. 41, no. 4, pp. 720-722, 1993, doi: 10.1109/22.231671.
- [524] T. Fujii, H. Mazaki, F. Takei, J. Bae, M. Narihiro, T. Noda, H. Sakaki, and K. Mizuno, "Coherent power combining of millimeter wave resonant tunneling diodes in a quasi-optical resonator," *IEEE MTT-S International Microwave Symposium Digest*, vol. 2, pp. 919-922, 1996, doi: 10.1109/MWSYM.1996.511177.
- [525] M. Reddy, S. C. Martin, A. C. Molnar, R. E. Muller, R. P. Smith, P. H. Siegel, M. J. Mondry, M. J. W. Rodwell, H. Kroemer, and S. J. Allen, "Monolithic Schottky-collector resonant tunnel diode oscillator arrays to 650 GHz," *IEEE Electron Device Letters*, vol. 18, no. 5, pp. 218-221, 1997, doi: 10.1109/55.568771.
- [526] R. P. Smith, S. T. Alien, M. Reddy, S. C. Martin, J. Liu, R. E. Muller, and M. J. W. Rodwell, "0.1  $\mu\text{m}$  Schottky-collector AlAs/GaAs resonant tunneling diodes," *IEEE Electron Device Letters*, vol. 15, no. 8, pp. 295-297, 1994. doi: 10.1109/55.296221.
- [527] R. E. Muller, S. C. Martin, R. P. Smith, S. A. Allen, M. Reddy, U. Bhattacharya, and M. J. W. Rodwell, "Electron-beam lithography for the fabrication of air-bridged submicron Schottky collectors," *Journal of Vacuum Science & Technology B: Microelectronics and Nanometer Structures Processing, Measurement, and Phenomena*, vol. 12, no. 6, pp. 3668-3672, 1994, doi: 10.1116/1.587636.
- [528] M. Reddy, M. J. Mondry, A. C. Molnar, U. Bhattacharya, and M. J. W. Rodwell, "Monolithic RTD array oscillators at 100 GHz and 200 GHz with on-Wafer bias stabilization," University of California, Santa Barbara (UCSB), 1997.
- [529] J. T. Wallmark and A. H. Dansky, "Nonlinear biasing resistors for microwave tunnel-diode oscillators," *IEEE Transactions on Microwave Theory and Techniques*, vol. 11, no. 4, pp. 260-262, 1963, doi: 10.1109/TMTT.1963.1125654.
- [530] M. Reddy, R. Y. Yu, H. Kroemer, M. J. W. Rodwell, S. C. Martin, R. E. Muller, and R. P. Smith, "Bias stabilization for resonant tunnel diode oscillators," *IEEE Microwave and Guided Wave Letters*, vol. 5, no. 7, pp. 219-221, 1995, doi: 10.1109/75.392280.
- [531] N. Orihashi, S. Suzuki, and M. Asada, "One THz harmonic oscillation of resonant tunneling diodes," *Applied Physics Letters*, vol. 87, no. 23, pp. 233501, 2005, doi: 10.1063/1.2139850.

- [532] M. Shiraishi, S. Suzuki, A. Teranishi, M. Asada, H. Sugiyama, and H. Yokoyama, "Fundamental oscillation up to 915GHz in InGaAs/AlAs resonant tunneling diodes integrated with slot antennas," *34th International Conference on Infrared, Millimeter, and Terahertz Waves*, pp. 1-2, 2009, doi: 10.1109/ICIMW.2009.5324766.
- [533] A. Teranishi, K. Shizuno, S. Suzuki, M. Asada, H. Sugiyama, and H. Yokoyama, "Fundamental oscillation up to 1.08 THz in resonant tunneling diodes with high indium composition transit layers," *23rd International Conference on Indium Phosphide and Related Materials*, pp. 1-4, 2011.
- [534] Y. Koyama, R. Sekiguchi, and T. Ouchi, "Oscillations up to 1.40 THz from resonant-tunneling-diode-based oscillators with integrated patch antennas," *Applied Physics Express*, vol. 6, no. 6, pp. 064102, 2013, doi: 10.7567/apex.6.064102.
- [535] T. Maekawa, H. Kanaya, S. Suzuki, and M. Asada, "Frequency increase in terahertz oscillation of resonant tunnelling diode up to 1.55 THz by reduced slot-antenna length," *Electronics Letters*, vol. 50, no. 17, pp. 1214-1216, 2014, doi: 10.1049/el.2014.2362.
- [536] K. Hinata, M. Shiraishi, S. Suzuki, M. Asada, H. Sugiyama, and H. Yokoyama, "High output power ( $\sim 400 \mu\text{W}$ ) oscillators at around 550 GHz using resonant tunneling diodes with graded emitter and thin barriers," *Applied Physics Express*, vol. 4, no. 6, pp. 064101, 2011, doi: 10.1143/apex.4.064101.
- [537] K. Kasagi, S. Suzuki, and M. Asada, "Large-scale array of resonant tunneling- diode terahertz oscillators for high output power at 1 THz," *Journal of Applied Physics*, vol. 125, no. 15, pp. 151601, 2009, doi: 10.1063/1.5051007.
- [538] M. Egard, M. Arlelid, L. Ohlsson, B. M. Borg, E. Lind, and L. -E. Wernersson, "In<sub>0.53</sub>Ga<sub>0.47</sub>As RTD-MOSFET millimeter-wave wavelet generator," *IEEE Electron Device Letters*, vol. 33, no. 7, pp. 970-972, 2012, doi: 10.1109/LED.2012.2194132.
- [539] J. Lee, M. Kim, and K. Yang, "A 1.52 THz RTD triple-push oscillator with a  $\mu\text{W}$  -level output power," *IEEE Transactions on Terahertz Science and Technology*, vol. 6, no. 2, pp. 336-340, 2016, doi: 10.1109/TTHZ.2015.2509358.
- [540] M. Kim, J. Lee, J. Lee, and K. Yang, "A 675 GHz differential oscillator based on a resonant tunneling diode," *IEEE Transactions on Terahertz Science and Technology*, vol. 6, no. 3, pp. 510-512, 2016, doi: 10.1109/TTHZ.2016.2554399.
- [541] A. Al-Khalidi, J. Wang, and E. Wasige, "Compact J-band oscillators with 1 mW RF output power and over 110 GHz modulation bandwidth," *43rd International Conference on Infrared, Millimeter, and Terahertz Waves (IRMMW-THz)*, pp. 1-2, 2018, doi: 10.1109/IRMMW-THz.2018.8510099.

- [542] K. Urayama, S. Aoki, S. Suzuki, M. Asada, H. Sugiyama, and H. Yokoyama, "Sub-terahertz resonant tunneling diode oscillators integrated with tapered slot antennas for horizontal radiation," *Applied Physics Express*, vol. 2, no. 4, pp. 044501, 2019, doi: 10.1143/apex.2.044501.
- [543] D. Horikawa, Y. Chen, T. Koike, S. Suzuki, and M. Asada, "Resonant tunneling-diode terahertz oscillator integrated with a radial line slot antenna for circularly polarized wave radiation," *Semiconductor Science and Technology*, vol. 33, no. 11, pp. 114005, 2018, doi: 10.1088/1361-6641/aae1ef.
- [544] K. Okada, K. Kasagi, N. Oshima, S. Suzuki, and M. Asada, "Resonant-tunneling-diode terahertz oscillator using patch antenna integrated on slot resonator for power radiation," *IEEE Transactions on Terahertz Science and Technology*, vol. 5, no. 4, pp. 613-618, 2015, doi: 10.1109/TTHZ.2015.2441740.
- [545] P. Ourednik, T. Hackl, C. Spudat, D. T. Nguyen, and M. Feiginov, "Double-resonant-tunneling-diode patch-antenna oscillators," *Applied Physics Letters*, vol. 119, no. 26, pp. 263509, 2021, doi: 10.1063/5.0068114.
- [546] P. Ourednik and M. Feiginov, "Double-resonant-tunneling-diode bridge-less patch-antenna oscillators operating up to 1.09 THz," *Applied Physics Letters*, vol. 120, no. 18, pp. 183501, 2022, doi: 10.1063/5.0090519.
- [547] J. Lee, M. Kim, and J. Lee, "692 GHz high-efficiency compact-size InP-based fundamental RTD oscillator," *IEEE Transactions on Terahertz Science and Technology*, vol. 11, no. 6, pp. 716-719, 2021, doi: 10.1109/TTHZ.2021.3108431.
- [548] K. Kasagi, S. Fukuma, S. Suzuki, and M. Asada, "Proposal and fabrication of dipole array antenna structure in resonant-tunneling-diode terahertz oscillator array," *41st International Conference on Infrared, Millimeter, and Terahertz waves (IRMMW-THz)*, pp. 1-2, 2016, doi: 10.1109/IRMMW-THz.2016.7758957.
- [549] K. H. Alharbi, A. Khalid, A. Ofiare, J. Wang, and E. Wasige, "Diced and grounded broadband bow-tie antenna with tuning stub for resonant tunnelling diode terahertz oscillators," *IET Colloquium on Millimetre-Wave and Terahertz Engineering & Technology 2016*, pp. 1-4, 2016, doi: 10.1049/ic.2016.0013.
- [550] R. E. Neidert, S. C. Binari, and T. Weng, "Dielectric constant of semi-insulating indium phosphide," *Electronics Letters*, vol. 18, no. 23, pp. 987-988, 1982, doi: 10.1049/el:19820675.

- [551] C. Hilsum, S. Fray, and C. Smith, "The optical frequencies and dielectric constants of InP," *Solid State Communications*, vol. 7, no. 15, pp. 1057-1059, 1969, doi: 10.1016/0038-1098(69)90470-0.
- [552] K. Hinata, M. Shiraishi, S. Suzuki, M. Asada, H. Sugiyama, and H. Yokoyama, "Sub-terahertz resonant tunneling diode oscillators with high output power ( $\sim 200 \mu\text{W}$ ) using offset-fed slot antenna and high current density," *Applied Physics Express*, vol. 3, no. 1, pp. 014001, 2009, doi: 10.1143/apex.3.014001.
- [553] R. Izumi, T. Sato, S. Suzuki, and M. Asada, "Resonant-tunneling-diode terahertz oscillator with a cylindrical cavity for high-frequency oscillation," *AIP Advances*, vol. 9, no. 8, pp. 085020, 2019, doi: 10.1063/1.5114963.
- [554] Z. Jéhn, "Cylindrical cavity optimization for resonant-tunneling diode oscillators," *IEEE Transactions on Microwave Theory and Techniques*, vol. 70, no. 5, pp. 2658-2667, 2022, doi: 10.1109/TMTT.2022.3150146.
- [555] M. Bezhko, S. Suzuki, and M. Asada, "Analysis of output power characteristics for resonant-tunneling diode terahertz oscillator with cylindrical cavity resonator," *Japanese Journal of Applied Physics*, vol. 12, no. 60, pp. 121002, 2021, doi: 10.35848/1347-4065/ac3721.
- [556] F. Han, K. Kobayashi, S. Suzuki, H. Tanaka, H. Fujikata, and M. Asada, "Impedance matching in high-power resonant-tunneling-diode terahertz oscillators integrated with rectangular-cavity resonator," *IEICE Transactions on Electronics*, vol. E104.C, no. 8, pp. 398-402, 2021, doi: 10.1587/transele.2020ECS6020.
- [557] X. Yu, Y. Suzuki, M. Van Ta, S. Suzuki, and M. Asada, "Highly efficient resonant tunneling diode terahertz oscillator with a split ring resonator," *IEEE Electron Device Letters*, vol. 42, no. 7, pp. 982-985, 2021, doi: 10.1109/LED.2021.3082577.
- [558] T. V. Mai, Y. Suzuki, X. Yu, S. Suzuki, and M. Asada, "Structure-simplified resonant-tunneling-diode terahertz oscillator without metal-insulator-metal capacitors," *Journal of Infrared, Millimeter, and Terahertz Waves*, vol. 41, no. 12, pp. 1498-1507, 2020, doi: 10.1007/s10762-020-00738-7.
- [559] M. V. Ta, Y. Suzuki, X. Yu, S. Suzuki, and M. Asada, "Structure dependence of oscillation characteristics of structure-simplified resonant-tunneling-diode terahertz oscillator," *Applied Physics Express*, vol. 4, no. 15, pp. 042003, 2022, doi: 10.35848/1882-0786/ac5b32.
- [560] S. Kitagawa, S. Suzuki, and M. Asada, "Wide frequency-tunable resonant tunnelling diode terahertz oscillators using varactor diodes," *Electronics Letters*, vol. 52, no. 6, pp. 479-481, 2016, doi: 10.1049/el.2015.3921.

- [561] K. Ogino, S. Suzuki, and M. Asada, "Spectral narrowing of a varactor-integrated resonant-tunneling-diode terahertz oscillator by phase-locked loop," *Journal of Infrared, Millimeter, and Terahertz Waves*, vol. 38, no. 12, pp. 1477-1486, 2017, doi: 10.1007/s10762-017-0439-1.
- [562] J. Lee, M. Kim, J. Lee and K. Yang, "A sub-mW D-band 2<sup>nd</sup> harmonic oscillator using InP-based quantum-effect tunneling devices," *26th International Conference on Indium Phosphide and Related Materials (IPRM)*, pp. 1-2, 2014, doi: 10.1109/ICIPRM.2014.6880527.
- [563] M. Feiginov, "Sub-terahertz and terahertz microstrip resonant-tunneling-diode oscillators," *Applied Physics Letters*, vol. 107, no. 12, pp. 123504, 2015, doi: 10.1063/1.4931727.
- [564] Z. Jéhn, "Simulation of traveling-wave resonant tunneling diode oscillator waveguides," *Optics Express*, vol. 30, no. 20, pp. 35725-35733, 2022, doi: 10.1364/OE.466405.
- [565] N. Nishigami, Y. Nishida, S. Diebold, J. Kim, M. Fujita. and T. Nagatsuma, "Resonant Tunneling Diode Receiver for Coherent Terahertz Wireless Communication," *2018 Asia-Pacific Microwave Conference (APMC)*, pp. 726-728, 2018, doi: 10.23919/APMC.2018.8617565.
- [566] Y. Takida, S. Suzuki, M. Asada, and H. Minamide, "Sensitive terahertz-wave detector responses originated by negative differential conductance of resonant-tunneling-diode oscillator," *Applied Physics Letters*, vol. 117, no. 2, pp. 021107, 2020, doi: 10.1063/5.0012318.
- [567] D. Pozar, "Microwave and RF design of wireless systems," *Wiley*, 2000.
- [568] T. Shiode, T. Mukai, M. Kawamura, and T. Nagatsuma, "Giga-bit wireless communication at 300 GHz using resonant tunneling diode detector," *Asia-Pacific Microwave Conference 2011*, pp. 1122-1125, 2011.
- [569] D. Schoenherr, C. Bleasdale, T. Goebel, C. Sydlo, H. L. Hartnagel, R. Lewis, and P. Meissner, "Extremely broadband characterization of a Schottky diode based THz detector," *35th International Conference on Infrared, Millimeter, and Terahertz Waves*, pp. 1-2, 2010, doi: 10.1109/ICIMW.2010.5613008.
- [570] S. Boppel, A. Lissauskas, M. Mundt, D. Seliuta, L. Minkevicius, I. Kasalynas, G. Valusis, M. Mittendorff, S. Winnerl, V. Krozer, and H. G. Roskos, "CMOS integrated antenna-coupled field-effect transistors for the detection of radiation from 0.2 to 4.3 THz," *IEEE Transactions on Microwave Theory and Techniques*, vol. 60, no. 12, pp. 3834-3843, 2012, doi: 10.1109/TMTT.2012.2221732.

- [571] M. Bauer, A. Ramer, S. A. Chevtchenko, K. Y. Osipov, D. ibiraitė, S. Pralgauskaitė, K. Ikamas, A. Lisauskas, W. Heinrich, V. Krozer, and H. G. Roskos, "A high-sensitivity AlGaIn/GaN HEMT terahertz detector with integrated broadband bow-tie antenna," *IEEE Transactions on Terahertz Science and Technology*, vol. 9, no. 4, pp. 430-444, 2019, doi: 10.1109/TTHZ.2019.2917782.
- [572] S. -P. Han, H. Ko, J. -W. Park, N. Kim, Y. -J. Yoon, J. -H. Shin, D. Y. Kim, D. H. Lee, and K. H. Park, "InGaAs Schottky barrier diode array detector for a real-time compact terahertz line scanner," *Optics Express*, vol. 21, no. 22, pp. 25874-25882, 2013, doi: 10.1364/OE.21.025874.
- [573] X. Yu, J. -Y. Kim, M. Fujita, and T. Nagatsuma, "Efficient mode converter to deep-subwavelength region with photonic-crystal waveguide platform for terahertz applications," *Optics Express*, vol. 27, no. 20, pp. 28707-28721, 2019, doi: 10.1364/OE.27.028707.
- [574] Y. Takida, S. Suzuki, M. Asada, and H. Minamide, "Sensitivity measurement of resonant-tunneling-diode terahertz detectors," *44th International Conference on Infrared, Millimeter, and Terahertz Waves (IRMMW-THz)*, pp. 1-2, 2013, doi: 10.1109/IRMMW-THz.2019.8873774.
- [575] Y. Takida, S. Suzuki, M. Asada, and H. Minamide, "Sensitive Continuous-Wave Terahertz Detection by Resonant-Tunneling-Diode Oscillators," *45th International Conference on Infrared, Millimeter, and Terahertz Waves (IRMMW-THz)*, pp. 1-2, 2020, doi: 10.1109/IRMMW-THz46771.2020.9370758.
- [576] K. Arzi, S. Clochiatti, E. Mutlu, A. Kowaljow, B. Sievert, D. Erni, N. Weimann, and W. Prost, "Broadband detection capability of a triple barrier resonant tunneling diode," *2nd International Workshop on Mobile Terahertz Systems (IWMTS)*, pp. 1-4, 2019, doi: 10.1109/IWMTS.2019.8823724.
- [577] K. Arzi, S. Clochiatti, S. Suzuki, A. Rennings, D. Erni, N. Weimann, M. Asada, and W. Prost, "Triple-barrier resonant-tunnelling diode THz detectors with on-chip antenna," *12th German Microwave Conference (GeMiC)*, pp. 17-19, 2019, doi: 10.23919/GEMIC.2019.8698124.
- [578] R. Sekiguchi, Y. Koyama, and T. Ouchi, "Subterahertz oscillations from triple-barrier resonant tunneling diodes with integrated patch antennas," *Applied Physics Letters*, vol. 96, no. 6, pp. 062115, 2010, doi: 10.1063/1.3315868.
- [579] K. Arzi, A. Rennings, D. Erni, N. Weimann, W. Prost, S. Suzuki, and M. Asada, "Millimeter-wave signal generation and detection via the same triple barrier RTD and on-

- chip antenna," *1st International Workshop on Mobile Terahertz Systems (IWMTS)*, pp. 1-4, 2018, doi: 10.1109/IWMTS.2018.8454700.
- [580] F. Sizov, "Terahertz radiation detectors: the state-of-the-art," *Semiconductor Science and Technology*, vol. 33, no. 12, pp. 123001, 2018, doi: 10.1088/1361-6641/aae473.
- [581] M. Asada and S. Suzuki, "Theoretical analysis of coupled oscillator array using resonant tunneling diodes in subterahertz and terahertz range," *Journal of Applied Physics*, vol. 103, no. 12, pp. 124514, 2008, doi: 10.1063/1.2947600.
- [582] K. Arzi, S. Suzuki, A. Rennings, D. Erni, N. Weimann, M. Asada, and W. Prost, "Sub-harmonic injection locking for phase and frequency control of RTD-based THz oscillator," *IEEE Transactions on Terahertz Science and Technology*, vol. 10, no. 2, pp. 221-224, 2020, doi: 10.1109/TTHZ.2019.2959411.
- [583] J. Wang, A. Al-Khalidi, S. Ahearne, and E. Wasige, "1080P HD video transmission using RTD transmitter," *14th UK-Europe-China Workshop on Millimetre-Waves and Terahertz Technologies (UCMMT)*, pp. 1-3, 2021, doi: 10.1109/UCMMT53364.2021.9569915.
- [584] L. Ohlsson and L. Wernersson, "A 15-Gb/s wireless ON-OFF keying link," *IEEE Access*, vol. 2, pp. 1307-1313, 2014, doi: 10.1109/ACCESS.2014.2364638.
- [585] N. Oshima, K. Hashimoto, S. Suzuki, and M. Asada, "Wireless data transmission of 34 Gbit/s at a 500-GHz range using resonant-tunnelling-diode terahertz oscillator," *Electronics Letters*, vol. 52, no. 22, pp. 1897-1898, 2016, doi: 10.1049/el.2016.3120.
- [586] K. Nishio, S. Diebold, S. Nakai, K. Tsuruda, T. Mukai, J. -Y. Kim, M. Fujita, and T. Nagatsuma, "Resonant tunneling diode receivers for 300-GHz-band wireless communications," *URSI-Japan Radio Science Meeting*, 2015.
- [587] N. Oshima, K. Hashimoto, S. Suzuki, and M. Asada, "Terahertz wireless data transmission with frequency and polarization division multiplexing using resonant-tunneling-diode oscillators," *IEEE Transactions on Terahertz Science and Technology*, vol. 7, no. 5, pp. 593-598, 2017, doi: 10.1109/TTHZ.2017.2720470.
- [588] T. Yamamoto, N. Nishigami, Y. Nishida, M. Fujita, and T. Nagatsuma, "16-QAM wireless communications using resonant tunneling diodes at 60 Gbit/s," *IEICE General Conference*, 2020.
- [589] J. Webber, A. Oshiro, S. Iwamatsu, Y. Nishida, M. Fujita, and T. Nagatsuma, "48-Gbit/s 8K video-transmission using resonant tunnelling diodes in 300-GHz band," *Electronics Letters*, vol. 57, no. 17, pp. 668-669, 2021, doi: 10.1049/ell2.12219.

- [590] S. Iwamatsu, N. Nishigami, Y. Nishida, M. Fujita, and T. Nagatsuma, "Broadband terahertz resonant tunnelling diode transmitter integrated with coplanar-waveguide-fed slot-ring antenna," *Electronics Letters*, vol. 57, no. 25, pp. 1001-1003, 2021, doi: 10.1049/ell2.12332.
- [591] X. Yu, R. Yamada, J. Kim, M. Fujita, and T. Nagatsuma, "Integrated circuits using photonic-crystal slab waveguides and resonant tunneling diodes for terahertz communication," *Progress in Electromagnetics Research Symposium (PIERS-Toyama)*, pp. 599-605, 2018, doi: 10.23919/PIERS.2018.8597616.
- [592] J. Webber, N. Nishigami, X. Yu, J. Kim, M. Fujita, and T. Nagatsuma, "Terahertz wireless communication using resonant tunneling diodes and practical radio-over-fiber technology," *IEEE International Conference on Communications Workshops (ICC Workshops)*, pp. 1-5, 2019, doi: 10.1109/ICCW.2019.8757176.
- [593] J. Webber, N. Nishigami, J. Kim, M. Fujita, and T. Nagatsuma, "Terahertz wireless CDMA communication using resonant tunneling diodes," *IEEE Globecom Workshops (GC Wkshps)*, pp. 1-6, 2019, doi: 10.1109/GCWkshps45667.2019.9024595.
- [594] S. Kitagawa, M. Mizuno, S. Saito, K. Ogino, S. Suzuki, and M. Asada, "Frequency-tunable resonant-tunneling-diode terahertz oscillators applied to absorbance measurement," *Japanese Journal of Applied Physics*, vol. 56, no. 5, pp. 058002, 2017, doi: 10.7567/JJAP.56.058002.
- [595] A. Dobroiu, R. Wakasugi, S. Suzuki, and M. Asada, "Toward a solid-state, compact, terahertz-wave radar," *AIP Conference Proceedings*, vol. 2067, no. 1, pp. 020004, 2019, doi: 10.1063/1.5089437.
- [596] A. Dobroiu, S. Suzuki, and M. Asada, "Terahertz-wave radars based on resonant-tunneling-diode oscillators," *Proceedings of the SPIE, Terahertz Emitters, Receivers, and Applications X*, vol. 11124, San Diego, California, 2019, doi: 10.1117/12.2526709.
- [597] T. Miyamoto, A. Yamaguchi, and T. Mukai, "Terahertz imaging system with resonant tunneling diodes," *Japanese Journal of Applied Physics*, vol. 55, no. 3, pp. 032201, 2016, doi: 10.7567/JJAP.55.032201.
- [598] O. K. Nilsen and W. D. Boyer, "Amplitude modulated CW radar," *IRE Transactions on Aerospace and Navigational Electronics*, vol. ANE-9, no. 4, pp. 250-254, 1962, doi: 10.1109/TANE3.1962.4201896.
- [599] A. Dobroiu, R. Wakasugi, Y. Shirakawa, S. Suzuki, and M. Asada, "Amplitude-modulated continuous-wave radar in the terahertz band using a resonant-tunneling-diode oscillator,"

*44th International Conference on Infrared, Millimeter, and Terahertz Waves (IRMMW-THz)*, pp. 1-2, 2019, doi: 10.1109/IRMMW-THz.2019.8874352.

- [600] A. Dobroiu, R. Wakasugi, Y. Shirakawa, S. Suzuki, and M. Asada, "Absolute and precise terahertz-wave radar based on an amplitude-modulated resonant-tunneling-diode oscillator," *Photonics*, vol. 5, no. 4, 2018, doi: 10.3390/photonics5040052.
- [601] A. Dobroiu, R. Wakasugi, Y. Shirakawa, S. Suzuki, and M. Asada, "Amplitude-modulated continuous-wave radar in the terahertz range using lock-in phase measurement," *Measurement Science and Technology*, vol. 31, no. 10, pp. 105001, 2020, doi: 10.1088/1361-6501/ab912a.
- [602] A. Dobroiu, K. Asama, S. Suzuki, M. Asada, and H. Ito, "Terahertz-wave three-dimensional imaging using a resonant-tunneling-diode oscillator," *Journal of Infrared, Millimeter, and Terahertz Waves*, vol. 43, no. 5, pp. 464-478, 2022, doi: 10.1007/s10762-022-00863-5.
- [603] T. Jaeschke, C. Bredendiek, and N. Pohl, "A 240 GHz ultra-wideband FMCW radar system with on-chip antennas for high resolution radar imaging," *IEEE MTT-S International Microwave Symposium Digest (MTT)*, pp. 1-4, 2013, doi: 10.1109/MWSYM.2013.6697495.
- [604] Y. Shirakawa, A. Dobroiu, S. Suzuki, M. Asada, and H. Ito, "Principle of a subcarrier frequency-modulated continuous-wave radar in the terahertz band using a resonant-tunneling-diode oscillator," *44th International Conference on Infrared, Millimeter, and Terahertz Waves (IRMMW-THz)*, pp. 1-2, 2019, doi: 10.1109/IRMMW-THz.2019.8873752.
- [605] H. Ito and T. Ishibashi, "InP/InGaAs Fermi-level managed barrier diode for broadband and low-noise terahertz-wave detection," *Japanese Journal of Applied Physics*, vol. 56, no. 1, pp. 014101, 2017, doi: 10.7567/JJAP.56.014101.
- [606] A. Dobroiu, Y. Shirakawa, S. Suzuki, M. Asada, and H. Ito, "Subcarrier frequency-modulated continuous-wave radar in the terahertz range based on a resonant-tunneling-diode oscillator," *Sensors*, vol. 20, no. 23, pp. 6848, 2020, doi: 10.3390/s20236848.
- [607] A. Dobroiu, J. Ito, S. Suzuki, M. Asada, and H. Ito, "Real-time subcarrier FMCW radar in the terahertz range based on a resonant-tunneling-diode oscillator: evaluation and demonstration," *47th International Conference on Infrared, Millimeter and Terahertz Waves (IRMMW-THz)*, pp. 1-2, 2022, doi: 10.1109/IRMMW-THz50927.2022.9895697.
- [608] Tanner L-Edit IC, *fact sheet*, Siemens EDA, 2020.

- [609] D. M. Pozar, "Microwave engineering," *Wiley*, 2011.
- [610] MICROPOSIT S1800 G2 SERIES PHOTORESISTS, *data sheet*, Rohm & Haas Electronic Materials, 2006.
- [611] LOR Lift-Off Resists, *data sheet*, MicroChem, 2002.
- [612] Positive PMMA E-Beam Resists AR-P 630 – 670 series, *data sheet*, Allresist, 2014.
- [613] MA6 Manual Mask Aligner, *user manual*, SÜSS MicroTec, 2006.
- [614] A. S. Gangnaik, Y. M. Georgiev, and J. D. Holmes, "New generation electron beam resists: a review," *Chemistry of Materials*, vol. 29, no. 5, pp. 1898-1917, 2017, doi: 10.1021/acs.chemmater.6b03483.
- [615] A. N. Broers, "Resolution limits for electron-beam lithography," *IBM Journal of Research and Development*, vol. 32, no. 4, pp. 502-513, 1988, doi: 10.1147/rd.324.0502.
- [616] N. Pala and M. Karabiyik, "Electron beam lithography (EBL)," in *Encyclopedia of nanotechnology*, Springer, 2012, doi: 10.1007/978-90-481-9751-4\_344.
- [617] EBPG 5200, *user manual*, Raith, 2016.
- [618] BEAMER, *web user guide*.
- [619] CJOB, *web user guide*.
- [620] B. El-Kareh, "Fundamentals of semiconductor processing technology," Springer, 1995.
- [621] MEB550S E-beam evaporator, *manufacturer website*, Plassys, 2018.
- [622] S. Masudy-Panah, Y. Wu, D. Lei, A. Kumar, Y. -C. Yeo, and X. Gong, "Nanoscale metal-InGaAs contacts with ultra-low specific contact resistivity: improved interfacial quality and extraction methodology," *Journal of Applied Physics*, vol. 123, no. 2, pp. 024508, 2018, doi: 10.1063/1.4997686.
- [623] J. Melngailis, "Focused ion beam technology and applications," *Journal of Vacuum Science & Technology B: Microelectronics Processing and Phenomena*, vol. 5, no. 2, pp. 469-495, 1987, doi: 10.1116/1.583937.
- [624] A. R. Clawson, "Guide to references on III–V semiconductor chemical etching," *Materials Science and Engineering: R: Reports*, vol. 31, no. 1-6, pp. 1-438, 2001, doi: 10.1016/S0927-796X(00)00027-9.
- [625] PI-2545 Polyimide, *data sheet*, HD MicroSystems, 2009.

- [626] Plasmalab 80 Plus, *fact sheet*, Oxford Instruments, 2009.
- [627] LEM Series: Camera Endpoint Monitor based on Real Time Laser Interferometry, *manufacturer website*, Horiba Scientific, 2022.
- [628] W. Zhou, R. Apkarian, Z. L. Wang, and D. Joy, "Fundamentals of scanning electron microscopy (SEM)," in *Scanning microscopy for nanotechnology*, Springer, 2006, doi: 10.1007/978-0-387-39620-0\_1.
- [629] UHR FE-SEM SU8200 Series, *fact sheet*, Hitachi High-Technologies Corporation, 2013.
- [630] DektakXT Stylus Profiler, *user manual*, Bruker Corporation, 2011.
- [631] 4155C Semiconductor Parameter Analyser, *user manual*, Keysight Technologies, 2020.
- [632] B. Streetman and S. Banerjee, "Solid state electronic devices," Pearson, 2005.
- [633] Precision Diamond Scriber model RV-129, *fact sheet*, ATV Technologie, 2018.
- [634] J. Wang, "Monolithic microwave/millimetrewave integrated circuit resonant tunnelling diode sources with around a milliwatt output power," PhD thesis, University of Glasgow, 2014.
- [635] J. R. Vig, "UV/ozone cleaning of surfaces," *Journal of Vacuum Science & Technology A*, vol. 3, no. 3, pp. 1027-1034, 1985, doi: 10.1116/1.573115.
- [636] Z. H. Lu, B. Bryskiewicz, J. McCaffrey, Z. Wasilewski, and M. J. Graham, "Ultraviolet-ozone oxidation of GaAs(100) and InP(100)," *Journal of Vacuum Science & Technology B: Microelectronics and Nanometer Structures Processing, Measurement, and Phenomena*, vol. 11, no. 6, pp. 2033-2037, 1993, doi: 10.1116/1.586539.
- [637] R. Driad, Z. H. Lu, S. Laframboise, D. Scansen, W. R. McKinnon, and S. P. McAlister, "Surface passivation of InGaAs/InP heterostructures using UV-irradiation and ozone," *Conference Proceedings. 1998 International Conference on Indium Phosphide and Related Materials (Cat. No.98CH36129)*, pp. 459-462, 1993, doi: 10.1109/ICIPRM.1998.712523.
- [638] T10XT10/OES/E ultra-violet ozone cleaning system, *brochure*, UVOCS, 2010.
- [639] MICROPOSIT REMOVER 1165, *technical data sheet*, Rohm & Haas Electronic Materials, 2014.
- [640] MICROPOSIT DEVELOPER CONCENTRATE, *safety data sheet*, Rohm & Haas Electronic Materials, 2018.
- [641] MICROPOSIT MF-319 DEVELOPER, *data sheet*, Rohm & Haas Electronic Materials, 2019.

- [642] J. Maassen, C. Jeong, A. Baraskar, M. Rodwell, and M. Lundstrom, "Full band calculations of the intrinsic lower limit of contact resistivity," *Applied Physics Letters*, vol. 102, no. 11, pp. 111605, 2013, doi: 10.1063/1.4798238.
- [643] A. Baraskar, A. C. Gossard, and M. J. W. Rodwell, "Lower limits to metal-semiconductor contact resistance: Theoretical models and experimental data," *Journal of Applied Physics*, vol. 114, no. 15, pp. 154516, 2013, doi: 10.1063/1.4826205.
- [644] D. K. Schroder, "Semiconductor material and device characterization," *John Wiley & Sons*, 2006, doi: 10.1002/0471749095.
- [645] A. K. Baraskar, M. A. Wistey, V. Jain, U. Singiseti, G. Burek, B. J. Thibeault, Y. J. Lee, A. C. Gossard, and M. J. W. Rodwell, "Ultralow resistance, nonalloyed Ohmic contacts to n-InGaAs," *Journal of Vacuum Science & Technology B: Microelectronics and Nanometer Structures Processing, Measurement, and Phenomena*, vol. 27, no. 4, pp. 2036-2039, 2009, doi: 10.1116/1.3182737.
- [646] R. Dormaier and S. E. Mohny, "Factors controlling the resistance of Ohmic contacts to n-InGaAs," *Journal of Vacuum Science & Technology B*, vol. 30, no. 3, pp. 031209, 2012, doi: 10.1116/1.4705730.
- [647] G. K. Reeves, "Specific contact resistance using a circular transmission line model," *Solid-State Electronics*, vol. 23, no. 5, pp. 487-490, 1980, doi: 10.1016/0038-1101(80)90086-6.
- [648] G. S. Marlow and M. B. Das, "The effects of contact size and non-zero metal resistance on the determination of specific contact resistance," *Solid-State Electronics*, vol. 25, no. 2, pp. 91-94, 1982, doi: 10.1016/0038-1101(82)90036-3.
- [649] J. H. Klootwijk and C. E. Timmering, "Merits and limitations of circular TLM structures for contact resistance determination for novel III-V HBTs," *Proceedings of the 2004 International Conference on Microelectronic Test Structures (IEEE Cat. No.04CH37516)*, pp. 247-252, 2004, doi: 10.1109/ICMTS.2004.1309489.
- [650] A. Baraskar, M. A. Wistey, V. Jain, E. Lobisser, U. Singiseti, G. Burek, Y. J. Lee, B. Thibeault, A. Gossard, and M. Rodwell, "Ex situ Ohmic contacts to n-InGaAs," *Journal of Vacuum Science & Technology B*, vol. 28, no. 4, pp. C5I7-C5I9, 2010, doi: 10.1116/1.3454372.
- [651] G. K. Reeves and H. B. Harrison, "Obtaining the specific contact resistance from transmission line model measurements," *IEEE Electron Device Letters*, vol. 3, no. 5, pp. 111-113, 1982, doi: 10.1109/EDL.1982.25502.

- [652] W. M. Loh, S. E. Swirhun, T. A. Schreyer, R. M. Swanson, and K. C. Saraswat, "Modeling and measurement of contact resistances," *IEEE Transactions on Electron Devices*, vol. 34, no. 3, pp. 512-524, 1987, doi: 10.1109/T-ED.1987.22957.
- [653] J. G. J. Chern and W. G. Oldham, "Determining specific contact resistivity from contact end resistance measurements," *IEEE Electron Device Letters*, vol. 5, no. 5, pp. 178-180, 1984, doi: 10.1109/EDL.1984.25875.
- [654] S. J. Proctor, L. W. Linholm, and J. A. Mazer, "Direct measurements of interfacial contact resistance, end contact resistance, and interfacial contact layer uniformity," *IEEE Transactions on Electron Devices*, vol. 30, no. 11, pp. 1535-1542, 1983, doi: 10.1109/T-ED.1983.21334.
- [655] F. M. Smits, "Measurement of sheet resistivities with the four-point probe," *Bell System Technical Journal*, vol. 37, no. 3, pp. 711-718, 1958, doi: 10.1002/j.1538-7305.1958.tb03883.x.
- [656] G. Stareev, and H. Künzel, and G. Dortmann, "A controllable mechanism of forming extremely low-resistance nonalloyed ohmic contacts to group III-V compound semiconductors," *Journal of Applied Physics*, vol. 74, no. 12, pp. 7344-7356, 1993, doi: 10.1063/1.355002.
- [657] A. G. Worthing, "The temperature scale and the melting point of molybdenum," *Physical Review*, vol. 25, no. 6, pp. 846-857, 1925, doi: 10.1103/PhysRev.25.846.
- [658] U. Singisetti, M. A. Wistey, J. D. Zimmerman, B. J. Thibeault, M. J. W. Rodwell, A. C. Gossard, and S. R. Bank, "Ultralow resistance in situ Ohmic contacts to InGaAs/InP," *Applied Physics Letters*, vol. 93, no. 18, pp. 183502, 2008, doi: 10.1063/1.3013572.
- [659] G. Klimeck, "Quantum and semi-classical transport in NEMO 1-D," *Journal of Computational Electronics*, vol. 2, no. 2, pp. 177-182, 2003, doi: 10.1023/B:JCEL.0000011421.53762.97.
- [660] T. Kubis and P. Vogl, "Self-consistent quantum transport theory: Applications and assessment of approximate models," *Journal of Computational Electronics*, vol. 6, no. 1, pp. 183-186, 2007, doi: 10.1007/s10825-006-0078-6.
- [661] S. Birner, T. Zibold, T. Andlauer, T. Kubis, M. Sabathil, A. Trellakis, and P. Vogl, "nextnano: General Purpose 3-D Simulations," *IEEE Transactions on Electron Devices*, vol. 54, no. 9, pp. 2137-2142, 2007, doi: 10.1109/TED.2007.902871.
- [662] W. M. Jubadi, M. A. Md Zawawi, and M. Missous, "Simulative study on physical modelling of submicrometer highly-strained In<sub>0.8</sub>Ga<sub>0.2</sub>As/AlAs resonant tunnelling diode,"

*The Tenth International Conference on Advanced Semiconductor Devices and Microsystems*, pp. 1-4, 2014, doi: 10.1109/ASDAM.2014.6998671.

- [663] A. Alqurashi and M. Missous, "Physical modeling of asymmetric spacers resonant tunneling diodes (RTDs)," *IEEE Latin America Electron Devices Conference (LAEDC)*, pp. 1-4, 2021, doi: 10.1109/LAEDC51812.2021.9437970.
- [664] A. L. Fetter and J. D. Walecka, "Quantum theory of many-particle systems," *McGraw-Hill*, 1971.
- [665] G. D. Mahan, "Many-particle physics," *Springer*, 2000, doi: 10.1007/978-1-4757-5714-9.
- [666] P. Roblin and W. -R. Liou, "Three-dimensional scattering-assisted tunneling in resonant-tunneling diodes," *Physical Review B*, vol. 47, no. 4, pp. 2146-2161, 1999, doi: 10.1103/PhysRevB.47.2146.
- [667] S. Datta, "Lessons from nanoelectronics: a new perspective on transport – Part B: quantum transport," *World Scientific*, 2018, doi: 10.1142/10440-vol2.
- [668] P. Vogl and T. Kubis, "The non-equilibrium Green's function method: an introduction," *Journal of Computational Electronics*, vol. 9, no. 3, pp. 237-242, 2010, doi: 10.1007/s10825-010-0313-z.
- [669] V. -N. Do, "Non-equilibrium Green function method: theory and application in simulation of nanometer electronic devices," *Advances in Natural Sciences: Nanoscience and Nanotechnology*, vol. 5, no. 3, pp. 033001, 2014, doi: 10.1088/2043-6262/5/3/033001.
- [670] S. Datta, "Nanoscale device modeling: the Green's function method," *Superlattices and Microstructures*, vol. 28, no. 4, pp. 253-278, 2000, doi: 10.1006/spmi.2000.0920.
- [671] N. Goldsman, L. Henrickson, and J. Frey, "A physics-based analytical/numerical solution to the Boltzmann transport equation for use in device simulation," *Solid-State Electronics*, vol. 34, no. 4, pp. 389-396, 1991, doi: 10.1016/0038-1101(91)90169-Y.
- [672] C. Jacoboni and P. Bordone, "The Wigner-function approach to non-equilibrium electron transport," *Reports on Progress in Physics*, vol. 67, no. 7, pp. 1033, 2004, doi: 10.1088/0034-4885/67/7/R01.
- [673] W. R. Frensley, "Wigner-function model of a resonant-tunneling semiconductor device," *Physical Review B*, vol. 36, no. 3, pp. 1570-1580, 1987, doi: 10.1103/PhysRevB.36.1570.
- [674] R. Lake, G. Klimeck, R. C. Bowen, and D. Jovanovic, "Single and multiband modeling of quantum electron transport through layered semiconductor devices," *Journal of Applied Physics*, vol. 81, no. 12, pp. 7845-7869, 1997, doi: 10.1063/1.365394.

- [675] L. Shifren, C. Ringhofer, and D. K. Ferry, "A Wigner function-based quantum ensemble Monte Carlo study of a resonant tunneling diode," *IEEE Transactions on Electron Devices*, vol. 50, no. 3, pp. 769-773, 2003, doi: 10.1109/TED.2003.809434.
- [676] M. Pourfath, "The non-equilibrium Green's function method for nanoscale device simulation," *Springer*, 2014, doi: 10.1007/978-3-7091-1800-9.
- [677] W. Pötz, "Microscopic theory of coherent carrier dynamics and phase breaking in semiconductors," *Physical Review B*, vol. 54, no. 8, pp. 5647-5664, 1996, doi: 10.1103/PhysRevB.54.5647.
- [678] J. Rammer, "Quantum field theory of non-equilibrium states," *Cambridge University Press*, 2009, doi: 10.1017/CBO9780511618956.
- [679] G. Stefanucci and R. van Leeuwen, "Nonequilibrium many-body theory of quantum systems: a modern introduction," *Cambridge University Press*, 2013, doi: 10.1017/CBO9781139023979.
- [680] R. C. Iotti, E. Ciancio, and F. Rossi, "Quantum transport theory for semiconductor nanostructures: A density-matrix formulation," *Physical Review B*, vol. 72, no. 12, pp. 125347, 2005, doi: 10.1103/PhysRevB.72.125347.
- [681] S. Datta, "Electronic transport in mesoscopic systems," *Cambridge University Press*, 1995, doi: 10.1017/CBO9780511805776.
- [682] R. D. Mattuck, "A guide to Feynman diagrams in the many-body problem," *McGraw-Hill*, 1976.
- [683] A. Wüthrich, "The genesis of Feynman diagrams," *Springer*, 2011, doi: 10.1007/978-90-481-9228-1.
- [684] S. Datta, "Quantum transport: atom to transistor," *Cambridge University Press*, 2005, doi: 10.1017/CBO9781139164313.
- [685] M. Cito, O. Kojima, B. J. Stevens, T. Mukai, and R. A. Hogg, "Photoluminescence excitation spectroscopy for structural and electronic characterization of resonant tunneling diodes for THz applications," *AIP Advances*, vol. 11, no. 3, pp. 035122, 2021, doi: 10.1063/5.0035394.
- [686] L. P. Kadanoff and G. Baym, "Quantum statistical mechanics: Green's function methods in equilibrium and nonequilibrium problems," *W. A. Benjamin*, 1962.
- [687] L. V. Keldysh, "Diagram technique for nonequilibrium processes," *Soviet Physics JETP*, vol. 20, no. 4, pp. 1018-1026, 1965.

- [688] P. C. Martin and J. Schwinger, "Theory of many-particle systems. I," *Physical Review*, vol. 115, no. 6, pp. 1342-1373, 1959, doi: 10.1103/PhysRev.115.1342.
- [689] O. Kurniawan, P. Bai, and E. Li, "Ballistic calculation of nonequilibrium Green's function in nanoscale devices using finite element method," *Journal of Physics D: Applied Physics*, vol. 42, no. 10, pp. 105109, 2009, doi: 10.1088/0022-3727/42/10/105109.
- [690] N. G. Einspruch and W. R. Frensley, "Heterostructures and quantum devices," *Academic Press*, 1994.
- [691] C. S. Lent and D. J. Kirkner, "The quantum transmitting boundary method," *Journal of Applied Physics*, vol. 67, no. 10, pp. 6353-6359, 1990, doi: 10.1063/1.345156.
- [692] Silvaco Atlas TCAD: Device Simulation Software, *user manual* (downloadable from Silvaco website), Silvaco, 2016.
- [693] R. C. Bowen, G. Klimeck, R. K. Lake, W. R. Frensley, and T. Moise, "Quantitative simulation of a resonant tunneling diode," *Journal of Applied Physics*, vol. 81, no. 7, pp. 3207-3213, 1997, doi: 10.1063/1.364151.
- [694] E. O. Kane, "Band structure of indium antimonide," *Journal of Physics and Chemistry of Solids*, vol. 1, no. 4, pp. 249-261, 1957, doi: 10.1016/0022-3697(57)90013-6.
- [695] S. C. Jain, M. Willander, and H. Maes, "Stresses and strains in epilayers, stripes and quantum structures of III - V compound semiconductors," *Semiconductor Science and Technology*, vol. 11, no. 5, pp. 641-671, 1996, doi: 10.1088/0268-1242/11/5/004.
- [696] W. F. Chow, "Principles of tunnel diode circuits," *Wiley*, 1964.
- [697] M. Cito, D. Cimbri, D. Childs, R. Baba, B. A. Harrison, A. Watt, T. Mukai, E. Wasige, and R. A. Hogg, "Micro-PL analysis of high current density resonant tunneling diodes for THz applications," *Applied Physics Letters*, vol. 119, no. 7, pp. 072102, 2021, doi: 10.1063/5.0059339.
- [698] R. K. Mains, J. P. Sun, and G. I. Haddad, "Observation of intrinsic bistability in resonant tunneling diode modeling," *Applied Physics Letters*, vol. 55, no. 4, pp. 371-373, 1989, doi: 10.1063/1.101874.
- [699] N. S. Wingreen, K. W. Jacobsen, and J. W. Wilkins, "Resonant tunneling with electron-phonon interaction: an exactly solvable model," *Physical Review Letters*, vol. 61, no. 12, pp. 1396-1399, 1988, doi: 10.1103/PhysRevLett.61.1396.
- [700] G. Klimeck, R. Lake, and D. K. Blanks, "Role of interface roughness scattering in self-consistent resonant-tunneling-diode simulations," *Physical Review B*, vol. 58, no. 11, pp. 7279-7285, 1998, doi: 10.1103/PhysRevB.58.7279.

- [701] F. Chevoir and B. Vinter, "Calculation of phonon-assisted tunneling and valley current in a double-barrier diode," *Applied Physics Letters*, vol. 55, no. 18, pp. 1859-1861, 1989, doi: 10.1063/1.102188.
- [702] K. J. P. Jacobs, B. J. Stevens, R. Baba, O. Wada, T. Mukai, and R. A. Hogg, "Valley current characterization of high current density resonant tunnelling diodes for terahertz-wave applications," *AIP Advances*, vol. 7, no. 10, pp. 105316, 2017, doi: 10.1063/1.4997664.
- [703] R. Lake, G. Klimeck, R. C. Bowen, C. Fernando, T. Moise, Y. C. Kao, and M. Leng, "Interface roughness, polar optical phonons, and the valley current of a resonant tunneling diode," *Superlattices and Microstructures*, vol. 20, no. 3, pp. 279-285, 1996, doi: 10.1006/spmi.1996.0079.
- [704] Victory Atomistic Device and Nanostructure Simulator, *web page*, Silvaco, 2022.
- [705] J. P. Sun and G. I. Haddad, "Self-consistent scattering calculation of resonant tunneling diode characteristics," *VLSI Design*, vol. 6, pp. 078412, 1998, doi: 10.1155/1998/78412.
- [706] T. S. Moise, Y. -C. Kao, A. J. Katz, T. P. E. Broekaert, and F. G. Celii, "Experimental sensitivity analysis of pseudomorphic InGaAs/AlAs resonant-tunneling diodes," *Journal of Applied Physics*, vol. 78, no. 10, pp. 6305-6317, 1995, doi: 10.1063/1.360511.
- [707] I. Mehdi, R. K. Mains, and G. I. Haddad, "Effect of spacer layer thickness on the static characteristics of resonant tunneling diodes," *Applied Physics Letters*, vol. 57, no. 9, pp. 899-901, 1990, doi: 10.1063/1.103398.
- [708] S. Alomari and J. Figueiredo, "Simulation and modelling of resonant tunneling diode peak voltage dependence on spacer layers," *2021 35th Symposium on Microelectronics Technology and Devices (SBMicro)*, pp. 1-4, 2021, doi: 10.1109/SBMicro50945.2021.9585751.
- [709] H. M. Yoo, S. M. Goodnick, and J. R. Arthur, "Influence of spacer layer thickness on the current-voltage characteristics of AlGaAs/GaAs and AlGaAs/InGaAs resonant tunneling diodes," *Applied Physics Letters*, vol. 56, no. 1, pp. 84-86, 1990, doi: 10.1063/1.102660.
- [710] D. Cimbri and E. Wasige, "Terahertz communications with resonant tunnelling diodes: status and perspectives," in *Next generation wireless terahertz communication networks*, *CRC Press*, pp. 25-87, 2021, doi: 10.1201/9781003001140-3.
- [711] B1500A Semiconductor Device Parameter Analyzer, *installation and service guide*, Keysight Technologies, 2022.
- [712] Agilent PNA Microwave Network Analyzers, *data sheet*, Keysight Technologies, 2009.

- [713] Agilent Technologies N5260A Millimeter Head Controller, *operation and service guide*, Keysight Technologies, 2013.
- [714] Keysight Technologies N5250C PNA Series Microwave Network Analyzer System, *installation and service guide*, Keysight Technologies, 2017.
- [715] Summit semi-automated Probe Station, *user manual*, CASCADE MICROTECH, 2000.
- [716] PICOPROBE MODEL 110H, *data sheet*, GGB INDUSTRIES.
- [717] C. Nasser, D. Ritter, and M. Rudolph, "Bias dependence of the access resistance in GaN HEMTs," *2018 22nd International Microwave and Radar Conference (MIKON)*, pp. 271-273, 2018, doi: 10.23919/MIKON.2018.8405197.
- [718] CPW (Coplanar Waveguide), *ADS documentation*, Keysight Technologies, 2008.
- [719] MLIN (Microstrip Line), *ADS documentation*, Keysight Technologies, 2008.
- [720] An Introduction to HFSS, *introduction manual*, Ansys, 2013.
- [721] A. Shedbalkar and B. Witzigmann, "Non equilibrium Green's function quantum transport for green multi-quantum well nitride light emitting diodes," *Optical and Quantum Electronics*, vol. 50, no. 2, pp. 67, 2018, doi: 10.1007/s11082-018-1335-1.
- [722] Y. Zohta and T. Tanamoto, "Improved optical model for resonant tunneling diode," *Journal of Applied Physics*, vol. 74, no. 11, pp. 6996-6998, 1993, doi: 10.1063/1.355054.
- [723] K. Miao, S. Sadasivam, J. Charles, G. Klimeck, T. S. Fisher, and T. Kubis, "Büttiker probes for dissipative phonon quantum transport in semiconductor nanostructures," *Applied Physics Letters*, vol. 108, no. 11, pp. 113107, 2016, doi: 10.1063/1.4944329.
- [724] P. Greck, "Efficient calculation of dissipative quantum transport properties in semiconductor nanostructures," PhD thesis, Technical University of Munich, 2012.
- [725] D. S. Ponomarev, A. Gorodetsky, A. E. Yachmenev, S. S. Pushkarev, R. A. Khabibullin, M. M. Grekhov, K. I. Zaytsev, D. I. Khusyainov, A. M. Buryakov, and E. D. Mishina, "Enhanced terahertz emission from strain-induced InGaAs/InAlAs superlattices," *Journal of Applied Physics*, vol. 125, no. 15, pp. 151605, 2019, doi: 10.1063/1.5079697.
- [726] M. V. Fischetti and S. E. Laux, "Monte carlo analysis of electron transport in small semiconductor devices including band-structure and space-charge effects," *Physical Review B*, vol. 38, no. 14, pp. 9721-9745, 1988, doi: 10.1103/PhysRevB.38.9721.
- [727] G. Liu and S. -L. Chuang, "Modeling of Sb-based type-II quantum cascade lasers," *Physical Review B*, vol. 65, no. 16, pp. 165220, 2002, doi: 10.1103/PhysRevB.65.165220.

- [728] T. B. Bahder, "Eight-band k-p model of strained zinc-blende crystals," *Physical Review B*, vol. 41, no. 17, pp. 11992-12001, 1990, doi: 10.1103/PhysRevB.41.11992.
- [729] G. Klimeck, R. C. Bowen, T. B. Boykin, and T. A. Cwik, "sp<sup>3</sup>s\* Tight-binding parameters for transport simulations in compound semiconductors," *Superlattices and Microstructures*, vol. 27, no. 5-6, pp. 519-524, 2000, doi: 10.1006/spmi.2000.0862.
- [730] B. G. Shohany, M. R. Roknabadi, and A. Kompany, "DFT-NEGF simulation of graphene-graphdiyne-graphene resonant tunneling transistor," *Computational Materials Science*, vol. 144, pp. 280-284, 2018, doi: 10.1016/j.commatsci.2017.12.031.
- [731] D. Cimbri, "Modelling the electronic structure of type-II superlattice photodetectors," MSc thesis, Boston University, Politecnico di Torino, 2017.
- [732] M. Ehrhardt and T. Koprucki, "Multi-band effective mass approximations: advanced mathematical models and numerical techniques," *Springer*, 2014, doi: 10.1007/978-3-319-01427-2.
- [733] C. Spudat, P. Ourednik, G. Picco, D. T. Nguyen, and M. Feiginov, "Limitations of Output Power and Efficiency of Simple Resonant-Tunneling-Diode Oscillators," *IEEE Transactions on Terahertz Science and Technology*, vol. 13, no. 1, pp. 82-92, 2023, doi: 10.1109/TTHZ.2022.3228069.
- [734] P. Ourednik, G. Picco, D. T. Nguyen, C. Spudat, and M. Feiginov, "Large-signal dynamics of resonant-tunneling diodes," *Journal of Applied Physics*, vol. 133, no. 1, pp. 014501, 2023, doi: 10.1063/5.0134223.
- [735] Y. Koyama, Y. Kitazawa, K. Yukimasa, T. Uchida, T. Yoshioka, K. Fujimoto, T. Sato, J. Iba, K. Sakurai, and T. Ichikawa, "A high-power terahertz source over 10 mW at 0.45 THz using an active antenna array with integrated patch antennas and resonant-tunneling diodes," *IEEE Transactions on Terahertz Science and Technology*, vol. 12, no. 5, pp. 510-519, 2022, doi: 10.1109/TTHZ.2022.3180492.
- [736] Y. Suzuki, T. Van Mai, X. Yu, S. Suzuki, and M. Asada, "Phase control of terahertz waves using injection-locked resonant tunneling diode oscillator," *IEEE Transactions on Terahertz Science and Technology*, vol. 12, no. 5, pp. 481-488, 2022, doi: 10.1109/TTHZ.2022.3170516.
- [737] Y. I. Vorontsov and I. V. Polyakov, "Study of oscillatory process in circuits with several series-connected tunnel diodes," *Radio Engineering and Electronic Physics*, vol. 10, pp. 758-763, 1965.

- [738] Y. Ookawa, S. Kishimoto, K. Maezawa, and T. Mizutani, "Novel resonant tunneling diode oscillator capable of large output power operation," *IEICE Transactions on Electronics*, vol. E89-C, no. 7, pp. 999-1004, 2006, doi: 10.1093/ietele/e89-c.7.999.
- [739] K. Lee, "Characteristics of series-connected resonant tunneling diode-pair configuration for high output power operation," *physica status solidi A*, vol. 219, no. 4, pp. 2100420, 2022, doi: 10.1002/pssa.202100420.
- [740] C. C. Yang and D. -S. Pan, "Theoretical investigations of a proposed series integration of resonant tunneling diodes for millimeter-wave power generation," *IEEE Transactions on Microwave Theory and Techniques*, vol. 40, no. 3, pp. 434-441, 1992, doi: 10.1109/22.121718.
- [741] O. Boric-Lubecke, D. -S. Pan, and T. Itoh, "RF excitation of an oscillator with several tunneling devices in series," *IEEE Microwave and Guided Wave Letters*, vol. 4, no. 11, pp. 364-366, 1994, doi: 10.1109/75.329707.
- [742] O. Boric-Lubecke, D. -S. Pan, and T. Itoh, "Fundamental and subharmonic excitation for an oscillator with several tunneling diodes in series," *IEEE Transactions on Microwave Theory and Techniques*, vol. 43, no. 4, pp. 969-976, 1995, doi: 10.1109/22.375262.
- [743] O. Boric-Lubecke, D. -S. Pan, and T. Itoh, "DC instability of the series connection of tunneling diodes," *IEEE Transactions on Microwave Theory and Techniques*, vol. 44, no. 6, pp. 936-943, 1996, doi: 10.1109/22.506454.